SINGLE CRYSTAL AND SUPPORTED NANO-CLUSTER COPPER-PALLADIUM/PLATINUM MODEL CATALYSTS

By

James P. Reilly B.Sc.(Hons.)

A Thesis presented to Dublin City University for the Degree of Doctor of Philosophy.

This work was carried out under the supervision of Dr. Colin J. Barnes, School of Chemical Sciences, at Dublin City University.

January 2000

Declaration

I hereby certify that this material, which I now submit for assessment on the programme of study leading to the award of Doctor of Philosophy is entirely my own work and has not been taken from the work of others save and to the extent that such work has been cited and acknowledged within the text of my work.

Signed: James P. Reilly

James P. Reilly

I.D. No.: 93700377

Date: 31/01/2000

Acknowledgements

Firstly, I would like to thank my supervisor Dr. Colin Barnes for his guidance and continued interest during my postgraduate studies. To this extent I would also like to thank Dr. Mike Hopkins and the members of his Plasma Research Group for their assistance and co-operation.

To my fellow group members, both past and present, namely Mick, Caroline, David and Ehab, I extend sincere appreciation for their assistance and valuable comments, not to mention the many interesting conversations had over coffee. I would also like to express my gratitude to the technical staff of both the Chemistry and Physics departments.

Furthermore, I wish to acknowledge the invaluable assistance provided by Prof. Mike Bowker and his Surface Science Research group in Reading University.

Finally, I would like to express sincere thanks to my family for the strong and constant support I have received over the past years.

Dublin, January 2000
James P. Reilly

CONTENTS

DECLARATION I

ACKNOWLEDGEMENTS II

CONTENTS III

LIST OF PUBLICATIONS VII

ABSTRACT 1

CHAPTER 1: INTRODUCTION

1.1. The importance of catalysis 4
1.2. Single crystal surfaces 8
1.3. Bimetallic surfaces 12
1.4. The CuPd system 13
1.5. Cu_xPd_{1-x} systems review
1.5.1. Cu_xPd_{1-x} bulk alloys 19
1.5.2. Ultra-thin Cu film growth on Pd single crystals 24
1.5.3. Pd growth on Cu single crystals 27
1.5.4. Supported Cu-Pd bimetallics 34
1.6. Overview 36

CHAPTER 2: PHYSICAL BASICS OF EXPERIMENTAL TECHNIQUES UTILISED

1. Surface structural determination 44
1.1. Scanning tunnelling microscopy (STM)
1.1.1. The birth of STM 45
1.1.2. STM: theory and operation 45
1.2. Low energy electron diffraction (LEED) 57
2. Surface compositional analysis
2.1. X-ray photoelectron spectroscopy (XPS)
2.1.1. The XPS process 64
2.1.2. The chemical shift 66
2.1.3. Core-level spectra 67
2.1.4. Valence levels 70
2.1.5. Secondary spectral structure 71
2.2. Auger electron spectroscopy (AES) 72
2.3. Growth modes 78
3. Surface bonding and reactivity
3.1. Temperature programmed desorption (TPD) 81

CHAPTER 3: THE GROWTH MECHANISM, THERMAL STABILITY AND REACTIVITY OF PALLADIUM MONO AND MULTILAYERS ON Cu(110)

1. Introduction 92
2. Experimental 97
3. Results
   3.1. Room temperature growth mechanism of Pd on Cu(110) – XPS, AES, and LEED 100
      3.1.1. XPS measurements 104
      3.1.2. STM measurements 107
   3.2. Thermal stability of the Cu(110)/Pd system
      3.2.1. LEED and XPS 108
      3.2.2. STM 114
   3.3. Reactivity of the Cu(110)/Pd system 122
4. Discussion 129
5. Conclusions 136

CHAPTER 4: AN XPS AND STM STUDY OF MONOMETALLIC Pd AND Cu, AND BIMETALLIC Pd-Cu CLUSTERS GROWN ON GRAPHITE

1. Introduction 143
2. Literature review
   2.1. Microscopy 145
   2.2. Integral techniques 148
3. Experimental 153
4. Results
   4.1. Absolute surface coverage determination for ultra-thin metal film deposition 156
      4.1.1. The glass-slide ex-situ calibration technique 158
   4.2. Nucleation and growth of monometallic Pd and Cu cluster catalysts grown on HOPG
      4.2.1. XPS and STM analysis 160
   4.3. Nucleation and growth of bimetallic CuPd cluster catalysts 174
      4.3.1. XPS analysis 175
      4.3.2. STM analysis 191
5. Discussion 198
6. Conclusions 203

CHAPTER 5: SURFACE ALLOY FORMATION: THE Cu(100)-c(2×2)-Pt SYSTEM

1. Introduction 211
2. Experimental 214
3. Results and discussion
   3.1. Structural transitions in the Cu(100)-Pt system 217
   3.2. CO adsorption 221
   3.3. Effect of surface alloy formation on formate decomposition kinetics 225
4. Conclusions 233

CHAPTER 6: CONCLUSIONS 237

APPENDICES 243

APPENDIX A: DESIGN AND APPLICATIONS OF A SIMPLE THERMAL MOLECULAR BEAM SYSTEM FOR REACTIVITY STUDIES

1. Introduction 245
2. Molecular beams 246
   - 2.1. Effusive beams 246
   - 2.2. Nozzle beams 247
3. The Dublin Molecular Beam System: design and technical considerations
   - 3.1. Molecular beam construction 253
   - 3.2. Beam genesis 253
     - 3.2.1. Beam alignment 256
   - 3.3. Spectrometer chamber 257
     - 3.3.1. Analytical techniques 259
4. Methodology
   - 4.1. Sticking probability measurements 261
   - 4.2. Examples of sticking probability Measurements 270
   - 4.3. Transient reaction studies 272
   - 4.4. Steady-state reactions – "mixed beam" techniques 276
5. Conclusions 278

APPENDIX B: AN EXPERIMENTAL INVESTIGATION OF THE RADIO FREQUENCY PLASMA-INDUCED MODIFICATION OF THE SURFACE MORPHOLOGY OF GRAPHITE

1. Introduction 283
2. Plasmas (glow discharges) 284
   - 2.1. Generation and general properties 285
   - 2.2. Plasma characteristics 288
   - 2.3. Radio frequency (RF) plasmas 290
3. Experimental
   - 3.1. The plasma etching system 293
     - 3.1.1. The RF circuit 293
     - 3.1.2. The power meter 296
     - 3.1.3. Langmuir probe diagnostic arrangement 297
     - 3.1.4. Plasma parameter analysis 300
     - 3.1.5. The tuned probe 302

3.2. HOPG etching arrangement and analysis set-up 303
4. Results
4.1. Plasma diagnostics
4.1.1. Plasma parameter measurements in argon 306
4.1.2. Plasma parameter measurements in hydrogen 309

4.2. RF plasma etching of HOPG with both argon and hydrogen: an STM and XPS study
4.2.1. Characterisation of freshly-cleaved HOPG 311
4.2.2. Argon RF plasma etched HOPG - power dependence 313
4.2.3. Argon RF plasma etched HOPG - time dependence 324
4.2.4. Hydrogen RF plasma etched HOPG - power dependence 326
4.2.5. Hydrogen RF plasma etched HOPG - time dependence 333
4.2.6. XPS of hydrogen and argon plasma etched HOPG 335
5. Discussion
5.1. Plasma parameters 340
5.2. Argon RF plasma etched HOPG surfaces 341
5.3. Hydrogen RF plasma etched HOPG surfaces 347
6. Conclusions 353

The following papers have been published or submitted for publication during the course of this work:

1. *"Morphology of Pd Multilayers on Cu(110)"*, R. A. Bennett, S. Poulston, N. J. Price, **J. P. Reilly**, P. Stone, C. J. Barnes and M. Bowker, Surface Science, 433-435 (1999) 816.

2. *"The Growth Mechanism, Thermal Stability and Reactivity of Palladium Mono and Multilayers on Cu(110)"*, **J. P. Reilly**, C. J. Barnes, N. J. Price, R. A. Bennett, S. Poulston, P. Stone and M. Bowker, Journal of Physical Chemistry B, 103 (1999) 6521.

3. *"Modification of Formate Stability by Alloying: the Cu(100)-c(2×2)-Pt System"*, **J. P. Reilly**, D. O'Connell and C. J. Barnes, Journal of Physics: Condensed Matter, 11 (1999) 1.

4. *"A Simple Method for Absolute Surface Coverage Determination for Metal Film Deposition"*, C. J. Barnes and **J. P. Reilly**, submitted to Surface Science Letters.

ABSTRACT

This work involved the experimental investigation of a variety of model copper-palladium/platinum heterogeneous catalysts in the form of single-crystal surfaces (Cu(110)/Pd and Cu(100)/Pt) and highly orientated pyrolytic graphite (HOPG) supported nano-clusters. The surface structural arrangement was primarily examined using scanning tunnelling microscopy (STM) and low energy electron diffraction (LEED) while X-ray photoelectron spectroscopy (XPS) and Auger electron spectroscopy (AES) were used to determine surface composition. In addition, temperature-programmed desorption (TPD) has been employed to probe the reactivity of the surfaces via the decomposition of formic acid (HCOOH).

In the case of the Cu(110)/Pd system XPS measurements backed up by STM/LEED clearly demonstrate the formation of regions of a Cu(110)-p(2×1)-Pd surface alloy at low Pd coverages (θ_{Pd}<1 ML) with considerable disorder in the form of monolayer deep pits and islands. Higher Pd coverages led to the formation of a granular film of epitaxial densely packed flat topped Pd clusters with largely a rectangular shape of average size 75×150 Å. The favoured growth mechanism is of multilayered Pd islands above a mixed (2×1) CuPd interface of two to three atomic layers thickness. Only after annealing to 600 K is the granular structure of the higher coverage Pd films disrupted due to inter-diffusion into the Cu substrate, leading to a surface with irregularly shaped flat domains separated by mono-atomic steps. Higher temperature (720 K) annealing led to further flattening and the appearance of regular parallel lines in STM images whose spacing varies with Pd loading, which is assigned to strain due to lattice mismatch between a "capping" outermost copper monolayer and the underlying mixed CuPd alloy. High Pd coverage samples annealed to 500 K displayed substantial destabilisation of the formate intermediate relative to clean Cu(110), attributed to formate adsorption on mixed CuPd sites.

The nucleation and growth of both monometallic and bimetallic Pd and Cu clusters on HOPG have been investigated. STM, and XPS measurements of monometallic films of Cu and Pd verified a Volmer-Weber growth mechanism with formation of

hemispherical monometallic clusters of average diameter ~4 nm (Pd) and ~8 nm (Cu).

Bimetallic films of Cu and Pd formed by sequential deposition revealed properties dependent on the sequence of metal deposition. In the case of Cu deposition on pre-deposited Pd clusters, preferential coating of Pd by a Cu thin film (themodynamically favourable in surface energy terms) at low Cu coverages is observed, followed by the formation of phase separated Cu clusters as the Cu coverage is increased. XPS measurements rule out substantial alloy formation. STM indicates the majority of hemispherical bimetallic clusters are 5 to 7 nm in diameter, intermediate in size compared to that found for both monometallic Cu and Pd films. For Pd deposition on pre-deposited Cu, XPS data indicate a growth mechanism whereby the simultaneous growth of Pd clusters on the HOPG surface and the alloying/capping of areas already covered by Cu clusters occurs. Shifts in the Cu 2p core-level to lower binding energies for increased Pd loading on all levels of Cu pre-dosed samples illustrate a strong Pd-Cu interaction and fully supports this theory. Again an intermediate cluster-size distribution was observed by STM.

In the course of this work a new simple and reliable method for the **absolute** calibration of surface coverage was developed, based on the ex-situ analysis of the absolute amount of the metal evaporated using graphite furnace atomic adsorption spectroscopy (GF-AAS). This method is shown to have an absolute sensitivity of better than 0.1 ML.

The Cu(100)/Pt bimetallic combination has been examined by LEED, AES and TPD. An underlayer c(2×2) CuPt alloy capped by a Cu monolayer may be formed by deposition of ~0.6 ML Pt followed by thermal activation. In contrast, higher coverages of Pt (1.0–2.5 ML) followed by annealing to 550 K led to a local order c(2×2) CuPt alloy with a mixed CuPt **top** layer. A top layer CuPt alloy led to a destabilisation of the formate intermediate due to adsorption on a mixed CuPt site although the surface chemistry is still similar to pure Cu(100). The underlayer CuPt c(2×2) also exhibits destabilisation of the formate intermediate but to a lesser extent than the c(2×2) mixed CuPt top layer

Chapter One

Introduction

1.1. The importance of catalysis

The Swedish Chemist Jöns Jakob Berzelius coined the term "catalysis" to describe chemical reactions in which a substance increases the rate of a chemical reaction yet remains unused. The origin of the term catalysis in a scientific context is revealed in the following quotation by Berzelius (1836) published in the Edinburgh New Philosophical Journal.

'*Many bodies....have the property of exerting on other bodies an action which is very different from chemical affinity. By means of this action they produce decomposition in bodies, and form new compounds into the composition of which they do not enter. This new power hitherto unknown is common both in organic and inorganic nature....I shall....call it catalytic power. I shall also call catalysis the decomposition of bodies by this force'.*

The German chemist Wilhelm Ostwald more clearly, although essentially only modernising the terminology used by Berzelius, defined a catalyst "as a substance that accelerates the rate of a chemical reaction without being part of its final products". Basically, the mechanistic variations, sometimes involving alternative intermediates, offered by a catalyst affords a more rapid path to the final products.

The importance of catalysis can not be over-emphasised and its application to both chemical and biological processes are well documented. In biological systems the most obvious catalysts are enzymes primarily involved in countless fundamental reactions that make up living organisms. Chemically catalysis has been strongly linked to the petrochemical industry. Environmentally, chemical processes such as detoxification of automobile pollutants is afforded by the employment of the catalyst commonly referred to as the "three-way catalyst" (Pt, Pd, Rh). The economic significance of catalysis is reflected in the fact that the worldwide market for solid catalysts in the automobile, petroleum and other industries is in the order of $100 billion per year and growing.

Table 1 reviews important milestones in the history of heterogeneous catalysis.

Year	Investigator(s)	Phenomenon
1796	van Marum	Dehydrogenation of alcohols contacted with metal surfaces
1817	Davy, Döbereiner	Glowing of metals in contact with mixtures of Ar and combustible gases
1825	Faraday	Surface-induced combustion of hydrogen
1831	Phillips	Patent for sulphur dioxide oxidation on platinum
1836	Berzelius	Definition of catalysis
1869	von Hoffmann	Partial oxidation of methanol to formaldehyde on silver
1875	Squire, Messel	Industrial scale oxidation of sulphur dioxide on platinum
1894	Takamine	First patent for an extracted enzyme catalyst
1905	Sabatier, Sanderens	Hydrogenation of unsaturated hydrocarbons on nickel
1913	—	First ammonia synthesis plant operated at Oppau, Germany (1.3×10^8 Kg fixed nitrogen per annum)
1915	Langmuir	First quantitative theory of adsorption
1925	H.S. Taylor	First detailed theory of contact catalysis

Table 1: Important early dates of advances in catalysis at surfaces [1].

The importance of catalysis to the chemical industry can not be over estimated. For example, in the USA some quite revealing statistics have been disclosed. In the total production of chemical products 43% is catalytically driven, 36% and 7% between heterogeneous and homogeneous respectively (oil refining is excluded). Even more amazing is the fact that just one product sulphuric acid, accounts for 10% of this total. Extraordinarily, one of the yardsticks proposed for judging the state of development of a nation is its production of sulphuric acid on a per capita basis. This leaves us without any doubt regarding the status of heterogeneous catalysis as a

mainstay of the world economy. A comprehensive list of the major industrial products reliant on solid catalysis is revealed in table 2 along with recent global production amounts.

Reactant(s)	**Product**	**Typical catalyst(s)**	**Global production/ Kg year^{-1}**
Crude oil	Hydrocarbon fuels	Platinum/silica-alumina Platinum/acidic alumina Metal-exchanged zeolites	1×10^{12}
SO_2, O_2	Sulphuric acid	V_2O_5	1.4×10^{11}
N_2, H_2	Ammonia	Fe	9×10^{10}
NH_3, O_2	Nitric acid	Pt/Rh	2.5×10^{12}
CO, H_2	Methanol	Cu/ZnO	1.5×10^{10}
C_2H_4, O_2	Ethylene oxide	Ag	1×10^{10}
Unsaturated vegetable oils	Hydrogenated vegetable oils	Ni	8×10^{9}
C_2H_4	Polyethylene	Cr(II), Ti(III)	6×10^{9}
CH_3OH, O_2	Formaldehyde	Mixed Fe, Mo oxides	5×10^{9}
C_3H_6, NH_3, O_2	Acrylonitrile	Mixed Bi, Mo oxides	3×10^{9}
o-xylene, O_2	Phthalic anhydride	V_2O_5	2×10^{9}
n-butane, O_2	Maleic anhydride	V_2O_5	4×10^{8}

Table 2: Major products of the usage of heterogeneous catalysis [1].

An example of an important industrial application of heterogeneous catalysis is its employment in air pollution control. The major problem in combustion emission is the unwanted production of nitrogen monoxide (NO). This pollutant species originates in the equilibrium represented as:

$$N_2 + O_2 \Leftrightarrow 2NO$$

established at high temperature within combustion chambers. This equilibrium is pushed strongly towards the left at elevated temperatures as the production of NO is exothermic. Consequently, it may be expected that the backward reaction process

should proceed rapidly enough to adjust NO levels to equilibrium levels as the temperature falls along the exhaust system, i.e. there would be no pollution problem. In the gas phase the actual rates of reaction are too slow to achieve significant adjustment for the high temp levels. This kinetic limitation suggests a potential for catalytic reduction of NO levels, together with those of carbon monoxide (CO) and hydrocarbon species which also emerge as a result of insufficient rates of homogeneous reaction in the exhaust system. The control of these emissions is afforded by the incorporation of catalytic converters into the exhaust manifold. Essentially, they comprise of coating a honeycomb ceramic material (monolith) with a precious metal catalyst combination of 90% platinum and 10% rhodium (not alloyed) to a mass loading of 0.25%. At operating temperature (1000 K), the metallic surfaces catalyse a series of reactions which result in the conversion of all these types of pollutants to the corresponding inert products, carbon dioxide, water, and nitrogen. The reduction in pollutant by an order of magnitude is achievable with the catalyst showing considerable resistance to sulphur poisoning. It should however be noted that the catalyst only works efficiently at operating temperature of 800–1000 K. The inability of catalytic converters to work at ambient temperature has fuelled interest in this area in an attempt to find materials that operate effectively at lower temperatures. Real catalysis transformation generally occurs in a flow reactor through which the reacting species pass. As they usually consist of finely divided particles (usually termed "nano-particles" i.e. metallic clusters of diameter between 1 and 100 nm) attached to an oxide support; complete and definite characterisation of the morphology of the particles and their local surface composition presents a considerable challenge. The inhomogeneous surfaces of such systems do not lend themselves to analysis by modern surface science techniques. Consequently, even in their preparation tried and tested techniques cannot always be relied upon. It seems extraordinary that such a vital scientific area is controlled by trial and error experimental methodology. Fundamentally, the insufficient understanding of "real catalysis" is more a consequence of the lack of catalyst characterisation rather than the innate complexity of such systems.

1.2. Single crystal surfaces

In order to investigate adsorption and surface reactivity phenomena in a more controlled manner single crystal surfaces have been utilised as model catalyst surfaces, reducing the complexity of the surface structure and allowing a more fundamental insight into adsorption phenomena.

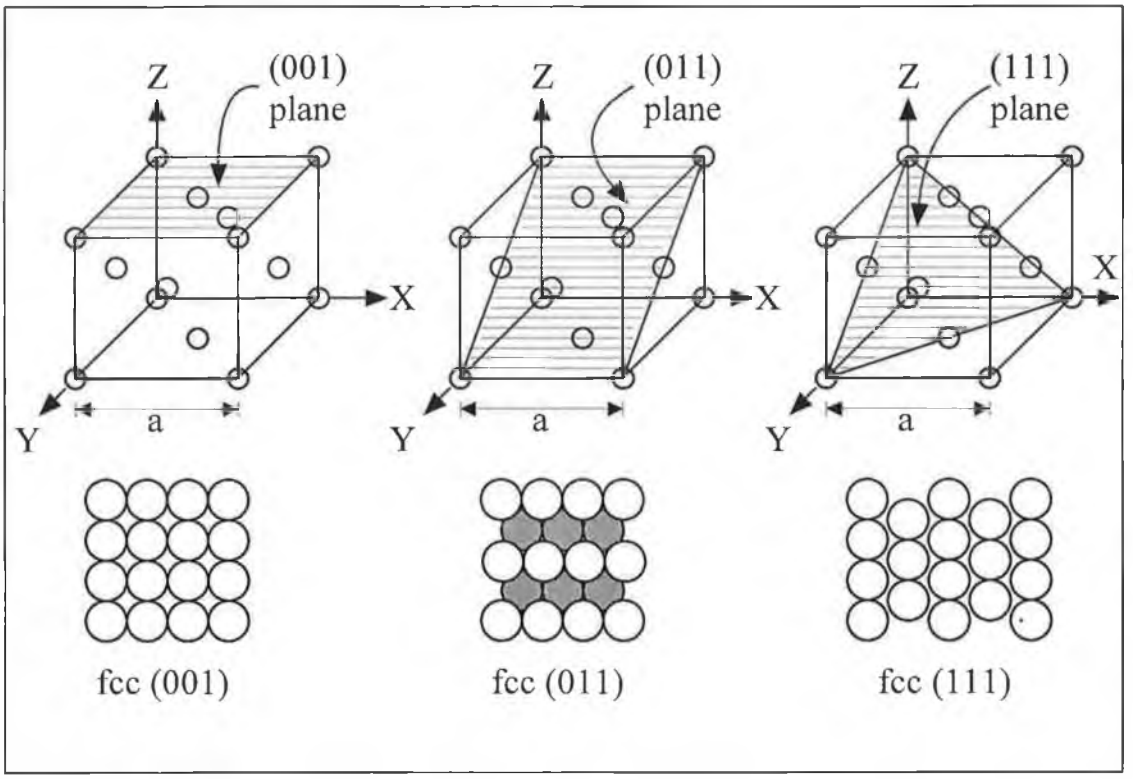

Figure 1: The three low-index faces of face centred cubic (fcc) materials. The hatched atoms in the (011) surface are second layer atoms.

The only type of surface which provides a uniform structure for well controlled fundamental study of adsorption and heterogeneous catalysis is a single crystal surface consisting of atoms arranged in an identical uniform repeating structure. Metal single crystals generally adopt close-packed crystal structures such as face-centred cubic (fcc) (e.g. Cu, Ni, Pd), body-centred cubic (bcc) (e.g. Fe, Cr, Mo) and hexagonal-close-packed (hcp) (e.g. Co, Ti, Ru). Figure 1 reveals the bulk unit cell of an fcc crystal, with different cross-sectional cuts yielding different surface atomic arrangements. The direction of cut with respect to the bulk unit cell is defined by

Miller indices [2]. The three low Miller index crystal surfaces (001), (011) and (111) are represented. Essentially these indices are defined as the reciprocal of the intersections of the particular plane with the x, y and z axes, respectively. The values are reduced to the lowest set of integer values and enclosed in brackets.

It is apparent that the surface atoms existing for the three low index faces experience loss of atomic co-ordination when compared to bulk atoms. For the (001) surface 4 nearest neighbours have been lost, while an atom located in the (011) surface has lost 5 nearest neighbours, and finally atoms in the (111) surface have lost 3 nearest neighbours. Thus, the properties of surfaces are significantly different than those of the bulk due to this loss of co-ordination. In some cases the surface will tend to compensate for the loss of atomic co-ordination by "reconstructing". The fcc (011) surface is a common example of this. A common reconstruction of the fcc (011) crystal face is the (1×2) "missing row" reconstruction shown in figure 2. This occurs both on clean single crystal surfaces (e.g. Au, Pt), or it may be induced by adsorbates (e.g. alkali metals, hydrogen on Pd or Ni (110)).

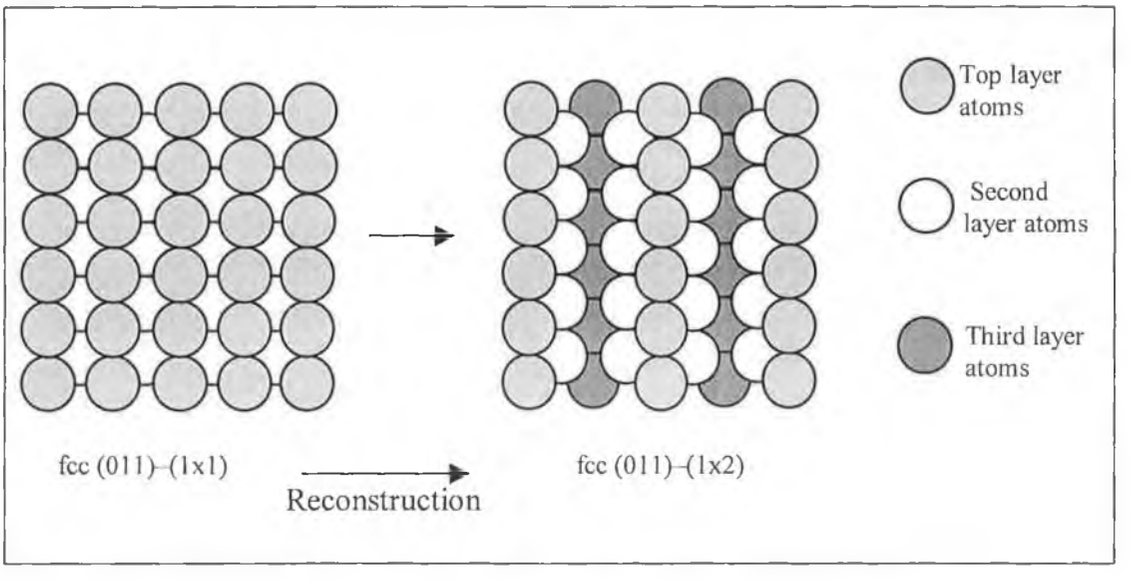

Figure 2: Typical reconstruction of a fcc (011) surface from a bulk truncated (1×1) structure to a (1×2) "missing row" surface.

Higher Miller index surfaces are comprised of a repeating pattern of atomically flat terraces and steps (and sometimes kinks) which correspond themselves to discontinuous low index surfaces. A notation for these surfaces, defined as the

compact-step notation [3] gives the surface structure in the general form $w(h_tk_tl_t) \times (h_sk_sl_s)$, where $(h_tk_tl_t)$ and $(h_sk_sl_s)$ are the Miller indices of the terrace and step plane, respectively, while w is defined as the number of atoms that is counted in the width of the terrace, including the step-edge atom and the in-step atom. These surfaces are particularly interesting as a result of the different chemistry that occurs at the step sites as opposed to the terrace sites. It is evident that the stepped sites will have a higher co-ordination for adsorbates than terrace sites, often leading to differing surface reactivity. Figure 3 illustrates the fcc (755) surface denoted by $7(111) \times (100)$.

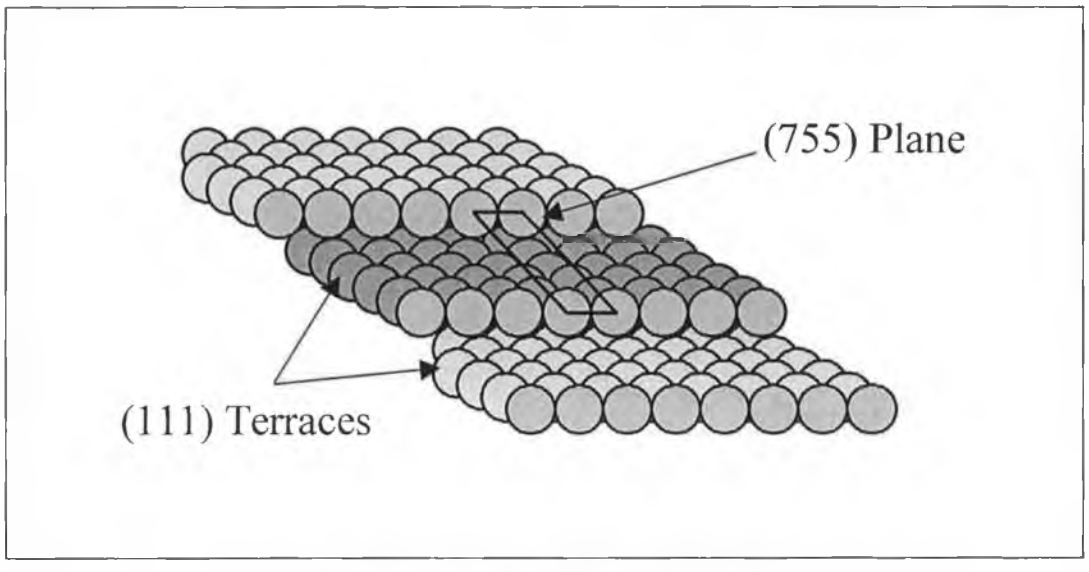

Figure 3: An fcc (755) surface.

The range of sites on most single-crystal surfaces are distinguished by the number of surface atoms the adsorbate may co-ordinate to. Figure 4 reveals the different high symmetry sites available on the low index fcc surfaces. For example, for CO adsorption any of the sites in figure 4 are possible while metal atoms generally (but not always) show a preference for the highly co-ordinated hollow sites.

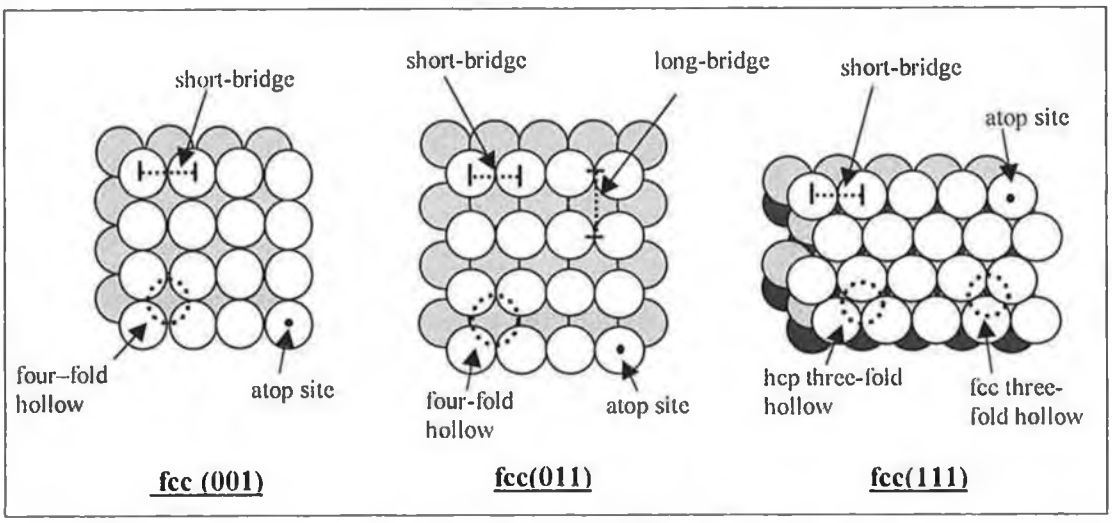

Figure 4: Different sites on the low Miller index fcc faces.

1.3. Bimetallic Surfaces

The use of bimetallic catalysts in industrial heterogeneous catalytic processes is widespread and explains the driving force behind the continued interest in this area. Understanding the correlation between the electronic and geometric structure of the bimetallic system and the induced reactivity changes is the goal. The tuning of the electronic properties of bimetallic systems seems to be a real possibility if the selvedge composition of the metals may be varied at will, opening up the possibility of "surface alchemy" and allowing control to be exerted on the stability of catalytic intermediates, reaction pathways and catalytic reaction rates.

In recent years, a large effort has been focused on understanding the chemical and physical properties of molecules and solids that have heteronuclear metal-metal bonds. Other areas to which mixed-metal systems have and continue to be applied include metallurgy, electrochemistry and microelectronics [4,5,6].

The factors which determine the properties of metallic centres and of heteronuclear metal-metal bonds are the metals involved, the local composition and the geometrical structure. In the formation of bimetallic surfaces two techniques are generally employed. The first involves the cutting and polishing of a sample of a bulk single-crystal alloy of the two metals followed by annealing and cleaning in ultra-high vacuum (UHV). The use of bulk alloys suffers from the problem of surface segregation, a phenomenon which dictates that the surface composition may be radically different from that of the bulk.

The surface composition of bulk alloys, either ordered or disordered, is dependent on a number of factors. Specifically, surface enrichment is usually dominated by the element with the lower heat of sublimation (lower metal-metal bond strength) [7,8,9]. This is directly related to a components surface energy. If the atoms are of substantially different radius ($\geq 10\%$) the element of greater size may segregate to the surface as a direct result of the contribution of the strain energy to the enthalpy of segregation. For exothermic alloys, a depletion of the element, which is enriched in the topmost layer, is often seen in the second layer. For endothermic alloys, surface enrichment is largely limited to the topmost atomic layer unless the sample is cooled to near the critical demixing temperature, where enrichment in the second layer can also be significant [7]. This leads to an inherent limitation in the flexibility of

producing surfaces of widely varying composition. Production of high quality single crystals is often a difficult and expensive task in the case of binary systems. Thus a second and more commonly used technique involves the deposition of one metal onto a single crystal face of a second to produce "bimetallic" surfaces [10]. In several cases careful control of the surface coverage and annealing conditions allows formation of "surface alloys", i.e. a two-dimensional mixed metal surface layer often of well-defined structure and composition.

1.4. The CuPd system

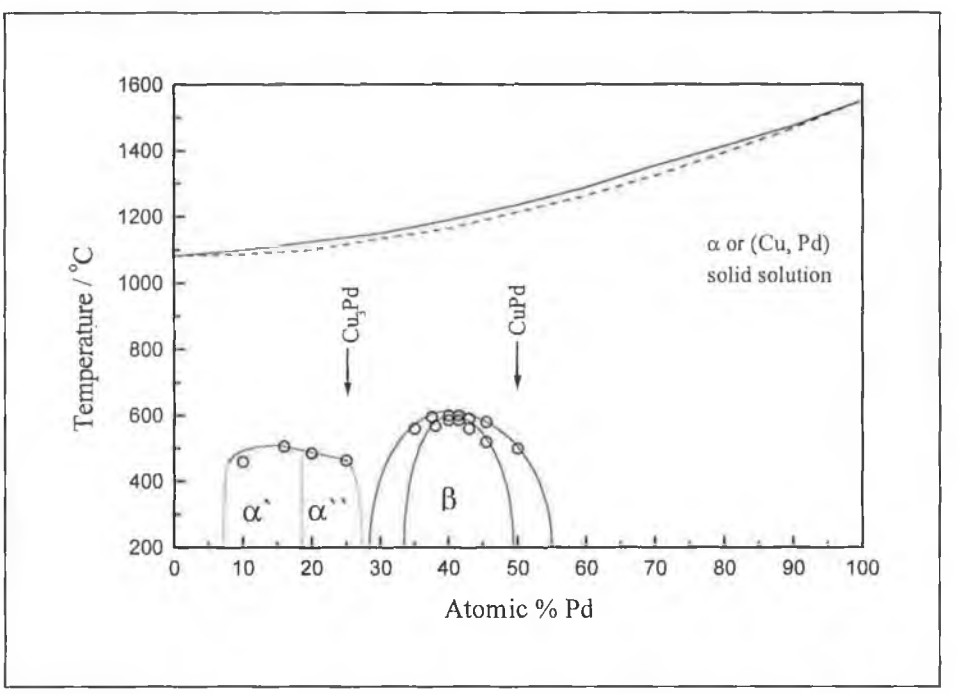

Figure 5: Cu-Pd phase diagram [11].

The CuPd system is of considerable interest in terms of its tendency to form a continuous series of solid solutions. Bulk CuPd alloys have received considerable scrutiny [12,13] regarding order-disorder transformations upon heat treatment and subsequent cooling experiments. Figure 5 reveals the bulk phase diagram of this system. The two common compounds formed are CuPd and Cu_3Pd, both undergoing an order-disorder transition to a solid disordered solution above a critical temperature. Alloys of the Cu_3Pd type have a disordered face-centred cubic (fcc)

structure at high temperature however assume an ordered structure of the Cu_3Au type after slow cooling to room temperature. The two structures are shown in figure 6. Previously, the structure based on Cu_3Pd was thought to be that of the Cu_3Au type within the entire range of about 10–25 atomic % Pd. However, alloys with 22, 24.4 and 25 atomic % Pd showed the presence of a tetragonal structure, the amount of which increased progressively as the temperature was lowered (α'' phase) [11]. Alloys with 10–19 atomic % Pd were confirmed to have the Cu_3Au type of lattice [14]. On the other hand alloys of the CuPd composition possess a fcc structure at high temperatures which is disordered while at lower temperature they are body-centred cubic (bcc) [15] and ordered i.e. the order-disorder transformation is accompanied by a transition in crystallographic structure.

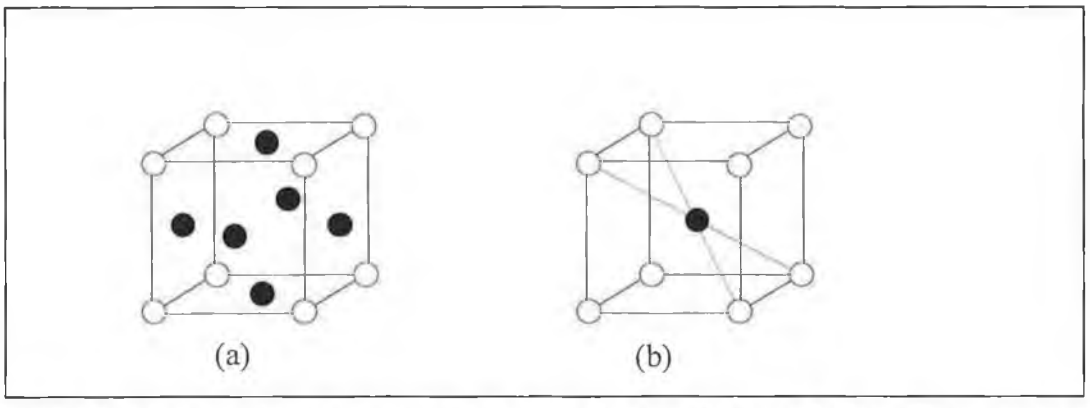

Figure 6: Models of the ordered (a) fcc Cu_3Pd and (b) bcc CuPd. The open and solid circles represent Pd and Cu atoms, respectively.

The factors deciding surface composition mentioned in the previous section are not adhered to in this system. The ~7.8% differences in atomic size between Pd (1.38 Å) and Cu (1.28 Å) would suggest that Pd extrusion to the surface would be preferred to compensate for the large degree of lattice strain in alloys dilute in Pd. However, surface energies dictate that Cu (1.934 Jm^{-2}) preferentially surface segregates as Pd (2.043 Jm^{-2}) has the higher surface energy [16,17]. Therefore the situation is one were surface energies are in opposition to atomic size differences for alloys dilute in Pd. For Pd rich alloys both factors favour Cu surface segregation. Cleavage of the Cu_3Pd structure in the <110> direction results in two possible terminations (figure 7).

The first results in a mixed top layer of alternating Cu and Pd atoms along the [1 $\bar{1}$ 0] direction with the second layer exclusively Cu (figure 7(a)). The second termination comprises of a top-layer of Cu atoms only with the second layer consisting of 50% Cu and Pd (figure 7(b)). Although it is important to realise that for bulk alloys a range of surface compositions are possible depending on the temperatures of sputtering and annealing used during their preparation.

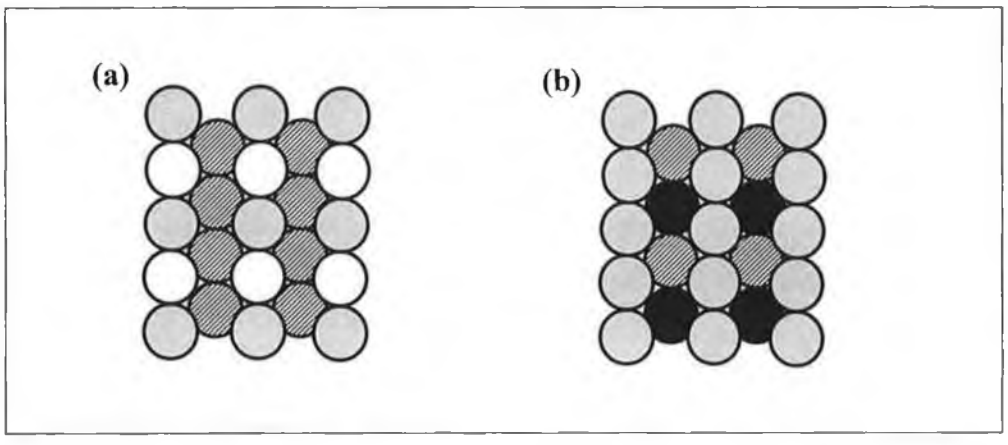

Figure 7: Plan views of the cross sections through the α' Cu_3Pd ordered structure shown in figure 6(a). The open circles represent top-layer Pd, the grey top-layer Cu, the filled circles to second-layer Pd and the hashed to second-layer Cu.

The electronic structure of the CuPd alloy system is also of interest being currently the focus of a lot of experimental and theoretical work [18,19,20,21]. One physical process observed in alloys is the rearrangement of electronic charge between the constituent atoms. Hence, the presence of Pd in dilute arrangement with Cu may allow the manipulation of its electronic structure which may be controllable by variation of the Pd concentration. This is clearly the case with Pd valence levels experiencing a shift in the centroid of the d-band emission to higher binding energy upon alloying with Cu (XPS core level shifts appear to mirror this shift). The 4d valence level peaks at about 0.6 eV below the Fermi level in pure palladium while in a CuPd surface alloy of Cu:Pd local stoichiometry varying between 3:1 to 20:1 it is located at approximately 1 eV higher binding energy [22]. Large shifts to higher binding energy have been reported for the Pd $3d_{5/2}$ core level relative to pure Pd

when in dilute arrangement with Cu. Shifts of ~0.75 eV have been measured for a Pd_8Cu_{92} alloy while a ~0.45 eV shift was recorded for a $Pd_{40}Cu_{60}$ bulk alloy [19]. For the Cu_xPd_{1-x} alloy system it has been observed both experimentally [19,23,24] and theoretically [25] that the Cu 3d partial density of states lies below the Fermi energy at all compositions. On the other hand the Pd d band is unfilled for $x<0.6$ [21,25].

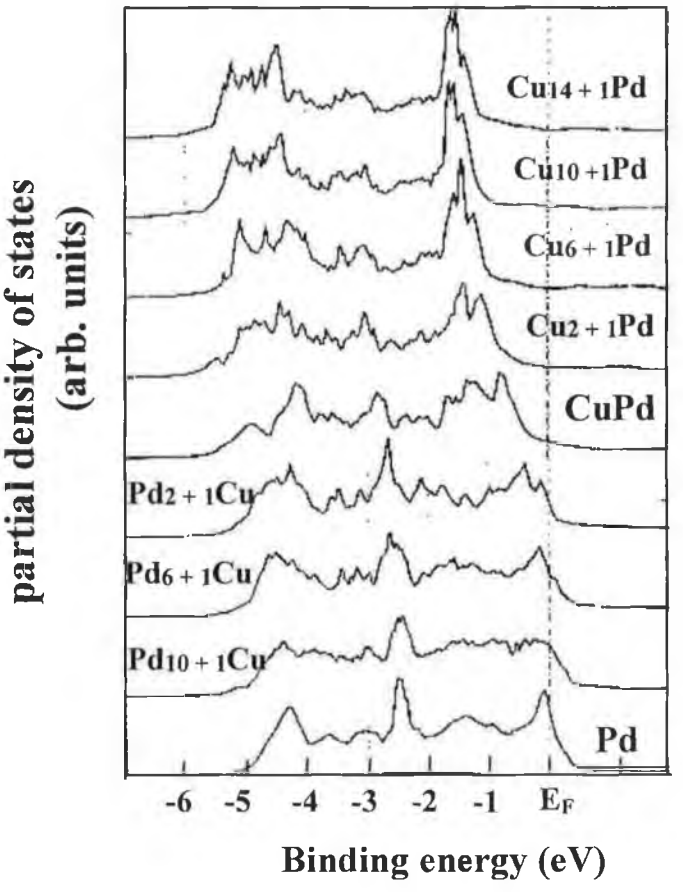

Figure 8: The variation in the (bulk) Pd d-density of electronic states for pure Pd and a number of alloys of decreasing Pd concentration, showing withdrawal of the Pd d-density of states from the Fermi level [26].

Calculations for Cu_3Pd indicates that ordering of the bulk serves simply to sharpen individual features in the band structure without generating any significant shifts when compared to a randomly distributed bulk mixture [27]. With reactivity directly

linked to the electronic states at the Fermi level it seems quite possible that we may exert some influence over reactivity by controlling the Pd surface concentration in CuPd alloys. Figure 8 reveals the Pd partial density of states at the Fermi level for a range of Cu_xPd_{1-x} alloys and how by varying the Pd concentration the "tuning" of the d-density of states at the Fermi level is possible.

Chemical wisdom suggests that an atom surrounded by "like" atoms will be neutral, while an atom bonded to all "unlike" atoms will experience charge 'transfer'/re-arrangement. This is evidently the case for the CuPd system revealing radical changes in the Pd electronic structure as its concentration is varied. At low Pd concentration with few Pd-Pd nearest neighbour bonds, Pd essentially becomes Cu-like, i.e. revealing filled d-band characteristics while normally pure Pd is an open d-band metal.

The reactivity of CuPd surfaces is also of interest. The interaction of CO with monometallic substrates has received considerable scrutiny with respect to its bonding mechanism. Recently, interest in the reactivity of CO with bimetallic surfaces has surged.

In general, it is found that weakening of the Pd-CO interaction occurs when Pd is incorporated in a bimetallic arrangement. A study examining the shift in both the binding energy of the Pd 3d core-level of the Pd overlayer, on both transition and s,p metals, and the CO desorption temperature reveal some interesting correlations [28]. A direct correlation between changes in electronic and chemical properties was discovered, i.e. the larger the shift in Pd 3d binding energy the lower the CO desorption temperature. In contrast, Cu experiences negative core-level shifts and an increase in CO desorption temperature when present as an admetal on the late transition metals [29].

The strength of CO bonding to a metal is thought to be dependent on the extent of π backdonation, i.e. electron transfer from the occupied bands of the metal into the CO($2\pi^*$) orbitals [30]. Moreover, d electrons are far more important in metal CO bonds than sp orbitals. The interaction of Pd with a metal substrate tends to move the 4d electrons to higher binding energy (away from the CO($2\pi^*$) orbitals). The d orbital population reduction is accompanied by a Pd(4d)→Pd(5s,5p) rehybridisation. The weakening of the carbon–metal bond subsequently strengthens the internuclear

CO bond which is easily characterised by the spectral location of the CO infrared stretching vibration. On the other hand, Cu as an admetal on the late-transition metals undergoes an increase in its 3d orbital population. This effectively strengthens the Cu(3d)-CO($2\pi^*$) bonding interaction.

Both Cu and Pd are catalytically active and as such their alloys may reasonably be thought to provide properties that are modified with respect to the pure components but which may enhance or poison specific reactions. Subsequently, the Cu_xPd_{1-x} bimetallic combinations have proven to be extremely relevant industrially and subsequently have received considerable attention. Their uses include CO and alkene oxidation [31], ethanol decomposition [32] and CO, benzene and toluene hydrogenation [33]. Transition metals can produce many useful industrial products upon hydrogenation including alcohols, hydrocarbons, aldehydes and acids. Supported bimetallic CuPd particles have been shown to maintain a high turnover rate for CO oxidation over a much wider temperature range than the elementary catalysts alone [31]. Hence, further interest has been generated into the CuPd system owing to the importance of CO oxidation/NO_x reduction to automobile pollution control (catalytic conversion) [34]. To this extent it seems that Pd and Cu have complementary activities. Pd is very active in CO oxidation and moderately active towards NO dissociation [35], while Cu shows little activity for CO oxidation but is active in NO dissociation [36]. Finally, the CuPd system has also been proposed as a bimetallic catalyst for reactions as diverse as methanol synthesis, where it is again believed to have superior reactivity, selectivity and stability properties when compared with the single component catalysts [37,38,34]. More specifically the addition of Pd to Cu based catalysts allows the favourable suppression of formate (HCOO) intermediate production in methanol oxidation. Formate formation is likely to lead to complete combustion of the methanol rather than the selective conversion to formaldehyde (H_2CO) [39].

1.5. Cu_xPd_{1-x} systems review

1.5.1. Cu_xPd_{1-x} bulk alloys

Studies on the $Pd_{50}Cu_{50}(111)$ single crystal indicate that CO and NO are more strongly bonded to the Cu atoms of the Pd-Cu alloy than on pure Cu and are less strongly bonded to the Pd atoms of Pd-Cu compared to pure Pd. In these studies the adsorption energies of CO and NO were calculated and compared to adsorption on the pure metals, with low energy ion scattering (LEIS) studies revealing the top layer to correspond to $Pd_{45}Cu_{55}$. The electronic changes recorded have been interpreted in terms of bond formation between the almost full valence 'sd' band of Pd and the resonant 'dsp' band of Cu near the Fermi level [40].

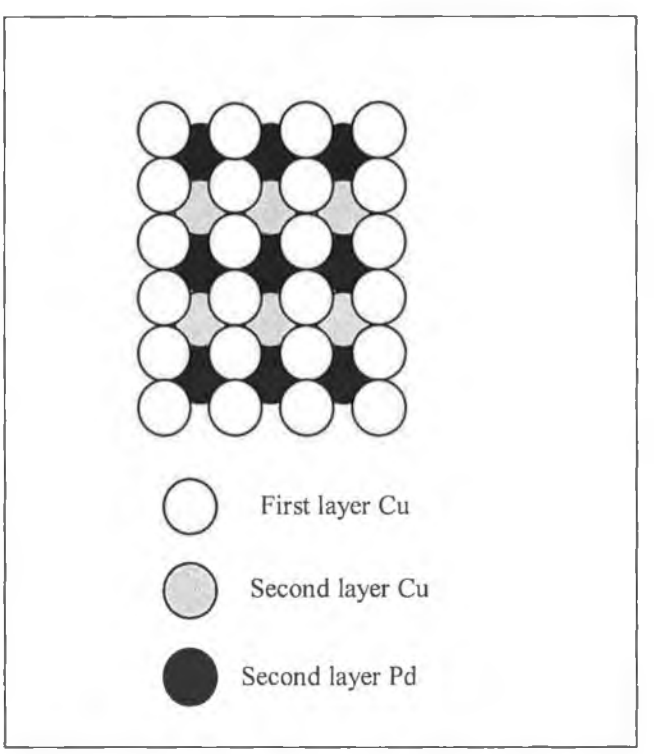

Figure 9: Proposed structure for the CuPd [85:15] (110) p(2×1) surface [46].

Regarding Cu_xPd_{1-x} bulk alloy crystals the expected depletion in the second layer of the component enriched in the topmost layer is seen in the CuPd [85:15] (110) crystal. This surface has received considerable attention [41,42,43,44,45]. The

surface layer is suggested to be Cu rich and essentially devoid of Pd [45]. The second layer is proposed to be an ordered layer of 50 at. % Cu and 50 at. % Pd giving rise to a p(2×1) LEED pattern [46,47]. Chemical ordering between Cu and Pd in the second layer is in the form of a mixed 50:50 second layer with Pd atoms occupying every second site along the close packed [1 $\bar{1}$ 0] rows. The surface bilayer therefore approximates to the ordered Cu_3Pd α' phase [48]. This is the only case of the ordered layer being formed below the top layer of a random substitutional alloy. Figure 9 reveals the proposed structure of the CuPd [85:15] (110) (2×1) surface. The surface represented is that of a pure Cu top layer although differing opinions exist regarding the purity of this Cu top layer. Newton et al [47] utilising angle dependent XPS and quantitative LEED support the theory of a Pd free top layer while the studies of Bergmans et al [41,42] using low energy ion scattering (LEIS) determined a top layer Pd concentration of 5–10%.

Regarding reactivity, the inclusion of Pd in the second layer of the CuPd [85:15] (110) alloy leads to an increase in reactivity towards dehydrogenation of adsorbed formate relative to Cu(110). Newton et al have reported a 7–10 kJ mol^{-1} destabilisation in the activation energy compared to Cu(110) [47]. No decomposition peaks attributable to surface Pd were reported. Cu(110) undergoes a facile reconstruction upon the adsorption of oxygen [49], causing a change in the observed LEED pattern from the (1×1) pattern to a p(2×1) structure complete at an oxygen coverage of 0.5 ML. The types of reconstruction possible include, a missing row type reconstruction or a buckled row with an added row model proposed more recently. The CuPd [85:15] (110) alloy undergoes a similar reconstruction to Cu(110) as observed using core level X-ray photoelectron diffraction (XPD) [45,50]. In terms of oxygen sticking probability the presence of Pd in the surface region of the alloy has led to little or no change in the observed trends when compared to Cu(110). The initial sticking probability, the coverage dependence of the sticking coefficient and the apparent activation energy for oxygen adsorption are the same as that observed for Cu(110) [51]. In a supersonic beam study of H_2 dissociation [44], a lower sticking probability was observed for the p(2×1) than that of the Cu(110) surface, reported similar to that found for the Cu(111) surface. Sputtering of the alloy at low temperature (280 K) results in a metastable disordered (1×1) surface revealing enhanced dissociative sticking compared to both the p(2×1) and Cu(110), although as

expected still significantly lower than that of pure Pd. It is suggested that this (1×1) surface contains small islands of Pd with TPD profiles revealing Pd derived features (a Pd enriched surface may be attributable to the higher sputtering yield of Cu compared to Pd).

Oxygen and nitrogen adsorption-desorption studies have also been carried out on the PdCu(110) bulk alloy with a Cu/Pd ratio of 1:1 in the bulk. Mousa et al [52] determined surface compositions using both AES and CO TPD measurements. Carefully chosen preparation procedures produced a 100% Pd top layer. LEED examination of an O_2 dosed crystal surface of a 100% Pd top layer and containing 13% Cu in the three subsurface layers, revealed a c(2×4) pattern at 295 K almost a 100 K less than that seen on the Pd(110) surface [53]. In effect Mousa et al observed a number of different oxygen adsorbate structures depending on the adsorption temperature, the subsequent annealing temperature, the concentration of Cu atoms in the surface region, and most importantly the type of crystal lattice present prior to adsorption. Evidence of the presence of subsurface oxygen was also found which influenced the building of oxygen adsorbate structures and surface reconstruction. Structurally the increase in concentration of Cu in the surface region to ~40% while still maintaining a 100% Pd top layer is proposed to have changed the crystal lattice from fcc to bcc(110). For a Pd-rich surface region with a Cu/Pd surface region ratio ≤0.1 CO TDS revealed desorption states resembling those from Pd(110), although two new desorption states at 250 and 190 K were observed indicative of alloy surface characteristics and strongly suggestive of a ligand effect regarding CO desorption [54]. Increasing the Cu/Pd surface region ratio to ≥0.3 reveals a loss in CO desorption for Pd-bridge sites (450 K) with a shift in the other two high temperature desorption sites to lower temperatures by ~50 K, suggested as an ensemble effect. CO oxidation rates for the PdCu(110) surface (surface Cu/Pd ratio ≤0.1, almost pure Pd top layer) exhibited lower reactivity compared to pure Pd. Increasing Cu surface region concentrations seemed to decrease the reactivity even further. Increasing Cu concentration possibly effects the sticking coefficient of CO on the surface [55].

Nitrogen desorption on the Pd rich surface of the PdCu(110) single crystal has also been studied [56]. Two desorption states at 130 and 445 K were observed with the latter not seen on the pure constituent metals and assumed to originate from alloy

sites. Higher N_2 doses showed more complicated desorption profiles with strongly bound nitrogen species revealing peak maxima at 445, 580 and 680 K.

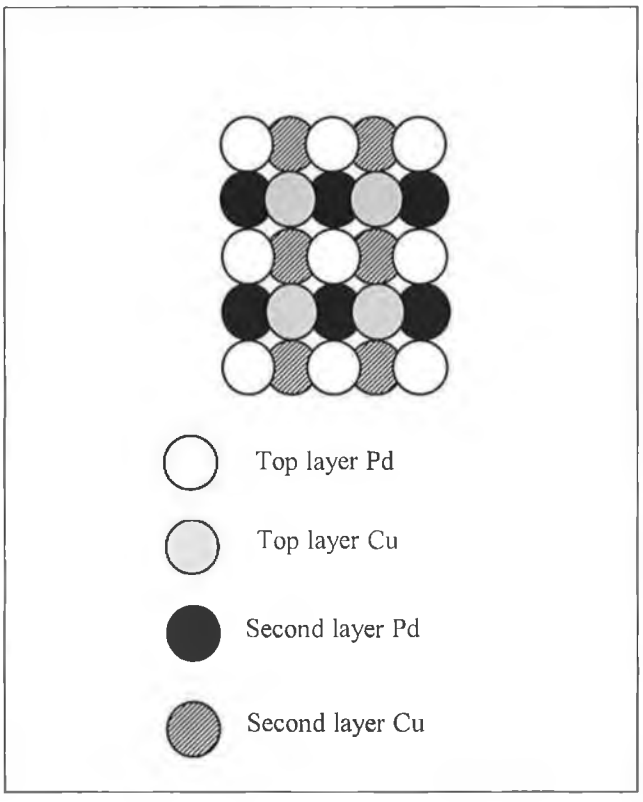

Figure 10: Termination of the β CuPd ordered structure [57].

Holroyd et al [57] have also studied the PdCu(110) bulk alloy (Cu/Pd surface region ratio = 0.55±0.05). The initial sticking probability for oxygen was found to be 0.10 and was found to vary only slightly by increasing the Pd concentration in the surface region (maximum sticking probability 0.13). Initial sticking probabilities for oxygen on the pure metals, Pd(110) and Cu(110), were found to be 0.4 and 0.2, respectively. So it is postulated that in the case of oxygen adsorption that going from an fcc to a bcc-type structure affects the barrier to adsorption. The composition of the CuPd(110) bulk alloy i.e. 1:1 means that it falls within the range expected for the bulk to order in the CuPd β bcc structure (figure 10).

Holroyd [57] studied formate decomposition on the PdCu(110) alloy (350 K) with stability intermediate between that of Cu(110) (450 K) and Pd(110) (240 K). The exact reasoning for this is unclear although it is suggested a formate bond is formed which is bidentate bridging between a Cu atom and a Pd atom. Narrow desorption

peaks for coincident CO_2 and H_2 were observed suggestive of a well-ordered surface. The structure pertaining to this desorption is stipulated to be a bcc-type model with a surface composed of alternate Pd and Cu rows along the $[1\,\bar{1}\,0]$ direction. Figure 11 illustrates this proposed bcc structure for the PdCu(110) bulk alloy with a mixed top layer. This surface has been offered as a possibility for the PdCu(110) bulk alloy with a Cu/Pd surface region ratio >0.2.

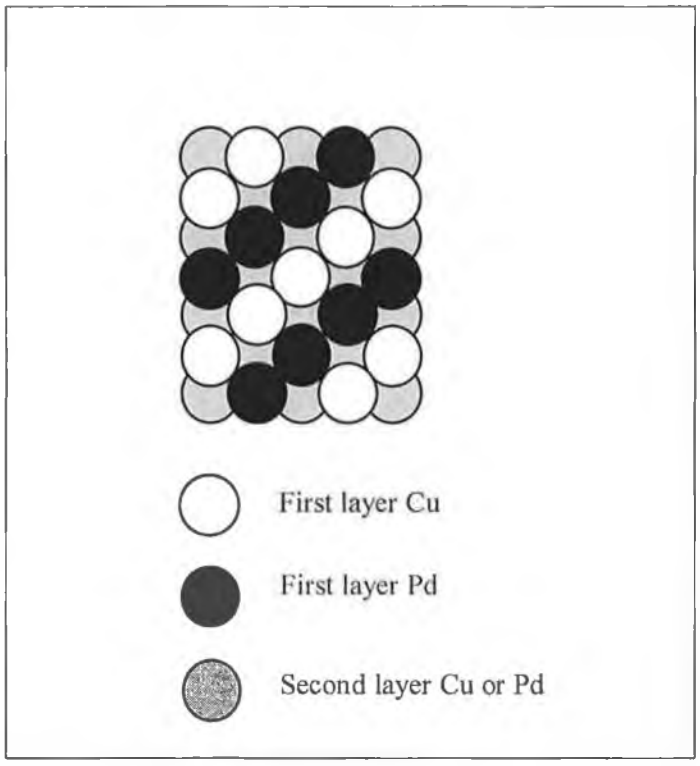

Figure 11: Body-centred cubic model proposed for the CuPd(110) bulk alloy for a Cu/Pd surface region ratio >0.2 [57].

Thin film growth:

The evaporation of one metal onto a second metal in the form of a single crystal is the most favoured technique of bimetallic formation. In this scenario if alloying occurs it only extends to the surface region and therefore the term '*surface alloy*' is used to describe these bimetallic arrangements. The first use of surface free energies to describe the modes of crystal growth was suggested by Bauer [58] in 1958 and has been frequently reviewed [59,60].

The prediction of growth depends on the relative surface free energies of the pure admetal (γ_A), the pure substrate (γ_S) and the interface ($\gamma_{A\text{-}S}$). The interface energy usually depends on the extent and nature of the bimetallic bond and is extremely important in determining the growth behaviour. However, unfortunately this thermodynamic quantity is poorly understood. Young's equation ($\Delta\gamma = \gamma_A + \gamma_{A\text{-}S} - \gamma_S$) as suggested by Bauer plays a large part in growth mode determination. Commonly, the growth modes experienced are divided into three categories: 3-dimensional island (Volmer-Weber, VW) where $\Delta\gamma>0$; layer plus island (Stranski-Krastanov, SK) where $\Delta\gamma<0$; and layer-by-layer (Frank van der Merwe, FM) growth where $\Delta\gamma\leq0$. Of course the prediction of growth using the rules above is only valid if the system is in thermodynamical equilibrium. In most cases growth occurs far from equilibrium.

1.5.2. Ultra-thin Cu film growth on Pd single crystals

Asonen et al [61] were the first to examine the Pd(100)/Cu system for growth at 300 K and suggested that the growth mechanism was Stranski-Krastanov according to LEED, angle-resolved ultraviolet photoelectron spectroscopy (ARUPS), AES and work function measurements. Pseudomorphic growth is observed initially, with the formation of clusters evident above 2 ML Cu deposition. Li et al [62] performed a LEED *I(V)* analysis from a 6 ML Cu film on Pd(100). Biaxial in-plane expansion of Cu to the Pd lattice parameter (2.75 Å) has been reported [63] with evidence of inter-layer spacing contraction (~1.55 Å). From this LEED analysis it was deduced that a body-centred tetragonal (bct) phase adopted by Cu was virtually strain free (bct is a local energy minimum of the distorted fcc structure) [64]. Valence band changes were seen with the appearance of new emission whose position varied between 4.35

and 4.85 eV below the Fermi level as a function of Cu coverage [61,62]. The feature was assigned to the surface state existing in the gap of the tetragonally distorted Cu band structure [65].

Vook et al [66] have studied Cu growth on a mica-supported Pd(111) film (thickness ~1500 Å). A layer-by-layer growth mechanism was confirmed by work-function measurements up to a critical coverage of 2 ML after which island formation is favoured. Elevated temperature studies concluded that Pd diffusion into the Cu film occurred at temperatures >500 K. The STM investigation of submonolayer Cu coverages on Pd(111) has shown Cu to grow in a single layer while the lattice mismatch strain is relieved via the formation of fcc hexagonal-closed packed (hcp) stacking domain walls [67]. Higher coverage studies by LEED, reported by Li et al [68], have predicted that Cu grows epitaxial yet incommensurate with Pd(111). The nucleation of multi-layered islands was suggested.

The growth of Cu on Pd(110) has been studied extensively using STM by Hahn et al [69,70,71,72] with particular emphasis on temperature dependent growth. A transition in growth mode is reported as changing from Volmer-Weber (VM) at 300 K to layer-by-layer at 600 K, with an intermediate Stranski-Krastanov (SK) mode observed at 400 K. The deposition of Cu on Pd(110) at 300 K reveals the formation of monoatomic chains extending along the $[1\,\bar{1}\,0]$ direction that exhibit lengths of several hundred Angstroms (θ_{Cu} = 0.07 ML). The difference in diffusion barrier to Cu in the longitudinal $[1\,\bar{1}\,0]$ and transverse [001] directions (there is a high diffusion barrier in transversing the close packed rows in the [001] direction) is the possible reason for their formation [73,74]. The transition of the one-dimensional (1-D) structures into two-dimensional (2-D) islands is observed upon annealing to 350 K. At higher coverages (θ_{Cu} = 0.35 ML) a change from 1-D chains to 2-D islands (width ~19 Å (5 atomic rows)) occurs. Island lengths similar to that seen at the lower coverage are observed. Increasing the coverage further (θ_{Cu} = 0.70 ML) results in filling the gaps between the islands increasing the average island width to ~40 Å. The formation of these islands allows the initiation of second layer growth proceeding in a more isotropic manner with extension along the $[1\,\bar{1}\,0]$ direction less

obvious. Again the morphology of the structures seen at this stage of growth is highly dependent on the deposition flux and substrate temperature [75].

Pseudomorphic growth is defined as the adoption by the overlayer of a lattice constant which differs from its own crystal structure but matches coherently the lattice constant of the underlying substrate. The continuation of growth generally results in the gradual change of the overlayer lattice constant to that normally seen for its bulk crystal structure. The strain in the overlayer can result in morphology changes and metastable structures. The increasing thickness of the overlayer sees the strain increase proportionally until the epitaxial film eventually finds a way to relieve this built-up strain. This is possible through the introduction of defects into the overlayer [76] or by the roughening of the surface [77].

An example of anisotropic strain relief is evidenced in the pseudomorphic growth of Cu on the (110) surface of Pd. At 600 K, the step-flow wetting of the substrate by Cu is the dominant process and is seen to continue up to almost 10 ML. Although the system exhibits direct wetting at 600 K evidence of alloying is only recorded at ~700 K. The (1×1) LEED pattern observed and the flat surface imaging by STM is difficult to understand as the total strain energy in the system increases linearly with film thickness [78]. The relief mechanism reported involves the appearance of banded stripes in the STM images after 5 ML deposition attributable to buckling in the $[1\,\bar{1}\,0]$ direction [70]. The banded appearance runs along the [001] direction. This periodic structure defines the uniaxial reduction in tensile strain for the system. The buckling height is about 0.5 Å and the absence of any additional LEED spots suggests that the reduction of the interatomic distance in the $[1\,\bar{1}\,0]$ direction is the only positional change taking place, with Cu locked in position between the closed packed atoms of the underlying layer in the [001] direction.

In summary, a considerable amount of work has been done on Cu deposition on Pd single crystal surfaces where two-dimensional monolayer formation is favoured. For deposition at 300 K strained epitaxial overlayers are formed with little intermixing on Pd(100) or Pd(110), with alloying occurring only at elevated temperatures. Generally ordered surface alloy formation between Cu and Pd is not observed. However it should be noted that Cu growth on the Pd(110) surface appears to differ from that on the low-index (111) and (100) surfaces. The first layer seems to grow

pseudomorphically essentially two dimensionally with cluster growth initiated beyond the completion of the first monolayer.

The adsorption and subsequent dissociation of H_2 on transition metal surfaces occurs quite readily while it is an activated process on noble-metal surfaces and on thin Cu layers on transition metal surfaces [79,80]. It is interesting to note that the adsorption of hydrogen on CuPd systems is suggested to be reliant on available surface islands of Pd in a (1×1) structure (nearest neighbour Pd sites are needed) [81]. This has important implications in the use of H_2 adsorption to selectively quantify the amount of active sites on transition-metal/Cu bimetallic catalysts [82]. Interestingly, oxygen adsorbed on submonolayer Cu on Pd(111) follows a room temperature reaction mechanism in the presence of hydrogen [67] which is commonly termed "spillover". This mechanism involves dissociation of H_2 on Pd which subsequently diffuses onto oxygen covered Cu regions (H_2 does not dissociate on oxidised Cu islands and only oxygen in hexagonal features ($Cu_2O(111)$) reacts with H_2). The rate of reaction is therefore dependent on the amount of bare Pd available to dissociate H_2. This reaction is found to occur at negligible rate on oxygen pre-dosed Cu(111) at 300 K. However it should be noted that the reaction of H_2 on oxygen pre-covered Pd(111) proceeds much more quickly.

1.5.3. Pd growth on Cu single crystals

It used to be widely accepted that systems exhibiting a negative enthalpy of bulk mixing to form stable bulk alloys are the most likely to form surface alloys, while bulk immiscible systems do not (highly positive heat of bulk alloy formation). Two-dimensional surface alloy formation involves the combination of two metals which are bulk immiscible. In these cases, surface alloy formation is limited to the outermost substrate layer. The two-dimensional alloy represents a minimum in the systems free energy and is a true equilibrium configuration. The earliest examples of these type of surface alloys are the c(2×2) structures resulting from the deposition of Cu, Ag and Au on W(100), initially discovered and studied by Bauer [83]. Subsequently, Attard and King [84] have verified the confinement of the surface alloy to the outermost layer using low-energy ion scattering (LEIS) spectroscopy

while Hu et al [85] using LEED $I(V)$ also supported the two-dimensional nature of the W(100)-c(2×2)-Cu alloy. A more recent case in point is the Au-Ni system for which a miscibility gap exists in the bulk binary phase diagram. Limited surface alloying occurs resulting in the formation of a novel 2-D confined surface alloy. In the adsorption of Au on Ni(110) at room temperature the alloy develops in the topmost layer [86,87]. The tendency for the Au atoms to diffuse along the troughs of the Ni substrate leads to, at certain points, the Au atoms squeezing out Ni atoms. STM studies supported by low-energy ion-scattering (LEIS) measurements and theoretical calculations based on the effective-medium theory (EMT) suggest the formation of a nearly 1:1 surface alloy of Au and Ni saturating at a Au coverage of ~0.45 ML. The substitution is linearly dependent on the amount of Au deposited with the expelled Ni growing anisotropically along the closed packed direction because of the much stronger nearest-neighbour bonding in the $[1\bar{1}0]$ direction. EMT calculations demonstrate that while second-layer Au atoms gain an energy of 0.03 eV, bulk substitution costs 0.21 eV for each Au atom substituted. Additional deposited Au reveals the formation of chemisorbed [001]-directed Au chains consisting of zig-zagging dimers and trimers, on top of a nearly 1:1 surface alloy of Au and Ni. A p(5×1) structure is observed upon an Au coverage of ~0.7 ML, transforming at 1 ML into a c(2×4) Au trimer structure.

In the case of metals which exhibit considerable bulk miscibility, the adlayer and the substrate may intermix. In most cases the composition and extent of the alloys formed is a function of the annealing temperature

For Pd-Cu which is a bulk miscible system, ordered stoichiometric surface alloys are common. In these cases surfaces alloys represent quasi-equilibrium structures kinetically frozen in a local free energy minimum. In this case it is probable that the surface alloy extends beyond the outermost layer essentially forming a compositionally graded interface.

Some of the earliest studies involving the deposition of ultra-thin Pd layers onto the low-index single crystal Cu surfaces were carried out by Fujinaga [88,89]. LEED and Auger investigations examined the conditions favourable to the formation of ordered alloy structures in the case of Pd evaporation on low index Cu crystals. No surface alloy formation was observed by LEED on the (111) surface with the (1×1)

LEED pattern persisting upon annealing. A c(2×2) CuPd surface alloy formed readily on the Cu(100) substrate after room temperature deposition of ~20 ML Pd although extended heating at 620 K caused the LEED pattern to fade. Other metals which exhibit c(2×2) structures on Cu(100) are Pb [90], Mn [91] and Au [92] at ~0.5 ML admetal coverage. Although no observable distortion of the c(2×2) structure due to the 8 % mismatch between Pd and Cu is noticed, the Au/Cu(100) with a 13% mismatch displays clear strain seen as surface ridges. Later scanning tunnelling microscopy (STM) work by Murray et al has shown that the origin of the c(2×2) LEED pattern from the CuPd is due to surface alloy formation via substitution of Pd adatoms into the outermost layer [93]. The formation of the alloy involves the preference of Pd atoms to occupy second nearest-neighbour sites of the Cu lattice. This results in the formation of short [001] and [010] directed chains which converge to form a c(2×2) structure as the coverage is increased. Cu atoms ejected by the incorporation of Pd into the surface form islands on the terraces [93].

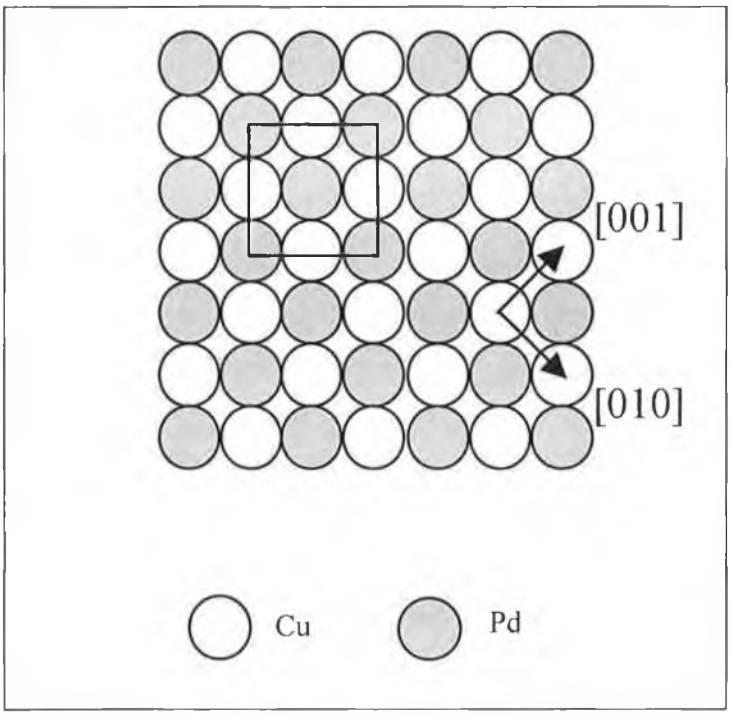

Figure 12: Schematic model of the Cu(100)-c(2×2)-Pd alloy structure. The c(2×2) unit cell is indicated.

Figure 12 illustrates an atomic model of the c(2×2) phase. The Pd atoms are relaxed 0.02 Å outwards from the Cu atoms in the outermost layer with the interlayer spacing of the first layer with regard to the second remaining similar to that of the copper substrate. The issue of most contention regarding this system is the exact coverage needed to complete an ordered c(2×2) structure and also the origin of a more ordered overlayer structure at higher coverages.

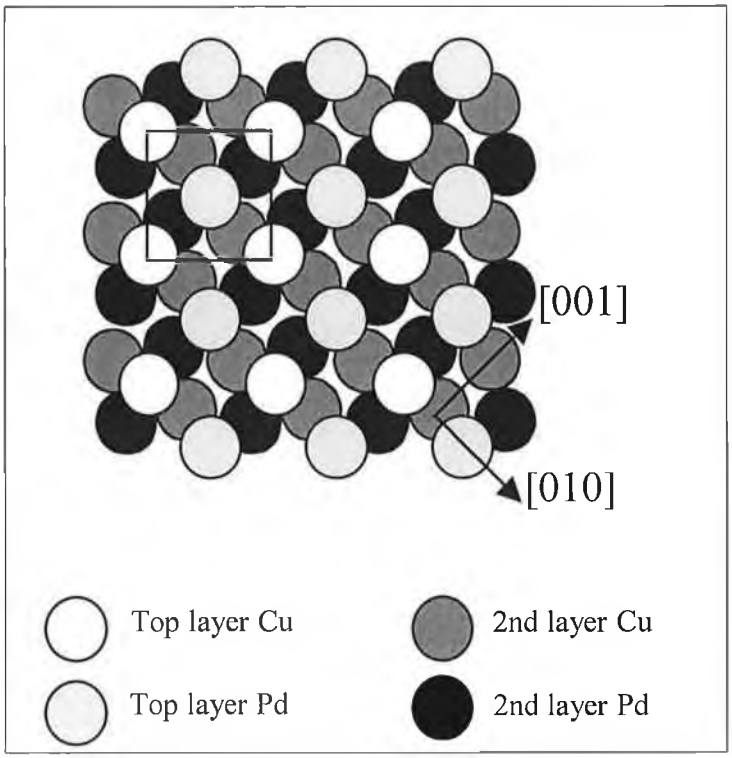

Figure 13: Proposed model for the (2×2)p4g structure based on the STM results of [93] and ion scattering [98]. The schematic reveals that the structure consists of two mixed Cu/Pd layers. The surface layer is a p(2×2) structure consisting of 0.25 ML Pd and 0.25 ML Cu, which is located on top of the "clock rotated" c(2×2) alloy phase. The (2×2) unit cell is marked.

Graham et al [94,95] suggest a coverage of 0.8 ML for an ideal c(2×2) while Pope et al [96] and Wu et al [97] agree on 0.55 ML. Both Graham [95] and Valden [98] et al report the presence of sub-surface Pd in the Cu(100)-c(2×2)-Pd system at "maximum perfection" as monitored by LEED. Valden et al, using CO as a probe molecule, propose the presence of pure Cu islands in the outermost layer due to ejected Cu

atoms coalescing after Pd place-exchange upon alloy formation. A value of 40% was calculated for the percentage of pure (non-alloyed) Cu in the outer layer for a Pd coverage of 0.5 ML. Valden also reports upper step and island edges to be Cu-rich regions. The Cu in these regions is suggested from STM examination to form a second layer structure classified as a p(2×2) [93]. This second layer seems to adopt a p4g symmetry from LEED while the topmost layer is seen from STM to contain one Pd and one Cu atom per unit cell. Thus, for continued deposition it is proposed that the topmost layer is a mixed alloy of Pd and Cu, forming on top of a p4g reconstructed c(2×2). Figure 13 illustrates the schematic of the model proposed by Murray et al [93]. According to their STM studies no rotation of the top layer takes place and subsequently the underlying c(2×2) layer is rotated in a clock-like mechanism. It is proposed that this restructuring leads to expansion of the fourfold hollow sites to accommodate the larger Pd atoms. It is suggested that the second layer consists of a 50% Pd and 50% Cu mix. The LEIS studies of Yao et al [99] confirmed the 50% Cu and Pd top layer composition.

Embedded atom method (EAM) calculations carried out by Pope et al [100] suggest that CuPd islands formed after Cu atom ejection upon initial Pd place exchange are most likely to reside on pure copper regions as opposed to CuPd c(2×2) alloy. Moreover, STM examinations at lower Pd coverages show that growth proceeds with Cu islands, resulting from Pd place exchange, tending to cover alloyed regions [93].

Pope et al [101] have examined CO desorption from the Cu(100)/Pd system. The presence of a CO desorption peak intermediate between Cu(100) (175 K) and Pd(100) (500 K) at 380 K is seen for Pd deposition at 110 K where Pd is kinetically inhibited by alloying. Pd growth at room temperature reveals the attenuation of the Cu-like CO desorption features found at 140 and 172 K and the development of a new feature at 270 K which is seen to increase in intensity with increasing Pd coverage. Increasing Pd coverage to 1 ML reveals a broadening of the Pd–CO feature, extending between 250 and 350 K. The width of this desorption feature suggests the presence of many different Pd–CO binding sites. Interestingly, annealing a 1 ML Pd film deposited at room temperature to 340 K reveals a Pd–CO desorption peak area of less than 35% of the as-deposited value, with a single desorption feature remaining at 315 K. The temperature of CO desorption from Cu atoms in the interfacial layers seems constant with increasing Pd coverage.

Moreover, only half the saturation CO desorption is from the c(2×2) alloy, the rest being from pure Cu. Pope et al [100,101] also suggest that the drop in CO saturation coverage by one-third seen over the first 0.25 ML of deposited Pd is due to CO adsorption-site blocking by top layer adatoms.

Bridge-site bonding of CO is preferable for adsorption on Pd(100) although the c(2×2) surface alloy has no nearest neighbour Pd pairs. Thus, the limitation of adsorption to atop sites is suggested for coverages less than 0.5 ML Pd and that the broadening of the 270 K feature to higher temperature is attributable to the bridge bonding and therefore increased stability of CO at Pd coverages above 0.5 ML.

Hydrogen chemisorption has also been used to probe the Cu(100)-c(2×2)-Pd surface alloy [100]. Hydrogen does not dissociatively adsorb on Cu(100) while it does readily on Pd(100) (main desorption peak at 355 K with a shoulder at 275 K). It is expected that, like other bimetallic systems, the extent of adsorption is proportional to the number of Pd atoms in (1×1) close packed islands [102]. Thermal desorption spectra of the 0.5 ML Pd room temperature deposited structure revealed no H_2 adsorption, evidence of a surface consisting of only c(2×2) alloy or pure Cu regions (no (1×1) Pd regions). For a 1 ML Pd film deposited at 100 K a broad desorption feature between 210 and 350 K results which is considerably different from that seen for a 1 ML Pd film deposited at 300 K. In this case as expected desorption after H_2 exposure is much smaller than the 100 K deposited film with the peak much narrower and extending from 230 to 300 K. Annealing the 300 K deposited film to 340 K did not affect the desorption peak.

A layer-by-layer room temperature growth mechanism has been suggested on the basis of Auger uptake studies for Pd on Cu(111) [88]. More recently for submonolayer Pd growth on Cu(111), STM indicates the random ordering of Pd at room temperature with the preferred structure that of single-layer dendritic islands nucleated at steps. At elevated temperature (~450 K) double-layer islands and pit formation is evidenced with the possibility of Cu capping the Pd islands [103]. Random Pd alloying with surface Cu results at higher temperatures (~500 K). The exact mechanism of Pd incorporation is unknown with the absence of any long-range ordering. It is however tenuously proposed that alloying of Pd into the terraces is concomitant with the removal of Cu from the step edges.

Aside from early LEED work by Fujinaga [88,89] the only detailed study to date of Pd growth on Cu(110) is that of Murray et al [104] who utilised STM to study the growth mechanism and structure of Pd films at low coverage (up to 0.3 ML). Initial alloying is seen as the formation of linear -Cu-Pd- chains in the $[1\,\bar{1}\,0]$ direction. Low Pd coverage leads to substitution of Pd atoms into the outermost Cu layer forming an ordered (2×1) CuPd surface alloy via periodic substitution of every second Cu atom along the $[1\,\bar{1}\,0]$ rows by Pd, with expelled Cu atoms diffusing to step edges. The coating of the alloy by expelled Cu in the form of islands produces a structure identical to the equilibrium structure of $Cu_3Pd(110)$ which is also terminated by a Cu layer. As the Pd coverage increases, larger domains of (2×1) alloy form and are covered by Cu originating not just from ejected Cu but also from step edges and from the Cu(110) terraces which exhibit monolayer deep "pits". It appears that a sub-surface second layer (2×1) CuPd alloy covered by a copper monolayer is the stable structure at higher Pd coverages. Further evidence for this mechanism is the lack of any indication of Pd atoms in the island or pit structures. In contrast the CuPd (2×1) chains formed at low Pd coverage ($\theta_{Pd} \leq 0.17$ ML) remain uncovered due to the necessary formation of a large number of high energy Cu edge atoms in a small 2-D island which would be required to "cap" the chain.

The stability of the double layer monolayer islands formed upon exposure to Pd was investigated by the adsorption of oxygen. Cu islands on a pure Cu lattice would be predicted to be eroded away due to the formation of -Cu-O- added rows [105]. Formation of added rows was observed although very little erosion of the islands took place. This provided evidence that the Cu atoms forming the islands are much more strongly bound than that expected if they were located on top of a pure Cu lattice. The Cu islands coating the alloy have been shown to be stable on the time scale of hours. However, upon exposure to CO increased mobility is noted. The increased mobility may in some ways be coupled to the fact that CO bonds to Pd more strongly in a Cu matrix than to Cu atoms themselves [101]. Under an ambient of CO, Pd atoms may be drawn from their subsurface positions to the surface layer thereby releasing the Cu atoms originally covering them. This type of chemical extraction has been previously observed. For example, the Pt rich Pt-Rh(100) surface sees Rh atoms in the second layer replace Pt atoms in the first upon exposure to

oxygen [106]. Figure 14 illustrates the most probable structure of a 0.5 ML Pd/Cu(110) film, illustrating a Cu coated p(2×1) CuPd alloy.

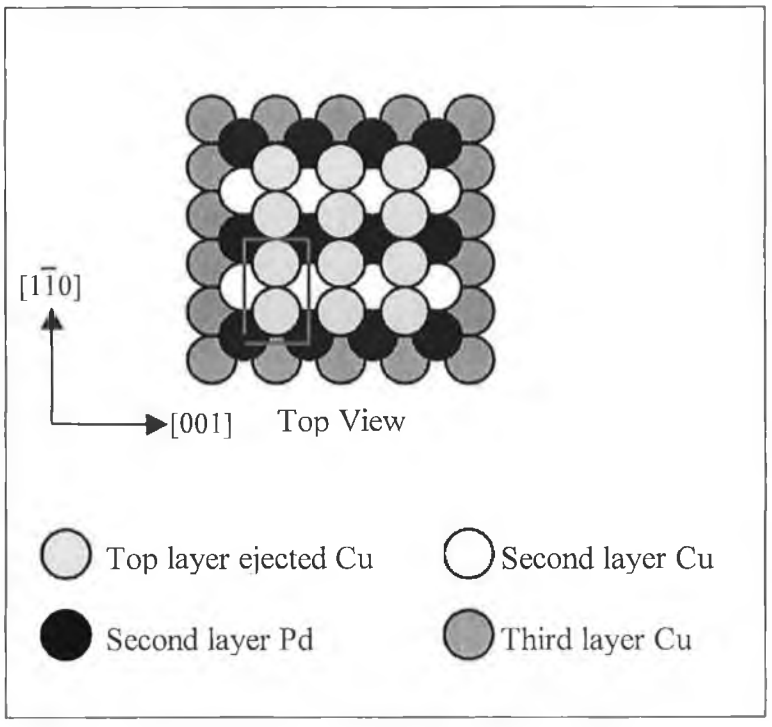

Figure 14: Proposed model for the p(2×1) CuPd alloy structure based on the STM results of [104] for 0.5 ML Pd on Cu(110). The (2×1) unit cell is marked.

1.5.4. Supported Cu-Pd bimetallics

The catalytic activity of supported metals may be often improved by the addition of a small amount of another metal or by completely alloying with another metallic component. Surprisingly, the number of studies pertaining to Pd-Cu supported catalysts is quite limited. Some of the few studies on this system include the following:

High-resolution transmission electron microscopy (HRTEM) and energy dispersive X-ray (EDX) studies have been carried out on Cu-Pd particles supported on amorphous carbon [107]. It is suggested that the sintering of formed particles in both CO and CO/H_2 environments favour Pd surface segregation owing to the large heat of adsorption of Pd for CO compared to Cu (36 kcal/mol and 18 kcal/mol,

respectively). Further examination using EDX microanalysis of particles, reacted in CO at 500–600 K, revealed particles with Pd-rich edges. Auger electron microscopy (AEM) also revealed Pd-rich particle surfaces after sintering in CO.

Kojima and Kurahashi [108] have carried out an STM study of bimetallic Cu-Pd clusters on graphite. Simultaneous UHV evaporation of 3 ML's of each metal, with the sample held at 550 °C, revealed epitaxial crystallites of 200 to 400 nm in width and 5 to 8 nm in height. Simultaneous deposition produced thinner crystallites than that seen for the single deposition of Pd. AES measurements revealed that co-deposited crystallites consisted mostly of Pd even though equal amounts of both metals were deposited on the surface. AES measurements also revealed the surface of the metallic particles to consist mostly of Pd atoms. STM images of the topmost layer of the (111) crystallite face exhibited a periodic structure with an observed atomic distance of 0.27 nm, slightly smaller than that of a bulk Pd crystal.

Gimenez et al [109,110] have studied the simultaneous growth of Cu-Pd on NaCl(100), held at 623 K, by HRTEM and EDX as examination techniques. It was reported that the initial condensation coefficients for Cu and Pd are around 0.01 and 0.3, respectively, when the metals are deposited alone. It is stipulated that Pd controls the evolution of the bimetallic particles during simultaneous deposition and that owing to the large disparity in condensation coefficients, Cu is only incorporated by the direct impingement on the nucleated particles as opposed to alloying after diffusion on the substrate. In these experiments the atoms with the higher energy of adsorption, Pd in Cu-Pd, form nuclei preferentially, and the composition of the growing film is initially enriched in the element that is most strongly bound to the surface. This theory is further supported by the fact that even when the particles are quite large (20 nm) the concentration in Cu is still well below the nominal concentration expected from the ratio of the beam fluxes. This is in agreement with the AES measurements of Kojima and Kurahashi [108] whom also reported Pd enrichment of the supported metallic particles after simultaneous deposition of similar Cu and Pd compositions. Studies involving Pd–Au systems have also been carried out [111,112]. Again the large difference in sticking coefficient between Pd and Au mirrors that of the Cu-Pd system. The incorporation of Au into the bimetallic particles is only significant when the probability of direct impingement on the growing clusters is high.

1.6. Overview

The work in this thesis is centred on the CuPd bimetallic system and includes (Chapters 3 and 4) results of the formation and structural and compositional characterisation of bimetallic CuPd surfaces by two different methods:

(a) formation of single crystal bimetallic and surface alloy systems by evaporation of Pd onto a Cu(110) single crystal;
(b) formation of model supported CuPd nano-particles by co-evaporation of Cu and Pd onto a highly orientated pyrolytic graphite (HOPG) support.

The study of a system closely related to that of CuPd namely the CuPt system has also been examined during the course of this thesis. In Chapter 5 both the structure and reactivity of a CuPt surface alloy formed by the evaporation of Pt onto a Cu(100) single crystal are considered.

Finally, two appendices are also included in this thesis. Appendix A comprises the design and construction of a molecular beam scattering apparatus (carried out in parallel to the characterisation of these model bimetallic catalysts) for the purpose of future studies of the adsorption and surface reactivity of these and other bimetallic systems, with facilities for temperature programmed thermal desorption spectroscopy (TPD), temperature programmed reaction spectroscopy (TPRS), measurement of gas sticking probabilities and catalytic reaction rates and mechanisms.
Appendix B outlines the characterisation of low-pressure argon and hydrogen capacitively coupled radio-frequency plasmas as well as the examination of plasma induced morphology changes on the HOPG surface, originally intended to be developed as a means of producing nucleation centres for anchoring nano-clusters.

References

[1] I. M. Campbell, Catalysis at Surfaces, University Press, Cambridge, (1988).

[2] M. A. van Hove, W. H. Weinberg and C. M. Chan, Low Energy Electron Diffraction: Experiment, Theory and Structural Determination, Springer-Verlag, Berlin, (1986).

[3] B. Lang, R. W. Joyner and G. A. Somorjai, Surf. Sci., 30 (1972) 440.

[4] G. A. Somorjai, Introduction to Surface Chemistry and Catalysis, Wiley Interscience, New York, (1994).

[5] T. N. Rhodin and G. Ertl, The Nature of the Surface Chemical Bond, North Holland Physics Publishing, Amsterdam, (1979).

[6] S. R. Morrison, The Chemical Physics of Surfaces, Plenum Press, New York, (1990).

[7] W. M. H. Sachtler and R. A. Van Santen, Adv. Catal., 26 (1977) 69.

[8] F. F. Abraham and C. R. Brundle, J. Vac. Sci. Technol., 18 (1981) 506.

[9] W. M. H. Sachtler and R. A. Van Santen, 3 (1979) 121.

[10] U. Bardi, Rep. Prog. Phys., 57 (1994) 939.

[11] F. W. Jones and C. Sykes, J. Inst. Metals, 65 (1939) 419.

[12] G. Borelius, C. H. Johansson and J. O. Linde, Ann. Physik, 86 (1928) 291.

[13] B. Svensson, Ann. Physik, 14 (1932) 699.

[14] J. O. Linde, Ann. Physik., 15 (1932) 249.

[15] C. H. Johansson and J. O. Linde, Ann. Physik, 82 (1927) 449.

[16] L. Z. Mezey and J. Giber, Jap. J. Appl. Phys., 21 (1982) 1569.

[17] W. R. Tyson and W. A. Miller, Surf. Sci., 62 (1977) 267.

[18] R. J. Cole, N. J. Brooks and P. Weightman, Phys. Rev. B, 56 (1997) 12178.

[19] N. Martensson, R. Nyholm, H. Calén, J. Hedman and B. Johansson, Phys. Rev. B, 24 (1981) 1725.

[20] G. G. Kleiman, R. Landers, S. G. C. de Castro and J. D. Rogers, Phys. Rev. B, 44 (1992) 8529.

[21] V. S. Sundaram, M. B. de Moraes, J. D. Rogers and G. G. Kleiman, J. Phys. F, 11 (1981) 1151.

[22] R. S. Rao, A. Bansil, H. Asonen and M. Pessa, Phys. Rev. B, 29 (1984) 1713.

[23] T. -U. Nahm, M. Han, S. -J. Oh, J. -H. Park, J. W. Allen and S. -M. Chung, Phys. Rev. B, 51 (1995) 8140.

[24] H. Wright, P. Weightman, P.T. Andrews, W. Folkerts, C. F. J. Flipse. G. A. Sawatzky, G. P. Diakun, D. Norman and H. Padmore, Phys. Rev. B, 35 (1987) 519.

[25] H. Winter, P. J. Durham, W. M. Temmerman and G. M. Stocks, Phys. Rev. B, 33 (1986) 2370.

[26] C. J. Barnes, M. Gleeson, S. Sarakorpi and M. Lindros, submitted to Surface Science.

[27] B. Ginatempo, G. Y. Guo, W. M. Temmerman, J. B. Staunton and P. J. Durham, Phys. Rev. B, 42 (1990) 2761.

[28] J. A. Rodriguez, J. Phys. Chem., 98 (1994) 5758.

[29] M. T. Paffett, C. T. Campbell, , T. N. Taylor and S. Srinivasan, Surf. Sci., 154 (1985) 284.

[30] K. Hermann, P. S. Bagus and C. J. Nelin, Phys. Rev. B, 35 (1987) 9467.

[31] K. I. Choi and M. A. Vannice, J. Catal., 131 (1991) 36.

[32] F. Skoda, M. P. Astier, G. M. Pajonk and M. Primet, Catal. Lett., 29 (1994) 159.

[33] J. A. Anderson, M. Fernández-Garcia and G. L. Haller, J. Catal., 164 (1996) 477.

[34] J. H. Sinfelt and J. A. Cusumano in: Advanced Materials in Catalysis, Eds., J. J. Burton and R. L. Garten, Academic Press, London, (1977) pp. 1–31.

[35] G. W. Graham, Surf. Sci., 268 (1992) 25.

[36] A. R. Balkenende, O. L. J. Gijzeman and J. W. Geus, Appl. Surf. Sci., 37 (1989) 189.

[37] V. Ponec, Surf. Sci., 272 (1992) 111.

[38] J. H. Sinfelt, Bimetallic Catalysts, Wiley, New York, (1983).

[39] J. F. Walker in: Formaldehyde, Reinhold, New York, (1964).

[40] Y. Debauge, M. Abon, J. C. Bertolini, J. Massardier and A. Rochefort, Appl. Surf. Sci., 90 (1995) 15.

[41] R. H. Bergmans, M. Van der Grift, A. W. Dernier van der Gon and H. H. Brongersma, Surf. Sci., 345 (1996) 303.

[42] R. H. Bergmans, M. Van der Grift, A. W. Dernier van der Gon, R. G. van Welzenis, H. H. Brongersma, S. M. Francis and M. Bowker, Nucl. Instrum. Methods B, 85 (1994) 435.

[43] M. A. Newton and M. Bowker, Surf. Sci., 307–309 (1994) 445.

[44] C. Cottrell, M. Bowker, A. Hodgson and G. Worthy, Surf. Sci., 325 (1995) 57.

[45] M. A. Newton, S. M. Francis and M. Bowker, Surf. Sci., 269/270 (1992) 41.

[46] D J. Holmes, D. A. King and C. J. Barnes, Surf. Sci., 227 (1990) 179.

[47] M. A. Newton, S. M. Francis, X. Li, D. Law and M. Bowker, Surf. Sci. 259 (1991) 45.

[48] Y. Fujinaga, Surf. Sci., 86 (1979) 581.

[49] S. A. Chambers, Surf. Sci. Lett., 248 (1991) L274.

[50] M. A. Newton, S. M. Francis and M. Bowker, Phys. Rev. B., 45 (1992) 9451.

[51] P. Pudney and M. Bowker, Chem. Phys. Lett., 171 (1990) 373.

[52] M. Mousa, J. Laboda-Cackovic, S. Jaenicke and J. H. Block, Surf. Sci., 307–309 (1994) 401.

[53] J. W. He and P.R. Norton, Surf. Sci., 204 (1988) 26

[54] M. S. Mousa, J. Laboda-Cackovic and J. H. Block, Vacuum, 46 (1995) 117.

[55] A. Hammoudeh, M. S. Mousa and J. Laboda-Cackovic, Vacuum, 54 (1999) 239.

[56] M. S. Mousa, A. Hammoudeh and J. Laboda-Cackovic, Vacuum, 54 (1999) 251.

[57] R. Holroyd, Ph.D. Thesis, Reading Catalysis Centre, University of Reading, United Kingdom.

[58] E. Bauer, Z. Kristallogr., 110 (1958) 372.

[59] B. Lewis and J. C. Anderson, Nucleation and Growth of Thin Films, Academic press, London, (1978).

[60] J. A. Venables, G. D. T. Spiller and M. Hanbucken, Rep. Prog. Phys., 47 (1984) 399.

[61] H. Asonen, C. J. Barnes, A. Salokatve and Vuoristo, Applic. Surf. Sci., 22/23 (1985) 556.

[62] H. Li, S. C. Wu, D. Tian, J. Quinn, Y. S. Li, F. Jona and P. M. Marcus, Phys. Rev. B, 40 (1989) 5841.

[63] E. Hahn, E. Kampshoff, N. Wälchli and K. Kern, Phys. Rev. Lett., 74 (1995) 1803.

[64] I. A. Morrison, M. H. Kang and E. J. Mele, Phys. Rev. B, 39 (1989) 1575.

[65] F. Maca and J. Koukal, Surf. Sci., 260 (992) 323.

[66] R. W. Vook, J. V. Bucci and S. S. Chao, Thin Solid films, 163 (1988) 447.

[67] F. Jensen, F. Besenbacher and I. Stensgaard, Surf. Sci., 269/270 (1992) 400.

[68] H. Li, D. Tian, F. Jona and P. W. Marcus, Solid State Commun., 77 (1991) 651.

[69] E. Hahn, E. Kampshoff and K. Kern, Chem. Phys. Lett., 223 (1994) 347.

[70] E. Hahn, E. Kampshoff, A. Fricke, J. -P. Bucher and K. Kern, Surf. Sci., 319 (1994) 277.

[71] E. Kampshoff, E. Hahn and K. Kern, Phys. Rev. Lett., 73 (1994) 704.

[72] J. -P. Bucher, E. Hahn, P. Fernandez, C. Massobrio and K. Kern, Europhys. Lett., 27 (1994) 473.

[73] C. Massobrio and P. Fernandez, J. Chem. Phys., 102 (1995) 605.

[74] H. Roeder, E. Hahn, H. Brune, J. P. Bucher and K. Kern, Nature, 366 (1993) 141.

[75] H. Röder, H. Brune, J. P. Bucher and K. Kern, Surf. Sci., 298 (1993) 121.

[76] F. C. Frank and J. H. Van der Merwe, Proc. R. Soc. London A, 198 (1949) 205.

[77] R. J. Asaro and W. A. Tiller, Metall. Trans., 3 (1972) 1798.

[78] J. G. Dash, J. Vac. Sci. Technol. A, 5 (1986) 1523.

[79] M. T. Paffett, C. T. Campbell, T. N. Taylor and S. Srinivasan, Surf. Sci., 154 (1985) 284.

[80] B. Hammer, M. Scheffler, K. W. Jacobsen and J. K. Nørskov, Phys. Rev. Lett., 73 (1994) 1400.

[81] K. Christmann, Surf. Sci. Rep., 9 (1988) 1.

[82] D. W. Goodman and C. H. F. Peden, J. Catal., 95 (1986) 321.

[83] E. Bauer in: Dynamic Processes at Solid Surfaces and Heterogeneous Catalysis, Vol. 3, Eds. D. A. King and D. P. Woodruff, Elsevier, Amsterdam, (1984) Chap. 1.

[84] G. A. Attard and D. A. King, Surf. Sci., 188 (1987) 587; 222 (1989) 360.

[85] P. Hu, A. Wander, L. Morales de le Garza, M. P. Bessent and D. A. King, Surf. Sci., 286 (1993) L542.

[86] L. Pleth Nielsen, I. Stensgaard, E. Lægsgaard and F. Besenbacher, Surf. Sci., 307-309, (1994) 544.

[87] C. T. Chan, K. P. Bohnen and K. M. Ho, Phys. Rev. Lett., 69 (1992) 1672.

[88] Y. Fujinaga, Surf. Sci., 84 (1979) 1.

[89] Y. Fujinaga, Surf. Sci., 86 (1979) 581.

[90] C. Nagl, E. Platzgummer, O. Haller, M. Schmid and P. Varga, Surf. Sci., 331–333 (1995) 831.

[91] R. G. P. van der Kraan and H. van Kempen, Surf. Sci., 338 (1995) 19.

[92] D. D. Chambliss and S. Chiang, Surf. Sci., 264 (1992) L187.

[93] P. W. Murray, I. Stensgaard, E. Lægsgaard and F. Besenbacher, Surf. Sci., 365 (1996) 591 (and references therein).

[94] G. W. Graham, P. J. Schmitz and P. A. Thiel, Phys. Rev. B, 41 (1990) 3353.

[95] G. W. Graham, Surf. Sci., 171 (1986) L432.

[96] T. D. Pope, G. W. Anderson, K. Griffiths, P. R. Norton and G. W. Graham, Phys. Rev. B, 44 (1991) 11518.

[97] S. C. Wu, S. H. Lu, Z. Q. Wang, C. K. C. Lok, J. Quinn, Y. S. Li, D. Tian, F. Jona and P. M. Marcus, Phys. Rev. B, 38 (1988) 5363.

[98] M. Valden, J. Aaltonen, M. Pessa, M. Gleeson and C. Barnes, Chem. Phys. Lett., 228 (1994) 529.

[99] J. Yao, Y. G. Shen, D. J. O'Connor and B. V. King, J. Vac. Sci. Technol. A, 13 (1995) 1443.

[100] T. D. Pope, M. Vos, H. T. Tang, K. Griffiths, I. V. Mitchell, P. R. Norton, W. Liu, Y. S. Li, K. A. R. Mitchell, Z. -J. Tian and J. E. Black, Surf. Sci., 337 (1995) 79.

[101] T. D. Pope, K. Griffiths, P. R. Norton, Surf. Sci., 306 (1994) 294.

[102] T. D. Pope, K. Griffiths, V. P. Zhdanov and P. R. Norton, Phys. Rev. B, 50 (1994) 18553.

[103] G. O. Pötschke and R. J. Behm, Phys. Rev. Lett., 44 (1991) 1442.

[104] P. W. Murray, S. Thorshaug, I. Stensgaard, F. Besenbacher, E. Lægsgaard, A. V. Ruban, K. W. Jacobsen, G. Kopidakis and H. L. Skriver, Phys. Rev. B, 55 (1997) 1380.

[105] F. Jensen, F. Besenbacher, E. Lægsgaard and I. Stensgaard, Phys. Rev. B, 41 (1990) 10233.

[106] T. Yamada, H. Hirano, K. Tanaka, J. Siera and B. E. Nieuwenhuys, Surf. Sci., 226 (1990) 1.

[107] P. L. Gai and B. C. Smith, Ultramicroscopy, 34 (1990) 17.

[108] I. Kojima and M. Kurahashi, J. Vac. Sci. Technol. B, 12 (1994) 1780.

[109] F. Gimenez, Ph.D. Thesis, Marseille, 1997.

[110] F. Gimenez, C. Chapon, S. Giorgio and C. R. Henry, Proc. ICEM 13, Paris, p. 354.

[111] A. Schmitz, V. Schünemann and R. Anton, Phys. Rev. B, 41 (1990) 11875.

[112] A. Schmitz, M. Spode, J. Heinrich and R. Anton, Thin Solid Films, 196 (1991) 253.

Chapter Two

Physical Basis of Experimental Techniques Utilised

1. Surface structural determination

In this chapter the basis of the techniques employed to examine the different forms of CuPd(Pt) bimetallic catalysts studied during this thesis is described. The unambiguous determination of catalyst systems involves the determination of both structure and reactivity, which are intimately linked.

In attempting to understand surfaces we must employ techniques which provide information on an adsorbate (if present), and the substrate selvedge (region of the solid in the vicinity of the mathematical surface). To this effect it is often necessary to use a combination of techniques. The information required consists of the physical morphology and surface structure, the chemical composition, the electronic structure and the molecular structure of adsorbed surface species. Subsequently, it is important to combine techniques which provide complementary information.

A number of surface sensitive electron spectroscopies have been utilised in the course of the research carried out in this thesis and include scanning tunnelling microscopy (STM), low energy electron diffraction (LEED), X-ray photoelectron spectroscopy (XPS) and Auger electron spectroscopy (AES). Reactivity studies have also been carried out using temperature programmed desorption (TPD). In the following section a brief overview of each technique is provided.

1.1. Scanning tunnelling microscopy (STM)

1.1.1. The birth of STM

STM is unique among imaging techniques in that it affords three-dimensional real space surface imaging. The concept of STM is quite simple with images obtained by scanning a sharp metal tip over the sample surface, analogous to the operation of a profilometer. The STM tip does not however make contact with the sample and is usually maintained at a distance of about 5–50 Å above the sample. The STM image is in fact a map of the surface electron density and for surfaces of fairly uniform electron density the STM image effectively represents the surface topography. The men recognised as developers of STM technology in the early 1980's are Binnig, Rohrer, Gerber and Weibel at the IBM Rüschlikon laboratory [1,2]. The early design incorporated a piezoelectric tripod scanner and a piezoelectric walker (the 'louse') to allow for the approach of the sample and tip. On 16 March, 1981, the first experiments, revealing an exponential dependence of the tunnelling current, *I*, on the tip–surface separation, *s*, were measured using a tungsten tip and a platinum sample. Surprisingly, atomic resolution was first achieved only a year later in the autumn of 1982 when the structure of the Si(111) 7x7 surface [3] was successfully imaged.
The unique ability to achieve atomic resolution in real time has become one of the STM's most valuable features. Its high lateral and vertical resolution make it an outstanding microscopy. Binnig and Rohrer were awarded the Noble prize for physics in 1986.

1.1.2. STM: theory and operation

If two conductors of differing work function are brought sufficiently close together, quantum mechanical tunnelling between them occurs leading to a small current flow between sample and tip. This is due to the electron wavefunctions leaking out of their confining potential wells in a solid with what is known as a characteristic exponential inverse decay length, *K*, given by

$$K = \frac{(2m\phi)^{1/2}}{\hbar} \qquad 1.1$$

where $\hbar$ is Planck's constant divided by 2π; ϕ is the effective local work function; and m the electron mass. It is often convenient to write $K \approx 0.51\ \phi^{1/2}$ where K is in Ångströms and ϕ in eV. If a conducting sample and tip are brought sufficiently close (about 4 Å) with a potential V applied between them, then quantum mechanical tunnelling occurs and a current I will flow across the gap.

At low voltages and temperatures:

$$I \alpha \exp(-2Kd) \qquad 1.2$$

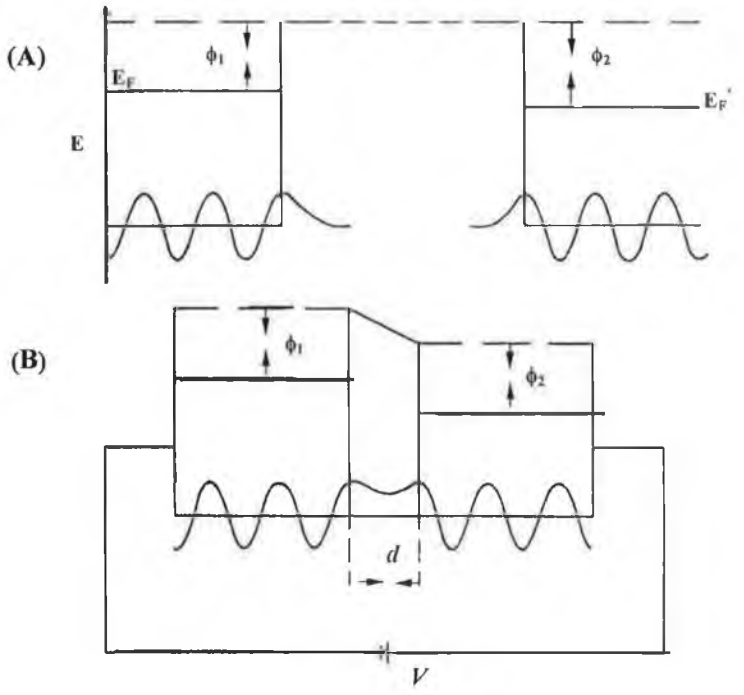

Figure 1: (A) Electron wavefunctions for two separate metals 1 and 2 with work functions ϕ_1 and ϕ_2. (B) Electron wavefunction for the same two metals separated by a small distance d; V is the bias potential. Tunnelling through the barrier may now proceed since the wavefunctions overlap.

where d is the distance between the electrodes, as shown in figure 1. For a work function of ~4 eV, $K = 1.0$ Å^{-1}. Typically, I decreases by an order of magnitude when the gap, d, is changed by only 1 Å. Alternatively, if the current is kept constant within a few percent, then the gap, d, remains constant within about 0.01 Å. This

forms the basis of the STM whereby an electrode, usually an atomically sharp tip, is scanned mechanically across a surface.

There are two basic modes of operation:

(a) Constant current

In this mode of operation the tip is brought sufficiently close to the surface (at a suitable bias voltage (typically up to 2 V) so that the tunnelling current is measurable. A feedback mechanism allows the distance, d, between the surface and the tip to change so as to maintain a constant tunnelling current as the tip is scanned laterally across the surface. Owing to the exponential dependence of I on d, this has the effect of scanning the tip over the surface at constant surface tip separation so that a plot of z versus the x and y co-ordinates of the tip is a set of contours of the surface below the tip. An image will actually comprise a set of multiple scans displaced laterally from each other in the y direction.

(b) Constant height

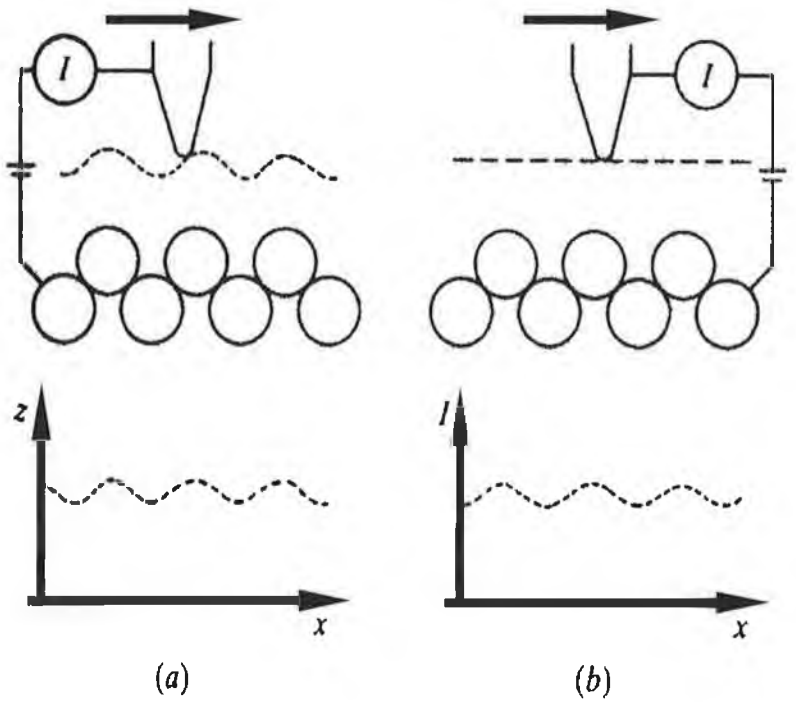

Figure 2: Scanning modes for STM: (a) constant current mode; (b) constant height mode. The dotted line represents the path traced by the tip.

During this mode of the operation the tip is scanned across the surface at a constant height and bias voltage, while the tunnelling current is measured. Again multiple scans displaced laterally in the y direction are carried out in capturing the image. Figure 2 illustrates both modes of operation.

The theory of tunnelling makes no distinction between the surface and the tip. This distinction is however critical, especially in STM. The difficulty arises due to the fact that the measured current involves a complicated convolution of the electron states of both surface and tip. The STM image obtained should ideally only represent the surface properties.

One means of achieving this involves the use of the s-wave model. Tersoff & Hamann [2] (1985) incorporating this model, successfully removed the tip properties from the image by considering a particular model for the tip in which the potential and wavefunctions were arbitrarily localised. In such a case, in the limit of small voltage, the tunnelling conductance, σ, is given by

$$\sigma \alpha \rho(\mathrm{r}_t, \mathrm{E}_F) \qquad 1.3$$

where r_t is the tip position, E_F is the Fermi energy, and

$$\rho(r, \mathrm{E}) \equiv \sum |\psi_v(\mathrm{r})|^2 \delta(\mathrm{E}_v - \mathrm{E}) \qquad 1.4$$

is the local density of states (LDOS) at point r and E.

Within these limitations the STM image may be interpreted directly by noting that the current is proportional to the surface LDOS at E_F, measured at the tip position. In other words, the tip path should map out a contour of constant Fermi-level LDOS for the bare surface. This result is true even if the tip is actually of arbitrary size as long as its wavefunction at E_F can be adequately approximated by a s-wave wavefunction, and r_t is taken to be the centre of curvature of the tip wavefunction [3].

Problems with these models have been encountered when it comes to proposed resolution capabilities of the STM. Suggestions that STM performance is largely

independent of tip material have also been questioned. Tersoff & Hamann (1985) [2] and Lang (1986) [3] predicted STM resolution of no better than 6–9 Å. This does not agree with experimental data where atomic resolution may be readily obtained. Chen (1989) [4] considered the actual electronic states of the real tip and predicted that closely packed metal surface atomic resolution with the STM requires localised metallic pz or dz^2 tip states. In consequence, the only tip materials providing this are d-band transition metals such as W, Pt and Ir. With these tip states, the nucleus of the apex atom of the tip follows a contour determined by the derivative of the surface wavefunction of the sample.

The microscope itself is shown in figure 3 demonstrating the atoms from which tunnelling takes place. This is known as the tripod scanner. The translation and distance determining devices are piezoelectric scanners upon which the tip is mounted and which can be built up by bars, tubes or biomorphs [5,6]. These units allow full three-dimensional movement of the tip. A compact single piezo-electrode scanner is generally used for full three-dimensional movement (figure 4(b)). The electrode is divided into four segments. Pairs of opposite outer electrode segments can be simply subjected to a voltage leading to bending of the tube in the x–y directions while z motion is achieved by expansion or contraction along the tube axis [7]. Application of a voltage to electrode segments opposite to each other i.e., two equal and opposite voltages on two opposite quadrants leads to movement of the tubes in the $x(y)$ direction. If a voltage Up is applied to opposite electrodes of a *piezoelectric tube* of thickness h and length l (figure 4(a)), the resulting length change Δl is given by

$$\Delta l = d_{31}\frac{l}{h}Up \qquad 1.5$$

where d_{31} is the relevant piezoelectric coefficient. On the other hand if a voltage is applied to just one quadrant (asymmetrically), then the deflection of the tube is exactly half of the deflection obtained for the symmetric case.

Piezoelectric materials are essentially ceramics which undergo a change in length on the application of an external electric field. Piezoelectric devices [8,9,10] used in STM, otherwise known as transducers convert electrical energy into mechanical

strains, or vice versa. The inducement of polarisation in ionic materials such as those used in piezo-drives, acts to displace cations in one direction and anions in the opposite direction. So for the arrangement in figure 4(b) lateral motion of scanning is achieved by the application of voltage across the tube while for vertical motion of scanning the voltage is applied between the inside and the outside of the tube.

The direction and extent of the applied field will determine the force exerted on the piezo-device. Piezoelectric materials include titanates of barium and lead, lead zirconate ($PbZrO_3$), ammonium dihydrogen phosphate ($NH_4H_2PO_4$), and quartz. This property is characteristic of materials having a complicated crystal structure with a low degree of symmetry.

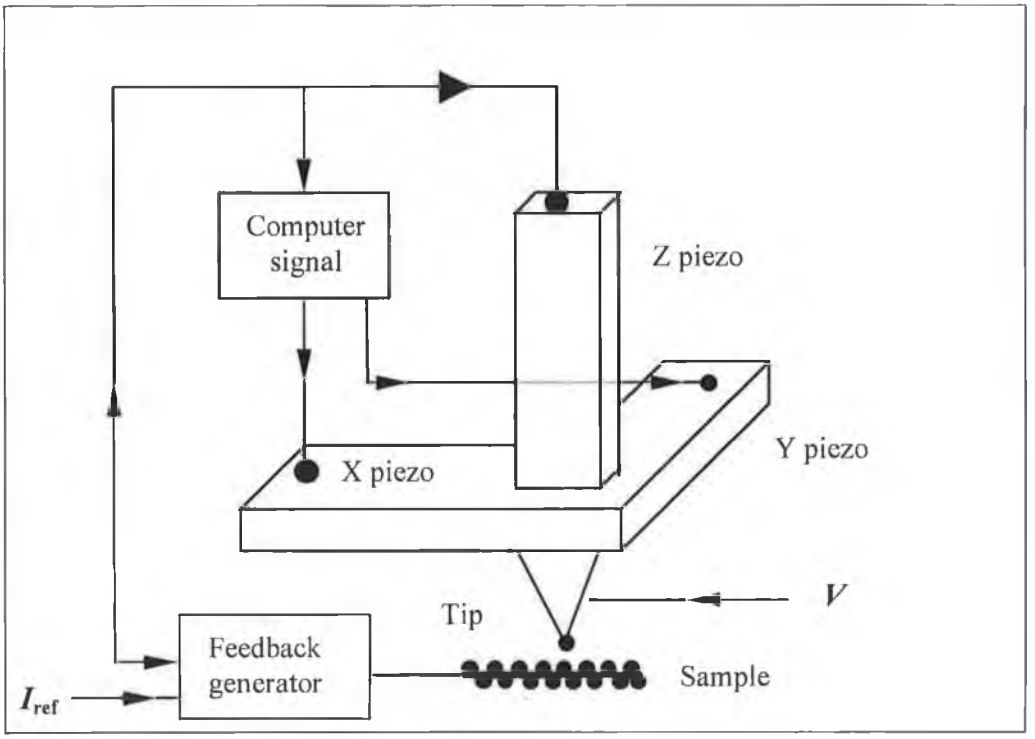

Figure 3: Schematic diagram of the STM.

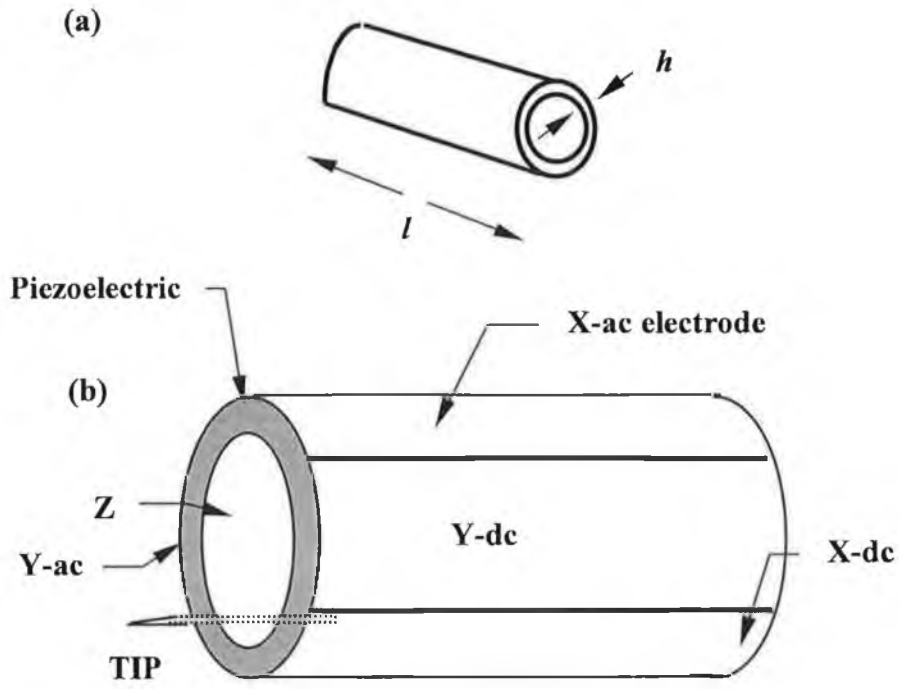

Figure 4: (a) Piezoelectric tube. (b) Tube scanner with the electrode sectioned into four equal areas parallel to the axis of the tube. As a voltage is applied to a single outside electrode the tube bends away from that electrode. Voltage applied to the inside electrode causes a uniform elongation. A small a.c. signal and a large d.c. offset can be separated on electrodes 180° apart.

The mechanical movement of the STM must be controlled by sensitive electronics. The tip (or sample) voltage is applied by a computer-controlled digital-to-analogue converter (DAC) using a low-voltage power supply. The tunnelling current is measured by a preamplifier with a gain of 10^6–10^9 V A^{-1}. A logarithmic amplifier linearising the tunnelling current signal, which is exponentially dependent on the separation between tip and sample, allows the dynamic range of the STM to be improved. This is important when scanning rough surfaces, while being essentially obsolete for atomically flat ones. The measured current is compared with that demanded (the reference current, typically 10 pA–10 nA) and the resultant error signal is fed into the feedback amplifiers which usually consist of a proportional amplifier and analogue integrator. The feedback signal is finally fed into a high-

voltage amplifier which generates the *z* piezoelectric drive. Scanning the tip in the *x–y* plane is achieved by using either computer-controlled DAC's or synchronised ramp generators with a subsequent signal amplification by high-voltage amplifiers. Typically to drive the piezoelectric elements variable gain high-voltage amplifiers are used. For example, using a gain of one, a 12-bit analogue to digital converter (ADC) and a piezoelectric constant of 15 Å/V, the smallest change in *z* displacement is 1.1 Å. However, if a gain of 20 is possible the potential resolution improves to 0.055 Å. In the case of the *x* and *y* scanners the range of the extension is reduced by increasing the gain of the amplifier; therefore, for large scale features or large scans the gain should be low but for high resolution, both vertical and lateral, the gain should be high. It is common to run the x and y scanners at a different gain than the *z* amplifier.

Vitally important in STM circuit design is to ensure the use of sufficiently high quality components which will prevent white noise interference. This should be kept to a minimum ideally between 0.2 and 0.5 Å.

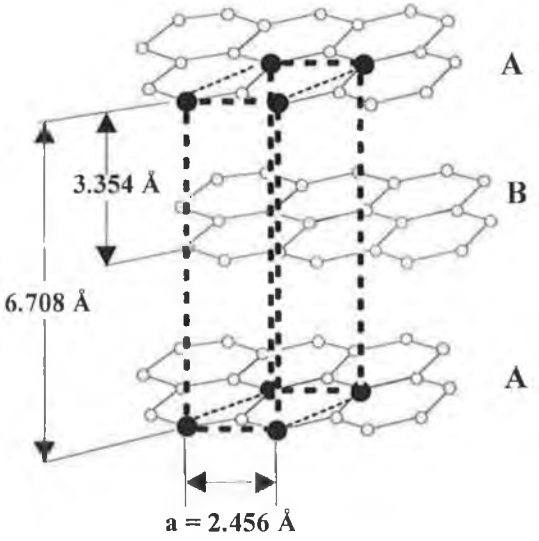

Figure 5: The structure of graphite showing the unit cell [11].

In terms of the tip geometry we ideally require a tip with a single atom at its apex to successfully achieve atomic resolution. The preparation of tungsten tips involves etching the tip with a NaOH solution while Pt-Ir tips are commonly prepared cutting the wire at an oblique angle. Other methods include applying a voltage pulse

between the tip and the sample which is suggested to draw atoms from the tip to it apex. The collision of the tip with the sample has also been used which is said to have the same effect. The tip structure has an important effect on the resolution of the image but also the nature of the image obtained. Variations in the tip atomic structure will no doubt effect the resulting image as the tunnelling current involves the wavefunctions of both the tip and the sample. The convolution of both the tip and sample structures make up the image. Effectively, an atomically sharp tip scanning a surface which contains an atomically sharp region will provide an accurate representation of the surface morphology. On the other hand if the tip is blunt and the region of the sample been scanned has dimensions smaller than the apex of the tip, then the surface may effectively image the tip. Other imaging anomalies also exist. The lateral resolution of an STM, unlike other conventional forms of microscopy, is limited only by the tip diameter and tip–sample spacing that can be achieved. Currently, this means resolution of about 1Å in the plane of the surface.

To obtain good quality images another vital factor in STM design is vibrational isolation. To achieve this the STM system must be as rigid as possible. Low frequency vibrations are usually those from buildings and are eliminated by elevating the system on an air table. In particular, the resonant frequencies of the individual translator elements (piezoelectric elements) ~1 kHz are usually eliminated by incorporating filters without altering the part of the signal that represents the structural image. Historically, vibrational isolation of the microscope assembly has ranged from superconducting levitation through damped springs (low-frequency elimination) to air tables and rubber mounts, although recent designs are very compact and have very high characteristic frequencies which are easy to filter out simply by using compact stacks of stainless steel sheet separated by viton (most effective for the elimination of medium range vibrations i.e. 20–200 Hz from pump motors and the resonances of the vacuum chamber).

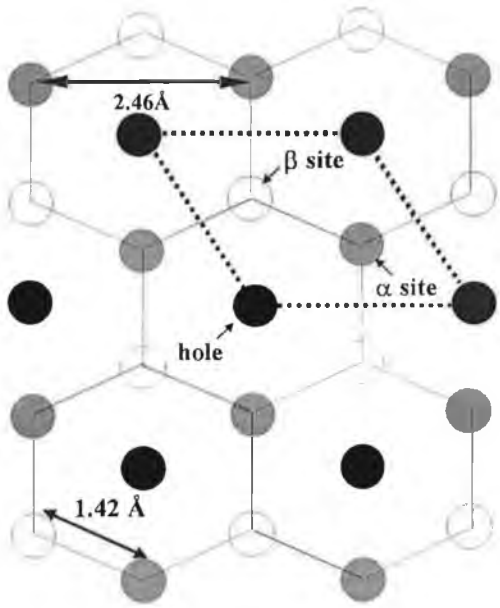

Figure 6: Schematic of the HOPG surface with the different atomic sites (α- and β-) and the hole-site. One unit cell is marked by thick dotted lines [14].

Finally, it should be emphasised that although STM is most efficient and reliable in UHV or high vacuum conditions, it is not exclusive to such conditions. STM has and continues to be used in many other environments including ambient and aqueous.

In all atmospheric STM studies carried out during this thesis the undamaged basal plane of HOPG has been used as a test of tip integrity and instrument stability. In graphite, there are both σ- and π- bonding holding the atoms in hexagonal two-dimensional networks. These layers are held rather loosely together by Van der Waals forces. The stacking of these layers follows a A.B.A.B pattern, i.e. hexagonal closely packed as illustrated in figure 5. Sub-nanometric STM studies of HOPG reveal its atomic structure to consist of a centred hexagonal arrangement of carbon atoms, including trigonally arranged β-atoms, separated by 0.246 nm [12,13]. The lattice of graphite contains in total three different atomic sites described as α, β and hole sites. As explained by Tománek et al [14], the β-atoms appear as bright spots in an STM image whereas the α-atoms are much less bright. In graphite we therefore see the different electronic environments for the differing sites on the surface. Figure 6 reveals a schematic drawing of the HOPG surface. At the α-sites the atoms in the

top layer have atoms in the layer underneath directly below them whereas the β-site atoms do not have a corresponding atom in the underlying layer. A differing tunnelling current is measured while scanning across the α- and β-sites, with the actual periodicity measured by STM found to be 2.46 Å. In this respect, graphite represents an important example in the way in which the corrugation reflects the local density of states (LDOS) at the Fermi level, and not the position of atoms.
Steps and grain boundaries may also perturb the electron density giving rise to the observation of superstructures. Large scale hexagonal superstructures have been observed with varying periodicity between 2 and 30 nm by Yang et al [15]. These superperiodic structures seem to have an irregular appearance and are suggested due to the misorientation of the two basal planes near the surface (commonly termed a Moiré effect).

STM has had an enormous impact on the study of growth phenomena (metal-on-metal systems, supported nano-clusters). One of the most significant advantages of STM is its large dynamic range of spatial resolution, ranging from the atomic scale to several micrometers. The information obtainable using the STM is wide and varied. Atomic-scale phenomena such as the atomistic processes governing the growth kinetics such as the motion of individual atoms and clusters, critical nucleus sizes, shape and branch thickness of dendritic adatom islands may be imaged. Larger scale regions reveal qualititative information such as island densities and defect and step densities etc.
Defects on alloy surfaces which are detectable by STM are generally undetectable using other techniques. The difficulty arising during atomic-resolution STM is the fact that it is generally difficult to distinguish the different atomic species present on the surface. However, in some cases the two metals may be resolved with the Cu(100)-c(2×2)-Au surface alloy being an example [16]. These differences are possibly due to changes in the tunnelling probability due to local electronic structure and work function changes. Even with the possibility of distinguishing species exact chemical identification is impossible. It should also be mentioned that examining the vertical relaxation of an element in a bimetallic surface is unsound using STM, as different vertical tip displacements are seen for different atomic species. STM is as already mentioned a surface confined technique and as such it is ineffective in

studying subsurface geometry. The lateral resolution is also limited by the area on the surface contributing current so that atomic resolution images cannot be determined with the same degree of precision as with LEED. Moreover STM is not able to obtain images fast enough to study local surface structure changes as images cannot be obtained on the same time scale compared to that of surface diffusion processes.

The major advances in understanding the growth mode and alloy formation for several metal-on-metal systems have come about through the employment of UHV STM [17]. Growth modes are generally more complicated than the original descriptions based on thermodynamical equilibrium arguments [18]. STM has also provided information on top-layer surface alloying for systems which are generally regarded to be immiscible in the bulk [19], and subsurface growth where the deposited layer forms one or more layers underneath the substrate surface [20,21]. Moreover STM quickly determines if the surface is ordered and whether more than one type of ordered structure is present. This sort of information is vitally important in for example LEED and X-ray photoelectron diffraction structure determinations.

Experimental difficulties often arise using STM. These include problems of reproducibly producing sharp tips and the requirement to isolate the STM from external vibrations. Other difficulties arising include artefacts in images, which may be mistaken for actual surface structure often attributable to imaging anomalies. Also, STM is often not well suited to the study of molecular adsorbates since interactions with the substrate and the tip may in some way influence the geometry of the adsorbates. However, several studies have been carried out including formic acid on Cu(110), confirming a previously debated aligned bridged site for the formate intermediate along the close packed rows [22,23].

1.2. Low energy electron diffraction (LEED)

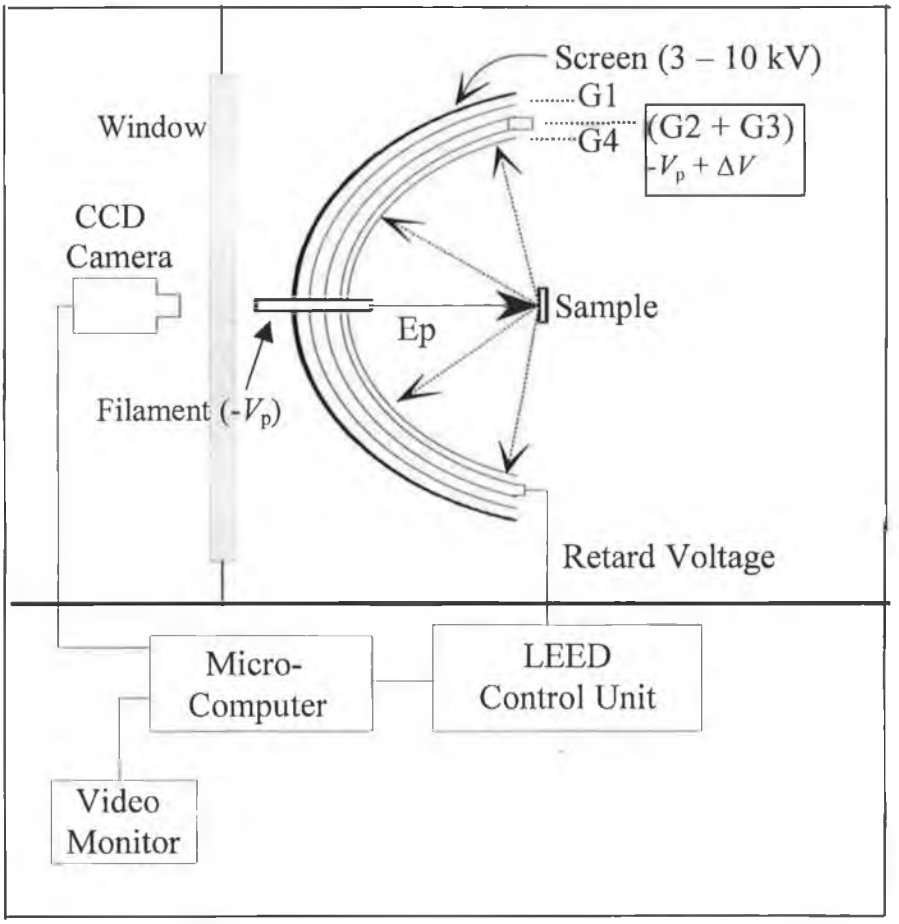

Figure 7: A schematic diagram of the experimental set-up for LEED with computer controlled data collection via a low light intensity CCD camera. ΔV is usually ~5 to 10% of V_p.

LEED is the oldest and probably still the most popular surface crystallographic technique. Effectively LEED is based on the diffraction of a monoenergetic electron beam when interacting with a periodic surface. This occurs because the de Broglie wavelength of electrons in the LEED energy range (20–500 eV) is of the same order of magnitude as the inter-atomic spacing at the surface of a single crystal. The high elastic back-scattering cross-sections for electrons with energies less than 1000 eV suggest that low energy electron diffraction should be extremely sensitive to surface atomic arrangements. A typical LEED system is shown in figure 7. In this arrangement a monoenergetic beam of variable energy is diffracted from a single crystal surface with the back-scattered beams moving through the field-free space

between the crystal and grid G4. Grids G2 and G3 act as filters and ensure that only quasi-elastically excited electrons reach the detector screen. G2 and G3 are held at a negative potential ($-E_p + \Delta V$) where ΔV is typically in the range 0–10 V.

The structural information determined using LEED includes the two dimensional periodicity of the surface unit cell along with any variations that occur upon adsorption. LEED also allows a complete surface map (bond lengths and angles) of the surface to be taken by monitoring the variation of the spot intensities with beam energy.

One way of representing the condition for diffraction is in terms of 'electron wavevectors' and so called 'reciprocal lattice vectors'. The magnitude of the wavevector k_0 is defined as:

$$|k_0| = \frac{2\pi}{\lambda} \tag{1.6}$$

substituting the de Broglie electron relationship:

$$\lambda = \frac{h}{mv} \tag{1.7}$$

reveals

$$|k_0| = \frac{2\pi}{h} mv \tag{1.8}$$

where mv is the electron momemtum. Substituting into the equation

$$\sin\theta_n = \frac{n\lambda}{a} \tag{1.9}$$

and eliminating λ gives

$$|k_0|\sin\theta_n = \left(\frac{2\pi}{a}\right) n \tag{1.10}$$

where $|k_0| \sin\theta_a$ is the component of momentum parallel to the surface of the incident electron ($k_{||}$), a is the lattice spacing and values of θ_a are allowed for which constructive interference results, corresponding to interger values of n. Therefore $2\pi/a$ is the magnitude of the one-dimensional **reciprocal lattice vector**.

In the case of a one-dimensional array, the diffraction pattern consists of a set of parallel lines. Periodicity in a second (orthogonal) direction with a lattice constant b will produce another set of diffracted beams perpendicular to the lattice direction a and again revealing an inversely proportional relationship to the lattice spacing, b. The LEED pattern resulting consists of diffraction spots resulting from the points of intersection of the two one-dimensional reciprocal lattice arrays. Therefore the exchange of parallel momentum is restricted to a two-dimensional reciprocal lattice vector (G) where

$$G = \Delta k_{\parallel} = n\frac{2\pi}{a} + m\frac{2\pi}{b} \qquad 1.11$$

The direction and number of diffraction beams originating from a surface in terms of primary energy beam and angle is more readily described in terms of reciprocal lattice (G vector) analysis. A reciprocal lattice results from a real space lattice upon diffraction, obeying the following rules:

$$G = na^* + mb^* \qquad \text{(n and m are integers)} \qquad 1.12$$

$$|a^*| = 2\pi/|a|; |b^*| = 2\pi/|b|; a \times b^* = a^* \times b = 0 \qquad 1.13$$

where a and b are the elementary vectors of the surface two-dimensional unit cell, and a^* and b^* are the elementary vectors of the corresponding reciprocal lattice. According to these equations a small distance in real space is a large distance in reciprocal space and vice-versa. In addition a and b are perpendicular to the direction of a^* and b^*, respectively. The condition of diffraction is then given by

$$k_0^{\parallel} = k_s^{\parallel} \pm G \qquad 1.14$$

where $k_s^{\parallel}$ is the parallel component of the scattered electrons wavevector. The conservation of parallel momentum $k_0^{\parallel} = k_s^{\parallel} \pm G$ means that if a G vector is exchanged with the surface, the incident electron must undergo a change in direction in order to conserve momentum.

The addition of an adsorbate adopting a different surface periodicity to that of the substrate may be described by means of the Woods notation [24]. The notation describes the ratio of the surface meshes to that of the substrate meshes including the angle of rotation (if different form zero) of the whole surface mesh with respect to that of the substrate. Observation of the LEED pattern of the overlayer (reciprocal lattice) and relating it to the real space lattice involves the following. The surface unit cell vectors of the overlayer are related to the substrate as follows:

$$a_O^* = G_{11}^* a_s^* + G_{12}^* b_s^*, \quad b_O^* = G_{21}^* a_s^* + G_{22}^* b_s^*. \tag{1.15}$$

For 0.25 ML atomic oxygen adsorption on Cu(100) this relates as follows (figure 8):

$$a_O^* = 1/2 a_s^* + 0 b_s^*, \quad b_O^* = 0 a_s^* + 1/2 b_s^* \tag{1.16}$$

therefore producing the matrix

$$G^* \begin{bmatrix} G_{11}^* & G_{12}^* \\ G_{21}^* & G_{22}^* \end{bmatrix} = \begin{bmatrix} 1/2 & 0 \\ 0 & 1/2 \end{bmatrix} \tag{1.17}$$

Converting the reciprocal space LEED pattern to a real space pattern involves taking the 'inverse transpose' of the matrix G^*. This results in the matrix

$$\begin{bmatrix} 2 & 0 \\ 0 & 2 \end{bmatrix}$$

In effect the matrix G yields the real space overlayer vectors (a_0 and b_0) in terms of the substrate unit vectors (a_s and b_s), i.e.

$$\begin{pmatrix} a_0 \\ b_0 \end{pmatrix} = G \begin{pmatrix} a_s \\ b_s \end{pmatrix} \qquad 1.18$$

Figure 8 reveals the LEED patterns of the substrate and the oxygen overlayer and also the corresponding real space structure. The real space structure is denoted as Cu(100)-p(2×2)-O. Simple inspection of the LEED pattern therefore reveals the relative size of substrate and overlayer cells.

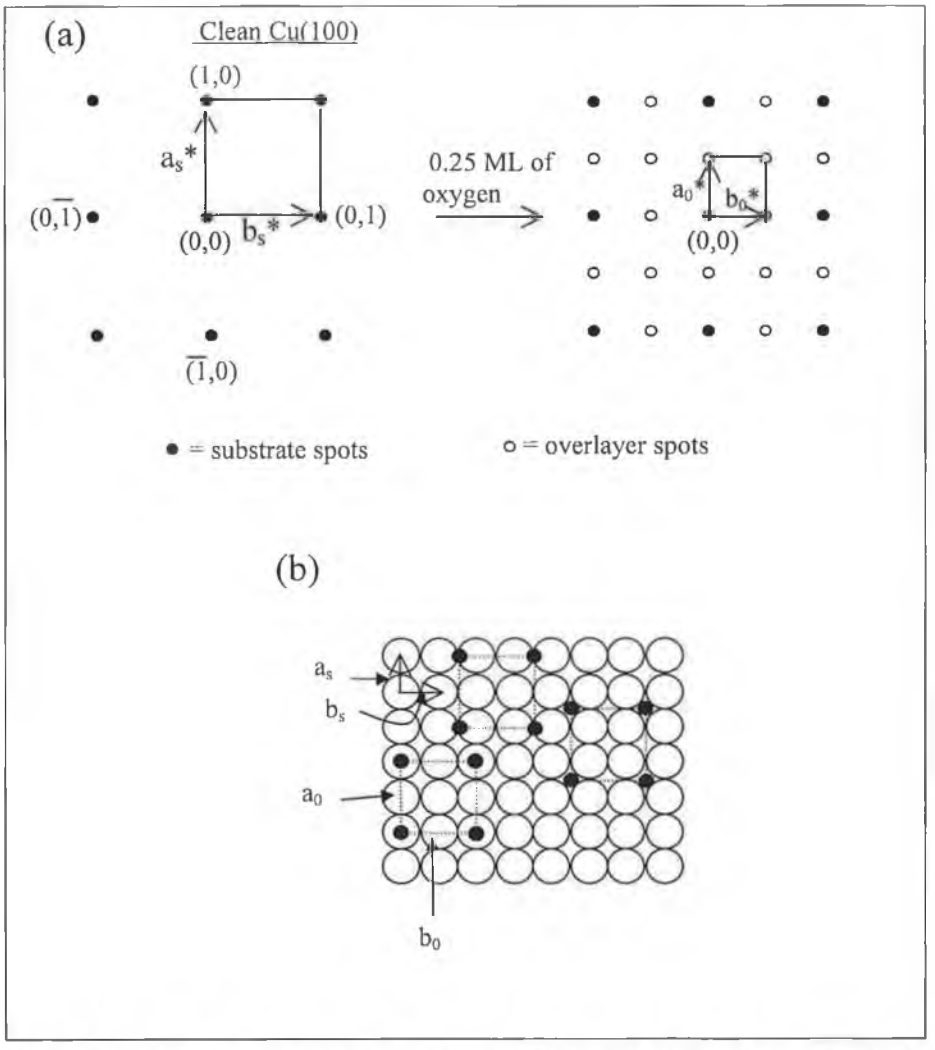

Figure 8: (a) Reveals the changes in the LEED pattern upon adsorption of oxygen on clean Cu(100). (b) The possible real space structures adopted by p(2×2) oxygen, included are atop, bridge and fourfold hollow site adsorption [25].

Another form of LEED commonly described as 'dynamical' or 'quantitative' LEED, or LEED *I–V* analysis (intensity versus potential), provides considerably more

surface information. In this case the intensity of diffracted beams is measured as a function of incident electron energy. The resulting intensity-energy or $I(E)$ spectra contain information on the surface atomic structure which may be retrieved by an indirect method. This involves calculation of the $I–V$ curves for a postulated surface structural model followed by comparison of theory and experimental data. The process is interactive and the surface structure is continually varied until the best fit between the theory and experimental data is obtained as indicated by an automatic R-factor (reliability) analysis [26,27]. Hence, from a comparison of measured and calculated $I–V$ curves it is possible to determine surface bond lengths to an accuracy of the order of ~0.02 Å.

The surface sensitivity of electron based spectroscopies such as LEED is controlled by the mean free paths for both elastic and inelastic scattering processes in the material of interest. Seah and Dench [28] have provided the most comprehensive study of the inelastic scattering of electrons as a function of energy from a number of different materials. Figure 9 reveals a collation of experimental values taken from an extensive survey of data by Seah and Dench.

In metals and alloys the inelastic-mean-free-path (IMFP) of an electron varies quite significantly with its kinetic energy. Essentially at very low kinetic energy electrons are unable to excite any of the most common loss mechanisms (plasmon excitation) and the mean free path is subsequently long. At very high energies the cross section for these losses is also low and again the mean free path is long. A minimum in mean free path is seen at energies between 50 and 70 eV where maximum surface sensitivity is encountered.

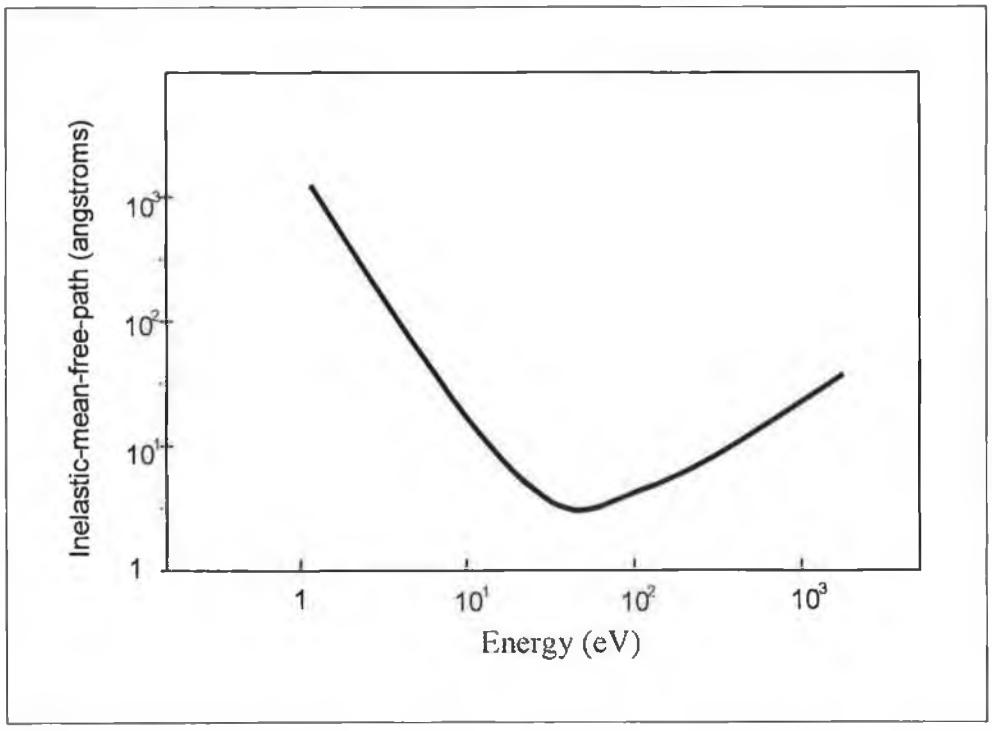

Figure 9: The variation of the inelastic-mean-free-path with electron kinetic energy.

2. Surface compositional analysis

2.1. X-ray photoelectron spectroscopy (XPS)

2.1.1. The XPS process

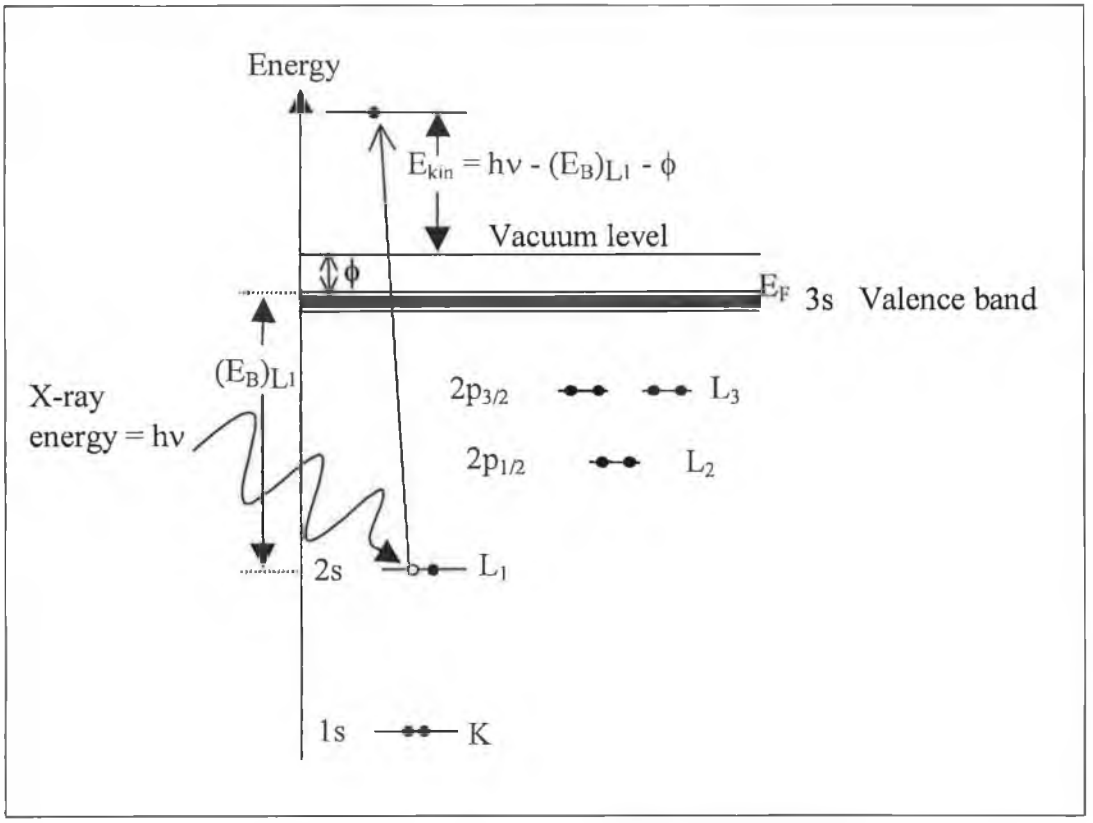

Figure 10: X-ray photoelectron excitation of a 2s electron (hν is the energy of the incident excitation photon). At the extreme right are the labels for the orbitals used in X-ray spectroscopy notation [29].

The principle behind XPS relies on the use of incident photons to ionise a surface localised atom, as shown in figure 10. As atoms of a given element have well defined binding energies the XPS process will give rise to electrons with well-defined kinetic energies. The relationship between the kinetic energy of an emitted electron and the orbital binding energies is defined by the Einstein equation:

$$E_{kin} = h\nu - E_B - \phi \qquad 2.1$$

where ϕ is the work function of the solid, defined as the minimum energy required to remove an electron from the highest occupied energy level in a solid to the 'vacuum level'. The vacuum level is the energy zero generally used in electron spectroscopy and corresponds to an electron at rest (zero kinetic energy) in a vacuum far removed from neighbouring particles so that it has no interaction with them (zero potential energy).

For a fixed photon energy, photoemission from an atom with well-defined core levels (with a characteristic binding energy) will produce photoelectrons with well-defined kinetic energies varying systematically from element to element thus allowing elemental identification. Incident photons are generally produced via an X-ray source with aluminium or magnesium anodes which when electron bombarded yield Kα photons of energies 1486.6 $\pm$ 0.85 eV and 1253.6 $\pm$ 0.7 eV, respectively. It is possible to monochromate the X-rays by single or multiple Bragg reflections from suitable crystals to pick out just a part of the dominant Kα line; this typically leads to photon energy spreads of ~0.2 eV although the loss in intensity is considerable. A thin Al or Be {~10–30 μm) window over the X-ray source aperture prevents the detection of secondary electrons from the X-ray source and isolates the pumping of the outgassing X-ray target from the UHV of the sample chamber [29,30].

An analyser commonly used for XPS is the electrostatic energy analyser consisting of two electrically isolated concentric hemispheres with a potential difference between them. The electrostatic field separates electrons by allowing only electrons of a specific energy through (commonly called the 'pass energy') to the detector. Electrons possessing a kinetic energy less than the chosen 'pass energy' are attracted by the inner positive hemisphere and neutralised. While the higher energy electrons hit the outer hemisphere and are lost. XPS spectrum production involves the pre-retarding of the electrons using a negative electrode allowing electrons of differing energy through to the analyser.

2.1.2. The chemical shift

The discovery, during the early days of XPS, that chemically non-equivalent atoms of the same element in a solid give rise to core level peaks with slightly different binding energies had a stimulating effect on the field. This discovery of "the chemical shift" by Seigbahn in the 1950's, led to the coining of the name "Electron Spectroscopy for Chemical Analysis". The corresponding acronym "ESCA" is widely used synonymously with the generic name "X-ray Photoelectron Spectroscopy". Non-equivalence of atoms can arise in several ways: difference in formal oxidation state, difference in molecular environment and so on.

The core-level binding energy is in effect a direct reflection of the electronic structure of an atom. As mentioned earlier the variation in both position and width of core-level peaks allows information on the atoms electronic environment to be deduced. The peak width, defined as the full width at half-maximum (FWHM), ΔE, is a convolution of several contributions:

$$\Delta E = \left(\Delta E_{\mathrm{n}}^2 + \Delta E_{\mathrm{p}}^2 + \Delta E_{a}^2\right)^{1/2} \qquad 2.2$$

where ΔE_{n} is the natural width of the core level, ΔE_{p} is the width of the photon source and ΔE_{a} the analyser resolution. Generally for unmonochromated Al Kα/Mg Kα radiation ΔE_{p} is dominant and the broadening due to the electron analyser is negligible hence $\Delta E \cong E_{\mathrm{p}} \cong 1$ eV.

Core-hole lifetimes are governed by the processes which follow photoemission, in which the excess energy of the ion is dissipated i.e. an Auger process or X-ray fluorescence. The longer the lifetime of the core-hole the narrower the core-level line width and vice versa. Lifetimes range between 10^{-14} and 10^{-15} s. For example, the line widths of the principle core levels of the light elements systematically increase with an increase in atomic number due to the increase in the number of electrons in higher energy levels which enhances the probability of an Auger process (electron emission), thus decreasing the lifetime of the core-hole [31].

The exact binding energies of core-levels reveal much about the emitting atom. As a rule, the binding energy will increase as the electronegativity of the attached atoms or groups to which the emitter is bonded increases. However, many cases arise in

which distinct chemical states give rise to photoelectron peaks whose relative chemical shift is sufficiently small for the peaks to overlap. In principle shifts of 0.1 eV are required to be measurable, however this is impossible if the contributory peaks have a line-width dictated by the width of Al Kα or Mg Kα sources. Deconvolution of these peaks may be and often is attempted.

2.1.3. Core-level spectra

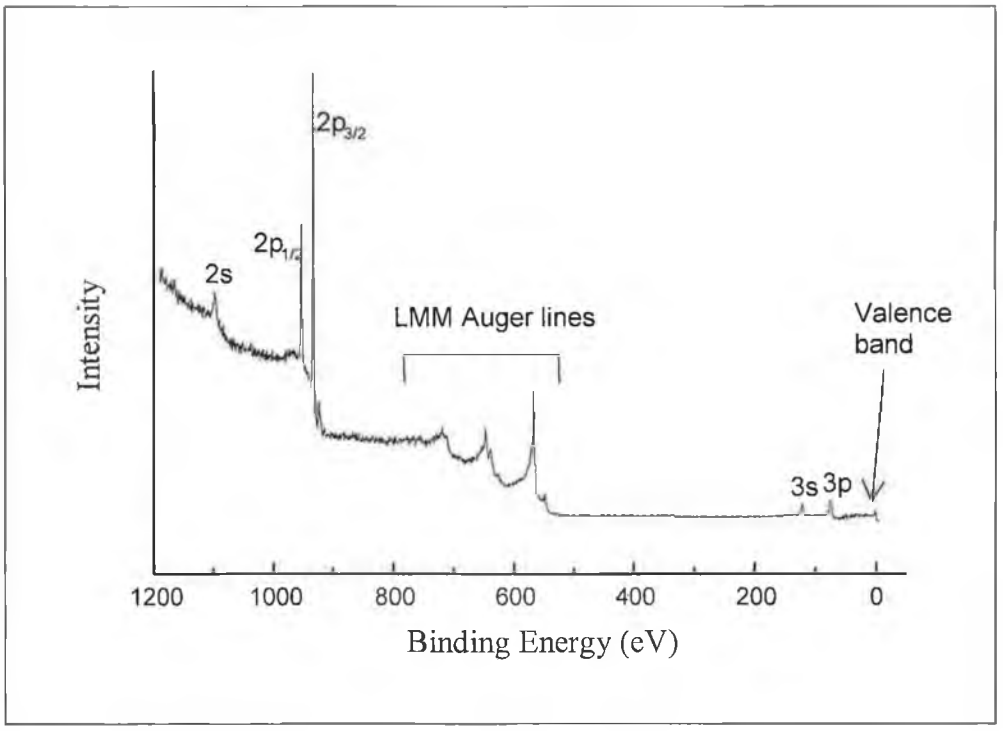

Figure 11: X-ray photoelectron survey-scan spectrum of Cu(110) excited by Al Kα radiation.

XPS helps to provide a compositional analysis of surfaces. The core-level structure shown in figure 11 is a direct reflection of the electron structure of a copper atom as excited by Al Kα radiation.

All core-levels with orbital angular momentum quantum number $\ell \geq 1$ (p, d, f, ...) are split into doublets by spin-orbit splitting (*j–j*), with the higher angular momentum state at higher kinetic energy. The separation can be many electron volts as seen for the 2p levels of Cu in figure 11. The separation also increases for a given subshell as the atomic number of the element increases, while increasing for decreasing ℓ i.e. 3p > 3d. On the other hand the relative intensities of the doublet peaks are given by the

ratio of their respective degeneracies ($2j+1$), i.e. total angular momentum values (j) for p-levels 1/2, 3/2 have corresponding peak area ratios of 1:2.

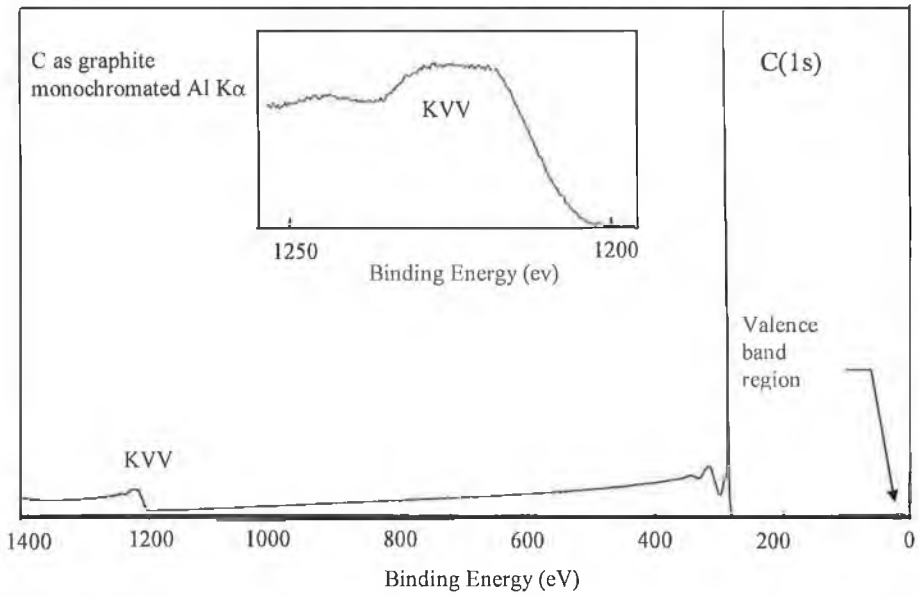

Figure 12: Al Kα-induced survey-scan XPS spectrum of graphitic carbon. The valence band region is just noticeable [32].

The intensities of the various core-level peaks are governed by the atomic photoemission cross sections. For conventional XPS our main concern is the variation of the cross-section with atomic number for given sub-shells at fixed photon energy. In 1976, Scofield carried out the relevant calculations for a wide range of accessible levels. Calculations were carried out for the fixed energies of both Al- and Mg-Kα photons. Scofield [33] has published an extensive list of X-ray absorption cross-sections for the sub-shells of electrons in the elements of the periodic table and has specifically utilised the X-ray energies of magnesium and aluminium to produce X-ray absorption coefficients relevant to ESCA measurements. His data have been normalised to a relative atomic sensitivity of 1.00 for C(1s).

An example of an Al Kα-induced survey-scan spectrum of as-cleaved graphite is shown in figure 12. The characteristic intense C(1s) core-level and the Auger KVV peaks are observed.

Core-peak intensities are also important in attempts to quantify the concentration of atoms of a specific element in the selvedge of the sample. The intensities are dependent on a number of factors including the concentration of the element present, the probability of photoemission occurring for the specific core level (photo-ionisation cross-section), the IMFP of the photoemitted electron, and the efficiency of the spectrometer for the detection of electrons as a function of kinetic energy (instrumental detection efficiency). Relative concentrations for two components can be determined if the binding energies of the two are similar (allowing IMFP and instrumental factors to be ignored), of course assuming that they are homogeneously distributed throughout the sampling depth. The following expression relates the relative concentrations:

$$\frac{C_A}{C_B} = \frac{I_A}{I_B} \times \frac{\sigma_B}{\sigma_A} \qquad 2.3$$

where C_A and C_B are the atomic concentrations of the two components A and B, respectively. I_A and I_B are the peak area of the two components while σ_A and σ_B are the respective photo-ionisation cross-sections of the core level of atom A and B.

In attempting to quantify the thickness of an overlayer material growing in a layer by layer fashion on a substrate we can follow the decay in the substrate XPS peak intensity which follows an exponential decay law. The equation is as follows:

$$I(d) = I_0 \exp\left[\frac{-d}{\lambda \cos\theta}\right] \qquad 2.4$$

where I_0 is the intensity of the clean substrate, d is the overlayer film thickness to be calculated, $I(d)$ is the substrate XPS signal intensity for a film thickness d, θ is the emission angle of the electrons with respect to the surface normal and λ is the IMFP of the substrate XPS peak defined using the formulism of Seah and Dench [31]:

$$\lambda(\text{nm}) = \left(538 \times E_{kin}^{-2}\right) + \left(0.41 \times a_m^{3/2} \times E_{kin}^{1/2}\right) \qquad 2.5$$

where E_{kin} is the kinetic energy of the substrate photoelectron and a_m is defined as:

$$a_m\,(\mathrm{nm}) = \left(\sqrt[3]{\frac{A_m}{\mathrm{N}\times P_m \times 1000}}\right)\times 10^9 \qquad 2.6$$

where A_m is the mean atomic weight of the overlayer material (g/mol), N is Avogadro's number and P_m is the density of the overlayer material (Kg/m^3).

2.1.4. Valence levels

The valence levels are those occupied by electrons of low binding energy (0–20 eV) which are involved in bonding. In metals, the Fermi level is defined as the highest occupied energy level and is sometimes referred to as the electron energy scale zero, with binding energies referenced to this point. However, the vacuum level is in fact the true zero with the work function of the material the difference in these two values.

Valence levels are seen to have low cross sections making XPS studies of such levels difficult as the photo-ionisation cross-section of a core level rises to a peak close to the threshold for ionisation and then falls monotonically as the emergent kinetic energy increases. For valence levels the exciting photon energy is far above the photo-ionisation threshold thus leading to a low cross-section. The electron analyser also has an effect on the intensity of the core levels. Its transmission characteristics being a function of electron energy.

It is seen that valence-level spectra have a strong dependence on the energy of the incident photon. Although the main features of the ultraviolet photoelectron spectroscopy (UPS) (excitation through helium resonance radiation with photon energies of 21.2 and 40.8 eV) and XPS spectra are in agreement there is considerably more structure in the data obtained by UPS. Although the UPS line-width is about 0.1 eV the main reason for enhanced sensitivity is the fact that photoelectrons leave with kinetic energies low enough to prevent elastic scattering.

For graphite, four peaks of interest have been identified in these spectra. These occur at binding energies of 17.2 eV, 10–15 eV, 8 eV and 4 eV below the Fermi level, corresponding to pure s bonding, two contributions due to a mixture of s and p bonding (p–σ), and p–π bonding, respectively [34].

The Al Kα-induced valence band spectrum of diamond is shown in figure 13. Peak I is due to pure 2p states, peak II composed of s–p hybridised states while peak III is proposed to be due to predominantly 2s states [35].

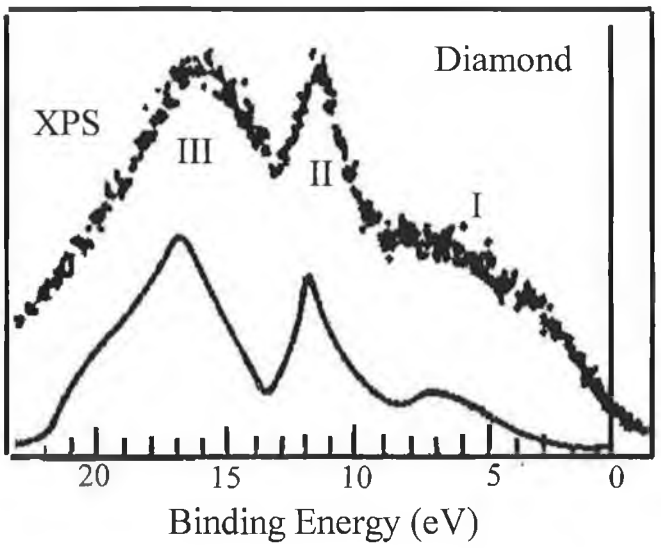

Figure 13: Al Kα-induced XPS spectrum of the valence bands of diamond (dots) compared with the results of tight-binding valence bands calculation with a plane wave final state (solid line) [35].

2.1.5. Secondary spectral structure

Electrons can lose energy by a number of quantised loss processes during phoionisation. The smallest energy losses are usually due to lattice vibrations or "phonons" and result in quite small losses in the kinetic energy of the emitted photoelectron (tens to hundreds meV). A more substantial loss mechanism is due to electron-electron interactions which lead to excitation of what is termed as a "plasmon" (a collective oscillation of conduction electrons). An electron that has given up an amount of energy equal to the characteristic plasmon energy is said to have suffered a plasmon loss. These fluctuations are quantisised with energies in the range 5–25 eV, the energy depending on the density of the electron gas and whether or not they are three-dimensional (bulk plasmons) or two-dimensional (surface plasmons). Plasmon features are often observed at lower kinetic energy (higher binding energy) than the main XPS line.

A third energy loss mechanism involves excitation of a valence electron to a higher unfilled level ('shake-up' satellite). The energy for this process is lost by the photoelectron and the 'shake-up' process results in a discrete structure on the low kinetic energy (high binding energy) side of the photoelectron peak. The shake-up satellite peak on the higher binding energy side of the C(1s) of graphite is indicative of aromaticity via a $\pi \rightarrow \pi^*$ transition. This satellite feature is centred for HOPG at a binding energy of ~6 eV higher than the C(1s). Other sp^2 systems such as fullerenes C_{60} and C_{84} have revealed $\pi \rightarrow \pi^*$ transitions at shifts as low as 1.9 eV and 1.4 eV, respectively. Conjugated and, especially, aromatic systems show shake-up satellites with intensities up to 5–10% of the primary peak. Strong satellites are also seen for the transition metals with unpaired electrons in the 3d shells.

In the event that a 'shake-up' valence electron is completely ionised the term 'shake-off' is used although this phenomenon is rarely discerned in the solid state.

2.2. Auger electron spectroscopy (AES)

As mentioned earlier the Auger process is an alternative to X-ray fluorescence and occurs after an atomic level has been ionised by incident photons or electrons in an XPS process. The process involves the loss in potential energy of the ion resulting from photoemission (excited by an incident photon or electron of sufficient energy) by filling the core hole with an electron from an outer level. The quantum of energy resulting (equal to the difference in energy between the core hole and the electron falling to fill it) can either be emitted as a photon (X-ray fluorescence) or transferred to a third electron which escapes as an 'Auger electron' provided the energy is sufficient to escape the binding of the atomic nucleus. The kinetic energy of this Auger electron is given in an example (figure 14) by:

$$E_{klm} \approx E_{\mathrm{K}} - E_{\mathrm{L_1}} - E_{\mathrm{L_{2,3}}} \qquad 2.7$$

where $E_{\mathrm{K}} - E_{\mathrm{L_1}}$ is the amount of energy released by an electron falling from the L_1 shell to the core hole in the K shell, with the electron escaping using up $E_{\mathrm{L_{2,3}}}$ of this amount of energy to escape the binding of the atomic nucleus. Again the emitted

electrons due to this process will have energies characteristic of the atoms whence they came and energy analysis will enable identification of the materials present. The Auger electron described by the process would be referred to as a $KL_1L_{2,3}$ Auger electron (figure 14). The probability of relaxation by Auger emission (as opposed to X-ray fluorescence) is the dominant process for core holes with binding energies below about 2 keV for K shell ionisation. The excitation of 'Auger electrons' is named after their discoverer, Pierre Auger [36].

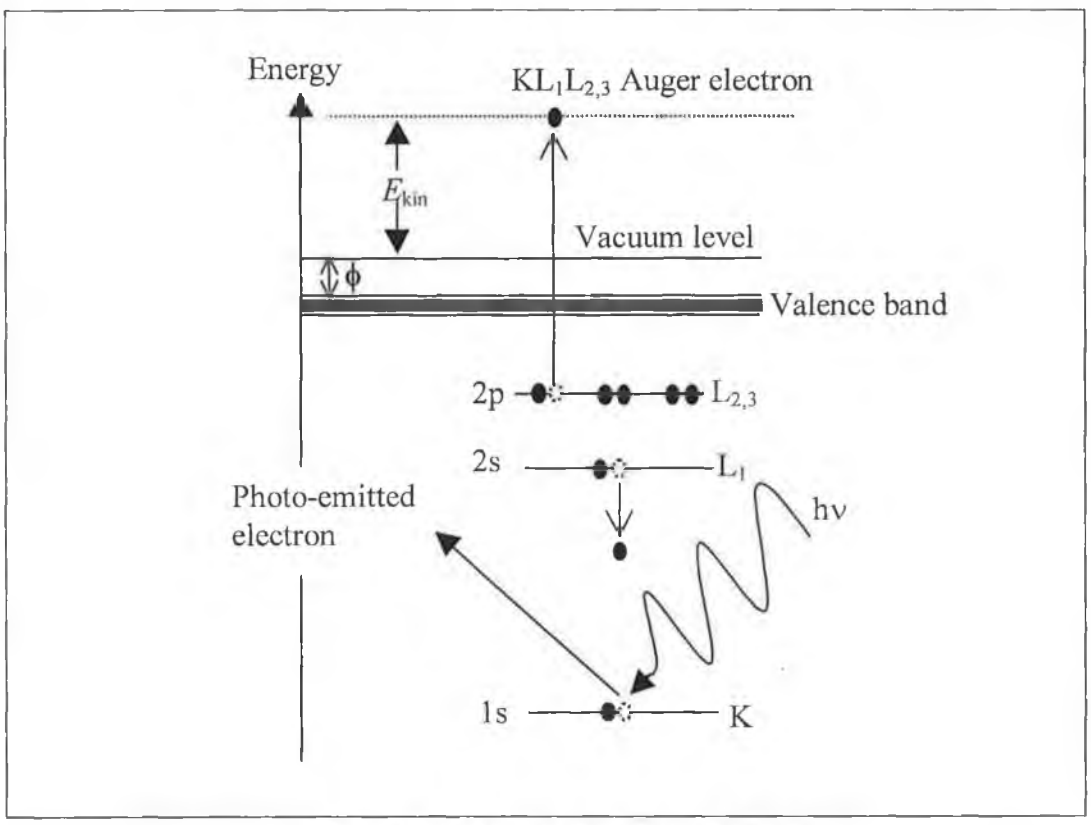

Figure 14: Auger electron emission.

The kinetic energy of the Auger electron is independent of the energy of the incident radiation giving rise to the initial core hole. The kinetic energy of the Auger electrons is exclusive to each element as they are merely a function of the internal atomic binding energies of each element. Each element thus has a unique set of Auger energies. Even when either or both electrons in the Auger process originate in the valence band the unique elementally specific nature of the transition is maintained as the dominant term in defining the Auger electron energy is the binding energy of the initially ionised core level.

Importantly, Auger electron emission is an efficient means of filling core holes of low binding energy, thus giving rise to relatively low kinetic energy Auger electrons of short mean-free-path. From this it is evident that the technique is highly surface sensitive. Auger excitation is usually carried out using electron sources due to the relative ease of producing sufficiently energetic beams of high intensity. For the light elements (atomic number $Z<20$) Auger emission is more probable than X-ray emission for a K-shell initial-state hole, and for $Z<15$ it is almost the exclusive process. For higher Z, Auger processes dominate for initial state holes in outer shells.

The use of electron beams to produce the initial ionisation process is an advantage in that the incident beam may be focused thus giving good spatial resolution.

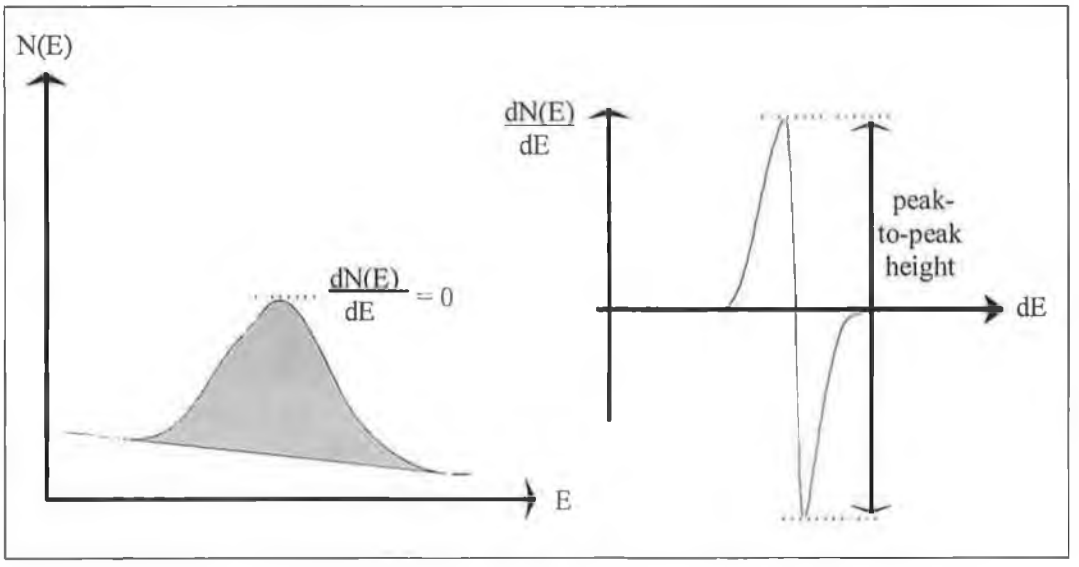

Figure 15: Illustration of an Auger ($N(E)$) peak and differentiated Auger ($dN(E)/dE$) peak.

The difficulty encountered in Auger spectroscopy is the fact that the spectrum recorded ($N(E)$ versus kinetic energy) generally consists of Auger electron peaks seen as small inflections on a high background. This background is attributable to secondary electrons (electrons that have undergone multiple energy losses by excitation of plasmons and/or interband transitions). The Auger peaks are often difficult to detect in this form and this is usually overcome by the electronic

differentiation of the electron energy distribution to yield a $dN(E)/dE$ curve, in which by convention the energetic position of the Auger peak is taken as that of the minimum in the high energy negative excursion (figure 15). In terms of quantification of surface species it maybe shown that the peak to peak height of the differentiated signal is directly proportional to the area under the $N(E)$ curve, providing peak shape changes do not occur as a function of coverage, and may be used as an approximation of surface concentration.

Strictly the correct energy of the Auger electron is not given by the differences in ground state binding energies. Examining the Auger transition in figure 14, once the L_1 electron has filled the initial-state hole in the K shell then the binding energy of the $L_{2,3}$ electron is increased because an L_1 electron has been removed. This hole-hole interaction in the final-state configuration will depend upon whether the holes are both in core levels, one in a conduction band, or both in a conduction band.

As three electrons are involved in an Auger process it is evident that the energy shifts and line shape witnessed in AES is considerably more complicated than the one-electron core level photoemission process involved in XPS. Of course all the complexities relevant to XPS such as chemical shift and inter and intra-atomic relaxation effects present in XPS also occur in AES, but with the complicating factors of hole-hole interactions in the final state and a great multiplicity of lines. The selection rules in the Auger process are generally much weaker than in photoemission, but certain transitions are nevertheless forbidden.

Initially Auger was developed using LEED optics as retarding field analysers (RFA). In this arrangement the surface is bombarded with a high energy (~3 keV) electron beam. The potential of Auger spectroscopy as a surface analytical technique was soon realised and detectors were constructed to specifically detect Auger electrons. The first of these was the cylindrical mirror analyser (CMA) [37]. In this arrangement the secondary electrons from the sample pass through an entrance slit in the centre of two concentric cylinders. A negative potential V is applied to the outer cylinder and electrons, which have the correct energy, are deflected through the exit slit and collected using an electron multiplier. By sweeping V over the desired range a spectrum can be generated. This type of analyser has excellent collection efficiency, high transmission and a good signal to noise ratio as only electrons with

the desired energy pass through the analyser. The CMA analyser is commonly used to carry out routine analysis such as depth profiling.

For submonolayer coverage provided no coverage dependent peak shape changes occur the signal is directly proportional to surface coverage. For multiple layer growth, effects such as inelastic scattering of the first layer signal by the overlying layers must be considered.

For many systems the monitoring of the Auger signals from the substrate and the adsorbate (condensate) as a function of the duration of exposure to a constant flux of impinging adsorbate is a means of defining the growth mechanism. The plot obtained is called an Auger signal versus deposition time plot or "AS–t" plot [38,39]. In a mechanism where the overlayer tends to grow layer-by-layer (Frank van der Merwe) initially straight line plots are obtained for both signals. A break or 'knee' in the straight line of each signal indicates the completion of the first layer and the beginning of the next. This is attributable to the attenuation of the signal from the underlying adsorbate layer(s) and to the fact that succeeding layers intercept more of the original substrate emission. The Volmer–Weber mode is a clustering adlayer growth mechanism where the growth of three-dimensional particles leaves much of the substrate uncovered. In this arrangement the AS–t plot will consist of a smooth decay in the substrate signal accompanied by an increase in that of the adlayer. The cluster size and shape will control the extent of the decay and increase in the substrate and adlayer signals, respectively. The third mechanism of growth, is that of Stranski–Krastanov. The AS–t plot for this mechanism is characterised by one of more linear segments indicating layer growth followed by the more gradual monotonic change resulting from bulk crystallites forming after one or several monolayers are complete. AS–t plots for these characteristic growth mechanisms are illustrated in figure 16. In the case of Stranski–Krastanov and Volmer–Weber growth for the same quantity of material, crystallites cover a relatively smaller area of the surface in comparison to extended monolayer growth, so both the net emission and attenuation effects are much lower.

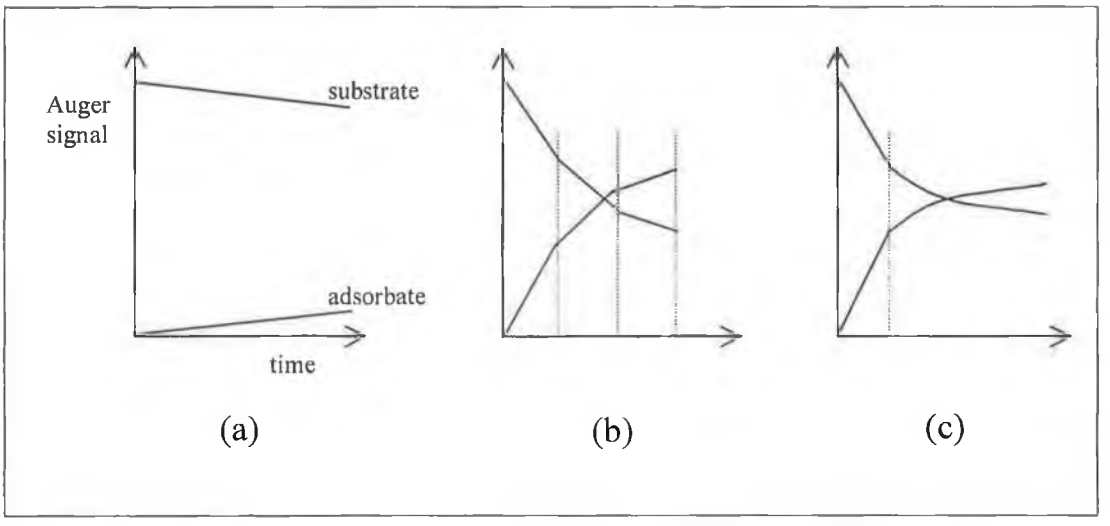

Figure 16: Schematic AS–t plots for the variation of the substrate and adsorbate signals for three different modes of film growth: (a) Volmer–Weber (nucleation of small particles or crystallites without prior formation of a monolayer); (b) Frank van der Merwe (layer-by-layer); (c) Stranski–Krastanov (nulceation of small particles or crystallites after the formation of one monolayer or in rare cases more than one monolayer). The dotted lines reveal the times for the completion of each subsequent monolayer.

The attenuation of the Auger electron signal from the substrate, I_s^n, at normal emission, associated with n atomic layers each of thickness, d_a, and an IMFP of λ_s is given by:

$$I_s^n = I_s^0 \exp(-nd_a / \lambda_s) \qquad 2.8$$

where I_s^0 is the Auger intensity from the clean substrate. Similarly, the increase in intensity of the adsorbate Auger peak, I_a^n, associated with n atomic adsorbate layers of thickness, d_a, and IMFP of λ_a is given by:

$$I_a^n = I_a^\infty [1 - \exp(-nd_a / \lambda_a)] \qquad 2.9$$

2.3. Growth Modes

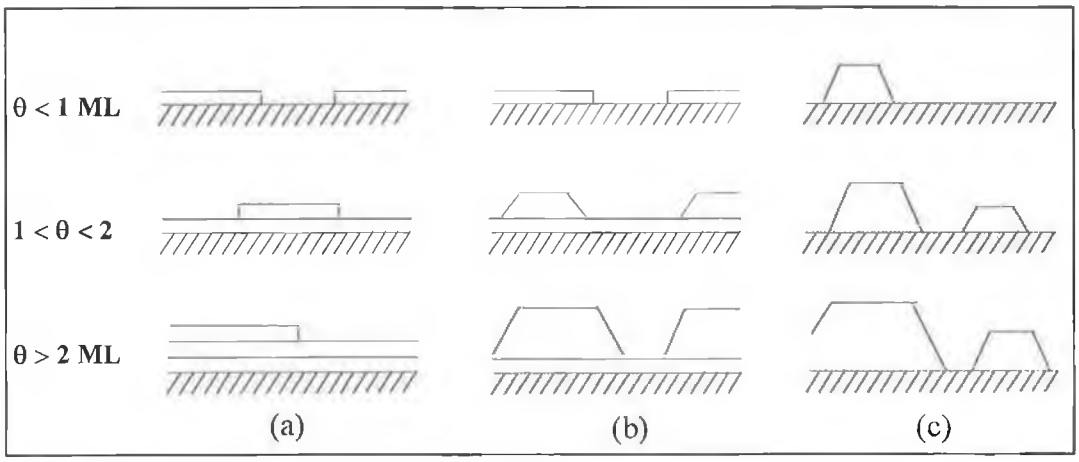

Figure 17: Schematic representation of the three crystal growth modes: (a) layer-by-layer, (b) layer plus island and (c) three-dimensional island growth. θ represents the coverage in monolayers (ML) [40].

The equilibrium growth mechanism depends on factors which include: (a) the surface energy of the substrate and adsorbate (and interface energy) and (b) the atomic size variation of the two metals. The first use of surface energies to describe the three modes of crystal growth was adopted by Bauer [41] in 1958 and has been subsequently reviewed several times since [42,43].

Commonly, the growth modes experienced are divided into three categories: (1) three dimensional island (Volmer-Weber, VW), layer plus island (Stranski-Krastanov, SK) and layer-by-layer growth (Frank van der Merwe, FM). The three growth modes are illustrated in figure 17. The factors vital to growth mechanism are the surface energies (which are proportional to the heats of sublimation) of the pure substrate (γ_S), the pure admetal (γ_A), and the interface ($\gamma_{A\text{-}S}$) [44,45]. The critical quantity which plays a large part in determination of the growth mode is, as suggested by Bauer: Young's equation [46]:

$$\Delta\gamma = \gamma_A + \gamma_{A\text{-}S} - \gamma_S \qquad 1.19$$

(i) Layer-by-layer growth:

The admetal tends to only grow in this mechanism if $\Delta\gamma \leq 0$ i.e. the difference in surface energy between substrate and adlayer is significant with the substrate having

a higher surface energy than the adsorbate. The continuance of this growth mode for increased adlayer coverage is dependant on the fulfilling of this criteria for each subsequent adlayer. The usual difficulty in homoepitaxial growth is the inherent lattice mismatch between substrate and adlayer atoms. Effectively, the continuance of FM growth is only possible for homoepitaxial growth, e.g. Cu on Cu, where the total strain energy of the system is equal to zero.

(ii) Stranski-Krastanov growth:

In this mechanism the interface layer energy is vitally important. The total surface energy remains $\Delta\gamma<0$ for a certain number of layers after which the interface energy increases causing the system to revert to island growth. This mode is intermediate between FM and VM growth.

(iii) Three-dimensional island growth:

The tendency of the adlayer to bond to itself more strongly than with the substrate epitomises this growth mechanism ($\Delta\gamma>0$). The resultant surface is a rough three-dimensional island topped surface.

Adopting this system for growth prediction leads to problems. For example, the use of surface energies calculated for bulk pure metals may not be a good approximation for a monolayer whose electronic structure may be strongly modified by the interaction with the substrate. This modification is partially contained in the interface energy. Furthermore, it should be noted that the growth mechanisms described above are idealised and only hold true if thermodynamic equilibrium is achieved. In many cases thin-layer growth occurs far from equilibrium. For kinetically hindered growth a number of external factors deciding the growth mechanism include substrate temperature and evaporation rate. So essentially the understanding of the atomistic processes which underlie and control the growth mechanism can obviously not be explained within the confines of the traditional growth modes described here. From the arrival of the initial atoms from the vapour phase to their coalescence or nucleation to form clusters which subsequently attach/diffuse to further islands, mobile or immobilised at step edges, to the final development of an overall growth mode. The ability to visualise and understand

such processes has only recently with the advent of scanning probe microscopies become possible.

3. Surface bonding and reactivity

3.1. Temperature programmed desorption (TPD)

Temperature programmed desorption (TPD) is a means of determining the binding energies of adsorbates by heating the surface after exposure to a gas and observing the temperature at which the gas or metal is desorbed using a quadrupole mass spectrometer. The application of a temperature ramp to the sample and monitoring the amount of adsorbate desorbed into the gas phase allows the rate of desorption to be monitored.

The TPD spectrum is achieved using a well-defined temperature–time heating schedule to facilitate quantitative analysis of the data. The heating rate (β) is generally linear with time (t) and obeys the relationship:

$$T(t) = T_0 + \beta t \qquad 3.1$$

where the initial sample temperature is T_0. Resistive heating of the sample is commonly afforded through the passing of an electric current through wires spot-welded to the edges of the crystal. Thermocouple attachment to the sample allows accurate sample temperature measurement. The mass spectrometer used to detect the desorbing species is usually orientated in the line-of-sight and quite close to the sample face. In this arrangement the surface coverage is proportional to the area under the desorption spectrum provided the pumping speed of the vacuum chamber remains constant.

Heating rates applied during TPD are typically between 1 and 100 K s^{-1}. The mechanism of desorption involves imparting sufficient energy to the atom/molecule to break its bond with the surface. The rate of desorption per unit surface area is given by:

$$-dN/dt = k_d N^m \qquad 3.2$$

where m is the order of the reaction and N is the number of adsorbed molecules. The rate constant for desorption, k_d, obeys an Arrhenius dependency and should therefore increase exponentially with temperature; k_d is defined as:

$$k_d = A\exp\left(-E_d / RT\right) \tag{3.3}$$

where E_d is defined as the activation energy for desorption and A is a pre-exponential factor. Substituting for the heating rate $\beta = dT/dt$ allows the desorption rate to be rewritten as:

$$-dN/dT = \frac{k_d}{\beta} N^m \tag{3.4}$$

and substituting for k_d gives the following:

$$-dN/dT = \frac{A}{\beta} N^m \exp\left(-E_d / RT\right) \tag{3.5}$$

At the maximum rate of desorption $\left(d^2N/dT^2 = 0\right)$; hence by differentiating with respect to T and equating to zero one can relate a general expression relating to the T_p, E_d and N:

$$\frac{E_d}{RT_p^2} = \frac{A}{\beta} mN^{m-1} \exp\left(-E_d / RT_p\right) \tag{3.6}$$

where T_p is the desorption peak maximum. In particular, for m = 1 (first order desorption):

$$\frac{E_d}{RT_p^2} = \frac{A}{\beta}\exp\left(-E_d / RT_p\right). \tag{3.7}$$

Thus as β is known and T_p is measurable, E_d can be calculated if the pre-exponential A factor is known. Typically A is set as 10^{-13} s^{-1} and for A/β between 10^8 and 10^{13} K^{-1}, equation 3.6 has been simplified [47,48] to:

$$E_d = RT_p\left[\log_e\left(\frac{AT_p}{\beta}\right) - 3.46\right] \qquad 3.8$$

where R = 8.314 J mol^{-1} K^{-1} and T_p is in Kelvin.

For any desorption other than first order it is seen that T_p is dependent on the initial surface coverage N. For first order desorption, T_p, will remain constant with increasing coverage with a simple increase in desorption intensity. The resultant peaks of first order desorption are asymmetric. For a second-order reaction it is seen that T_p is now dependent on N and decreases with increasing coverage although the peaks remain symmetrical. Thus, the behaviour in the maximum in the desorption as a function of coverage can be used to determine the desorption order if the activation energy for desorption is independent of coverage (no lateral adatom-adatom interactions or coverage dependent site switching). A first order desorption process with a coverage-dependent desorption energy which decreases with increasing coverage will also result in a decreasing peak temperature with increasing coverage. This behaviour can often be distinguished from second order desorption for the case of weak lateral interactions as shifts of more than 100 K are generally seen for second-order kinetics. Combinations of the two effects will however be difficult to distinguish. The desorption equation reveals the dependence of T_p on surface coverage, N, for second-order kinetics:

$$\frac{E_d}{RT_p^2} = \frac{2AN}{\beta}\exp\left(-E_d / RT_p\right). \qquad 3.9$$

For reaction orders less than one, the peak temperature is also dependent on initial surface coverage with T_p shifting to higher temperature with increasing coverage. Fractional order desorption processes are quite uncommon and are limited mainly to the desorption of metal atoms from the edges of islands [49,50,51]. Zero-order kinetics on the other hand is often found for multilayered systems. In mutilayer

systems while the first monolayer is bonded via a strong chemisorption bond to the surface, the second and subsequent layers interaction with the surface is weak and appears as a lower temperature desorption peak relative to the chemisorbed layer. As more and more material is condensed on the surface the multilayer peak will increase in intensity. General observations for multilayer desorption include the increase in T_p to higher temperature for increasing coverage although all desorption curves have a common leading edge.

The popularity of TPD is attributable to a number of factors. Firstly, it is essentially a simple and low cost analysis method. Secondly, as the adsorption process is generally nonactivated, the desorption energy may be approximated to the differential heat of adsorption allowing access to the variation in adsorption energy with coverage. The integration of the areas under the TPD peaks is also a good method of obtaining relative surface coverages again providing the chamber pumping speed remains constant.

The difficulty in the interpretation of TPD spectra is reduced if there is some knowledge of the surface structure of the adsorbate and its variation with surface coverage. The strong interrelationship between structure and kinetics implies that knowledge of the surface structure is vital if the latter is to be understood. In particular complex desorption spectra, consisting of multiple peaks and shoulders maybe interpreted in terms of a set of physically and chemically distinct binding sites, each having a characteristic desorption energy. Other reasons proposed for the multiple desorption states include lateral repulsive interactions which tend to destabilise neighbouring atoms leading to a lowering in their adsorption energy, hence producing a shift of the desorption maximum to lower temperature with increasing coverage and in some cases the emergence of a new low temperature desorption state. In this scenario a single high temperature desorption peak is seen for coverages less than 0.5 ML on systems exhibiting fourfold symmetry and nearest-neighbour repulsive interactions. At 0.5 ML the desorption spectrum splits with the appearance of a low temperature peak due to the necessary placement of adsorbates in excess of 0.5 ML in nearest neighbour sites.

The equation describing the rate of desorption, proposed by Redhead [47,48], has come under some scrutiny. A variety of procedures have been developed for the

analysis of desorption spectra based on this equation. Calculation of the activation energy of desorption, E_d, in terms of the pre-exponential factor, A, the peak maximum, T_p, and the heating rate, β, by setting $\left(d^2N/dT^2 = 0\right)$ has already been described. Usually a guess is made for A, and it is commonly set at 10^{-13} s^{-1} for first order kinetics. However, provided that the experimental results are sufficiently accurate, a full lineshape analysis can be employed. Several methods have been described, including: (a) computer fitting by adjusting A and E_d; (b) a comparison of peak temperatures obtained over a range of heating rates, since the slope of $\ln(T_p^2/\beta)$ against $1/T_p$ gives E_d/R; or (c) from both T_p and w, the full-width at half maximum, using the expressions:

$$E_d = 2.52\left(RT_p^2/w\right) - 2RT_p \qquad 3.10$$

for first-order kinetics, and

$$E_d = 3.54\left(RT_p^2/w\right) - RT_p \qquad 3.11$$

for second-order kinetics. Nevertheless, the preferable technique is one which is based on the analysis of a family of spectra with variable surface coverage [52,53]. This method negates the need to assume that A and E_d are coverage independent. This is commonly termed the 'leading edge analysis' method. In the relation

$$pressure\,(p) = -dn_{ad}/dT = \frac{A}{\beta}N^m\,exp\left(-E_d/RT\right) \qquad 3.12$$

it is found that a plot of ln p versus $1/T$ will give a straight line with slope $-E/R$. Numerical simulations of desorption spectra with coverage dependent E and the pre-exponential factor, A, show that E may be extracted from ln p versus $1/T$ plots if the p, T data are restricted to the onset of desorption at the low temperature tail of desorption spectra [54]. Hence, $E(\theta)$ values are accessible by this procedure as long as A does not change by decreasing the coverage by some percent in the low temperature region of the desorption experiment. Subsequently, A values can be calculated form equation 3.7. For the desorption spectra of CO on Co(10$\bar{1}$0) it was

found that a linear relationship between ln p versus $1/T$ was valid up to a coverage decrease of about 4% from the initial coverage present preceding the desorption experiment [54].

Decomposition mechanisms of adsorbed intermediates may also be probed by desorption techniques commonly described as temperature programmed reaction spectroscopy (TPRS). In certain cases a molecule adsorbed on a surface may overcome a dissociation barrier during the heating cycle and at least one of the dissociation products may be created at a temperature well above its desorption temperature leading to immediate release into the gas phase. Therefore, the desorption of this species is controlled by this dissociation step as opposed to the desorption and is said to be decomposition limited. An example of one such reaction is the desorption of the reaction products subsequent to formic acid (HCOOH) adsorption on Cu(110) [55]. Two differing reactions occurring in stepwise fashion were shown to occur via study of the decomposition of HCOOD. The presence of a D_2 peak at 273 K and coincident CO_2 and H_2 at 473 K provided clear evidence for the formation of a surface formate species (HCOO). The reaction scheme proposed is as follows:

$$\mathrm{HCOOD_{(a)} \rightarrow HCOO_{(a)} + D_{(a)}}$$

$$\mathrm{2D_{(a)} \rightarrow D_{2(g)}} \qquad 273\ \mathrm{K}$$

and

$$\mathrm{HCOO_{(a)} \rightarrow \frac{1}{2}H_{2(g)} + CO_{2(g)}} \qquad 473\ \mathrm{K}$$

The use of HCOOD allowed positive identification of these two processes, as only D_2 is evolved at 273 K and only H_2 was seen at 473 K. A quantitative evaluation of the amounts of H_2 and CO_2 evolved at 473 K verified the stoichiometry of 1:2 expected from the decomposition of $HCOO_{(a)}$.

TPRS allows mechanistic analysis to be conducted for rather complex surface reaction processes utilising temperature programming, mass spectrometry and

isotope labelling. Quantitative determination of rate constants, reaction orders, and activation energy barriers is possible. Such procedures may be applied to a number of different and varying natured surfaces including clean metals, metal-adatom overlayers, alloy surfaces and supported catalysts.

References

[1] G. Binnig, H. Rohrer, C. Gerber and E. Weibel, Phys. Rev. Lett., 50 (1983) 120.

[2] J. Tershoff and D. R. Hamann, Phys. Rev. B, 31 (1985) 805.

[3] N. D. Lang, Phys. Rev. Lett., 56 (1986) 1164.

[4] Y. -Chen, W. -Xu, and J. Huang, J. Phys. E, 22 (1989) 455.

[5] J. E. Demuth, R. J. Hamers, R. M. Tromp, and M. E. Welland, IBM J. Res. Develop., 30 (1986) 396.

[6] M. P. Cox and P. R. Griffin, J. Vac. Sci. Technol. A, 6 (1988) 376.

[7] G. Binnig and D. P. E. Smith, Rev. Sci. Instrum., 57 (1986) 2630.

[8] G. Binnig and H. Rohrer, Helv. Phys. Acta, 55 (1982) 726.

[9] G. Binnig and D. P. E. Smith, Rev. Sci. Instrum., 57 (1986) 1688.

[10] S. Gregory and C. T. Rogers, J. Vac. Sci. Technol. A, 6 (1988) 390.

[11] G. R. Hennig, Chemistry & Physics of Carbon, Ed. P. L. Walker, Marcel Dekker, New York, (1970) Vol. 2.

[12] S-II. Park and C. F. Quate, Appl. Phys. Lett., 48 (1986) 112.

[13] I. P. Batra and S.Ciraci, J. Vac. Sci. Technol. A, 6 (1988) 313.

[14] D. Tománek, S. G. Louie, H. J. Mamin, D. W. Abraham, R. E. Thomson, E. Ganz and J. Clarke, Phys. Rev. B, 35 (1987) 7790.

[15] X. Yang, Ch. Bromm, U. Geyer and G. von Minnigerode, Ann. Physik., 1 (1992) 3.

[16] D. D. Chambliss and S. Chiang, Surf. Sci. Lett., 264 (1992) L187.

[17] P. W. Murray, S. Thorshaug, I. Stensgaard, F. Besenbacher, E. Lægsgaard, A. V. Ruban, K. W. Jacobsen, G. Kopidakis and H. L. Skriver, Phys. Rev. B, 55 (1997) 1380.

[18] E. Bauer, Z. Kristallogr., 110 (1958) 372.

[19] L. Pleth Nielsen, I. Stensgaard, E. Lægsgaard and F. Besenbacher, Surf. Sci., 307-309 (1994) 544.

[20] A. K. Schmid, D. Atlan, H. Itoh, B. Heinrich, T. Ichinokawa and J. Krschner, Phys. Rev. B, 48 (1993) 2855.

[21] E. Hirschorn, D. S. Lin, E. D. Hansen and T. -C. Chiang, Surf. Sci., 323 (1995) L299.

[22] S. Poulston, R. A. Bennett, A. H. Jones and M. Bowker, Phys. Rev. B, 55 (1997) 12888.

[23] S. Poulston, A. H. Jones, R. A. Bennett and M. Bowker, Surf. Sci., 379 (1997) 66.

[24] E. Wood, J. Appl. Phys., 35 (1964) 1306.

[25] G. Attard and C. J. Barnes, Surfaces: Oxford Chemistry Primers, Oxford University Press, Oxford, (1998).

[26] J. B. Pendry, J. Phys. C, 13 (1980) 937.

[27] E. Zanazzi and F. Jona, Surf. Sci., 62 (1977) 61.

[28] M. P. Seah and W.A. Dench, Surface Interface Analysis, 1 (1979) 2.

[29] M. Prutton, Surface Physics, Oxford University Press, New York, (1983).

[30] D. P. Woodruff and T. A. Delchar, Modern Techniques of Surface Science, Eds. R. W. Cahn, E. A. Davies and I. M. Ward, Cambridge University Press, New York, (1986).

[31] D. Briggs and M. P. Seah (Eds.), Practical Surface Analysis by Auger and X-ray Photoelectron Spectroscopy, Wiley, New York, (1983).

[32] T. Takahagi and A. Ishitani, Carbon, 22 (1984) 43.

[33] A. W. Czanderna and S. P. Wolsky (Eds.), Methods and Phenomena, Vol. 1 - Methods of Surface Analysis, Chap. 4, Elsevier, New York, (1975) p. 110–113.

[34] S. C. Sharma, M. Green, R. C. Hyer, C. A. Dark, T. D. Black, A. R. Chourasia, D. R. Chopra and K. K. Mishra, J. Mater. Res., 5 (1990) 2424.

[35] H. K. V. Lotsch, Topics in Applied Physics: Photoemission in Solids (I, II), Eds. M. Cardona and L. Ley, Springer–Verlag, New York, (1978) Vol. 26/27.

[36] M. T. Anthony and M. P. Seah, J. Electr. Spectrosc., 32 (1983) 73.

[37] P. W. Palmberg, F. K. Bohn and J. C. Tracy, Appl. Phys. Lett., 15 (1969) 254.

[38] G. E. Rhead, J. Vac. Sci. Technol., 13 (1976) 603.

[39] C. Argile and G. E. Rhead, Surf. Sci., 53 (1975) 659.

[40] J. A. Venables, G. D. T. Spiller, Surface Mobilities on Solid Materials, Ed. Vu-Thien Binh, Plenum NATO ASI Series B86, (1982) p. 341.

[41] E. Bauer, Z. Kristallogr., 110 (1958) 372.

[42] B. Lewis and J. C. Anderson, Nucleation and Growth of Thin Films, Academic Press, London, (1978).

[43] J. A. Venables, G. D. T. Spiller and M. Hanbucken, Rep. Prog. Phys., 47 (1984) 399.

[44] E. Bauer and J. H. van der Merwe, Phys. Rev. B, 33 (1986) 3657.

[45] A. Zangwill, Physics at Surfaces, Cambridge Press, New York, (1988).

[46] T. Young, Philos. Trans., 95 (1805) 65.

[47] P. A. Redhead, Trans. Faraday Soc., 57 (1961) 641.

[48] P. A. Redhead, Vacuum, 12 (1962) 203.

[49] J. R. Arthur and A. Y. Cho, Surf. Sci., 36 (1973) 641.

[50] J. R. Arthur and A. Y. Cho, Surf. Sci., 38 (1973) 394.

[51] J. McCarthy and R. J. Madix, Surf. Sci., 54 (1976) 210.

[52] D. A. King, Surf. Sci., 47 (1975) 384.

[53] J. L. Falconer and R. J. Madix, J. Catal., 48 (1977) 262.

[54] E. Habenschaden and J. Küppers, Surf. Sci., 138 (1984) L147.

[55] R. J. Madix, Surf. Sci., 89 (1979) 540.

Chapter Three

The Growth Mechanism, Thermal Stability and Reactivity of Palladium Mono and Multilayers on Cu(110)

1. Introduction

The interest in metal-on-metal growth continues to grow, with bimetallic systems of considerable relevance to many different technological processes including catalysis, electrochemistry and corrosion passivation [1]. The growth mechanisms are far more complex than originally anticipated and often diverge far from that expected based on thermodynamical equilibrium arguments [2]. An example of this is surface-alloy formation in which the deposited metal substitutes into the outermost atomic or several atomic layers of the substrate yielding a mixed and often ordered array rather than forming a simple overlayer structure [3]. The study of surface alloys is for the most part motivated by the possibilities of modifying both the catalytic and electronic properties of thin films and also examining the unique effect the interface buffer layer has on subsequent epitaxial growth, i.e. the stabilisation of lattice expansions/contractions or thermodynamically metastable phases.

Copper-palladium bimetallic combinations have received considerable attention due to their use industrially for CO and alkene oxidation [4], ethanol decomposition [5] and CO, benzene and toluene hydrogenation [6]. Basically, the CuPd system is an example of a bulk miscible system where a homogeneous alloy may form across the entire compositional range. Bulk CuPd alloys have received considerable scrutiny [7,8,9] regarding order-disorder transformations. It has been established that transformations of the order-disorder type occur in alloys of composition approximating to Cu_3Pd and CuPd. Alloys of the Cu_3Pd type have a disordered face-centred cubic (fcc) structure at high temperature and assume an ordered structure of the Cu_3Au type after slow cooling to room temperature. On the other hand alloys of CuPd composition possess a fcc structure at high temperatures which is disordered while at lower temperature they are body-centred cubic (bcc) and ordered with the CsCl structure, i.e. the order-disorder transformation is accompanied by a transition in crystallographic structure

Fundamentally Pd in its atomic ground state has a valence electronic configuration of $d^{10}\ s^0$ [10]. In general, Pd adatoms exhibit shifts of both core and valence levels to higher binding energy with respect to pure Pd when alloyed to Cu. The extent of the shift depends on the alloy composition [11,12], with the extent of the admetal core level shift being dependent on the fraction of empty states in the valence band of the

substrate. The greater the occupancy of the admetal d-band, the bigger the core-level shift it experiences Ni<Pt<Pd. It follows that the greatest shifts are seen for bimetallics with adsorbates with electron-rich d-bands and substrates with electron deficient valence regions. Pd has the largest d-occupancy of the group-10 metals. This would suggest that the extent of electron density transfer to the interface region in a bimetallic arrangement is greatest for Pd and therefore promotes a strong admetal-substrate bond.

Several theoretical studies are available on the deposition of group-10 atoms as clusters modelling the surfaces of transition and s,p metals [13,14]. There findings suggest a d/s-p rehybridisation that shifts d electrons from around the group-10 metal into the metal-metal interface. This has the effect of making Pd behave like a closed d-band metal in its surface chemical behaviour [15,16].

In general, ordered surface alloy formation occurs more readily in the case of growth of high melting point/surface energy metals (e.g. Pd) onto lower surface energy substrates e.g. Cu. As already noted a considerable amount of work has been done on the opposite combination i.e. Cu deposition on Pd single crystal surfaces where two-dimensional monolayer formation is favoured. For deposition at 300 K strained epitaxial overlayers are formed with little intermixing, with rapid alloying occurring only at elevated temperatures and generally ordered surface alloy formation between Cu and Pd is not observed. Hahn et al [17,18,19,20] have studied the Cu on Pd(110) system extensively by STM with emphasis on temperature dependent growth. In general, the growth mode extends from Volmer-Weber (VM) at 300 K to layer-by-layer at 600 K, with an intermediate Stranski-Krastanov (SK) mode observed at 400 K. Cu grows pseudomorphically at 600 K even up to coverages as high as 10 ML. A sharp (1×1) LEED pattern and flat STM imaging discloses this phenomenon which is unexpected since the total strain energy of the system increases linearly with film thickness [21]. Although the system exhibits direct wetting at 600 K evidence of alloying is only recorded at ~700 K. Worthy of note at this interval is the strain relief mechanism employed by this system. Uniaxial buckling of the surface in the $[1\,\bar{1}\,0]$ direction is suggested [18] to relieve this strain. STM images reveal this as a striped pattern in the image running in the opposite [001] direction. This occurrence is further developed during the discussion of this chapter.

In contrast, Pd deposition onto Cu single crystal surfaces at 300 K leads to ordered surface alloys via place exchange of the Cu substrate with Pd atoms in the outermost layers favoured both by the enhanced kinetics due to the relative ease of breaking Cu-Cu bonds compared to Pd-Pd bonds and the additional thermal energy of the incoming hot Pd atoms.

Fujinaga's [22,23] LEED and Auger measurements were the earliest concerning the conditions favourable to the formation of ordered alloy structures in the case of Pd evaporation on low index Cu crystals. Most work to date has centred around the formation of the c(2×2) CuPd surface alloy formed readily on the Cu(100) substrate, upon deposition at 300 K, due to surface alloy formation via substitution of Pd adatoms into the outermost layer [24]. Other metals which exhibit c(2×2) structures on Cu(100) are Pb [25], Mn [26] and Au [27] at ~0.5 ML admetal coverage. Although no observable distortion of the c(2×2) structure due to the 8 % mismatch between Pd and Cu is noticed, the Au/Cu(100) with a 13 % mismatch displays clear strain seen as surface ridges. However, Pd atoms are relaxed 0.02 Å outwards from the Cu atoms in the outermost layer with the interlayer spacing of the first layer with respect to the second remaining similar to that of the copper substrate. The issue of most contention regarding this system is the exact coverage needed to complete an ordered c(2×2) structure and also the origin of a second ordered overlayer structure at higher coverages.

Graham et al [28,29] suggest a coverage of 0.8 ML for an ideal c(2×2) while Pope et al [30] and Wu et al [31] agree on 0.55 ML. Both Graham [29] and Valden [32] et al report the presence of subsurface Pd in the Cu(100)-Pd- c(2×2) system at "maximum perfection" as monitored by LEED. Valden et al, using CO as a probe molecule, propose the presence of pure Cu islands in the outermost layer due to ejected Cu atoms coalescing after Pd place exchange upon alloy formation. Valden also reports upper step and island edges to be Cu-rich regions. The Cu in these regions is suggested from STM examination to form a second layer structure classified as a p(2×2) [24]. This second layer seems to adopt a p4g symmetry from LEED while the topmost layer is seen from STM to contain one Pd and one Cu atom per unit cell. Thus, for continued deposition it is proposed that the topmost layer is a mixed alloy

of Pd and Cu, forming on top of a p4g reconstructed c(2×2) (see Chapter 1 – figure 13).

It is suggested that CuPd islands formed after Cu atom ejection upon initial Pd place exchange are most likely to reside on pure copper regions as opposed to CuPd c(2×2) alloy [33]. STM examinations of lower Pd coverages reveal that growth proceeds with Cu islands formed after Pd place exchange tending to cover alloyed regions [24].

In the case of Pd growth on Cu(111) at 300 K, a layer-by-layer room temperature growth mechanism has also been suggested on the basis of Auger uptake studies [22]. More recently for submonolayer Pd growth on Cu(111), STM indicates the random ordering of Pd at room temperature with the preferred structure that of single-layer dendritic islands nucleated at steps [34]. Random Pd alloying with surface Cu results at higher temperatures (~500 K). The exact mechanism of Pd incorporation is unknown with the absence of any long-range ordering. It is however tenuously proposed that alloying of Pd into the terraces is concomitant with the removal of Cu from the step edges.

Aside from early LEED work by Fujinaga [22,23] the only detailed study to date of Pd growth on Cu(110) is that of Murray et al [35] who utilised STM to study the growth mechanism and structure of Pd films at low coverage (up to 0.3 ML). Low Pd coverages lead to substitution of Pd atoms into the outermost Cu layer forming an ordered (2×1) CuPd surface alloy via periodic substitution of every second Cu atom along the $[1\,\bar{1}\,0]$ rows by Pd, with expelled Cu atoms diffusing to step edges. As the Pd coverage increases, larger domains of (2×1) alloy form and are covered by a monolayer of Cu originating both from step edges and from the Cu(110) terraces which exhibit monolayer deep "pits". It appears that a sub-surface second layer (2×1) CuPd alloy covered by a copper monolayer is the stable structure at higher Pd coverages. The area covered by islands at this stage is roughly twice that of the Pd coverage. Further evidence for this mechanism is the lack of any indication of Pd atoms in the island or pit regions. In contrast the CuPd (2×1) chains formed at low Pd coverage ($\theta_{Pd} \leq 0.17$ ML) remain uncovered due to the necessary formation of a large number of high energy Cu edge atoms in a small 2D island which would be required to "cap" the chain. While Murray et al [35] only studied Pd coverages up to about 0.3 ML, it appears reasonable that at coverages of 0.5 ML, large areas of a

copper capped p(2×1) CuPd underlayer will be the dominant structure, with the top two layers having a similar structure to that determined for a bulk $Cu_{0.85}Pd_{0.15}(110)$ alloy ($Cu_3Pd(\alpha')$)[36].

In this chapter we will outline a number of previously unreported aspects for the growth of Pd on Cu(110) for coverages above 0.5 ML indicating a growth model in which further alloying occurs with the outermost copper monolayer forming a bi- or tri-layer of CuPd alloy upon which pure Pd eventually grows in the form of flat topped epitaxial platelets. The aim of this study is to extend the work of Murray et al [35] up to high Pd coverages for room temperature growth, to study the thermal stability of the Pd/Cu(110) layers by STM and XPS and to examine the surface reactivity of the composite CuPd layers by monitoring the thermal stability of a reactive intermediate – a formate species formed by adsorption of formic acid.

2. Experimental

Experiments were performed in two separate ultra-high vacuum (UHV) chambers operated at base pressures in the low 10^{-10} Torr range. The first chamber was equipped with low energy electron diffraction (LEED) optics for surface crystallographic characterisation and unmonochromated XPS (single-channeltron angle-resolved analyser) facilities coupled with a VG quadrupole mass spectrometer (MS) both for monitoring gas purity and as a detector for temperature programmed desorption (TPD). The second chamber consisted of a variable temperature Oxford Instruments STM. This STM system was also equipped with a quadrupole MS and accompanied by LEED characterisation facilities, the latter also serving as a retarding field analyser for surface elemental characterisation by Auger electron spectroscopy (AES).

The Cu sample was oriented to within 0.5° of the (110) plane (Metal Crystals and Oxides Ltd.). Cleaning of the sample typically involved repeated cycles of argon-ion bombardment, initially with the sample at room temperature and finally at ~700 K. Upon ceasing ion bombardment the sample was annealed in UHV at around 700 K for several minutes to restore surface order producing a sample surface which exhibited a sharp low background (1×1) LEED pattern. XPS and AES indicated no contaminants above their respective noise limits.

A standard TPD set-up was employed during the work, comprising of line-of-sight geometry between sample and MS as well as a linear sample heating rate (~1.5 K s^{-1}). Formic acid (97% purity, Aldrich Chemicals Ltd.) dosing was carried out via a liquid reservoir attached to a fine-control leak valve and checked for purity with the quadrupole MS. Gas exposures were measured using an uncalibrated Bayard-Alpert ionisation gauge and are quoted in Langmuirs (L). All XPS experiments were recorded using Al-Kα radiation ($h\nu$ = 1486.6 eV) with XPS binding energies referenced to the Cu $2p_{3/2}$ core-level intensity at 932.7 eV [37]. The electrostatic hemispherical analyser was operated with a fixed analyser transmission energy of 44 eV (FAT mode). The accuracy of the measured binding energies is ± 0.05 eV.

Palladium was evaporated using a home-built sublimation source. This was achieved via the resistive heating of a 0.3-mm diameter tungsten filament around which a 0.125-mm high-purity Pd wire (Goodfellows Metals Ltd., (99.97 % purity)) was

wound. The evaporators were outgassed until they could be used with the chamber pressure remaining in the 10^{-10} Torr range. Deposited films were shown to be spectroscopically pure by XPS/AES analysis with a homogeneous Pd coverage across the entire surface. Palladium deposition rates (approximately 2×10^{-3} ML s^{-1}) were calibrated as follows: - for all TPD experiments the deposition rate was monitored by recording the ratio of the Pd $3d_{5/2}$ (KE ~1150 eV) and Cu $2p_{3/2}$ (KE ~550 eV) core-level intensities as a function of evaporation time. In the STM chamber the growth rate of Pd on Cu(110) was estimated by construction of Auger signal versus evaporation time (AS-t) plots. This was achieved by monitoring the ratio of the peak-to-peak amplitudes of the derivative spectra of the Pd $M_{4,5}N_{4,5}N_{4,5}$ (KE = 326, 330 eV) and the Cu $M_{2,3}VV$ (KE = 59, 61 eV) Auger transitions employing the LEED optics as a retarding field analyser (RFA). We estimate the coverages quoted should be accurate to within about ±50% between chambers.

Modelling thin layer metal-on-metal growth by comparison to that expected for layer-by-layer growth is commonly attempted to determine the metal growth mode and calibrate the surface coverage. The theoretical spectral intensity ratios are calculated for both XPS and AES from equation 2.1:

$$\frac{I_{Pd}}{I_{Cu}} = \frac{I_{Pd}^{\infty}}{I_{Cu}^{o}} \left[\frac{1 - \exp\left[\frac{-d}{\lambda_{Pd} \cos\theta} \right]}{\exp\left[\frac{-d}{\lambda_{Cu} \cos\theta} \right]} \right] \qquad 2.1$$

where

I_{Pd}^{∞} is the Pd $3d_{5/2}$ (Pd MNN) signal from a "bulk" Pd overlayer.

I_{Cu}^{o} is the Cu $2p_{3/2}$ (Cu MVV) intensity from the clean Cu(110) crystal.

θ is the emission angle of the electrons with respect to the surface normal (θ = 40 deg. for XPS).

d is the distance travelled through the Pd overlayer by the emitted electrons in Å (Pd(110) interlayer spacing = 1.37 Å).

A "bulk" Pd overlayer was considered to be an overlayer of sufficient thickness to completely damp the XPS signal from the underlying copper substrate. λ_{Pd} & λ_{Cu} are the inelastic mean free paths (IMFP) of the Pd $3d_{5/2}$ (Pd MNN) and the Cu $2p_{3/2}$ (Cu MVV) core-levels calculated to be 16.7 Å (9.0 Å) and 10.5 Å (5.2 Å), respectively, using the formalism of Seah and Dench [38]:

$$\lambda_m(\text{nm}) = \left(538 \times E^{-2}\right) + \left(0.41 \times a_m^{1.5} \times E^{0.5}\right) \qquad 2.2$$

where

- λ_m is the IMFP of the material,
- E the electron kinetic energy (eV),
- $a_m(\text{nm}) = \left(\sqrt[3]{\frac{A_m}{\text{N} \times \rho_m \times 1000}}\right) \times 10^9$

  where

  - A_m is the mean atomic weight of material (g/mol) (Cu = 63.5, Pd = 106.4),
  - N is Avogadro's number (6.023×10^{23} particles/mol),
  - ρ_m is the density of material (Kg/m^3) (Cu = 8920, Pd = 12250).

Cu (a_m) = 0.2278 nm and Pd (a_m) = 0.2423 nm.

3. Results

3.1. Room temperature growth mechanism of Pd on Cu(110) - XPS, AES, and LEED

Figure 1 shows a plot of Pd $3d_{5/2}$/Cu $2p_{3/2}$ XPS intensity ratio for Pd adsorption on Cu(110). The areas plotted are integrated peak areas after a linear background subtraction. Use of a ratio rather than plotting Cu or Pd peak intensities individually serves to remove errors in re-positioning of the sample after evaporation relative to the XPS gun/electron energy analyser and changes in X-ray flux. All evaporations were carried out with the sample held at room temperature (300 K). On the same graph we show the theoretical layer-by-layer (Frank van der Merwe) growth curve for Pd on Cu(110).

Figure 2 on the other hand reveals a corresponding Auger signal versus deposition

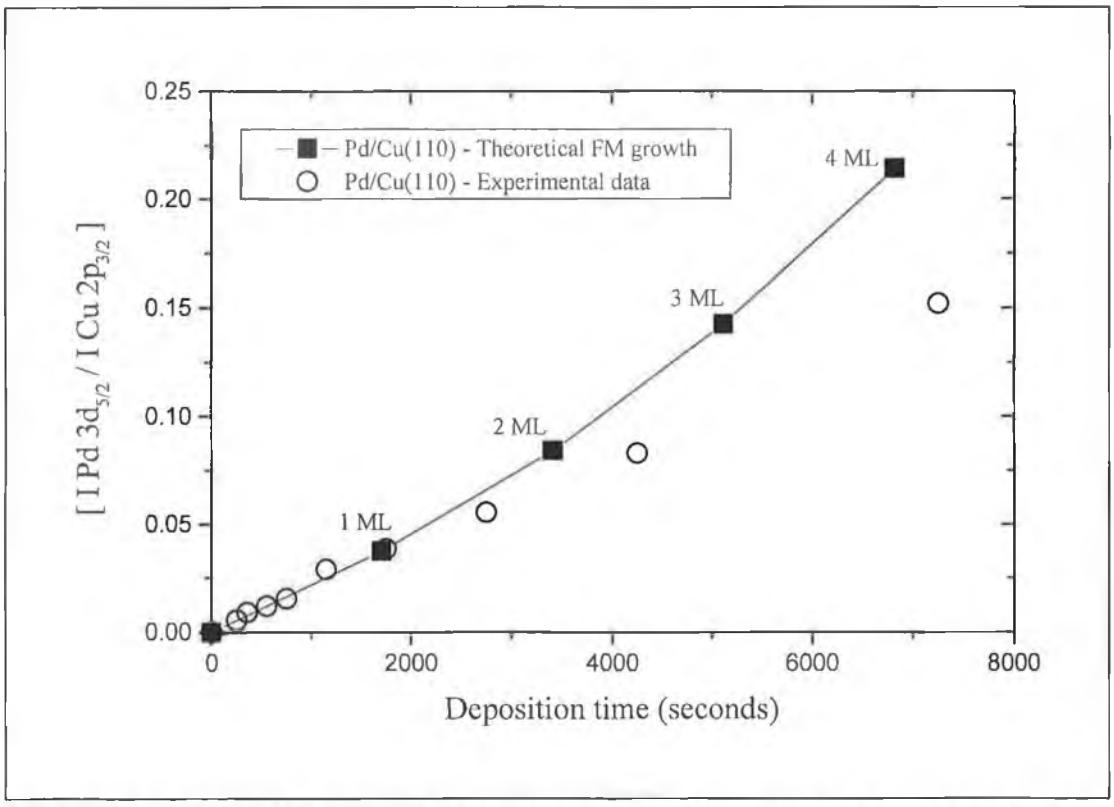

Figure 1: Variation of the integrated area of the Pd $3d_{5/2}$ core level ratioed to that of the Cu $2p_{3/2}$ level (open circles) for deposition of Pd onto Cu(110) at 300 K. Also shown is a theoretical prediction for a perfect layer-by-layer (Frank van der Merwe = FM) growth mechanism.

time plot utilising the ratio of Pd MNN (KE = 326, 330 eV) and the Cu MVV (KE = 59, 61 eV) peaks for sequential depositions of Pd at 310 K. Peak intensities were measured peak-to-peak. The theoretical curve for Frank van der Merwe (layer-by-layer) growth has been included and the data has been scaled to give a best fit to the theory. The theoretical curve was calculated by employing the elemental sensitivity factors determined directly for our own analyser with Pd and Cu single crystals of (110) orientation. Clearly the curve shows no break points that would be reminiscent of layer-by-layer growth and so we use the film thickness' derived by this method as merely a guide to the deposited coverage in the STM experiments.

As it is known that for coverages at least up to 0.3 ML, Pd essentially grows two-dimensionally via substitution into the top copper layer of the substrate forming a (2×1) CuPd surface alloy [35]. The theoretical layer-by-layer growth curve has been fitted to the experimental curve at low Pd coverages assuming a layerwise growth mechanism. It is anticipated that a small error will exist in quoted coverages using a

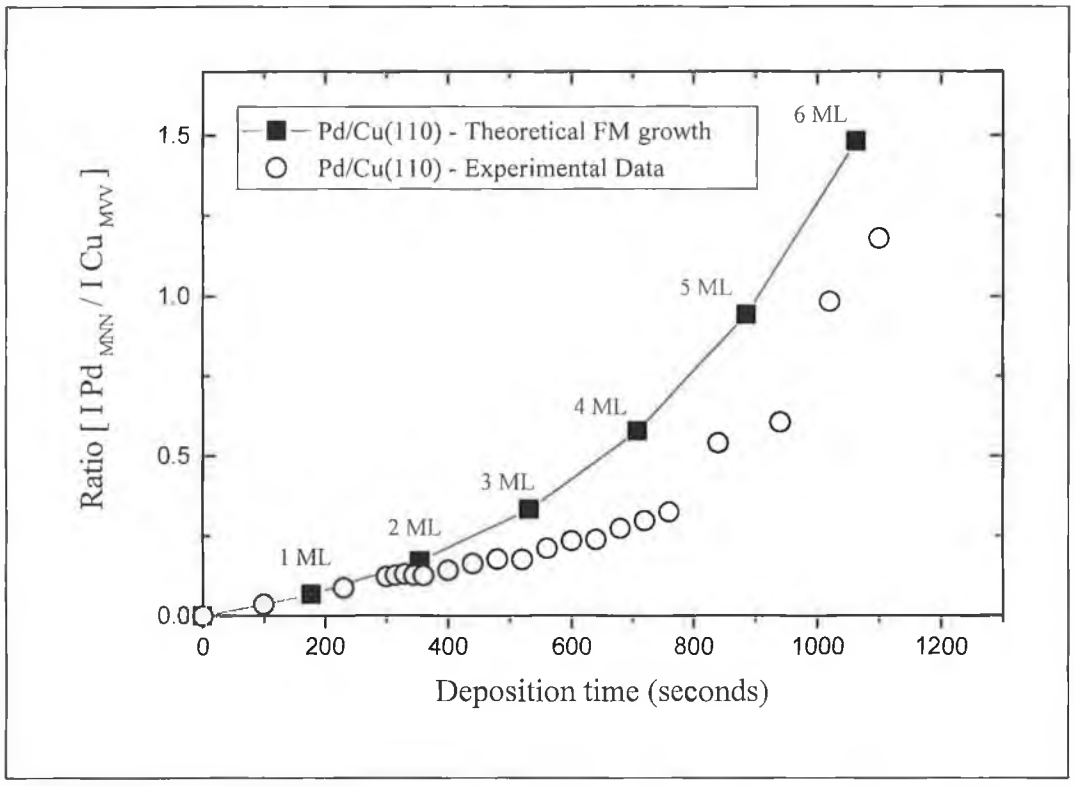

Figure 2: Uptake curve showing the variation of the ratio of Pd MNN (KE = 326, 330 eV) and Cu MVV (KE = 59, 61 eV) Auger lines with increased deposition time. The theoretical points for a layer-by-layer growth mechanism are plotted along with the measured Auger ratios.

fitting of this type as the majority of Pd atoms, while growing in a two-dimensional layer, are covered by a copper monolayer as outlined in the introduction. This will serve to make the actual coverages of Pd on the surface slightly higher than that predicted by figure 1. A simple calculation based on comparing a 0.5 ML Pd film in a true layer-by-layer growth mode and in a copper coated sub-surface (2×1) layer indicates coverages will be underestimated by approximately 15%. All coverages quoted have thus been adjusted for this effect. It should be stressed that even after this adjustment the XPS coverages quoted must only be viewed as estimates due to uncertainties in the inelastic mean free paths utilised and possible photo-electron diffraction effects within the film leading to enhancements or reductions of the measured XPS signal from geometric rather than compositional effects. It would seem reasonable to assume that the quoted absolute coverages are accurate to within ±30%.

Inspection of figure 1 illustrates that the experimental data fall below that predicted for pure layer-by-layer growth. This clearly signals departure from simple two-dimensional growth already at coverages above 1 ML. This is not surprising as the Pd surface energy (2.043 J m^{-2}) is higher than that of Cu (1.934 J m^{-2}) [39,40] which, along with the 7.7% lattice mismatch favours a growth mechanism in the form of clusters. The higher surface energy of Pd is verified experimentally both by the fact that Murray and co-workers find that the (2×1) CuPd alloy prefers to be covered by a copper monolayer [35], that growth of Cu on Pd(110) is two-dimensional up to completion of the first atomic layer [18], and that the bulk alloy is found to be Cu terminated [36].

The XPS data shown in figure 1 indicate that the Pd:Cu XPS ratio increases in an approximately linear fashion. This may be explained if at coverages beyond 1 ML a linear increase in the density of Pd clusters occurs as a function of evaporation time with little change in the cluster base-to-height ratio. The clusters must have a high base to height ratio to mimic quite closely layer growth as the experimental data points do not fall that significantly below the theoretical. Due to the propensity for the Cu(110)/Pd system to mix for deposition at 300 K [35], it is likely that at coverages >0.5 ML further intermixing with the outermost copper monolayer, will initially occur leading to growth of a second mixed CuPd layer above the (2×1) CuPd surface alloy. This mixing will clearly be limited, as the amount of copper directly

available for further alloying is the single outermost monolayer capping the (2x1) CuPd alloy unless we invoke transport from deeper layers. It would thus appear likely that either two or three alloyed layers will form prior to nucleation of pure Pd clusters, signalled by the deviation from the theoretical curve between 1 and 2 ML coverage.

With regards to the AS-t plot, shown in figure 2, clear deviation from linearity is found between 1 and 2 ML similar to XPS observations. The departure from FM growth, as the curve falls below that theoretically predicted, suggests in a similar manner as for the XPS curve that cluster formation dominates after initially alloying. Unfortunately, the exact extent of this initial interfacial alloying is difficult to quantify. In essence this plot only serves to emphasise the high base to height ratio of the clusters formed, evident by only a slight deviation from the FM growth curve even up to high Pd coverages (~6 ML). Strong clustering producing taller islands would lead to a more significant divergence in the experimental data below the modelled FM growth.

The adsorption of Pd was also followed qualitatively by observing changes in the LEED pattern with increasing Pd exposure at 300 K in the STM chamber. The Cu(110) surface exhibited a sharp low background (1×1) LEED pattern. Exposure to Pd led initially to an increase in diffuse background intensity with the formation of a p(2×1) LEED pattern (~0.7 ML Pd) as expected from the surface alloy [22,41]. The quality of the p(2×1) increased (sharpest at ~1.2 ML Pd), although for deposition at 300 K there always remained clear signs of disorder evidenced by high background and the rather weak nature of the superlattice beams. Streaking and elongation of the (2×1) beams in the [001] direction was observed suggestive of poor long range order of the (2×1) CuPd alloy in this direction. Increasing the Pd coverage beyond 1.2 ML led to a further increase in diffuse background scattering and a gradual weakening in the half order beams. At high coverages only a poor quality (1×1) pattern super-imposed on a high background persisted.

The predicted growth mechanism for Pd on Cu(110) up to and beyond completion of interfacial alloy formation Pd coverages is shown schematically in Figure 3. At Pd coverages ~2 ML the postulated growth mode is that of the nucleation of Pd clusters above a mixed p(2×1) CuPd alloy "buffer" layer.

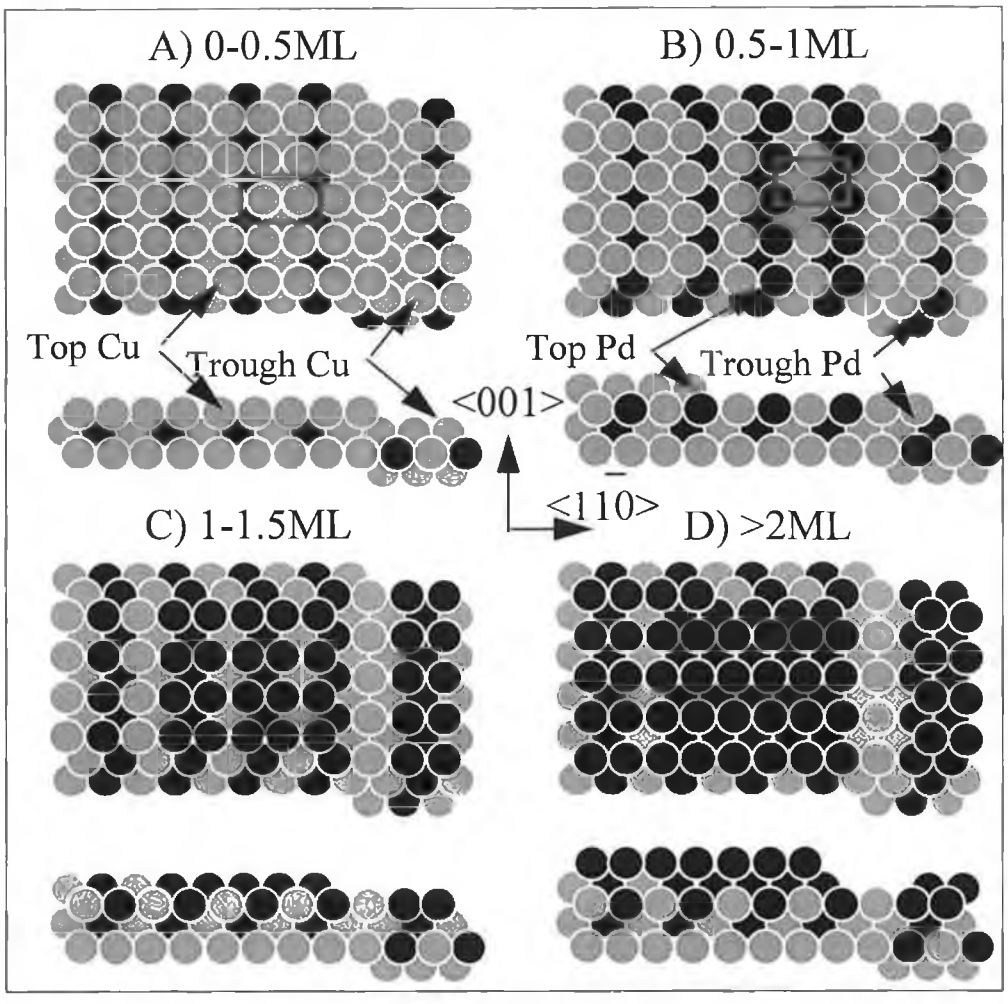

Figure 3: Schematic model of the suggested growth mechanism of Pd on Cu(110) at 300 K. The model does not necessarily imply that Pd grows in a layer-by-layer fashion upon the CuPd interface.

3.1.1. XPS measurements

Figure 4 illustrates the evolution of the Pd 3d core-level with increasing Pd coverage for deposition at 300 K. A small shift to lower binding energy of 0.3±0.1 eV and broadening is observed with increasing coverage. The observed changes in XPS line shape are in line with the postulated growth mechanism. At lower coverages (up to coverages around 1 ML) emission is predominantly from Pd in a CuPd alloy environment (higher binding energy XPS peak) [42,43], while for higher coverages emission occurs from both Pd in the mixed alloy buffer layer and metallic Pd clusters above the mixed interface. The observed broadening may thus be assigned both to the convolution of the chemically shifted "alloyed" Pd and metallic Pd but also to the

larger width of the Pd core level in an epitaxial film than in an alloyed state (see thermal stability section). We postulate that the range of differing local geometries in the epitaxial film leads to a wider range of core binding energies than in a CuPd alloy for which all Pd atoms are in a similar local environment.

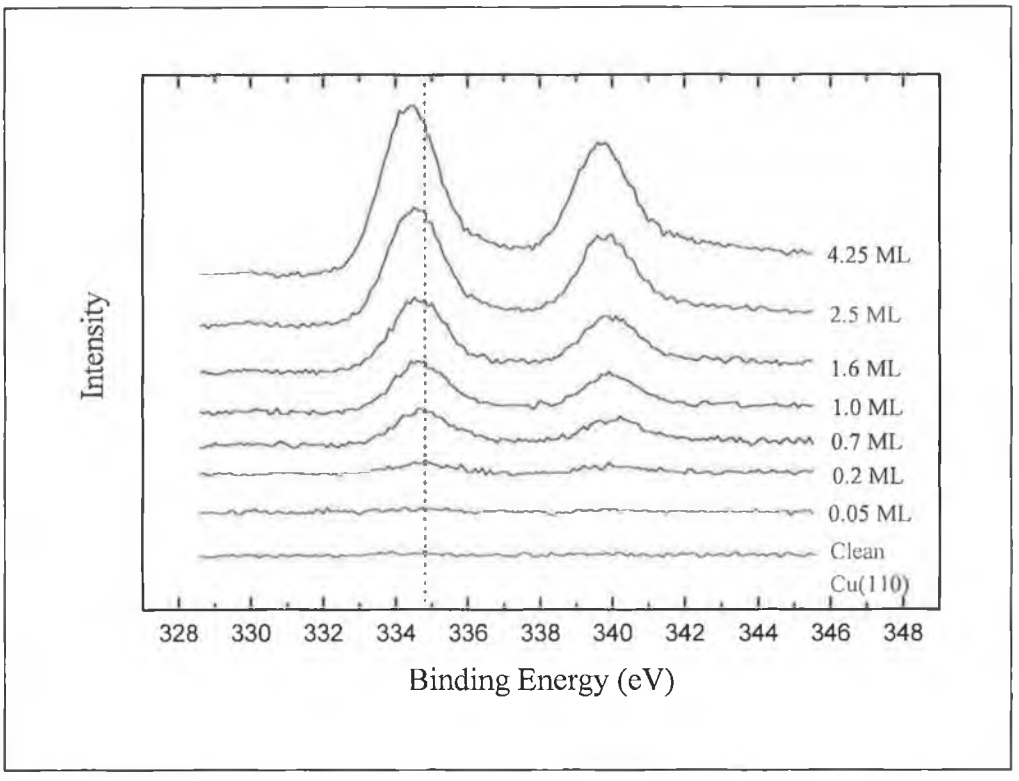

Figure 4: Palladium 3d core-level spectra as a function of surface coverage for Pd films grown on Cu(110) at 300 K. The dotted line is to aid visualisation of the core-level chemical shift with increasing coverage.

The observation of a shift to lower binding energy as the Pd coverage is increased agrees with previous observations of Pope et al [41]. These authors report that a c(2×2) CuPd alloy formed with Cu(100) at Pd coverages of 0.5 ML have a 0.4 eV higher binding energy than for 2 ML and 4 ML Pd films. Pope's value compares with the measurements of Graham et al for Pd growth on Cu(100) [28] whom reported a positive 0.3 eV binding energy shift. Pope et al also noted an increase in the full-width-at-half-maximum (FWHM) as the Pd coverage is increased which they attribute to a similar reason as postulated here i.e. a range of different environments for Pd.

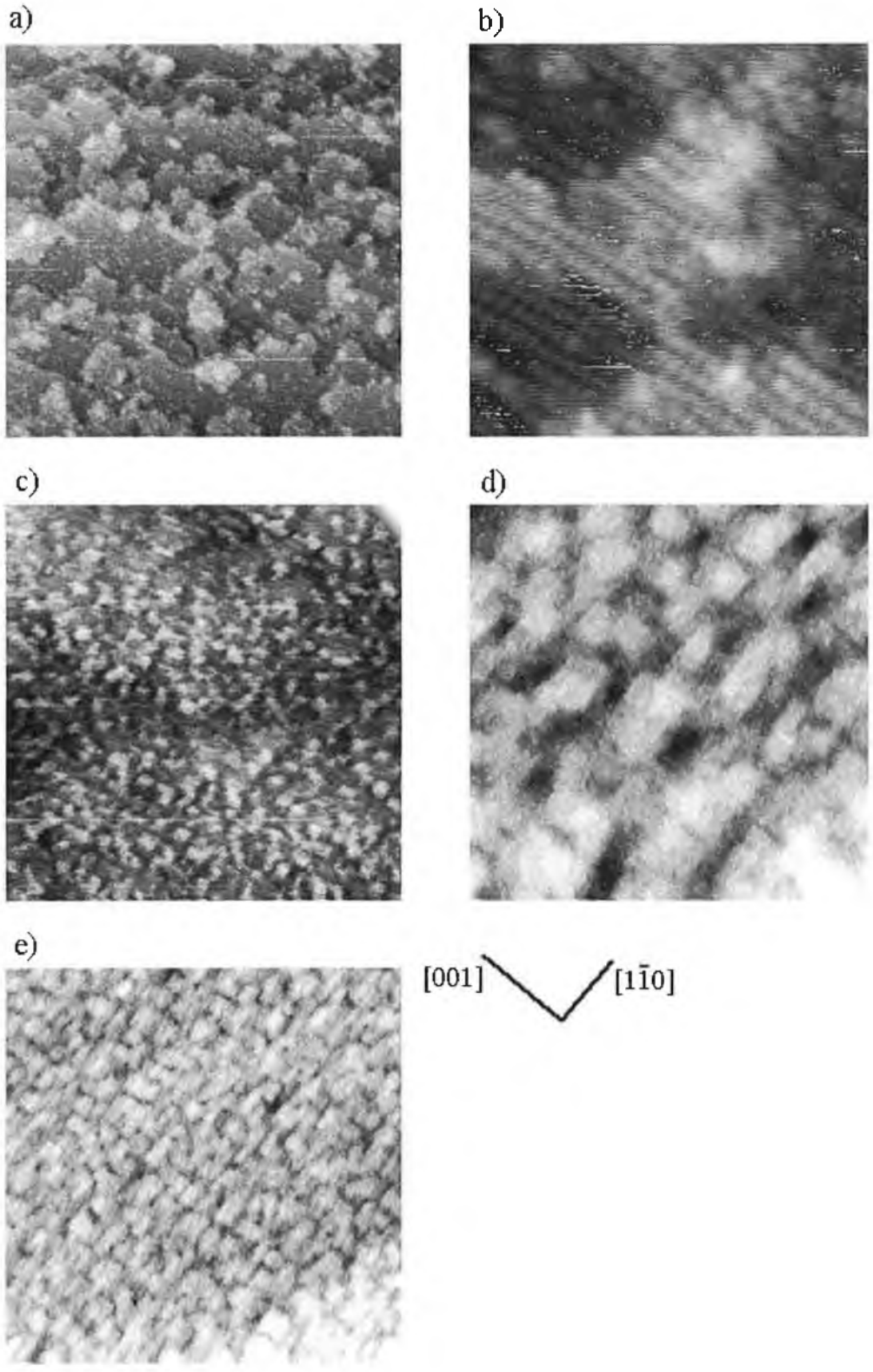

Figure 5: A series of representative STM images for Pd adsorption on Cu(110) at 300 K, (a) (100 × 100 nm^2) and (b) (10 × 10 nm^2) 1 ML; (c) (200 × 200 nm^2) 2.5 ML; (d) (100 × 100 nm^2) 4 ML; and (e) (177 × 177 nm^2) 10 ML. Tunnelling current = 1 nA (all images), bias voltage = -500 mV (a,b), 500 mV (c–e).

3.1.2. STM measurements

In order to examine the room temperature growth mechanism at a nanoscopic level STM was applied. The STM images were recorded in constant current mode for a range of Pd coverages with each film being freshly prepared by deposition at 300 K. Figure 5 illustrates a selection of STM images for increasing Pd coverage from sub-monolayer to thick films. Crystal orientation as indicated in figure 5 is the same for all subsequent images shown.

Figure 5(a) shows a 100 × 100 nm image of a 1 ML Pd film. The surface is highly heterogeneous and consists of monolayer deep pits, terraces and monolayer high islands. The edges of the islands and terraces are not aligned in any ordered way. Figure 5(b) illustrates a 10 × 10 nm image of the same surface at atomic resolution indicating widespread formation of a (2×1) structure both within the islands and on terraces. This surface displayed a (2×1) LEED pattern. Closer inspection of the terrace structure shows a (2×1) surface termination on two different levels of terrace. These images suggest that for Pd coverages above 0.5 ML further alloying occurs leading to formation of large areas of surface with a mixed CuPd (2×1) alloy layer outermost, which contrasts with the findings of Murray et al for lower coverages for which the (2×1) mixed layer is capped by a copper monolayer. For coverages beyond 0.5 ML (where the surface is dominated by the aforementioned CuPd underlayer capped by a copper monolayer) arriving Pd atoms appear to substitute within the outer copper monolayer thus forming a top layer (2×1) alloy. Ejected copper atoms form islands above the alloyed double layer which may themselves mix with further Pd atoms arriving at higher coverages. Unlike the case at Pd coverages ≤0.5 ML, no surface copper is available for alloying (other than from the bulk) once the "capping" copper monolayer has been used up.

Figure 5(c) illustrates a 200 × 200 nm image of a 2.5 ML Pd film illustrating a surface upon which Pd clusters have begun to nucleate above the CuPd alloyed buffer layer. The image shows a high density of platelets covering a large fraction of the surface with monolayer and in some cases bilayer heights. The platelets adopt a range of shapes and sizes and there is clearly significant heterogeneity within the surface as would be expected as the 1 ML film does not present an ideal template upon which further Pd clusters may grow. Figure 5(d) illustrates a 100 × 100 nm

image of a palladium film of 4 ML coverage clearly indicating growth of multilayered Pd platelets which are densely packed. The clusters are predominantly rectangular in shape and aligned with their edges parallel to the two high symmetry directions of the Cu(110) substrate. The clusters are now multilayered with a high base to height ratio, readily explaining that while the XPS- and Auger-time plots do differ from that expected for a simple layer-by-layer growth mode the deviation is far from significant. Finally, figure 5(e) (177 × 177 nm) illustrates an image from a "thick" (~10 ML) Pd film indicating a high density of clusters densely packed, separated by crevices. The clusters are predominantly flat topped in shape and the film has a clearly granular appearance. Moreover, for coverages <1 ML we observe similar rough step edges and islands on terraces as for the ~1 ML images while coverages between 4 and 10 ML maintain the rectangular/granular appearance.

3.2. Thermal Stability of the Cu(110)/Pd System

3.2.1. LEED and XPS

It is observed that the annealing of low coverage surfaces displaying a (2×1) LEED pattern to 470 K generates better ordering of the (2×1) overlayer with sharper overlayer LEED spots, while annealing to 670 K and maintaining this temperature slowly degrades the (2×1) overlayer and leaves a high background (1×1). This suggests that the formation of a well-ordered (2×1) is kinetically hindered for growth at 300 K. In order to investigate the thermal stability of the bimetallic interface further, the ratio of the palladium $3d_{5/2}$ to copper $2p_{3/2}$ XPS core lines were monitored as a function of stepwise annealing for 30 seconds to increasingly high temperature (with XPS spectra being recorded on cooling to 300 K). Figure 6 reveals the resulting data for (a) 3 ML and (b) 8 ML films. In the case of the thinner film the XPS ratio remains relatively constant up to ~500 K with a sharp drop between 500 and 700 K clearly illustrating that alloying is rapid on an experimental time scale for temperatures above 500 K. In the case of the 8 ML film signs of intermixing occur even earlier, at around 450 K.

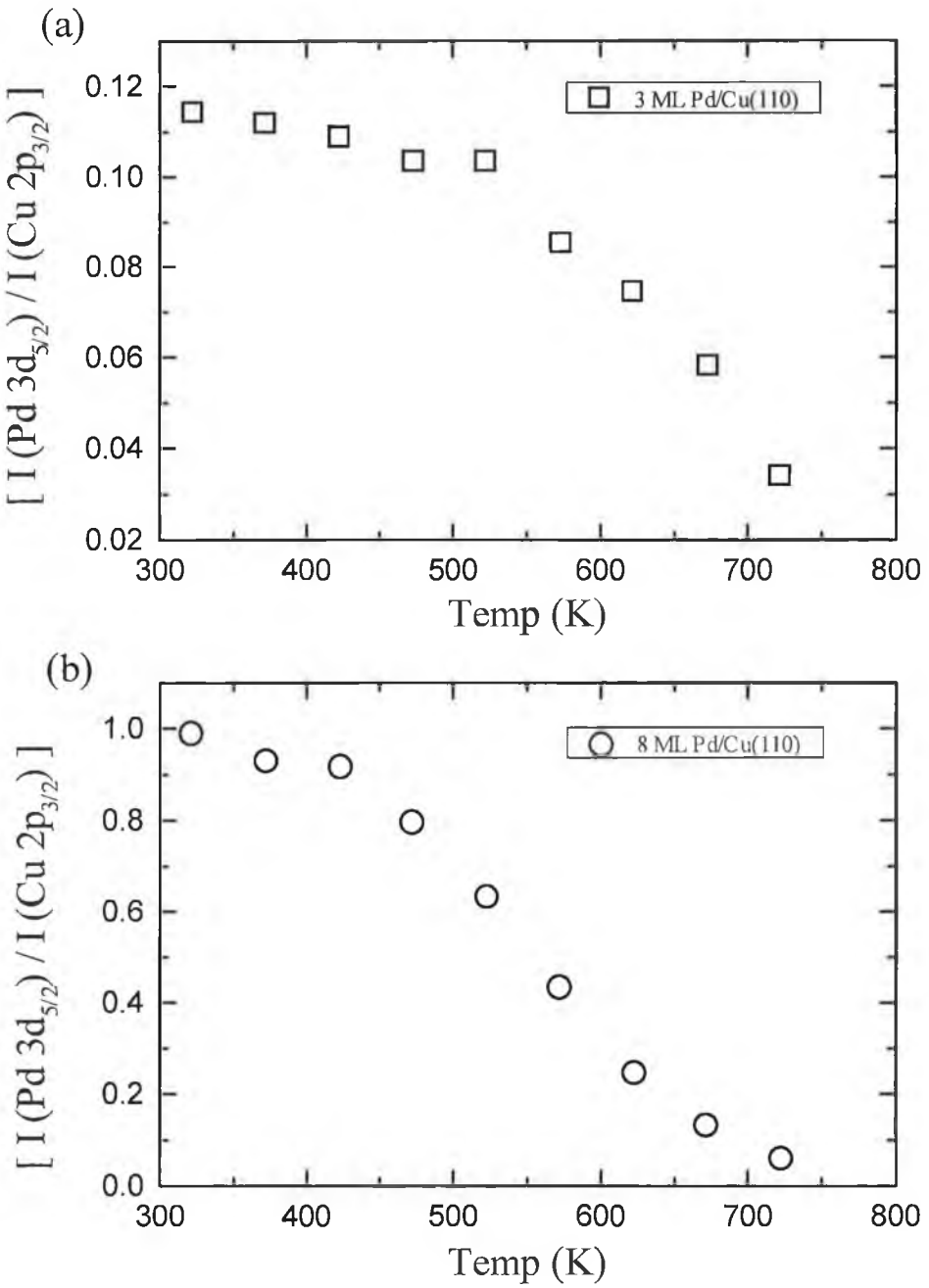

Figure 6: Variation of the background subtracted XPS palladium $3d_{5/2}$ to copper $2p_{3/2}$ core level ratio as a function of annealing temperature for (a) 3 ML and (b) 8 ML Pd films. In each case the sample was held at the annealing temperature for 30 seconds and re-cooled to room temperature prior to the measurement.

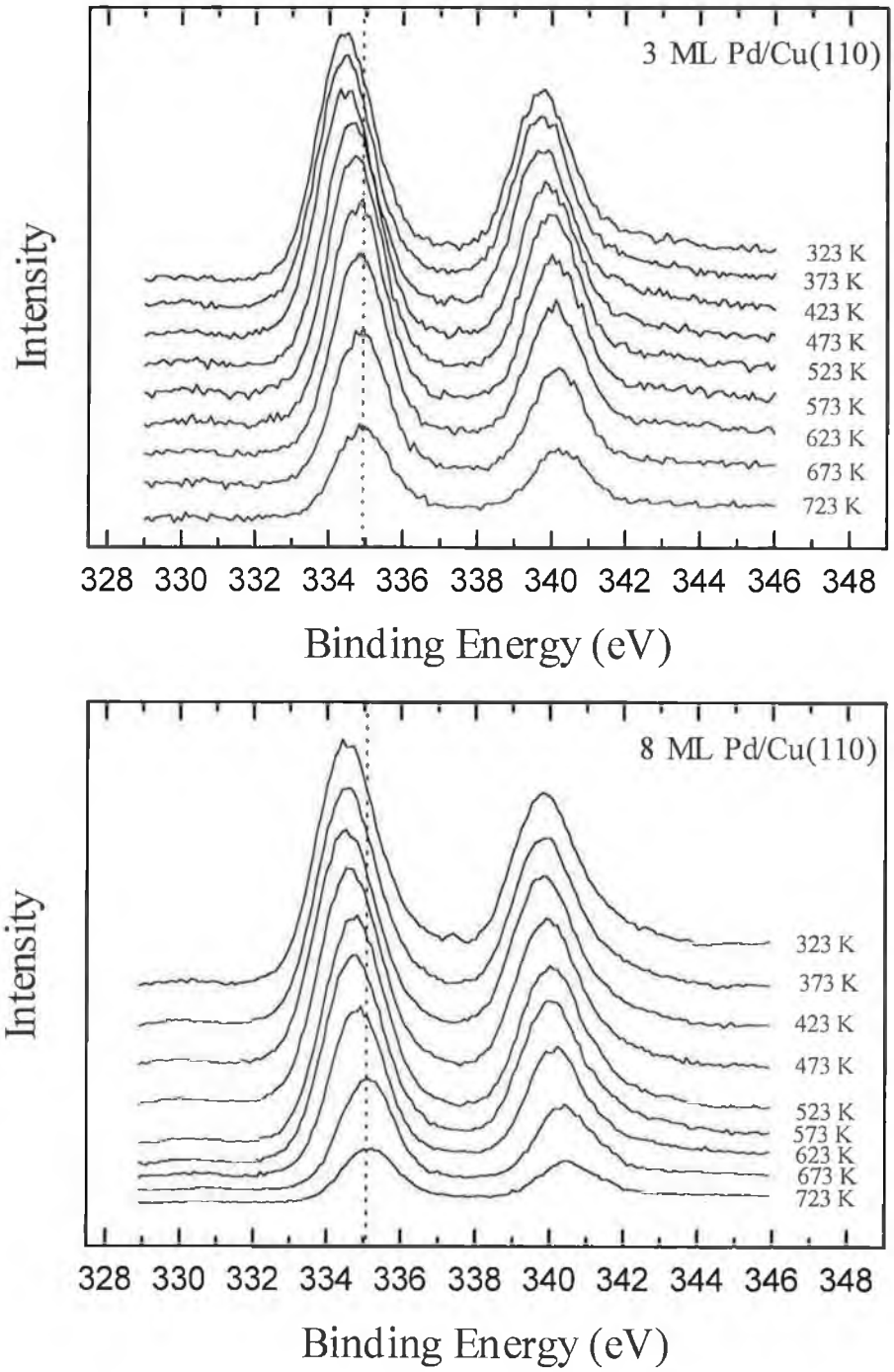

Figure 7: Palladium $3d_{5/2}$ XPS core levels for a 3 ML and 8 ML Pd film as a function of annealing temperature.

Figure 7 illustrates the effect of annealing on the palladium 3d XPS core lines, again for a 3 ML and 8 ML film. In both cases the unannealed film exhibits a binding

energy of 334.4 ± 0.05 eV. The binding energies and full-widths-at-half-maximum (FWHM) remain constant for annealing up to approximately 473 K after which a shift towards higher binding energy occurs along with a concomitant decrease in peak intensity due to thermally induced intermixing. Heating to 725 K leads to an intermixed alloy surface with a large shift of 0.6 ± 0.05 eV to higher binding energy relative to the as-deposited film and a marked reduction in FWHM. The XPS core level shift appears to mirror that reported for the Pd valence levels upon alloying with Cu, in which a shift in the centroid of the d-band emission to higher binding energy occurs. The 4d valence level peaks at about 0.6 eV below the Fermi level in pure palladium while in a CuPd surface alloy of Cu:Pd local stoichiometry varying between 3:1 to 20:1 it is located at approximately 1 eV higher binding energy [44]. As discussed earlier, Pd adatoms in CuPd alloys exhibit core and valence shifts towards higher binding energy with respect to those of pure Pd [11,12].

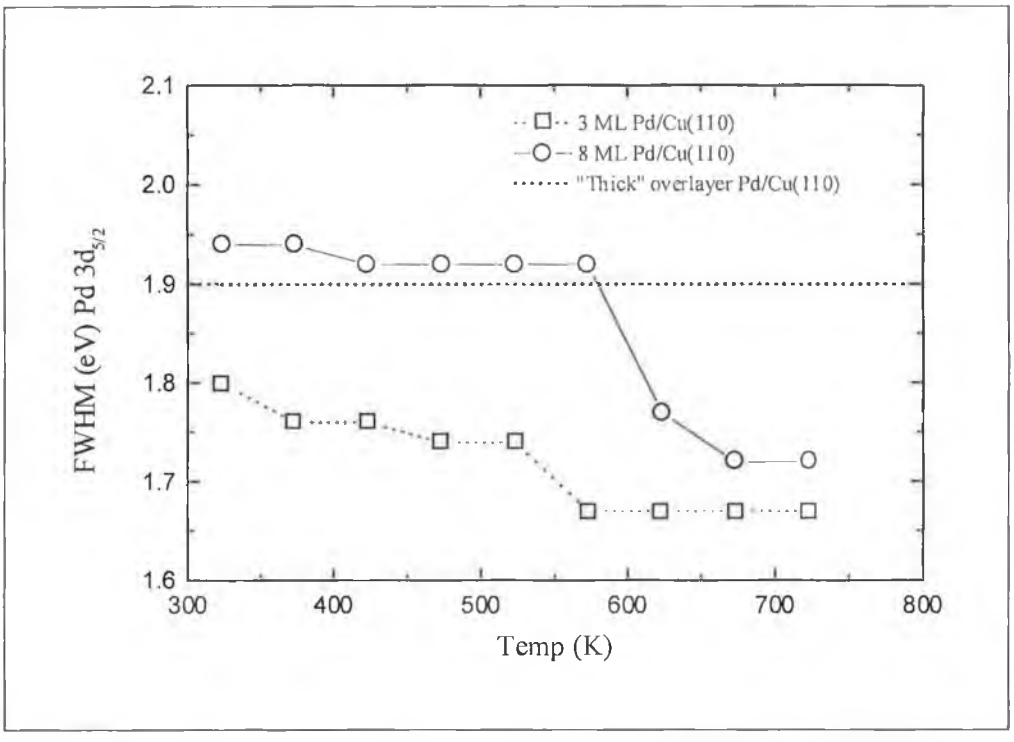

Figure 8: Variation of the full-width-at-half-maximum (FWHM) of the palladium $3d_{5/2}$ XPS core level as a function of annealing temperature for the 3 ML and 8 ML film.

Figure 8 represents the change in FWHM clearly illustrating a decrease of 0.2 eV which predominantly occurs between 500 and 650 K for a thick Pd film. The decrease in FWHM is somewhat sharper than the loss in intensity of the palladium

XPS peak and may suggest that while alloying is essentially complete by 600 K leading to a reduction in FWHM, the continued drop of the XPS ratio in figure 6 simply reflects slow diffusion of alloyed Pd deep into the crystal and out of the region probed by XPS (approx. 3λ, $\cong$ 30 Å for 1000 eV electrons). The reduction in FWHM is interpreted as due to emission from Pd in a single alloy environment for high temperature annealed films as opposed to the range of environments within the multilayer film with a corresponding range of core-level binding energies (cluster surface atoms, cluster bulk atoms, substrate cluster interface atoms and intermixed buffer layer Pd). Valence band examination of various bimetallics with Pd as the admetal growing essentially epitaxially help to clarify this hypothesis. Pd grows in a layer-by-layer mechanism on tungsten (high surface energy and small lattice mismatch compared to Pd) [45]. A monolayer of Pd on W(100) and (110) exhibits a narrow 4d band (Pd essentially in one environment) at higher binding energy in contrast to multilayers of Pd or bulk Pd which reveal a wider density of states (DOS) much nearer the Fermi level.

Finally, figure 9 illustrates the effect of annealing a 8 ML Pd film on the Cu $2p_{3/2}$ core level and its FWHM. As expected the copper intensity begins to increase for annealing temperatures above 473 K as diffusion is activated with a clear increase in the Cu $2p_{3/2}$ binding energy by 0.3 ± 0.05 eV attributable to CuPd alloying. A clear decrease in FWHM of between 0.2 to 0.35 eV occurs upon alloying depending on the initial Pd coverage, with the final value equal to that of clean Cu(110).

These shifts in peak maximum and FWHM agree with the measurements of Pope et al [41] who report a decrease in binding energy of the Cu $2p_{3/2}$ core level of 0.25 eV relative to clean Cu(100) for deposition of a 2 ML Pd film (no change in the Pd 3d core-level binding energy was seen upon increasing the Pd coverage to 4 ML, indicative of either bulk-like Pd binding energy or an intermediate plateau) at 300 K, with an accompanying increase in FWHM. The decrease in binding energy is consistent with an increase in electron density for some portion of Cu in the near surface region. This 'interface peak', as it is described, contributes to the observed broadening on the lower binding energy side of the Cu $2p_{3/2}$ peak. Pope et al postulate that this is due to surface alloying between Cu and Pd. The observed increase in binding energy in our case is interpreted as production of clean copper and/or alloy very dilute in Pd by heating to high temperature. The decrease in

FWHM may in a similar way be interpreted as emission from a single pure Cu-like environment after high temperature annealing as opposed to a range of mixed (pure Cu, CuPd alloy etc.) environments in the as-deposited films.

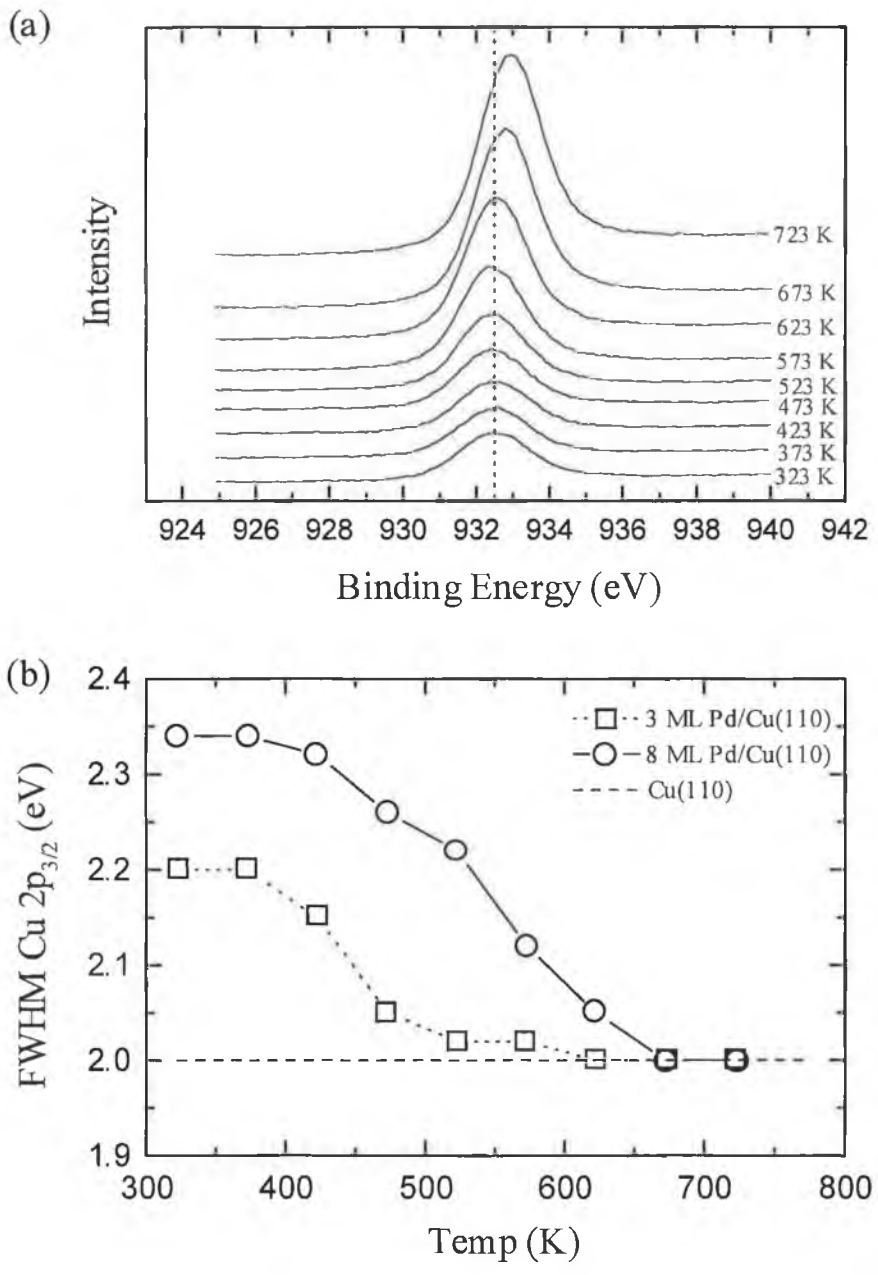

Figure 9: (a) Copper $2p_{3/2}$ core levels for a 8 ML Pd film as a function of annealing temperature; (b) variation of the Cu $2p_{3/2}$ FWHM as a function of annealing temperature for a 3 ML and 8 ML Pd film.

3.2.2. STM

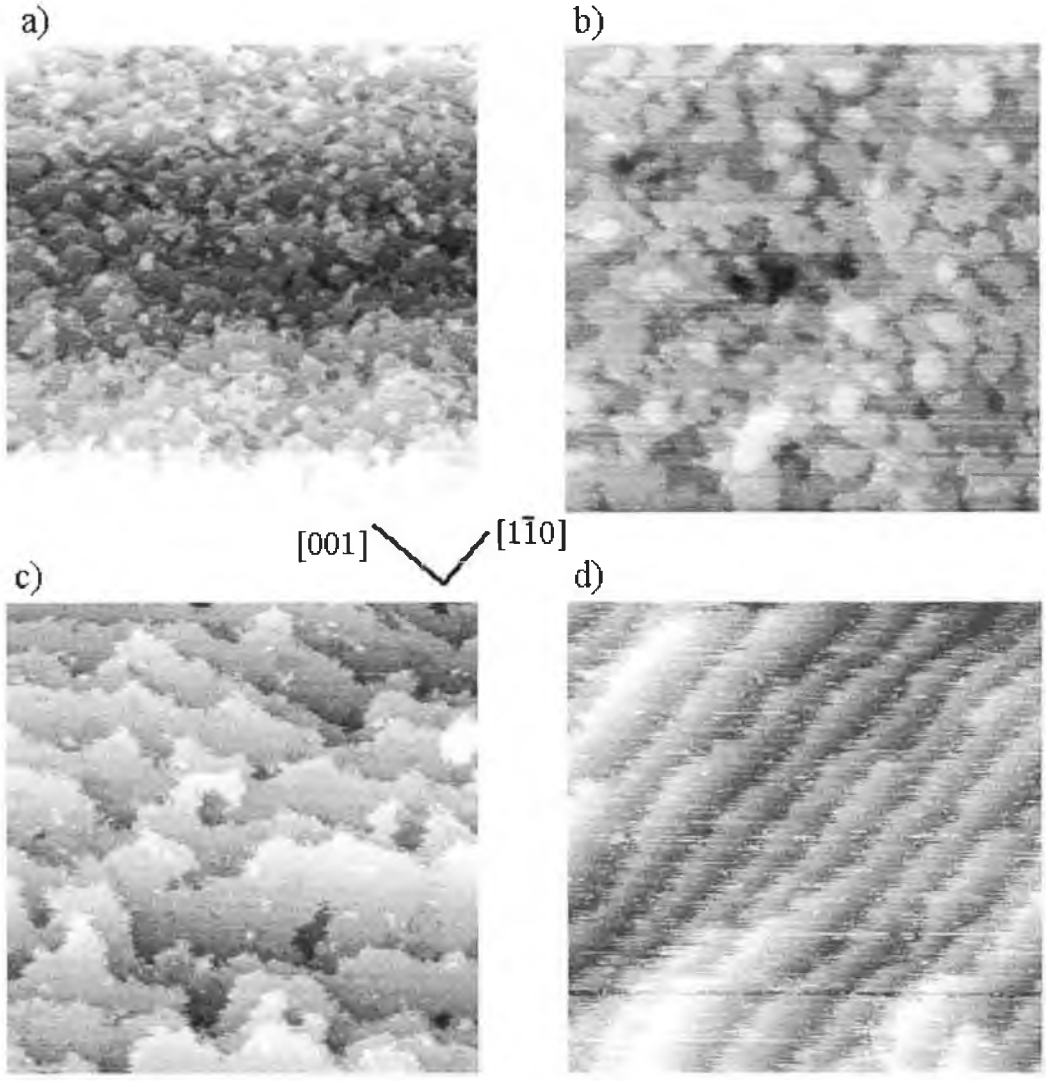

Figure 10: STM images characterising the structural change of a 1 ML Pd film grown at room temperature on Cu(110), (a) 300 K (200 × 200 nm^2), and upon annealing to (b) 500 K (200 × 200 nm^2); (c) 600 K (100 × 100 nm^2); and (d) 720 K (50 × 50 nm^2) with subsequent cooling to room temp before imaging. Tunnelling current = 1 nA (all images), bias voltage = 500 mV (a), 1000 mV (b-d).

Figures 10 to 14 represent the effect of annealing on the morphology of the palladium films. The general procedure followed in these measurements was to anneal the films to temperatures of 500 K, 600 K and 720 K for 30 seconds with images collected upon re-cooling to 300 K. The heating was performed sequentially on the same palladium film. The first annealing temperature (500 K) represents a temperature at which minimal change has occurred with respect to XPS ratios. In

contrast 600 K represents a temperature at which alloying is activated yet is incomplete while the highest annealing temperature (720 K) is one sufficient for bulk intermixing to be driven to completion.

Figure 10 illustrates images from the 1 ML Pd film. In comparison to the as-deposited film imaged in figure 10(a) annealing to 500 K (as indicated in figure 10(b)) produces a somewhat smoother surface with monolayer high islands seemingly larger than those found for the as-deposited film. Hence, at 500 K no drastic changes have occurred with the surface still consisting of islands and pits with three or more layers separated by atomic height steps. However, atomic resolution imaging of the previously observed (2×1) superstructure was not possible suggesting that while no gross changes occur it may be possible even at 500 K that copper capping of the CuPd domains occurs. In contrast, at 600 K, significant changes have occurred in the surface morphology as illustrated in the 100 × 100 nm image shown in figure 10(c). Terraces appear to elongate with steps between neighbouring domains oriented predominantly in the [001] direction. Annealing to 720 K (figure 10(d)) leads to a significant flattening of the surface in the $[1\,\bar{1}\,0]$ direction with atomically flat terraces extending for large distances also in the $[1\,\bar{1}\,0]$ direction with shorter terraces in the [001] direction.

Figure 11(a) illustrates the effect of heating a 2.5 ML Pd film to 500 K which maintains the granular structure of the film observed at room temperature. Figures 11(b) and (c) show the effect of annealing to 720 K where the granular structure is lost and has been replaced by a surface consisting of large flat domains separated from neighbouring regions by mono-atomic non-linear steps. There is significant ordering of the surface as expected after such a high temperature anneal. The evidence of what seems like a faint periodic band-like structure in images (b) and (c) will be discussed later.

Figure 12(a), illustrates a 100 × 100 nm image, for a 4 ML Pd sample after annealing to 500 K. The annealing appears to lead to formation of large islands. Within the islands and in other areas of the surface is a granular structure composed of a number of apparently nucleated (but not Ostwald ripened) Pd clusters. In contrast to the as-deposited film, the clusters seem to adopt a more hemispherical shape with an

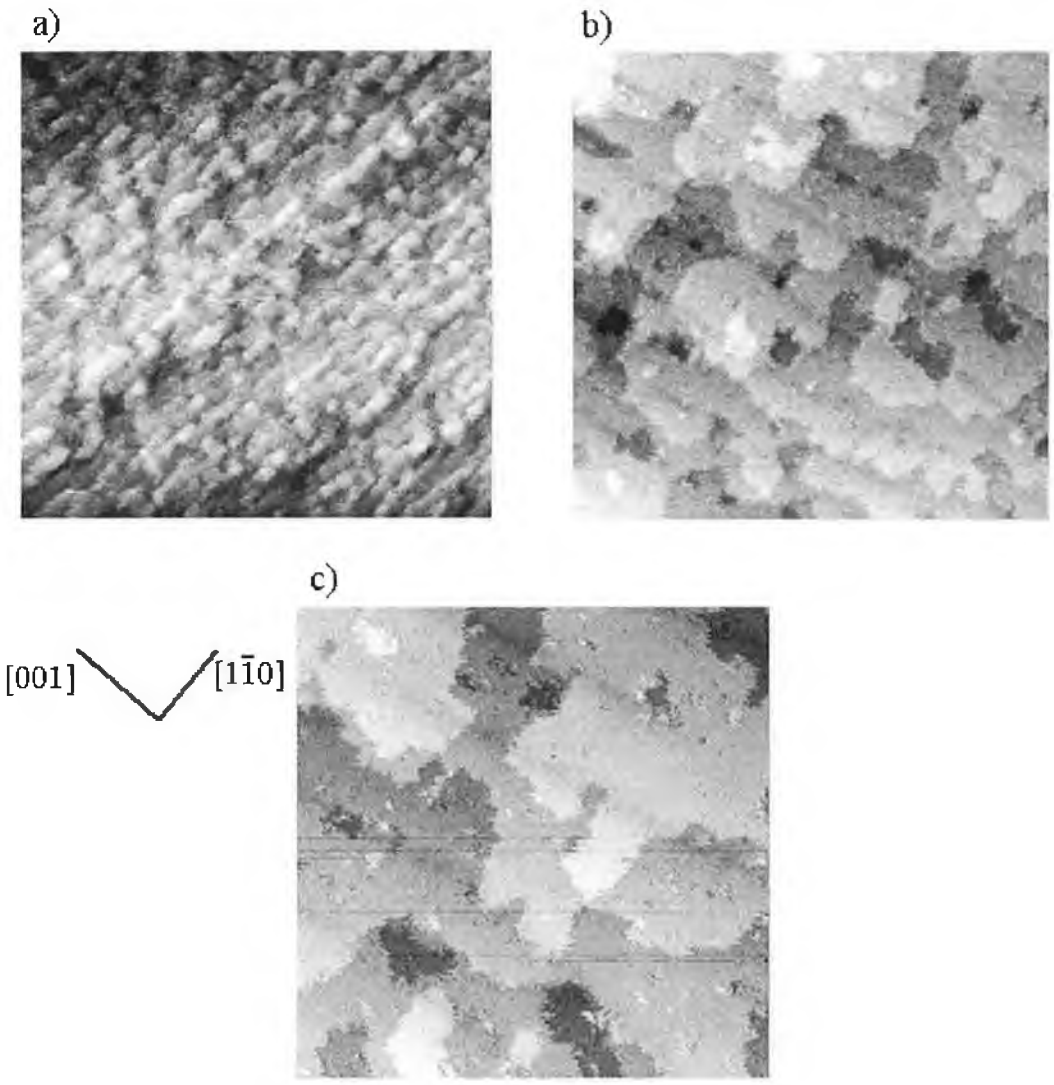

Figure 11: Selected STM images illustrating the effect of annealing on a 2.5 ML Pd film, (a) annealing to 500 K (200 × 200 nm^2); (b) (100 × 100 nm^2) and (c) (60 × 60 nm^2) annealing to 720 K. Tunnelling current = 1 nA (all images), bias voltage = 500 mV (a), 1000 mV (b,c).

average diameter of around 30 Å. Further annealing to 600 K (figure 12(b)) leads to loss of the Pd clusters and formation of a surface consisting of atomically flat islands of irregular shape with neighbouring terraces separated by mono-atomic steps. Small monolayer deep "pits" of varying shape and size also appear within the terraces. Figure 12(c) represents a higher resolution image of a region of the 600 K annealed surface showing the widespread formation of "strings" or atomic chains orientated

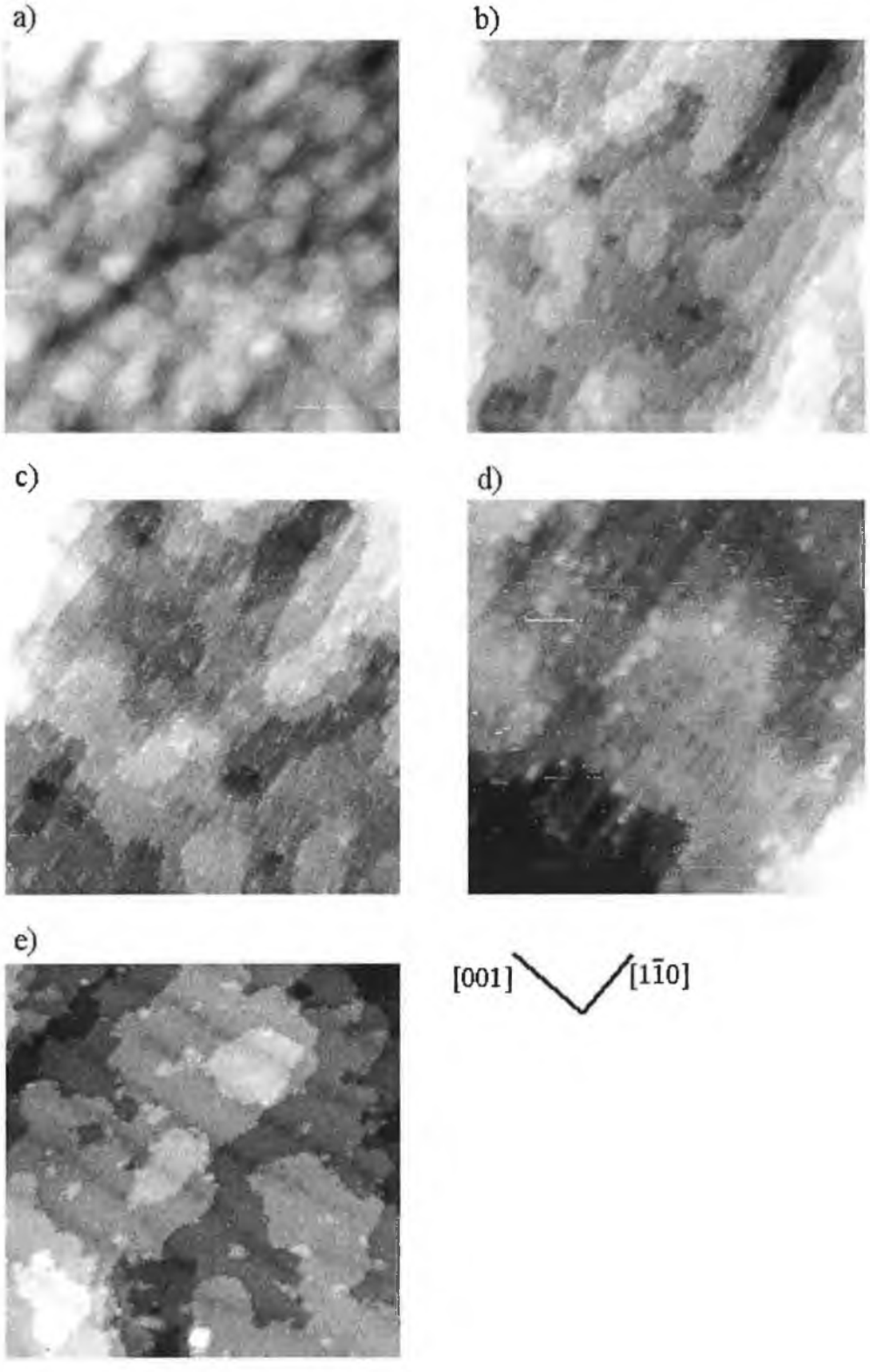

Figure 12: Representative STM images illustrating the effect of annealing on the morphology of a 4 ML Pd film, (b)→(d) are images acquired after heating to 600 K and (e) to 720 K. (a) The surface morphology at 500 K (100 × 100 nm^2); (b) (70 × 70 nm^2), (c) (50 × 50 nm^2) and (d) (20 × 20 nm^2); and (e) (70 × 70 nm^2). Tunnelling current = 1 nA (all images), bias voltage = 500 mV (a–d), 1000 mV (e).

along the [1 $\bar{1}$ 0] direction. Figure 12(d) reveals this atomic phenomenon more clearly. These "strings" exhibit structure with ~4.9Å periodicity as would be expected for an alternating Pd-Cu chain structure (similar therefore to the extended (2×1) regions seen after ~1 ML deposition).

Finally, annealing to 720 K results in a further flattening of the surface as shown in figure 12(e). Again a multilayer surface is formed with a meandering step direction. Interestingly, a longer range superstructure becomes apparent in the form of parallel lines which are approximately evenly spaced or periodic and run roughly parallel to the [001] direction. To further investigate this, a sample was prepared with 7–8 ML of Pd and the sample was sequentially heated to higher temperature and was subsequently held at this temperature while imaging (no cooling to room temperature prior to imaging) in an attempt to pinpoint the onset of 'band' formation. This was found to happen around 600 K as illustrated in figure 13(a). Again the bands are quite apparent and regularly spaced with a periodicity of ~90 Å. In general, for coverages of ~3 and 10 ML Pd annealing produces significant banding on the surface with spacings between bands varying from 70 to 150 Å. The spacing between the bands seem to increase with decreasing coverage, although a direct correlation between band spacing and Pd coverage has yet to be identified.

Such structures have been previously observed for the Pd(110)/Cu system [18] with their origin proposed to be due to lattice strain, a consequence of the 7.8% lattice mismatch between the Pd(110) surface and the growing copper film. A sharp (1×1) LEED pattern was observed for growth at 600 K up to 5 ML, with the films appearing to grow pseudomorphically. Above this critical coverage of 5 ML a partial stain relief mechanism through buckling in the [1 $\bar{1}$ 0] direction is effected and observed as a striped pattern with the stripes directed as here in the [001] direction. A 79 Å band periodicity is seen and proposed to be due to the uniaxial reduction of the tensile strain to 4% along the [1 $\bar{1}$ 0] direction. The height variation from light to dark stripes is reported by Hahn to be 0.5 Å and found to be 0.7–0.8 Å for the Cu(110)/Pd system examined here (measured for 7–8 ML of Pd/Cu(110) at 600 K). The reconstruction of the Pd(110)/Cu was not detected by LEED due to the limited resolution of their instrument. While the absence of any additional LEED spots is suggested to support the theory that the Cu atoms are still locked in their positions

between the close packed atom rows of the underlying layer in the [001] direction. From the observed periodicity it is calculated that the average interatomic spacing has been reduced to 2.66 Å (from 2.75 Å for Pd(110)) along the [1 $\bar{1}$ 0] direction.

Hence, the buckling pattern is suggested to arise from the occupancy by Cu of alternating regions of near bridge sites and near fourfold hollow sites. While this strain relief mechanism is plausible it must be noted that the occupancy of near bridge sites is energetically quite unfavourable and will be minimised with the Cu density possibly reduced in these bridging regions compared to that found in fourfold hollow regions. Moreover, the evidence of increased surface discontinuity (imperfections and pits) recorded in images after high temperature anneals may in some way aid strain relaxation.

Nevertheless, it should be noted that this relief mechanism although applicable to Cu on Pd(110) is not equally so for Pd on Cu(110) due to the opposite sign in the lattice mismatch. However, if the interface between Cu and Pd was not abrupt (i.e. a PdCu alloy formed) then the buckling could be attributable to mismatch between alloy and Cu (overlayer or bulk). The XPS results for Pd on Cu(110) add credence to this argument indicating significant alloying for films annealed at high temperature, with the surface found to consist of a dilute CuPd alloy phase. It is therefore perhaps more likely that the long range periodicity is due to mismatch between either the CuPd alloy and the underlying Cu(110) bulk or between the copper capping monolayer and an underlying CuPd alloy. The requirement that the surface is annealed at elevated temperatures to form the banded structure suggests that alloy formation is important in both Pd on Cu(110) and Cu on Pd(110). Furthermore our observation that the bands are still apparent at elevated temperatures (figure 13(a)) for extended periods of time suggest that the structure is reasonably stable and not a result of quenching a metastable state.

STM examination of a 2.5 ML Pd coverage sample annealed to 720 K and imaged at 300 K reveals surface structure consisting of the expected and already imaged periodically "banded" monoatomic islands (figure 13(b)). Reactivity studies reveal these surfaces to exhibit properties quite similar to that of pure Cu. Cross-sections of these surfaces (figure 13(b)) also indicate the possibility of a Cu surface region with

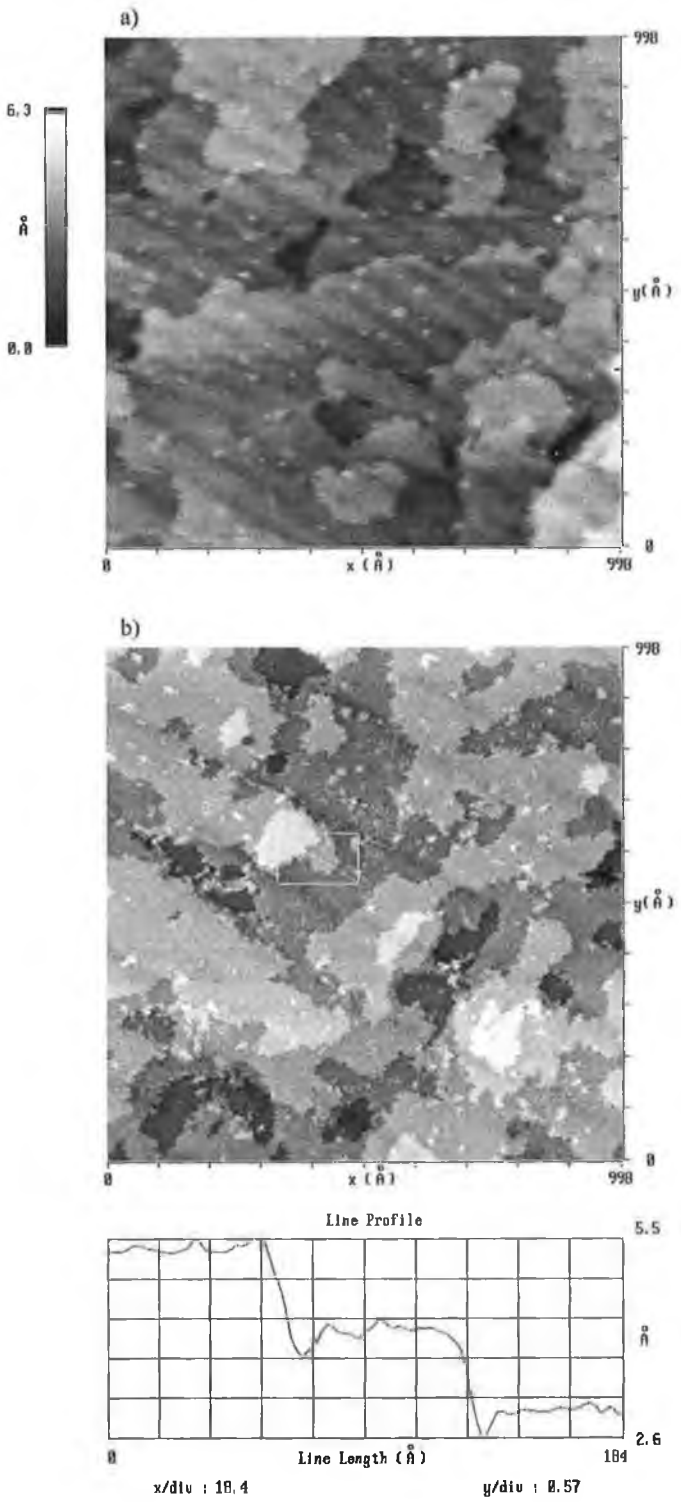

Figure 13: (a) Surface morphology of a thick Pd film of 7–8ML on Cu(110) showing significant "banding" even while imaged at 613 K; (b) room temperature STM image of a 2.5 ML Pd film after annealing to 720 K for 30 seconds, showing formation of extended flat terraces with ragged step edges. The line profile shown below (b) is the height difference for the diagonal line shown.

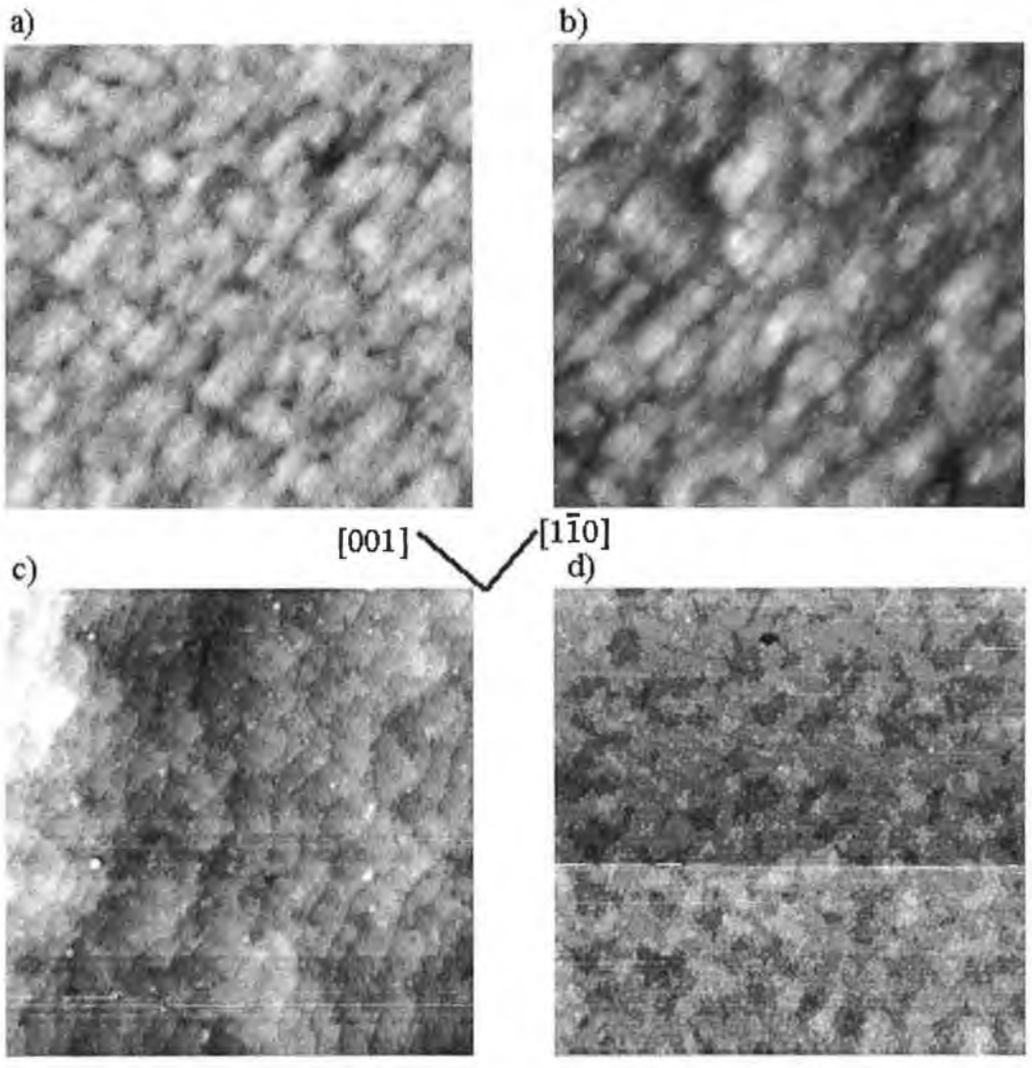

Figure 14: Selected STM images illustrating the effect of annealing on the film morphology for a ~10 ML Pd film heated to increasingly high temperature. (a) 300 K (100 × 100 nm^2); (b) 500 K (100 × 100 nm^2); (c) 600 K (100 × 100 nm^2); and (d) 720 K (200 × 200 nm^2). Tunnelling current = 1 nA (all images), bias voltage = 1000 mV (all images).

the interlayer spacing measured to be ~1.25 Å, more in keeping with the interlayer spacing of Cu(110) (1.3 Å) than Pd(110) (1.37 Å).

Finally, figure 14(b) shows a 10 ML palladium film annealed to 500 K, and again illustrates that no major morphological changes seem to occur for the lowest temperature anneal, although the surface is smoother than that seen after room temperature deposition (figure 14(a)). Moreover, large islands consisting of seemingly nucleated Pd clusters are also evident after annealing to 500 K, somewhat similar to that observed for the 4 ML Pd film. Heating to 600 K leads to a

transformation to a surface consisting of small flat terraces (figure 14(c)) with a staircase type structure while a high temperature anneal (720 K) leads to formation of flat domains of irregular shape separated from neighbouring atomically flat domains by single atomic height steps with highly non-linear step edges (figure 14(d)).

3.3. Reactivity of the Cu(110)/Pd system

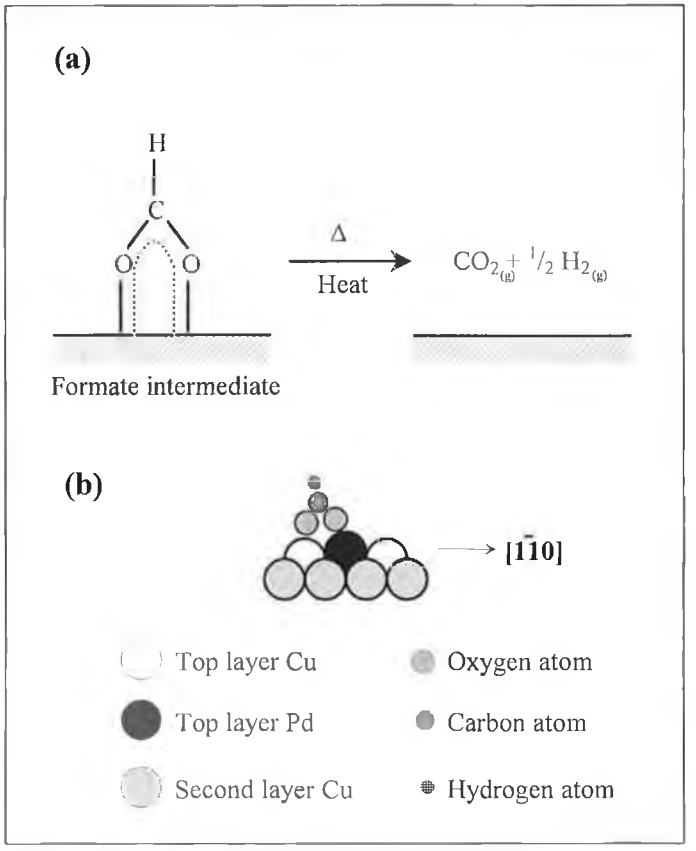

Figure 15: (a) Molecular orientation of the formate intermediate on Cu(110); (b) formate on a mixed CuPd site bonded to both Pd and Cu.

The reactivity of the Cu/Pd interfaces was investigated via adsorption of formic acid on various Cu(110)/Pd surfaces with subsequent decomposition being monitored by TPD. Formic acid (HCOOH) decomposition has been widely employed as a reaction to probe model catalysts [46,47] and is well documented on Cu(110) [46,47,48,49,50] and Pd(110) [51]. On Cu(110) adsorption at low temperature occurs molecularly. As the temperature is raised, the bond to the acidic hydrogen breaks producing an adsorbed formate intermediate and chemisorbed atomic

hydrogen, the hydrogen desorbs as H_2 at ~280 K. The formate is stable up to ~440 K when simultaneous desorption of H_2 and CO_2 occurs in a decomposition limited desorption peak. Hence the temperature of CO_2/H_2 desorption may be used to monitor the stability of the formate intermediate. On Cu(110) the adsorbed formate species is orientated parallel to the close-packed $[1\,\bar{1}\,0]$ direction with the two oxygen's bound to the surface in locally identical sites [50]. The structure of formate on Cu(110) after room temperature adsorption is suggested to consist of domains containing short rows parallel to the $[1\,\bar{1}\,0]$ direction, with an inter-row spacing of two lattice spacings in the [001] direction of the unconstructed (1×1)-Cu(110) termination. Adjacent domains were offset in the [001] by one lattice spacing suggesting relatively short-range order in the $[1\,\bar{1}\,0]$ direction [50]. Figure 15(a) displays more clearly the molecular orientation of the formate intermediate on Cu(110). This simple reaction mechanism for formic acid adsorption/desorption on Cu(110) is summarised below:

$$HCOOH_{(g)} \rightarrow HCOOH_{(ad)}$$
$$HCOOH_{(ad)} \rightarrow HCOO_{(ad)} + H_{(ad)}$$
$$2H_{(ad)} \rightarrow H_{2(g)}$$
$$2HCOO_{(ad)} \rightarrow 2CO_{2(g)} + H_{2(g)}$$

In contrast, formic acid decomposition on Pd(110) is not so straight forward. Upon low temperature (140 K) adsorption, HCOOH decomposes to yield CO, CO_2, H_2 and H_2O during TPD. At low coverage, the major peaks are coincident CO_2 and H_2O evolving at 237 K and CO and H_2 which evolve as desorption-limited peaks at 470 and 320 K, respectively. Coincident CO and H_2O resultant from formate dehydration occurs to only a limited degree, while CO_2 and H_2 evolution from formate dehydrogenation continues to increase with dose. Hence, CO_2 which evolves in a decomposition-limited peak at 237 K moves to lower temperature with increasing coverage, evidenced as CO_2 peak broadening [51]. It is proposed that the decomposition of adsorbed formate follows two routes implying a common rate-determining step for dehydrogenation and dehydration.

(i) $HCOO_{(ad)} \rightarrow H_{(ad)} + CO_{2(g)}$

$H_{(ad)} + H_{(ad)} \rightarrow H_{2(ad)}$

(ii) $HCOO_{(ad)} \rightarrow HCO_{(ad)} + O_{(ad)}$

$HCO_{(ad)} \rightarrow CO_{(ad)} + H_{(ad)}$

$H_{(ad)} + O_{(ad)} \rightarrow OH_{(ad)}$

$OH_{(ad)} + H_{(ad)} \rightarrow H_2O_{(g)}$

$CO_{(ad)} \rightarrow CO_{(g)}$

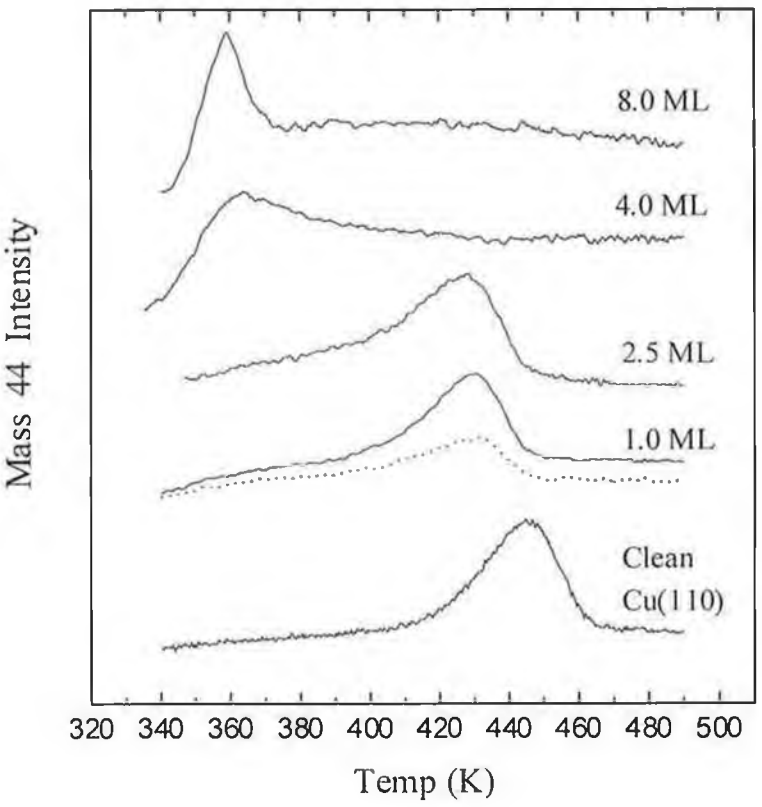

Figure 16: Mass 44 (CO_2) TPD spectra from clean Cu(110) and for Pd films of 1 ML (coincident H_2 (mass 2) desorption is indicated by the dotted line); 2.5 ML; 4 ML; and 8 ML. All Pd films were pre-annealed to 500 K and re-cooled to 300 K prior to dosing with saturation formic acid coverage.

Figure 16 illustrates the TPD spectrum of formic acid monitoring CO_2 evolution (mass 44) for a range of Pd coverages. The Cu(110)/Pd surfaces were pre-annealed

(500 K) prior to room temperature formic acid dosing to minimise compositional/morphological changes induced during the TPD ramp. In the case of the 1 ML Pd films, coincident CO_2 and H_2 desorption evident at ~430 K, is clearly indicative of formate decomposition. Similar TPD spectra were recorded for surfaces annealed to higher temperatures (up to 600 K).

From figure 16 it is clear that a slight decrease in formate stability is apparent for the low coverage Cu(110)/Pd systems (1 and 2.5 ML Pd coverages). The temperature of CO_2 desorption decreases from 445 K for pure Cu(110) to ~430 K for a 2.5 ML Cu(110)/Pd annealed alloy surface. In energy terms this corresponds to only a reduction of ~3 kJ mol^{-1} in the activation energy for formate decomposition compared to Cu(110). Table 1 documents the activation energy for formate decomposition from various surfaces.

Substrate	**β/K s^{-1}**	**T_{max}/K**	**E_d/kJ mol^{-1}**
Pd(110)	3.0	237[a]	60
Cu(110)	1.8	445	117.7
1–2.5 ML Pd/Cu(110)	1.2	430	115
4 ML Pd/Cu(110)	1.5	363	95.9
8 ML Pd/Cu(110)	1.2	358	95.2
CuPd[85:15](110)	2.65	445[b]	116.2
CuPd[50:50](110)	2.5	346[c]	89.8

[a] ref. [51], [b] ref. [60], [c] ref. [53].

Table 1: Comparison of the activation energy (E_d) for formate decomposition on various CuPd model catalysts calculated using the Redhead approximation, with a pre-exponential factor $\nu = 10^{-13}$ s^{-1}, assuming the reaction follows first order kinetics (β = heating rate).

Higher doses of Pd (4 and 8 ML) result in TPD profiles which reveal considerable loss in formate stability. In these cases CO_2 evolution occurred at ~360 K with no evidence of Cu(110) like states, corresponding to a ~22 kJ mol^{-1} reduction in decomposition activation energy. Desorption from such high coverage Pd surfaces without prior annealing revealed only Pd-like characteristics with only CO desorbed

above room temperature, suggesting that annealing to 500 K already leads to the transformation from a Pd-like outer layer to a layer with considerable copper character. This intermediate activity (intermediate between elemental Cu and Pd) would seem to be the product of a bimetallic surface layer.

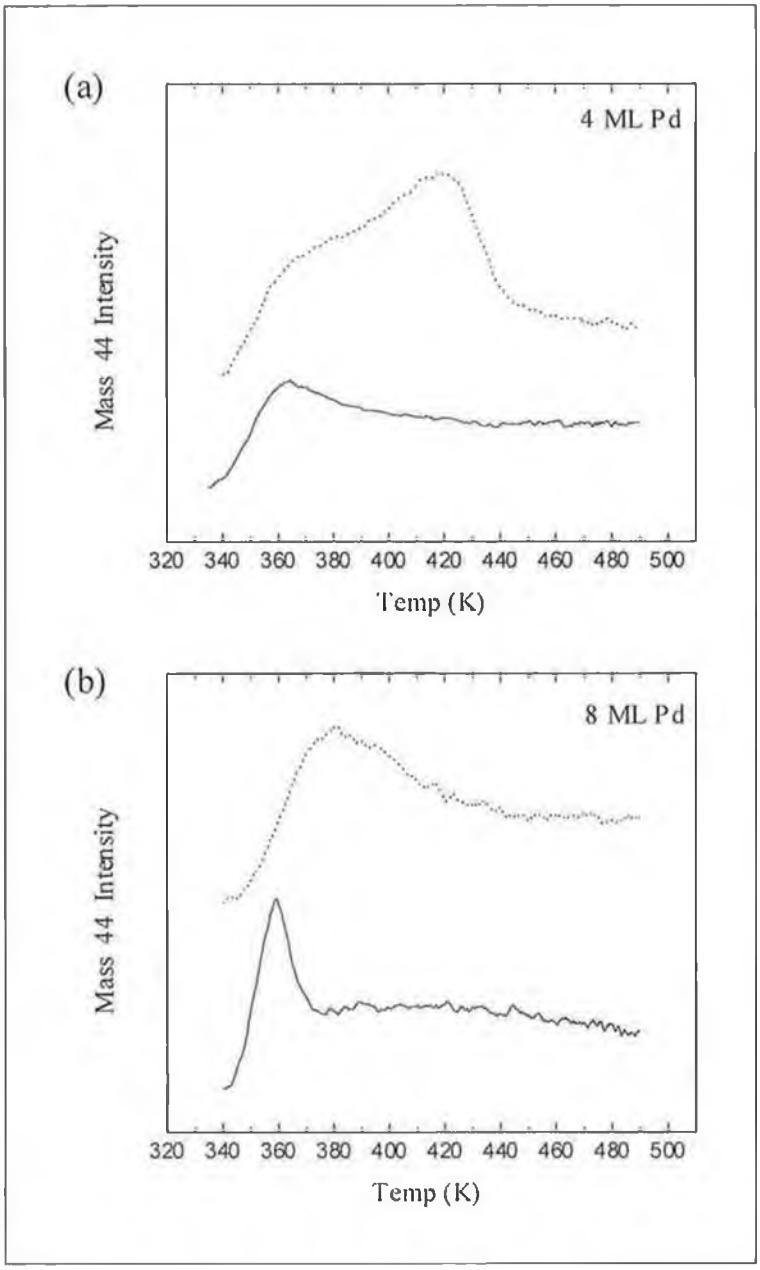

Figure 17: Effect of annealing of a (a) 4 ML and (b) 8 ML Pd film to 500 K (full line) and 600 K (dotted line) on formate thermal stability.

As already mentioned, the low coverage Pd/Cu(110) system (1, 2.5 ML Pd coverages) exhibits a dominant CO_2 desorption peak quite similar in temperature to Cu(110), although there is a significant tailing on the low-temperature side of the peak. In the case of a CuPd[85:15](110) bulk alloy with an ordered CuPd second alloy layer below a Cu terminated surface, geometrically similar to Cu(110), it was observed that the formate was uniformly destabilised relative to Cu(110) with respect to dehydrogenation by around 7–10 kJ mol^{-1} [52]. Thus we conclude that pre-annealing to 500 K while having relatively little effect in XPS spectra terms may lead to capping of the surface by copper. This is in keeping with STM results for 500 K annealed films which show no evidence of a (2×1) CuPd alloy surface layer.

On the other hand intermediate formate stability is clearly evidenced for the high coverage Cu(110)/Pd alloy systems (4, 8 ML Pd coverages). The intermediate CO_2 desorption peak is neither Cu nor Pd like, suggesting that an alloy state dominates its surface chemistry. Referring to table 1 it is clear that this alloy state exhibits similar desorption characteristics to the PdCu(110) bulk alloy with a Cu/Pd surface region of 0.55±0.05, as observed by Holroyd [53]. Several models have been proposed to explain this intermediate activity although they tenuously suggest that for such a large shift in formate stability the most probable scenario is a so called 'inter-atom' bidentate formate intermediate, bound to both a Cu and a Pd atom simultaneously [53]. Whether the adsorbed species adopts this geometry requires further quantitative structural work.

The effect of further annealing (600 K) on the higher coverage Pd samples (4, 8 ML Pd/Cu(110)) was also examined. Figure 17(a) reveals the variation in chemical reactivity of a 4 ML Cu(110)/Pd surface upon annealing from 500 to 600 K. The spectrum obtained after annealing to 600 K illustrates some interesting points, the most striking being the presence of two distinct CO_2 desorption states. The first peak corresponding to the alloy state (~360 K) and a second peak found at ~420 K. This latter state is to some extent Cu-like in origin. For the 4 ML Pd film the presence of mixed desorption peaks upon annealing to 600 K suggests that one of the surface components is Cu-like i.e. Cu surface islands with CuPd alloy below exist leading to the high temperature desorption peak at ~420 K perturbed by Pd in deeper layers. The fact that the CuPd alloy state persists (~360 K) suggests mixed CuPd regions are still present in the outermost layer.

Finally, the CO_2 desorption from a 8 ML Pd film pre-annealed to 500 K exhibits a well defined narrow peak (figure 17(b)) at ~360 K. This peak shape suggests that only one adsorption/desorption site is present for the formate. Unlike the less Pd-rich surfaces, this rules out a random dilute CuPd alloy system and would support a surface region consisting of a more homogeneous alloy top layer. Upon annealing to 600 K a broadening of the alloy-state peak occurs suggesting a number of locally different CuPd alloy sites in the surface layer as shown in figure 17(b). Annealing of this surface layer (including any lower Pd coverage surface) to even higher temperature (~720 K) does however lead to a surface with desorption properties similar to clean Cu(110).

4. Discussion

This study appears to be the first detailed investigation of the nature of the growth mechanism of Pd onto low index Cu surfaces for coverages beyond 0.5 ML. To date little work exists for Pd growth on low index Cu surfaces over a wide coverage range other than an Auger uptake study for the growth of Pd onto Cu(111) and Pd on Cu(100) where for the former the author favoured a layer-by-layer growth mechanism [22,23]. The close similarity of Auger or XPS signal versus deposition time plots for a system with initial interfacial mixing followed by layer-like growth and a true layer-by-layer mechanism may however lead to uncertainty in conclusions regarding growth mechanisms from spectroscopic uptake data alone. The initial growth mechanism for Pd on Cu(110) has significant similarities to Pd on Cu(100) where initial growth leads to formation of a surface alloy consisting of a surface of mixed CuPd and pure Cu domains formed due to Cu having been expelled from the outermost layer upon CuPd alloy formation [24,30]. Little is known about the growth of Pd on Cu(100) at higher coverages (>1 ML), however it is highly likely that the growth adopts a similar form to that reported here with clusters of Pd growing above a mixed CuPd interface of two or three layers thickness [41].

The general growth mechanism of Pd on Cu(110) at 300 K is suggestive of growth of a high density of flat topped Pd(110) orientated clusters above a bi- or tri-layer mixed CuPd interface. The initial observation of growth of considerable areas of a p(2×1) CuPd top layer at coverages around 1 ML can be understood on the basis of the model suggested by Murray et al for low Pd coverages which consisted of an outermost Cu layer covering a p(2×1) CuPd underlayer with the "capping" of the growing Pd film with Cu occurring to minimise the surface energy. Thus incoming Pd atoms at coverages $\geq$ 0.5 ML will impinge largely on a Cu outermost layer. The most likely scenario is that Pd substitutes within the outermost Cu monolayer, pushing further Cu islands above the mixed interface which can then alloy with further Pd forming an intermixed bi/tri-layer. At this stage arriving Pd is inhibited from further mixing with the Cu due to the mixed CuPd buffer layer, hence pure Pd islands begin to grow above the mixed interface with both Auger and XPS signal versus deposition time plot data suggesting these islands to have a large base to height ratio as evidenced by the small deviation from theoretically predicted layer-by-

layer growth. Such a growth mechanism is quite different than that proposed for Cu on Pd(110) [18,19,54,55] where little intermixing appears to occur for deposition at 300 K, rather the first monolayer grows pseudomorphically and epitaxially capping the Pd substrate as expected from surface energy considerations.

Our XPS and STM data clearly indicate strong intermixing of the Pd with the Cu substrate at temperatures above 500 K. In particular STM elegantly shows the loss of the granular Pd structure for annealing above 600 K with Pd presumably fully dissolved into the Cu substrate, as expected as the thermodynamically stable state of the Cu(110)/Pd system is an intermixed dilute CuPd alloy.

An interesting point in relation to the STM work of Hahn et al [18] for Cu on Pd is their observations of a large period super-structure revealed as repeating dark lines across the STM image which the authors assign to strain mismatch of the pure Cu film to the Pd(110) substrate (~7.8 % lattice mismatch). As we observe similar long period structures for the Pd/Cu(110) system after annealing to 725 K when CuPd intermixing is complete as determined by XPS, we cannot invoke a similar film/substrate mismatch argument. In our case, it is likely that the long period structure in our images is due to a mismatch of the "capping" Cu monolayer with the underlying CuPd alloy due to the differing lattice parameters of Cu with a CuPd alloy. However, as already mentioned, the possibility of mismatch between the CuPd alloy and underlying Cu substrate can not be ruled out. Thus, it would be expected that the period would be larger than for Cu on Pd(110) due to the smaller mismatch between an alloy and pure metal. This is indeed what is observed with the period being ~100 Å compared to that of ~80 Å observed by Hahn et al.

The XPS core level data in the form of peak binding energy position as a function of coverage and annealing temperature allows further insight into the nature of the CuPd interface. Previous studies on CuPd alloys indicate that large shifts to higher binding energy occur in the Pd $3d_{5/2}$ core level relative to pure Pd. Shifts of ~0.75 eV have been measured for a Pd_8Cu_{92} alloy while a ~0.45 eV shift was recorded for a $Pd_{40}Cu_{60}$ bulk alloy [42]. A recent cluster calculation has reproduced the systematics of this concentration dependent shift for the aforementioned alloys. Therefore, on this basis, we would expect the Pd 3d binding energy to be highly sensitive to changes in the Pd environment, undergoing a considerable shift to higher binding energy when a metallic-like Pd film is transformed into a dilute alloy via annealing.

For films deposited at 300 K, it is likely that the relatively large escape depth of the Pd $3d_{5/2}$ electrons (16.7 Å [38]) will lead to the 3d envelope containing contributions from Pd atoms in a range of environments including pure Pd clusters (bulk and surface atoms) and alloyed interface Pd. At low Pd coverages (≤ 1 ML), if our postulated model of an intermixed CuPd alloy is correct, we would expect to find a high binding energy peak of narrow half-width (due to Pd in a single alloyed environment). Increasing weight should occur on the low binding energy side of the peak as metallic Pd clusters grow above the mixed interface with a shift in the peak maximum to lower binding energy at high coverages where the metallic Pd begins to dominate. Indeed, in figure 6 we see growth of a high binding energy peak (~334.8 eV) for coverages up to ~1 ML when CuPd alloying readily occurs with subsequent additional emission at lower binding energy owing to metallic Pd clusters at ~334.4 eV. Hence, the XPS data fully supports our mechanism for growth of a mixed CuPd alloy interface up to ~1 ML coverage followed by growth of pure Pd clusters.

In contrast, annealing the Pd film, which promotes further intermixing at temperatures above ~500 K as shown by the decreasing Pd/Cu XPS ratio, would be expected to reveal a decrease in the Pd 3d FWHM due to the loss of Pd clusters. Such a decrease is clearly observed between 500 and 600 K. Annealing to high temperatures yields a dilute CuPd alloy which should in turn show a shift in the core-level binding energy from lower (pure metallic Pd clusters dominating for high coverage 300 K films) to higher values as a dilute CuPd alloy is formed. Again this prediction is indeed what takes place, with a clear reduction in the FWHM between 500 and 600 K and with a loss of peak weight at the low binding energy signifying the dissolving of the Pd clusters into the Cu substrate. Net upwards shifts of 0.5 ± 0.05 eV and 0.7 ± 0.05 eV is observed for the Pd 3d core-level of 725 K annealed films of 3 and 8 ML Pd, respectively, when compared to the room temperature deposit in-line with formation of a dilute CuPd alloy.

A smaller shift to higher binding energy (0.3 ± 0.05 eV) is observed for the Cu $2p_{3/2}$ core-level upon intermixing along with a clear decrease in the FWHM which is already beginning at ~400 K. Interestingly, a plot of the variation in intensity of the Cu $2p_{3/2}$ core-level alone for Pd films of 3 and 8 ML coverage indicate a significant increase in the Cu $2p_{3/2}$ intensity between 400 and 500 K, whereas the Pd $3d_{5/2}$ intensity remains unaltered. This is perhaps indicative of out-diffusion of copper to

alloy with, or to encapsulate, areas of overlying Pd clusters, a point of considerable importance when addressing the desorption behaviour of the formate intermediate. Even for low sub-monolayer coverages of Pd on Cu(111) capping by Cu is evidenced after annealing at ~430 K [56]. Low temperature capping by Cu substrate atoms has been observed for other systems, for example Co on Cu(111) experiences Cu capping even at room temperature [57].

As previously mentioned, formate decomposition on Cu(110) was observed and identified by the simultaneous desorption of CO_2 and H_2 in a decomposition limited peak at 445 K (β = 1.8 K s^{-1}). The temperature of the desorption peak may be utilised to estimate the formate stability, and the decomposition activation energy on Cu(110) has been found to be 118 kJ mol^{-1} using the Redhead approximation [58]. In comparison, Pd(110) is much more active towards formate dehydrogenation. Aas et al [51] report simultaneous desorption of CO_2 and H_2 for formic acid adsorbed at low temperature in a decomposition limited peak at 237 K (β = 3 K s^{-1}) with the desorption following first order kinetics and exhibiting an activation energy of 60 kJ mol^{-1}. Molecular CO remains on the surface above 250 K yielding a desorption limited peak at ~470 K.

At low Pd coverages (1 and 2.5 ML), following a pre-anneal to 500 K, co-incident CO_2/H_2 desorption at ~430 K is observed indicative of a decomposition limited fragmentation of a formate intermediate rather close to that for a pure Cu(110) surface although a small destabilisation of the formate is apparent.

Newton and co-workers [52] have studied the thermal decomposition of formic acid on a $Cu_{0.85}Pd_{0.15}$(110) bulk alloy. The structure of the surface which exhibits a (2×1) superstructure in LEED has been the focus of considerable attention [36,52,59,60,61,62]. It has been unequivocally demonstrated that the (2×1) periodicity has its origin in chemical ordering between Cu and Pd in the second layer in the form of a mixed 50:50 second layer with Pd atoms occupying every second site along the close packed [1 $\bar{1}$ 0] rows. The top layer is Cu rich [59,60]. Newton et al observed a co-incident CO_2/H_2 TPD peak at 445 K (β = 2.65 K s^{-1}) on the CuPd alloy along with a small amount of molecular formic acid desorption. Again using the Redhead approximation and assuming first order kinetics, an activation energy of 116 kJ mol^{-1} is calculated and found to be slightly less than that determined for Cu(110)

here (118 kJ mol^{-1}). However, Newton et al [60] suggest that the destabilisation of adsorbed formate to dehydrogenation on the $Cu_{0.85}Pd_{0.15}(110)$ bulk alloy relative to Cu(110) is more in the region of 7–10 kJ mol^{-1}. Nevertheless, it is clear that the inclusion of Pd in the second layer of the alloy leads to an increase in the reactivity towards dehydrogenation of the formate relative to Cu(110).

A possible explanation of the similarity of the formate decomposition from the low Pd loading films with that of the $Cu_{0.85}Pd_{0.15}(110)$-(2×1) alloy is that the pre-annealing to 500 K leads to a pure or almost pure Cu layer capping a mixed CuPd alloy. A recent STM study of Pd deposition ($\theta_{Pd} \leq 0.5$ ML) on Cu(111) at ~530 K led to a surface with Pd atoms substituted into the top Cu layer with roughly half of the Pd atoms sub-surface [56]. As it is likely that place exchange on the close-packed (111) surface will have a higher activation energy than on the more open (110) surface, capping of the Pd films on the (110) surface is quite possible upon annealing to 500 K for a short period.

At higher Pd coverages (4 and 8 ML) a considerable destabilisation of the formate intermediate occurs indicative of a surface intermediate in stability between pure Cu and Pd(110). Auger data for the thicker Pd films suggests that significant changes in surface composition do not occur upon annealing up to 500 K. This observation is backed up by STM data, which illustrates that the Pd morphology is not significantly altered upon annealing to 500 K for a short period. It is thus surprising that the formate stability remains intermediate between Cu and Pd if the surface were to consist of pure Pd clusters in the 4 and 8 ML films.

The models for formate adsorption on surfaces include (a) monodentate formate bonding to just one atom on the surface (observed on Cu and Ni surfaces following low temperature adsorption of formic acid); (b) chelating or aligned top bidentate structure with the formate oxygens in between atoms in the close-packed rows rather than directly above them (figure 18). This latter orientation has been suggested by surface extended X-ray-adsorption fine-structure (SEXAFS) and near-edge X-ray-adsorption fine-structure (NEXAFS) data [63]. This is, however at variance with the photoelectron diffraction (PhD) work of Woodruff who suggests an aligned bridge formate bonding orientation [64].

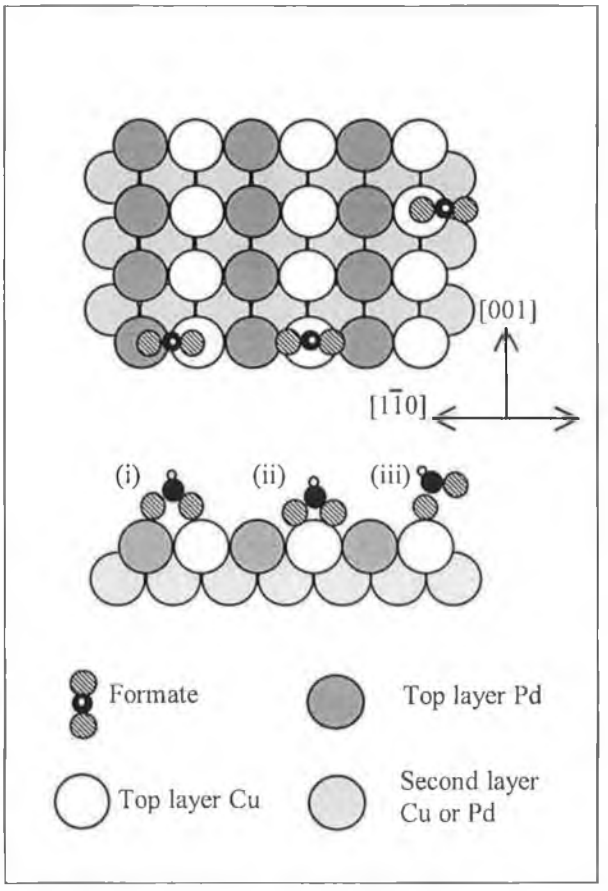

Figure 18: Models for the adsorption site of formate on an ordered CuPd alloy surface. The bridging bidentate structure (i) is preferred, although for a more disordered surface the (ii) chelating bidentate (atop site) and the (iii) monodentate structure are known configurations.

The monodentate bonding site effectively contains one less bond to the surface than the bridging bidentate structure and is thought to be less stable. Whether this is a possibility regarding the CuPd surface synthesised here, is as of yet unclear, although the possibility of various surface structural arrangements of Cu and Pd allowing such an intermediate cannot be completely dismissed. Another model for adsorption is the chelating (atop) site were formate bond formation is suggested to be little different in energy terms with respect to bridge bonding and as such increased formate stability is expected if bonded atop a Pd atom (relative to Pd(110)) with stability decreased if bonded atop a Cu atom (relative to Cu(110)) for a mixed CuPd surface. Regarding the 8 ML Pd film it is unclear whether this argument is applicable with a narrow decomposition peak suggesting only one type of adsorption site. On the other hand

the 4 ML Pd film seems to reveal a broad desorption peak indicative of more than one desorption site (figure 17).

The final formate binding site model to discuss is the bridging bidentate structure and as revealed earlier is the most favoured formate bonding arrangement [50,64], especially on Cu(110). Whether the bonding site is one where bridging between two Pd atoms, two Cu atoms, or 'inter-atom' bridging between Cu and Pd occurs has not as of yet been unequivocally determined. We propose that 'inter-atom' bonding is the most likely to afford a binding energy intermediate between that of Pd(110) and Cu(110). Inter-atom site bonding for the formate species has been previously proposed for the adsorption of formic acid on reduced $CuO/ZnO/SiO_2$ with the formate species inter-bonding between Cu and Zn sites.

The fact that the formate decomposition kinetics do not resemble those of Pd(110) suggest that while the surface is still dominated by Pd clusters, Cu atoms are present within the outermost layer. As mentioned earlier contact with Cu atoms leads to large changes in the Pd valence band structure in the form of withdrawal of the d-partial density of states on Pd sites from the Fermi level. The exact d-density of states at the Fermi level is critically dependent on the CuPd stoichiometry and recent work indicates that withdrawal is effectively complete at a CuPd stoichiometry of about 1:1 [65]. Hence, we propose that annealing the thicker films to 500 K leads to out-diffusion of Cu from the CuPd interface to partially mix with the Pd clusters resulting in an outermost mixed CuPd surface with intermediate formate desorption kinetics. Previous work on a Cu(100)-c(2×2) Pd surface alloy for which significant Pd is present in the outermost layer gave evidence of a large destabilisation in the CO desorption activation energy to a value intermediate between pure Pd(100) and Cu(100) for which the main CO desorption peak occurs at 500 K and 170 K, respectively [41,32]. This result further attests to the fact that a mixed CuPd outermost layer leads to an adsorbate stability intermediate between the two pure metals.

5. Conclusions

A complex growth mechanism for palladium on Cu(110) has been demonstrated in which initial growth occurs via intermixing to form an ordered CuPd(2×1) surface alloy of two to three layers thickness resulting in a heterogeneous surface consisting of monolayer high two-dimensional islands and monolayer deep "pits". Subsequent growth takes place in the form of densely packed (110) orientated palladium platelets. The platelets have a large base-to-height ratio and vary in shape and size although some preference for rectangular islands aligned with their edges parallel to the high symmetry substrate directions is detected.

XPS data has shown that rapid alloying occurs at temperatures between 500 and 600 K. While not detected readily by XPS, capping of the resulting CuPd alloy for temperatures as low as 500 K by a low surface energy copper monolayer is suspected, as indicated by STM and formate decomposition measurements. Temperature induced morphological transformations have been followed by STM, which indicates that the granular platelet structure of the higher coverage palladium films is maintained upon heating to 500 K without significant Ostwald ripening or cluster coalescence. However, large changes are induced by heating to 600 K and beyond: the granular palladium film is lost, transforming into a multi-level surface with large flat domains bounded by non-linear mono-atomic steps with areas of raised islands and large pits formed by palladium substitutionally transplanting into the copper lattice, with ejected copper atoms growing as islands and leading to the multilayered structure observed.

Morphological changes are mirrored in XPS core level binding energies and peak widths with a large shift of the palladium $3d_{5/2}$ core level to higher binding energy and an accompanying narrowing of the line width as the transition from a granular metal film to a CuPd alloy is induced. The narrowing in peak width is in keeping with the evolution from a highly heterogeneous palladium environment (surface Pd atoms at cluster edges, bulk Pd atoms within clusters, Pd in an intermixed interface, etc.) to a dilute CuPd alloy where palladium atoms are all in similar local environments. The effect of intermixing (shift to higher binding energy of core levels and narrowing of peak width) leads to XPS spectra similar to those obtained from a 1 ML film consisting of a thin intermixed CuPd interface.

Finally, the reactivity of the CuPd interface has been probed by monitoring the changes in stability of the formate intermediate. Low Pd coverages (1 and 2.5 ML) show only a small destabilising of the formate relative to clean Cu(110) suggestive that the surface is largely copper monolayer capped. Thicker Pd films show a marked destabilisation of the formate (decomposition activation energies of 118 and 95 kJ mol^{-1} on Cu(110) and a 8 ML Pd film, respectively). This destabilisation is attributed to desorption from a mixed CuPd surface, indicating that the stability of the formate intermediate may be altered to a state intermediate between pure Cu and Pd via surface alloy formation.

References

[1] C. T. Campbell, Annu. Rev. Phys. Chem., 41 (1990) 775.

[2] E. Bauer, Z. Kristallogr., 110 (1958) 372.

[3] U. Bardi, Rep. Prog. Phys., 57 (1994) 939.

[4] K. I. Choi and M. A. Vannice, J. Catal., 131 (1991) 36.

[5] F. Skoda, M. P. Astier, G. M. Pajonk and M. Primet, Catal. Lett., 29 (1994) 159.

[6] J. A. Anderson, M. Fernández-Garcia and G. L. Haller, J. Catal., 164 (1996) 477.

[7] G. Borelius, C. H. Johansson and J. O. Linde, Ann. Physik, 86 (1928) 291.

[8] B. Svensson, Ann. Physik, 14 (1932) 699.

[9] F. W. Jones and C. Sykes, J. Inst. Metals, 65 (1939) 419.

[10] J. Elmsley, The Elements, Clarendon Press, Oxford, (1990).

[11] J. A. Rodriguez, Surf. Sci., 318 (1994) 253.

[12] J. A. Rodriguez, Surf. Sci., 304 (1994) 366.

[13] J. A. Rodriguez, Surf. Sci., 345 (1996) 347.

[14] J. A. Rodriguez and M. Kuhn, J. Phys. Chem., 100 (1996) 381.

[15] V. S. Sundaram, M. B. de Moraes, J. D. Rogers and G. G. Kleiman, J. Phys. F, 11 (1981) 1151.

[16] H. Winter, P. J. Durham, W. M. Temmerman and G. M. Stocks, Phys. Rev. B, 33 (1986) 2370.

[17] E. Hahn, E. Kampshoff and K. Kern, Chem. Phys. Lett., 223 (1994) 347.

[18] E. Hahn, E. Kampshoff, A. Fricke, J. -P. Bucher and K. Kern, Surf. Sci., 319 (1994) 277.

[19] E. Kampshoff, E. Hahn and K. Kern, Phys. Rev. Lett., 73 (1994) 704.

[20] J. -P. Bucher, E. Hahn, P. Fernandez, C. Massobrio and K. Kern, Europhys. Lett., 27 (1994) 473.

[21] J. G. Dash, J. Vac. Sci. Technol. A, 5 (1986) 1523.

[22] Y. Fujinaga, Surf. Sci., 84 (1979) 1.

[23] Y. Fujinaga, Surf. Sci., 86 (1979) 581.

[24] P. W. Murray, I. Stensgaard, E. Lægsgaard and F. Besenbacher, Surf. Sci., 365 (1996) 591 (and references therein).

[25] C. Nagl, E. Platzgummer, O. Haller, M. Schmid and P. Varga, Surf. Sci., 331–333 (1995) 831.

[26] R. G. P. van der Kraan and H. van Kempen, Surf. Sci., 338 (1995) 19.

[27] D. D. Chambliss and S. Chiang, Surf. Sci., 264 (1992) L187.

[28] G. W. Graham, P. J. Schmitz and P. A. Thiel, Phys. Rev. B, 41 (1990) 3353.

[29] G. W. Graham, Surf. Sci., 171 (1986) L432.

[30] T. D. Pope, G. W. Anderson, K. Griffiths, P. R. Norton and G. W. Graham, Phys. Rev. B, 44 (1991) 11518.

[31] S. C. Wu, S. H. Lu, Z. Q. Wang, C. K. C. Lok, J. Quinn, Y. S. Li, D. Tian, F. Jona and P. M. Marcus, Phys. Rev. B, 38 (1988) 5363.

[32] M. Valden, J. Aaltonen, M. Pessa, M. Gleeson and C. Barnes, Chem. Phys. Lett., 228 (1994) 529.

[33] T. D. Pope, M. Vos, H. T. Tang, K. Griffiths, I. V. Mitchell, P. R. Norton, W. Liu, Y. S. Li, K. A. R. Mitchell, Z. -J. Tian and J. E. Black, Surf. Sci., 337 (1995) 79.

[34] G. O. Pötschke and R. J. Behm, Phys. Rev. Lett., 44 (1991) 1442.

[35] P. W. Murray, S. Thorshaug, I. Stensgaard, F. Besenbacher, E. Lægsgaard, A. V. Ruban, K. W. Jacobsen, G. Kopidakis and H. L. Skriver, Phys. Rev. B, 55 (1997) 1380.

[36] M. A. Newton, S. M. Francis and M. Bowker, Surf. Sci., 259 (1991) 56.

[37] J. F. Moulder, W. F. Stickle, P. E. Stickle and K. D. Bomben in: Handbook of X-ray Photoelectron Spectroscopy, Ed. Jill Chastain, Perkin-Elmer, US, (1992).

[38] D. Briggs and M. P. Seah, Practical Surface Analysis, John Wiley & Sons, New York, (1990).

[39] L. Z. Mezey and J. Giber, Jap. J. Appl. Phys., 21 (1982) 1569.

[40] W. R. Tyson and W. A. Miller, Surf. Sci., 62 (1977) 267.

[41] T. D. Pope, K. Griffiths, P. R. Norton, Surf. Sci., 306 (1994) 294.

[42] N. Martensson, R. Nyholm, H. Calén, J. Hedman and B. Johansson, Phys. Rev. B, 24 (1981) 1725.

[43] V. S. Sundaram, M. B. de Moraes, J. D. Rogers and G. G. Kleiman, J. Phys. F, 11 (1981) 1151.

[44] R. S. Rao, A. Bansil, H. Asonen and M. Pessa, Phys. Rev. B, 29 (1984) 1713.

[45] G. W. Graham, J. Vac. Sci. Technol. A, 4 (1986) 760.

[46] M. Bowker and R. J. Madix, Surf. Sci., 102 (1981) 542.

[47] R. J. Madix, Surf. Sci., 89 (1979) 540.

[48] M. Bowker, E. Rowbotham, F. M. Leibsle and S. Haq, Surf. Sci., 349 (1996) 97.

[49] S. Poulston, A. H. Jones, R. A. Bennett and M. Bowker, Surf. Sci., 377 (1997) 66.

[50] S. Poulston, R. A. Bennett, A. H. Jones and M. Bowker, Phys. Rev. B, 55 (1997) 12888 (and references therein).

[51] N. Aas, Y. Li, and M. Bowker, J. Phys.: Condens. Matter, 3 (1991) 1.

[52] M. A. Newton and M. Bowker, Surf. Sci., 307–309 (1994) 445.

[53] R. Holroyd, Ph.D. Thesis, Reading Catalysis Centre, University of Reading, United Kingdom.

[54] C. Barnes and M. Gleeson, Surf. Sci., 319 (1994) 157.

[55] R. W. Vook and J. V. Bucci, Thin Solid Films, 163 (1988) 447.

[56] A. Bach Aaen, E. Lægsgaard, A. V. Ruban and I. Stensgaard, to be published.

[57] M. Ø. Pedersen, I. A. Bönicke, F. Lægsgaard, I. Stensgaard, A. Ruban, J. K. Nørskov and F. Besenbacher, Surf. Sci., 387 (1997) 86.

[58] P. A. Redhead, Vacuum, 12 (1962) 203.

[59] D J. Holmes, D. A. King, and C. J. Barnes, Surf. Sci., 227 (1990) 179.

[60] M. A. Newton, S. M. Francis, X. Li, D. Law and M. Bowker, Surf. Sci., 259 (1991) 45.

[61] C. Cottrell, M. Bowker, A. Hodgson and G. Worthy, Surf. Sci., 325 (1995) 57.

[62] M. A. Newton, S. M. Francis and M. Bowker, Surf. Sci., 269/270 (1992) 41.

[63] A. Puschmann, J. Haase, M. D. Crapper, C. E. Riley and D. P. Woodruff, Phys. Rev. Lett., 54 (1985) 2250.

[64] D. P. Woodruff, C. F. McConville, A. L. D. Kilcoyne, Th. Lindner, J. Somers, M. Surman, G. Paolucci and A. M. Bradshaw, Surf. Sci., 201 (1988) 228.

[65] C. J. Barnes, M. Gleeson, S. Sarakorpi and M. Lindroos, submitted to Surface Science.

Chapter Four

An XPS and STM Study of Monometallic Pd and Cu, and Bimetallic Pd-Cu Clusters Grown on Graphite

1. Introduction

Heterogeneous catalysis spans a number of diverse areas from organic synthesis to automobile pollution control. The preparation of catalysts involves mainly tried and tested empirical techniques essentially relying on trial and error methodology. The reason for such an approach is the complex nature of real working heterogeneous catalysts which generally consist of several elements in precise proportion supported on an oxide support. Indeed, 'real catalysts' as they are commonly termed comprise, for the most part, of small metal sub-micrometer particles dispersed on and within the surfaces of porous materials. The precise characterisation of such particles has proven extremely difficult. However, with the advent of modern surface science techniques coupled with the development of "model catalysts" consisting of nanometre scale particles on planar supports this problem is beginning to be redressed. Essentially, the methodology utilised is that heterogeneous catalysis is undertaken on model catalysts in ultra-high vacuum (UHV) conditions often with the possible incorporation of 'high pressure cells' within UHV apparatus to mimic real catalysis working conditions.

The effect that particle size and shape has on both the reactivity and selectivity of a catalyst is well known [1]. Also, the catalyst support may some times act as more than just a mechanical inert support with encapsulation of the catalyst by the support material known to occur [2] as well as the modification of its electronic properties [3]. These limitations have led to the introduction of a new type of model catalyst: *the supported model catalyst*. This involves the examination of small metal particles prepared in UHV environment supported on planar substrates allowing their direct characterisation by many of the modern surface science techniques [4].

The supports are generally single crystal materials (oxides of Mg, Al, Ti, Si, Ce, Zr and Zn; lamellar supports: graphite, mica and MoS_2) exhibiting large atomically flat domains. Only a few oxide supports can be cleaved (MgO and ZnO). The cleavage of these surfaces is either carried out in air or UHV conditions depending on the support and specific experimental arrangement available. The most commonly used catalyst supports are alumina, silica and titania surfaces of various orientations which are generally obtained by the cutting of rutile single crystals. The cut surfaces are chemically polished and cleaned in UHV or under oxygen environment or after ion

bombardment. The lamellar surfaces including graphite [5], employed as a support in this study, are generally prepared and regenerated by simple cleavage in air followed by annealing in UHV at ~800 K to remove physisorbed hydrocarbons adsorbed from the ambient.

Graphite as a substrate offers many advantages. Firstly, as it is a conductor it opens the possibility of probing the metal particle size distribution of the catalyst and monitor changes in the particle size distribution with exposure to reactive gases by scanning tunnelling microscopy (STM) [6,7]. Graphite in its highly orientated pyrolytic (HOPG) form is a single crystal in nature and offers large areas of several thousand square Angstroms of atomically flat surface which is relatively inert to chemisorption from the ambient environment at 300 K. Hence HOPG acts as an ideal single crystal support and circumvents the problem of porosity of standard oxide support materials such as Al_2O_3 in which the majority of the metal clusters exist in the micropores of the material, hard to access by traditional surface sensitive spectroscopies.

Metal deposition on graphite surfaces continues to be a highly active area and a large number of studies exist incorporating a wide range of surface spectroscopies dealing with this subject matter including variation of particle size and shape with coverage and surface temperature, convergence of electronic properties as a function of particle size, and effects of particle size and shape on chemisorption properties and surface reactivity. However, the majority of the available literature covers monometallic systems. The area of bimetallics is much less investigated.

In the case of bimetallics a number of additional questions require addressing including the nature of the metal film i.e. alloy or phase separated, also whether "egg-shelling" of one metal by another occurs and whether the nanocluster microstructure is dependent on the evaporation sequence and growth temperature. To our knowledge little work exists on photoemission and/or STM studies of bimetallic clusters of Pd and Cu on solid substrates. Our interest revolves around the extent of interaction between the two metals in bimetallic supported cluster catalysts, and the subsequent effect on core-level binding energies and cluster sizes when compared to their single metal counterparts. We have chosen a model bimetallic system CuPd for study which is interesting for a variety of reasons. Firstly, the CuPd system is highly catalytically relevant being used in automobile pollution control of CO oxidation

[8,9] and for the reforming of hydrocarbons in the petroleum industry [10,11]. It is not clear a-priori if the CuPd bimetallics will phase-separate or form binary alloys. Both metals adopt a face-centred-cubic (fcc) bulk crystal structure, with Pd having an 8% larger lattice parameter (a_{Cu} = 3.61 Å, a_{Pd} = 3.89 Å), yet exhibit different surface energies with Cu preferring to surface segregate in CuPd bulk alloys due to its lower surface energy.

In this paper we present an XPS study (along with an ancillary STM study) of the growth of both the monometallic films of Cu and Pd and of bimetallic systems of Cu and Pd on HOPG. In addition a novel method of determination of absolute metal coverages as an aid to growth mechanism evaluation is described.

2. Literature review

2.1. Microscopy

The characteristics of a model catalyst surface as already suggested are dependent on a number of factors, although those of significant importance include the nature of the support, the substrate temperature, metal evaporation rate and the residual vacuum. Effectively, the easiest way to control the deposition process is to evaporate at elevated temperature allowing the surface to reach thermodynamic equilibrium. UHV compatible deposition sources must produce a steady stable, reproducible flux and include the Knudsen cell, the most reliable source, and also the resistively heated tungsten wire source around which the metal of interest is wound. Electron bombardment heating of sources is employed in the evaporation of refractory metals however the high-energy electrons utilised in the e-beam process are known to create nucleation sites on the surface of graphite [5] and ionic substrates.

The quantification of surface coverage commonly involves the use of a quartz crystal monitor (QCM).

In general, regarding epitaxy of supported metal clusters on oxides and graphite two main epitaxial orientations, (100) and (111), are observed for fcc metals which will lead to different morphologies for the particles. STM examination of graphite supported Pd crystallites suggest the particles are tetrahedra with either four (111) facets or one (111) at the interface and three (100) exposed faces [12].

Those metals receiving the most attention are Pd, Ni and Au while only a couple of studies to date have been reported for Cu. The discussion will be limited here to work on Cu and Pd.

Graphite supported Pd model catalyst studies have been extensive and numerous. The control of surface morphology maybe afforded to some extent by the creation of nucleation sites on the substrate surface generally through ion bombardment. Granjeaud et al [13,14] revealed through a transmission electron microscopy (TEM) study an increase in the density of Pd clusters on graphite by effectively two orders of magnitude coupled with a significant decrease in cluster size upon ion bombardment prior to metal deposition.

Granjeaud also discusses the relative merits and limitations of TEM and STM in their use as techniques for heterogeneous catalysis structural examination [15]. In the examination of Pd clusters on HOPG it is found that TEM is an extremely powerful tool regarding nucleation studies as it allows the examination of large areas of the surface, although its limited resolution means it is difficult to make statistical measurements on smaller clusters (1-1.5 nm). The non-in-situ nature of TEM is also relevant regarding the effect of air on cluster morphology. STM measurements by Granjeaud allow the smallest cluster sizes ranging from 1 to 4 nm to be examined as well as the larger clusters evidenced by TEM, although the imaging of extremely large regions is impractical.

STM has proven itself to be one of the most rewarding techniques in this field. Atomic resolution of 2D and 3D clusters is possible in both UHV and air environments. The comparison of air exposed and UHV graphite supported Pd clusters has been addressed by Humbert et al [14]. No discernible differences in morphology were observed between air exposed and unexposed samples, however it should be mentioned that pre-damaged substrate surfaces were used. Smaller clusters (1.5 nm) have a regular crystallographic habit and reveal the ledges of their triangular base to be 30° off the STM graphite lattice proving the epitaxial orientation of the clusters with respect to the lattice. The largest isolated clusters (10-20 nm) were found to be triangular or hexagonal in shape [16]. Generally in UHV large, flat clusters were observed with evidence of a high growth rate at the lateral faces.

Kojima et al [17] have studied Pd model catalysts formed at elevated temperatures (70 and 450 °C). With the graphite substrate held at 70 °C, smaller clusters (3–5 nm)

were observed after 4 ML Pd deposition when compared to those (50–100 nm) with the surface at 450 °C. The coalescence and nucleation seen at the higher temperature reveal epitaxial triangular and hexagonal crystallites with all surfaces directed towards the (111) plane.

Murakami et al [18] have reported the association or aggregation of Pd clusters on HOPG for a 1.7 ML coverage. Atomic force microscopy (AFM) images indicate Pd cluster agglomerates with lateral sizes of 30 nm and heights of 6.5 nm. Furthermore, Cadete Santos Aires et al [19] in an attempt to produce uniform cluster sizes and limit cluster coalescence, utilised cluster beam deposition involving the laser evaporation of Pd and the size selection of neutral Pd clusters with a size distribution around 50 atoms. An approximate 3 ML coverage on pristine HOPG was examined. Cluster aggregation as well as surface defect decoration was observed for a 2 ML coverage, with a mean particle size of 3.8 nm, somewhat larger than the size of the incoming particles (supported Pd particles = 60 atoms). Effectively, mass-selected clusters were found to diffuse and coalesce on the surface in a similar manner to that found using other less precise deposition techniques.

Aiyer et al [20] report an increase in cluster size for Pd on HOPG upon going from "low" to "medium" coverage (average of 1.6 nm and 3.3 nm at "low" and "medium" coverage, respectively) although the authors do not provide any detailed information on the absolute metal loadings. High resolution electron microscopy (HREM) and STM reveal generally rounded cluster morphologies although it is hinted that at higher coverages the cluster shapes deviate from sphericity along with an increase in their size distribution. Bifone et al [21] suggest that deposition with the substrate at room temperature allows clusters to remain on the terraces with little or no movement observed during scanning. Lateral dimensions of Pd clusters at low coverage (absolute coverage not quoted) range from sub- to tens of nanometres, with heights ranging from 0.5 to 2 nm observed. Deposition with the substrate at higher temperature results in clusters found only at defected sites due to increased cluster mobility. The migration of clusters to form rows along the steps was also observed.

In the only reported UHV STM study of Cu model catalysts, Ganz et al [22] have attempted to clarify the static and dynamic nature of Cu on HOPG. For deposition of approximately 1 ML of Cu on pristine graphite, clusters of average size 4.4 nm are

found to decorate the steps with a cluster size distribution ranging from 2 to 8 nm. Ganz reveals the beauty of the STM study of such systems, with atomic resolution of both the substrate and metal cluster obtained in the same image affording information about the structure and epitaxy of the clusters. Atomic resolution images suggested the metal adatoms occupied β-sites on the graphite lattice. Diffusion tendencies of clusters on the basal plane of inert graphite are also discussed. Whelan et al [23] have examined high Cu coverages (3 to 75 ML) on pristine HOPG with imaging performed in air after vacuum deposition of the model catalysts. A cluster size distribution of 5 to 10 nm was found with the most probable cluster size of ~7.5 nm. The preferred decoration of stepped our defected surface regions was also reported. The Cu particles were reported to be hemispherical in shape.

In discussing the relative merits of microscopy for the study of particle size and structure it is clear that the unambiguous determination of exact structure is best achieved through STM. However, the finite curvature of the STM tip may lead to objects appearing rounded because of the convolution of the tip shape with the actual shape of the object if the tip is not carefully prepared. Deconvolution is only possible if the actual shape of the tip is exactly known. AFM is more promising in that it is not restricted to conducting samples. AFM of a 10 nm (as detected by a QCM) Pd film on HOPG, grown at 500 °C revealed hexagonal flat-topped crystallites typically of 30 nm in height and 100 nm in length [24]. Limitations of AFM, include for example, its use in contact mode where it is known to move clusters on the surface, however, a non-contact mode which is less damaging also exists with the tip far from the surface. The microfabrication of AFM tips usually leaves the tip apex in the region of 50 nm resulting in a much more difficult tip-surface deconvolution problem.

2.2. Integral techniques

For Pd clusters deposited on polycrystalline graphite, a hybridisation model has been suggested in which Pd 4d filled bands and π* empty graphite sites strongly hybridise in the Fermi energy region. This is deemed responsible for the variation of the full

and empty states of Pd observed using XPS, AES and Bremstrahlung isochromat spectroscopy (BIS) [25].

In the spectroscopic comparison of polycrystalline and single crystal graphite as supports for model catalysts differences have been recorded. Egelhoff and Tibbetts [26] in an UPS study of Pd and Cu suggest that even for low coverages (submonolayer) these metals reveal electronic properties quite similar to bulk when deposited on the basal plane of cleaved crystalline graphite. Amorphous graphite supported clusters display quite a different trend with submonolayer coverages found with core level binding energies 0.6 eV higher than bulk values for the metals. The valence band region shifts almost mirror those of the core levels for the amorphous substrate. Egelhoff reports that for 5×10^{14} Pd atoms per cm^2 (ca. 0.5 ML) deposited on a crystalline graphite surface valence properties quite similar to the bulk are observed. The trend is reported quite consistent for Cu (ca. 0.25 ML), although the Cu 3d levels within the valence band are somewhat narrower than that of the bulk suggested to be due to the absence of interlayer (3-dimensional) broadening i.e. that two-dimensional islanding of Cu occurs [27]. Egelhoff cites the work of Arthur and Cho [27] who demonstrate that submonolayer coverages of Cu and Au on single crystal graphite aggregate quickly into islands following growth at 300 K. These islands are claimed to display bulk-like properties. It appears that for even submonolayer coverages of Cu deposited on pristine HOPG bulk properties are exhibited while this does not carry over to polycrystalline carbon supports where the particle size is reduced as the defected surface limits diffusion and coalescence of smaller particles.

Di Nardo et al [28] in the study of Cu on polycrystalline graphite have mirrored the results of Egelhoff and Tibbetts in terms of valence band shifts. Again a significant shift of almost 1 eV to higher binding energy is seen in the 3d UPS valence band spectra of Cu in the transition from bulk to the smallest clusters. This is accompanied by a concomitant decrease in FWHM from 2 eV in the bulk to 1.6 eV for the lowest Cu coverages. Interestingly, the 2p core level peaks of Cu only reveal a 0.4 eV increase in binding energy following the same coverage transition.

In examining the electronic nature of supported metal particles one must firstly realise that their electronic properties, especially at low metal loadings may differ dramatically from those of their bulk metal counterparts. Small isolated clusters are

known to be subject to so called quantum size effects. In core level terms positive shifts i.e. increasing binding energy shifts are observed by decreasing the amount of metal deposited [29]. The core level shift (CLS) in supported model catalysts is essentially a contribution of two factors: initial state [29] and final state effects [30]. The discussion of such effects centre around the differences in the potential experienced by atoms in the bulk metal compared to small clusters where metallic properties are reduced and the electronic levels approach those of an isolated atom [31,32]. The metallicity of a cluster is determined by the average co-ordination number of the atom in the particle [33]. There is predicted to be a size-induced metal–insulator transition at a critical cluster size. While initial state effects are concerned with the variation of the electronic structure as a function of the size of the metal cluster, on the other hand final state effects are directly related to the screening of the photoemission core hole which depends strongly on the cluster size, shape and on the nature of the substrate.

If final state effects were to dominate the measured variations in electronic properties in the metal to non-metal transition with decreasing cluster size, we would expect identical shifts in both the valence and core levels. In the examination of noble metals such as Ag, Au and Cu as well as the transition metals Pd and Ni on amorphous graphite, Vijayakrishnan et al [34] have noticed considerable deviation. Therefore, it is proposed that the most significant contribution originates from initial state effects.

We have seen that on the basal plane of pyrolytic graphite deposited metals have a tendency to rapidly diffuse and agglomerate into quite large particles owing to the low nucleation site density of a pristine crystalline surface. In fact, it has been reported that even at low temperature (100 K) diffusion and coalescence on graphite is rapid [35]. Generally, as mentioned earlier clusters grow more quickly on crystalline graphite [36] than on amorphous carbon as the density of nucleation sites is much lower.

Pristine single-crystal graphite exhibits another interesting property regarding the growth of metal clusters i.e. its sticking coefficient for metals. The sticking coefficient for silver on HOPG even at low temperature is reported to be far below unity [22,27]. Patthey and Schneider [37] have measured a sticking coefficient of lower than 0.1 for Ag on freshly cleaved HOPG at 50 K. This was confirmed by the

deposition of Ag^+ ions with a cluster source [38] and comparing the measured ion current on the substrate with the Ag 4d photoemission signal. Ultraviolet photoelectron spectroscopy (UPS) studies reveal the decay length of the Ag(111) surface state wave function allowing the distribution of island heights to be measured. Assuming the sticking probability of Ag on Ag to be unity it is clear that the growth mechanism of Ag on HOPG will be determined by the nucleation sites on the surface combined with the frequency of Ag clusters on the surface. Evidently, a silver atom incident on a bare surface has only a small possibility of staying on the surface while a particle incident on a cluster or nucleation site will most likely adsorb. This will lead to formation of larger particles exhibiting bulk-like properties even at low coverages.

Bulk Pd has an unfilled d-band with isolated Pd atoms having a full d^{10} configuration. It is proposed that as cluster size increases hybridisation between the initially empty s states and the filled d states occurs. Thus, the electron structure of a small metal cluster is somewhat between that of an isolated atom and a bulk metal. The variations of electronic configuration or orbital occupation numbers with metal cluster or particle sizes have been predicted theoretically. It has been proposed that a metal cluster of 140 atoms, corresponding to a radius of ~10 Å for transition metals already leads to convergence to bulk properties [39]. Likewise, The central atom in a cluster of Cu containing 79 atoms is predicted to have a local density of states of the bulk metal, with the less co-ordinated atoms approaching surface properties [40].

In examining the valence band of supported metal clusters three effects are observed when the cluster size is reduced: the valence band width decreases, the density of states (DOS) at the Fermi level drops and the gravity centre of the band shifts towards higher binding energy. Effectively, the narrowing of the valence band arises from the decrease of the mean co-ordination of the atoms in the clusters. Linking of the decreased DOS at the Fermi level with size effects in catalysis has been suggested [1,41]. One such example of this is the fact that very small clusters of Pd show entirely different reactivity with respect to CO, compared to large metal clusters. Of course the co-ordination of clusters is not just size dependent, shape is also important, with the variation of substrate temperature the most effective way to control cluster shape. Pd clusters having the same size but grown at different temperatures exhibit different valence band features [42].

Relating the results of photoemission experiments to actual catalytic activity is not a facile process. The photoemission process provides information arising from the whole cluster although chemical reactions take place on the surface. With the variation of the co-ordination number from one site to the next it is clear that the averaging nature of the valence band spectra leaves many questions unanswered. There is a general problem in relating the changing electronic structure with cluster size to reactivity in that changing the cluster size also changes the nature of sites, i.e. steps/boundaries, which may be the "active site" for a reaction.

In summary, the STM examination of the nucleation and growth of both Cu [22,23] and Pd [13–21] on HOPG reveals similar trends. Essentially three-dimensional clustering is the favoured growth mechanism for both metals at 300 K. Moreover, at higher coverages large rafts (between 10–70 nm and 20–100 nm for Cu and Pd, respectively) of aggregated clusters are observed while at lower coverages individual clusters (2–8 nm for Cu and 1–5 nm for Pd) are found to reside at defect sites i.e. active sites on the surface.

The electronic properties of both graphite-supported Cu and Pd clusters have also been widely investigated with extensive studies existing regarding changes in energy position and width of valence band and core levels as a function of their size. In general a shift to higher binding energy is observed for both the core and valence levels, using XPS and UPS, when the cluster size decreases. The actual reasoning behind this has been discussed in terms of initial and final state effects and the weight of contribution from each to the observed shifts is as of yet unresolved.

3. Experimental

All ultra-high vacuum experiments were carried out in a custom built Vacuum Generators chamber consisting of a main spectrometer vessel linked to a preparation chamber with facilities for rapid sample insertion via a load-lock system.

The main spectrometer vessel was pumped by a combination of trapped diffusion and sublimation pumps and had a base pressure of 1×10^{-10} Torr. Facilities were available for sample cleaning by argon ion bombardment, X-ray photoelectron spectroscopy using a dual anode Mg/Al Kα X-ray gun and CLAM (combined lens analyser module) electron energy analyser with three channel detection and variable entrance aperture to allow angle resolved XPS and X-ray photoelectron diffraction (XPD). A high-resolution electron gun for scanning Auger microscopy was also available.

The preparation chamber which could be isolated from the spectrometer vessel by a gate valve also operated in the low 10^{-10} Torr region. Rapid sample transfer between the two chambers was possible using a rack-and-pinion linear motion with wobble sticks mounted for sample transfer. The preparation chamber was utilised for Cu/Pd film preparation. Dual evaporators were mounted side-by-side and consisted of 0.3 mm diameter tungsten spirals around which was carefully wrapped 0.125 mm diameter high purity Cu and Pd wire (Goodfellow Metals Ltd., 99.99 % purity). The filaments were mounted on multipin electrical feedthroughs and shrouded using stainless steel cylinders which surrounded the filaments and acted to collimate the metal flux. The evaporators were heated with a stabilised dc power supply and were shown to afford spectroscopically pure Cu and Pd after prolonged outgassing as judged by XPS analysis. Bimetallic films were formed by sequential evaporation of Cu/Pd or Pd/Cu. The evaporation rate under well defined operating conditions was calibrated by evaporating onto glass slides positioned in sample evaporation conditions in conjunction with ex-situ atomic absorption analysis of the coverage of metal evaporated (described in more detail in results section).

High quality freshly cleaved HOPG samples of dimensions $6 \times 6 \times 1$ mm were employed as supports (Burleigh Instruments Ltd.). The samples were attached by UHV compatible silver paint onto the XPS sample stubs. Clean HOPG was ensured by simple mechanical cleavage of its basal plane prior to insertion into the vacuum

chamber. The crystalline quality of surfaces produced in this manner was verified by air-STM analysis with samples reproducibly yielding images containing large atomically flat terraces of width between several hundred and thousands of Angstroms separated by atomic steps (height < 10 Å) and cleavage steps (height = 10–100's Å) a consequence of the mechanical cleavage process. Occasional high-resolution studies on atomically flat terraces yielded atomically resolved images of the expected hexagonal graphite surface.

Samples were inserted via a rotary pumped load lock system into the preparation chamber. Past experience indicated that despite best efforts including the use of a nitrogen glove box, surfaces always exhibited carbon and oxygen contamination due to the physisorption of low vapour pressure hydrocarbons probably from the rotary pumped load-locked chamber. However, these contaminants could be effectively removed via vacuum annealing at elevated temperature. Hence, after transfer all graphite samples were subjected to a 5-min anneal at 1000 K. Upon cooling the HOPG samples were transferred to the spectrometer chamber and analysed by XPS. No contaminants above the noise level were revealed after annealing. Graphite is also noted to be highly inert relative to residual gas pick-up and no time dependent contamination problems on the graphite were ever noted.

Metal films were formed by deposition for a fixed length of time a calibrated Cu or Pd flux at 300 K and the sample then directly transferred into the spectrometer vessel for analysis. Annealing experiments were also possible by heating the sample to a pre-set temperature as measured by a thermocouple located in a sample heating facility in the preparation chamber. Quoted temperatures are upper limits of the actual annealing temperatures as a small thermal lag may exist between the heater and the sample temperature.

In all studies performed, samples were characterised in-situ by interrogating both core levels and valence bands. In all XPS work the binding energy scale was calibrated by setting the carbon 1s core peak to a binding energy of 284.4 eV [43,44]. Finally, several of the samples were removed for STM analysis after XPS characterisation. This necessarily involved transfer through the load-lock into an atmospheric environment, hence the films imaged may be partially covered with a thin carbonaceous layer. Partial oxidation at the cluster/air interface may also occur. In all STM experiments the samples were first prepared in vacuum before removal to

be examined by a commercial Burleigh STM (Burleigh Instruments Inc.) operated in air. All STM images were recorded in the constant current mode.

4. Results

4.1. Absolute surface coverage determination for ultra-thin metal film deposition

In many aspects of surface science work, determination of the growth mechanism and the related surface coverage calibration is often a crucial precursor to the measurement of the film geometric, electronic or magnetic properties or chemisorption/catalytic activity. Examples of specific applications of these properties include optically transparent electrodes [45] and selective surfaces [46], catalysis [47] and electron induced light emission [48]. Determination of the true growth mechanism is a notoriously difficult task. The majority of workers have in the past relied heavily on construction of the so-called Auger signal versus deposition time (AS-t) plots or an equivalent uptake mechanism based for example on X-ray photo-electron signal intensities [49]. In order to draw reliable and unambiguous conclusions regarding the film growth mode great care must be taken in the measurement and collection of a large number of evaporation time-intensity data points. As such plots often take a considerable length of time to construct, even highly painstaking work can suffer from the problem of residual gas adsorption, leading to changes in the growth mode from that under clean surface conditions. In particular, the common case of loss of adsorbate material into the substrate via surface or bulk alloying is a common problem in miscible metal-on-metal systems. Rhead has critically evaluated growth mode determinations using spectroscopic uptake measurements [50].

To progress from the growth mechanism to the absolute coverage of metal deposited requires knowledge of the metal packing density for at least one point in the Auger or XPS uptake curve. This may only be provided if a complimentary structural probe such as low energy electron diffraction (LEED) is available in situ.

The lack of cheap and easily applied absolute coverage calibration methods remains a problem for the majority of workers in the field of metal thin film growth. It should however be pointed out that reliable methods of absolute coverage calibration are presently available. For example, Rutherford backscattering spectroscopy (RBS) is a highly accurate method which has been successfully utilised by a number of groups

[51]. More recently, the application of the Scanning Tunnelling Microscope (STM) has revolutionised the study of metal thin film growth providing insight at an atomic level to the metal growth processes from submonolayer to multilayer coverages [52]. The STM has been utilised to provide coverage calibration via statistical counting of island sizes and heights. This method works well provided a large enough statistical average is taken but in certain cases suffers from disadvantages due to loss of adsorbate into the substrate via film/substrate alloying or the concealment of adsorbate at step edges and other defect sites. While the above two techniques are clearly useful, many laboratories involved in thin film growth do not have access to these expensive and in the case of RBS, highly specialised facilities.

Perhaps the most common method of film thickness/coverage calibration is via the use of an in-situ Quartz Crystal Microbalance (QCM). This method is known to give accurate and reliable relative thickness'/coverages. However, due to problems involving the accurate specification of the source/oscillator relative geometry, obtaining absolute coverages by this method is often more problematic.

A new simple and accurate method for absolute metal coverage calibration is described based upon the assumption of a coverage independent metal sticking probability from substrate to substrate which may be applied to a wide range of metals and is particularly relevant to the large number of workers possessing fast entry lock rapid sample insertion facilities.

The usefulness of the method is highlighted by two examples including the determination of the growth mechanism of Pd on highly oriented pyrolytic graphite (HOPG) and the growth and morphology of PdCu bimetallics on HOPG later in the Chapter.

4.1.1. The glass-slide ex-situ calibration technique

The method employed for the absolute coverage calibration consisted of preparation of glass slide segments from standard optical microscope slides. These glass samples were then attached to stainless steel sample stubs. The slides were carefully introduced into the sample preparation chamber and metal was evaporated for fixed lengths of time from evaporators operating under conditions consistent with their day to day operation for metal film growth (filament current, warm-up time, etc.). Care was taken to place the slides in identical positions relative to the evaporator as those used in film growth. The glass slides were then carefully removed via the load lock taking care not to touch the surface exposed to the metal flux for calibration by ex-situ graphite furnace atomic adsorption spectrometry (GF-AAS) analysis.

In order to perform the AA analysis the metal was first removed from the surface of the glass slide into solution using Analar grade acid digestion employing protocols, dependant on the nature of the metal digested. For Pd Aqua Regia acid was used (3 volumes conc. HCL:1 volume conc. HNO_3). Cu on the other hand requires a less vigorous acidic solution, namely conc. HCL. Subsequently, the glass slide was placed in a beaker which was carefully pre-cleaned via acid washing according to standard analytical techniques (steeped in Aqua Regia overnight, followed by steeping in chromic acid (5 % solution of potassium dichromate in conc. H_2SO_4) overnight, and finally conc. nitric acid overnight to remove residual chromate). This technique is applied to remove traces of metals adsorbed on the walls of the beaker. The solution was boiled to near dryness to ensure all the metal is removed from the glass.

Care was taken to ensure the dissolution was vigorous enough to remove all the metal from the surface of the glass slide. By performing a second acid digestion and a subsequent AA analysis it was verified that no additional metal was present on the slide and that the background signal from the acid itself, the acid-washed glassware and the glass slide was minimal.

A simple calculation assuming a metal monolayer density equal to that of HOPG (1.9×10^{15} atoms cm^{-2}) indicates that 3.2×10^{-9} moles of analyte is taken into solution if a monolayer of metal is deposited. Hence dissolution in 100 cm^3 of buffer yields a concentration of 3.2×10^{-8} moles per litre (3.2 μg/litre) which is well above the

detection limit of GF-AAS [53]. Pre-concentration to a volume of 10 cm^3 gives an order of magnitude advantage allowing even lower metal coverages to be detected. While the sensitivity of AA varies from metal to metal (electrothermal AAS is an order of magnitude more sensitive to Cu compared to Pd), we estimate the technique is capable of detecting surface coverages $\leq$0.10 ML for most commonly deposited metals.

The absolute amount of metal deposited on the glass slide was determined via construction of a standard AA curve following standard analytical chemistry techniques [53]. The concentration range typically used for Cu and Pd was 5–100 p.p.b. The copper and palladium calibrations were performed on a Spectra Varian 100 graphite furnace atomic absorption spectrometer (GF-AAS) with calibrant solutions prepared by serial dilution of a 1000 p.p.m. bench standard ($Cu(NO_3)_2$ and $Pd(NO_3)_2$ AA standards, BDH, SpectroscoL). The absorbance of the solution containing the copper or palladium obtained from the glass slide was then measured by interpolation from the calibration curve (serial dilutions may be made if the measured concentration is initially too high). The number of atoms evaporated onto the glass slide may then be simply calculated via knowledge of the solution concentration and the volume of acid the metal was dissolved in.

Typically, for a practitioner familiar with AA analysis and the associated analytical procedures, a standard curve and several concentration determinations from glass slides of differing evaporation times may be comfortably made within a day. Thus, the technique is not particularly time consuming. Furthermore, this method may be widely adopted as most Universities or modern research facilities will have access to atomic absorption facilities in-house.

It has been realised for some time that destructive techniques utilising dissolution of evaporated materials into solution followed by analysis by techniques such as spectrophotometry, polarography and atomic absorption or emission spectroscopy may be used for metal analysis [54], however, they do not appear to have been widely used by the surface science community. Prutton quotes an approximate sensitivity for flame spectrometry in emission mode as ~0.1 ML cm^{-2} [55]. On the other hand an approximate minimum amount of metal required is quoted to be 10^{-4} grams which approximates to 10^{-6} mole of metal, assuming a typical metal molecular weight of 100 grams i.e.10^2–10^3 monolayers per square centimetre. This rather high detection

limit has perhaps led to the belief that ultra-thin films of thickness in the submonolayer, monolayer and early stages of multilayer regimes provide insufficient material for successful ex-situ spectroscopic analysis. It is clear that the minimum amount of metal quoted by Prutton is too high based on modern analytical methodology.

4.2. Nucleation and growth of monometallic Pd and Cu cluster catalysts grown on HOPG

4.2.1. XPS and STM analysis

Figure 1 illustrates an XPS uptake curve for the growth of Pd on HOPG at 300 K. The curve was constructed utilising the Al Kα excited C 1s substrate XPS peak (E_{kin}=1202.2 eV) and the Pd $3d_{5/2}$ (E_{kin}=1151.2 eV) as palladium is deposited onto spectroscopically pure HOPG. The peak intensities measured correspond to the integrated areas under the C 1s and Pd $3d_{5/2}$ peaks with a linear background subtraction applied. In the case of the carbon signal, the intensity of the $\pi \rightarrow \pi^*$ shake-up peak was not included in the peak integration. We plot the XPS ratio rather than the individual intensities to minimise errors due to re-positioning of the sample with respect to the X-ray source/analyser after each subsequent evaporation and time dependent changes in the X-ray flux and detector gain.

Most importantly, use of the glass-slide absolute calibration method allows us to use absolute coverages on the ordinate axis rather than simply evaporation time, hence at all times we have knowledge of the metal loading on the HOPG surface. Thus, no fitting to straight-line segments need be attempted as in traditional growth mechanism determination. Instead, we simply calculate the expected Pd/C ratio based on a layer-by-layer growth mechanism, obtained utilising equation 4.1:

$$\frac{I_{Pd}}{I_C} = \frac{I_{Pd}^{\infty}}{I_C^{0}} \left[\frac{1 - \exp\left[\frac{-d}{\lambda_{Pd} \cos\theta} \right]}{\exp\left[\frac{-d}{\lambda_C \cos\theta} \right]} \right] \qquad 4.1$$

Values for the inelastic mean-free-paths of the C 1s and Pd $3d_{5/2}$ photoelectrons were calculated to be 17.1 and 16.7 Å respectively using the formalism of Seah and Dench [56]. The absolute XPS intensity ratios for pure HOPG (I_C^∞) and Pd (I_{Pd}^∞) were approximated using the relative photoionisation cross sections taken from Schofield [57] and the analyser transmission function measured to be $(E_{kin})^{-0.65}$ for our own XPS instrument.

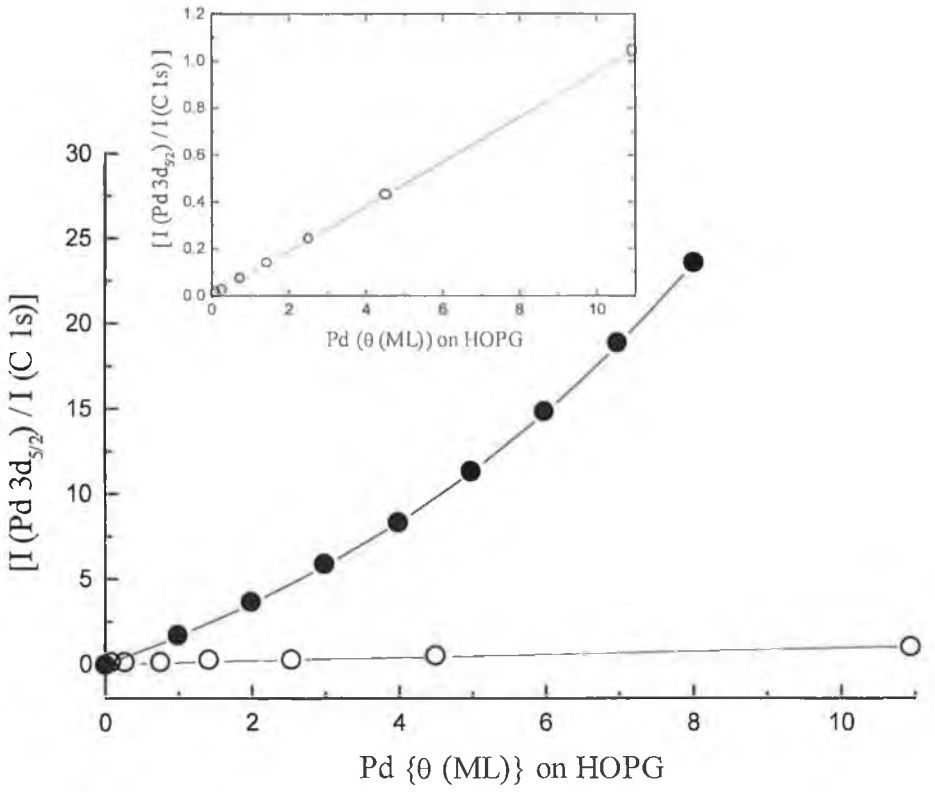

Figure 1: Variation of the background subtracted Integrated area of the Pd $3d_{5/2}$ core level ratioed to that of the C 1s level (open circles) for deposition of Pd onto HOPG at 300 K. Also shown is a theoretical prediction for layer-by-layer growth (filled circles). The linear increase for the experimental data set is revealed in the inset.

It is quite clear that at all coverages (even submonolayer), the experimental curve falls well below the layer-by-layer prediction allowing us to immediately rule out layer-by-layer or Stanski-Krastanov growth [58]. As the Pd $3d_{5/2}$ core level binding

energy and peak shape are very similar to those from bulk Pd we may also conclude that significant intercalation of Pd into the graphite lattice has not occurred. Hence, we may unambiguously say that Pd grows in the form of three-dimensional clusters on HOPG at 300 K.

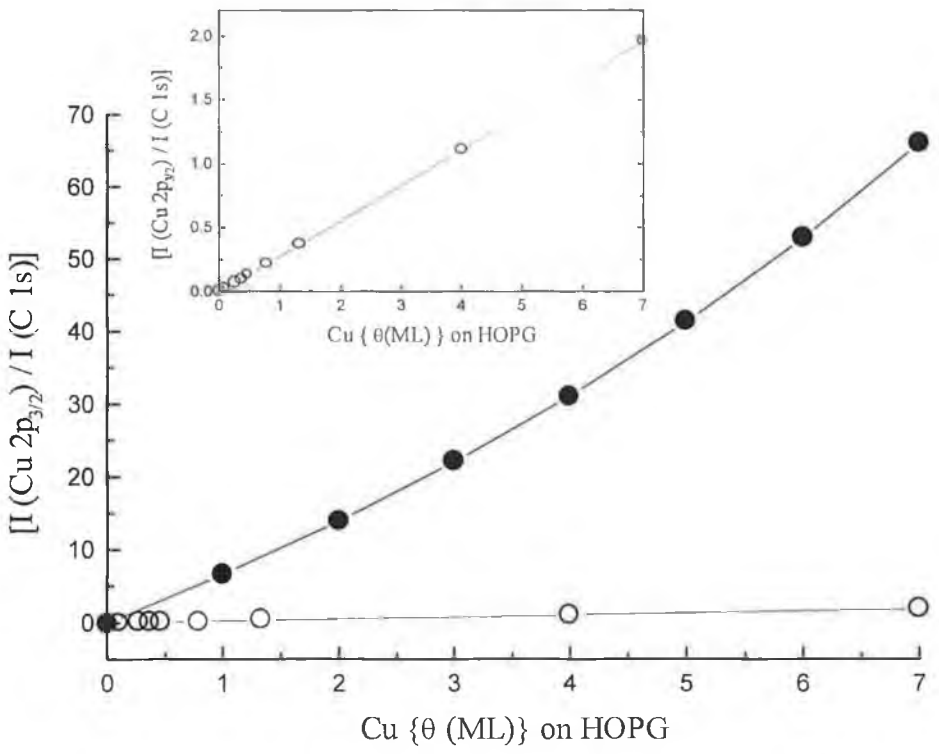

Figure 2: Variation of the background subtracted Integrated area of the Cu $2p_{3/2}$ core level ratioed to that of the C 1s level (open circles) for deposition of Cu onto HOPG at 300 K. Also shown is a theoretical prediction for layer-by-layer growth (filled circles). The linear increase in the experimental data set is revealed in the inset.

Similarly, figure 2 illustrates the background subtracted integrated area of the Cu $2p_{3/2}$ core-level ratioed to the C 1s core level at constant take-off angle ($\theta = 30°$) for the room temperature deposition of copper on HOPG. The experimental data again approximates rather well to a straight line in the coverage regime illustrated as shown in the inset. Also shown in figure 2 is a model calculation for Cu growing in a layer-by-layer mode utilising, as in the case of Pd, the inelastic mean free paths (IMFP) for the C 1s and Cu $2p_{3/2}$ core levels found to be 15.5 and 10.5 Å, respectively [56].

Again at all coverages including submonolayer the experimental data falls substantially below the layer-by-layer curve allowing us to again unambiguously rule out layer-by-layer and Stranski-Krastanov growth. Thus, the growth mechanism for Cu on HOPG appears, as for Pd, to be Volmer Weber. This conclusion is in line with expectations based on Bauer's classification [59] as the surface free energies of both Cu and Pd are considerably higher than that of HOPG [60]. Also, the cohesive energy of Cu is greater than its chemisorption enthalpy on the graphite surface [61].

The linear variation of the Cu/C and Pd/C core-level area ratios is worthy of comment. Essentially, this linear variation is suggestive of a mechanism in which simply the proportion of the HOPG surface covered with clusters scales linearly with coverage. Continuing deposition of metal does not lead to changes in morphology of existing clusters but rather forms new clusters indicating that a "critical cluster size" exists as a stable entity. In fact, these conclusions are in good agreement with an ex-situ STM study of Whelan and Barnes [23] in which both Pd and Cu possess strongly peaked cluster size distributions appearing to be relatively constant throughout the coverage regime examined with a simple increase in the area of HOPG covered.

Figures 3(a) illustrates the evolution in the Al Kα-induced Cu $2p_{3/2}$ core level with increasing coverage. The Cu $2p_{3/2}$ core peak maximum for highest coverage was located at a binding energy of 932.70 ± 0.05 eV and represents bulk Cu. For the lowest coverages a small shift to higher binding energy of ~0.3 eV is observed. Figure 3(b) represents the corresponding FWHM of the Cu $2p_{3/2}$ core levels as a function of coverage. A distribution in cluster sizes containing a sizeable fraction of particles of sizes differing significantly enough to lead to core level shifted XPS peaks will lead to a broadening of core level signals [30,31,42]. The FWHM shows no strong variation with coverage even at submonolayer coverages where the shift in the peak centroid indicates a decrease in cluster size. Thus, we tentatively deduce that while at low submonolayer coverages the Cu cluster size is reduced, a narrow size distribution still exists with only small quantities of large clusters present. Although at very low coverages small particles dominate and the FWHM is broader due to emission from Cu atoms in a number of different environments i.e. surface, bulk and interface (associated with the substrate) states. At higher coverages bulk Cu atom emission dominates resulting in a narrow FWHM.

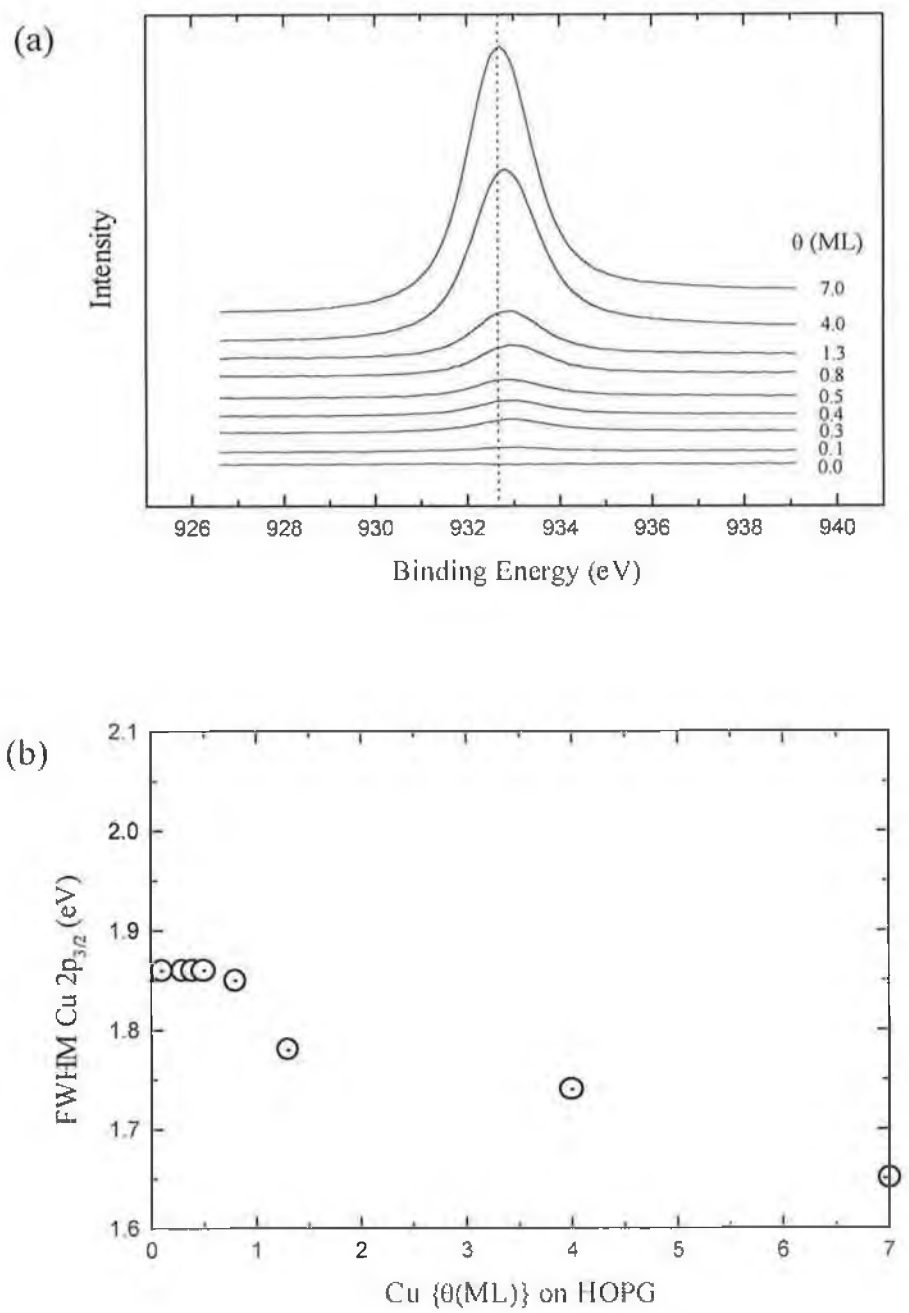

Figure 3: (a) Cu $2p_{3/2}$ core-levels; (b) FWHM as a function of Cu (ML) deposited on HOPG excited by Al Kα radiation. The binding energy scale is referenced with respect to the C 1s of the HOPG set at 284.4 eV [43,44]. The dotted line in (a) is to aid visualisation of the observed shift for lower coverages.

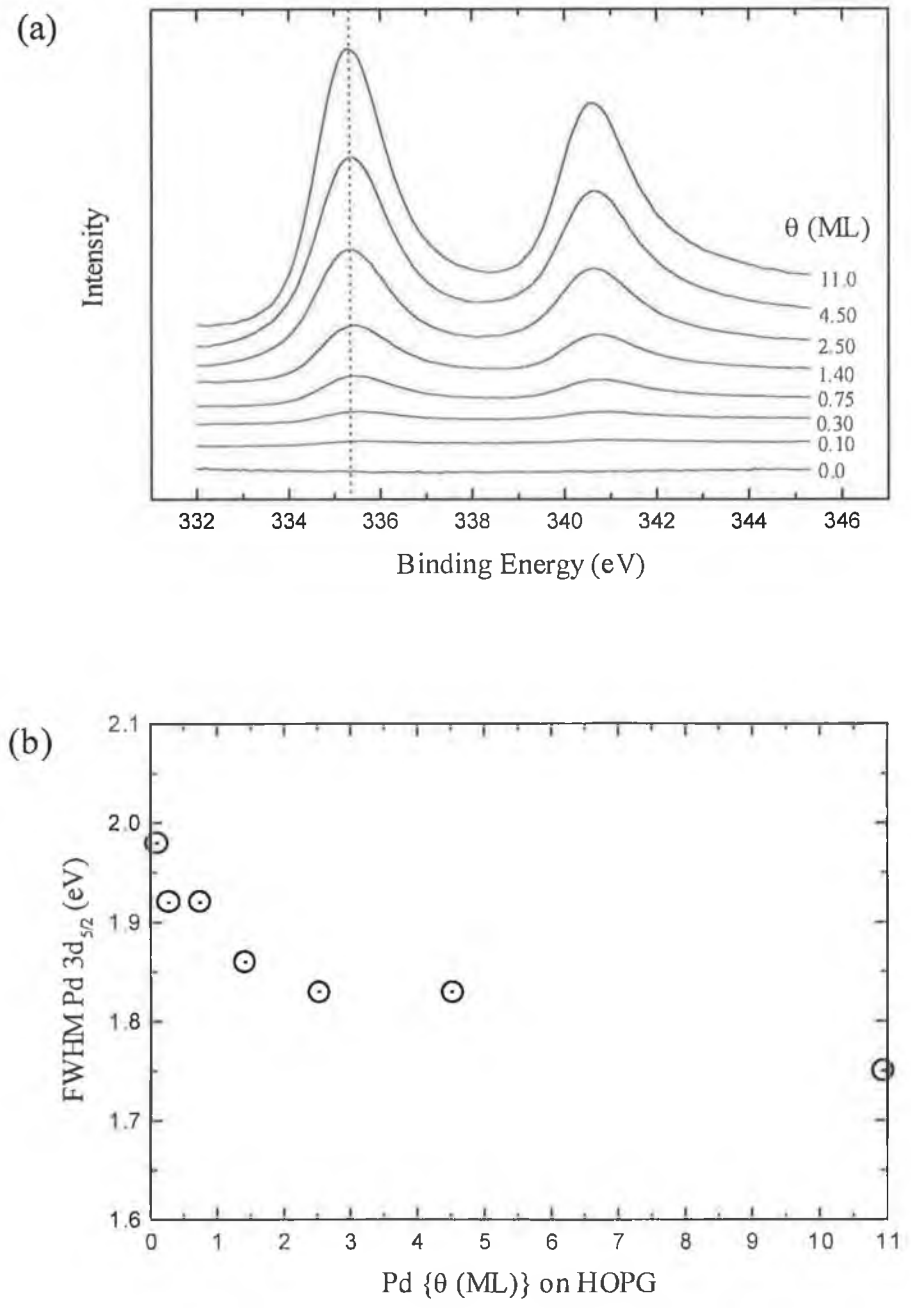

Figure 4: (a) Pd $3d_{5/2}$ core-levels; (b) FWHM as a function of Pd coverage (ML) as excited by Al Kα radiation. The binding energy scale is referenced with respect to the C 1s of the HOPG set at 284.4 eV [43,44]. The dotted line in (a) is to aid visualisation of the observed shift for lower coverages.

Figure 4(a) illustrates the Pd 3d core electron spectra of Pd for increasing coverage on HOPG. A small shift to lower binding energy (~0.3 eV) is observed with increase

in Pd coverage as expected for the transition to bulk like properties, for coverages of just over a monolayer. We note however that although the binding energy approaches that of the bulk metal it does not actually reach it (335.1 eV for bulk Pd), and even for the largest coverage examined (11 ML) it remains at 0.2 eV higher binding energy. The shift in core level binding energy for Pd is of a similar magnitude to that found for the Cu core-levels. The coverage dependence of the FWHM of the Pd $3d_{5/2}$ peak is shown in figure 4(b) and mirrors the trend seen for the Cu $2p_{3/2}$ core level with a significant increase in FWHM for submonolayer coverages compared to thicker films which display bulk like Pd properties. Again the presence of a varied and differing arrangement of clusters in the submonolayer domain leads to broadening of the core-level signals, with a high surface to bulk ratio.

The increase in core level binding energy observed for the lower Cu and Pd coverages is suggested, especially in the case of graphite as substrate, to be either a consequence of a metal-nonmetal transition, materialising as a variation in the electronic structure of the particles (an initial state effect) or as a result of the hole created upon photoemission which is not compensated for by the transfer of a screening electron from the substrate (final state effect). A contribution from both effects is also a possibility.

During photoemission studies there is no actual insight into the cluster sizes under scrutiny and therefore no evidence for a cluster size decrease at lower coverages. Independent assistance from the air-STM measurements of submonolayer coverages for both Cu and Pd revealed no further insight, with repeated attempts to image clusters at these low coverages failing. Interestingly Aiyer et al [20] have reported quite substantial Pd 3d core level binding energy increases with decreasing Pd coverage on HOPG. STM and HREM measurements allowed insight into cluster sizes revealing average sizes of 1.6 and 5.0 nm for Pd coverages of ~0.4 ML and ~7 ML, respectively. This supports the theory of reduced cluster sizes at low coverages for Pd on pristine HOPG. A substantial increase in Pd 3d binding energy (~1.0 eV) was recorded for the smallest clusters compared to the largest. This binding energy increases seen at low coverages (low cluster size), although significantly greater than those recorded here, are proposed to reflect the metal-nonmetal transition. More importantly, shifts in the centroids of the valence bands and the core-level binding

energies of the Pd clusters are not identical, ruling out the exclusive influence of final state effects.

Identical shifts have been observed in the Fermi edge, d-valence states and core levels (a shift in the whole electronic structure of the cluster with respect to that of the bulk) in the XPS spectra of Au and Ag clusters deposited on graphite [30,62] suggestive that the influence of final state effects is dominant. Although contradicting views also exist and more recently it has been proposed that changes observed in the electronic structure of both Cu [28] and Pd [25] deposited on graphite, as a function of particle average size can be explained in terms of interaction with the substrate. This interaction is described as a hybridisation between the filled d-states of the metal and the π^* empty graphite states, with this coupling constant proportional to the cluster size. This model has been invoked to explain the different shifts observed for the binding energies of the valence band, core levels and Fermi edge of Cu clusters on graphite [28]. Changes in the electron energy loss spectra (EELS) for decreasing Cu cluster sizes on polycrystalline graphite [63] cannot be attributed to final state effects since no uncompensated charge is created in the process. Therefore it is likely that the redistribution of states within the cluster d-band is the reason for this observed effect (initial state).

Importantly, valence band shifts to higher binding energy and a detectable narrowing of the lineshape have also been observed for discontinuous metal films on noble metal substrates, including Pd on Aluminium or silver [64] and Cu on zinc [65] where size effects due to charging cannot be present. In our case the use of graphite as a support ensures, due to its low reactivity with metals, cluster catalyst formation although its poor conducting nature [30,62] prevents us from discriminating between initial and final state effects and in effect deciphering the relative weight of contribution from each. However, it should be noted that the shift in the Cu $2p_{3/2}$ core-level (figure 3(a)) is to ~0.3 eV higher binding energy for the lowest Cu coverages with respect to the highest Cu coverages examined here, quite similar to the 0.4 eV shift measured by Di Nardo et al [28].

The Al Kα valence band spectra as collected for both Pd and Cu deposition on HOPG is represented in figure 5. As the cluster size decreases, the 3d peak, which is located in bulk Cu at about 2.4 eV [28], moves slightly towards higher binding

energy (figure 5(a)). Due to our limited experimental resolution (≥ 1 eV) no sizeable narrowing of the d-bands can be observed. The effect of Pd deposition on the valence band region is to attenuate graphite features and to introduce Pd-derived features (figure 5(b)). Even at low coverages a high density of states at the Fermi level is observed.

Both the core level binding energy and valence band maxima for thicker films of Cu and Pd are in good agreement with bulk values [30,26,34]. This is strongly suggestive that for all but the lowest coverages studied electronic properties have converged to their bulk values. The ratio of bulk to surface atoms in a Pd cluster of radius 13.6 Å is 2:1 [66]. Moreover, the cluster distribution for both Cu and Pd in a number of UHV- and air-STM studies reveal cluster sizes, for even the lowest coverages (~2 ML), of this size and greater when deposited on pristine HOPG [21,23].

Interestingly, the air-STM studies carried out on bimetallic arrangements to be discussed later, consistently failed to allow the imaging of submonolayer coverages, therefore, denying access to characterisation of cluster size distributions at low coverage. This applied to pure metals also [23]. This indicates the highly mobile nature of the clusters on HOPG at 300 K. A possible explanation is the evidence of electrostatic interactions between the tip and the surface in STM reported by Ohmori et al leading to clusters being pushed away from the tip during scanning at low coverages [67]. Loss of metal to surface defects such as cleavage steps is also possible.

While the growth mechanism deduced from XPS and ex-situ STM are in good agreement; we finally focus on the nature of the particles with respect to their structure. Ex-situ STM work indicates that Cu and Pd particles adopt a hemispherical droplet-like conformation in preference to growing epitaxially in orientated flat topped single crystal-like islands. However, it should be noted that the finite curvature of STM tips (10 nm) may make a small 3D object appear rounded because of the convolution of the tip shape with the actual shape of the cluster being imaged. In addition, as the STM analysis was performed in air, the clusters are undoubtedly partially oxidised which may lead to a change in morphology relative to their UHV prepared counterparts.

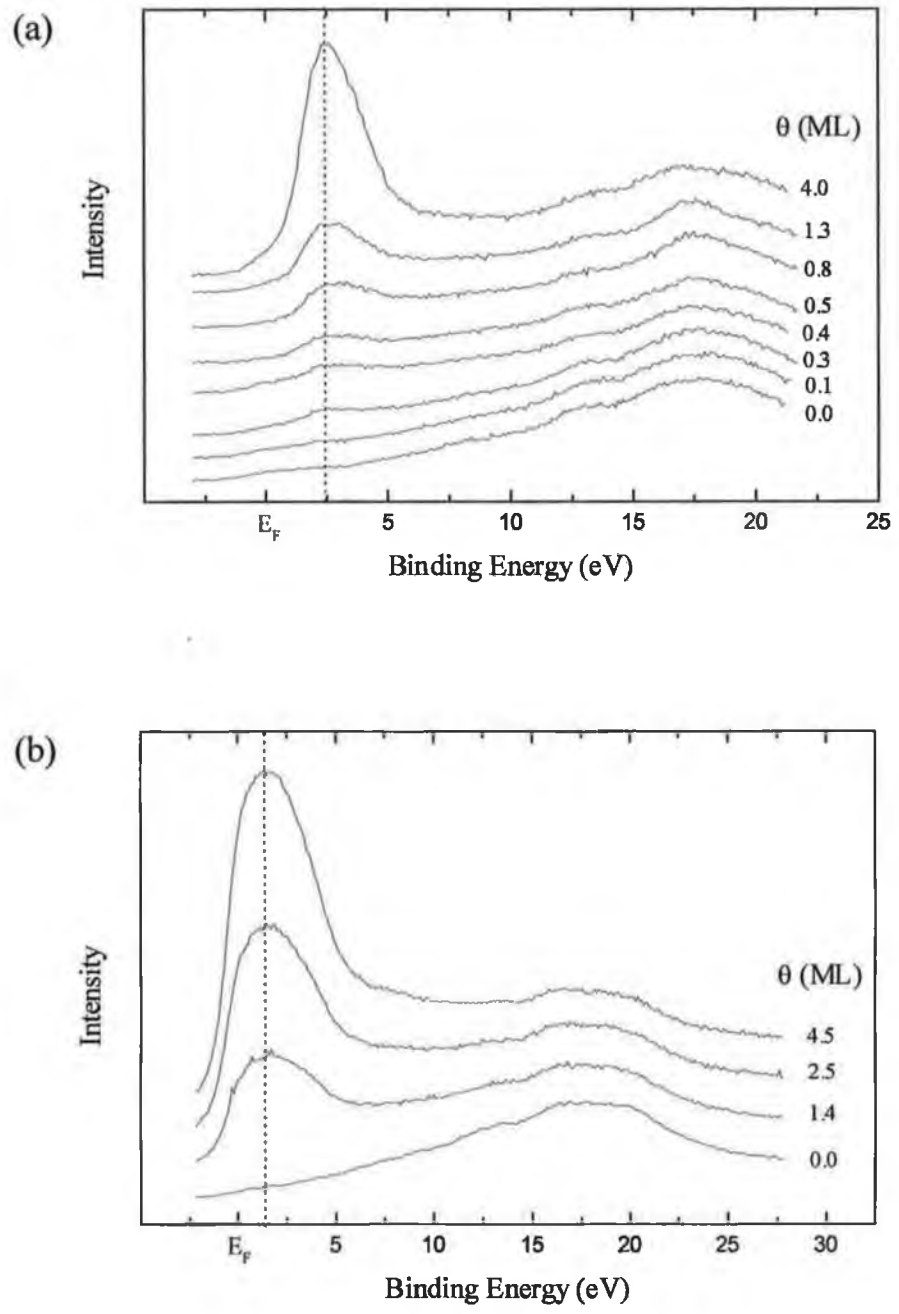

Figure 5: X-ray photoelectron spectra of the valence band of (a) Cu and (b) Pd for increasing metal coverage on HOPG , as excited by Al Kα radiation. The dotted line in (a) and (b) marks the position of maximum emitted intensity from the respective d-bands for the thickest films studied.

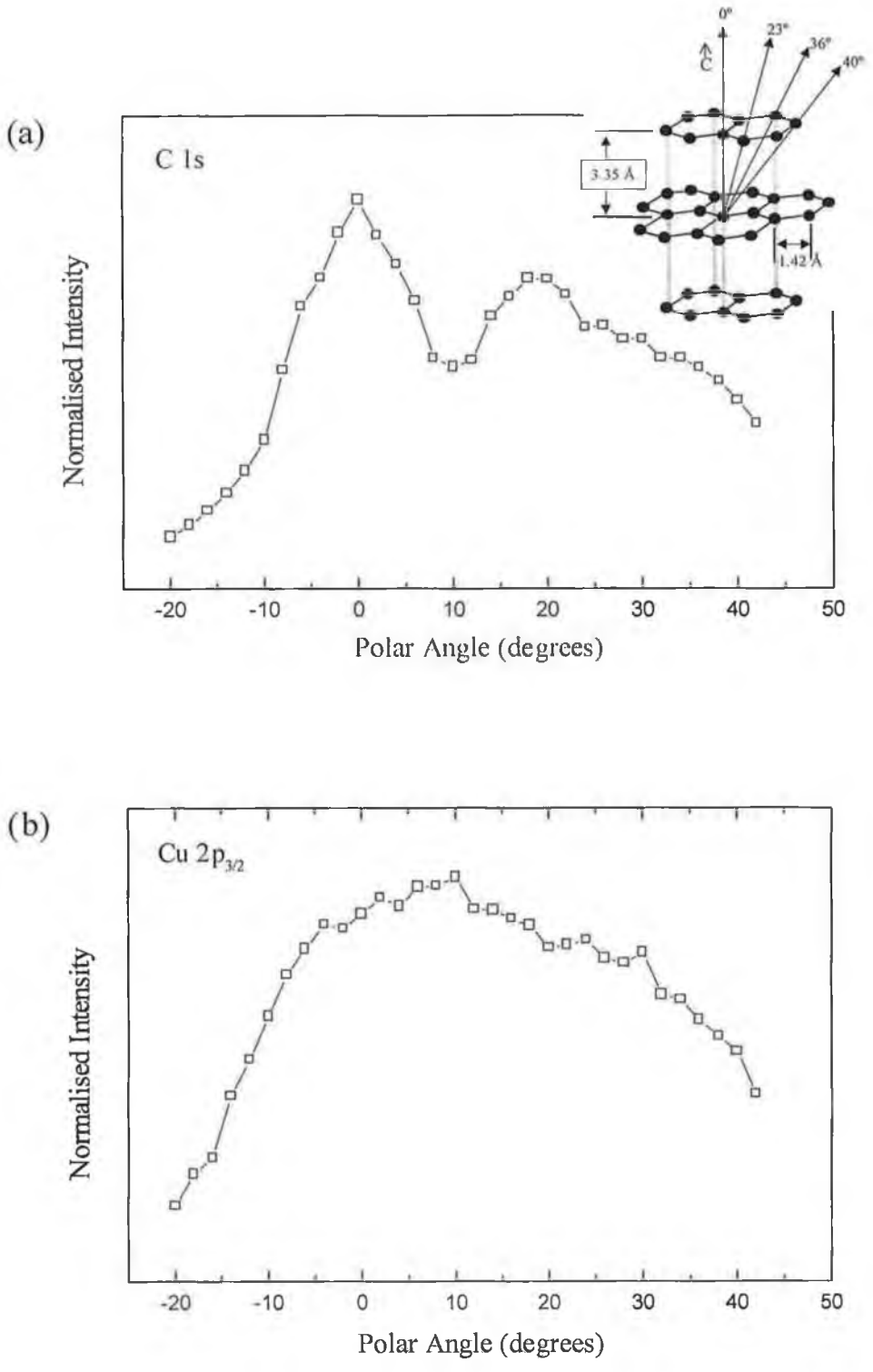

Figure 6: (a) Polar XPD scans from the C 1s core level from a 4 ML Cu film deposited at 300 K (the inset reveals the internuclear vectors (0°, 23°, 36° and 40°) between the atoms on neighbouring layers with respect to the c-axis which is normal to the HOPG surface); (b) polar XPD from the Cu $2p_{3/2}$ core level from the film deposited at 300 K.

The technique of X-ray photoelectron diffraction (XPD) was utilised as a probe to further determine the UHV structure. Polar plots of core-level peaks are known to contain significant structure from single crystal orientated surfaces due to photoelectron diffraction of emitted electrons within the sample selvedge when measurements are performed with an analyser of small angular acceptance [68,69]. In particular, at medium outgoing kinetic energies the diffraction is dominated by so called "forward focussing" in which emitted photoelectrons are "focussed" along internuclear bond axes of overlying atoms. This phenomenon has been much used in examining thin film epitaxy.

Figure 6(a) illustrates a polar plot in two degree steps from the C 1s core level induced by Al Kα radiation (E_{kin} ~1202.2 eV). The data represents the integrated area of the core peak with a linear background subtraction applied and was obtained by rotating the sample with the X-ray source and analyser fixed. Care was taken to ensure that during rotation the area analysed corresponded to the well-orientated surface of the HOPG sample. Clear diffraction peaks are observed. The peak at normal emission is due to forward focussing between adjacent layers as shown in the inset of figure 6(a) and should be present in all azimuthal directions. The second diffraction at an emission angle of 20 degrees cannot be definitely assigned as the exact polar direction scanned is not known as LEED optics were not available. Nevertheless, qualitatively the presence of normal emission and off-normal diffraction peaks are evidence of a well-orientated single crystal surface.

In contrast, the polar scan taken from a 4 ML Cu film (figure 6(b)) in the same azimuth utilising emission from the Cu $2p_{3/2}$ core level (E_{kin} ~553 eV) shows no evidence of the normal emission diffraction feature expected if the crystallites were single crystal and flat topped in nature. This is definitive proof that the Cu clusters are not epitaxial and flat topped in nature.

Heating the Cu sample to ~900 K tends to lead to a net decrease in metal XPS signal relative to the C 1s signal. This may be interpreted as (a) desorption of metal, (b) intercalation of the metal into the graphite lattice or (c) Ostwald ripening leading to an increase in the cluster size and consequent decrease in the metal signal due to a lowering in the proportion of the graphite being covered by the metal and a higher degree of self-attenuation. As the peak positions and the line shape of the C 1s remains similar before and after annealing as does the Cu $2p_{3/2}$ line we do not favour

intercalation as an explanation. Cu desorption experiments from HOPG have revealed the onset of desorption to occur at ~1150 K for a Cu coverage similar to that examined here. The desorption of metals at temperatures as low as 900 K is unlikely [70], hence we conclude that Ostwald ripening occurs.

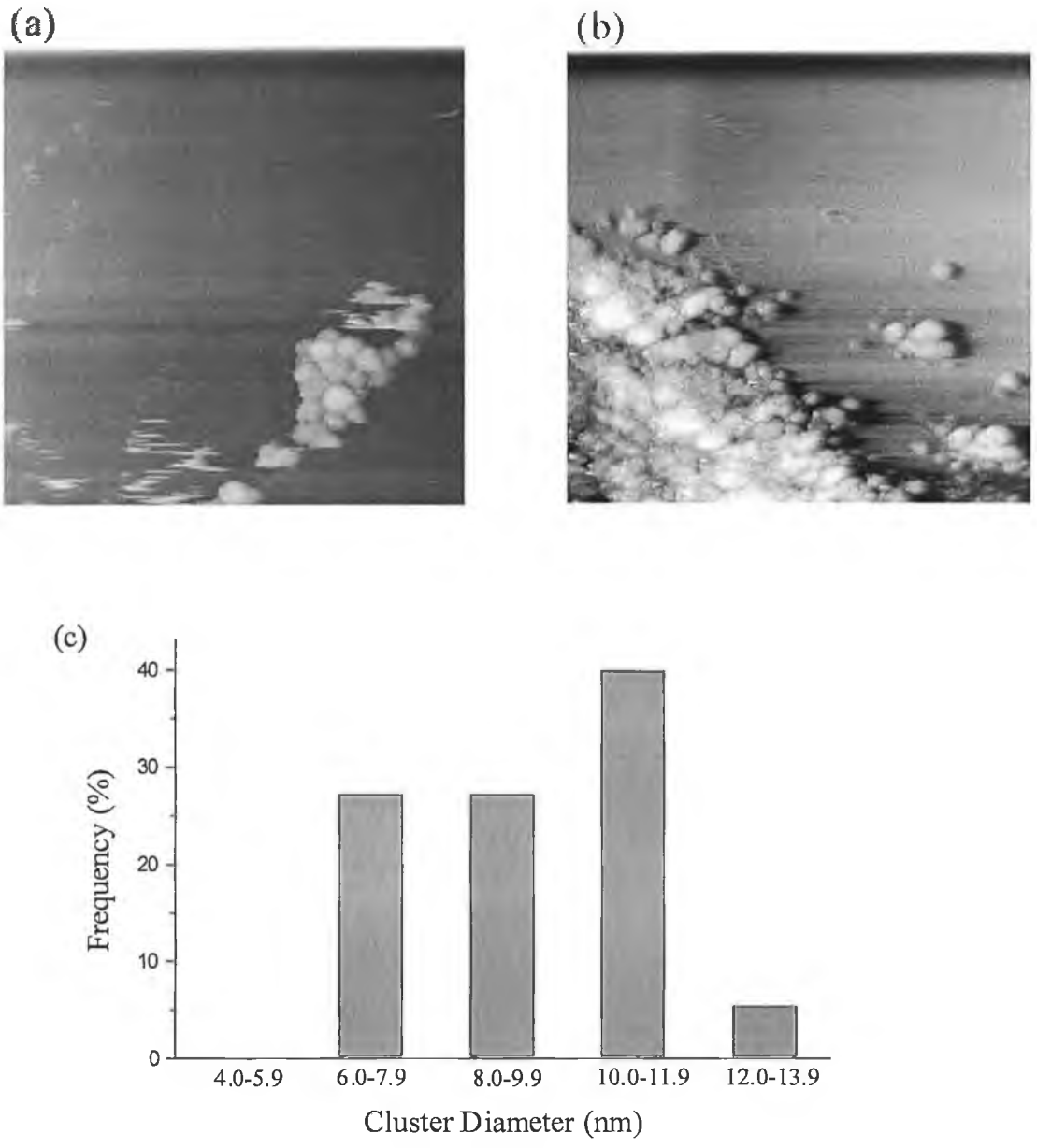

Figure 7: STM topographic images of an annealed (900 K) 4 ML Cu film on HOPG. Bias voltage (V) = 200 mV, tunnelling current (I) = 1 nA. (a) and (b) (200 × 200 nm) images of hemispherical cluster particles; (c) is a measured cluster size distribution for the Cu film.

Ex-situ STM examination of an as-deposited 4 ML Cu film heated to ~900 K is illustrated in figure 7. The images seem to emphasise that although Ostwald ripening does occur it is not to any significant extent for annealing to ~900 K (figure 7(b)) with hemispherical shaped clusters still present on the surface (figure 7(a)). The cluster size histogram corresponding to the analysis of several images revealing hemispherical clusters is illustrated in figure 7(c). The statistics were obtained from the individual measurement of each cluster with no automation. Expectantly the majority of clusters analysed are somewhat larger than those observed in the case of unannealed Cu samples [23], indicative of cluster coalescence.

4.3. Nucleation and growth of bimetallic CuPd cluster catalysts

To date, only a few works have been devoted to bimetallic supported model catalysts. The effect of gas treatment on various vacuum deposited silica supported bimetallic arrangements has been studied by TEM including, Pt-Pd [71] and Pt-Rh [72,73]. Other studies utilising HRTEM and EDX have been carried out on Pd-Cu on carbon [74] and Pt-Pd particles vacuum grown on both graphite and amorphous carbon [75]. However, none of these studies were concerned with the nucleation of the bimetallic particles.

The only STM study on bimetallic Cu/Pd clusters on graphite is that of Kojima and Kurahashi [76] in which only one coverage was studied. Samples were prepared by the simultaneous UHV evaporation of 3 ML's of each metal at a substrate temperature of 550 °C. Large crystallites growing epitaxially of 200 to 400 nm in width and 5 to 8 nm in height were formed. Simultaneous deposition produced smaller crystallites than that seen for the single deposition of Pd. Interestingly, AES measurements reveal that co-deposited crystallites consisted mostly of Pd even though equal amounts of both metals were deposited on the surface. Moreover, surface composition/analysis of the crystallites quantified by AES reveal a surface consisting of mostly Pd atoms. STM images of the topmost layer of the (111) crystallite face exhibited a long periodic structure with an observed atomic distance of 0.27 nm, slightly smaller than that of a bulk Pd crystal.

This work is in some ways clarified by the studies of Gimenez et al [77,78]. Again the elevated temperature growth of Pd–Cu particles is observed. Using HRTEM and EDX as examination techniques it was reported that on NaCl(100), held at 623 K, initial condensation coefficients for Cu and Pd are around 0.01 and 0.3, respectively, when the metals are deposited alone. It is suggested that Pd controls the evolution of the bimetallic particles during simultaneous deposition and that owing to the large disparity in condensation coefficients, Cu is only incorporated by the direct impingement on the nucleated particles as opposed to alloying after diffusion on the substrate. This theory is further supported by the fact that even when the particles are quite large (20 nm) the concentration in Cu is still well below the nominal concentration expected from the ratio of the beam fluxes. Similar studies involving Pd–Au systems have also been carried out [79,80]. Again the large difference in

sticking coefficient between Pd and Au mirrors that of the Pd-Cu system. The incorporation of Au into the bimetallic particles is only significant when the probability of direct impingement on the growing clusters is high. In these experiments the atoms with the higher energy of adsorption, namely Au in Ag-Au, or Pd in Pd-Cu, form nuclei preferentially, and the composition of the growing film is initially enriched in the element that is most strongly bound to the surface. The composition approaches that of the sources only after long times, or under complete condensation conditions.

It is quite evident that in the tailoring of bimetallic particle compositions a number of factors are quite important i.e. metals used, deposition time, substrate temperature and metal flux ratio and sequence (if not simultaneously deposited).

In this section results regarding the growth mechanism and morphology of bimetallic Cu-Pd catalysts supported on HOPG from both XPS and STM analysis are presented.

4.3.1. XPS analysis

Firstly, we should discuss the various possibilities regarding the sequential deposition of two different metals. A range of possibilities exist including (a) complete phase separation into monometallic clusters, (b) partial phase separation but with "egg-shelling" of metal A with metal B and (c) formation of mixed metal (alloy clusters). In a system involving HOPG, where the nucleation sites are low in concentration and randomly distributed, it is safe to assume that in the coverage regime studied we are still not sure that all the nucleation sites are occupied by the first metal evaporated before deposition of the second metal. The growth of bimetallic clusters upon deposition of a second metal can be expected, provided that the interaction between the two metals is stronger than the interaction of the second deposited metal with the substrate. The interaction strength of metals with carbon substrates is unknown but it is generally assumed to be weak.

Bimetallic PdCu surfaces were firstly probed by measurement of the core level binding energies and full widths of the Pd $3d_{5/2}$ and the Cu $2p_{3/2}$ core-levels and to a lesser extent consideration of the photoelectron line intensities.

In figure 8 we show the variation in the shift of the Pd $3d_{5/2}$ core level binding energy (BE) and FWHM for the incremental evaporation of Pd on various coverages of pre-

deposited Cu (1–7 ML). In all cases we plot, ΔE, the shifts in the BE for the bimetallic combination relative to bulk Pd and Cu (measured from very thick layers of single phase Pd and Cu on HOPG) found to be 335.3 and 932.7 eV, respectively. Absolute coverages were calculated using the glass slide method described in section 4.1.

For incremental Pd dosing on a 1 ML Cu film it is evident that at submonolayer Pd coverages there is a similar variation in the Pd $3d_{5/2}$ core-level BE when compared to similar coverages of the pure Pd metal on HOPG (figure 8(a)). As the Pd loading increases, the trend in BE follows that of pure Pd on HOPG. Incremental Pd coverages on 4 ML Cu is not that different from that seen for Pd deposition on 1 ML Cu, although for very low coverages of Pd (~0.1 ML) a 0.2 eV higher BE shift is observed relative to the smallest coverages (also ~0.1 ML Pd) of pure Pd on HOPG, which in turn is a shift to 0.5 eV higher BE compared to a bulk monometallic Pd overlayer. For an even higher pre-dosed Cu film (7 ML) Pd continues to adopt, as for the other Cu coverages, a BE pattern for increasing Pd loading quite similar to that for the pure metal on HOPG.

The BE data for Pd on pre-dosed Cu films as revealed above is quite suggestive of phase separated Pd, apart from one statistic i.e. the lowest coverage of Pd (~0.1 ML) on the pre-dosed 4 ML Cu film. In this case a 0.2 eV shift to higher binding energy is observed compared to a ~0.1 ML pure Pd film on HOPG. In a situation were alloying between Pd and Cu occurs and Pd is the dilute component, a 0.75 eV shift to higher BE is observed for the Pd 3d core level of a Pd_8Cu_{92} alloy compared to pure Pd. This shift is reduced to ~0.45 eV as the concentration of Pd increases i.e. a $Pd_{40}Cu_{60}$ alloy [81]. In our case the expectant shift to higher BE for Pd (submonolayer coverages) associating itself in a dilute alloy with already formed Cu clusters does not materialise.

On the other hand FWHM's of the Pd $3d_{5/2}$ (figure 8(b)) seem to contradict this hypothesis of phase separated Pd. On pre-deposited Cu samples, submonolayer Pd exists in a number of different forms revealed through a broad FWHM. A ~0.2 eV increase in full-width is seen for Pd on 1 ML Cu compared to the smallest Pd clusters on pure HOPG. This suggests that Pd exists largely as phase separated clusters as well as involving itself in a Cu-Pd interaction. High coverage pre-dosed Cu seems to behave quite differently. At 7 ML Cu coverage the HOPG surface is expected to be

considerably covered by Cu clusters. In fact assuming an average cluster size of ~75 Å [23] and that clusters are invariably hemispherical in shape, almost 60% of the surface is covered. As a result the probability of incident Pd atoms impinging directly on Cu clusters is therefore quite high. The constant and narrow FWHM (~1.7 eV) of Pd even at low coverages (0.75 ML) on Cu suggests a single Pd state presumably in a homogeneous arrangement with Cu, as phase separated Pd cluster FWHM's at this coverage are much higher (~1.9 eV) (see inset figure 8(b)). Interestingly the FWHM of ~1.7 eV observed is very similar to the width of the Pd 3d core level of a CuPd alloy, which is dilute in Pd (Cu(110)/Pd system - see Chapter 3).

The effect of Pd adsorption on the BE of the Cu $2p_{3/2}$ core level is shown in figure 9(a). A decrease in BE is experienced by all coverages of Cu and further decreases with continuing Pd deposition. On substrates with a valence band more than half occupied (Ru, Rh and Pt), Cu adatoms exhibit negative BE shifts in their 2p core levels and 3d band [82,83]. As expected the effect is most apparent for the low coverage Cu sample (1 ML) with a ~0.4 eV decrease in binding energy observed as the transition from Pd low submonolayer to multilayer deposition is made. However, for the 7 ML pre-dosed Cu sample the eventual 2p BE decrease is of a similar magnitude, however, requiring a far greater Pd loading (~11 ML). The reported trends reveal clear evidence of interaction between Pd and Cu as complete phase separation would show no change in Cu core-level BE as a function of Pd coverage.

An examination of the FWHM of the Cu $2p_{3/2}$ core-level is suggestive of Cu alloying with Pd. Figure 9(b) reveals a broadening in the FWHM for all coverages of pre-dosed Cu with increasing sequential dosing of Pd. The greatest increase in width is seen for the 7 ML Cu sample which experiences a ~0.3 eV increase. The increase in FWHM is interpreted as due to emission from Cu in a range of environments with a corresponding range of core-level binding energies. The increase in FWHM is not as extreme for the lower coverage Cu samples, as they don't initially exhibit the uniform bulk-like properties such as the narrow FWHM seen for the 7 ML Cu sample. More enlightening is the fact that the final degree of disorder of Cu for all samples is quite similar for all levels of Cu i.e. 1, 2.5 and 7 ML pre-dosed samples. The only differing factor been the amount of Pd needed to achieve this, found to be

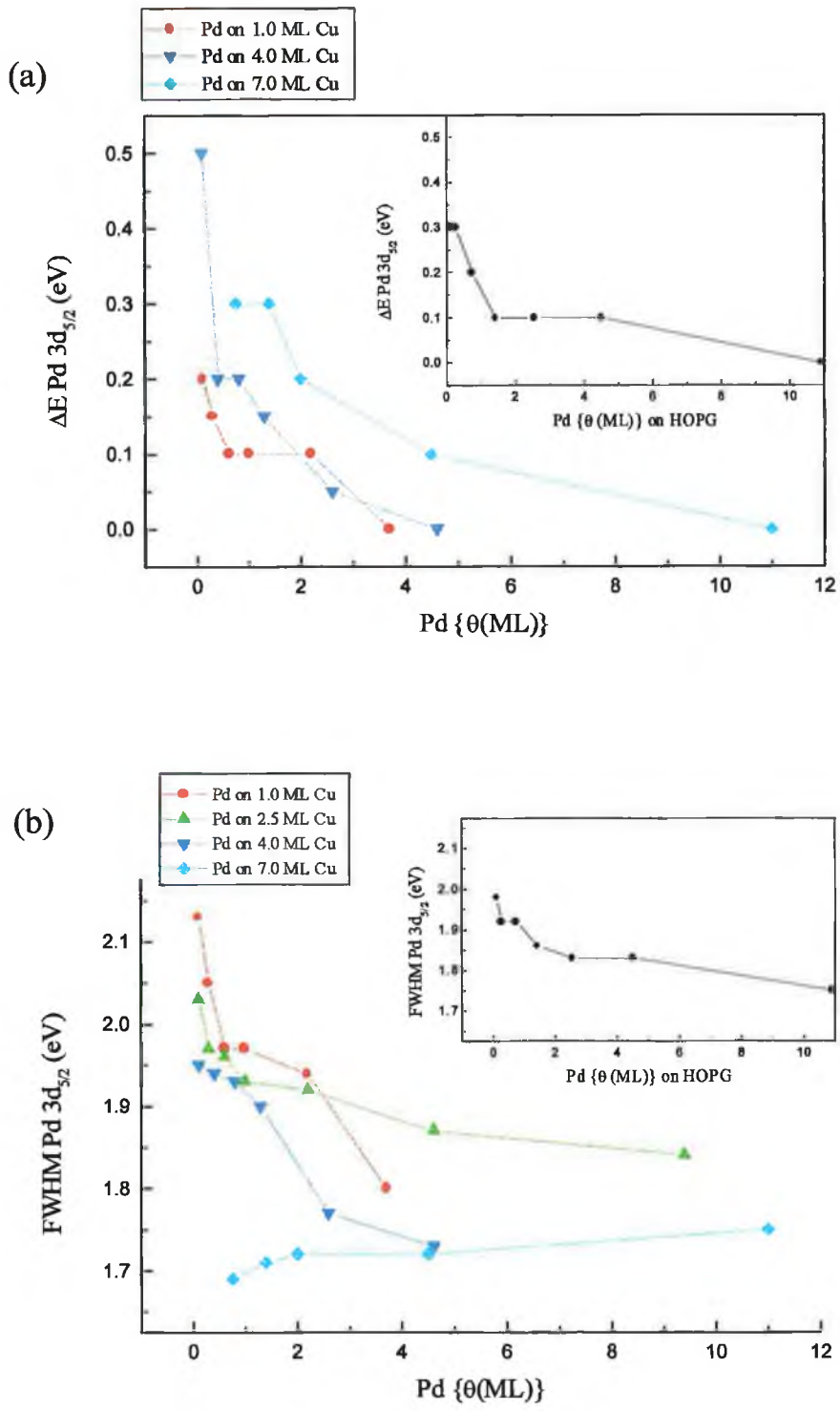

Figure 8: (a) Variation of the shifts in the binding energy of the Pd $3d_{5/2}$ core level (relative to bulk Pd), ΔE, and (b) the FWHM of the Pd $3d_{5/2}$ for incremental Pd deposition on different loadings of Cu pre-deposited on HOPG. The inset in (a)/(b) reveals the variation in the core level binding energy/FWHM of Pd monometallic clusters with respect to coverage.

(a)

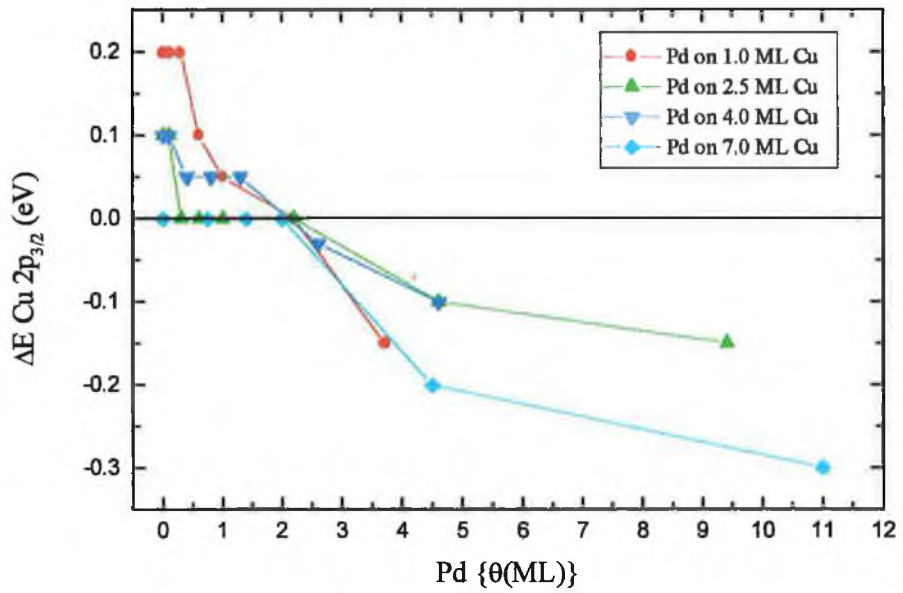

(b)

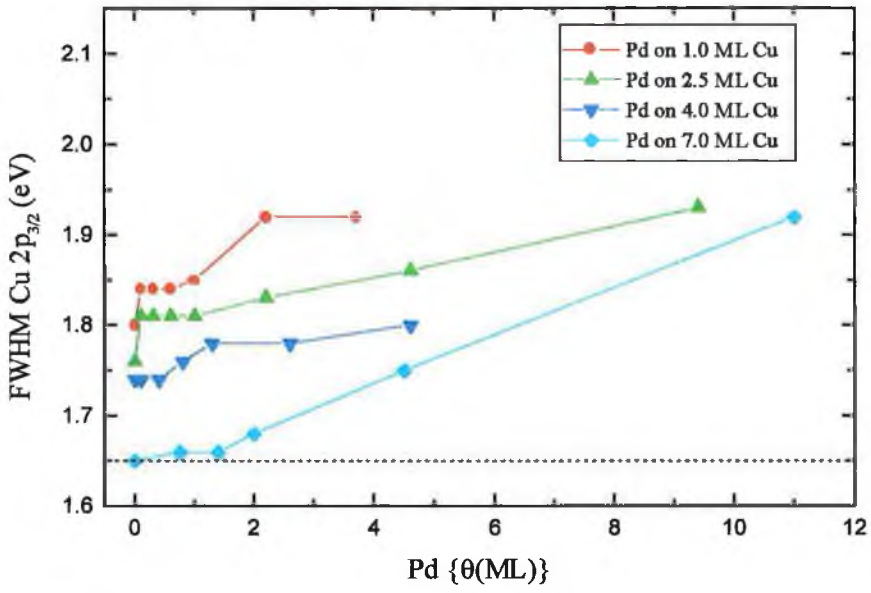

Figure 9: (a) Variation of the binding energy of the Cu $2p_{3/2}$ (relative to bulk Cu), ΔE, and (b) the FWHM of the Cu $2p_{3/2}$ for incremental Pd deposition on different loading of Cu pre-deposited on HOPG. The dotted line in (b) is the FWHM for bulk Cu.

~4 ML Pd for the 1 ML Cu pre-dosed sample and between 10 and 11 ML Pd for the 11 ML Cu pre-dosed sample. Surface alloy formation is common for the deposition of Pd onto Cu single crystals. The extent of alloying is usually determined by the crystal face, and tends to be limited to the first couple of substrate layers for the more open (100) and (110) faces. On the other hand alloying of Pd with Cu(111) requires thermal activation. For Pd deposition onto Cu(100) a 0.3 eV shift of the Cu 2p core level to lower binding energy is seen for a 2 ML film deposited at room temperature, with no change observed upon further deposition [84]. If Pd simply coats Cu ("egg-shelling") we would expect an increase in the Cu 2p BE due to the loss of Cu surface atoms (calculated values for surface core level shifts BE shifts vary but are negative compared to bulk BE values and found to be between 0.2 and 0.5 eV for the various low index faces of Cu [85,86]). The BE decrease observed in figure 9(a) is therefore consistent with an increase in the electron density for some portion of Cu in the near surface region. A contribution from this interfacial alloying region at low BE explains the observed broadening of the Cu signal (Cu $2p_{3/2}$ FWHM increases). In bulk alloy CuPd arrangements the Cu 2p core level binding energy is seen to decrease for increasing Pd composition in CuPd alloys [81,87]. Hence, it seems that our Cu core level shift may be indicative of an alloying interaction between Pd and Cu.

Regarding Pd incremental dosing on varying Cu coverages on HOPG we may suggest some initial theories. In BE and FWHM terms Pd will possibly preferentially associate with Cu although the extent of interaction is unclear. On the other hand, it seems that Pd exists in a uniform environment for submonolayer coverages on a high loading of Cu exhibiting a FWHM quite similar to a uniform CuPd alloy dilute in Pd. The probability of interaction with a Cu cluster as opposed to interaction with free graphite surface will also determine the extent of Cu-Pd interaction and will be greater for higher coverage pre-dosed samples. The decrease in BE of the Cu $2p_{3/2}$ to values below that of the bulk is relevant as it indicates that Cu exists as a CuPd alloy as the amount of Pd on the surface increases, suggestive that even for growth at 300 K the catalyst surface region probed by XPS is an alloy at the surface of the Cu microclusters. The Cu increasing FWHM's suggest an increasing number of differing Cu environments with increasing Pd coverage.

From the binding energy and peak width data discussed above it appears that the growth mechanism for Pd deposition on pre-dosed Cu is as follows: the simultaneous

growth of Pd clusters on the HOPG surface and the alloying/ capping of the areas already covered by Cu clusters. This is perhaps not too surprising for growth at 300 K. Figure 10(a) reveals the variation in the ratio of the integrated areas of the Pd $3d_{5/2}$ core-level to that of the C 1s as a function of Pd coverage on different pre-dosed Cu samples. A linear variation in this ratio is seen for all pre-dosed Cu coverages. This is a mechanism whereby the proportion of the surface covered with clusters scales linearly with coverage with a quite constant cluster size distribution. The trend seems to be one of increasing Pd/C ratio (compared to that seen for monometallic Pd growth on HOPG) as the amount of pre-dosed Cu on the surface increases, supporting the capping of Cu clusters with Pd. Figure 10(b) reveals the percentage attenuation in the Cu $2p_{3/2}$ signal as a function of Pd coverage for the same pre-dosed Cu samples and is compared to that of theoretically predicted layer-by-layer Pd growth on Cu(111). For all Cu coverages the attenuation of the Cu signal upon Pd deposition is less than that expected if Pd growth involved the exclusive coating of the Cu clusters in a layer-by-layer growth mode. This growth mechanism (unfavourable thermodynamically) is easily dismissed. Moreover, figures 10(a) and (b) emphasise the limited nature of the Pd-Cu interaction and the greater tendency of Pd to form phase separated clusters when deposited on pre-deposited Cu.

The systematics of Cu on Pd seems to follow a more predictable route. Figure 11(a) reveals the evolution of the BE of the Cu $2p_{3/2}$ core level for Cu incrementally dosed on a range of pre-deposited coverages of Pd. The shift to lower binding energy at low Cu coverages is suggestive of Cu existing as adatoms on Pd clusters (layer-by-layer Cu growth is observed on Pd(111) up to a coverage of 2 ML and thereafter in the form of clusters [88]) in good agreement with thermodynamic considerations. This immediately suggests that particularly for low Cu coverages, where a significant fraction of clean HOPG exists, Cu atoms incident upon these areas may rapidly diffuse and "coat" the Pd clusters. For the 1 ML pre-dosed Pd sample (21% of surface is covered if a 40 Å hemispherical Pd cluster size is assumed) the addition of ~3 ML of Cu returns the BE of the $2p_{3/2}$ to that expected for bulk-like Cu. This suggests that Cu may simply cap or eggshell the Pd clusters.

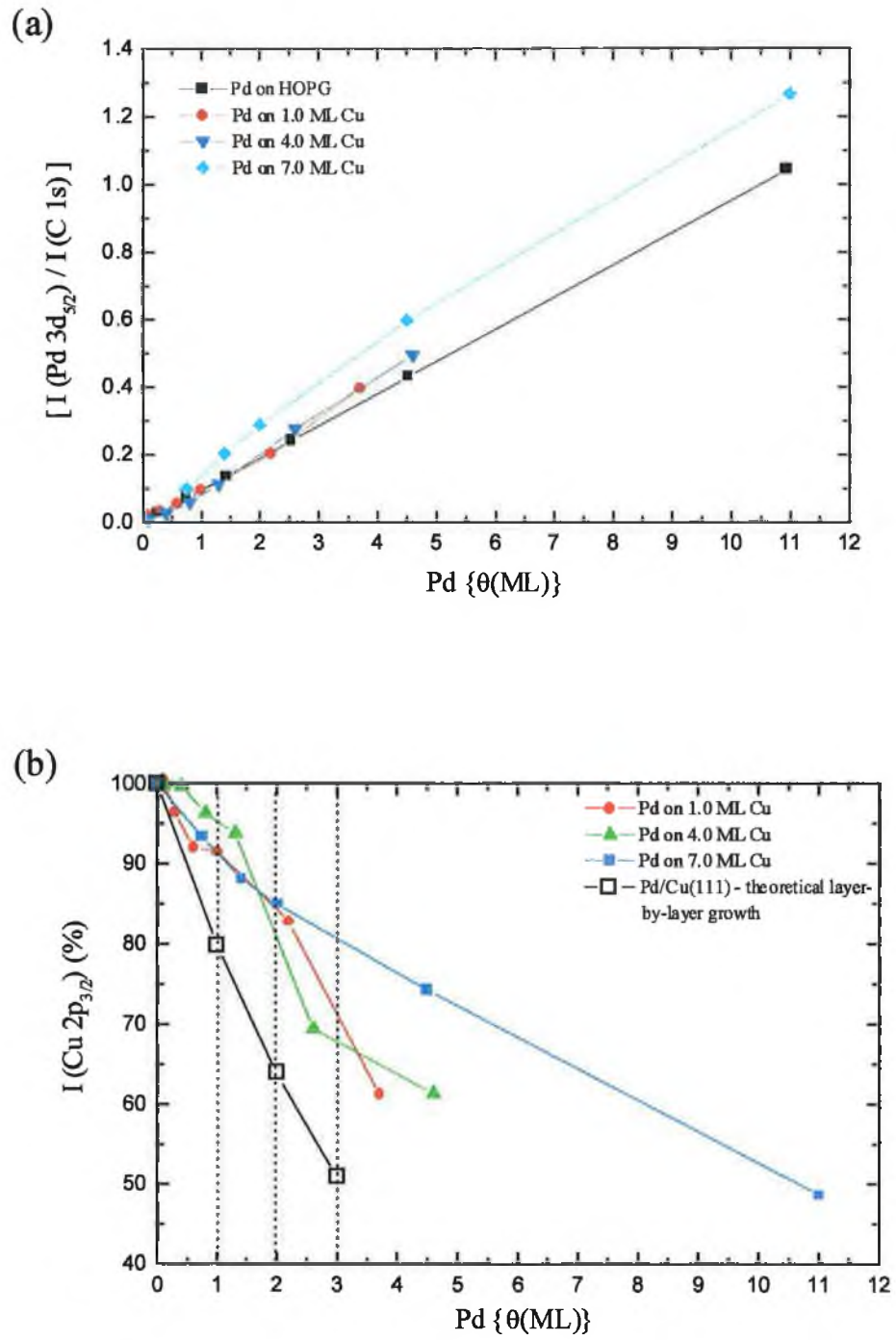

Figure 10: (a) Variation of the ratio of the Pd $3d_{5/2}$ and C 1s photoelectron core levels and (b) the percentage decrease in intensity of the Cu $2p_{3/2}$ core level, as a function of Pd deposition on different loadings of Cu pre-deposited on HOPG. Theoretical layer-by-layer growth for Pd on Cu(111) is also indicated.

There is no evidence for deposition at 300 K that significant alloying between Pd and Cu occurs as this would result in a shift to a different BE relative to bulk Cu. Consideration of the BE of the Cu $2p_{3/2}$ core level dosed onto 11 ML Pd supports more clearly this growth mechanism. The fact that the Cu $2p_{3/2}$ never attains the BE of bulk-like Cu for even 7 ML Cu coverage attests to the dominant force driving the growth mechanism i.e. the interaction of Cu with Pd as opposed to the formation of pure Cu clusters, although it is noted that according to our calculations no free graphite is available for 11 ML Pd pre-dosed samples.

The FWHM of the Cu $2p_{3/2}$ follows the trend expected if Cu preferably coats Pd as opposed to forming phase separated clusters (figure 11(b)). On pre-dosed 1 ML Pd, Cu in the low submonolayer range reveals a higher FWHM by ~0.25 eV than that expected for monometallic Cu clusters on HOPG. This trend is repeated for the 2.5 ML Pd coverage sample. The decrease in the FWHM to values approaching pure Cu clusters is observed as the Cu coverage increases above 1.5 ML on both the 1 and 2.5 ML pre-loaded Pd samples. For the low and intermediate levels of Pd predosing (1,2.5 and 4 ML) the Cu FWHM decreases with increasing Cu coverage all except for the high coverage 11 ML Pd sample. The increase in FWHM seen for the transition between the Cu monolayer to the multilayer range for this Pd coverage (11 ML) is a result of convoluted emission initially from Cu in a homogeneous Cu-Pd surface arrangement (narrow FWHM) as well as from size distributed pure Cu clusters (broader FWHM). At high Pd coverage the probability that Cu will impinge directly on a Pd cluster is increased (narrow FWHM). In contrast, the probability of Cu directly impinging with a nucleation substrate site is far greater than that of directly hitting a Pd cluster on the low Pd coverage pre-dosed samples (broader FWHM). As the Cu coverage increases on the high coverage Pd sample (11 ML) we see a slight increase in FWHM attributable to the convolution of the chemically shifted Cu-Pd surface interaction and the evolution of pure Cu derived features. We postulate that the broadening of the FWHM to values equivalent to that seen for submonolayer Cu coverages on low pre-dosed Pd coverages (1 and 2.5 ML Pd) is evidence of the existence of Cu-Pd interaction and a range of Cu clusters existing in tandem, having chemically shifted states producing the observed broadening. The 0.5 eV decrease in BE for 1 ML Cu on 11 ML Pd compared to bulk Cu is evidence of the extremely dilute Cu nature of the Cu-Pd interaction, essentially Cu capping.

Therefore as the Pd-to-Cu ratio increases, the Cu 2p peaks shift to lower binding energy consistent with that measured for PdCu bulk alloys [81,87,89].

The constancy of the BE values of the Pd $3d_{5/2}$ for all Pd coverages reinforces the hypothesis that Cu-Pd alloying does not occur to any considerable extent. In figure 12(a) we have plotted the shifts in the BE of Pd $3d_{5/2}$ against Cu coverage for several Pd pre-dosed graphite samples. The non-variance of the BE representing bulk Pd properties is in keeping with the growth of Cu mono and multilayers above Pd clusters similar to the tendencies of Cu on Pd single crystals [90,91,92], and is good proof that bulk alloying does not occur for the deposition of Cu on Pd at 300 K. Formation of a CuPd alloy would lead to a shift of the Pd $3d_{5/2}$ core level to higher BE relative to bulk Pd.

The variation in the width of the Pd $3d_{5/2}$ core-level for several Pd films as a function of Cu coverage is plotted in figure 12(b). The constancy of the FWHM for both 1 and 2.5 ML Pd pre-dosed samples again suggests that the continued addition of Cu leads to the coating ("egg-shelling") of the Pd clusters and that alloying is not significant with increasing Cu coverage. The levels of Cu necessary to coat low coverage Pd samples is quite small, essentially complete in the submonolayer Cu range and manifesting as a constant Pd FWHM from the submonolayer to multilayer Cu range. The FWHM of the Pd $3d_{5/2}$ core-level for high coverage pre-dosed Pd (4 and 11 ML) samples is found to reduce below the values of bulk Pd with increasing Cu coverages. The marked reduction in FWHM with increasing Cu dosing to a value below that of a thick bulk Pd layer on HOPG maybe explained as follows: the FWHM of a Pd thick layer on HOPG represents Pd atoms in a range of environments (surface atoms, bulk atoms and substrate-film interface atoms) with a corresponding range of core-level binding energies. The narrowing of the Pd $3d_{5/2}$ core line to a value less than bulk Pd maybe a result of Cu capping of the clusters leading to a return of surface atoms to a binding energy closer to that of bulk Pd thus leading to a narrowing of the FWHM of the Pd $3d_{5/2}$ core level with increasing Cu coverage.

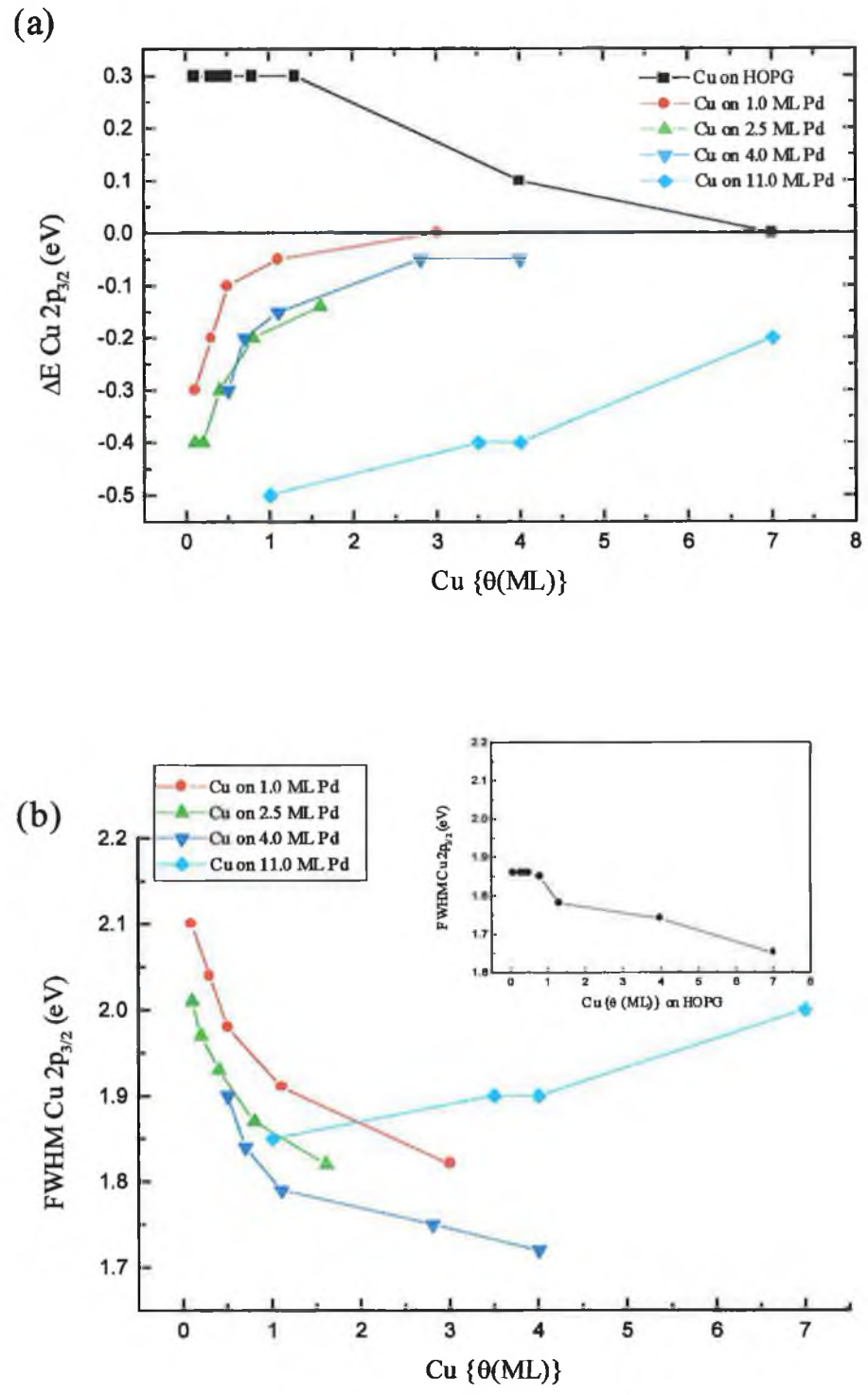

Figure 11: (a) Variation in the Cu $2p_{3/2}$ binding energy (relative to bulk Cu), ΔE, and (b) the Cu $2p_{3/2}$ FWHM for incremental Cu deposition on several different loading of Pd pre-deposited on HOPG. The inset in (b) reveals the variation in the FWHM of Cu monometallic clusters with respect to coverage.

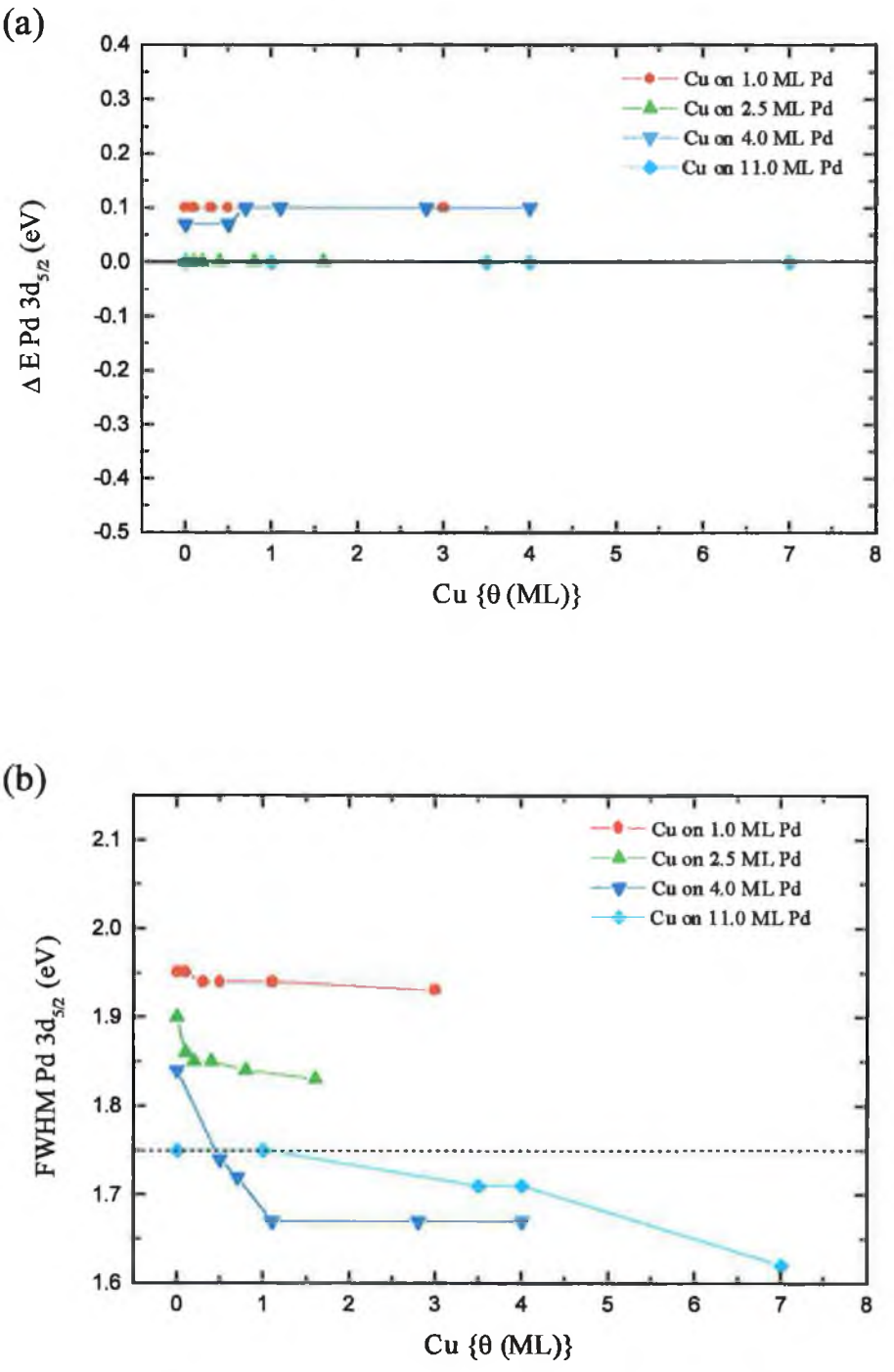

Figure 12: (a) Variation of the Pd $3d_{5/2}$ binding energy (relative to bulk Pd) and (b) the Pd $3d_{5/2}$ FWHM for incremental Cu deposition on several different loadings of Pd on HOPG.

The absence of shift in the binding energy of Pd 3d XPS peaks for amorphous carbon supported Pd-Cu samples have been previously reported [93]. Similar to our

observations concomitant shifts of the Cu 2p peaks to lower binding were recorded. Of interest is the suggestion that this may not rule out Pd-Cu alloy formation. It is proposed that in the case of a large Pd particle size distribution, Cu may preferentially interact with larger Pd particles (> 50 Å) and the dominant XPS signal from the smaller pure Pd particles may potentially mask the XPS signal from Pd in the larger Pd-Cu bimetallic particles (to be discussed further in the discussion).

Further examination of the Cu-Pd system is provided by the consideration of the valence band spectra revealing the progressive development of the Cu 3d and Pd 4d bands as the relative concentration of the metals on the surface changes. For Cu deposition on a 1 ML Pd film (figure 13(a)), an increase in θ_{Cu} leads to the development of the Cu 3d band at ~2.5 eV binding energy and at 3.0 ML the spectrum resembles that of pure Cu. Even if the initial loading of Pd on the surface is increased (θ_{Pd} = 4 ML) (figure 13(b)) an almost identical behaviour is observed.

The deposition of Pd on 1 ML Cu reveals the evidence of Pd clusters for coverages as low as 0.1 ML, seen as a shoulder on the lower BE side of the Cu 3d band (figure 14(a)). The comparison of the valence band region of samples containing equal loading of Pd and Cu (~4 ML of each metal) formed differently i.e. one by Cu deposition on Pd (figure 14(b)) and the other by Pd deposition on Cu (figure 13(b)) is quite interesting. The increased intensity at low binding energies witnessed for Pd on Cu compared to the that observed for Cu on Pd suggests as may be expected that a more Pd rich surface results in the former case.

Figure 15 shows an XPS survey scan of a 1.2 ML Cu film deposited on a 1.5 ML Pd film. The survey scan of the 1.5 ML Pd film prior to Cu deposition is included for comparative purposes. The Pd MVV Auger transition is particularly surface sensitive and experiences considerable quenching after deposition of the Cu. On the other hand the Pd 3d core-level quenching is less evident presumably due to the longer inelastic-mean-free-path. Some interesting points are raised in a similar experiment for Pd (8 ML) deposition onto a 5 ML Cu film. The deposition of Pd results in the partial quenching of the Cu 2p signal, as seen in survey scan (b) of figure 16, interpreted as the attenuation of Cu due to interaction with deposited Pd. As the C 1s signal is also seen to decrease somewhat it would appear that some Pd clusters also nucleate on free areas of HOPG.

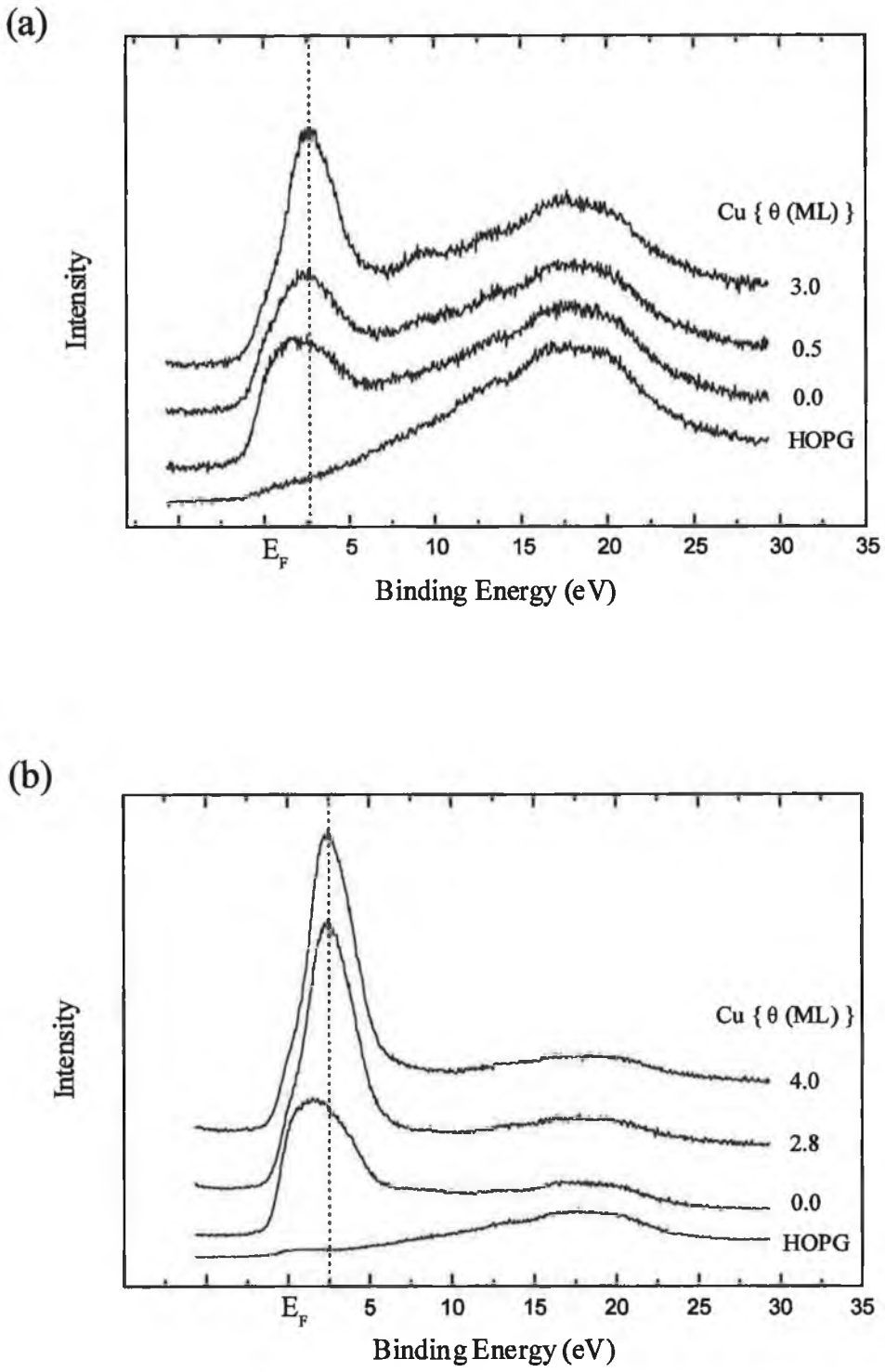

Figure 13: Al kα induced X-ray photoelectron valence band spectra for increasing Cu coverages on a (a) 1 ML Pd film and (b) 4 ML Pd film.

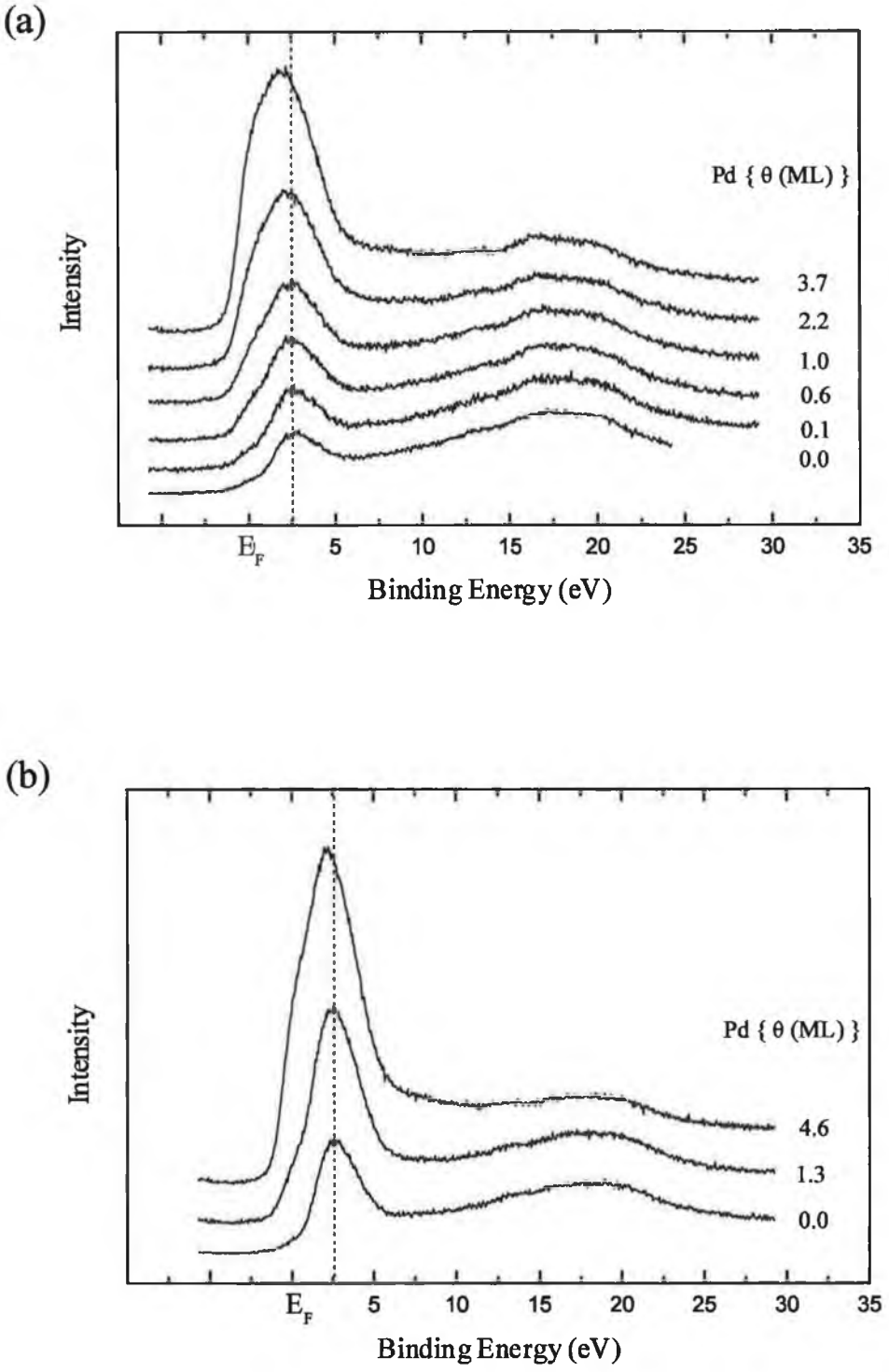

Figure 14: Al kα induced X-ray photoelectron valence band spectra with increasing Pd coverage for (a) 1 ML and (b) 4 ML Cu films. The dotted line in both plots indicates the point of maximum emission from the Cu 3d band.

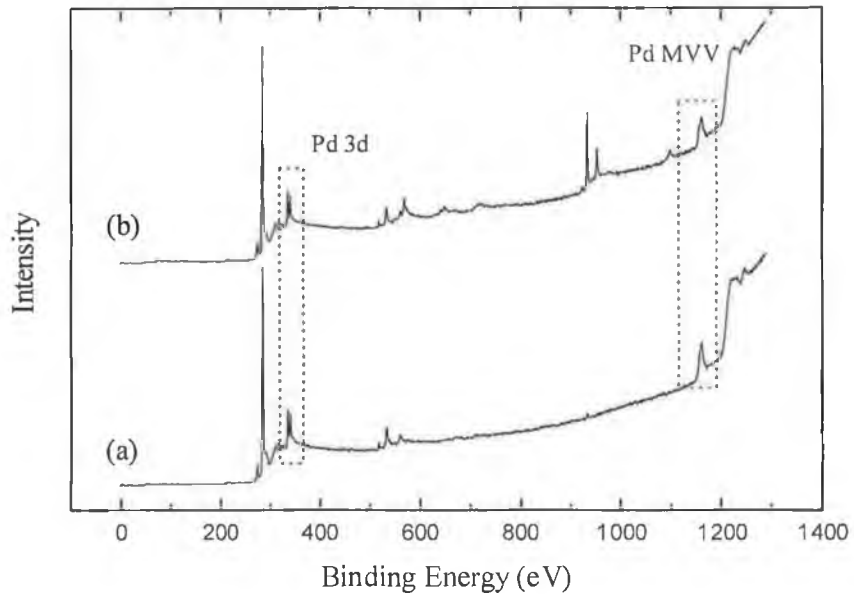

Figure 15: Survey scan of (a) 1.5 ML Pd deposited on HOPG and (b) 1.2 ML Cu co-deposited onto the pre-dosed 1.5 ML Pd film.

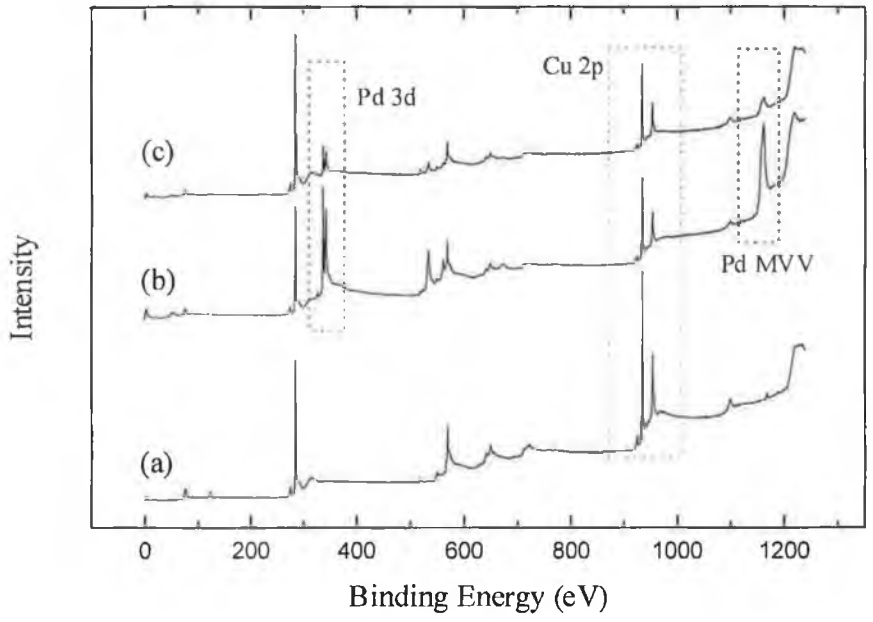

Figure 16: Comparison of the survey scan spectra of (a) 5 ML Cu on HOPG, (b) 8 ML Pd deposited onto 5 ML Cu and (c) annealing of the resulting film to 900 K. The pronounced intensity change of the Pd MVV and Pd 3d transitions are noted upon annealing.

Heating the resulting film to 900 K causes an increase in the C 1s but more importantly significant damping of the Pd core and Auger levels and supports the loss of Pd from the surface. Upon deposition of Pd the Cu $2p_{3/2}$ core-level exhibits broadening (~0.2 eV) as expected due to the increase in varying Cu environments as discussed earlier. A concurrent decrease in BE by ~0.3 eV is also observed compared to the BE of the as deposited Cu film. Upon annealing the PdCu film the Cu $2p_{3/2}$ FWHM is seen to narrow by ~0.2 eV although strangely no change in the BE is observed. The narrowing of the Pd 3d lines by almost 0.2 eV upon annealing, to a FWHM value of 1.6 eV (~0.15 eV lower than that of bulk Pd) is clear evidence of Pd dissolving into Cu forming an alloy. Similar extremely low FWHM's are only evident for submonolayer coverages of Pd on high coverage pre-dosed Cu samples with presumably Pd also in a homogeneous environment. An increase of ~0.3 eV in the Pd $3d_{5/2}$ BE is also seen upon annealing (900 K) when compared to the as-deposited PdCu film. Alloy formation between Cu and Pd has shown unequal core level shifts of opposite sign for the BE of the Pd 3d (seen to increase by 0.5 eV) and Cu 2p core levels (seen to decrease by only 0.1 eV) [81].

4.3.2. STM analysis

Verification of the three-dimensional islanding (Volmer-Weber growth) of the metal and the quantification of cluster size, structure and morphology are all possible utilising STM.

As mentioned earlier, with regards bimetallic films two extreme possibilities may be envisaged. Firstly, that a bimetallic film formed by the deposition of one metal on a pre-dosed film of the other, supported on HOPG, is composed of essentially monometallic Cu and Pd clusters (phase segregation). In such case a cluster size distribution between 3 and 10 nm would be expected spanning the total range recorded for the Cu and Pd cluster size as reported by Whelan and Barnes [23]. For complete phase separation we may expect a double peak structure reflecting the most probable diameters of monometallic Pd and Cu cluster diameters of 40 and 80 Å, respectively. However, this notion of complete segregation seems highly unlikely if the XPS observations of section 4.3.1. are considered. Interaction between Cu and Pd to form alloy clusters or alternatively "egg-shelled" clusters where one metal coats

the other should lead to a cluster size distribution which differs significantly from a simple superposition of the individual Cu and Pd sizes, with somewhat larger clusters observed.

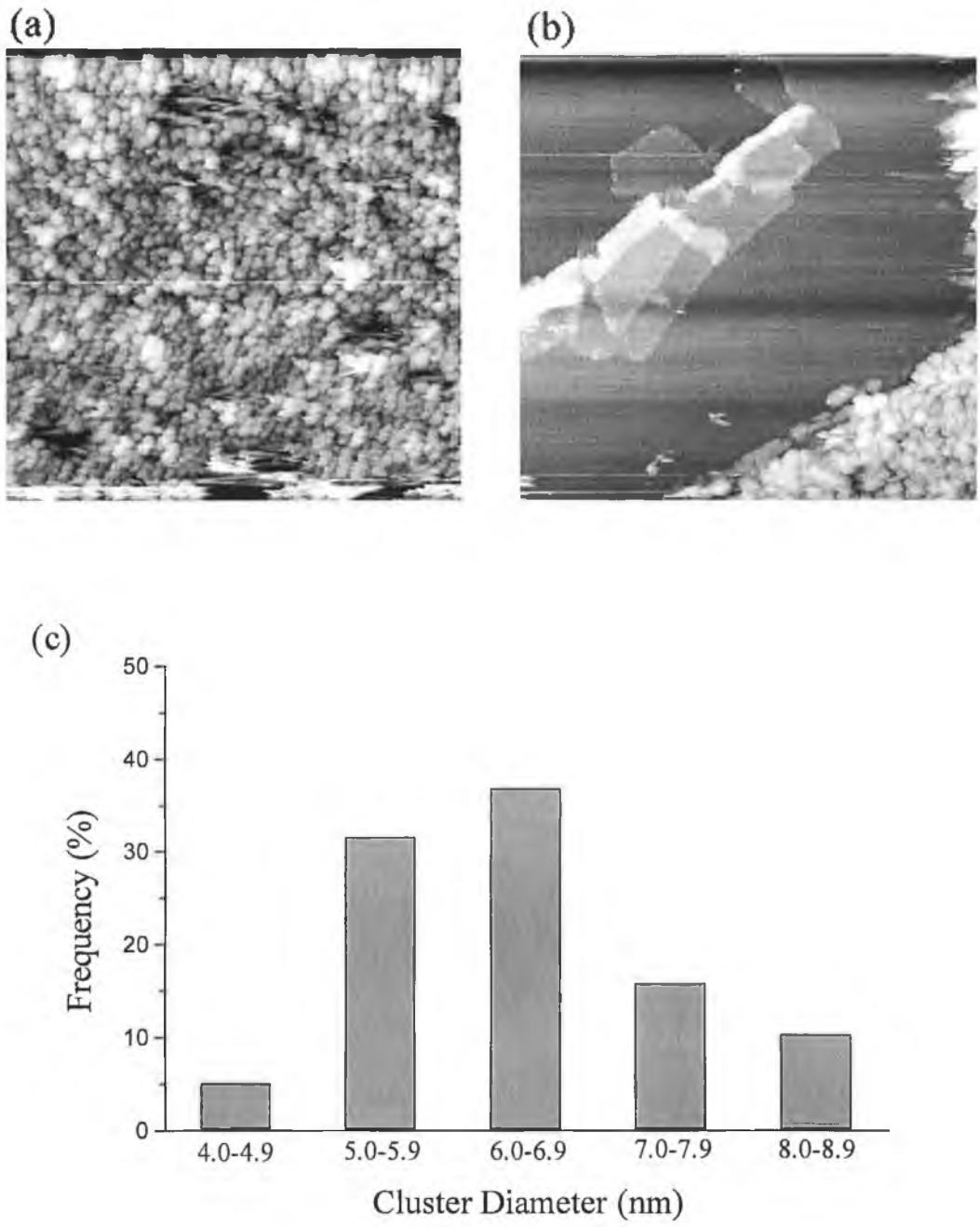

Figure 17: STM topographic images of 1.5 ML Cu deposited onto a 1.5 ML Pd film. V = 250 mV, I = 1.5 nA. (a) and (b) (200 × 200 nm) images of hemispherical clusters; (c) the measured cluster size distribution for the bimetallic film.

Figure 17 represents images typically obtained for the sequential evaporation of 1.5 ML of Cu onto 1.5 ML of Pd on HOPG. What is clearly evident in (a) is the narrow size distribution of the particles shown in histogram form in figure 17(c). At this loading of metal, areas of free graphite are quite frequent. The morphology is essentially the adorning of the surface with large flat unconnected islands of metal 100 to 200 nm in diameter comprising of individual small hemispherical clusters. The majority of clusters are found to be between 5 and 7 nm in diameter which is somewhat intermediate to that found for the most probable diameter of monometallic Cu (7.5 nm) and Pd (4.2 nm) clusters [23]. Interestingly, the size distribution suggests that phase separation is unlikely as hardly any clusters sizes indicative of monometallic Pd are witnessed. A possible explanation for this is that the deposition of Cu onto Pd may result in the thermodynamically favourable coating of Pd clusters with Cu effectively reducing the surface energy of the system and resulting in this observed intermediate cluster size. The nucleation of clusters into the large rafts illustrated in figure 17(a) is clear evidence of individual cluster diffusion and mobility. Because of the inherent relatively weak interaction between the metal particles and the graphite support, one might expect that the STM tip may easily manipulate the metal particles. Also the use of a metallic STM tip may cause it to pick-up metal clusters upon close approach.

A set of images typical for the opposite combination i.e. 1.5 ML Pd deposited onto 1.5 ML Cu is shown in figure 18. Figures 18(a) and (b) are quite revealing in that they exhibit clusters with a seemingly large size distribution. Centrally located clusters are generally smaller and there is a broad size distribution. Figure 18(c) illustrates a collection of large, flat and unconnected rafts of clusters measuring 200 to 250 nm in diameter and 15 to 20 nm in height. The tendency for cluster plateau's to be connected is also evident although at this coverage (~3 ML) isolated rafts of clusters are most prevalent. Figure 18(d) is a magnified image of these raft-like structures. The interesting variation in cluster sizes is seen clearly in figure 18(b). A careful examination of this image reveals the smaller clusters to be somewhat evenly distributed between the larger ones.

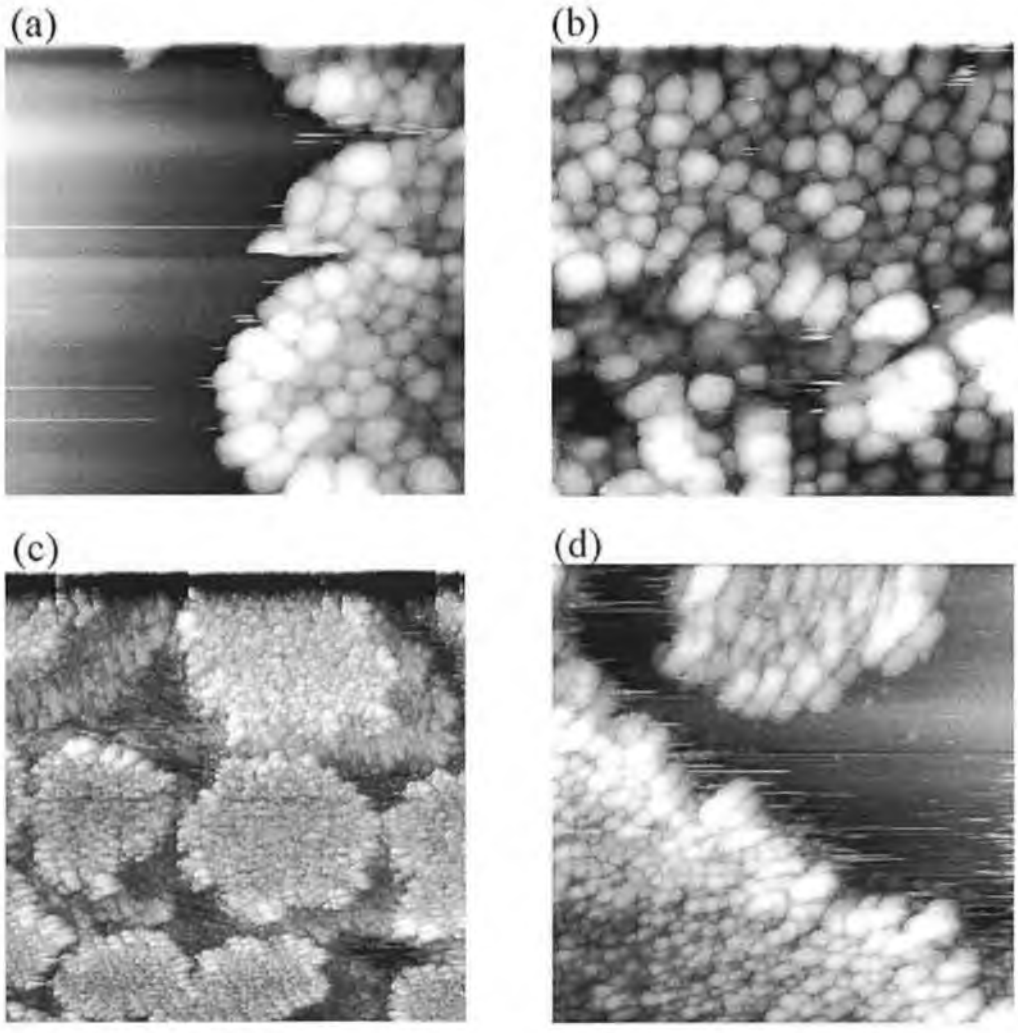

Figure 18: Topographic images of 1.5 ML Pd deposited onto a 1.5 ML Cu film on HOPG. V = 200 mV, I = 1.0 nA. Large variations in cluster size are quite evident in (a) and (b) (100 × 100 nm) while a large area scan in (c) (500 × 500 nm) reveals large, flat and connected plateau's of clusters; (d) (200 × 200 nm) is a magnified image of one of these cluster rafts.

Figure 19 reveals images of the 1.5 ML Pd on 1.5 ML Cu film obtained 22 hrs after deposition. The images are typical of the surface and depict that the rafts have aggregated to a greater extent. Figure 19(a) illustrates a rather large raft of clusters draped over a cleavage plane on the graphite surface. At this time after deposition the surface is more ordered mostly consisting of large rafts of clusters draped over step areas. The central region of (a) is imaged in figure 18(b) showing the nucleation of a small group of clusters at the cleavage plane. The size distribution of these

clusters is quite varied, also the alignment of the clusters along the step edge should be noted.

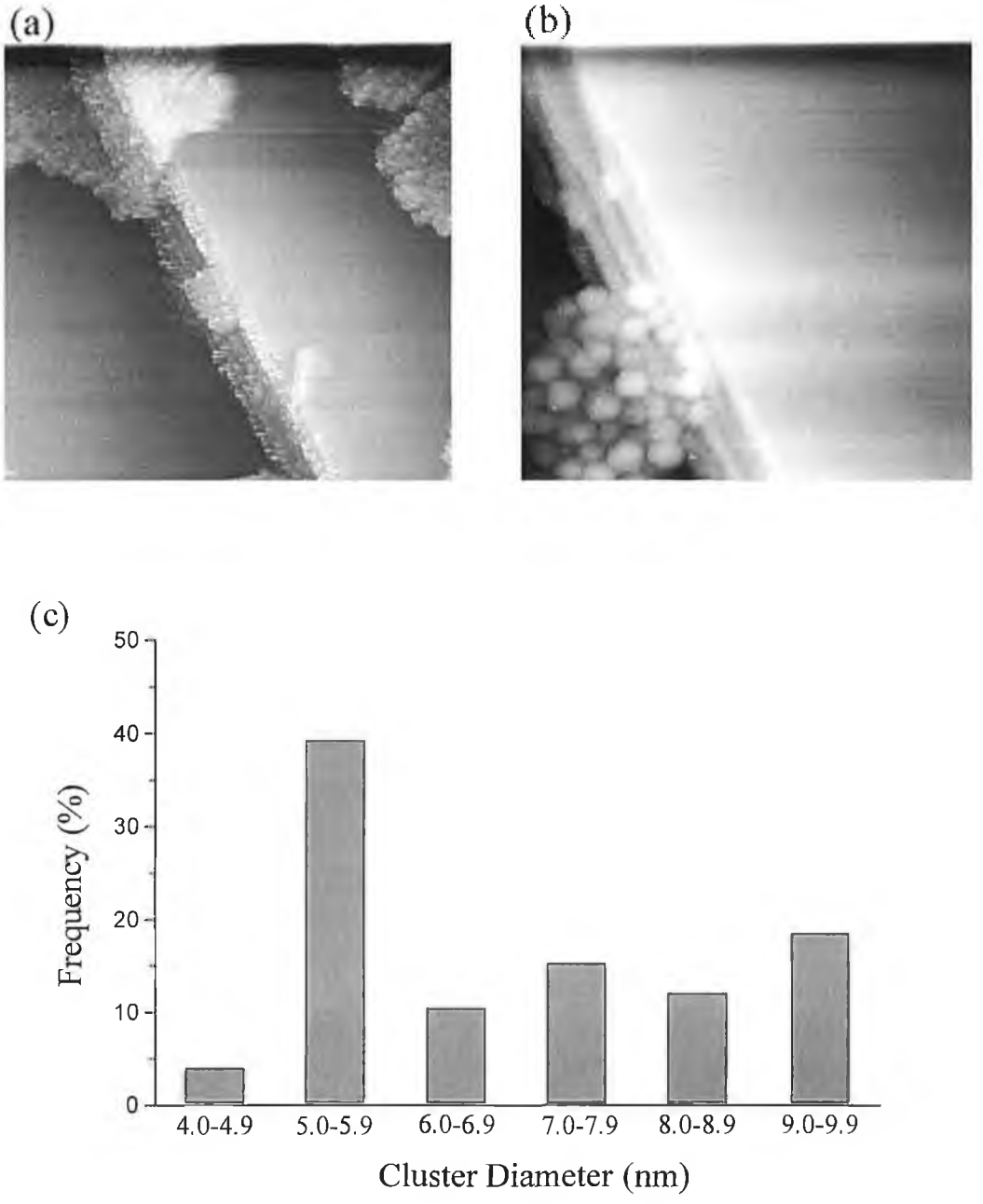

Figure 19: STM topographic images of 1.5 ML Pd deposited onto a 1.5 ML Cu film on HOPG. V = 200 mV, I = 1.0 nA. Showing (a) (500 × 500 nm) a large area scan and (b) (100 × 100 nm) a magnified image of the central region of (a); (c) is a measured cluster size distribution for the film (averaged statistics shown in (c) were taken from a number of images representative of the film, such as those shown in figure 18).

The measured size distribution of clusters for this film is illustrated in figure 19(c). Examining this distribution more clearly it seems that clusters smaller than 4 nm are not observed and that 50% of all clusters recorded range between 6 and 10 nm. Again this is essentially intermediate between Cu and Pd monometallic cluster distribution sizes. The association of pure large Cu clusters with Pd seems to deplete the extent of large Cu clusters (7.5 nm) with little evidence of monometallic Pd cluster sizes. Moreover, the existence of quite large clusters (~10 nm) may involve the direct "egg-shelling" or alloying of incoming Pd with already formed Cu clusters. Overall, this suggests a quite heterogeneous surface arrangement, which may involve random Cu-Pd alloy formation owing to the non-equilibrium nature of the film.

Finally, a repeat experiment of this film i.e. 1.5 ML Pd deposited onto a pre-dosed 1.5 ML Cu layer is illustrated in figure 20(a). This 100 × 100 nm image contrasts with the previous experiment, revealing that cluster sizes suggested representative of pure Pd [23] are in fact imaged. This image was recorded 5 min after the film was made and reveals quite stunningly the hemispherical nature of the clusters. The cluster distribution for this film (figure 20(b)) indicates that a large number of clusters of size expected for Pd occurs. The low density of Cu cluster sizes is unexplained at this time and requires further investigation.

It should be noted that the surface mobility and structural modification as reported for single-phases systems [23] was observed just as readily during scanning of the bimetallic surfaces. It should also be noted that for STM imaging in air the coalescence of smaller particles into larger particles, in an attempt to minimise the surface free energy by decreasing the surface to bulk ratio (Ostwald-Ripening) does not occur, possibly due to an oxide shell surrounding the inner metal-core coupled with insufficient cluster mobility, preventing gross structural rearrangement.

Elevated temperature work involving both deposition at high temperature and annealing to high temperature after room temperature deposition would elucidate information regarding whether the system is trapped in a local free energy minimum (metastable state) at 300 K.

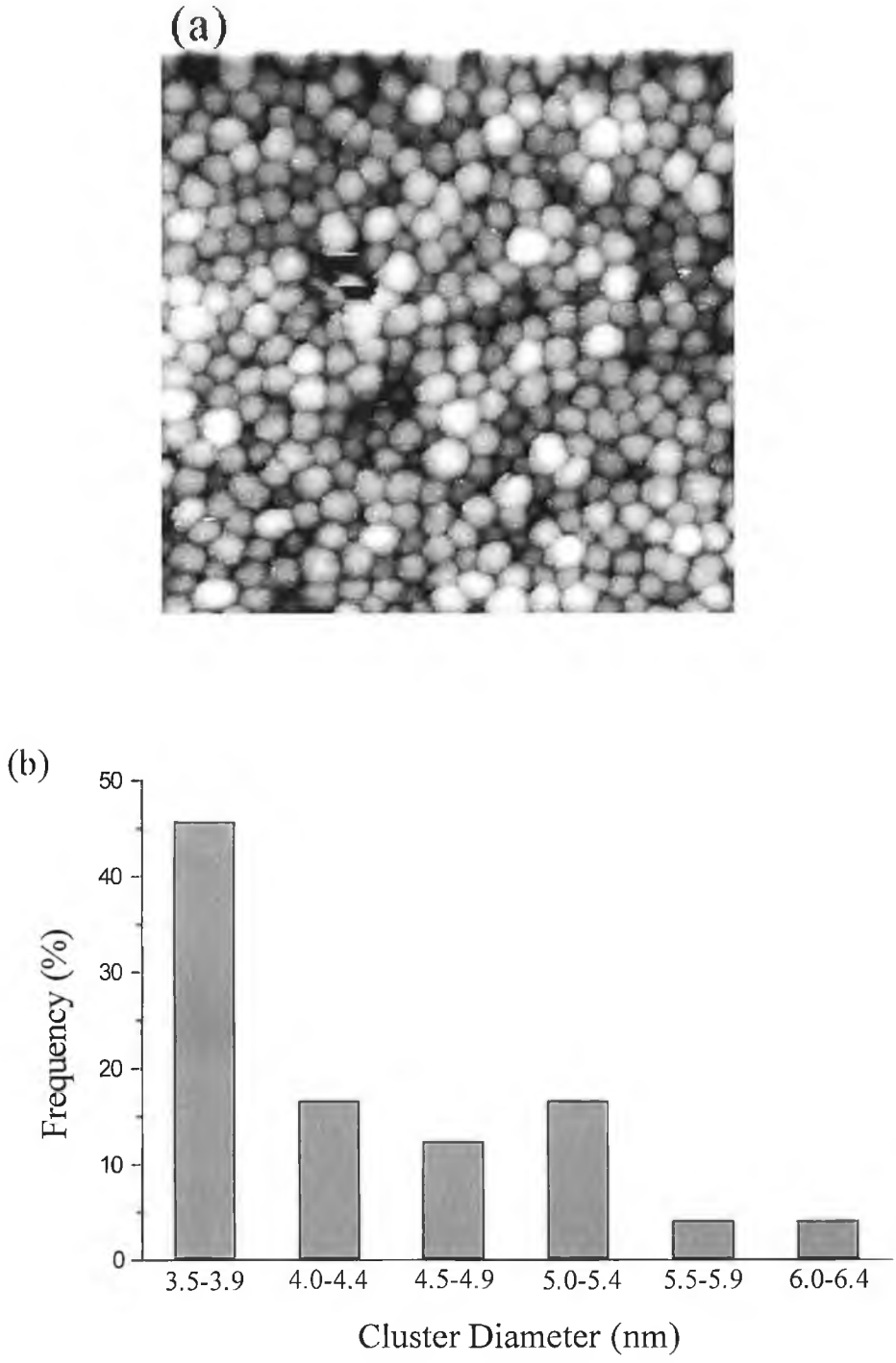

Figure 20: (a) STM topographic image (100 × 100 nm) of 1.5 ML Pd deposited onto a 1.5 ML Cu film on HOPG. This represents a repeat experiment of that shown in figures 18 and 19. V = 150 mV, I = 1.5 nA. The measured cluster size distribution for the film averaged over several scan areas is shown in (b).

5. Discussion

In the determination of the properties of supported bimetallics it has been suggested that the core-level binding energy shifts determined are completely different from those found in bimetallic overlayers formed by the deposition of one metal on the surface of a second [94]. In bimetallic clusters, the binding energy of either metallic component generally increases with decrease in coverage or cluster size. The lack of literature available on bimetallic supported clusters is an indication of the difficulty of understanding such phenomena. The difficulty arises from the necessary consideration of a number of different factors. This most obvious include the non-equilibrium nature of a room temperature deposited bimetallic film, the possible attempt of system surface free energy minimisation [95] by the enrichment of the component with the lowest surface energy to the surface, and the role played by the initial and final state effects in the observed binding energy shifts. Changes in the electron configuration of the component atoms during alloying, charge transfer between them or changes in the atomic volumes of clusters are all possibilities. Moreover, the shifts of binding energies in the core levels of alloy components credibly involve the superposition of alloy shifts and cluster size shifts.

In the use of pristine pyrolytic graphite it is believed that the adoption of bulk like properties by supported metal clusters occurs in the submonolayer coverage range, as evidenced by Arthur and Cho [27] for both Cu and Au on single crystal graphite. It has been proposed that the aggregation of metal adatoms on defect sites of crystalline graphite occurs even at very low temperature (100 K) [35]. The lower density of clusters is also believed to enhance the rate at which the metal clusters grow [96]. This results in the possible minimisation of initial state effects in any studies carried out on crystalline graphite although the non-screening nature of graphite owing to its poor conducting qualities is not so easily compensated for [30]. Contrarily, the FWHM increase observed at submonolayer coverages for both monometallic Cu and Pd is suggestive of a reduced cluster size, although the independent verification of this utilising STM has yet to be achieved.

For the monometallic systems of Pd and Cu, the increase in binding energy observed (~0.3 eV for both Cu 2p and Pd 3d core levels) at low coverage may be due to final state effects [29], with a possible contribution from the electronic structure change

for the metal to non-metal transition seen as cluster sizes decrease [31,32,97]. A similar shift (0.4 eV decrease) was observed in the Cu 2p core levels, by Di Nardo et al [28], for decreasing Cu coverages on graphite. It is claimed that the different shift in the binding energies of the core levels, 3d states and the Fermi edge as recorded by Di Nardo et al rules out the exclusive influence of final state effects. Rather a model involving the interaction of the Cu d-states and the π^* states of graphite was described to explain the observed shift variations. Furthermore, the assignment of the growth mechanism of both Cu and Pd on HOPG (at 300 K) as clustering 3-dimensional growth has been unambiguously verified by XPD.

In bulk metals the pseudo-continuous valence band allows the screening charge to be transferred to the atom being ionised. Less screening due to small particle size means a lower relaxation energy and thus a higher BE. Theoretical calculations for the ionisation potential of small Cu particles reveal a value of 5–6 eV, which is smaller than that of a free atom, 7.24 eV, but higher than the work function of Cu metal (4.5–5 eV) [98]. Interestingly, a shift to lower BE would be expected for the smaller clusters if we were to invoke surface core level shift (SCLS) theory, as the surface to bulk ratio is $\leq$0.40 for a Pd cluster size of ~40 Å and will increase with decreasing cluster size. For example, the Pd $3d_{5/2}$ BE of the surface atoms of Pd(100) is found to be 0.43 eV smaller than that of bulk Pd [99]. However, this is certainly not the case here with a shift to higher BE observed for both low coverages of Cu and Pd when compared to the bulk. It is a well established phenomenon that small metal particles bind their core electrons more tightly, and this has been accepted by many as evidence of the electron deficiency of small metal particles [1]. FWHM values of core levels are generally ~0.2 eV broader at low coverages, proposed to be due not only to the size distribution of small clusters of the film at decreasing coverages but also to the increased proportion of surface like-atoms in small metal clusters

In the case of the bimetallic layers core-level spectroscopy has been studied as a function of incremental deposition of one metal on a pre-dosed layer of the other. In particular for the examination of Pd incremental deposition on Cu, BE's of the Pd $3d_{5/2}$ core-level seem to allow little insight into the growth mechanism while the FWHM of the Pd core level seems to suggest a number of different Pd states at low coverages for all Cu pre-dosed levels, for the most part greater than that seen for

monometallic Pd. The 0.2 eV increase in FWHM seen for the lowest coverages of Pd on 1 ML Cu is suggestive of a Cu-Pd interaction. The rather sharp fall of the FWHM to values of bulk Pd after ~2 ML deposition is indicative of the absence of bulk intermixing. The constancy of the Pd FWHM values when deposited on 7 ML Cu suggests the preferable association of Pd with Cu as opposed to monometallic cluster formation, although almost 60% of the surface is already covered by Cu clusters before deposition of Pd (assuming an average Cu cluster size of ~80 Å).

Regarding Cu characteristics for Pd on pre-dosed Cu levels, any significant decrease in BE seen for the Cu $2p_{3/2}$ in dilute arrangements with transition metals [82,83] is only evidenced during our experiments when the relative concentration of Pd surpasses that of Cu and even then the shift is small (0.1-0.3 eV). In FWHM terms the Cu $2p_{3/2}$ core-level seems to converge at ~1.9 eV after Pd saturation dosing, suggestive of an equilibrium (a local free energy minimum) Cu-Pd interaction.

In the reverse scenario i.e. the deposition of Cu on Pd, increasing the Cu coverage seems to have no effect on the Pd core-level BE's. On the other hand the Cu $2p_{3/2}$ BE reveals a large decrease for submonolayer Cu coverages on all Pd films. This negative BE shift of ~0.3 eV for submonolayer Cu is supportive of a configuration whereby Cu coats the Pd clusters. The shift is in agreement with the SCLS (towards lower BE) expected for Cu [85,86]. Increasing Cu coverage results in an increase in co-ordination of Cu and an increase in the $2p_{3/2}$ BE to that of bulk Cu. Once the coverages of Cu and Pd on the surface reach similar levels the BE of the Cu $2p_{3/2}$ core level matches that of bulk Cu. Whereas the Cu $2p_{3/2}$ BE and FWHM values testify to Cu interaction with Pd it is quite clear according to the Pd signals that this interaction is limited to the Cu submonolayer range proposed as a consequence of Cu "egg-shelling" the Pd clusters.

The above phenomenon i.e. the non-variance of the BE of the Pd 3d peaks in Pd-Cu amorphous carbon supported samples has been previously reported [93]. A decrease in the BE of the Cu 2p core levels with decreasing Cu coverage was also observed, as during these studies, yet attributed to bimetallic Pd-Cu particle formation as opposed to the Cu capping theory proposed here. Gustafson and Wehner [93] hypothesise that the interaction of Cu is exclusively restricted to larger Pd particles (>50 Å) of low density on the surface. The dominant Pd XPS signal from the greater number of smaller particles is suggested to mask the XPS signal from Pd in the larger Pd-Cu

bimetallic particles. The reasoning behind the restricted Cu interaction is not discussed. Alumina (Al_2O_3) supported Cu-Pd bimetallic catalysts revealed a similar trend with no change in the Pd 3d core-level BE when Pd was added first. Whether we invoke our own arguments or those of Gustafson it is nonetheless obvious that the Cu-Pd interaction is dependent on the sequence of metal addition. The addition of Pd before Cu providing us with the most apparent proof of limited Cu-Pd interaction. The decrease in the binding energy of the Cu $2p_{3/2}$ peak seen as the Pd-to-Cu ratio increases correlates to that expected upon bimetallic particle formation. This is substantiated by the numerous studies of the core-level binding energies of Cu and Pd in substitutionally disordered Cu_xPd_{1-x} alloys [85,87,89]. However, the corresponding increase in the binding energy of the Pd 3d peaks expected upon alloy formation is not observed, hence ruling out bulk Cu-Pd intermixing (limited Cu-Pd interaction). Interestingly, X-ray diffraction (XRD) studies by Gustafson [93] have argued that smaller Pd clusters i.e. smaller than the cluster sizes observed for monometallic Pd studies, may result when incorporated with Cu. The results are however inconclusive as the presence of varying Cu-Pd particle compositions may also account for the observed line broadening in the XRD pattern as suggested by Mallat et al [100].

A study of co-deposited Cu and Pd on HOPG, although at elevated temperature (823 K), by Kojima and Kurahashi produced Pd enriched bimetallic particles even with equal amounts of each metal deposited [76]. The co-deposition of Pd and Cu on NaCl(100) has also revealed Pd to be the dominant metal in bimetallic particles examined after continued growth at 673 K even when the flux ratios of Pd and Cu were similar [79,80]. This may suggest the tendency for Pd to dominate the bimetallic particles no matter which sequence of metal growth is followed i.e. Cu on Pd or Pd on Cu. The tendency for Cu to cap Pd (favourable thermodynamically) along with this observed non-variance in Pd core-level BE's supports this theory with Pd bulk-like properties dominating. The XPS characteristics of Cu at low coverages on Pd do not support phase separation and more so hint at the adlayer association of Cu with Pd.

The non-variance in Pd XPS signals seen for this Cu on Pd experiment is most likely attributable to the bulk-like nature of the pre-deposited Pd particles (at ~2 ML Pd

coverage monometallic clusters exhibit bulk-like properties) coupled with the restricted surface nature of the Cu-Pd interaction as opposed to bulk intermixing.

In STM terms the deposition of Cu onto Pd supports the proposed theory of "egg-shelling" in that the cluster size distribution resulting is intermediate between that found for the single-phase Cu and Pd systems [23]. The deposition of Pd onto Cu is not as clear-cut in that the non-reproducible nature of the cluster size distribution for a repeat experiment of 1.5 ML Pd on 1.5 ML Cu supports our theory of the system being trapped in a local free energy minimum (metastable state). The increase in the number of smaller clusters (35–39 Å) seen for this surface when compared to pure Pd is of interest and supports Gustafson's preliminary suggestion of an increased number of smaller Pd clusters when Cu is present on the surface. Nevertheless, further STM studies are necessary to verify this phenomenon.

The time dependent nature of these systems for the low doses studied in which areas of free graphite dominate is suggestive that STM examination is a mere snapshot in time. The inherent mobility of the clusters owing to the weak interaction with the substrate will only heighten their dynamic nature [35,36] and consequently the difficulty in studying them. Only very high coverages seem to exhibit stability where a high degree of co-operative motion is required to facilitate mobility [23].

6. Conclusions

In this study the complementary techniques of XPS and STM have been employed to investigate the nucleation and growth of both mono-and bimetallic Pd and Cu clusters grown on HOPG. We have described in detail a simple and reliable method for the absolute calibration of surface coverage for metal growth studies based on ex-situ analysis of the absolute amount of the metal evaporated onto a glass slide using graphite furnace atomic adsorption spectroscopy (GF-AAS). This method is shown to have an absolute sensitivity of better than 0.1 ML.

The growth of monometallic films of Cu and Pd on pristine HOPG grown at room temperature on pristine graphite is essentially of the Volmer-Weber growth mode where the forces between the metal atoms are the dominant force expected as the graphite substrate is weakly interacting. STM, XPS and XPD results have verified this proposed mechanism. Growth occurs as hemispherical shaped clusters with STM statistics revealing average cluster diameters of ~8 and ~4 nm in the case of Cu and Pd, respectively [23]. In both cases a small decrease in the core level binding energy and FWHM is observed as a function of metal coverage. Shifts to higher binding energy for low coverages (especially in the submonolayer range) are proposed attributable not only to the imperfect screening of small particles by the graphite substrate (final state effects) but also to the suggested interaction of the metal filled d-states with the π^* empty graphite states [25,28]. The different shifts recorded for the d-band, core levels and Fermi edge upon cluster size reduction by other workers [25,28] may require further clarification here.

Bimetallic films of Cu and Pd formed by sequential deposition reveal properties dependent on the sequence of metal deposition. In the case of Cu deposition on pre-dosed Pd films it seems that the growth mechanism initially involves the preferential coating of Pd by a Cu thin film (themodynamically favourable in surface energy terms) followed by the formation of phase separated Cu clusters. The constancy of the Pd core-level binding energy for all Cu coverages (ruling out substantial alloy formation) coupled with the substantial decrease in Cu binding energy (~0.5 eV) at low submonolayer Cu coverages on Pd supports this hypothesis. STM examination again reveals a Volmer-Weber growth mechanism with the majority of hemispherical

clusters between 5 and 7 nm in diameter somewhat intermediate between monometallic Cu and Pd films.

For Pd deposition on Cu, characterisation is more difficult. Cu core level binding energies decrease for increasing Pd coverages illustrating clear Pd-Cu interaction. Pd core level binding energy shifts for increasing coverage on Cu show little insight following trends expected for monometallic Pd deposition. The extent of Pd-Cu interaction is unclear although the constancy of FWHM values for all Pd coverages on high loading Cu samples (~7 ML) may suggest the preference for a somewhat homogeneous (as opposed to disordered interaction) Pd-Cu interaction. Again STM examination reveals cluster sizes somewhat intermediate between those of Pd and Cu monometallic films. Moreover, the dynamic nature of the Pd-Cu system on the lubricating HOPG surface is clearly evidenced by STM.

References

[1] M. Che, C. O. Bennett, Adv. Catal., 36 (1989) 55.

[2] R. Persaud and T. E. Madey, The Chemical Physics of Solid Surfaces and Heterogeneous Catalysis, Vol. 8, Eds. D. A. King and D. P. Woodruff, Elsevier, Amsterdam, (1997).

[3] S. Ogawa, S. Ichikawa, Phys. Rev. B, 51 (1995) 17231.

[4] G. A. Somarjai, Introduction to Surface Chemistry and Catalysis, Wiley, New York, (1994).

[5] J. J. Metois, J. C. Heyraud and Y. Takeda, Thin Solid Films, 51 (1978) 105.

[6] A. K. Santra, S. Ghosh and C. N. R. Rao, Langmuir, 10 (1994) 3937.

[7] Y. Takasu, T. Sakuma, Y. Matsud and I. Toyoshima, Surf. Sci., 152/153 (1985) 479.

[8] K. I. Choi and M. A. Vannice, J. Catal., 131 (1991) 36.

[9] A. D. van Langeveld and V. Ponec, Surf. Sci., 126 (1983) 702.

[10] J. A. Anderson, M. Fernández-Garcia and G. L. Haller, J. Catal., 164 (1996) 477.

[11] J. T. Kummer, J. Catal., 38 (1975) 166.

[12] A. Piednoir, E. Perrot, S. Granjeaud, A. Humbert, C. Chapon and C. R. Henry, Surf. Sci., 391 (1997) 19.

[13] S. Granjeaud, Ph.D. Thesis, Marseille (1995).

[14] A. Humbert, M. Dayez, S. Granjeaud, P. Ricci, C. Chapon and C. R. Henry, J. Vac. Sci. Technol., B 9 (1991) 804.

[15] S. Granjeaud, K. Yckache, M. Dayez, A. Humbert, C. Chapon and C. R. Henry, Micros. Microanal. Microstruct., 4 (1993) 409.

[16] A. Humbert, M. Dayez, S. Sangay, C. Chapon and C. R. Henry, J. Vac. Sci. Technol. A, 8 (1990) 311.

[17] I. Kojima, A. K. Srivastava and M. Kurahashi, Jpn. J. Appl. Phys., 30 (1991) 1852.

[18] Y. Murakami, K. Naoi, K. Yahikozawa and Y. Takasu, J. Electrochem. Soc., 141 (1994) 2511.

[19] F. J. Cadete Santos Aries, P. Sautet., J. -L. Rousset, G. Fuchs and D. Melinon, J. Vac. Sci. Technol. B, 12 (1994) 1776.

[20] H. N. Aiyer, V. Vijayakrishnan, G. N. Subbanna and C. N. R. Rao, Surf. Sci., 313 (1994) 392.

[21] A. Bifone, L. Casalis and R. Riva, Phys. Rev. B, 51 (1995) 11043.

[22] E. Ganz, K. Sattler and J. Clarke, Surf. Sci., 219 (1989) 3.

[23] C. M. Whelan and C. J. Barnes, Appl. Surf. Sci., 119 (1997) 288.

[24] H. Y. Nie, T. Shimizu and H. Tokumoto, J. Vac. Sci. Technol. B, 12 (1994) 1843.

[25] M. Cini, M. De Crescenzi, F. Patella, N. Motta, M. Sastry, F. Rochet, R. Pasquali, A. Balzarotti and C. Verdozzi, Phys. Rev. B, 41 (1990) 5685.

[26] W. F. Egelhoff, jr. and G. G. Tibbetts, Solid State Commun., 29 (1979) 53.

[27] J. R. Arthur and A. Y. Cho, Surf. Sci., 36 (1973) 641.

[28] S. Di Nardo, L. Lozzi, M. Passacantando, P. Picozzi, S. Santucci and M. De Cresenzi, Surf. Sci., 307-309 (1994) 922.

[29] S. Kohiki and S. Ikeda, Phys. Rev. B, 34 (1986) 3786.

[30] G. K. Werthiem, S. B. Di Censo and D. N. E. Buchanan, Phys. Rev. B, 33 (1986) 5384.

[31] M. G. Mason, Phys. Rev. B, 27 (1983) 748 (and references therein).

[32] G. K. Werthiem, S. B. Di Censo, D. N. E. Buchanan and P. A. Bennett, Solid State Commun., 53 (1985) 377.

[33] P. A. Douben, D. LaGraffe, D. Li, G. Vidali, L. Zhang, L. Dotte and M. Onellion, Phys. Rev. B, 43 (1991) 10677.

[34] V. Vijaykrishnan, A. Chainani, D. D. Sarma, and C. N. R. Rao, J. Phys. Chem., 96 (1992) 8679.

[35] W. F. Egelhoff, jr. and G. G. Tibbetts, Phy. Rev. B, 19 (1979) 5028.

[36] S. B. Dicenzo and G. K. Wertheim, Comments Solid State Phys., 11 (1985) 203.

[37] F. Patthey and W. -D. Schneider, Surf. Sci., 34 (1995) L715.

[38] H. -V. Roy, P. Fayet, F. Patthey, W. -D. Schneider and C. Massobrio, Phys. Rev. B, 49 (194) 561.

[39] R. Unwin and A. M. Bradshaw, Chem. Phys. Lett., 58 (1978) 58.

[40] B. Delley, D. E. Ellis, A. J. Freeman, E. J. Baerends and D. Post, Phys. Rev. B, 27 (1983) 2132.

[41] V. de Gouveia, B. Bellamy, Y. Hadj Romdhane, A. Masson and M. Che, Z. Phys. D, 12 (1989) 587.

[42] Ch. Kuhurt and M. Harsdorff, Surf. Sci., 245 (1991) 173.

[43] T. L. Barr and M. P. Yin, J. Vac. Sci. Technol. A, 13 (1995) 1239.

[44] G. Johansson, J. Hedman, A. Berndtsson, M. Klasson and R. Nilsson, J. Electron Spectros., Related Phenom., 2 (1993) 1327.

[45] J. L. Vossen, Physics of Thin Films, Eds. G. Haass, H. H. Francombe and R. W. Hoffman, Vol. 9, Academic Press, New York, (1977).

[46] C. G. Granqvist, J. Appl. Phys., 50 (1979) 2916.

[47] L. H. Dubois, P. K. Hansma and G. A. Somorjai, Appl. Surf. Sci., 6 (1980) 173.

[48] P. K. Hansma and H. P. Broida, Appl. Phys. Lett., 32 (1978) 595.

[49] M. Valden, J. Aaltonen, M. Pessa, M. Gleeson and C. Barnes, Chem. Phys. Lett., 228 (1994) 519.

[50] G. E. Rhead, M. -G. Barthés and C. Argile, Thin Solid Films, 82 (1981) 201.

[51] P. W. Murray, I. Stensgaard, E. Lægsgaard and F. Besenbacher, Surf. Sci., 365 (1996) 591.

[52] P. W. Murray, S. Thorshaug, I. Stensgaard, F. Besenbacher, E. Lægsgaard, A. V. Ruban, K. W. Jacobsen, G. Kopidakis and H. L. Skriver, Phys. Rev. B, 55 (1997) 1380.

[53] H. H. Willard, L. L. Meritt, jr., J. A. Dean and F. A. Settle, jr., Instrumental Methods of Analysis, 7th Edition, Wadsworth Publishing Co., CA, (1988).

[54] L. I. Maissel and R. Chang, Handbook of Thin Film Technology, McGraw-Hill, New York, (1970).

[55] M. Prutton, Surface Physics, Oxford Physics Series, 2nd edition, Oxford University Press, New York, (1983).

[56] D. Briggs and M. P. Seah, Practical Surface Analysis, John Wiley & Sons, New York, (1990).

[57] J. H. Scofield, J. Electron. Spectosc. Relat. Phenom., 8 (1976) 129.

[58] E. Bauer and J. H. van der Merwe, Phys. Rev. B, 33 (1986) 3657.

[59] E. Bauer, Z. Kristallogr., 110 (1958) 372.

[60] R. C. Weast and D. R. Linde (Eds.), Handbook of Chemistry and Physics, 70th edition, CRC Press, Boca Raton, FL, (1989).

[61] G. K. Wertheim, Z. Phys. B, 66 (1984) 55.

[62] G. K. Wertheim, S. B. Di Censo and S. E. Youngquist, Phys. Rev. Lett., 51 (1983) 2310.

[63] M. De Crescenzi, M. Diociaiuti, L. Lozzi, P. Picozzi and S. Santucci, Solid State Commun., 74 (1990) 115.

[64] B. Frick and K. Jacobi, Surf. Sci., 178 (1986) 907.

[65] I. Abbati, L. Braicovich, C. M. Bertoni, C. Calandra and F. Manghi, Phys. Rev. Lett., 40 (1978) 469.

[66] Y. Hu, T. J. Wagener, Y. Gao, H. M. Meyer III and J. H. Weaver, Phys. Rev. B, 38 (1988) 3037.

[67] T. Ohmori, K. Hashimoto and A. Fujishina, Jpn. J. Appl. Phys., 30 (1991) 1826.

[68] W. F. Egelhoff, Phys. Rev. B, 30 (1984) 1052.

[69] W. F. Egelhoff, J. Vac. Sci. Technol. A, 2 (1984) 350.

[70] M. Bäumer, J. Libuda and H. -J. Freund, Surf. Sci., 327 (1995) 321.

[71] M. Chen and L. D. Schmidt, J. Catal., 56 (1979) 198.

[72] Y. Zhu and L. D. Schmidt, Surf. Sci., 129 (1983) 107.

[73] T. P. Chojnacki and L. D. Schmidt, J. Catal., 115 (1989) 473.

[74] P. L. Gai and B. C. Smith, Ultramicroscopy, 34 (1990) 17.

[75] J. L. Rousset, A. M. Cadrot, F. J. Cadete Santos Aires, A. Renouprez, P. Melinon, A. Perez, M. Pellarin, J. L. Vialle and M. Boyer, J. Chem. Phys., 102 (1995) 8574.

[76] I. Kojima and M. Kurahashi, J. Vac. Sci. Technol. B, 12 (1994) 1780.

[77] F. Gimenez, Ph.D. Thesis, Marseille, (1997).

[78] F. Gimenez, C. Chapon, S. Giorgio and C. R. Henry, Proc. ICEM 13, Paris, p. 354.

[79] A. Schmitz, V. Schünemann and R. Anton, Phys. Rev. B, 41 (1990) 11875.

[80] A. Schmitz, M. Spode, J. Heinrich and R. Anton, Thin Solid Films, 196 (1991) 253.

[81] N. Martensson, R. Nyholm, H. Calén, J. Hedman and B. Johansson, Phys. Rev. B, 24 (1981) 1725.

[82] M. L. Shek, P. M. Stefan, I. Lindau and W. E. Spicer, Phys. Rev. B, 27 (1983) 7277; 27 (1983) 7301.

[83] W. K. Kuhn, R. A. Campbell and D. W. Goodman, J. Phys. Chem., 97 (1993) 446.

[84] T. D. Pope, K. Griffiths, P. R. Norton, Surf. Sci., 306 (1994) 294.

[85] N. Martennson, H. B. Saalfield, H. Kuhlenbeck and M. Neumann, Phys. Rev. B, 39 (1989) 8181.

[86] W. F. Egelhoff jr., Surf. Sci. Rep., 6 (1987) 253.

[87] R. J. Cole, N. J. Brooks and P. Weightman, Phys. Rev. B, 56 (1997) 12178.

[88] R. W. Vook, J. V. Bucci and S. S. Chao, Thin Solid films, 163 (1988) 447.

[89] V. Sundaram, M. De Moraes, J. Rogers and G. Kleiman, J. Phys: F, 11 (1981) 1151.

[90] H. Li, S. C. Wu, D. Tian, J. Quinn, Y. S. Li, F. Jona and P. M. Marcus, Phys. Rev. B, 40 (1989) 5841.

[91] H. Li, D. Tian, F. Jona and P. W. Marcus, Solid State Commun., 77 (1991) 651.

[92] E. Hahn, E. Kampshoff, A. Fricke, J. -P. Bucher and K. Kern, Surf. Sci., 319 (1994) 277.

[93] B. L. Gustafson and P. S. Wehner, Appl. Surf. Sci., 52 (1991) 261.

[94] J. A. Rodriguez and D. W. Goodman, J. Phys. Chem., 95 (1991) 4196.

[95] M. P. Seah, J. Catal., 57 (1979) 450.

[96] S. B. Dicenzo and G. K. Wertheim, Comments Solid State Phys., 11 (1985) 203.

[97] C. N. R. Rao, V. Vijaykrishnan, H. N. Aiyer, G. U. Kulkarni and G. N. Subbanna, J. Phys. Chem., 97 (1993) 11157 (and references therein).

[98] R. P. Messener, S. K. Knedson, K. H. Johnson, J. B. Diamond and C. Y. Yang, Phys. Rev. B, 13 (1976) 1396.

[99] J. N. Andersen, N. Qvarford, R. Nyholm, S. L. Sorensen and C. Wigren, Phys. Rev. Lett., 67 (1991) 2822.

[100] T. Mallat, S. Szabo and J. Petro, Appl. Surf. Sci., 40 (1990) 309.

Chapter Five

Surface Alloy Formation:
the Cu(100)-c(2×2)-Pt System

1. Introduction

Miscible bimetallic combinations which form exothermic alloys for which the adsorbed metal has a higher surface energy than the substrate have a tendency to form ordered bimetallic underlayers to minimise the surface energy [1]. However, the energy gain by forming an ordered underlayer may, in certain cases, be couterweighed by additional strain if there is a considerable size mismatch between substrate and adsorbate. In general it is expected that the element of lowest surface energy and largest atomic size will surface segregate in bulk alloys. In several systems the surface energy and strain factors may work against each other leading for example to top layer surface alloy formation at low overlayer coverages due to the additional freedom for incorporation of the adsorbate at the vacuum interface despite the unfavourable surface energy of this arrangement. In such cases it is often difficult to predict whether it is the ordered bimetallic outer layer or underlayer which dominates the surface alloy metastable phase. Bimetallic surface alloys are of considerable use to probe surface reaction kinetics and dynamics as surface composition can often be more easily controlled than in the case of bulk alloys. It is thus vital for such studies to gain knowledge as to whether adsorbate atoms are located within the outermost layer or occupy sub-surface sites and to quantify the thermal stability of the overlayer in order to understand how the incorporated adsorbate alters the surface reactivity.

Copper forms exothermic alloys with the neighbouring transition metal group Ni, Pd and Pt. The bulk phase diagrams for these systems indicate that alloys form throughout the composition range [2]. In the case of Ni a substitutionally disordered fcc alloy is formed while in the cases of Pd and Pt ordered phases also form, particularly around the compositions $Cu_3Pt(Pd)$ and CuPt(Pd) [2].

Of this grouping of surface alloys the Cu(100)-c(2×2)-Pd structure has been and continues to be the most extensively studied. A well developed c(2×2) structure is formed at submonolayer Pd coverages upon deposition at 300 K which appears to be best developed at a Pd coverage between 0.5 and 0.8 ML [3,4]. While early structural work favoured a simple outermost layer surface alloy of Cu:Pd composition 50:50 [5], more recent work has indicated that the surface layer is heterogeneous with areas of top layer c(2×2) CuPd alloy co-existing with areas of

pure Cu [6]. A significant quantity of Pd has been shown to reside in the second layer due to capping c(2×2) CuPd top layer domains by ejected copper atoms. Much less is known regarding the surface chemistry of this system with reported work being limited to CO adsorption/desorption which has been extensively probed [7]. Significant changes have been reported in the CO chemisorption bond strength on Pd surface sites in the Cu(100)-c(2×2)-Pd surface alloy with desorption maxima being significantly shifted to lower temperature due to modification of the Pd electronic structure towards a d^{10} closed d-band configuration [8]. Significant ongoing interest in this surface alloy remains due to the large changes in the Pd surface electronic structure and reports of Pd-induced lattice distortions within the alloy selvedge [9,10].

The CuPd(Pt) systems are of particular interest catalytically in a range of important reactions including oxidation of CO to CO_2 in automobile catalytic converters [11] and in a range of hydrocarbon reactions. In particular, the CuPt system has a higher selectivity for hydrocarbon reforming reactions than pure Pt [12]. In addition the CuPd system has relevance to methanol synthesis for which copper is unique in its ability, although Pd is also known to exhibit activity [13,14].

In contrast to the CuPd system, little is known of its CuPt counterpart. As Pd and Pt have identical lattice constants and similar electronic properties we may expect similarities between the CuPd and CuPt systems. However, the fact that Pt has a significantly higher surface energy than Pd may also lead to differences in surface geometry and reactivity. Thus we have undertaken a study of the surface geometric structure and reactivity of the Cu(100)-Pt system and in particular the related Cu(100)-c(2×2)-Pt surface alloy system. In this case the surface free energy of the adsorbate (Pt) significantly exceeds that of the substrate (Cu) with a surface energy difference of 0.76 J m^{-2} [15]. We illustrate that for low Pt coverages, the chemical ordering has its origin in a mixed CuPt underlayer below a Cu outer monolayer with the bimetallic surface exhibiting a significant "electronic effect" as monitored by the significantly reduced stability of a formate reactive intermediate relative to clean Cu(100). In contrast higher Pt loadings, while still leading to a well-ordered c(2×2) alloy interface, have a top layer mixed CuPt layer. The reactivity of this surface is compared with both clean Cu(100) and the c(2×2) CuPt underlayer indicating that

significant alteration in the surface chemistry of Pt occurs when incorporated into a copper lattice.

2. Experimental

All measurements were performed in a custom built ion and titanium sublimation pumped ultra-high-vacuum chamber operating at base pressures in the low 10^{-10} Torr regime described in detail elsewhere [16]. The chamber possesses facilities for quantitative monitoring surface crystallography by low energy electron diffraction via 4-grid Vacuum Generators reverse view optics. Quantitative measurements of

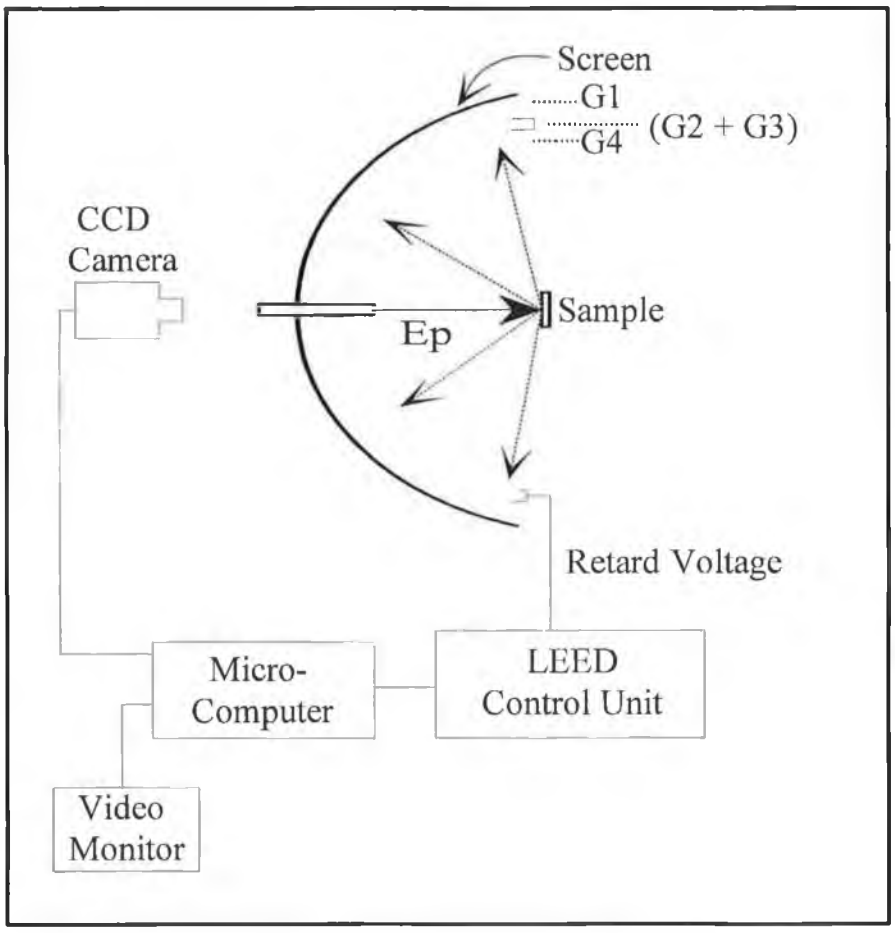

Figure 1: LEED system.

spot intensities and beam profiles can be made with a CCD video camera interfaced to a micro computer (figure 1) using data acquisition software supplied by Data-Quire corporation (Stony-Brook, New York). The LEED optics also served as a retarding field analyser for surface elemental analysis by Auger electron spectroscopy (AES). A VG Quasar quadrupole mass spectrometer was utilised for residual gas analysis and as a detector for temperature programmed desorption measurements (TPD).

The Cu sample of dimensions 14 × 10 × 1.5 mm was oriented to within 0.5° of the (100) plane (Metals Crystals and Oxides Ltd, Cambridge, UK) and was supplied with four 0.25 mm diameter holes spark eroded into the corners of the sample to aid sample mounting. A fifth 0.25 mm hole was drilled for location of a chromel-alumel thermocouple for temperature measurement. The sample was mounted on a high precision LEED goniometer via suspension between two stainless steel blocks by 0.25 mm diameter tantalum wire passed through the four 0.25 mm holes at the corners of the sample. Heating was achieved by passing a direct current through the tantalum mounting wires allowing temperatures of up to 1000 K to be attained. The sample was cleaned by repeated cycles of argon ion bombardment (3 kV) while annealing at 800 K and was deemed clean when no contaminants could be observed above the AES noise level. At this stage the sample exhibited a sharp p(1×1) LEED pattern with normal incidence $I(V)$ spectra in excellent agreement with literature reports [17].

Platinum was dosed from a home made evaporator consisting of a 0.30 mm tungsten filament around which was tightly wound 0.125 mm Pt wire (Goodfellows Metals: 99.995 % purity). The filament was mounted on a titanium sublimation pump feedthrough and shrouded with a stainless steel shield. After thorough outgassing the source provided a slow Pt flux of approximately 0.025 ML min^{-1} at the sample surface which was checked to be homogeneous across the sample. The evaporation rate was calibrated by monitoring the time dependent decrease in the Cu MVV 59/61 eV Auger peak for coverages up to 1 ML and locating the evaporation time which lead to a decrease in the substrate MVV signal to 60 % of its clean surface value. A decrease of 60 % corresponds to that calculated upon assumption of layer-by-layer growth and utilising an inelastic mean-free-path of 5.2 Å calculated using the formalism of Seah and Dench [18]. This method obviously relies on the growth mechanism being true layer-by-layer and will tend to underestimate the true Pt coverage if deviations from layerwise growth occurs. The Auger data were cross checked by quantitatively monitoring the dose time required to obtain a high quality c(2×2) LEED pattern. The LEED intensity maximising at approximately 20% higher evaporation time than that calculated on the basis of AES for formation of a 0.5 ML film.

There is a problem with the AES calibration of this system as the Pt 64 eV transition and the Cu 59/61 eV transition overlap. Hence as you deposit Pt the Pt transition will distort the Cu transition. The coverage calibration technique used here involved the measurement of the evaporation time necessary to reduce the Cu intensity to 60% of its original value, expected for 1 ML Pt layer-by-layer growth. This coverage calibration will have an associative uncertainty due to the distortion of the Cu 59/61 eV peak which is likely to be severe as the cross sections for both the Pt and Cu transitions are approximately equal at 3 keV primary beam energy. Further uncertainty is added by the fact that it is unlikely that Pt will grow in an atomically flat layer. It is more likely at 300 K that the Pt exists as a PtCu surface alloy. However the fact that the c(2×2) structure maximised in perfection at 0.6 ML it is suggested that the coverage calibration is not substantial in error.
An absolute surface coverage determination technique for calibration of a Pt source would be the ex-situ GF-AAS glass-slide analysis technique described in detail in Chapter 4 (unfortunately this was not possible during the time of this thesis).

For desorption experiments formic acid (97 % purity, Aldrich chemicals) was further purified by several freeze-pump-thaw cycles prior to dosing. Gas purity was checked using the quadrupole mass spectrometer and dosing performed through an all-metal leak valve with exposures measured using an uncalibrated Bayard-Alpert ionisation gauge. CO was dosed from ultra-high purity Messer-Greisheim gas bottles. Desorption spectra were collected in line-of-sight geometry with variable linear heating rates between 1 and 10 K s^{-1} employed.

3. Results and discussion

3.1. Structural transitions in the Cu(100)-Pt system

Room temperature adsorption of Pt onto the (1×1) surface led initially to a slow increase in the background of the substrate LEED pattern with diffuse low intensity c(2×2) superstructure beams appearing after evaporation times of approximately 9 minutes. In contrast to the Cu(100)-c(2×2)-Pd system, a good quality c(2×2) was never obtained in the Pt coverage range 0–1 ML, upon Pt adsorption at 300 K. Formation of a crystallographically high quality surface as judged by LEED required thermal activation to temperatures in excess of ~500 K. Upon cooling to 300 K, a well contrasted c(2×2) LEED pattern with intense and sharp half order beams was obtained. In order to examine the optimal Pt coverage and annealing conditions to form a well ordered c(2×2) LEED pattern, LEED beam profiles were measured as a function of dose time at constant beam energy. Figure 2(a) illustrates selected LEED beam profiles collected at a primary beam energy of 124 eV as a function of Pt evaporation time. The Pt was evaporated at a sample temperature of 330 K with the c(2×2) ordering being activated by ramping the temperature to 520 K at a rate of 5 K s^{-1}. The LEED profiles were measured upon re-cooling to a constant temperature of 330 K. The annealing temperature was chosen for its ability to promote surface ordering yet to prevent significant loss of Pt from the outermost bilayer by dissolution into the Cu bulk. The data indicate that the c(2×2) becomes visible at an evaporation time of >9 minutes which corresponds to a Pt coverage of 0.2 ML based on Auger calibration. Figure 2(b) illustrates the variation of the (1/2,1/2) beam intensity and the full-width-at-half-maximum (FWHM) with deposition time. The half-order beam intensity increases up to an evaporation time of 27 minutes (0.61 ML) after which it slowly decreases. The FWHM decreases for evaporation times between 9 and 25 minutes indicating an increase in the long range order of the c(2×2) superstructure.

The LEED data suggests that at low Pt coverages (<0.2 ML) no two-dimensional islanding of areas of CuPt alloy occurs. Rather it appears that substitution into the copper substrate follows a somewhat random pattern. Ordering on a scale detectable by LEED only becomes apparent at coverages above 0.2 ML at which stage the half-order LEED beams are rather broad and diffuse. Thus, we propose at this critical

coverage small areas of c(2×2) CuPt alloys form, similar to that observed for the Pd/Cu(100) system where the convergence of short rows of Pd atoms (occupying the second-nearest neighbour sites) along the [001] and [010] directions results in localised domains of c(2×2) [19]. As the Pt coverage increases the domain size grows, until finally at the optimal coverage the half-order beam widths are comparable to those of the clean Cu(100) surface indicating a high degree of long range order. Based on an AES calibration assuming layer-by-layer growth a Pt coverage of 0.61 ML is required to give the "best" c(2×2).

The temperature dependence for activation of formation of a well-ordered surface alloy was investigated by evaporation of a Pt coverage corresponding to the optimal coverage required for c(2×2) formation with the substrate held at 320 K during film growth. The sample was then annealed step-wise to increasingly high temperature and held at temperature for 30 seconds. LEED beam profiles were then acquired upon re-cooling to 320 K. Figure 3(a) illustrates a selection of beam profiles for different annealing temperatures. Figure 3(b) illustrates that a rapid increase in half-order beam intensity is observed between ~430 and 540 K. There is no obvious plateaux region and the intensity almost immediately begins to decrease for annealing temperatures above ~540 K with only a weak c(2×2) remaining upon annealing to 650 K. The increase in beam intensity is accompanied by a decrease in the half-order FWHM with the minimum half width signifying the optimally ordered surface occurring at ~540 K, the same temperature at which the beam has attained its maximum intensity. Thus we conclude that an 'optimal' c(2×2) surface is formed by annealing a Pt coverage of 0.6 ML briefly to ~540 K and re-cooling. It is important to remember that the "optimal" coverage obtained for c(2×2) formation is the minimum true coverage due to possible deviation from true layerwise growth. Thus, for this system it seems that Pt coverages in excess of the ideal 0.5 ML value are required to bring the c(2×2) to "maximum perfection" as judged by half-order beam intensities and widths. The Cu(100)-c(2×2)-Pt system appears to behave significantly differently than the related Cu(100)-c(2×2)-Pd surface alloy where a high quality c(2×2) is observed *directly* after deposition at 300 K. In fact, for the Cu(100)-Pd system recent work indicates that heating to between 400 and 550 K leads to a marked decrease in half order beam intensity in direct contrast to the increase reported here for the Pt system [20]. We suggest this difference has its

origin in the variation in surface thermodynamics for Pd and Pt when deposited on Cu(100).

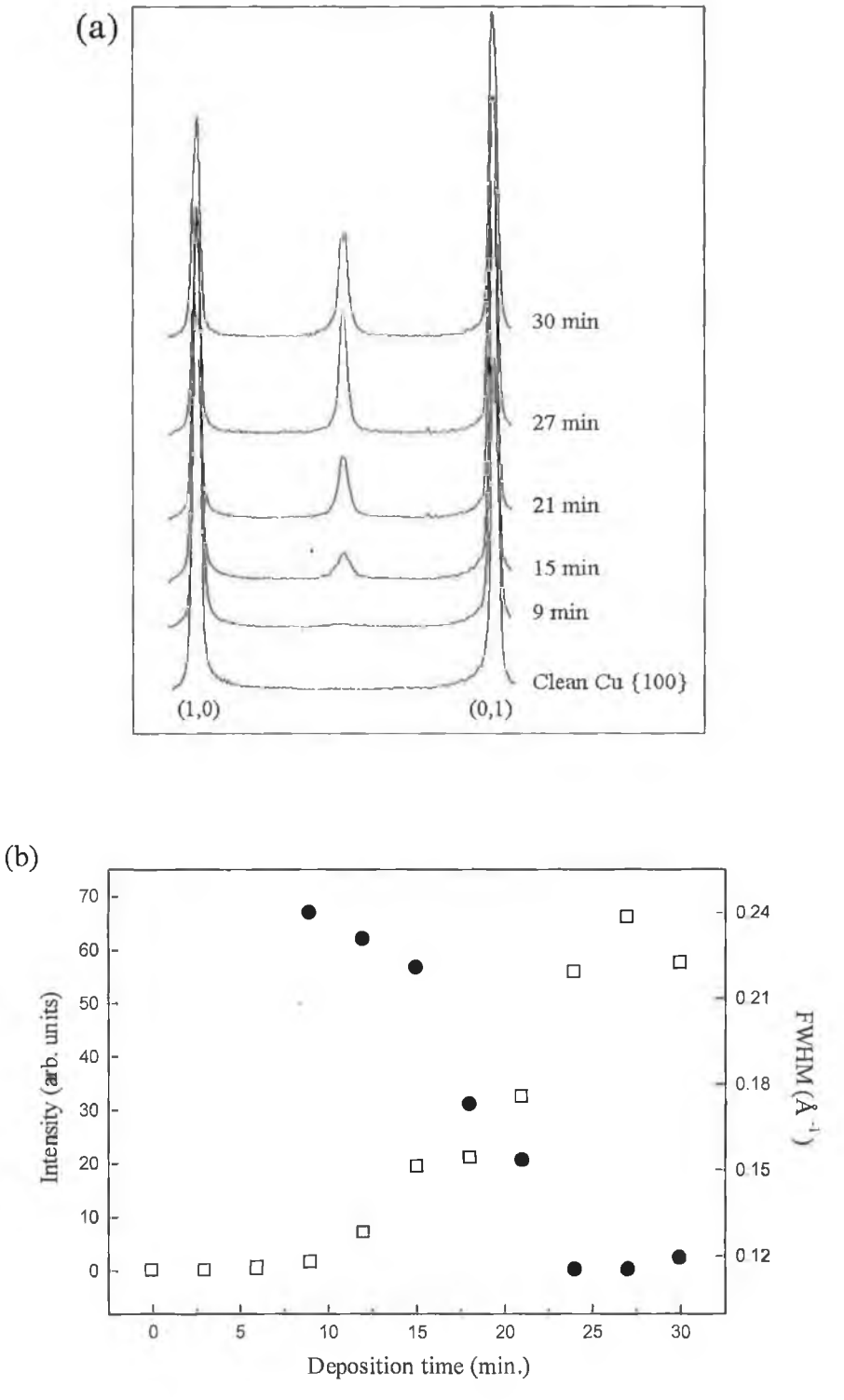

Figure 2: (a) Selected LEED beam profiles measured at 124 eV primary beam energy as a function of Pt coverage. All surfaces were pre-annealed to ~520 K prior to profile acquisition at 320 K. (b) Variation of the (1/2,1/2) beam integrated intensity (□) and full-width-at-half-maximum (●) with deposition time.

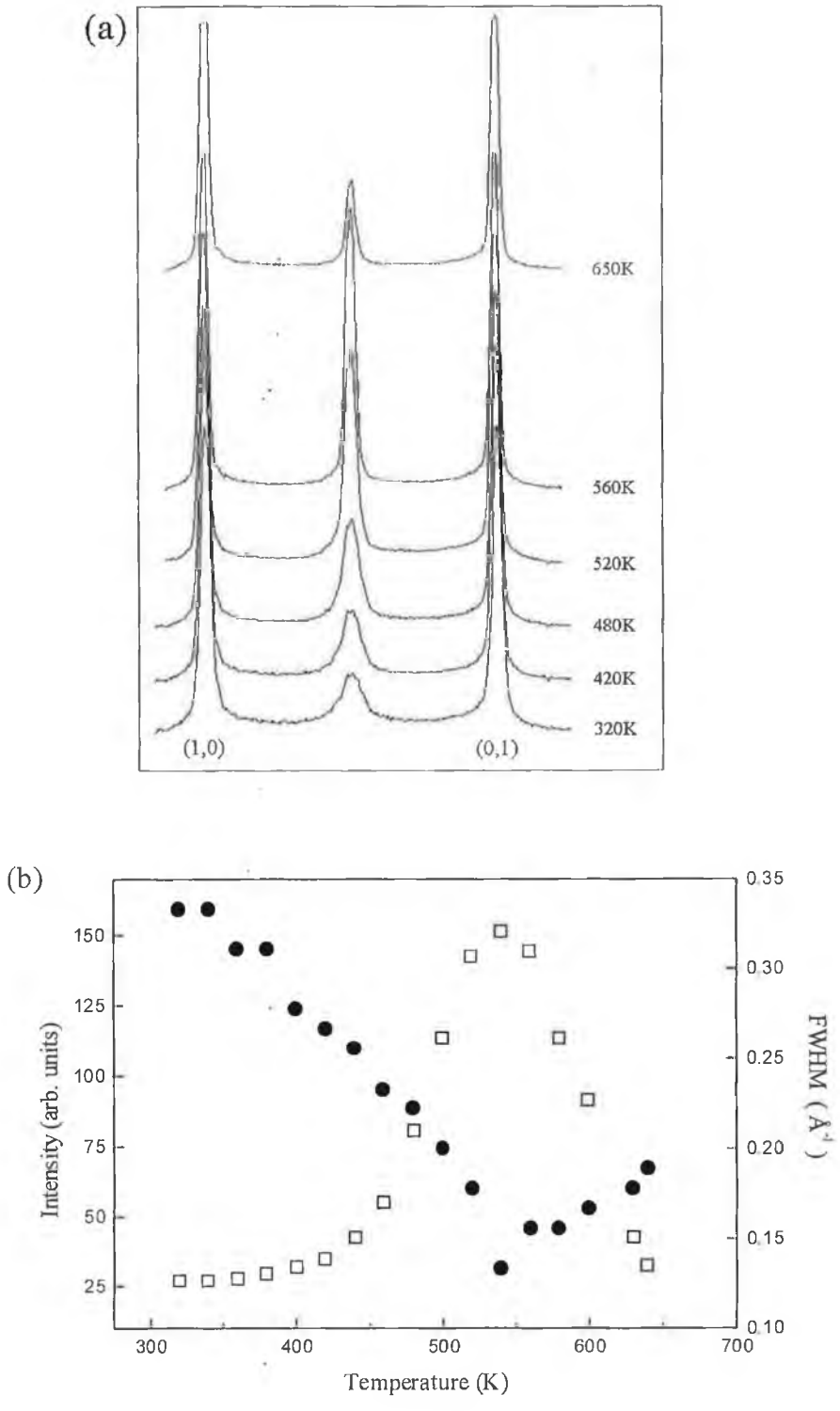

Figure 3: (a) Selected LEED beam profiles measured at a beam energy of 122 eV as a function of annealing temperature for a 0.6 ML Pt film deposited on Cu(100) at 320 K. The profiles were collected after annealing to the quoted temperature for 30 s with beam profiles being collected on re-cooling to ~320 K. (b) Variation in the (1/2, 1/2) beam integrated intensity (□) and full-width-at-half maximum (●) with annealing temperature.

It is well documented that the c(2×2) CuPd alloy formed at 300 K is the result of substitution of Pd into the *outermost* copper monolayer [19]. The outermost layer is however heterogeneous due to partial covering of the growing c(2×2) surface alloy by ejected copper atoms. In fact recent work has indicated that annealing this surface to 500 K leads to capping of the c(2×2) CuPd regions by a copper monolayer and formation of a c(2×2) CuPd underlayer [20] similar to that postulated here for Pt on Cu(100). The lack of formation of a well ordered c(2×2) CuPt alloy on deposition at 300 K cannot be explained by kinetic limitations for Pt compared to Pd as both Pt and Pd have identical atomic size and the arriving Pt atoms have thermal energy well in excess of that of Pd and would be expected to have similar heats of adsorption hence favouring increased kinetics of surface alloy formation in the case of Pt adsorption. Formation of an outermost layer surface alloy must be prohibited on thermodynamic grounds due to the higher difference in surface energy (γ) between adsorbate and substrate i.e. γ_{Pt}-γ_{Cu} (0.76 J m^{-2}) relative to γ_{Pd}-γ_{Cu} (0.11 J m^{-2}) [15]. The stronger Pt-Pt bond energy compared to Pd may result in clustering if top layer alloy formation is thermodynamically unfavourable and underlayer alloy formation kinetically inhibited. The metastable local free energy minimum in the case of Pt adsorption is likely to be a c(2×2) CuPt *underlayer* which has a higher activation energy barrier to formation compared to the top layer alloy due to the correlated atomic motion of adsorbate and substrate atoms required. For deposition at 300 K there is insufficient thermal energy for underlayer penetration to go to completion. However, it is clear that some limited alloying does occur as indicated by the observation of weak diffuse c(2×2) beams directly upon adsorption.

3.2. CO adsorption

In order to probe the change in surface stoichiometry which takes place upon annealing, CO desorption spectroscopy was utilised as a probe. Figure 4 illustrates the mass 28 desorption spectra acquired after saturating a 0.5 ML Pt film deposited at 310 K with CO. A large desorption peak was observed (T_p= 415 K) with a low temperature shoulder. Assumption of a pre-exponential factor of 10^{13} s^{-1} and first order desorption kinetics yields a desorption activation energy of 106 kJ mol^{-1}. It is interesting to note that the desorption spectrum obtained resembles that from a

metastable Pt(100)-(1×1) single crystal surface. Thus, the CO TPD is supportive of the earlier postulation that the major proportion of Pt upon deposition at 300 K is in the form of a thin Pt(100) pseudomorphic monolayer or Pt(100) crystallites.

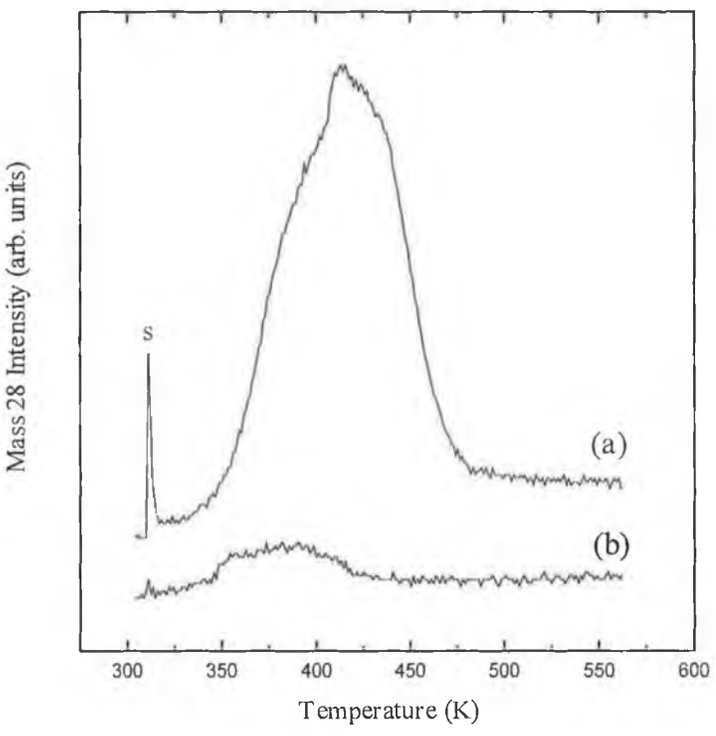

Figure 4: (a) Mass 28 TPD spectra (heating rate 4.5 K s^{-1}) from 0.5 ML of Pt deposited on Cu(100) at 310 K; (b) repeat of (a) performed after re-cooling to 310 K. In both cases the alloy surface was saturated with 100 L of CO at 310 K (s corresponds to the desorption peak from the support wires).

In contrast, the same surface when re-saturated with CO at 310 K after the previous activation to 550 K yields only a very weak desorption (figure 4(b)). Clearly a considerable redistribution of Pt at the interface occurs. It is tempting to simply interpret this result as the substitution of Pt atoms into second layer sites thus forming a c(2×2) underlayer below an outermost copper layer as illustrated in figure 5(a), thus leaving a Cu monolayer outermost which is inert to CO adsorption at 300 K. However, a second possibility which consists of a change to a top layer surface alloy, as shown in figure 5(b) is also possible. This second alternative would clearly require a significant alteration in the Pt surface chemistry to an extent that the CO

desorption is shifted to well below room temperature. Such an effect is indeed possible as Pt is in a significantly altered local environment with no Pt-Pt nearest neighbours in the surface alloy. However, previous work on a $Cu_3Pt(111)$ bulk alloy in which the top layer consists of a p(2×2) mixed Cu_3Pt layer of composition close to that of the bulk is not supportive of such a significant downshifting of the CO desorption. A more detailed analysis of the surface region of the $Cu_3Pt(111)$ alloy revealed a surface composition of 80 % Cu and 20 % Pt in the first layer, while the second layer was 69 % Cu–31 % Pt. In the first layer Pt and Cu atoms were found to be coplanar [21]. This surface, which consists of isolated Pt atoms co-ordinated exclusively to Cu in the outermost layer exhibits a CO desorption above room temperature (T_p= 340–380 K, β =7 K s^{-1}), although a significant downshifting of the desorption maximum was observed relative to Pt(111) [22,23]. As the CO is bound on top sites [22] on the Cu_3Pt alloy, it would be unusual to find significantly different desorption behaviour for the Cu(100)-c(2×2)-Pt surface alloy which also consists of isolated Pt atoms available for atop CO bonding if a top layer c(2×2) CuPt alloy where formed. Hence, the loss of the major CO desorption is assigned to penetration of the Pt into the second layer of the copper sample to form a c(2×2) CuPt underlayer.

The idea that alloying takes place for the Pt/Cu(111) system prior to annealing is proposed in a recent study by Bönicke et al [24], with STM indicating Pt atoms to be alloyed into the Cu(111)-surface for low Pt coverages (~0.1 ML) upon deposition at room temperature. It is further suggested that the formation of an ordered row type structure at the step edges (θ_{Pt} <0.5 ML) accompanied by finger shaped islands growing out from steps on the lower terraces is associated with the formation of an ordered Cu_3Pt surface alloy. It is apparent that further investigation into this system is necessary.

It is interesting to note that the small residual CO TPD signal centred at ~360 K from the annealed Cu(100)/Pt surface alloy is similar to that observed by Schneider et al [22] for the aforementioned $Cu_3Pt(111)$ single crystal, suggesting that while the majority of Pt does go sub-surface a small number of Pt atoms remain in the outermost layer (possibly at defect sites), although they are minority species with an estimated coverage of <0.05 ML. Thus, it is possible that after annealing, small areas of top layer c(2×2) CuPt alloy may be present with the exact amount depending

on the surface coverage of Pt deposited and the thermal treatment that the overlayer has been subjected to.

The conclusion that annealing for a short time to 550 K leads to penetration of the surface localised Pt to sub-surface sites is in full agreement with a low energy ion scattering (LEIS) study of Graham et al [25]. These authors noted that sub-monolayer films prepared by direct deposition at room temperature had significant quantities of Pt in the outermost layer. However, LEIS also indicated a higher Cu concentration in the outermost layer than that expected on the basis of fitting AES results to a layer-by-layer growth mechanism, suggestive of either loss of Pt to sub-surface sites upon deposition or cluster formation. For example, at a Pt coverage of 1 ML (as calibrated by AES) the substrate ISS intensity decreases to 40 % of its clean surface value. A brief anneal to 525 K was sufficient to reduce the Pt ISS signal to close to zero, indicative of place-exchange of Pt into sub-surface sites, in full agreement with the CO TPD results reported here.

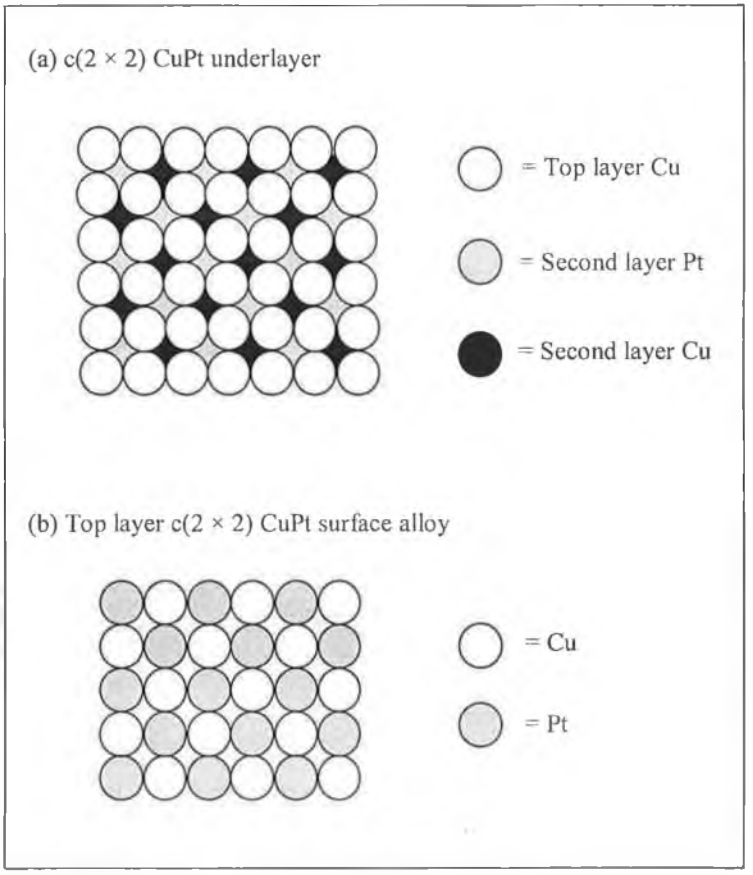

Figure 5: Models for the c(2x2) CuPt surface alloy: (a) a c(2x2) CuPt underlayer below an outermost copper monolayer; (b) a mixed outermost alloy layer.

A number of studies have been carried out in recent years for Pt deposition on the Cu(111) surface [26,27,28,29,30]. Most studies conclude a room temperature layer-by-layer growth mechanism for at least the first three monolayers. Core-level photoelectron studies suggest that there exists a sharp interface with no evidence of interdiffusion [26]. Furthermore, the inducement of alloying is concluded only possible after heating to 580 K [27]. In contrast a recent STM study suggests alloying at room temperature for extremely low coverages (~0.1 ML) of Pt on Cu(111). Moreover, at higher coverages (~0.5 ML) the formation of what appears to be an ordered row structure is observed at the step edges, tentatively attributed to an ordered Cu_3Pt surface alloy. Therefore, it remains unclear whether alloying occurs at room temperature for Pt growth on the Cu(111) face. In contrast, Pt interdiffusion although limited occurs at room temperature on the Cu(100) face (diffuse c(2×2) lead pattern), proposed due to Cu surface segregation which is more favoured on the (100) face relative to that of the (111) [40].

3.3. Effect of surface alloy formation on formate decomposition kinetics

The reactivity of the Cu(100)-c(2x2)-Pt alloy was monitored by study of the thermal decomposition of a formate intermediate formed upon dosing of formic acid at room temperature. For adsorption of formic acid on Cu(100) a formate intermediate is formed. Most of the recent structural work is indicative of a geometry in which the two oxygen atoms of the formate bridge two nearest neighbour copper atoms [31,32]. The formate is stable to temperatures above 400 K after which it decomposes, signalled by simultaneous evolution of CO_2 and hydrogen and small amounts of molecular formic acid. Figure 6 illustrates the temperature programmed desorption spectra for formate decomposition for saturation formic acid coverage on clean Cu(100) and on a c(2×2) underlayer alloy (formed by pre-annealing a 0.5 ML dose of Pt to 530 K). Mass 44 (CO_2), mass 2 (H_2) and mass 46 (HCOOH) desorption spectra are illustrated. The clean Cu(100) surface shows simultaneous desorption of CO_2 and H_2 at 461 K, along with a broad molecular desorption peak. Assuming first order formate decomposition kinetics and a pre-exponential factor of 10^{13} s^{-1} an activation energy of 119 kJ mol^{-1} is obtained for formate decomposition on clean Cu(100).

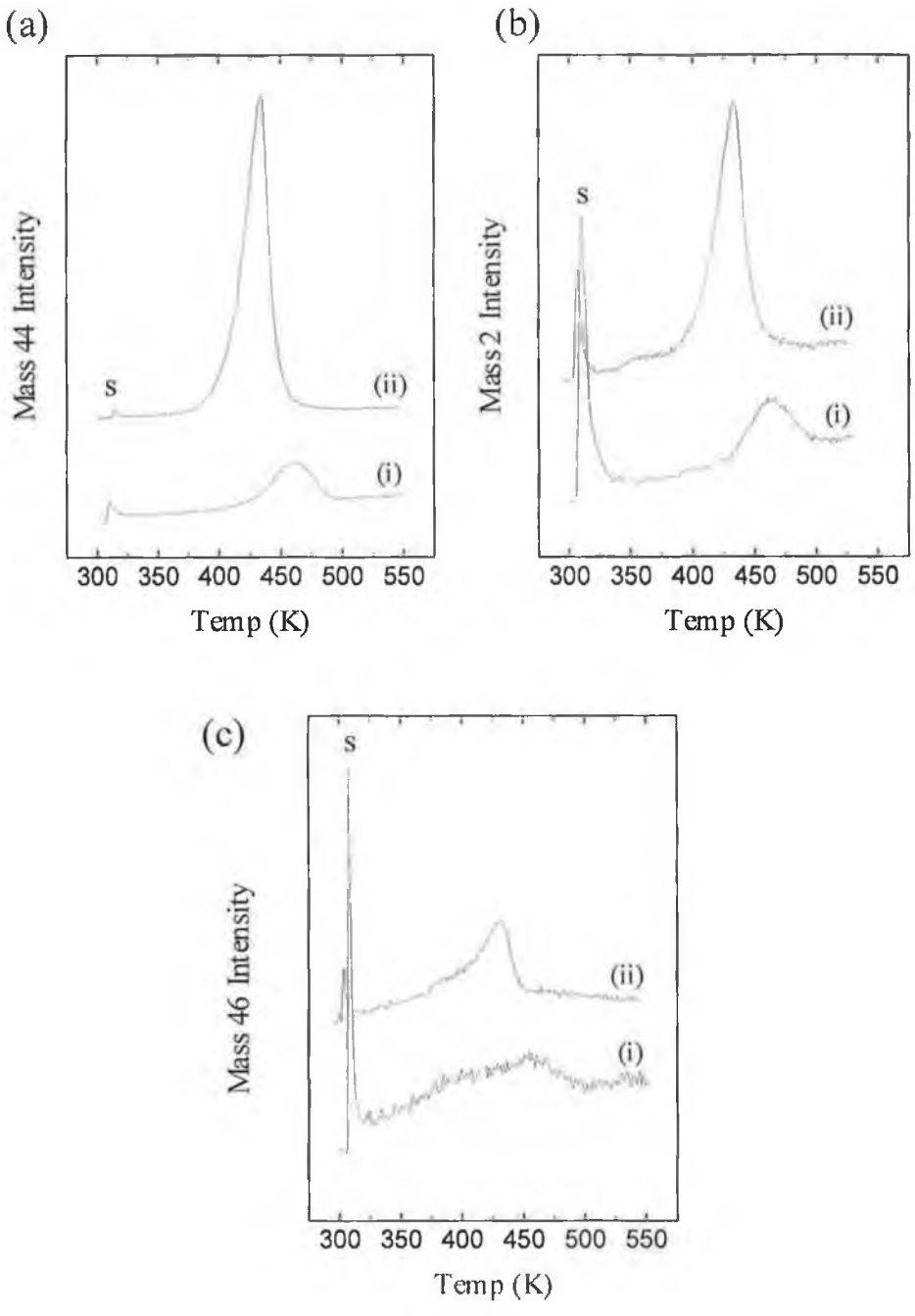

Figure 6: Temperature programmed thermal desorption spectra for saturation coverage of formic acid (HCOOH) on: (i) Cu(100) and (ii) the c(2x2) CuPt underlayer alloy, (a) mass 44 (CO_2); (b) mass 2 (H_2); (c) mass 46 (HCOOH). All spectra were recorded with a linear heating rate of 5.0 K s^{-1} (s corresponds to the desorption peak from the support wires).

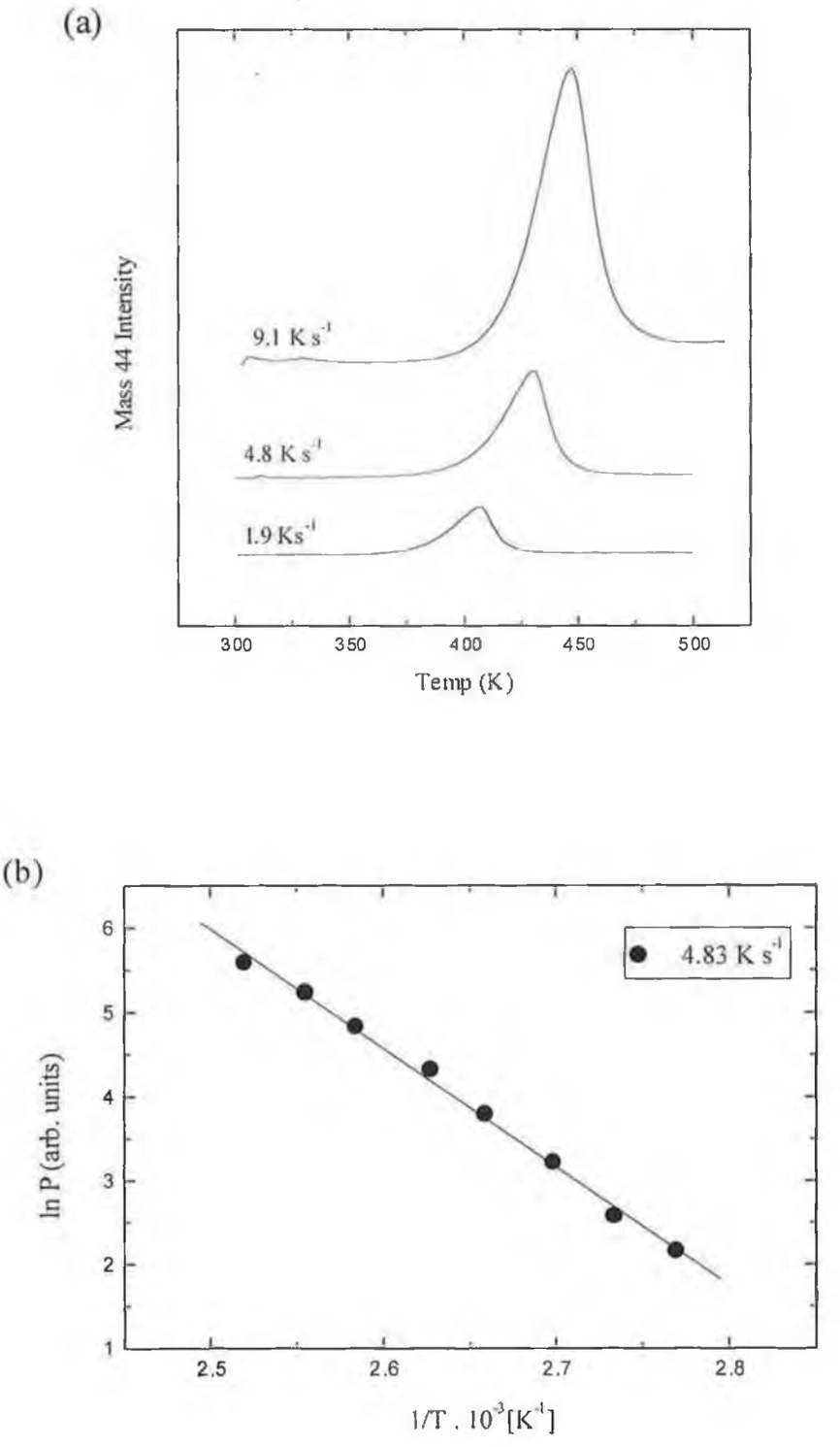

Figure 7: (a) Effect of heating rate on the mass 44 (CO_2) peak for the c(2x2) CuPt underlayer alloy; (b) an example of an Arrhenius plot utilising the leading edge analysis method.

The corresponding spectra from the c(2x2) surface alloy show a significant downward shift of the desorption peak maximum to 432 K, with again a coincident CO_2/H_2 signal. Application of the Redhead approximation leads to a decrease in the activation energy for decomposition to 110 kJ mol^{-1}. Interestingly, a decrease in the full width at half maximum from 39 K on clean Cu(100) to 23 K on the c(2x2) Pt alloy for CO_2 desorption is observed. Attempts were made to monitor other masses including H_2O (mass 18) and CO (mass 28), however the only signals seen were coincident with the CO_2/H_2 peaks and were thus assigned to cracking processes of the desorbing CO_2/H_2/HCOOH.

Figure 7 illustrates the effect of heating rate on the CO_2 TPD peak for the Cu(100)-c(2x2)-Pt underlayer alloy. The quality of the data was sufficient and the desorption significantly removed from the support peak to allow a full analysis utilising the leading edge of the peak [33,34]. Such an analysis in conjunction with heating rate variation data yielded a conclusion that the decomposition occurs via first order decomposition kinetics on the alloy surface with an activation energy for decomposition of 116(±3) kJ mol^{-1} and a pre-exponential factor of $4.2(\pm4.8)\times10^{13}$ s^{-1} from the 4.83 K s^{-1} heating rate, in reasonable agreement with the value obtained by the Redhead method. A leading edge Arrhenius plot for the 4.83 K s^{-1} heating rate is shown in figure 7(b).

As the c(2×2) structure corresponds to a mixed CuPt underlayer with a copper monolayer outermost, then the decreased formate stability may be due to an "electronic effect" for formate of the second layer Pt on the top layer Cu atoms if we assume that the formate adopts a similar geometry to that found on Cu(100). Alternatively a change in the bonding site for the formate intermediate (ensemble effect) cannot be completely dismissed. While there have been no past studies of the effect of Pt on the reactivity of copper surfaces with respect to formate decomposition, the CuPd system has received considerably attention. Newton and Bowker [35] have studied the effect of a sub-surface p(2×1) CuPd underlayer below a Cu rich top layer for a $Cu_{0.85}Pd_{0.15}$(110) bulk alloy. These authors report using the complete analysis approach [33,34] that sub-surface Pd in a 50:50 % local composition leads to a destabilisation of the formate intermediate from a decomposition activation energy of 136.4(±3) kJ mol^{-1} on clean Cu(110) to 125(±3) kJ mol^{-1} on the alloy surface, while a Redhead analysis also leads to a Pd induced destabilisation a smaller (2%) decrease in decomposition activation energy is

indicated. This 6 % decrease in activation energy is similar in magnitude to that on the Cu(100)-c(2×2)-Pt underlayer surface (slightly higher at 7%), although the absolute activation energies of Newton and Bowker are somewhat higher than those obtained in this work. Table 1 illustrates formate decomposition activation energies for a range of Cu, Pd and CuPd alloy surfaces calculated using he Redhead method along with results of this study on Cu(100)-Pt. We believe the Redhead method although not exacting, is the best way to compare the sets of data taken in different laboratories. The coverage dependence of the formate stability was also investigated on the Cu(100)-c(2×2)-Pt underlayer by dosing 0.1 L of formic acid. A leading edge and Redhead analysis indicated that within the accuracy of either analyses, no coverage dependent changes in the stability of the formate species occurs.

Substrate	**β/K s^{-1}**	**T_{max}/K**	**E_d/kJ mol^{-1}**	**Ref.**
Pd(110)	3.0	237	60.0	[36]
Cu(110)	1.8	445	117.7	[39]
1 ML Pd/Cu(110)	1.2	430	115.0	[39]
4 ML Pd/Cu(110)	1.5	363	95.9	[39]
CuPd[85:15](110)	2.65	445	116.2	[37]
CuPd[50:50](110)	2.5	346	89.8	[38]
Cu(100)	5.0	461	118.5	This work
Cu(100)-c(2×2)-Pt	5.0	432	109.7	This work
Cu(100)-c(2×2)-Pt*	5.0	406	104.0	This work

* mixed CuPt top layer.

Table 1: Comparison of the activation energy (E_d) for formate decomposition on various model catalysts calculated using the Redhead approximation, with a pre-exponential factor $\nu = 10^{-13}$ s^{-1}, assuming the reaction follows first order kinetics (β = heating rate).

We have recently shown that for CuPd systems formed by sublimation of Pd onto a Cu(110) surface, the stability of the formate intermediate is altered depending on the Pd loading and thermal processing undergone by the system [39]. In particular, from copper capped p(2×1) surfaces of similar local geometry/composition to the bulk

alloy of Newton and Bowker, a similar de-stabilisation of the formate intermediate is encountered as that previously reported [35].

The mechanism of formation of a c(2×2) CuPt underlayer requires further comment. Substitution of 0.5 ML of Pt into the outermost layer of the Cu(100) substrate naturally requires that 0.5 ML of Cu is expelled. These copper atoms must then reside above the surface with the natural conclusion that a somewhat heterogeneous surface will initially arise with large areas consisting of an outermost copper monolayer above a c(2×2) mixed CuPt layer. As the Pt c(2×2) films for Pt coverages of 0.5 ML yield no evidence of a high temperature desorption state reflecting coincident CO_2/H_2 at 461 K (CO_2 peak from clean Cu(100)), we may conclude that we have indeed deposited the minimum Pt coverage of 0.5 ML required to form a homogeneous c(2×2) CuPt second layer. Hence, the additional 0.5 ML of Cu required to fully cap the c(2×2) CuPt underlayer must be transported from step edges. Additional Pt over and above that required to form the mixed underlayer is then likely to be located within the outermost layer as it is unlikely that a brief anneal to 520 K will provide sufficient activation energy to transport a significant number of Pt atoms into the copper bulk, possibly explaining the small residual CO desorption (figure 4(b)). The lack of formate decomposition at ~460 K and the narrow FWHM of the formate decomposition is thus clear evidence that no areas of un-alloyed clean Cu(100) surface remain i.e. a rather homogeneous c(2×2) underlayer forms.

In order to investigate the possibility of stabilising Pt in the outermost layer, interfaces of higher Pt loading were produced. Graham et al [25] has observed that thicker films (>1ML) annealed to 525 K have a significant Pt content in the **outermost** layer. For example, a Pt coverage of 3 ML deposited at 300 K yields a pure Pt surface as analysed by ISS. Annealing to 525 K leads to a reduction in the Pt signal and re-appearance of a Cu ISS signal in keeping with a mixed CuPt outermost layer. Belkhou et al [40] have reported that deposition of thicker Pt films followed by annealing to 575 K lead to a well ordered c(2×2) alloy with a mixed CuPt outermost layer in agreement with the ISS work of Graham et al [25]. Utilising the technique of surface core level shift spectroscopy Belkhou et al observed that the Pt 4f core level had a significant surface component which the authors ascribed to Pt atoms within a mixed *outermost* CuPt layer above an alloyed interface of average composition Cu_3Pt. Thus while it would appear that in the sub-monolayer regime the

mixed CuPt layer prefers to be sub-surface at higher Pt loading the role is reversed with the mixed layer being outermost.

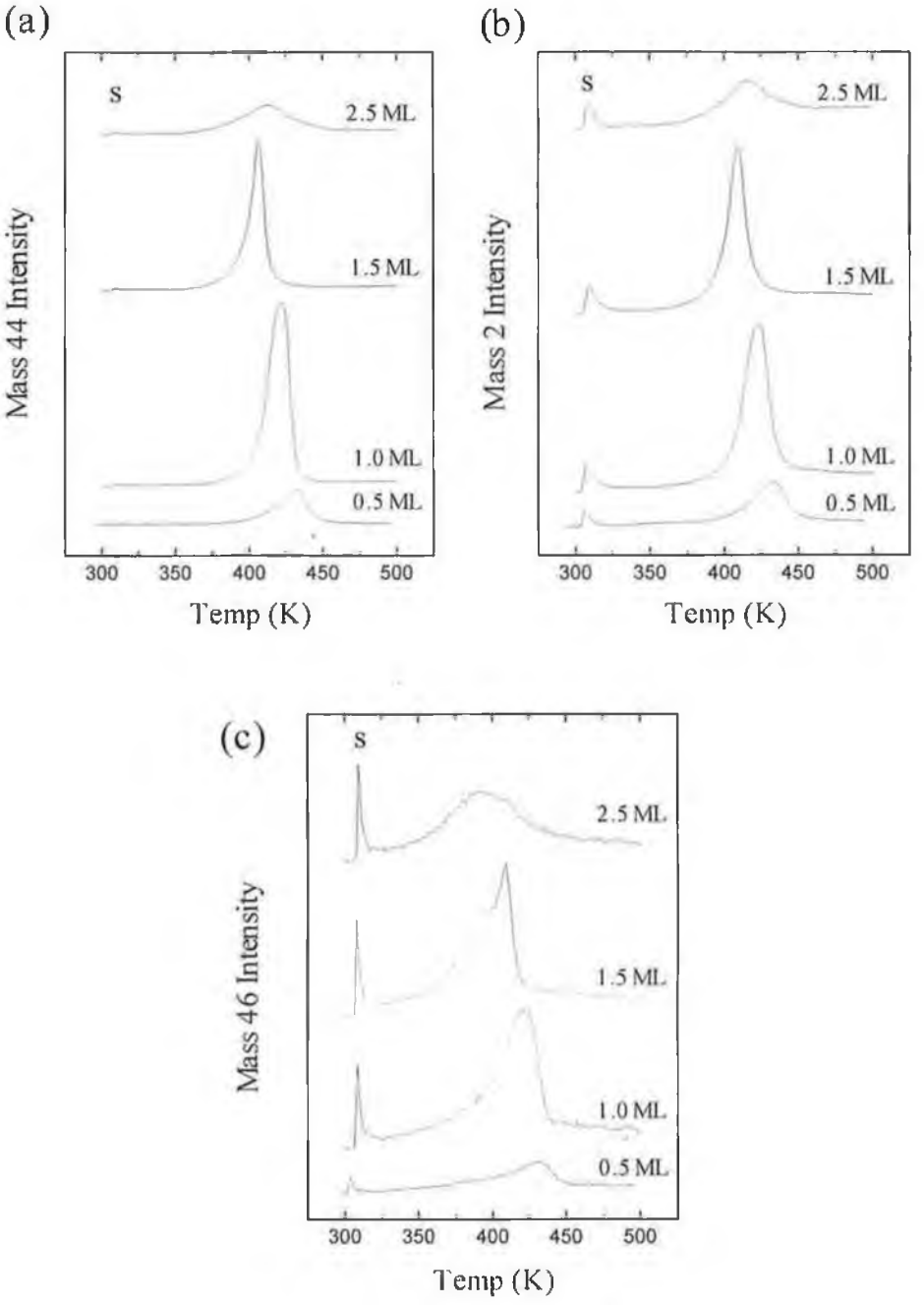

Figure 8: Effect of higher Pt loadings on the formate decomposition kinetics (a) mass 44 (CO_2); (b) mass 2 (H_2); (c) mass 46 (HCOOH). All surfaces were pre-annealed to 530 K prior to dosing to saturation HCOOH coverage (10 L) (s corresponds to the desorption peak from the support wires).

Figure 8 illustrates the mass 44, mass 2 and mass 46 TPD spectra for Pt films of thickness 0.5, 1, 1.5 and 2.5 ML. The 1 ML film illustrates strong simultaneous CO_2/H_2 desorption at 426 K. The LEED pattern in this case remained an excellent c(2×2). The CO_2 desorption peak has a particularly narrow half-width (11 K) at Pt coverages of 1.5 ML indicative of a highly homogeneous surface. Again this surface exhibits an excellent c(2×2) LEED pattern. The simultaneous CO_2/H_2 evolution is further downshifted to 406 K. As the 1.5 ML c(2×2) surface has a mixed CuPt layer outermost we therefore have direct evidence of a significant alloying induced change in the Pt surface chemistry. Madix [41] has shown that on Pt(110) the maximum rate of formate decomposition occurs below room temperature at ~250 K. Thus, while the mixed CuPt surface does show a formate stability intermediate between that of Pt and Cu, the surface chemistry remains more similar to that of Cu(100). This is perhaps not surprising given that a c(2×2) CuPt outermost layer requires formate to bond at CuPt sites if it is to bridge two nearest neighbour atoms in the outermost layer. The UPS work of Schneider et al [23] along with band structure calculations of Banhart et al [42], indicates that for dilute CuPt alloys the platinum atoms adopt a d^{10} filled d-band configuration which may be expected to passify their reactivity towards formate decomposition and yield properties more similar to those encountered on copper. Finally, In the case of 2.5 ML of Pt the LEED pattern degraded substantially to a high background c(2×2). The CO_2 and H_2 peaks are substantially broadened relative to the 1.5 ML film, indicating considerable surface heterogeneity. The simultaneous CO_2/H_2 desorption is centred at 412 K with significant desorption at lower temperatures, indicative of regions of the surface containing alloyed Pt in the outermost layer possibly with varying degrees of Pt-Pt nearest neighbour bond formation. This should lead to a gradual destabilisation of formate on Pt rich areas of the surface and the concomitant broadening in the formate decomposition [39]. Nevertheless, the fact that the surface chemistry has not fully crossed over to Pt-like behaviour clearly illustrates that large regions of pure Pt clusters are still not present at the surface.

4. Conclusions

Copper-platinum surface alloys have been formed by deposition of Pt onto Cu(100) and structural transitions as a function of Pt coverage and thermal processing have been followed by LEED and desorption spectroscopy. Adsorption of Pt leads to the formation of a c(2×2) surface alloy. Formation of a well ordered high crystallographic quality surface requires thermal activation to 540 K while annealing above this temperature leads to slow dissolution of Pt into the bulk. Combination of AES analysis and CO TPD strongly suggests that a surface subject to a brief anneal to temperatures in excess of 500 K results in the formation of a c(2×2) CuPt *underlayer* below an outermost pure Cu monolayer.

Platinum exerts a considerable "ligand" effect on the outermost copper monolayer de-stabilising the formate intermediate which undergoes a first order decomposition with an activation energy of 110 kJ mol^{-1}, a 7 % decrease in the formate decomposition activation energy relative to clean Cu(100). Higher Pt coverages lead to the formation of a c(2×2) overlayer with a mixed CuPt layer outermost. On these surfaces formate decomposition is further destabilised with a decomposition activation energy of 104 kJ mol^{-1} (a 13 % decrease in the activation barrier relative to clean Cu(100)). Alloying platinum with copper at higher Pt coverages leads to significant chemical modification of the chemistry of Pt sites, however this 'electronic effect' is mixed with a geometric effect due to the mixed metallic nature of the site (if formate remains bridging two nearest neighbour metal atoms) on the high Pt loading CuPt interface.

References

[1] U. Bardi, Rep. Prog. Phys., 57 (1994) 939.

[2] M. Hansen, Constitution of Binary Alloys, 2nd Ed., McGraw-Hill, New York, (1958).

[3] G. W. Graham, Surf. Sci., 171 (1986) L432.

[4] G. C. Smith, C. Norris and C. Binns, Vacuum, 31 (1981) 523.

[5] S. H. Lu, Z. Q. Wang, S. C. Wu, C. K. C. Lok, J. Quinn, Y. S. Li, D. Tian, F. Jona and P. M. Marcus, Phys. Rev. B, 37 (1988) 4296; S. C. Wu, S. H. Lu, Z. Q. Wang, C. K. C. Lok, J. Quinn, Y. S. Li, D. Tian, F. Jona and P. M. Marcus, Phys. Rev. B, 38 (1988) 5363.

[6] M. Valden, J. Aaltonen, M. Pessa, M. Gleeson and C. J. Barnes, Chem. Phys. Lett., 228 (1994) 529.

[7] T. D. Pope, K. Griffiths and P. R. Norton, Surf. Sci., 306 (1994) 294.

[8] R. S. Rao, A. Bansil, H. Asonen and M. Pessa, Phys. Rev. B, 29 (1984) 1713.

[9] M. Bowker, M. Newton, S. M. Francis, M. Gleeson and C. J. Barnes, Surf. Rev. and Lett., 1 (1994) 569.

[10] M. Newton, M. Bowker, P. Weightman, M. Gleeson and C. J. Barnes, submitted to Phys. Rev. Lett.

[11] F. J. C. H. Toolenar, F. Stoop and V. Ponec, J. Catal., 83 (1983) 1.

[12] H. C. de Jonste and V. Ponec, J. Catal., 63 (1980) 389.

[13] M. L. Poutsma, L. F. Elek, R. A. Ibarbia, A. B. Rich and J. A. Rabo, J. Catal., 52 (1978) 152.

[14] V. Ponec, Surf. Sci., 272 (1992) 111.

[15] W. R. Tyson and W. A. Miller, Surf. Sci., 62 (1977) 267; L. Z. Mezey and J. Giber, Jpn. J. Appl. Phys., 21 (1982) 1569.

[16] C. J. Barnes, D. O'Connell and M. Gleeson, in preparation.

[17] H. L. Davis and J. R. Noonan, J. Vac. Sci. Technol., 20 (1982) 842.

[18] M. P. Seah. and W. A. Dench, Surface Interface Anal., 1 (1979) 2.

[19] P. W. Murray, I. Stensgaard, E. Lægsgaard and F. Besenbacher, Surf. Sci., 365 (1996) 591 (and references therein).

[20] E. Al Shamaileh and C. J. Barnes, work in progress.

[21] Y. G. Shen, D. J. O'Connor, K. Wandelt and R. J. MacDonald, Surf. Sci., 328 (1995) 21.

[22] U. Schneider, H. Busse, R. Linke, G. R. Castro and K. Wandelt, J. Vac. Sci. Technol. A, 12 (1994) 2069.

[23] U. Schneider, H. Busse, T. Janssens and K. Wandelt, Surf. Sci., 269/270 (1992) 316.

[24] I A. Bönicke, M. Ø. Pedersen, I. Stensgaard, E. Lægsgaard and F. Besenbacher: Growth and reactivity of Cu on Pt(110) and Pt on Cu(111), to be published.

[25] G. W. Graham, P. J. Schmitz and P. A. Thiel, Phys. Rev. B, 41 (1990) 3353.

[26] R. Belkhou, N. T. Barrett, C. Guillot, A. Barbier, J. Eugne, B. Carrire, D. Naumovic and J. Osterwalder, Appl. Surf. Sci., 65/66 (1993) 63.

[27] R. Belkhou, N. T. Barrett, C. Guillot, M. Fang, A. Barbier, J. Eugne, B. Carrire, D. Naumovic and J. Osterwalder, Surf. Sci., 297 (1993) 40.

[28] J. Fusy, J. Menaucourt, M. Alnot, C. Huguet and J. J. Erhardt, Appl. Surf. Sci., 93 (1996) 211.

[29] U. Schneider, R. Linke, J. -H. Boo and K. Wandelt, Surf. Sci., 357/358 (1996) 873.

[30] Y. G. Shen, D. J. O'Connor, K. Wandelt and R. J. MacDonald, Surf. Sci., 357/358 (1996) 921; Phys. Rev. Lett., 71 (1993) 2086.

[31] D. P. Woodruff, C. F. McConville, A. L. D. Kilcoyne, T. Linder, J. Somers, M. Surman, G. Paolucci and A. M. Bradshaw, Surf. Sci., 201 (1988) 228.

[32] S. P. Mehandru and A. B. Anderson, Surf. Sci., 219 (1989) 68.

[33] E. Habenschaden and J. Kuppers, Surf. Sci., 138 (1984) L147.

[34] D. A. King, Surf. Sci., 47 (1975) 384.

[35] M. A. Newton and M. Bowker, Surf. Sci., 307 (1994) 445 (and references therein).

[36] N. Aas, Y. Li and M. Bowker, J. Phys.: Condens. Matter, 3 (1991) 1.

[37] M. A. Newton, S. M. Francis, X. Li, D. Law and M. Bowker, Surf. Sci., 259 (1991) 45.

[38] R. Holroyd, Ph.D. Thesis, Reading Catalysis Centre, University of Reading, United Kingdom.

[39] J. P. Reilly, C. J. Barnes, N. J. Price, S. Poulston, R. A. Bennett, P. Stone and M. Bowker, J. Phys. Chem. B, 103 (1999) 6521.

[40] R. Belhou, J. Thiele and C. Guillot, Surf. Sci., 377 (1997) 948.

[41] R. Madix, Surf. Sci., 102 (1981) 542.

[42] I. Banhart, P. Weinberger and J. Voitlander, Phys. Rev. B, 40 (1989) 12097.

Chapter Six

Conclusions

1. Conclusions and suggestions for further studies

Bimetallic combinations have revealed superior properties for a number of catalytic reactions. Moreover, in many cases improvements in activity, selectivity or even greater resistance to poisoning have been reported compared to the constituent monometallic catalysts. To this extent, the Cu-Pd/Pt bimetallic system is of particular interest having shown itself to be active in NO reduction by CO, with turnover rates comparable to those of the expensive yet efficient Rh/Al_2O_3 catalyst. Cu-Pd/Pt catalysts have also shown particular relevance to a number of other industrially important reactions, including CO and alkene oxidation, ethanol decomposition and CO, benzene and toluene hydrogenation. For instance, the addition of Cu has been found to improve methane and methanol yields in the Pd catalysed CO hydrogenation. From a theoretical point of view the Pd-Cu is especially interesting in that it forms a continuous series of solid solutions above a critical temperature (773 K) with two ordered phases (Cu_3Pd and CuPd) occurring in the phase diagram. Whereas the Cu_3Pd belongs to the fcc lattice, CuPd forms a bcc lattice with the CsCl structure. Similarly Cu and Pt form a continuous series of solid solutions at high temperature, while at low temperature various ordered phases exist. The study of single crystal and supported nano-cluster copper-palladium(platinum) model catalysts has comprised the bulk of this thesis.

In Chapter 3 the growth mechanism, thermal stability and reactivity of the Cu(110)/Pd system were discussed with particular emphasis on the transition from single to multilayer Pd growth (to date most effort has been devoted to characterisation of the structure and chemical reactivity of sub-monolayer Pd coverages). The room temperature growth mechanism for the Cu(110)/Pd system initially involved the intermixing of Pd and Cu to form an ordered Cu(110)-p(2×1)-Pd surface alloy of two to three layers thickness although the surface was essentially heterogeneous as opposed to uniform, consisting of monolayer high two-dimensional islands and monolayer deep "pits" (Pd coverage ~1 ML). For multilayer Pd coverages, densely packed palladium platelets were formed with some preference for rectangular island shapes.

The thermal stability of the system has been examined by XPS and primarily STM. STM revealed the loss of the granular palladium film structure at 600 K, with a

multi-level surface dominated topography. The surface consisted of large flat domains bounded by non-linear mono-atomic steps and raised islands and large pits. Pit formation is attributed to palladium substitutionally transplanting into the copper lattice with the ejected copper atoms growing as islands and leading to the multilayered structure observed. XPS Pd 3d core level peak widths (narrowing FWHM) and shifts (to higher binding energy) upon annealing are suggestive of CuPd alloy formation. Capping of the resulting CuPd alloy by a low surface energy copper monolayer is suspected for temperatures as low as 500 K. The appearance of periodic bands running across the surface structure, as indicated by STM, at elevated temperature (>600 K) reveal striking similarity to those seen for elevated temperature deposition of Cu on Pd(110). These have been attributed to strain relaxation between Cu and alloy layers.

Thicker Pd films showed a marked de-stabilisation to the formate intermediate (decomposition activation energies of 118 and 95 kJ mol^{-1} on Cu(110) and a 8 ML Pd film, respectively). This destabilisation is attributed to desorption from a mixed CuPd surface indicating that the stability of the formate intermediate may be altered to a state intermediate between pure Cu and Pd via surface alloy formation.

In Chapter 4 a study of Cu, Pd and Pd-Cu HOPG supported nano-clusters was presented. XPS studies of monometallic Cu and Pd supported nano-clusters revealed an increase in core-level binding energy with decreasing coverage in keeping with the tendency of small metal clusters to bind their core electrons more tightly. STM, XPS and XPD results have verified a Volmer-Weber growth mechanism.

In the case of bimetallic films, non variance of the Pd 3d core level binding energies for increasing Cu coverages on pre-dosed Pd was noted, ruling out substantial alloy formation. On the other hand a decrease in binding energy was observed for the Cu 2p core levels for submonolayer Cu coverages on all Pd films. This negative BE shift for submonolayer Cu is indicative of a surface configuration for Cu, i.e. coating the Pd clusters (thermodynamically favourable). The growth mechanism is therefore one where Cu preferentially coats or "eggshells" Pd clusters in the low coverage Cu regime with subsequent phase separated Cu clusters formed with increasing Cu coverage.

In the reverse scenario i.e. Pd incremental deposition on Cu, Pd XPS core levels seem to be more complex. Bulk intermixing is ruled out as Pd core level binding

energies and FWHM values for the most part generally mirror those of monometallic Pd. The suggested growth mechanism is one involving the simultaneous growth of Pd clusters and the capping/surface alloying of areas already covered by Cu clusters (due to the direct impingement of Pd on such areas). STM results have verified a Volmer-Weber growth mechanism for the bimetallic films as for their single metal counterparts. A double-peaked cluster size distribution indicative of phase separated clusters (with the most probable diameters of monometallic Pd and Cu clusters dominating) was not observed for either scenario i.e. Pd on Cu or Cu on Pd. Intermediate cluster sizes between those dominant for pure Cu and Pd clusters were observed in both cases supportive of Cu-Pd interaction.

In Chapter 5 the structural transitions following the deposition of Pt onto Cu(100) have been followed by LEED and desorption spectroscopy. Thermal activation to 540 K was required to produce a c(2×2) surface alloy of high crystallographic quality after ~0.60 ML Pt deposition. Moreover, AES and CO TPD fully support the theory that a surface subject to a brief anneal to temperatures in excess of 500 K results in the formation of a c(2×2) CuPt *underlayer* below an outermost pure Cu monolayer. A considerable "ligand" effect was exerted by the Pt on the outermost copper monolayer de-stabilising the formate intermediate with an activation energy of 110 kJ mol^{-1} recorded, a 7 % decrease in the formate decomposition activation energy relative to clean Cu(100). The c(2×2) LEED pattern persisted for even higher Pt coverages (1–2.5 ML) with a mixed CuPt layer outermost. Further formate destabilisation was observed with a first order decomposition activation energy of 104 kJ mol^{-1} calculated (a 13 % decrease in the activation barrier relative to clean Cu(100)). It is suggested that the significant chemical modification of Pt in an alloy with copper at the higher Pt coverages is attributable to both an electronic and geometric effect due to the mixed metallic nature of the formate binding site (assuming formate remains bridging two nearest neighbour metal atoms) on the CuPt interface.

The thermal molecular beam system designed and constructed during the course of this thesis (Appendix A) is ideal for future progress resolving microscopic details of the kinetics of surface reactions of all systems investigated, i.e. graphite supported nano-cluster CuPd bimetallic catalysts, the Cu(110)/Pd and Cu(100)/Pt systems . In

all cases, information regarding the extent of phase separation, alloying and/or coating of one metal by the other for various loading of each metal should be easily obtainable from CO and formic acid adsorption/desorption profiles. Moreover, the beam system presented here allows the techniques of LEED and mass spectrometry (MS) to be used in tandem i.e. facilitating the monitoring of changes in both the surface structure and reactivity simultaneously.

Of particular relevance to the supported nano-clusters are transient measurements involving CO oxidation (beam temperature variation) after oxygen predosing on Pd supported particles. Oxygen atoms are suggested to diffuse into Pd particles with smaller particles found to be more reactive than larger ones. This should allude information regarding cluster sizes for the Pd monometallic system at lower coverages. NO dissociation (if it occurs) is also found to be particle size dependent, increasing with decreasing particle size. Sticking probability measurements for CO and NO will also be of interest.

Furthermore, Pd is capable of dissociatively adsorbing hydrogen, while Cu is not. Hydrogen dissociative adsorption requires the presence of (1×1) Pd close packed surface regions. Hydrogen adsorption/desorption trends regarding the surface arrangement of the bimetallic clusters (surface alloy formation and Cu coating of Pd clusters will most likely prevent dissociative adsorption while phase separated Pd clusters will readily adsorb H_2) will be of interest in comparison to monometallic Pd supported cluster adsorption/desorption profiles.

The Cu(110)/Pd system is also open to further structural investigation. Initially, it is important to spend further time investigating the formate adsorption site for the pre-annealed Pd films (~4 and 8 ML Pd), which reveals intermediate reactivity to formate decomposition when compared to Cu(110) and Pd(110). We have suggested an 'inter-atom' formate binding site assuming bidentate formate adsorption. Photoelectron diffraction or near-edge X-ray-adsorption fine structure (NEXAFS) and surface extended X-ray-adsorption fine structure (SEXAFS) measurements are required to confirm the co-ordination and orientation of the formate species, i.e. whether it has changed from the aligned bridge adsorption orientation proposed for it on Cu(110). Formate binding site determination is also highly relevant to the Cu(100)/Pt system.

In addition, further low temperature desorption studies (formic acid/CO/H_2) are required to answer questions regarding the surface composition of the intermediate to high Pd coverage samples upon mild annealing to 500 K i.e. whether the surface consists solely of a Pd-Cu mixed top layer; or contains Pd islands, and finally to what extent, if any, does Cu surface segregation occur. Other questions which require addressing include the extent of Cu segregation to the surface upon (a) initial p(2×1) alloy formation were the thermodynamical favourable coating of the PdCu alloy by ejected and step edge Cu is seen and (b) upon the annealing of thicker Pd films. Again low temperature formic acid desorption studies will complement any further studies on the Cu(100)/Pt system.

APPENDICES

Appendix A

Design and Applications of a Simple Thermal Molecular Beam System for Reactivity Studies

1. Introduction

The very first gas phase molecular beam experiments were those carried out by Dunoyer in 1911 [1,2], while Stern and his collaborators in Hamburg further developed many of the principles, which are followed even to this day. The development of beam technology around the 1920's and 1930's centred around experiments involving the evolution of quantum mechanics, including the famous Stern-Gerlach experiment of 1922 [3].

The elevation of molecular beam technology to a position of extreme importance in the field of surface science to study gas-solid interactions coincided with the development of UHV technology. The principles of beam technology and furthermore their applicability to the examination of surface kinetics are dependent on one factor and that is the effective isolation of the atoms or molecules incident on the surface. This involves the production of a collision-free environment in which the incident gas particles become far removed from other particles. Of course the difficulty in any gas-surface reaction is the collision of incident gas molecules with other gas phase molecules present in the environment. The results of such collisions include the loss of energy, direction and chemical identity of the molecule whose interaction with the surface is under investigation. The difficulty that arises from such perturbations is not only the loss of uniform energy of the incident species but also the loss of beam intensity at the surface.

In this chapter the design and construction of a simple thermal molecular beam system built within the Chemistry Department of Dublin City University (DCU) is described and examples in its future use in determination of sticking probabilities, reaction probabilities and reaction mechanisms are outlined.

2. Molecular beams

A molecular beam is a collimated stream of electrically neutral molecules traversing an area of sufficiently low pressure such that the number of collisions that the particles within the beam undergo is negligible. Moreover, the beam characteristics include a well-defined spatial distribution, particle flux, and, in certain cases, energy distribution among the internal modes of freedom (translational, vibrational, rotational and electronic). The beauty of molecular beam technology is the ability to finely tune the energy of the beam. The control ranges from the 'thermal' excitation of the beam producing essentially a Maxwell-Boltzmann distribution of internal energies to the use of supersonic beams, which will allow access to manipulate all quantum states of the gas molecules.

2.1. Effusive beams

These sources involve the effusion of a source gas through an orifice, tube or array of tubes which is then allowed to pass through a collimating aperture or apertures to finally produce the molecular beam [2]. The source chamber (oven) containing the gas is at a low operational pressure to ensure that the gas follows molecular flow through the orifice of the chamber. In effect, the pressure in the source chamber is such that the mean free path (MFP) of the molecules is much larger than the dimensions of the orifice which means that the probability of the gas moving through the orifice is exactly the same as the probability of the gas hitting the wall in the area of the orifice. Therefore, at low pressure the flux is directly proportional to the pressure. The flow is described to be of the Knudsen type and is defined as the ratio of the mean free path of the gas in the source to the smallest dimensions in the source (the source orifice diameter (d)). In effusive arrangements the Knudsen number (K_n) is large. The velocity distribution of the emerging gas along the beam axis undergoes no mass transport and is said to be Maxwellian, and characteristic of molecules having the source temperature. The velocity distribution of the flux ($I(v)$) in the beam is defined as [4]:

$$I(v)\alpha\ v^3 \exp\left(-\frac{Mv^2}{2kT}\right) \qquad 2.1$$

where M is the molecular weight, k is the Boltzmann constant and T is the source temperature. The beam flux at the surface is then given by:

$$I = 1.118 \times 10^{22} P_s A_s / l^2 (MT)^{\frac{1}{2}} \qquad 2.2$$

where P_s is the source pressure in Nm^{-2}, A_s (m^2) area of source aperture, l(m) the source to surface distance and T the source temperature. The energy range obtainable by this type of source is 0.008–0.32 eV for source temperatures ranging from 77–3000 K, respectively. The limitations of effusive beams soon becomes clear, as the beam is thermalised to the temperature of the source the 'thermal' range of the orifice material is the limiting factor.

2.2. Nozzle beams

First discovered by Rodebush in 1931 nozzle beams were developed and proposed by Kantrowitz and Grey in 1951, allowing the production of beam intensities orders of magnitude higher than those of effusive sources [5]. The conventional oven source must be modified to consider a low-density supersonic free-jet. The difficulty with these systems is that for even a small supersonic jet the gas flowing through the nozzle is extremely large, and of course to maintain the beam without significant collisions with out-of-beam gas molecules, the stray gas which leaves the source must be pumped away before entry into the scattering chamber to maintain good background pressure. So obviously the greater the beam intensity the greater the pumping power necessary to remove the out-of-beam gas from the chamber. It was not until the efforts of Becker and Bier in 1954 that the potential of supersonic beam technology was realised [6].

As in thermal beams, the system consists of a nozzle aligned with a hollow truncated cone often referred to as a skimmer. The skimmer serves to define the beam by removing or skimming the out-of-beam particles. The beam is usually subject to a final collimation in the analysis chamber. Figure 1 reveals the schematics of both the

effusive and nozzle sources. In supersonic beams the pressure in the source chamber has increased and the Knudsen number becomes less than one, as the MFP is much smaller than the orifice dimensions. The gas is literally forced through the orifice of the nozzle by the very large number of collisions occurring as the gas expands into the lower pressure region. This expansion is termed isentropic as the thermal molecular motion is almost completely converted to directed motion producing an almost monoenergetic beam that is more focussed and intense than an effusive beam.

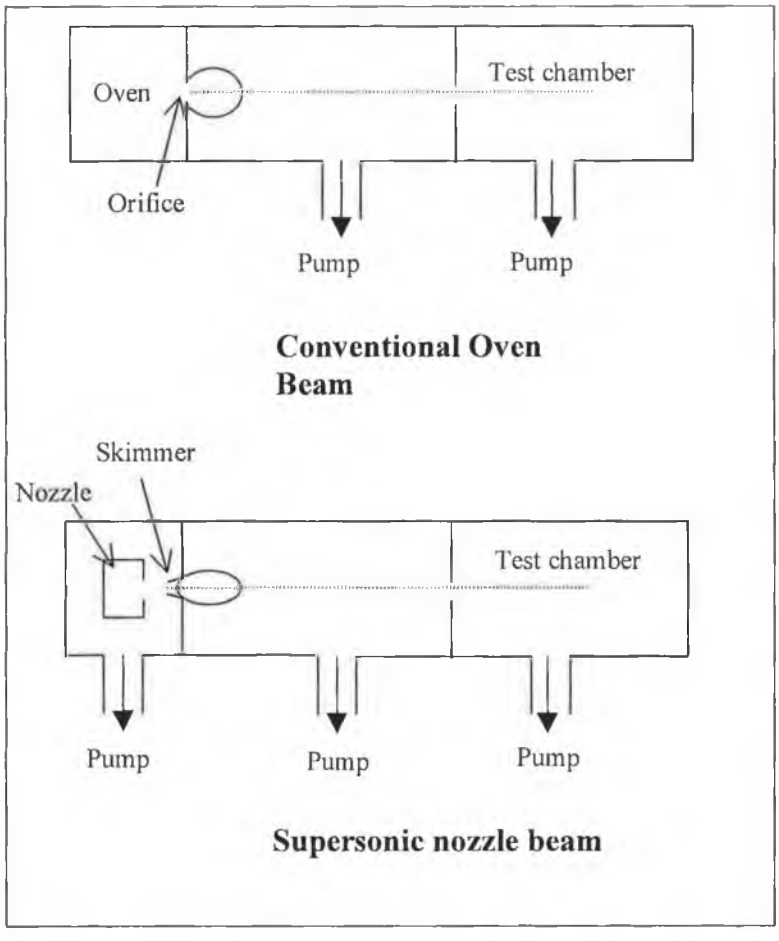

Figure 1: Comparison of oven beam and nozzle beam sources. The relative intensity distributions are indicated by the closed curves downstream of the slit and the skimmer, respectively.

In the high-pressure regime of the supersonic beam the flow becomes turbulent and reverts to laminar flow. The conductance now becomes proportional to the square of the pressure in the source chamber. Figure 2 reveals a plot of conductance down a capillary as a function of the pressure behind the source for a capillary. Molecular

flow is obtained at low pressure where the conductance of the capillary is constant with increasing pressure. At this point the flux is directly proportional to the pressure as the flow is of Knudsen type in the source. At increased pressure the molecules flow at much higher speeds in the flow direction and a change to laminar flow is observed. Conductance now becomes a function of pressure and the flux rate is then proportional to the square of the pressure.

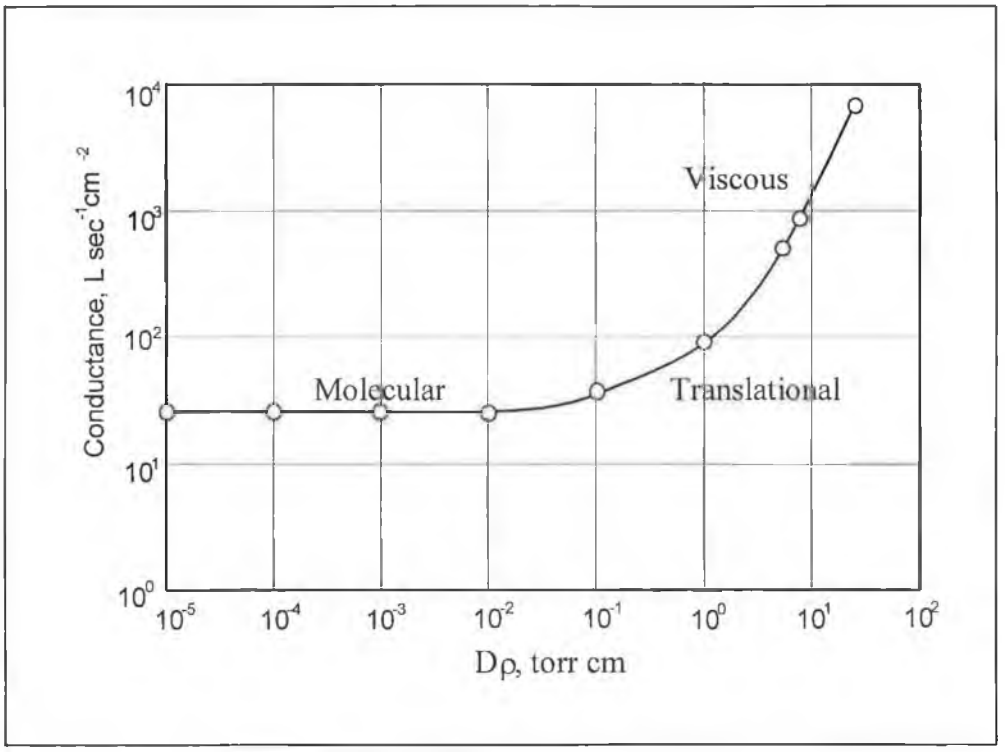

Figure 2: Conductance dependence of the average pressure across a capillary showing a constant value in the molecular flow region and an increase with the pressure in the viscous flow region. The beam flux is proportional to the product of conductance and pressure [7].

The distribution of velocities in the emerging molecules of a supersonic beam is extremely narrow. The high energy of the beam is coupled with what is described as 'cooling' of the gas molecules. This arises from the conversion of the total enthalpy into beam translational energy. The freezing of the internal degrees of freedom of the gas, including rotational and vibrational degrees of freedom are all possible and in some instances clustering or condensation of the beam molecules is observed. The

quantum states of the molecules are therefore under complete control allowing the selective excitation of the beam en-route to the sample. Laser technology is usually employed and when tuned to a particular molecular vibrational frequency the required internal energies of the molecule can be controlled (rotational/vibrational/electronic). A spread of 10% in velocities is common, however, a 0.1% spread has been obtained for cooled, highly expanded helium beams [8].

In terms of velocities achieved in nozzle sources, variations are easily achieved by changing the source conditions. The velocities reached are defined as 'Mach' numbers (M_n) or the speed ratio, defined as the ratio of the terminal velocity to the local speed of sound. This will effect the velocity spreads of supersonic beams as can be seen from figure 3 [9].

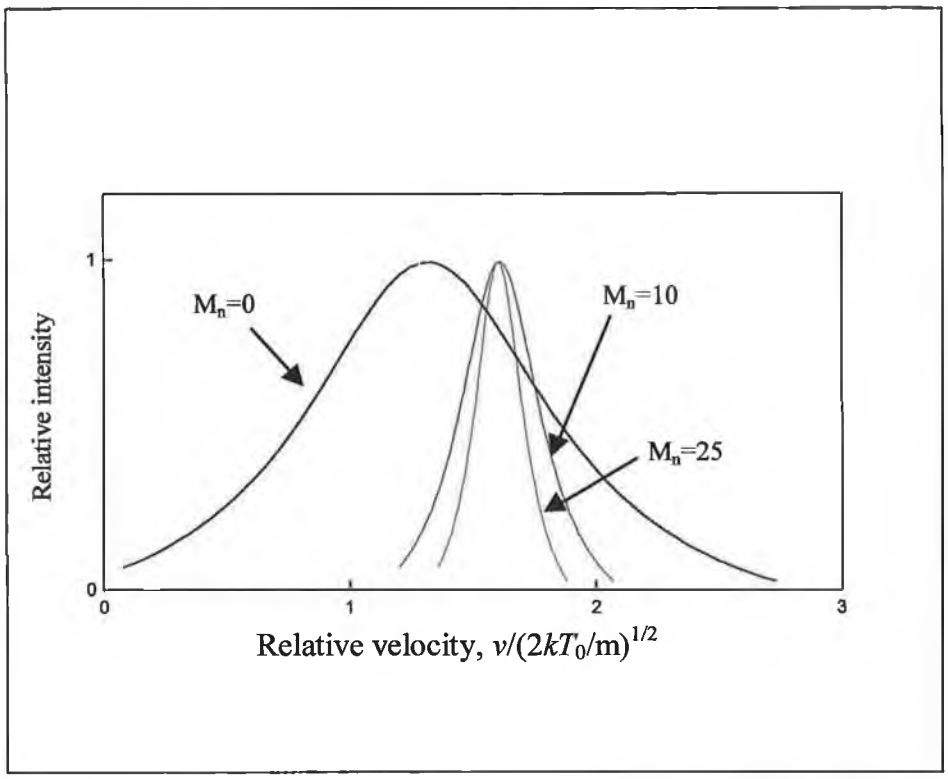

Figure 3: Comparison of the velocity distribution in thermal (M_n=0) and supersonic beams at the skimmer entrance [10].

For an effusive beam only about 11% of the total flux is within 5% of the mean molecular velocity, whereas in a supersonic beam at a 'Mach' number of 25 this

fraction becomes about 80%. The average translational energy of a supersonic molecular beam due to the streaming motion of the molecules is:

$$\overline{E} = \frac{1}{2}mv^2 = \int_{T\to 0}^{T_0} C_p dT \approx \frac{RT_0\gamma}{(\gamma - 1)} \qquad 2.3$$

where v is the flow velocity, m is the molecular mass, C_p is the molecular specific heat at constant pressure, R is the Universal gas constant, γ is the heat capacity ratio, T_0 is the source temperature and T is the static temperature in the nozzle.

In the nozzle source the average translational energy is 5/2 kT, in effect only slightly higher than that of an oven source (3/2 kT). The seeding technique which involves the introduction of a lighter gas (usually H_2 or He) with considerably higher average velocities (note: the introduction of H_2 into the source may cause it to react with the surface, therefore noble gases are more commonly used for metal/alloy studies) into the source accelerates the heavier gas molecules to higher energies. This ensures effective translational beam energies far higher than that characteristic of nozzle wall temperatures. The energies obtainable are far greater than that seen for the oven sources (0.008–0.32 eV), and can be in excess of 1 eV. For example, in the case of 1% argon in helium the argon molecules are said to approach the energy of the light component, reaching kinetic energy values ten times higher than if only pure argon was utilised [11]. Xe in a similar arrangement has reached translational energies as high as 14.4 eV when the nozzle is heated to ~3000 K [12]. At first glance, it would appear that the seeding technique will encounter the problem of low incident surface intensities, as the concentration of the reactant gas is quite small when diluted with smaller faster molecules. However, the intensity obtainable by the supersonic system is so large that the required signal-to-noise ratio to ensure usable results is easily achieved. Moreover it is found that the heavier particles in the beam possess a preference for alignment along the centre of the beam. Thermal fluxes are typically in the order of $\sim 1\times10^{17}$–10^{18} molecules m^{-2} s^{-1} and can be several orders of magnitude greater for supersonic beam systems.

The schematics of a supersonic beam apparatus are shown in figure 4. A number of differential pumping stages are required to maintain a good background pressure in the analysis chamber. The presence of defining beam chambers also allows the

incorporation of features such as beam choppers. The purpose of a beam chopper is to cut the beam into short temporal segments (pulsed beam) allowing fast transient kinetic measurements. Chopping the beam is also important when combined with time of flight measurements to characterise the energy distribution of the beam. The comparison of the surface desorption pulse with that directly from the source is easily achievable with this technique allowing the extraction of information eluding to reaction kinetics. The employment of more precise systems such as double disc choppers allows the selection of species with a specific velocity i.e. those species that pass the distance between the two discs in a specific time. This technique is useful for the study of the dynamics of reactions. The schematics of a supersonic beam apparatus arrangement are shown in figure 4.

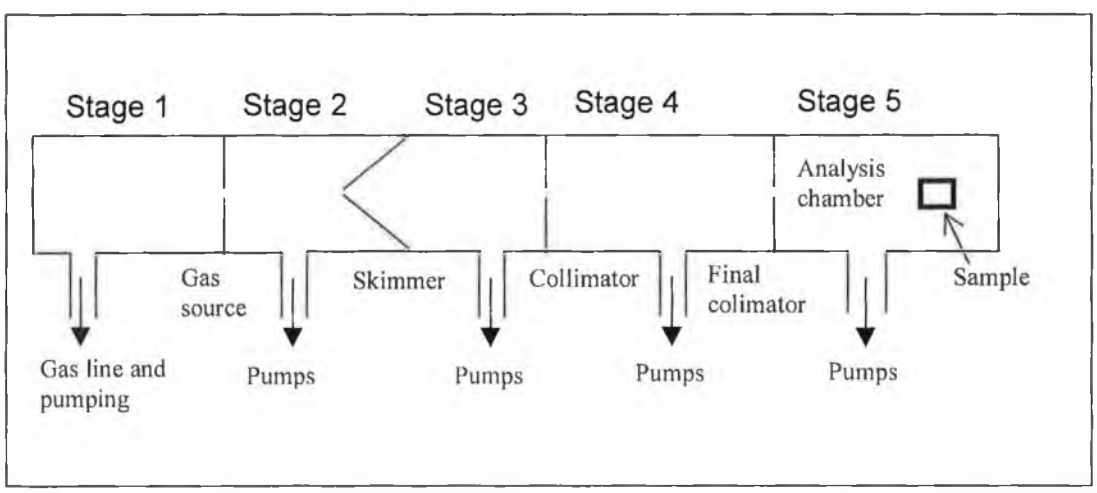

Figure 4: Schematic layout of a typical molecular beam system with several stages of differential pumping.

3. The Dublin Molecular Beam System: design and technical considerations

3.1. Molecular beam construction

The molecular beam system planned and constructed consists of a simple yet effective thermal beam allowing the accurate measurement of absolute sticking probabilities (± 0.01) and examination of surface reaction rates and mechanisms, and their variation with (a) sample temperature, (b) beam temperature and (c) angle of incidence with respect to the sample (important for stepped surfaces). This system is based on the original design of King and Wells [13] which consisted of four differentially pumped stages. Simplification of this system was carried out by Bowker and King [14], with only three stages of differential pumping producing a beam size at the sample of 1 to 2 mm. This system (constructed from pyrex glass) was later further modified by Bowker, Pudney and Barnes to be constructed in stainless steel as a compact cheap "add-on" to a standard UHV chamber [15]. The system described in detail here represents a further evolution and improvement of this basic design. The essentials of this system involve three basic components: the source, skimmer and final collimator, each of which is housed in a differentially pumped vacuum chamber. These chambers are essentially standard stainless-steel six-way crosses (70-mm o.d.). The apparatus and the alignment of the beam components are illustrated in figure 5. The basic design is very similar to that of Bowker, Pudney and Barnes [15]. The system consists of a molecular beam generation stage with two stages of differential pumping coupled to the ultra-high-vacuum stage.

In the following sections the beam will be discussed in more detail and possible applications discussed.

3.2. Beam genesis

The first stage in the beam section is the source chamber allowing gas pressures of typically 5–50 Torr to be generated. The gas for beam generation is stored in a four-way cross attached to the x-y-z manipulator controlling the source position (figure 5). The source chamber is pumped by a rotary pump where the ultimate vacuum

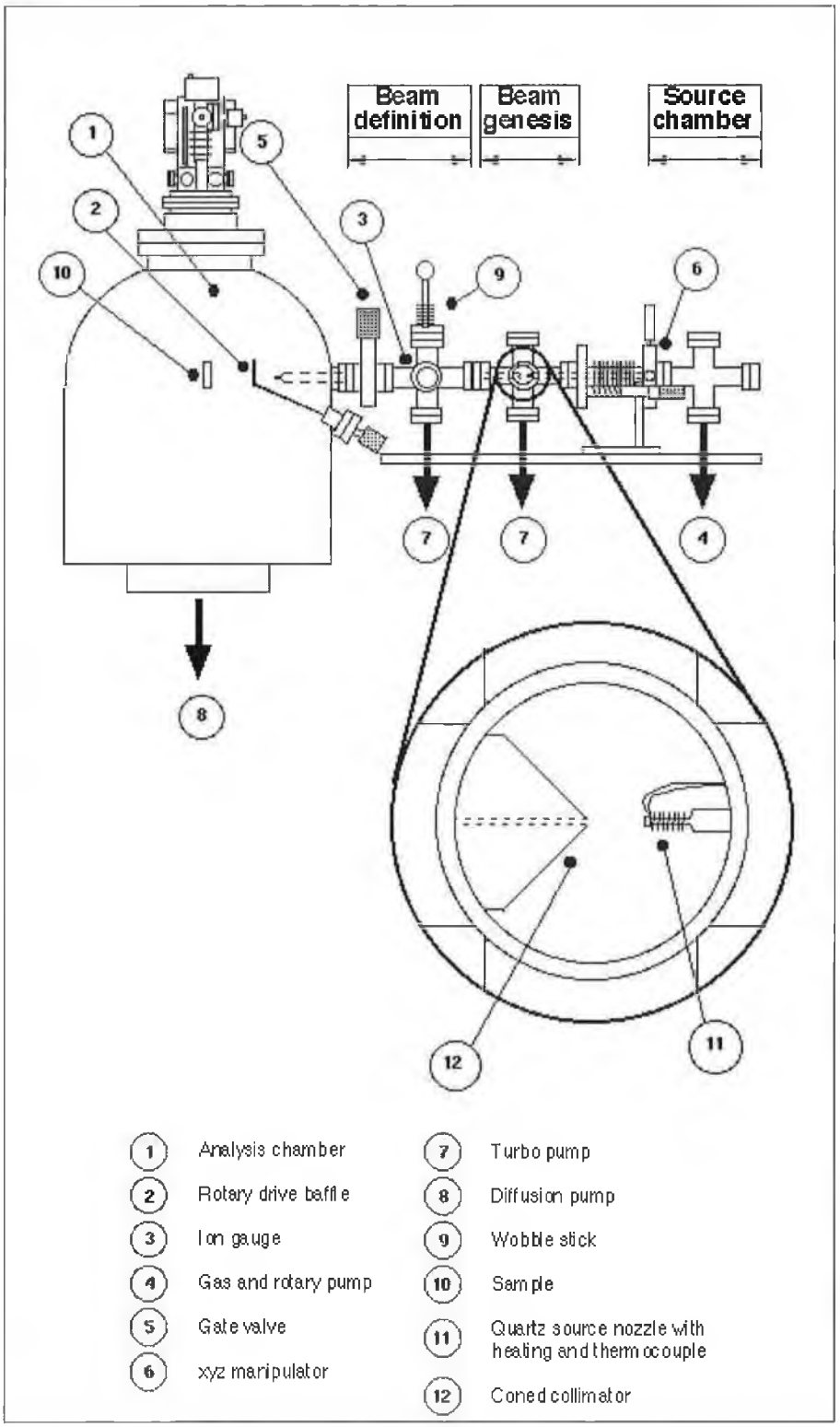

Figure 5: Schematic of the thermal molecular beam system designed and constructed in Dublin.

obtained should be less that 10^{-2} Torr. Pressure measurement requires a gauge capable of measuring pressures from 10^{-2} Torr to several tens of Torr facilitated by Pirani/baratron gauges.

The gas effuses through a quartz capillary 0.2 mm in diameter and 20 mm in length. As the capillary is made of quartz it can be heated to high temperature and will not corrode if reactive gases are used. Passing a current through a platinum wire wrapped around the source allows variation of source temperature. Thermocouple attachment allows the accurate measurement of source temperature. Once the beam leaves the source and enters the first stage of differential pumping gas scattered out of the beam by collisions is pumped by a rotary backed turbomolecular pump (Edwards EXT 70, pumping speed of 65 l s^{-1}).

The beam is then collimated. The collimator prevents the shock wave formed during expansion of the beam from collapsing on itself and thus degrading the monoenergisity of the beam. This collimator is more aptly described as a conical shaped skimmer. A fine edge and steep angle are essential in minimising the disturbance to the beam. The skimmer is constructed from stainless steel. In our arrangement the cone angle of the skimmer was 90° with an aperture of 0.3 mm diameter. The beam then enters the second stage, itself pumped by an identical Edwards EXT 70 turbomolecular pump backed by a rotary.

The final collimator is a 2.5 mm diameter glass tube 20 mm in length located within the scattering chamber. The effect of the collimator is twofold: (1) to define the final size of the beam at the sample and (2) to reduce the effusive gas load in the analysis chamber. In this arrangement the collimator is attached to a glass sleeve and is approximately 6 cm from the centre of the chamber. The projected size of the beam on the sample was reported to be ~2.8 mm by Bowker, Pudney and Barnes [15], when source pressures of 30 Torr are used. It is important that the beam intensity is as homogeneous as possible at the sample surface. The considerations necessary to ensure this are either a very small source or a small ratio of L_1/L_2 where L_1 is the defining collimator–sample distance and L_2 is the source–sample distance. In our case the source–sample distance is ~50 cm and the defining collimator–sample distance is as already stated 6 cm. Figure 6 reveals a schematic of the profile of the beam across the surface illustrating the presence of penumbra. Clearly minimisation of the width of the penumbra is critical to the quality of beam experiments.

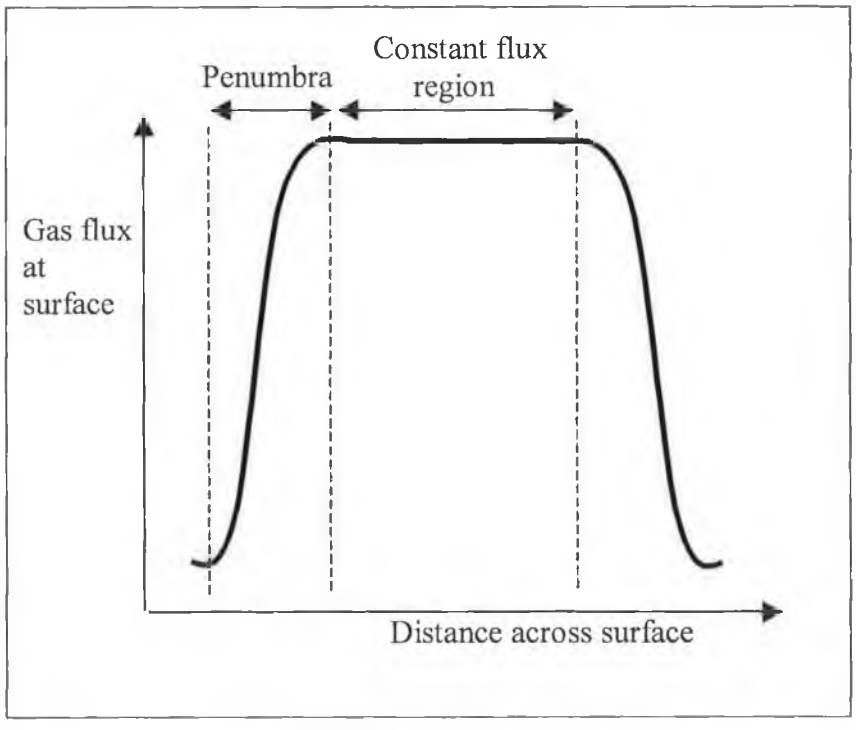

Figure 6: A plot of flux of gas at the surface as a function of distance across the sample surface. Essentially good beam design will result in the minimisation of the penumbra.

3.2.1. Beam alignment

The alignment of the source, skimmer and collimator is important in achieving a high intensity beam along with preventing excessive gas scattering in the different differential pumping stages. A low cost precision x-y-z manipulator (Vacuum Generators, z-travel 100 mm, x,y travel ±12.5 mm) facilitates source movement. This allows the external adjustment of the source to ensure optimal beam intensity when source–skimmer alignment is optimal. Alignment may be achieved by using a laser beam which is sighted through the skimmer (ideally the skimmer should be mounted on an x-y manipulator) until the light is concentric with the skimmer aperture. The skimmer is subsequently positioned to maximise the quality of the final reflection of light in the main chamber. The difficulty with this is that the laser beam source should follow the relative movements of the skimmer. Alternatively, a white light source can remain in a fixed position while the position of the skimmer is finely adjusted.

The x-y-z manipulator must also have sufficient drive to allow the source–skimmer distance to be adjusted. Bowker et al [15] selected an optimum distance of ~18 mm which allowed a high intensity beam at the surface while still maintaining reasonable pressure in the second stage of differential pumping (10^{-7} Torr). Bowker et al calculated a first stage pressure of 2.5×10^{-4} Torr for a source pressure of 30 Torr. The further the source moves away from the skimmer the greater the loss in beam intensity due to gas phase collisions.

The pumping of the two differential stages in the beam system described is afforded through the use of rotary-backed turbomolecular pumps. The minimisation of the distance between the sample and the source is important as the intensity of the beam decreases as the inverse square of the distance from the source orifice. In choosing small turbomolecular pumps we prevent the possibility of oil vapour contamination quite common in the use of oil diffusion pumps, while their compact size allows us to minimise the source–sample distance.

In addition to the basic structure of the molecular beam stage a wobble stick is included allowing the placement of a blocking flag in front of the beam when necessary. This is contained in the beam definition stage of the system. Another useful feature is a gate valve in the same stage which allows the isolation of the molecular beam stage from the analysis chamber. This allows the beam to be vented independently of the analysis chamber and prevents the impractical venting and baking of the analysis chamber if a small problem is encountered within the molecular beam stage.

3.3. Spectrometer chamber

We have discussed in detail the concept of producing a collimated molecular beam at the sample surface. The analysis chamber is now briefly outlined.

It is of paramount importance that provision should be made to house all available sample analysis techniques including any which may be acquired in the future. The chamber itself was manufactured by Vacuum Generators in accordance with our design specifications. Figure 7 reveals the experimental set-up of the system which must operate at pressures of $\sim 10^{-10}$ Torr. The chamber is pumped with an oil diffusion pump (Edwards EO6K with a pumping speed of 1350 l s^{-1}) which accommodates the pumping of both active and inert gases without memory effects.

The diffusion pump is also baffled by a liquid nitrogen trap to effectively eliminate backstreaming of the pump fluid. In addition, a titanium sublimation pump is incorporated in the services well of the chamber and is shrouded by a liquid nitrogen cooled cryopanel.

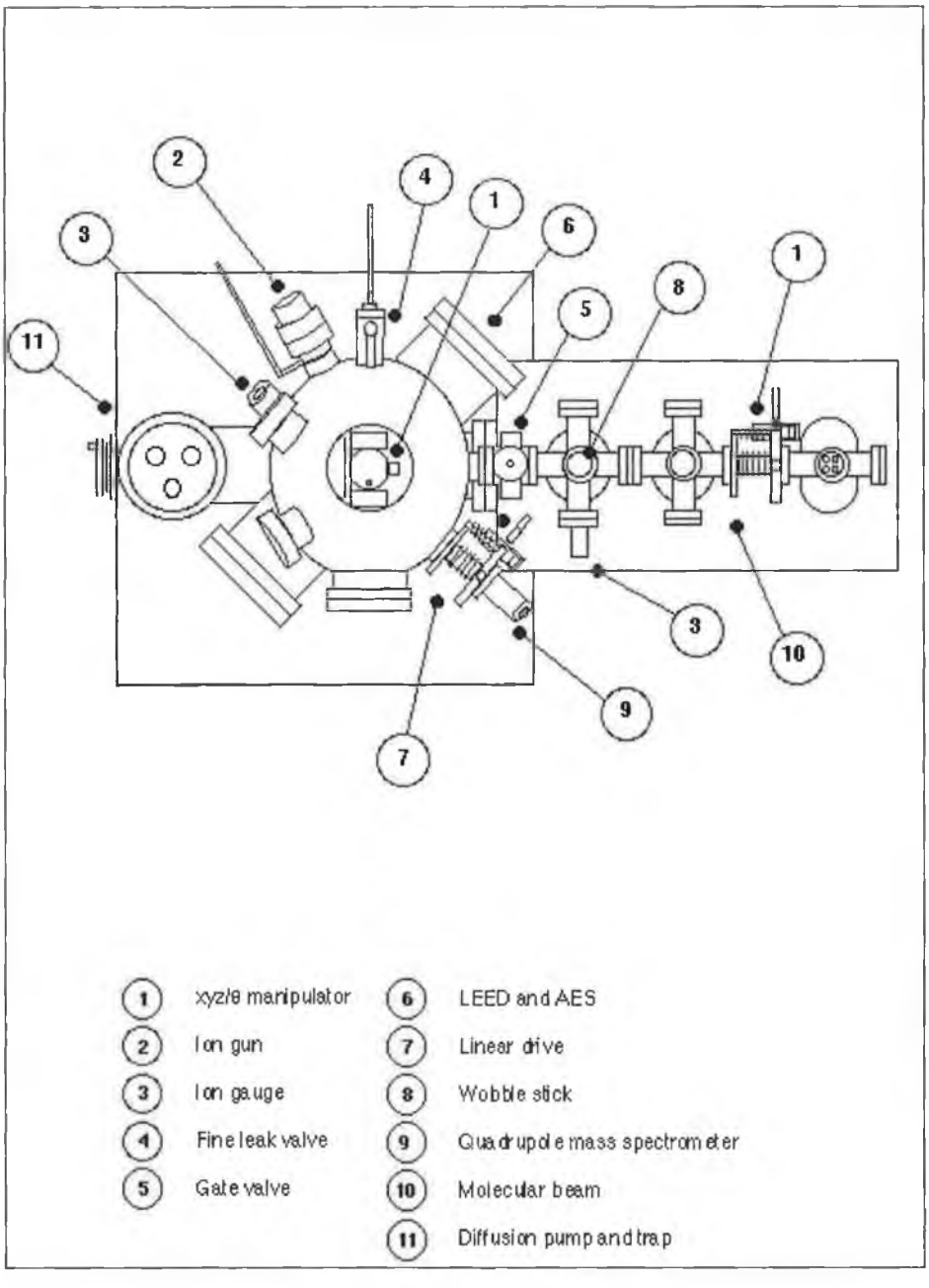

Figure 7: Schematic of the configuration of the molecular beam and main analysis chamber.

The sample is mounted on a high precision x-y-z manipulator (Huntington PM-600) which offers x-, y- and z- translation coupled with angular and azimuthal rotation. The sample may be resistively heated with sample temperature measurement made using a chromel-alumel thermocouple spot-welded to the sample. Sample cleaning is planned to be via argon ion bombardment.

3.3.1. Analytical techniques

In the beam system presented here we have added a novel yet simple aspect to the design in terms of the characterisation of the sample. Essentially, the techniques of low energy electron diffraction (LEED) and mass spectrometry (MS) are to be used in tandem i.e. facilitating the monitoring of changes in both the surface structure and reactivity simultaneously. Surface structure and reactivity are often interdependent. Figure 8 reveals this concept of simultaneous structure/reactivity measurements.
The mass spectrometer fitted to the chamber is a fixed Vacuum Generators (VG) Quasar quadrupole capable of monitoring several masses simultaneously. Improvements in the performance of the mass analyser could involve the mounting of a specially designed glass enclosure around the ionisation area of the mass analyser in accordance with Feulner and Menzel's design [16]. The advantage of the housing is to prevent the interaction of scattered molecules with the walls of the chamber and other devices such as pumps and ion gauges prior to detection. Improvement in the mass spectrometer signal to noise ratio is also seen with such an arrangement.

Before we continue and examine the experiments possible with this, let us point out the features of this simple thermal molecular beam. Firstly, the molecular beam source system is not expensive in surface science terms costing only ~£25,000, included in this is the x-y-z movement of the source, gate-valved differential turbo-molecular pumping and complete gauging of the system. The system allows access to the study of reaction rates and mechanisms both over model single crystal samples and real and model supported catalysts. Low source pressures allow the use of the low vapour pressure molecules such as formic acid. The compact nature of the system allows it to be utilised as a 'bolt-on' accessory adaptable to most surface science systems. The drawbacks in relation to the system include its limitation to use

at low pressures (low pumping capacity) excluding it from the examination of adsorption dynamics.

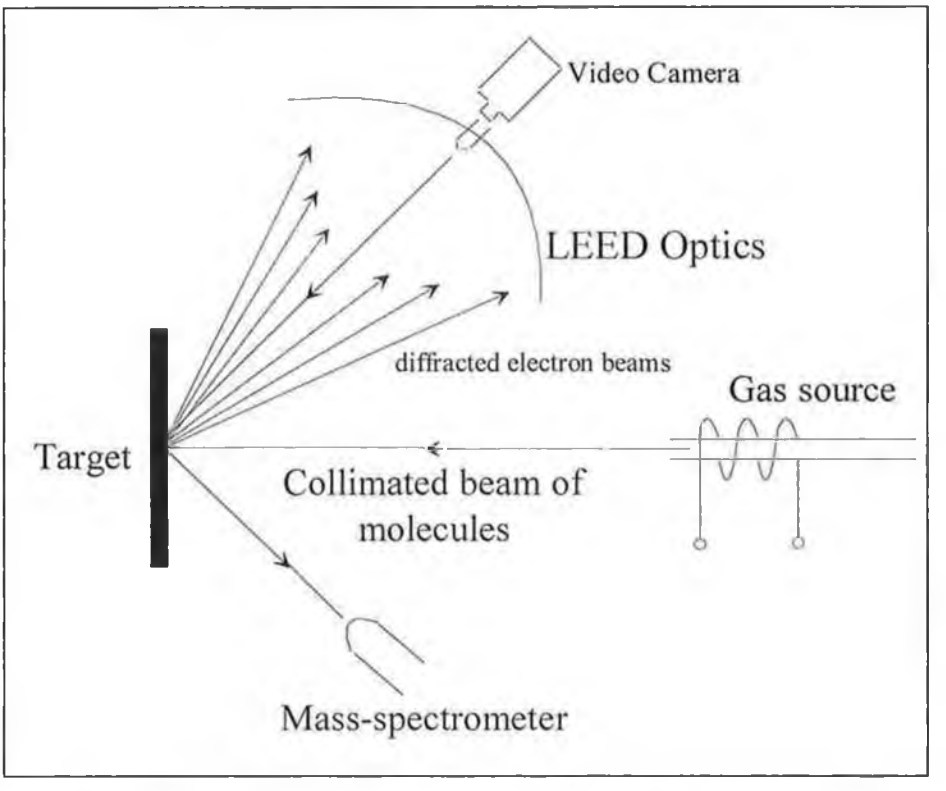

Figure 8: Schematic of molecular beam design allowing structural (LEED) and reactivity to be measured simultaneously.

4. Methodology

4.1. Sticking probability measurements

One of the most useful quantities measurable by the beam is the sticking probability allowing access to the adsorption rate dependence on sample surface coverage. The sticking probability (S) of a molecule is defined as the proportion of molecules striking the surface that successfully lead to adsorption (eqn. 4.1):

$$S = \frac{\text{rate of adsorption of molecules by the surface}}{\text{rate of collision of molecules with the surface}} \qquad 4.1$$

The sticking probability, S, is directly linked to the rate of adsorption R [17,18]. According to the kinetic theory of gases the rate of collision with the surface (Z) is given by:

$$Z = \frac{P}{\sqrt{2\pi\, MkT}} \qquad 4.2$$

where P is the pressure of adsorbing gas and M is the molecular mass of the gas. From this it is clear that the rate of adsorption $R(t)$ can be easily calculated from the following equation:

$$R(t) = S(\theta) \cdot \frac{P}{\sqrt{2\pi\, MkT}} \qquad 4.3$$

The methodology has been previously described by King and Wells [13,19]. The remarkable 1974 paper by King and Wells [19] introduced the now generally applied King and Wells method to determine sticking coefficients. The appeal of this technique is the ability to determine absolute values of sticking probabilities without the need for calibration.

The procedure is schematically represented in figure 9. With the beam blocker in place the background pressure of the gas is measured as a function of time. The beam is then unblocked and enters the chamber but is prevented from impinging on

the sample by a baffle. Once equilibrium within the chamber is reached, in terms of mass spectrometer signal (P_2), the sample is then exposed to the beam and molecules will be adsorbed, seen as a pressure drop to ($P_1(t)$). As the sample surface saturates with the gas, so the sticking diminishes until complete saturation occurs and no further adsorption takes place. The pressure will return to that seen (P_2) for beam impingement on an inert substrate and therefore total reflection (no adsorption). The surface behaves as a fast pump in the experiment and the tendency for it to adsorb particles is generally coverage dependent. The sticking probability at any particular adsorption time (t) may be calculated from the following equation:

$$S(t) = \frac{[P_2 - P_1(t)]}{P_2} \qquad 4.4$$

However, a more accurate method is to background subtract the data so that the partial pressure is zero before opening of the baffle and normalise the data to a pressure of unity, and then directly extrapolated the sticking probability (Figure 9).

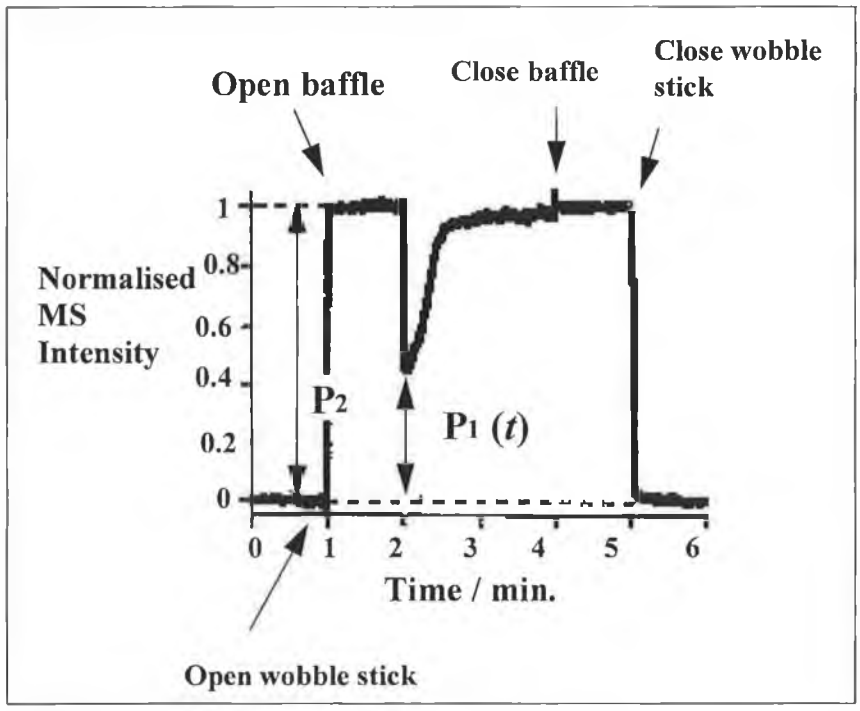

Figure 9: Example of experimental data illustrating the measurement of the sticking probability.

The corresponding surface coverage [$\theta(t)$] may be then determined provided that the beam flux (F) in molecules cm^{-2} s^{-1} is known, where:

$$\theta(t) = F \int_0^t S(t)\, dt \qquad 4.5$$

The integral in equation 4.5 is equal to the shaded area in figure 10. This figure indicates the evolution of pressure as a function of time for beaming onto two different samples. The dashed blue line illustrates the partial pressure of the system for beaming onto a surface with a time/coverage dependent sticking coefficient, while the black line represents that seen where the beam is incident upon an inert surface in which all molecules are reflected (no adsorption).

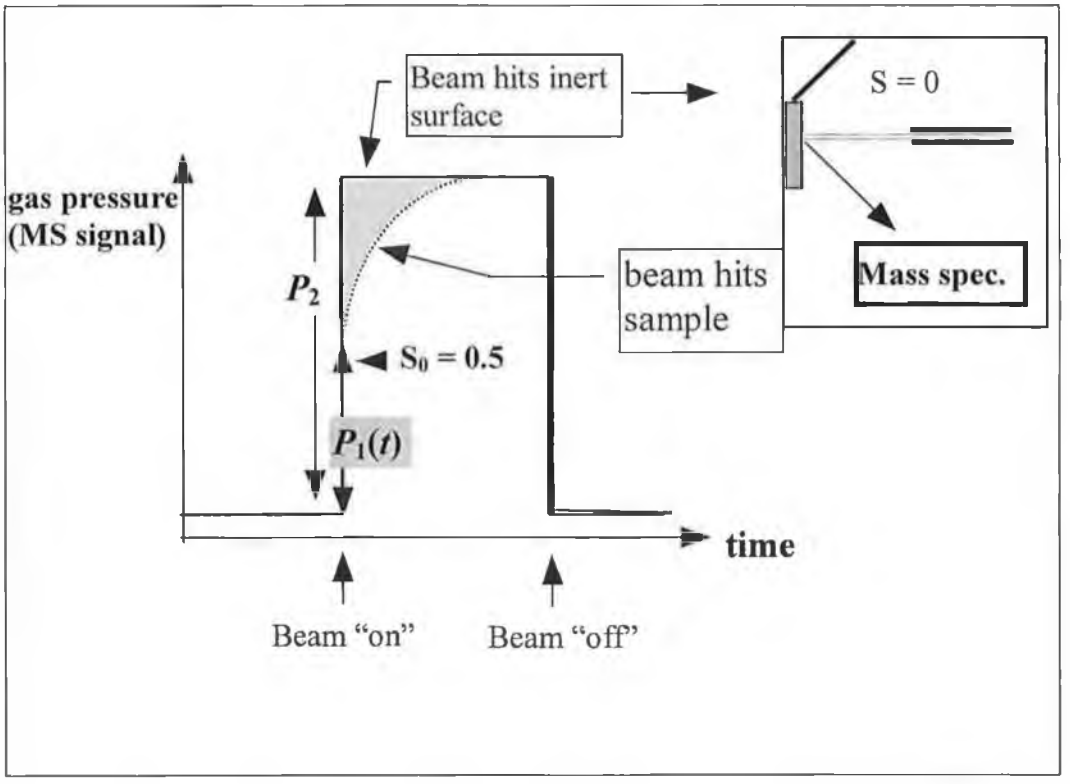

Figure 10: The measurement of beam sticking probabilities using the molecular beam method. S_0 is the sticking probability at zero surface coverage and is 0.5 in this case.

We have seen how we can calculate sticking probability as a function of time and how it is possible to calculate the corresponding surface coverage. This allows the plotting of sticking probability (S) versus surface coverage (θ) which can give information on the adsorption mechanism. In many cases the greater the number of vacant adsorption sites the greater the probability of adsorption. The simplest mechanism describing the adsorption process related to non-dissociative adsorption is known as Langmuir kinetics [20]. If this is obeyed a molecule incident on an empty surface site will adsorb with a sticking probability of S_0, whereas in the case that a molecule impinges on an already filled sight it will be reflected (S=0). Therefore the sticking probability is merely a function of the surface coverage (θ) and decreases linearly with θ:

$$S = S_0(1-\theta) \qquad 4.6$$

where S_0 is the initial sticking probability [21,22].

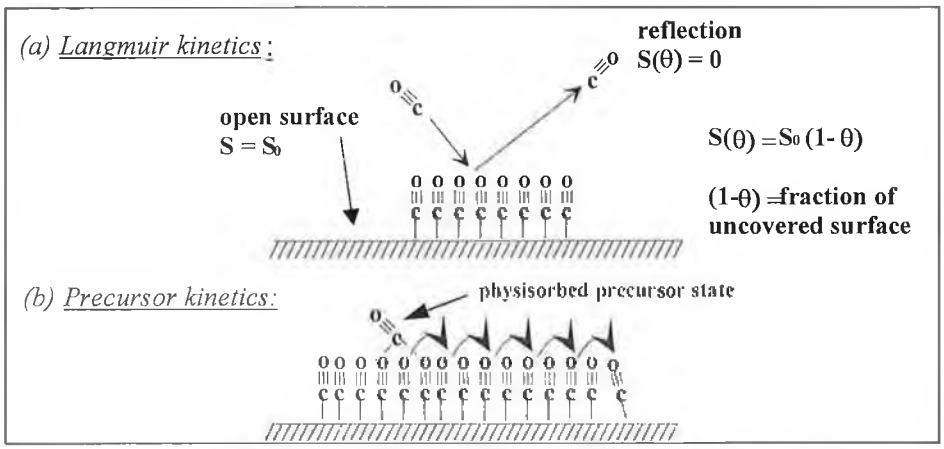

Figure 11: Langmuir and precursor adsorption kinetics.

It is seen that S in some cases behaves quite differently. A common adsorption mechanism involves the existence of a 'precursor' state. In such cases S remains constant or decreases slowly with increasing coverages with a rapid drop off in the sticking probability upon saturation. This adsorption scenario is quite common

[23,24] and was initially observed by Langmuir [20] before been further expanded by Kisliuk [25]. In this mechanism molecules incident on a filled site instead of rebounding, may initially become trapped on the surface in a weak physisorbed or 'precursor' state. The molecule may migrate along the surface (continuously losing energy) until it finds a vacant site and then become chemisorbed. Two separate types of precursor state have been identified. The first refers to a molecule physisorbed to a vacant site on the surface known as an "intrinsic precursor" and the second is the physical association of a molecule with a filled site i.e. an "extrinsic precursor" [26]. Figure 11 reveals the schematics of both Langmuir and precursor state adsorption.

Hence, within the precursor model the adsorbate is capable of migrating over both the empty and the filled sites on the surface until a favourable configuration for chemisorption is attained. Obviously the kinetics of precursor and Langmuir adsorption are quite different and the effect on the sticking probability with increasing surface coverage for both scenarios is illustrated in figure 12.

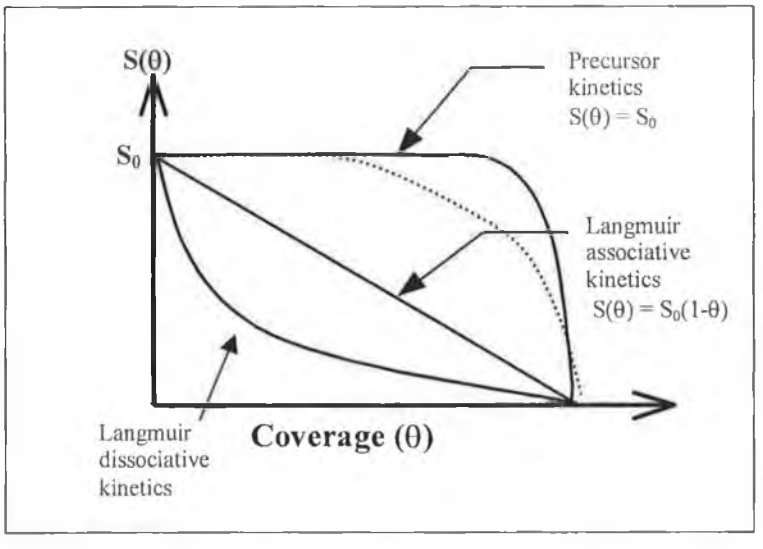

Figure 12: The variation of sticking probability with surface coverage for precursor, Langmuir associative and Langmuir dissociative adsorption in which the precursor lifetime is long compared to the diffusion length on the surface before adsorption. A shorter precursor lifetime would result in a faster deviation from S_0 (dotted line).

To quantify the effect of the precursor state on the adsorption kinetics, namely on the coverage dependence of $S(\theta)$, we initially consider the physical parameters the initial sticking probability depends on:

$$S_0 = \frac{\alpha\, k_c}{k_c + k_d} \tag{4.7}$$

where α is the trapping probability or condensation coefficient and is more clearly defined as the rate at which molecules colliding with the surface can lose their energy and become adsorbed, k_c and k_d are the rate constants for chemisorption and desorption from the intrinsic precursor state, respectively [24]. The trapping probability α is dependent on the translational and internal energy of the incident molecule and can be either dependent or independent on the surface temperature T_s. The rate constants k_c and k_d are only dependent on T_s (assuming trapping is complete).

In attempting to extend this theory to higher surface coverage, a number of other factors must be considered: whether the adsorption is molecular or dissociative, the dependence of α on coverage and the molecular interactions within the adsorbed layer. If we try and simplify the situation by assuming non-dissociative molecular adsorption and that α is independent of coverage, we obtain the following expression, referred to as the Kisliuk precursor model. This effectively relates the sticking probability to coverage by using a statistical approach for successive site adsorption and considering the adsorbed layer as a non-interacting lattice gas [22,24,25]

$$S(\theta, T_s) = S_0(T_s)\left(1 + \frac{\theta}{1-\theta} K\right)^{-1} \tag{4.8}$$

The precursor state parameter K is defined as:

$$K = \frac{(k_c + k_d + k_m)}{(k_c + k_d)} \cdot \frac{k'_d}{(k'_d + k'_m)} \tag{4.9}$$

where k_c, k_d and k_m are the rate constants for chemisorption, desorption and migration, respectively, from the intrinsic precursor state whereas k'_d and k'_m are the rate constants for desorption and migration from the extrinsic precursor state, respectively.

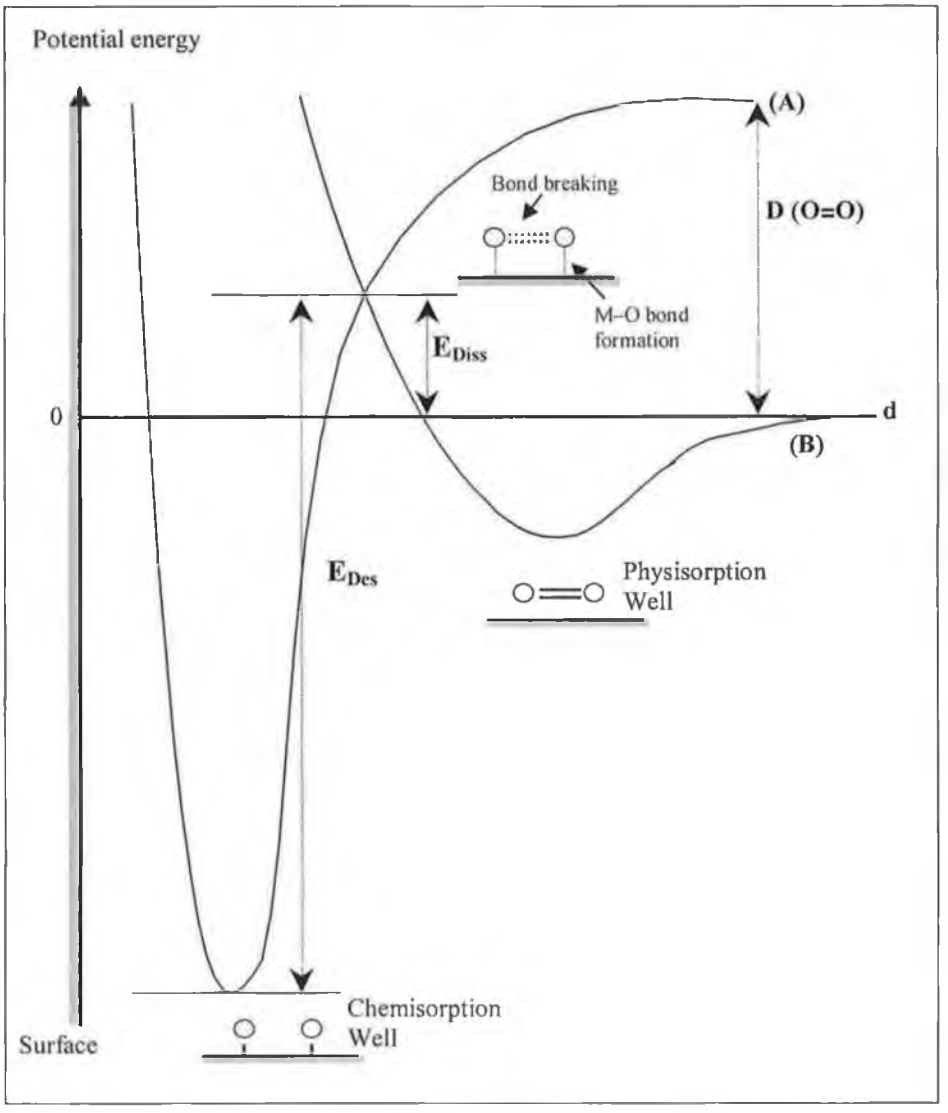

Figure 13: One-dimensional potential energy diagram for dissociative chemisorption [27].

The precursor state parameter K has a well-defined physical meaning. For values of $K<1$, the prediction based on the Kisliuk model yields an independence of the sticking probability on surface coverage, which has been experimentally observed for many adsorption systems [28]. We have indicated that if K is assumed to be less

than one, the factor $k'_d/(k'_d + k'_m)$ in equation 4.7 must be far less than one since (k_c + k_d + k_m)/(k_c + k_d) is always greater or equal to one. This means that the rate constant for desorption from the extrinsic precursor state is much smaller than the rate constant for migration from the extrinsic precursor state i.e. $k'_d << k'_m$. Hence, this provides evidence for the existence of the extrinsic precursor state [22,28].

For many systems energy is necessary to cleave or break a bond before sticking can occur, with sticking being an activated process. At low temperature the probability of sticking will be low, as most molecules do not possess the necessary energy to afford sticking. Variation of beam temperature allows us to probe the activation barrier. For example, as an oxygen molecule approaches a surface, it first enters a weak physisorbed state, however, for the molecule to proceed into the more thermodynamically favourable dissociative chemisorption state an activation energy barrier must be often overcome. The cross over between physisorption and chemisorption represents a state in which the molecular oxygen bond is partially broken and the surface–oxygen bond partially formed. Figure 13 is a one-dimensional plot of the potential energy versus reaction co-ordinate for the reaction:

$$O_{2(g)} \rightarrow O_{2(precursor)} \rightarrow 2O_{(ads)}$$

The interaction of the diatomic molecule with the surface is represented by curve B revealing that adsorption in a precursor state is a non-activated process. In the case of chemisorption (curve A) the activation barrier to dissociation (E_{Diss}) must be overcome. Figure 13 also reveals the energy needed for gas phase dissociation (D(O=O)) which is much larger than the barrier to dissociation via surface adsorption. The cross over of curves A and B lies above the energy zero. Non-activated adsorption is said to occur when the crossing lies below the energy zero.

The monitoring of sticking probability (dissociative adsorption) in such a system with increasing beam temperature will allow the activation energy for adsorption to be estimated. The zero-coverage sticking probability (S_0) generally follows an Arrhenius-type response. The initial sticking probability obeys the relationship:

$$S_0 = S' \exp\left(\frac{-E^a_{Diss}}{RT}\right) \qquad 4.10$$

where T is the absolute temperature of the incident gas molecules, $E_{\mathrm{Diss}}^{\mathrm{a}}$ the molar activation energy barrier to dissociation and S' is the sticking probability in the absence of an energy barrier. Hence measurement of S_0 for a range of temperatures allows the activation energy to be deduced via a plot of $\ln(S_0)$ versus 1/T:

$$\ln(S_0) = \ln(S') - \frac{E_{\mathrm{Diss}}^{\mathrm{a}}}{\mathrm{R}}\left(\frac{1}{T}\right). \qquad 4.11$$

4.2. Examples of sticking probability measurements

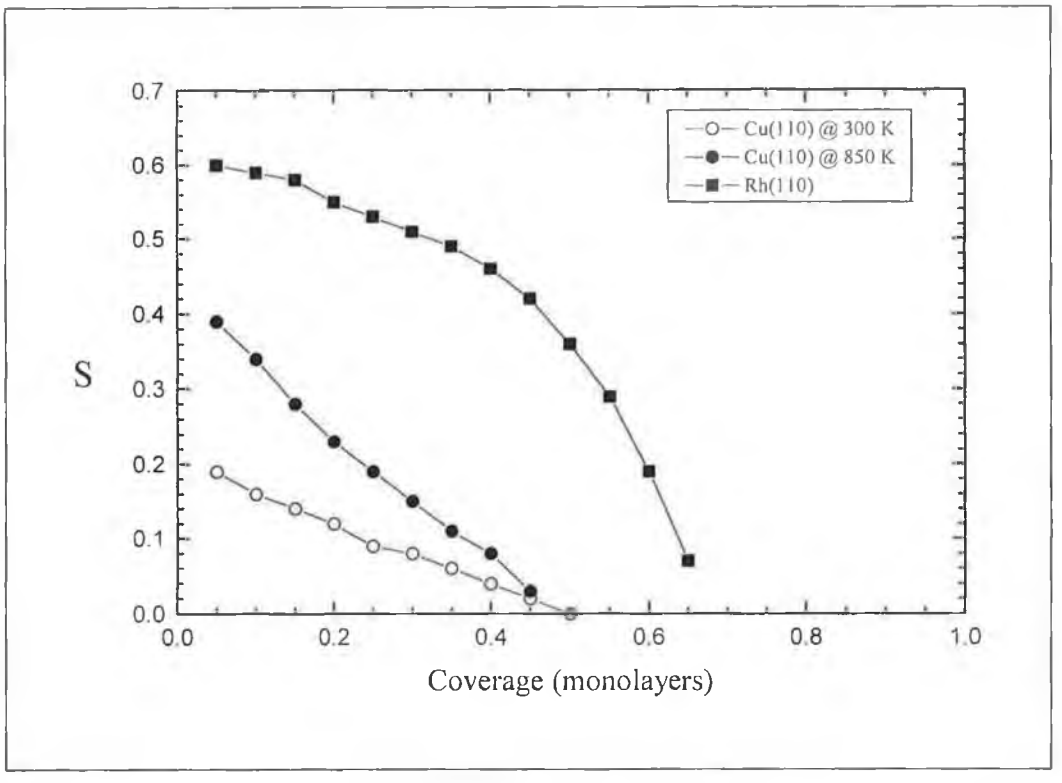

Figure. 14: The coverage dependence of the sticking probability for oxygen on Cu(110) [29] and Rh(110) [30].

The sticking probability for O_2 on Cu(110) has been well examined by Bowker et al [15,29] and has been compared to that on Rh(110) [30]. Figure 14 reveals the dependence of the sticking probability of O_2 on Cu(110) at two different beam temperatures. In the temperature range 300–650 K it is found that the initial sticking probability, S_0, is found to be independent of temperature. At higher temperature (~850 K) the zero coverage sticking probability increases to 0.4 from ~0.2 at 300 K. The interesting point is the linear dependence of the sticking on coverage even at high temperature where dissociative adsorption is known to occur. The adsorption kinetics thus do not follow either classical Langmuir dissociative or precursor behaviour. It is suggested that the strong islanding of oxygen occurs on the surface in the form of p(2×1) islands. In the case of Cu sticking (although dissociative) obeys Langmuir kinetics and is directly proportional to the coverage of un-oxidised Cu surface. The mechanism is believed to consist of the activated dissociation of the oxygen on the clean surface followed by migration to the edge of the growing p(2×1)

islands. This has indeed been observed by STM [31]. On the other hand O_2 sticking on Rh reveals little gas temperature dependence and the shape of the sticking curve suggests precursor mediated kinetics.

Previously the Kisliuk model in describing the precursor state kinetics of adsorption was described. Figure 15 reveals the CO sticking probability as a function of coverage (relative to the saturation coverage θ_{sat} = 1.0 ML) on Rh(110) [30]. Both the experimental curve and the theoretical curve generated using the Kisliuk precursor model (equation 4.8) are shown.

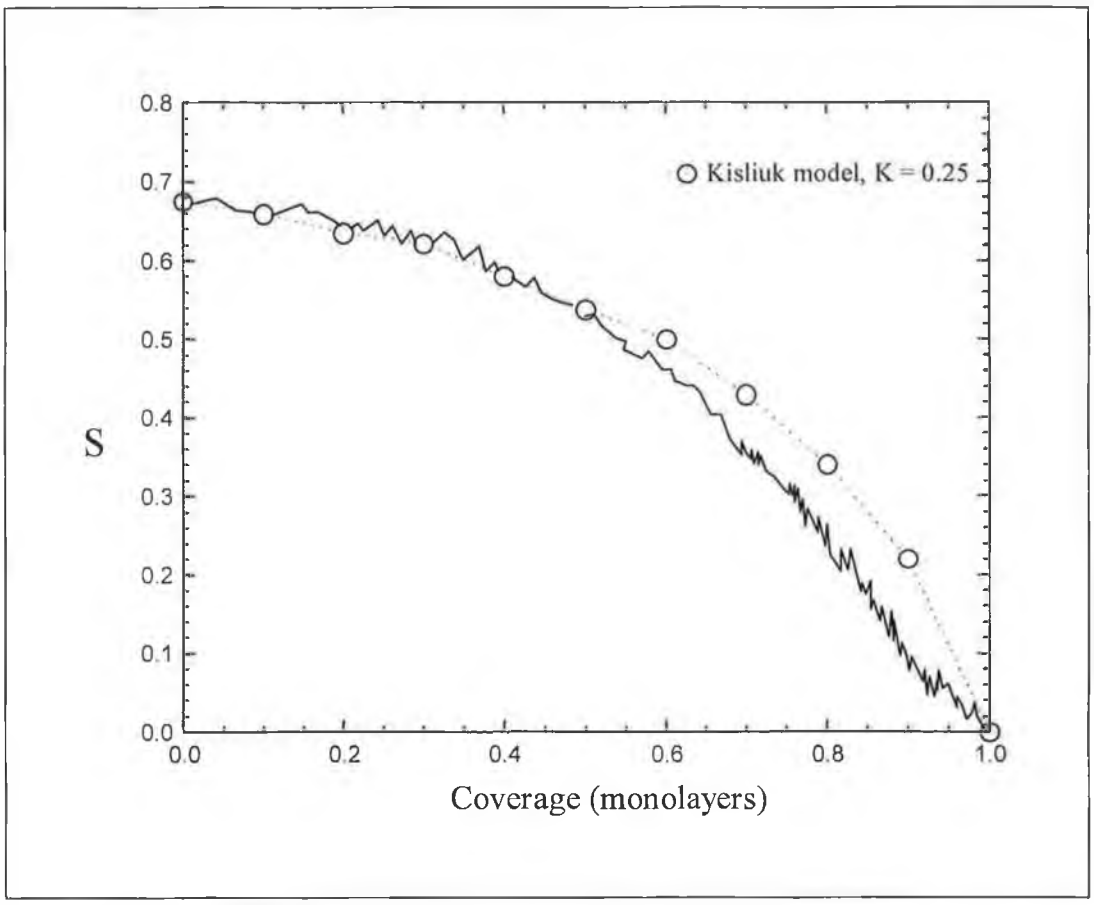

Figure 15: The dependence of CO sticking probability on surface coverage on Rh(110) at a surface temperature of 320 K. The solid curve represents the experimental data while the circles represent the modelled fit using the Kisliuk precursor kinetics with an optimised precursor state parameter of 0.25 [30,32].

Bowker [30] and Valden [32] are in good agreement regarding this mechanism of adsorption. Regarding initial sticking probability of CO on Rh(110) no dependence

on surface temperature was observed in the range 320–473 K the latter temperature corresponds to the desorption maximum of CO. This is quite confusing in terms of the precursor state models where it is necessary for the molecule to dump energy into the solid for adsorption to occur. Effectively, the existence of the intrinsic precursor state is directly related to the behaviour of the initial sticking as a function of surface temperature and energy of the incident molecules. In elevating the temperature of the surface initial sticking should be reduced as the 'hot' gas molecule in the precursor physisorbed state will not have time to dissipate energy before chemisorption. The most likely occurrence is that the excess thermal energy will result in desorption from the precursor state. We would therefore expect a decrease in sticking probability as the surface temperature increases [33]. However, this is not the case in CO adsorption on Rh(110). D'Evelyn et al [24] have proposed a theory regarding the nature of this precursor state. This "dynamical" precursor state, as it has been named, is suggested to require no secondary minimum in the gas-surface interaction potential, with it properties and lifetime determined only by the dynamics of the accommodation process. Hence, it is proposed that no surface temperature dependence of the sticking probability would be observed. Surprisingly, other surfaces have shown temperature independent sticking probabilities for CO including Ni(111) [34], Pd(111) [35], Pt(111) [23] and Ru(001).

4.3. Transient reaction studies

The inducement of transients is usually afforded through the variation of one or more of the independent variables of the system. In molecular beam studies the variation of surface temperature and/or reactant partial pressures are common examples of transients [36].

One extremely important reaction in automobile pollutant control is the oxidation of CO to CO_2. This is normally carried out using Pt and/or Pd catalysts although rhodium has often been used [37,38,39]. This is one of the fundamental reactions of the so-called 'three-way catalyst' (which consists of a mixture of Rh, Pt, and Pd supported on an oxide monolith). Figure 16 reveals the formation of transient CO_2 from CO oxidation on Rh(110) at 320 K, following predosing of oxygen. In carrying out this reaction scheme, Valden et al [32] followed the formation of CO_2 from

adsorbed CO and dissociated oxygen. The rate laws cannot be simply described in terms of reaction temperature as the rate constant is not fixed at constant temperature but is dependent on the surface concentrations of both species, which change as the reaction proceeds. Thus to obtain an in-depth understanding of the factors controlling reaction rate, a range of experiments at different adsorbate pre-coverages and substrate/beam temperatures is required.

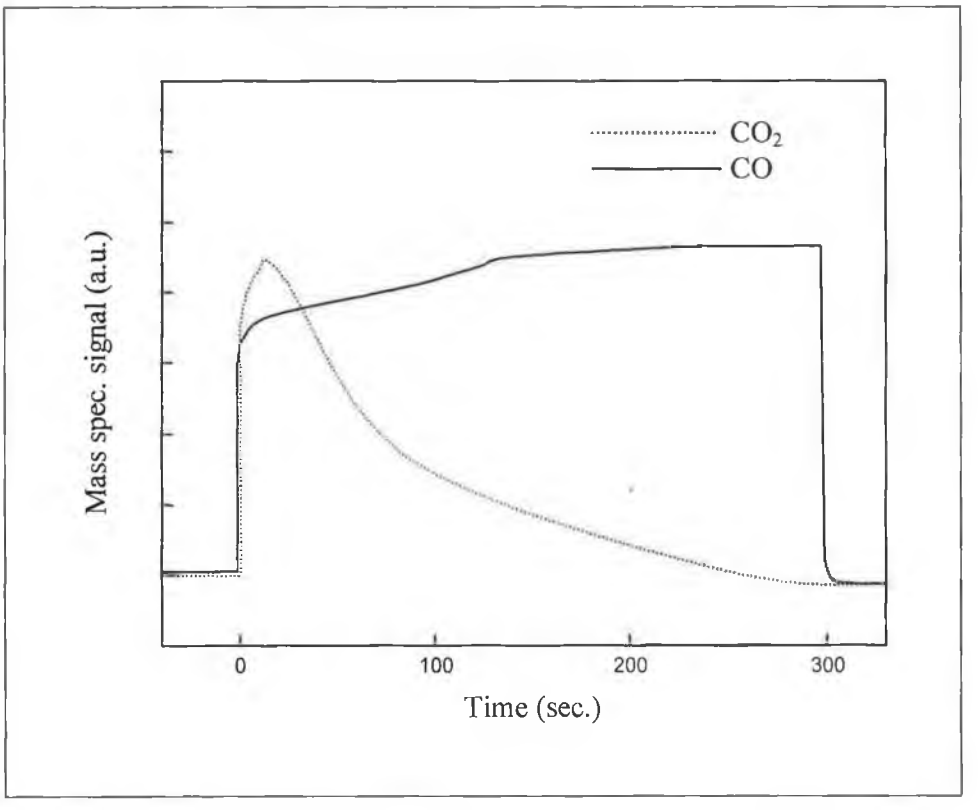

Figure 16: Molecular beam data for a transient reaction in which CO reacts with a pre-adsorbed layer of oxygen on Rh(110) at 320 K. Taken from [32].

The detailed kinetic rate law for CO oxidation obtained was:

$$R_{CO_2} = A\exp\left(\frac{-E_{LH}(\theta_O,\theta_{CO})}{RT}\right)\theta_O\theta_{CO} \qquad 4.12$$

where A is the pre-exponential factor and $E_{LH}(\theta_O,\theta_{CO})$ is the activation energy of the reaction which is a function of oxygen and CO coverages (LH = Langmuir-

Hinshelwood mechanism). The activation energy of the reaction is difficult to determine and changes as the lateral interaction between CO and oxygen changes with coverage. The further complication of the system is that oxygen is known to induce six different reconstructed phases on Rh(110) depending on coverage. Valden et al have examined transient CO_2 formation at 560 K as shown in figure 17.

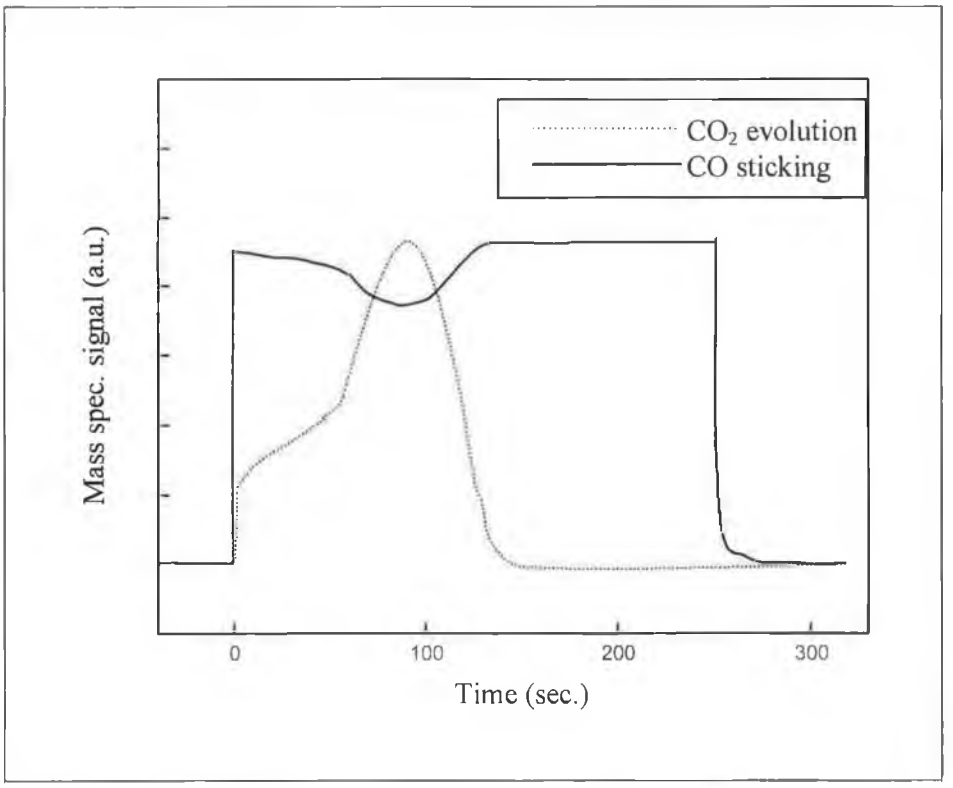

Figure 17: Molecular beam data for a transient reaction in which CO reacts with a pre-adsorbed layer of oxygen (θ_O = 0.68 ML) on Rh(110) at 560 K [32]. Note the induction time required until the CO_2 rate reaches its maximum.

It is obvious that the reaction scenario is completely different from that seen at 320 K. It is proposed that dosing the surface with oxygen, to a coverage of 0.68 ML, at 560 K results in a (100)-like surface (oxygen adsorption on Rh(110) can induce several different reconstructed phases depending on the oxygen coverage and the adsorption temperature as indicated by LEED analysis). It is thought that in this structure some of the oxygen resides in subsurface sites [40]. The evidence of an induction period for maximum rate of CO_2 production is due to only a small amount of oxygen being present initially on top of the Rh-layer. Once the top-layer oxygen

has been used, sub-surface oxygen will return to the surface for further CO_2 formation and affording a somewhat delayed maximum. Valden et al's work is in good agreement with the molecular beam studies of CO oxidation on Rh(110) carried out by Bowker et al [41,42].

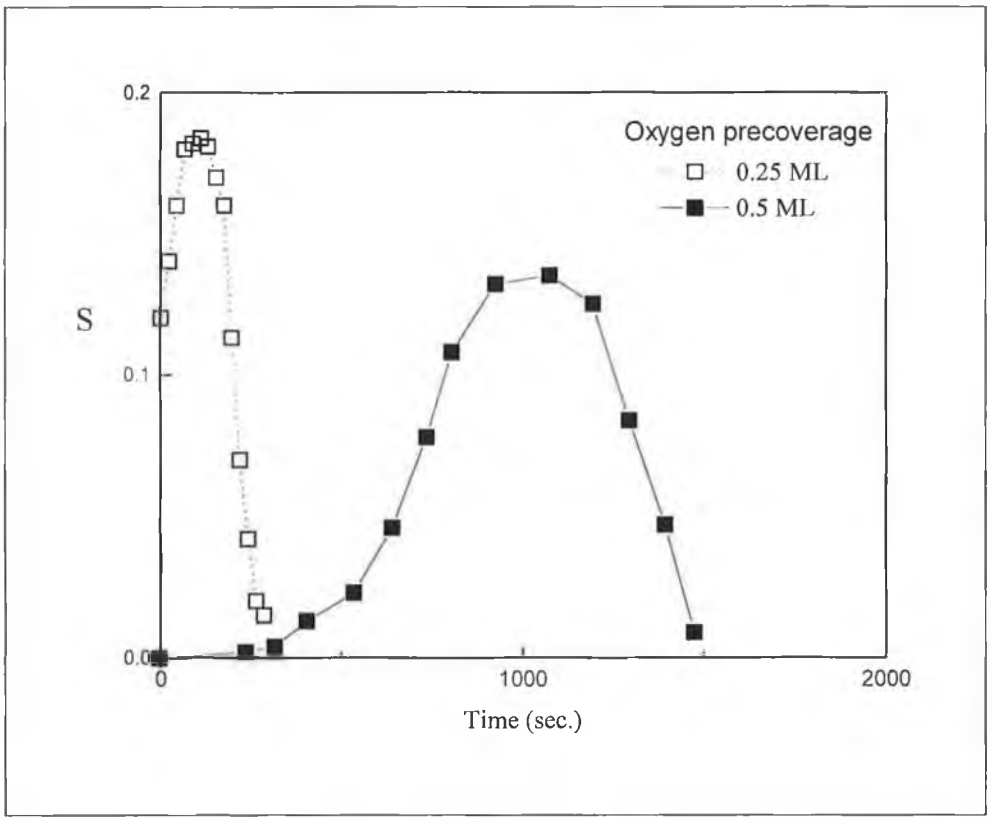

Figure 18: The sticking probability dependence on time for methanol reacting with two different coverages of pre-adsorbed oxygen on Cu(110) at 353 K. The induction period for the reaction is greater for the complete p(2×1) as well as taking far longer for the reaction to run to completion [43].

Another interesting reaction, although far more complex, is the production of formaldehyde by the oxidative dehydrogenation of methanol:

$$2CH_3OH + O_T \rightarrow 2H_2CO + H_2O + H_2 + O_V.$$

This catalytically relevant reaction seems to be considerably oxygen coverage dependent. Figure 18 compares data obtained at two different pre-coverages of

oxygen on Cu(110) [43]. O_T in the above equation is the active site (oxygen at the end of (2×1) Cu–O strings) and O_V is an oxygen vacancy formed by the loss of these terminal atoms.

The main products in this reaction are the H_2, H_2O and H_2CO. It is observed that methanol does not adsorb on clean Cu at these temperatures (353 K) while if oxygen is pre-dosed onto the surface methanol adsorption is promoted. However, if the oxygen pre-dosed coverage is high the reaction is poisoned. There is the suggestion that at low oxygen coverage specific oxygen sites are available for reaction, these have been assigned as oxygen atoms located at the edges of the (001) orientated p(2×1) islands which form even at very low oxygen coverages. The prevalence of these sites at low oxygen coverage is seen in the high initial methanol sticking probability while at higher coverages the concentration of these sites is reduced until a saturation p(2×1) structure results. This leads to the induction period for reaction seen for the 0.5 ML oxygen coverage where initially reaction only occurs at these step edges. The decomposition of a methoxy intermediate follows which in turn produces oxygen vacancies which act as nucleation sites for reaction. This process has been verified on the atomic scale by STM [44]. Kinetic modelling based on this scheme has also provided qualitative evidence for the proposed reaction mechanism.

4.4. Steady-state reactions – "mixed beam" techniques

Another scenario exists in which the two reactants are beamed simultaneously onto the surface. In this case there is a transient region where the reactant and the product coverages approach steady state and the adsorption and desorption rates become constant. The transient period varies in length, depending on the system and temperature of the reactants with longer transient times seen for lower temperatures (low reaction rate constants). Such measurements are isothermal with steady-state measurements possible at various temperatures. An alternative to variation of the beam temperature is the variation of sample temperature (pseudo-steady-state). The advantage of surface temperature variation is the speed at which changes can be made.

Steady-state studies are a natural progression from transient measurements. They involve mixing the reactant gas within the beam as opposed to pre-dosing. These studies allow true catalytic turnover to be monitored. In the case of CO oxidation, figure 19 reveals the reaction rate for a number of different temperatures [45]. According to Bowker et al the rate maximum is evidence of high CO adsorption with the temperature of maximum rate being a balance between the CO residence time on the surface and the need for a sufficiently high temperature to activate the CO/O reaction. Increasing the temperature causes rapid CO desorption with oxygen the main surface component and little CO_2 formation resulting.

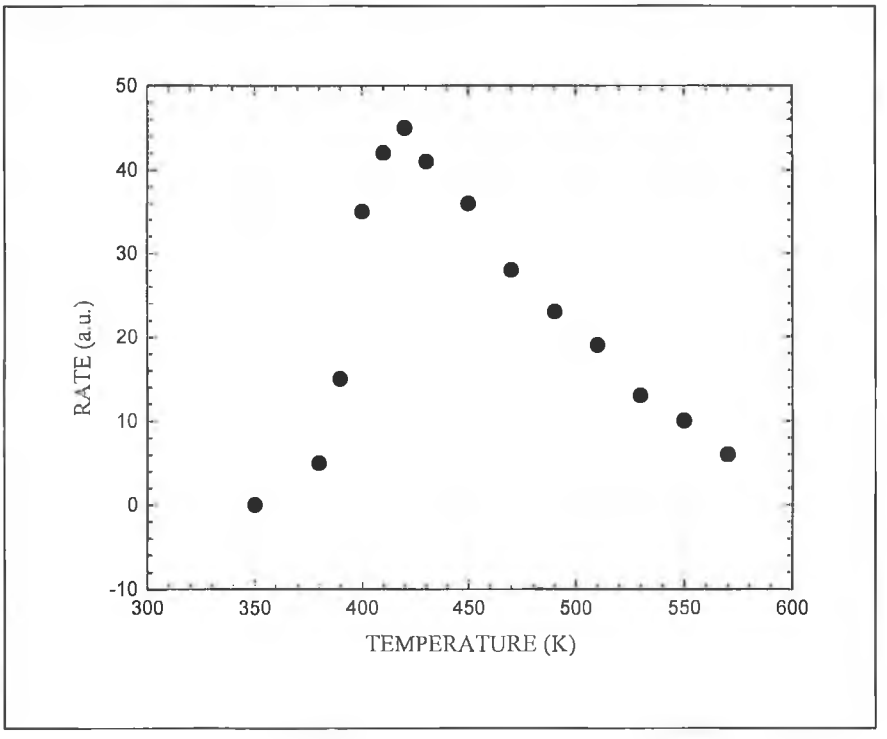

Figure 19: Steady-state measurements of the rate of CO_2 production from a mixed beam of CO and O_2 impinging on Rh(110) for a range of substrate temperatures [45].

5. Conclusions

In this chapter the principles and considerations necessary in the design and construction of a low cost simple thermal molecular beam scattering system have been presented. Furthermore, we have introduced the fundamentals of molecular beam technology and their physical properties.

Molecular beam technology has and continues to be applied to a range of catalytic reactions of practical interest, and helps in the understanding of the elementary steps which make up a catalytic reaction mechanism. The capabilities of the system designed and constructed here include the accurate measurement of sticking probabilities and their dependence on surface coverage; determination of activation barriers to adsorption by gas temperature variations; and for reactive scattering measurements to determine reaction probabilities, mechanistic pathways, and the kinetics of surface reactions. These capabilities have been illustrated with suitable examples.

References

[1] L. Dunoyer, Comptes Rend., 152 (1911) 594.

[2] N. Ramsey, Molecular Beams, Oxford, Oxford University Press, (1956).

[3] O. Stern and W. Gerlach, Z. Phys., 8 (1922) 349.

[4] J. A. Barker and D. J. Auerbach, Surf. Sci. Rep., 4 (1985) 1.

[5] A. Kantrowitz and J. Grey, Rev. Sci. Instr., 22 (1951) 328.

[6] E. W. Becker and K. Bier, Z. Naturforsh, 9a (1954) 975.

[7] A. Roth, Vacuum Technology, North-Holland, (1976).

[8] J. Wang, V. A. Shamamian, B. R. Thomas, J. M. Wilkinson, J. Riley, C. F. Giese and W. R. Gentry, Phys. Rev. Lett., 60 (1988) 696.

[9] J. B. Anderson, R. P. Andres and J. B. Fenn, Adv. Chem. Phys., 10 (1966) 275.

[10] D. P. Woodruff and T. A. Delchar, Modern Techniques of Surface Science, Eds. R.W. Cahn, E. A. Davies and I. M. Ward, Cambridge University Press, (1986).

[11] N. Abuaf, J. B. Anderson, R. P. Andres, J. B. Fenn and D. G. H. Mardsen, Science, 155 (1967) 997.

[12] H. F. Winters, H. Coufal, C. T. Rettner and D. S. Bethune, Phys. Rev. B, 41 (1990) 6240.

[13] D. A. King and M. Wells, Surf. Sci., 29 (1972) 454.

[14] M. Bowker and D. A. King, Surf. Sci., 94 (1980) 564.

[15] M. Bowker, P. Pudney and C. J. Barnes, J. Vac. Sci. Technol. A., 8 (1990) 816.

[16] P. Feulner and D. Menzel, J. Vac. Sci. Technol., 17 (1980) 662.

[17] D. A. King, CRC Crit. Rev. Solid State Sci., 7 (1978) 167.

[18] D. O. Hayward and B. M. Tapnell, Chemisorption, Butterworths, London, (1964).

[19] D. A. King and M. W. Wells, Proc. Roy. Soc. London, Ser. A, 339 (1974) 245.

[20] I. Langmuir, J. Am. Chem. Soc., 40 (1918) 1361.

[21] J. B. Taylor and I. Langmuir, Phys. Rev., 44 (1933) 23.

[22] S. L. Tang, J. D. Beckerle, M. B. Lee and S. T. Leyer, J. Chem. Phys., 84 (1986) 6488.

[23] C. T. Campbell, G. Ertl and J. Segner, Surf. Sci., 107 (1981) 207.

[24] M. P. D'Evelyn, H. P. Steinruck and R. J. Madix, Surf. Sci., 180 (1987) 47.

[25] P. J. Kisliuk, J. Phys. Chem. Solids, 3 (1957) 95.

[26] H. J. Kreuzer and Z. W. Gortel, Physisorption Kinetics, Vol. 1, Springer Verlag, (1986).

[27] G. Attard and C. Barnes, Oxford Chemistry Primers: Surfaces, Oxford Science Publications, (1998).

[28] W. H. Weinberg, C. M. Comrie and R. M. Lambert, J. Catal., 41 (1976) 489.

[29] P. Pudney and M. Bowker, Chem. Phys. Lett., 171 (1990) 373.

[30] M. Bowker, Q. Guo and R. W. Joyner, Surf. Sci., 253 (1991) 33.

[31] D. Coulman, J. Wintterlin, R. Behm and G. Ertl, Phys. Rev. Lett., 64 (1990) 1761.

[32] M. Valden, Licentiate Thesis, Molecular Beam-Surface Scattering Studies of the Gas-Surface Interaction, (1993).

[33] A. Zangwill, Physics at Surfaces, Cambridge University Press, Cambridge, (1988).

[34] J. C. Campuzano, R. Dus and R. G. Greenler, Surf. Sci., 102 (1982) 172.

[35] T. Engel, J. Chem. Phys., 69 (1978) 373.

[36] J. R. Creighton and J. M. White, Catalysis Under Transient Conditions, Eds. A. T. Bell and L. Hegdus, Amer. Chem. Soc., Washington, DC, (1982) Chap. 2.

[37] M. Bowker, Q. Guo, Y. Li and R. W. Joyner, J. Chem. Soc. Faraday Trans., 91 (1995) 3663.

[38] T. Engel and G. Ertl, Adv. Catalysis, 28 (1979) 1.

[39] C. T. Campbell, S. K. Shi and J. M. White, Appl. Surf. Sci., 2 (1979) 382.

[40] M. Bowker, Q. Guo, P. Pudney and R. W. Joyner, Catalysis and Automotive Pollution Control II, (1991) 409.

[41] Q. Guo, R. W. Joyner and M. Bowker, J. Phys.: Condens. Matter, 3 (1991) 55.

[42] M. Bowker, Q. Guo and R. W. Joyner, Catalysis Today, 10 (1991) 409.

[43] S. Francis, F. Leibsle, S. Haq, N. Xian and M. Bowker, Surf. Sci., 315 (1994) 284.

[44] F. Leibsle, S. Francis, S. Haq, X. Nign and M. Bowker, Phys. Rev. Lett., 72 (1994) 2569.

[45] M. Bowker, Q. Guo and R. W. Joyner, Surf. Sci., 280 (1993) 50.

Appendix B

An Experimental Investigation of the Radio Frequency Plasma-Induced Modification of the Surface Morphology of Graphite

1. Introduction

The interaction of plasmas with solid surfaces plays a key role in many applications including many economically relevant industrial processes, i.e., dry etching of polymers and resist removal of semiconductors. It is generally regarded that the central scientific problem underlying plasma processing concerns the interaction of the plasma with solid surfaces [1]. To date plasma treatment is regarded as probably the most versatile surface treatment technique. Different types of gases such as argon, oxygen, nitrogen, fluorine, carbon dioxide, and water can produce unique surface properties required by various applications, i.e., metal hardening, and paper/fabric treatment. Of further interest is the fact that plasma modification is usually confined to the top several hundred Ångstroms and does not alter bulk properties. The necessity for a vacuum environment also endears plasma technology to the surface scientist, however, at present surface science studies on plasma-surface interactions are hampered by the fact that plasmas and well defined and controlled surfaces require different environments: mTorr to Torr pressures for generation of plasmas and UHV for the in situ study of surface processes, (excluding optical methods).

Formation of model cluster catalysts with high dispersion, by vacuum deposition of metal onto single crystal surfaces, has met with many problems. The highly mobile nature of these catalysts on the substrate surface along with the lubricating nature of many substrates (e.g. HOPG) combine in causing the catalyst particles to coalesce and agglomerate into large islands ("Ostwald-Ripening"), in effect severely reducing their efficiency. The defects present on the surface of HOPG including atomic steps and those resulting from the cleavage mechanism i.e. cleavage steps and graphitic debris help to reduce this process by providing nucleation sites for cluster growth. However, these defects are not widespread on the surface of high-quality single crystal graphite required as substrates in model surface science studies. Real-time STM studies have revealed the highly mobile nature of such systems with the continuous diffusion of clusters in and out of scanned areas.

Damaging the graphite basal plane offers a means of creating the necessary nucleation centres for cluster growth. Ion or electron bombardment techniques are the most commonly used, allowing the production of highly specific and efficient

catalysts consisting of mostly small clusters of a few nanometres in diameter. Plasma processing is interesting in this respect for a number of reasons. Firstly, the surface modification can be varied by changing the etching gas, with both physical etching and chemical etching possible. Secondly, surface modification is fairly uniform over the whole surface and, finally, subtle variations in plasma parameters are possible i.e. RF volume, RF frequency, power level, gas flow rate, gas composition, gas pressure, sample temperature, and reactor geometry. It should be noted, however, that plasma processing is quite complicated with difficulties arising in achieving a good understanding of the interactions between the plasma and the surface.

In this study it is hoped that the use of glow discharges (plasmas), both reactive and non-reactive, may offer an alternative controllable route of producing reproducible nucleation sites on the graphite surface, hence offering a means of controlling catalyst cluster size. This may prevent, to some extent at least, the coalescence of mobile clusters into larger particles as seen on the basal plane of freshly cleaved HOPG. This alteration in cluster morphology may provide valuable information relevant to the possible enhancement of both catalyst reactivity and selectivity.

2. Plasmas (glow discharges)

Gas discharge plasmas have been the subject of study for well over a hundred years. Scientists such as Michael Faraday, James Clerk Maxwell, J. J. Thomson, Ernest Rutherford, J. S. E. Townsend, and Irving Langmuir, to name but a few, have contributed greatly to our understanding of gas discharge phenomena. It is also of interest that the development of atomic physics was synonymous with gas discharge physics.

Although plasma fusion and space plasma science continue to dominate plasma physics, non-equilibrium glow discharge plasma interest has never been greater. It is estimated that up to ~30% of all process steps in the manufacture of integrated circuits involve plasmas in one way or another. Plasma etching initially used as a direct replacement of liquid etching underwent rapid growth during the late 1970's, early 1980's and has become indispensable in semiconductor chip manufacture.

2.1. Generation and general properties

Plasmas, often referred to as the fourth state of matter, are constituted of charged and neutral species. The charged species are predominantly positive ions and electrons; a contribution from negative ions is only present in plasmas of electronegative species. The neutral species are atoms and molecules in the respective ground states or attainable excited states.

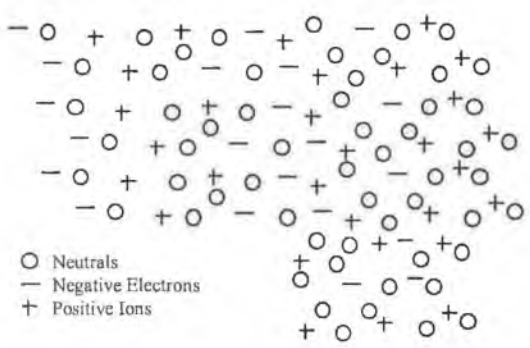

Neutrals: $m = 6.6 \times 10^{-23}$ g
$T = 20\ ^{\circ}C = 293\ K \cong 0.025$ eV
mean speed = $\bar{c} = 4.0 \times 10^{2}$ m/sec

Ions: $m_i = 6.6 \times 10^{-23}$ g
$T_i = 500\ K \cong 0.04$ eV
$\bar{c}_i = 5.2 \times 10^{2}$ m/sec

Electrons: $m_e = 9.1 \times 10^{-28}$ g
$T_e = 23\,200\ K \cong 2$ eV
$\bar{c}_e = 9.5 \times 10^{5}$ m/sec

$$\bar{c} = \left(\frac{8kT}{\pi m}\right)^{\frac{1}{2}}$$

Figure 1: Typical parameter values for an argon glow discharge plasma.

In low pressure plasmas addressed here, collisions between neutrals and energetic electrons produce the ions. The application of an external electric field supplies the energy to accelerate electrons (easily achieved due to their small mass). Even at a small mean free path length an inelastic collision between an energetic electron and a neutral is an effective process and will result in ionisation. On the other hand, energy

extraction by ions is a slow process so that their contribution to ionisation through inelastic ion–neutral collisions can be neglected. Figure 1 shows typical values for the different constituents of such a discharge.

It is important to note, that unlike elastic collisions between particles of masses *m* and *M*, in inelastic collisions the mass ratio of the colliding particles is not relevant for energy transfer. Essentially, elastic collisions (momentum-transfer collisions) involving electrons and ions tend to restrict electron velocity in the direction of the field. Use of the collisional cross-section concept to describe the probability of elastic collision of an argon atom with a 15 eV electron predicts that at 10 mTorr (3.54×10^{14} atoms/cc) the probability of elastic collision is 0.89 cm^{-1}. In terms of inelastic collisions provided that the electrons energy is above certain thresholds for excitation, ionisation or dissociation of a neutral, electrons effectively excite target particles. For example, the threshold energy for an electron to ionise an argon atom is 15.7 eV with the acceleration and subsequent energy gain of the removed electron by the powering electric field allowing it to partake in further ionisation. It is this multiplication process which maintains a glow discharge. Photon excitation of atoms also occurs.

Ionisation of an atom involves the removal of an electron from the atom. The removal of an electron in such a collision results in a positive ion and two electrons. Excitation on the other hand merely involves the excitation of an electron into a higher energy level, somewhat of a less dramatic energy transfer than ionisation. The minimum energy of excitation of argon is 11.56 eV. Further excitation of an excited state may lead to ionisation since the excited electron is less tightly bound. Metastable states are also produced during excitation and may have lifetimes of greater than 1 ms. For argon, the threshold for their production is 11.7 eV.

Other important plasma processes are discussed below:

Recombination:

$$X^+ + A + e^- \rightarrow X + A$$

The recombination process is simply a reversal of ionisation. However, it does not happen as we would expect, by a simple ion–electron collision/coalescence. There is

generally a third party involved which can be an atom, electron or even the chamber wall (A).

Examining more closely the role of the chamber walls, we realise just how important they are. Basically they could be described as catalysts speeding up certain reactions that would otherwise proceed many orders of magnitude slower. Examples of such reactions include the recombination of atoms:

$$\mathbf{H + H \xrightarrow{wall} H_2},$$

the neutralisation of charged particles:

$$\mathbf{H_n^+ (n = 1,2, \text{ or } 3) \xrightarrow{wall} neutrals},$$

and relaxation of internal energy in $\mathbf{H_2}$,

$$\mathbf{H_2(v'', j'') \xrightarrow{wall} H_2(v', j')},$$

where **v"** and **j"** are respectively the vibrational and rotational excitation states of hydrogen.

Relaxation:

$$X^* \rightarrow X + h\nu$$

The glow from a plasma discharge is a consequence of the electronic de-excitation of atoms and molecules. The process involves the emission of a photon of energy whose frequency is equal to the difference in the excited and ground electron energy states.

Other collisional processes

These processes include dissociation, electron attachment and ion-neutral collisions. Dissociation of a molecule can result in either neutral or charged particles. The latter process more frequently defined as dissociative ionisation.

Electron attachment in noble gases is unknown owing to their inherent stability (filled outer electron shell). On the other hand, halogens have a tendency to form

negative ions as their outer electron states are unfilled. The rate of dissociative attachment of electrons to hydrogen molecules is dependent on the excited state of $\mathbf{H_2}$ [2,3,4],

$$\mathbf{e^- + H_2(v'') \rightarrow H^- + H.}$$

For neutral molecules in very high vibrationally excited states (**v"≈ 9**) the reaction proceeds 10^5 times quicker than for **v" = 0** states. For deuterium the corresponding factor is $> 10^7$.

2.2. Plasma characteristics

Various physical quantities are used to characterise the state of a plasma, of which density and temperature are the most important. It is generally important as a rule to determine plasma parameters such as plasma potential, V_p, the electron and ion number densities, n_e and n_i, and the effective electron temperature, T_e, for a given set of discharge conditions so as to allow the reproducible transfer of plasma processes from one reactor to another.

The strong Coulomb interaction warrants that the charge corrected densities of charged species must be equal in sufficiently big volume elements in the plasma i.e. $n_e = n_i$. A measure of the size of volumes in which deviations from this neutrality can occur is given by the Debye length. The Debye length is a physical length, typically ~100 μm, in a plasma described as follows: from the perspective of a particular point in the plasma, we need to consider the sum of the individual interactions with all of the other charged particles contained within a sphere centred on a particular point having a radius of one or two Debye lengths. Outside of this sphere, the detailed nature of the plasma becomes immaterial and the net interaction is zero. Hence, the unperturbed plasma is equipotential except for small fluctuating voltages which are attenuated over distances of the order of a Debye length [5]. In other words the Debye length (λ_d) defines the scale length of departure from neutrality:

$$\lambda_d = \left(\frac{kT_e \varepsilon_0}{n_e e^2} \right)^{\frac{1}{2}}$$

where ε_0 is the vacuum permittivity and e is the electron charge. The electrons have a Maxwellian distribution characterised by the mean energy kT_e.

Another important phenomenon in plasmas is the sheath potential, which has a significant effect in the interaction of plasmas with surfaces. In the situation of a plasma in contact with a conducting plate, electrons which have a higher velocity than ions tend to reach the surface more frequently than ions. It is seen that the potential of the plasma is always positive with respect to the potential of a conducting plate (walls of the chamber or electrodes). The region in which the potential drops from the plasma potential to the plate potential is called the sheath and the potential drop is referred to as the sheath potential. Sheath potentials can achieve values in the range of 100 eV. This potential difference extends over a few Debye lengths, typically from a fraction of a mm to several mm.

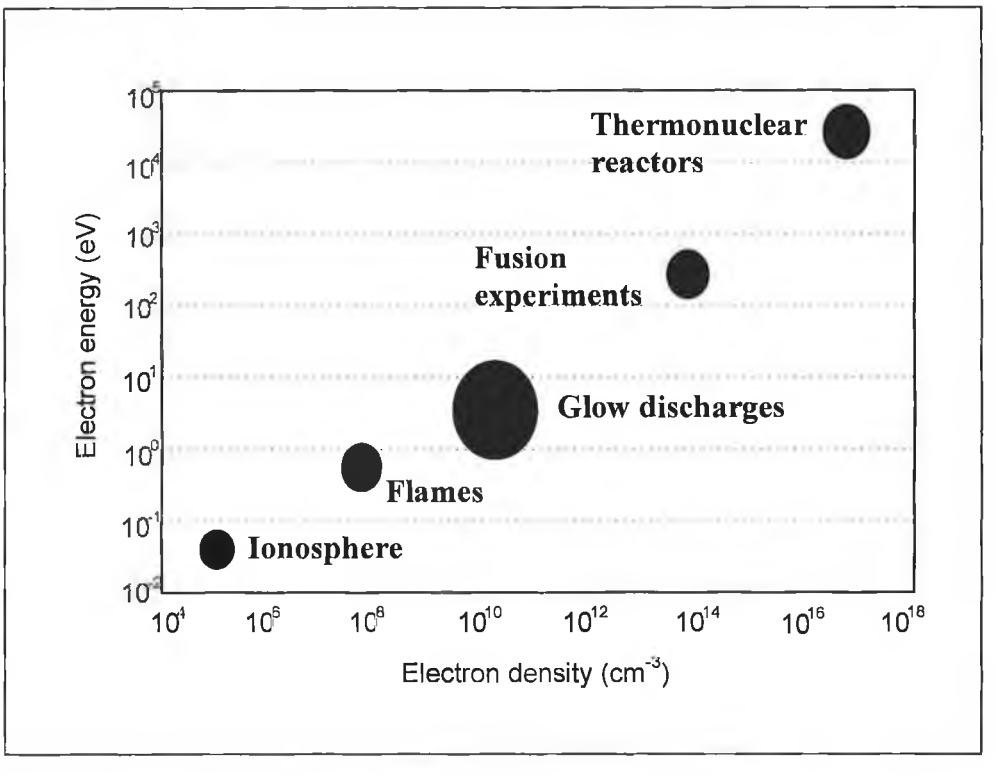

Figure 2: Electron density versus electron energy for a variety of plasmas. Laboratory and industrial plasmas are summarised as glow discharges.

If the potential at the plate is only due to the plasma characteristics, one calls the plate negatively self-biased. On the other hand the application of an external voltage allows the manipulation of the energies of the ions impacting the surface, their energy determined by the sheath potential or bias potential rather than their temperature in the plasma. Accordingly, a proper arrangement of potentials at plasma facing surfaces enables one to manipulate energies of particles which are of interest in plasma-surface interaction over a wide range and allows specific surface processes to be promoted or suppressed. Of these processes physical sputtering proceeding simultaneously with neutral particle/surface reactions is the most important.

The most convenient method of plasma classification is with two parameters, electron temperature, T_e, and electron density, n_e. These quantities are often referred to as plasma temperature and plasma density. Figure 2 reveals the classification of all known plasma types using these criteria.

Plasmas with very small densities and small energies are found in the ionosphere, starting about 50 km above sea level. These plasmas are generally fully ionised. Laboratory plasmas exhibit much higher electron temperatures than ion temperatures, $T_e \gg T_i$, and are non-equillibrium plasmas with the ratio of ions to neutrals of between 10^{-6} and 10^{-2}. Fusion plasmas, on the other hand , are almost equilibrium plasmas i.e. $T_e = T_i$, and are fully ionised. Due to this difference, laboratory plasmas with low ion energies are often called cold or low temperature plasmas, whereas fusion plasmas are called hot plasmas.

2.3. Radio frequency (RF) plasmas

Damage to a surface in a plasma is due to either of two mechanisms: – reactive ion etching (RIE), physical etching commonly known as 'plasma etching' or both. The basis of RIE is quite simple: use of a molecular gas glow discharge to dissociate relatively stable molecules forming chemically reactive atoms and/or molecular radicals, these species subsequently react with the solid to be etched. RIE is a predominantly chemical process accompanied by the simultaneous energetic ion bombardment of the processed surface. On the other hand physical etching, as its name suggests, is basically a physical effect with no chemical interaction between the surface and the plasma components. In this process damage to the surface is

mainly caused by ion-bombardment otherwise known as "sputtering", this essentially involves knocking an atom or cluster of atoms out of the surface of a target by impact of a chemically unreactive incident ion such as a noble gas ion. By repeating this process over and over we sputter etch the target surface, for example to clean it or to make it thinner, or selectively to generate a topographic pattern on the surface. Figure 3 illustrates all the possibilities within such a technique.

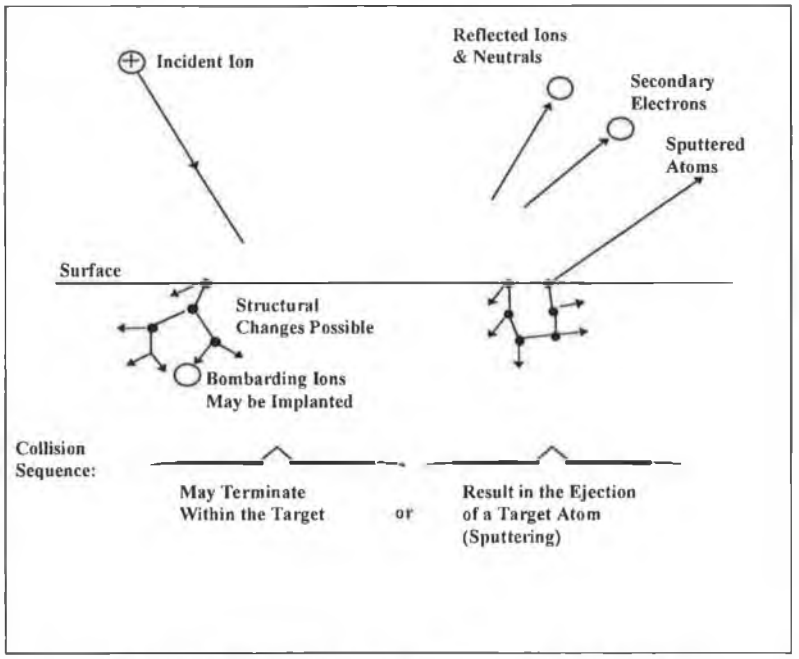

Figure 3: Interactions of ions with surfaces.

Radio-frequency discharges (most often operating at a frequency of 13.56 MHz due to legal restrictions), employed during these studies, have many advantages over conventional d.c. systems. These include their efficiency at promoting ionisation and the ease of use at quite low gas pressures. The main reason behind such efficiency is the ability of the electrons to follow the applied electric field while the other elements of the plasma remain essentially unperturbed. It also happens that RF discharges allow more current to be driven through the plasma for a given voltage, this being a direct result of decreasing impedance with increasing driving frequency. The incorporation of RF discharges (a.c. discharges) in industry for use in both etching and deposition arrangements is a consequence of the ease at which the flux of charged particles to a surface can be controlled, with the surface continuously charging and discharging. Unlike a.c., d.c. discharges are unable to control the flux at a surface. Materials processed in such discharges obtain the plasma floating

potential quite quickly resulting in equal fluxes of electrons and ions to the material surface. This flux is for the most part independent of changes in applied potential with the material behaving like a capacitor within a d.c. circuit.

The powered electrode, often referred to as the 'driven' electrode, in a capacitively coupled parallel plate arrangement attracts electrons to itself during the positive half of the RF cycle. The electrons which have greater mobility than the ions, subsequently bombard the electrode. In turn the ions are attracted during the negative half of the cycle, however they are slow in responding due to their size. The outcome of this is the build up of a negative d.c. bias on the driven electrode reducing the number of electrons collected, allowing the acceleration of ions to the substrate which is usually attached to this electrode. The net effect is a continuous flux of ions towards the substrate.

Many systems favour the use of what is known as asymmetry, i.e. electrodes of uneven size, as opposed to a symmetric electrode system. More commonly the driven electrode is small compared to the grounded, which usually consists of an electrode and the chamber walls. This is not to say that an arrangement like this is perfect. For example, with the substrate attached to the driven electrode and because the powered electrode has a smaller area than the rest of the chamber walls which are in turn grounded, the resulting production of an RF-self bias tends to drive ions into the substrate with a higher energy than those experienced by a sample attached to the grounded electrode. In addition, RF sources can operate, unlike d.c. sources, effectively at gas pressures below 20 mTorr.

3. Experimental

3.1. The plasma etching system

The experimental system employed the use of a parallel plate capacitively coupled asymmetric etching arrangement (figure 4). The system used had to be assembled for this purpose. The discharge chamber, walls and electrodes are made of stainless steel with the powered electrode being water cooled. The power to the grounded electrode is small and therefore active cooling of this electrode is not required. The walls of the chamber and grounded electrode were connected together leaving the system asymmetrical in arrangement. The spacing between the electrodes was set at ~6 cm.

Pressure measurement was carried out using baratron, penning and pirani gauges, with the first two employed for low-pressure work. The base pressure of the system was better than 10^{-7} Torr achieved through the use of an Edward's EO2 diffusion pump backed by a two-stage rotary pump. A steady flow of research quality gas was afforded through the employment of an Edward's LV10K leak value and the resulting gas pressure checked and successfully maintained using a MKS baratron pressure gauge within the chamber.

3.1.1. The RF circuit

A type ENI (model ACG-3) RF generator was used to source RF power to the plasma discharge. A circuit was designed to enable the transfer of maximum power to the plasma.

A number of factors have to be considered when using RF. Stray RF radiation is a problem which can interfere with sensitive equipment. The power radiated from an oscillating voltage source is proportional to the fourth power of the oscillation frequency. Shielding of any potential sources is therefore necessary, such as lead connections etc. Equipment liable to be affected, such as Langmuir probe diagnostic electronics, were housed in Faraday cages.

Other complications arise using RF, when for example circuit components acquire properties unseen at d.c. or low frequencies. A case in point, is the way RF inductance which appears insignificant at low frequencies become very significant at

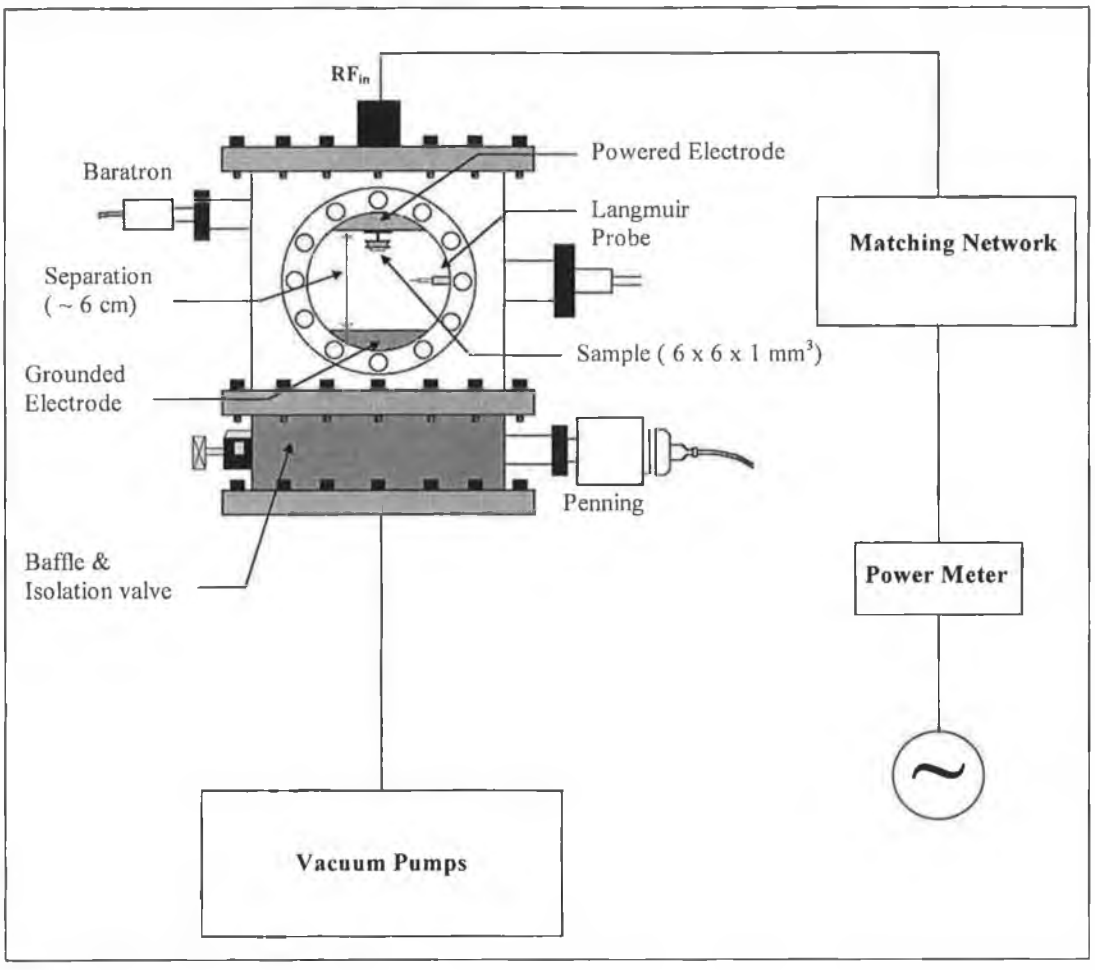

Figure 4: Schematic diagram of parallel plate plasma reactor.

13.56 MHz. At low frequencies the inductance of a wire is insignificant, but the situation changes drastically at high frequency. Specifically, a magnetic field is set-up at the centre of the conductor and effectively impedes the flow of current down the centre of the conductor, so that more of the current flows around the perimeter. This is commonly referred to as the skin depth effect. A copper wire of 1 m in length has a resistance of 0.02 Ω for d.c. which subsequently increases to almost 1 Ω at 13.56 MHz. The effect of increased conductor impedance at RF means that care should be taken in the design of earth leads. Ideally grounding leads should have as large a surface area as possible as most RF current flows near the conductor surface. Usually braided wire or straps of copper or aluminium are used.

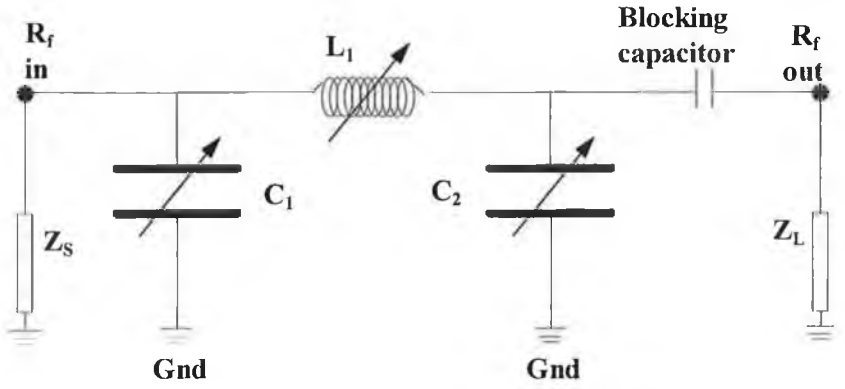

Figure 5: Schematic diagram of the matching unit.

The new terms introduced in this section are "impedance" and "reactance". Essentially, the behaviour of capacitors and inductors in a circuit is frequency dependent. Effectively, replacing the word "resistance" with "impedance" allows us to describe any circuit containing resistors, capacitors, and inductors. Impedance is the "generalised resistance": inductors and capacitors have reactance (they are "reactive"); resistors have resistance (they are "resistive"). In other words, impedance = (resistance + reactance).

The amount of power transfer between generator and plasma is vital and controlled by what is known as 'matching'. The use of a matching unit (figure 5) allows us to successfully match the output impedance of the RF generator (source) to the input impedance of the plasma (load) [6]. This is achieved by inserting the appropriate reactances between the two. Since we are dealing with reactances, which are frequency dependent, a perfect match is achievable at only one frequency. Hence variable reactances are employed in RF matching units. The reasoning behind this comes about through the manipulation of the maximum power theorem which states that the impedance of the load ($\mathbf{Z_L}$) must equal the complex conjugate of the source impedance ($\mathbf{Z_S}$) [7]. When this is achieved maximum power is transferred to the load with no power reflected back to the source:

$$R_S + jX_S = R_L - jX_L$$

where $\mathbf{R_S}$ and $\mathbf{R_L}$ are, respectively, the resistances of the source and plasma (load), while $\mathbf{X_S}$ and $\mathbf{X_L}$ are their corresponding reactances. This essentially means that the

50 Ω source must be matched by the resistive and inductive component of the plasma, both combining to give its impedance. The additional circuitry in the matching unit allows this to happen. Since the impedance of the plasma varies with pressure, power etc., the components of the matching unit are generally variable so that optimum power transfer is maintained for any number of plasma conditions. As already noted variable capacitors are used as the presence of the plasma will also affect the impedance of the load.

The blocking capacitor incorporated in the design of the matching unit (figure 5) ensures that no d.c. current can flow through the plasma. This is particularly favourable in etching arrangements as a negative offset is maintained most efficiently, so facilitating ion bombardment of the substrate. The removal of the blocking capacitor in d.c. coupled systems allows current flow.

3.1.2. The power meter

The RF power entering the matching unit is measured by a directional, Bird model 43 power meter with a power range of 1 W to 1 kW and a frequency range of 0.45–2300 MHz. The rotatable element within the meter allows both forward and reverse power measurements.

In practice, not all of the forward power measured by the power meter will be deposited in the plasma. As much as 90% can be lost in the RF circuit, yet there exists several methods of estimating it's efficiency. A novel technique used to determine the power dissipated in a discharge is simply to subtract the power dissipated in the circuit with a plasma present from that dissipated when the plasma is absent. This involves firstly matching the plasma i.e., minimising the reflected power when the plasma is on and determining the forward power using the power meter coupled with the measurement of the peak to peak voltage on an oscilloscope employing an RF voltage probe. The power to the system is then reduced until the plasma extinguishes. The power is then increased, this time with no matching and therefore no plasma, until the peak to peak voltage reaches the value measured when the plasma was on. The forward power on the meter is again read and the difference in the two readings i.e., when the plasma is on and off, is the power which reaches the plasma discharge.

3.1.3. Langmuir probe diagnostic arrangement

Two tuned probes were installed on the chamber both through "Wilson seals". These type of connectors facilitate the movement of the probes therefore allowing parameter measurement at different positions in the discharge (figure 6). The charged gas-phase components of plasmas may be sampled directly by drawing currents between a pair of conductors immersed in it. This forms the basis of Langmuir probe design. In recent years, probes have been used to obtain useful information regarding the spatial variation of density and temperature in RF etching plasmas. The main advantages of the Langmuir probe compared to other diagnostic techniques include its ability to measure local plasma information as opposed to volume averaged results, its simplistic design, stability for real-time in-situ measurements, and the extensive established theoretical information available.

The basis of Langmuir probe operation involves the application of a changing sweeping potential to the probe. The circuit is subsequently completed through a second (reference) electrode or a grounded electrode (usually including the chamber walls). As the voltage applied changes so does the current drawn. The *I–V* characteristic curve resulting allows the calculation of the various plasma parameters.

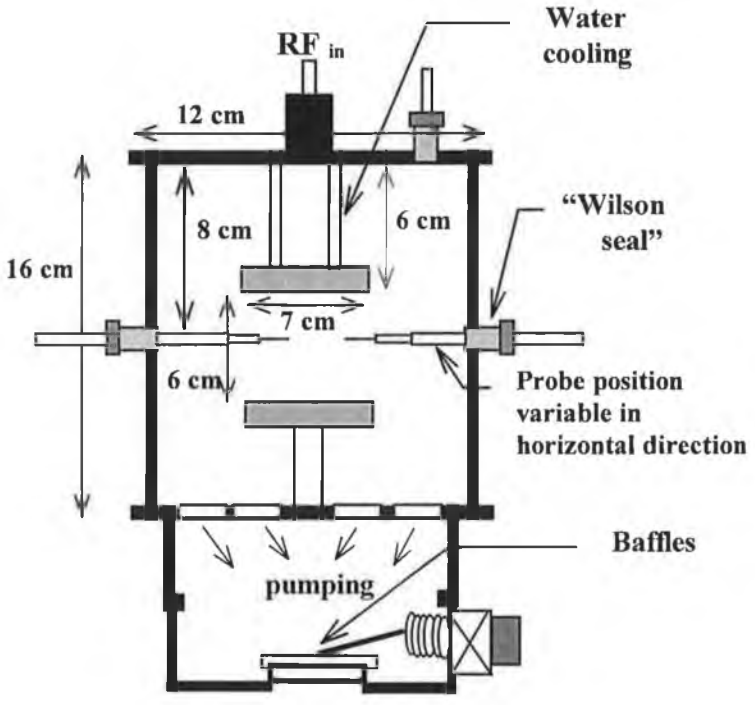

Figure 6: Chamber dimensions and Langmuir probe positioning.

The probe itself can be a number of different shapes, however the cylindrical probe has proved most popular because probe size is essentially kept to a minimum, in addition extensive theory already exists on the use of such probes [8,9].

A typical Langmuir probe *I–V* curve is shown in figure 7. Voltage applied to the probe attracts charge of opposite sign and repels charges of the same sign. If the probe is biased negatively with respect to the plasma potential then the plasma electrons are repelled while only positive ions are collected. The current collected is I_{+sat}, the ion saturation current:

$$I_{+sat} = \frac{1}{4} n_0 \, e \, S \, \bar{v}_s$$

where S denotes the probe sheath area, n_0 is the ion density in the unperturbed plasma and $\bar{v}_s$ the ion acoustic velocity defined as:

$$\bar{v}_s = \left(\frac{kT_e}{m_+} \right)^{\frac{1}{2}}.$$

This velocity is more generally regarded as the minimum velocity these ions must achieve to enter the probe sheath.

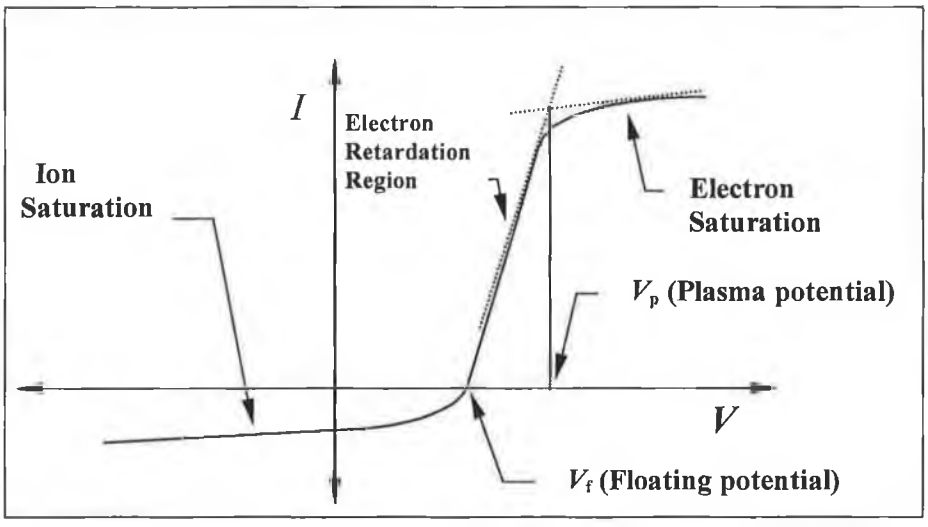

Figure 7: *I–V* probe characteristic of a Langmuir probe [10].

Reducing the negativity of the applied potential allows the probe to draw electron current. Increasing the potential even further positive to a value known as the floating potential, V_f, is the point at which there is no net current drawn i.e., ion and electron currents are equal. Increasing the bias voltage past this point allows more electrons to collect on the probe as they are able to overcome the retarding potential: - initially the very energetic electrons are collected and then the less energetic.
In this region, commonly known as the electron retardation region, the random current to the probe collected at the sheath edge like that for the ion current equation is given as:

$$\mathbf{I}_e = -\frac{1}{4} n_0 \, e \, \bar{\mathbf{v}}_e \, S$$

where S is the area of the sheath and $\bar{\mathbf{v}}_e$ is the average electron velocity calculated from the Maxwell–Boltzmann distribution and found to be:

$$\bar{\mathbf{v}}_e = \sqrt{\frac{8\mathbf{k}\mathbf{T}_e}{\pi \mathbf{m}_e}}$$

The total current to the probe in this region of retarding potential is then:

$$I_{\text{probe}} = I_{+\text{sat}} + I_e \exp\left(\frac{eV_p}{kT_e}\right).$$

A further increase in potential results in more and more electrons collecting at the probe until a point known as the plasma potential, V_p, is reached. At this potential the sheath around the probe disappears with the current drawn due only to the thermal flux of electrons and ions. The resulting current at this potential is due mainly to electrons owing to their higher mobility than heavy ions. Raising of the probe voltage above the plasma potential significantly reduces the number of ions reaching the probe as they are unable to overcome the potential drop within the sheath [11]. The electron saturation current is quickly reached as only electrons are collected by the probe. This current is defined as:

$$I_{e\,sat} = -\frac{1}{4}\mathbf{n}_0\, e\, \bar{\mathbf{v}}_e\, S\,.$$

The performance of the probe is in part dependent on the ratio of the probe radius, r_p, to the Debye length, λ_d. Also, the probe collecting area of the cylindrical probe, S, is related to the probe sheath radius, r_s, as follows:

$$S = 2\pi\, r_s\, L$$

where L is the probe radius and r_s is defined as:

$$r_s = r_p\left(1 - \frac{\left(V - V_p\right)}{kT_e}\right)^{\frac{1}{2}},$$

where V represents the probe bias.

In the ion saturation (collection) region the probe bias can be 50–60 volts less than the plasma potential producing a sheath radius of approximately 3 times the probe radius, consequently leading to an extremely large probe collection area. Contrarily, the probe bias in the electron saturation (collection) region is only a few volts above the plasma potential, with the sheath radius almost equal to the probe radius. This significantly reduces the probe collection area. In this case the sheath radius is quite small, comparable to a Debye length, ~100 μm. This variation in S during the acquisition of an I–V curve will lead to anomalies during both electron and ion density measurements.

The physical integrity of the probe tip must be continually checked during use in all etching processes. A reliable cleaning process must also be employed to maintain a smooth surface and structurally consistent probe tip.

3.1.4. Plasma parameter analysis

The measurement of the various plasma parameters important in plasma discharges incorporates the manipulation of the I–V characteristic curve. Determination of the

electron temperature involves first the use of the equation defining the electron current to the probe in the electron retardation region, defined as

$$I_e = -\frac{1}{4} n_0 \, e \, \bar{v}_e \, S \exp\left(\frac{eV_p}{kT_e}\right).$$

Taking the log of this equation and differentiating both sides with respect to the probe voltage reveals:

$$\frac{d \ln I_e}{dV} = \frac{e}{kT_e}.$$

The inverse of the slope of a plot of $\ln I_e$ versus probe voltage reveals the electron temperature, T_e.

The first derivative of the I–V characteristic should in principle divulge the value of, V_p, the plasma potential:

$$\left|\frac{dI}{dV}\right|_{max} = V_p.$$

The use of the current and voltage values found at the maximum of the derivative should increase the accuracy of V_p:

$$I_{max\ deriv.} = I_{e\ sat} \exp\left(\frac{V_{max\ deriv.} - V_p}{kT_e}\right)$$

where $I_{e\ sat}$ is the electron saturation current and V_p is then calculated as:

$$V_p = V_{max\ deriv.} + kT_e \ln\left(\frac{I_{e\ sat}}{I_{max\ deriv.}}\right).$$

The calculation of electron density, n_e, is easily accomplished when the electron saturation current and electron temperature, T_e, are known where:

$$n_e = \frac{4I_{e\,sat}}{e\,v_e S} = \frac{4I_{e\,sat}}{eS}\left(\frac{\pi m_e}{8kT_e}\right)^{\frac{1}{2}}.$$

The floating potential, V_f, is where the I–V curve crosses the voltage axis.

3.1.5. The tuned probe

Usually time dependant potentials are problematic in RF plasmas. In a.c. plasmas, the plasma potential varies with time therefore a fixed d.c. bias probe will draw a time dependant current as the voltage drop across the plasma probe sheath changes. The overall result of this is an over-estimation of the electron temperature, kT_e, and an under-estimation of the electron density, n_e. A means of overcoming this problem is achieved through the use of what is known as a tuned Langmuir probe [12,13,14,15] (figure 8).

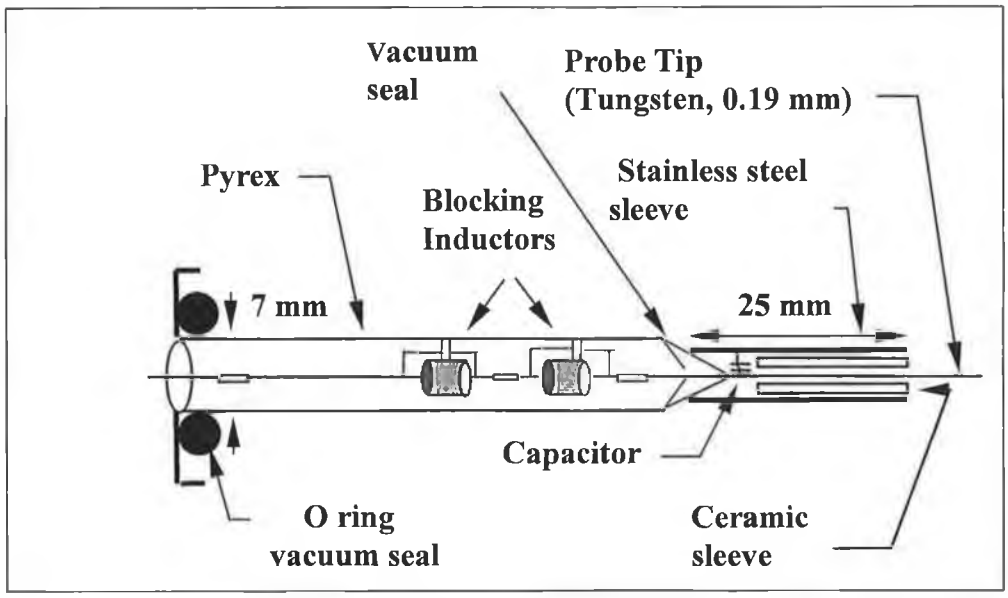

Figure 8: The tuned probe.

The employment of a tuned probe allows us to filter out the RF signal before it reaches the probe diagnostic hardware. In effect allowing us to acquire an undistorted probe characteristic.

3.2. HOPG etching arrangement and analysis set-up

HOPG samples (6 mm x 6 mm x 1 mm, Burleigh Instruments, Inc.) were cleaved in air with adhesive tape and subsequently placed into the capacitively coupled RF plasma-etching chamber of unconfined geometry as shown in figure 4. The sample was attached to the powered electrode in an inverted arrangement. The steady flow of research quality gas into the RF chamber was achieved and maintained as described in section 3.1. The pressure, as measured by a baratron, was stabilised at 75 ± 5 mTorr for argon RF plasma discharges whereas for hydrogen RF discharges 60 ± 5 mTorr was used as the working pressure.

Argon RF plasma etching of separate freshly cleaved HOPG samples was carried out at input powers of 5, 15, and 25 W for a period of 10 min, respectively. A comparison of both 3 and 5-min samples etched at a fixed input power of 20 W was also attempted. Hydrogen RF plasma etched samples, etched at a number of different powers, were also subjected to STM examination. Discharge powers of 15, 20, 30 and 40 W were employed during these experiments.

The striking of a hydrogen discharge proved difficult at low pressures (below 60 mTorr). The placing of magnets of alternate polarity around the chamber walls was carried out in an attempt to improve electron confinement and increase ionisation. In a conventional discharge chamber, electrons are soon lost through absorption at the chamber walls. The effect of a magnetic field is to induce the electrons into a circular motion around the field. After each revolution of this induced helical motion, the electron will return to the same radial position around the axis of the discharge. The total path travelled by the electron is also increased thus enabling it to cause more ionisation and excitation. The use of magnetic confinement did improve the situation yet the striking of a hydrogen plasma was only achieved at pressures ~60 mTorr. Moreover, upon visual examination the hydrogen plasma seemed to contain a bright region within the bulk of the plasma. This region appeared to be outside the sheath regions.

The STM used during this study was a commercial Burleigh STM (Burleigh Instruments Inc.). Mechanically prepared Pt/Ir (90/10) tips were utilised during all experiments. Calibration of the STM was carried out on a regular basis. Lateral calibration involved examination of pristine freshly cleaved HOPG samples with the characteristic centred hexagonal pattern, consisting of trigonally arranged β atoms

(separation 2.46 Å), identified from atomic resolution STM images. Horizontal and vertical calibration required the use of two gold-coated holographic gratings with periodicities of 200 and 400 nm, respectively.

STM data were taken (in topographical imaging mode (constant current)) with the following experimental conditions: tunnelling voltage 50–200 mV, tunnelling current 1–2 nA, and scan areas ranging from 500 × 500 to 10,000 × 10,000 $Å^2$. These setting were used for all experiments. For each sample examined, STM data were taken at a number of different areas on its surface. The only filtering treatment used was tilt removal which corrects for any physical tilt of the mounted sample. All STM images chosen for this report were carefully selected to be representative of the sample surfaces resulting from the etching processes. It is hoped that the images chosen will highlight both the similarities and variations existing between samples resulting from the various RF plasma etching parameters employed.

The r.m.s. roughness was calculated for all recorded topographs. This initially involves the subtraction of a best-fit base plane from each topograph which in effect is a two dimensional surface minimising the height difference between image points (x_i,y_i) and their corresponding points on this plane. The r.m.s. roughness is defined as:

$$\textbf{roughness (r.m.s.)} = \left\{ \sum_{i}^{N} \left(Z_i - ax_i - by_i - c \right)^2 / N \right\}^{1/2}$$

where Z_i is the observed height at point (x_i, y_i), $ax + by + c$ is the best fit plane, and N is the total number of data points. Interactive Data Language (IDL, Research Systems Inc.) mathematical analysis of the recorded topographs was used for r.m.s. calculations.

Since the STM has extremely high resolution and no mechanical contact [16,17,18], it is suitable for surface roughness measurements. The simultaneous high resolution of the STM both in the lateral and vertical directions suggest that the STM is uniquely suited to study processes as well as topographies. More specifically, in the study of non-equilibrium surfaces, STM offers opportunities to examine radiation induced erosion allowing quantitation of both height and lateral profiles of damage created.

Frequency-size distribution analysis of the features found on HOPG samples after plasma treatment was also carried out for a number of samples for each separate set of plasma processing conditions. Lateral sizes of features within images recorded are expressed as the square root of the product of the length in the short and long axis directions. Height distributions were recorded as the highest point on each individual surface feature measured.

4. Results

4.1. Plasma diagnostics

4.1.1. Plasma parameter measurements in argon

Table 1: Argon RF plasma parameters: (pressure = 75 mTorr).

Power (W)	"V_f" (V)	"V_p" (V)	"kT_e" (eV)	"n_e" ($\times 10^{+9}$ cm^{-3})	"n_i" ($\times 10^{+9}$ cm^{-3})	"Ion Current" (mA cm^{-2})
5	15.6	25.8	3.1	0.76	0.43	0.04
10	17.0	28.5	3.2	1.87	1.13	0.07
15	18.2	29.2	3.0	3.04	1.93	0.10
20	19.2	30.7	2.9	4.30	2.72	0.12
25	20.0	30.9	2.7	5.26	3.34	0.14
30	20.4	30.9	2.6	6.34	3.96	0.16
40	21.1	31.6	2.4	9.06	5.74	0.19
50	21.5	31.0	2.1	11.1	7.71	0.22

The probe characteristics reported were measured in argon discharges of 75 mTorr over a number of power settings between 10 and 50 W. The measurements taken were corrected for sheath resistance as this resistance makes up part of the probe current path. In RF plasmas the sheaths are mainly capacitive, so the conduction current of the sheaths and the discharge current are very different resulting in comparable electrode and probe sheath resistances. This leads to distortion in the current curve characteristic of the probe. As a rule the probe sheath resistance is important with its measurement allowing correction of the current curve of the probe. According to Godyak et al [8] its affect on plasma parameters increases as electrode size decreases. In these experiments the probe sheath resistance had a maximum value of ~0.5 kΩ and was seen to decrease with increasing applied power. A

complete examination of plasma parameter variation with power is seen in table 1. Results are comparable to those in the literature [19,20,21].

Ion density measurements show ion populations to be less than that of electron populations observed at all plasma conditions measured. In a quasineutral system one would expect ion and electron densities to be similar. However, a trend is observed with both ion and electron densities increasing linearly with increasing plasma power. The observed densities for both ions and electrons were in the range of 10^9 per cm^3, these values are typical of capacitively coupled systems. The electron temperature in capacitively coupled systems at low pressures is essentially higher due a lower probability of collision. The electron inelastic collision frequency increases at higher pressures and therefore electrons lose more energy resulting in lower electron temperatures. At this time, it is important to stress that measurements were repeated a number of times over a few months with the data recorded showing good consistency.

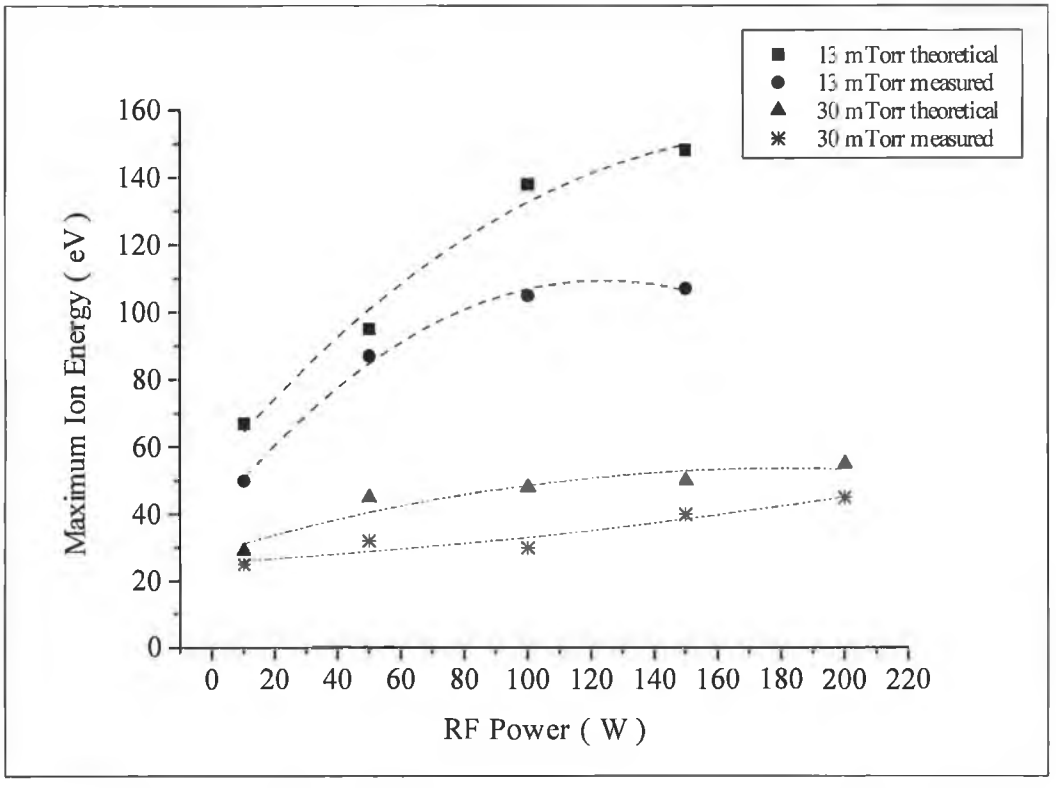

Figure 9: Measured and theoretical values of the maximum ion energies for an argon discharge at pressures of 30 and 13 mTorr [10].

Examination of plasma potential reveals that it reaches a maximum and begins to level off after 30 W. Theoretical work indicates that plasma potential tends to decrease at high powers in an argon discharge [22]. In relation to electron temperature it is known that at higher pressures, 50 to 250 mTorr, the electron temperature attains a value of approximately 3 eV, decreasing to ~1 eV as the pressure is reduced to 10 mTorr. At the plasma pressure employed, 75 mTorr, we measure an electron temperature of ~3 eV which is consistent with that expected. Table 1 reveals a trend of decreasing electron temperature with increasing power. A temperature of ~3.1 eV recorded at 5 W reduces to ~2.1 eV for an input power of 50 W. This temperature was measured in the bulk plasma region as was the case for all plasma parameters measured. The visual uniformity of the bulk plasma region in argon should ensure constant plasma parameters across it. The large voltage drop across the sheath region distorts the probe characteristic when recorded in this area.

The measurement of ion energies in the argon discharge was not carried out. Generally a retarding grid energy analyser consists of planar grids of fine wire mesh. A potential difference of typically - 40 V is maintained between the first and second grid to prevent electrons from the discharge penetrating further into the analyser. A variable, retarding potential difference of up to 100 V is maintained between the first and the third grids to determine the energy distribution of the positive ions striking the grounded counter electrode. The fourth grid is maintained at a small positive potential (~2 V) with respect to the ion collecting electrode. Typical ion currents measured for a capacitively coupled argon RF discharge of 10 W at 30 mTorr vary from 0.5×10^{-9} A to zero as the retarding potential is increased from zero to 40 V. At 50 W the ion current is as expected far greater, initially 2.0×10^{-9} A [10].

Theoretical and measured maximum ion energies for argon at two different pressures are shown in figure 9 [10]. It is observed that argon ion energies are quite significant and decrease as the pressure is increased to 30 mTorr. From such calculations, it is clear that even in a reactor with a large area ratio (area ratio = area of grounded electrode/area of driven electrode) impacting of electrodes with energetic ions occurs to a large extent.

4.1.2. Plasma parameter measurements in hydrogen

The measurement of plasma parameters in a hydrogen RF plasma is more difficult than in argon. While a substantial body of data exists on the use of Langmuir probes in gases such as argon, the information available on the performance of reactive gases is less extensive. The increased complexity and variation of species in hydrogen plasma (both atomic and molecular) not to mention its tendency to combine with electronegative species such as oxygen, lead to more difficulties during characterisation.

Table 2: Hydrogen RF plasma parameters: (pressure = 60 mTorr).

Power (W)	"V_f" (V)	"V_p" (V)	"kT_e" (eV)	"n_e" (x 10^{+8} cm^{-3})	"n_i" (x 10^{+8} cm^{-3})	"Ion Current" (mA cm^{-2})
10	26.7	33.0	5.1	5.87	8.75	0.18
20	25.5	29.6	6.9	8.40	13.70	0.28
30	26.8	28.5	6.1	11.00	17.60	0.35
40	27.9	28.8	5.7	14.40	21.60	0.43
50	-	29.0	-	17.10	23.40	0.46

The species existing in hydrogen plasmas include among others H_2, H, e^-, H^+, H_2^+, $H_3^+$and H^-. Of these elemental constituents only H_2^+, H_3^+ and H_2 possess the three states of excitation i.e., rotational, vibrational and electronic. Generally ions experience many reactions before impacting the chamber walls. The exception to this rule is H^+ which does not undergo any changes under the discharge conditions used during these experiments. The contribution to the H^+ ion concentration through the electronic dissociative ionisation of H_2 is weak under our plasma conditions. H^+ ions are primarily created by direct ionisation of atomic hydrogen. Hence, the dominant ion species in the plasma arrangement employed is proposed to be H_3^+ created through H_2^+/H_2 collisions. Atomic hydrogen is also produced during this

collisional process and also through H_3^+/H_2 collisions. Neutrals generally have a large mean free path while some ions such as H_2^+ and H_3^+ have extremely fast rates of recombination with thermal electrons.

Table 2 summarises the measured probe characteristics for a hydrogen discharge of 60 mTorr at a number of power setting between 10 and 50 W. The electron and ion density trends are similar to those seen for argon with populations increasing as power is increased at fixed pressure. However, both electron and ion densities are smaller than those found for the argon plasma. This reflects the lower ionisation cross-section of hydrogen in comparison with argon.

The trends observed for both plasma potential and electron temperature are less obvious. The plasma potential is 33 V at 10 W and decreases significantly when the power is increased.

4.2. Radio frequency (RF) plasma etching of HOPG with both argon and hydrogen: an STM and XPS study.

4.2.1. Characterisation of freshly-cleaved HOPG

The STM imaging of freshly cleaved HOPG reveals large atomically flat domains stretching over thousands of Ångströms. Characterisation of the pre-etched substrate is essential before etching not only to ensure the structural integrity of the pre-treated surface but also to identify the many surface defects (pits, graphitic debris, and steps both atomic and cleavage) arising from the mechanical cleavage process. Figure 10(a) shows a typical image of the freshly cleaved basal plane of HOPG revealing steps running diagonally across the image. A tiny piece of graphitic debris is evident on the step running through the centre of the image. These cleavage steps are found regularly throughout the surface and range in height from 50–500 Å. Naturally occurring atomic single layer steps are also seen on the surface and are less than 1 nm in height. These steps (atomic and cleavage) are for the most part featureless and linear extending for many thousands of Ångströms. Figure 10(b) reveals an image of yet another cleavage step, this time tearing of the graphite basal plane has occurred producing the characteristic graphitic debris seen in many STM images. The presence of a bubble like feature in the bottom right hand corner of the image may be the result of air trapped under the basal plane or alternatively of an STM imaging anomaly.

Figure 10(c) displays an image of a highly damaged graphite basal plane. The presence of a seemingly large-scale superperiodic hexagonal structure in the top left hand corner of the image is proposed as a consequence of the rotational misorientation of the two top graphite layers or of two successive graphite layers near the surface. The presence of large-scale hexagonal structures with different periodicity's have been occasionally observed on graphite in air [23,24,25]. In principle, the characterisation of the inherent structural features of pristine HOPG will allow us to successfully distinguish them from damage resultant after plasma treatment.

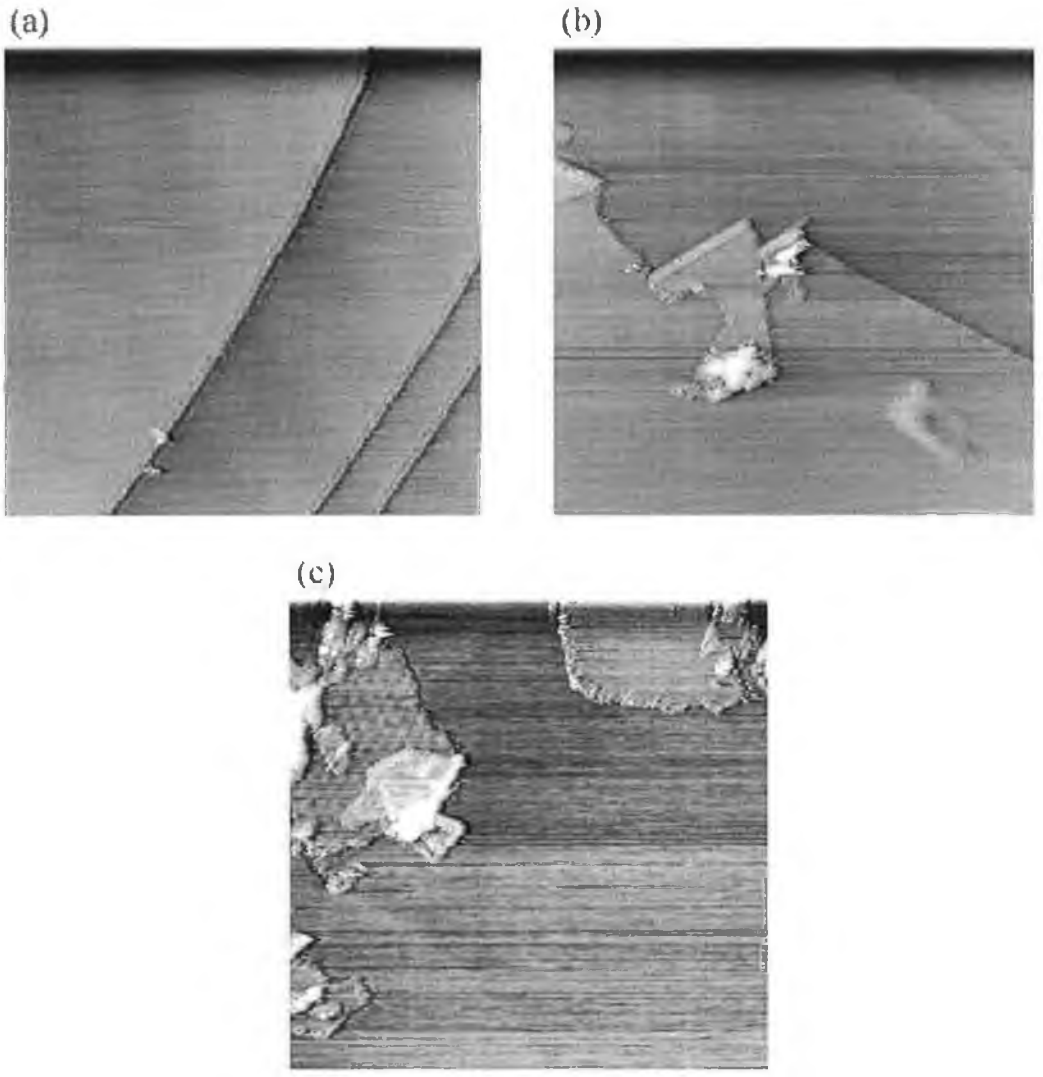

Figure 10: STM topographic mode images of the freshly cleaved basal plane of HOPG. (a) An (5000 Å x 5000 Å x 198 Å) image revealing atomic steps; (b) an (5000 Å x 5000 Å x 211 Å) image illustrating the local mechanical damage arising from the cleavage process; and (c) an (5000 Å x 5000 Å x 104 Å) image revealing a large-scale superperiodic hexagonal structure on the terrace in the top left hand corner.

4.2.2. Argon RF plasma etched HOPG: - power dependence

(i) 5 W:

Figure 11(a) illustrates the effect of the etching process on the topography of HOPG. The surface is completely altered, bearing no resemblance to the pristine graphite structure seen in figure 10. This image, from a sample etched at 5 W for 10 min, reveals a surface morphology consisting of semi-regular oval shaped protrusions (hillocks). Figure 11(b) is a magnified image of the central area of the sample surface region imaged in figure 11(a). This image emphasises the reproducible nature of the hillock-like surface features with the structures quite similar in both lateral size and height. The area imaged in figure 11(b) also reveals the presence of cavern-like regions on the surface seen as dark areas on the image. These are tentatively attributed to the preferential sputter removal of carbon atoms from defected sites on the basal plane of HOPG.

The image of a cleavage step shown in figure 11(c) supports the proposal of the preferential etching of defected basal plane graphite. A large, deep cavern-like region extends along the step edge with the characteristic hillock-like protrusions evident on the upper terrace of the step. Figure 11(d) reveals a similar topography to that seen in figure 11(c) with hillock-like protrusions evident on both the upper and lower terraces of the stepped region.

Figure 12(a) exhibiting an area of graphite near the top of the image also reinforces this hypothesis of the preferential etching of certain areas on the graphitic surface. These areas of graphite seemingly revealing less damage are proposed due to different sputtering probabilities on either side of the grain boundaries rather than the erosion of the exposed edges of the basal plane of graphite. Figures 12(b) and (c) are images of two different plasma etched samples illustrating similar topographies. These images seem to consist of large pieces of graphitic debris maybe as a consequence of the break-up of the graphite basal plane estimated to occur for incident ion energies of ~28 eV or more [26].

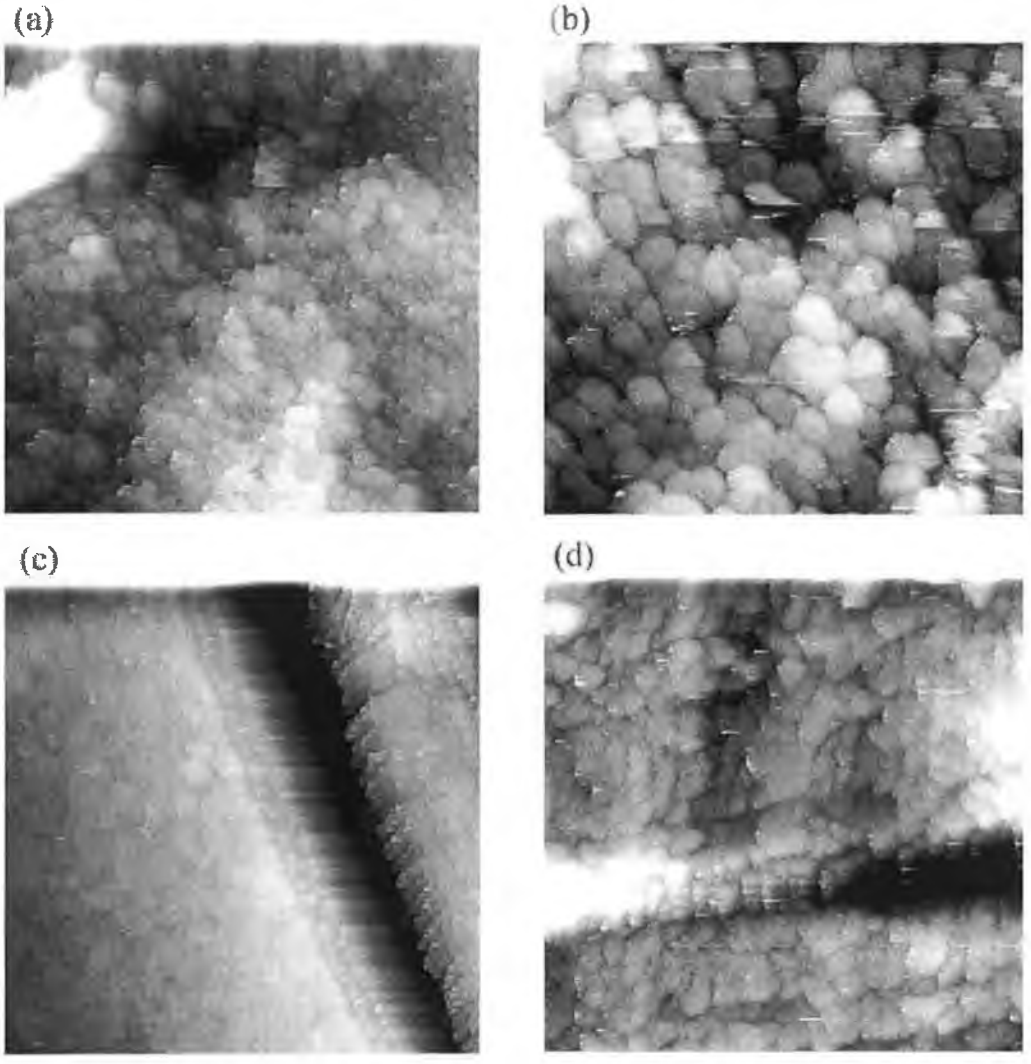

Figure 11: Typical STM images of the surface of HOPG showing the hillock-like structural features resulting after argon RF plasma treatment at 5 W for 10 min. (a) A typical STM (5000 Å x 5000 Å x 504 Å) image; (b) magnification of the central region in (a) (2500 Å x 2500 Å x 216 Å); (c) an STM (5000 Å x 5000 Å x 677 Å) image revealing a deep cavern-like region extending along a step edge; and (d) another stepped region image (5000 Å x 5000 Å x 280 Å).

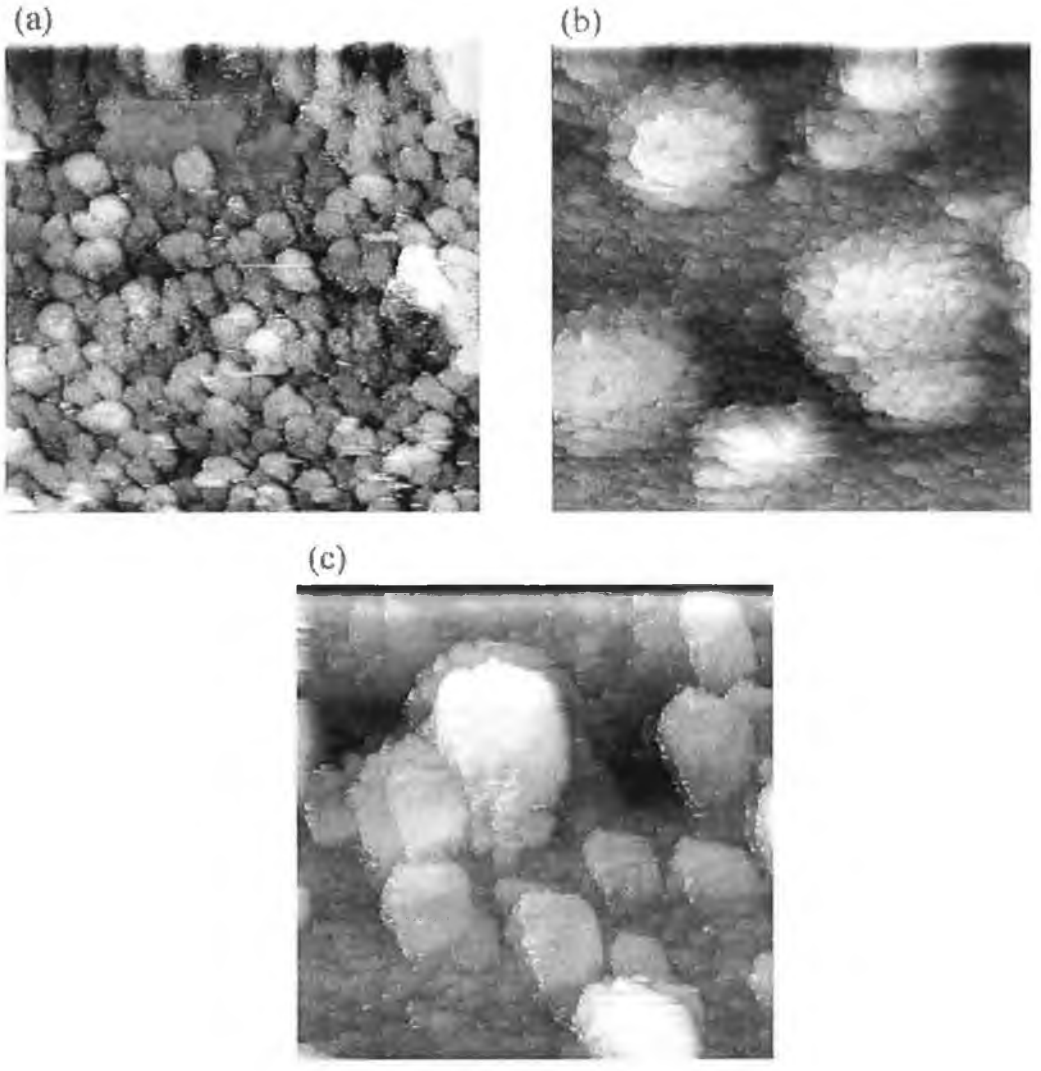

Figure 12: Typical STM images of the surface of HOPG after argon RF plasma treatment at 5 W for 10 min. (a) STM topographic mode image (2500 Å x 2500 Å x 112 Å) revealing a structural boundary on the surface of HOPG; (b) STM image (5000 Å x 5000 Å x 606 Å) showing several large structures suggested to be attributable to the break-up of the graphite lattice; and (c) an STM image (5000 Å x 5000 Å x 518 Å) revealing large pieces of graphitic debris.

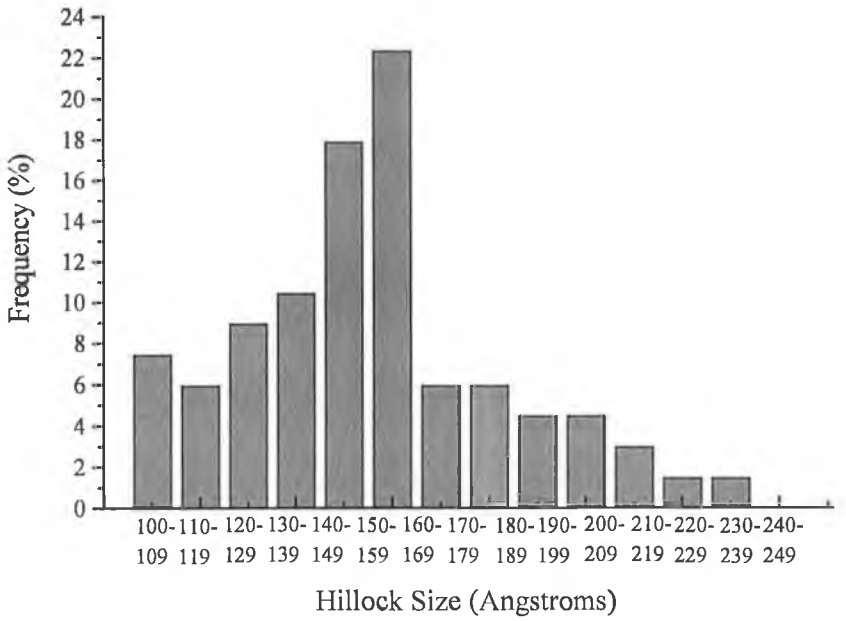

Figure 13: Measured % frequency size-distribution histogram of hillock-like protrusions deduced from STM topographs. The data shown is an average of a number of HOPG samples RF plasma etched in argon at 5 W.

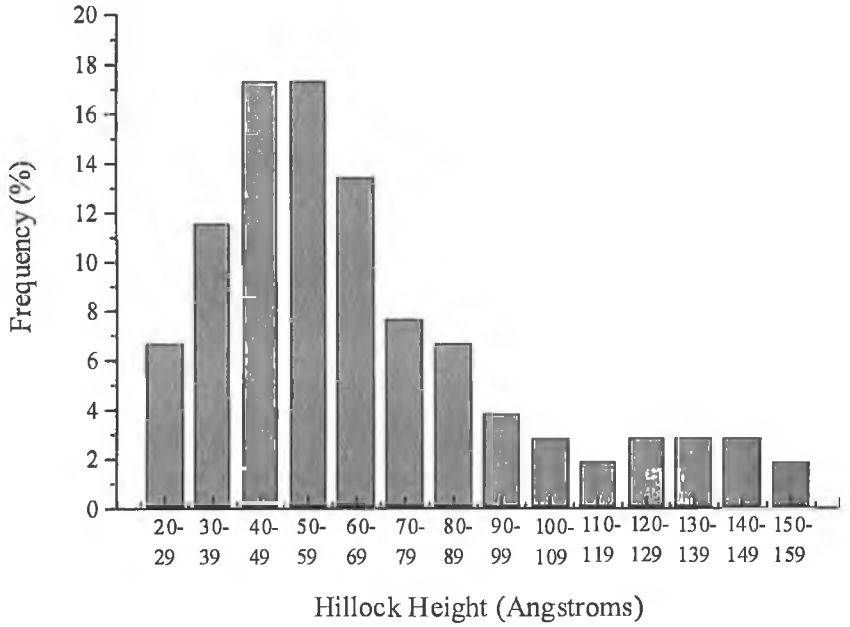

Figure 14: Measured % frequency height-distribution histogram of hillock-like protrusions deduced from STM topographs. The data shown is an average of a number of HOPG samples RF plasma etched in argon at 5 W.

Although variations in surface features are evident on samples etched at an input power of 5 W, the examination of a number of different areas on numerous samples affords the histogram of frequency-size distribution of hillock-like protrusions shown in figure 13. It exhibits mainly two large peaks illustrating highest frequencies for hillock protrusions of sizes ranging from 140–160 Å. The height frequency distribution of the hillocks was also calculated and is illustrated in figure 14. The figure shows clearly that most features (≈80%) found on images of 5 W plasma-etched samples have heights ranging between 20 and 80 Å, however are most frequently found with heights of between 40 and 60 Å.

(ii) 15 W:

Figure 15(a) represents a large-scale image of 15 W argon RF plasma etched HOPG. The characteristic features observed for the 5 W etch are as expected also evident. An increase in feature size is also noted compared to features on HOPG samples plasma treated at 5 W. The increase in plasma input power to 15 W increases the ion impact energies bombarding the surface. Nevertheless, the increase in ion energy as the input power is increased from 5 to 15 W is not that substantial as reported by Al-Assadi et al [10] (section 4.1.1). However, as recorded in Table 1, the increase in ion densities detected as power is increased produces an increased ion flux to the surface. Thus, this is likely the origin of increased damage to the surface seen at the higher powers.

The increase in the frequency of the cavern-like regions compared to those seen for 5 W etched samples is illustrated in figure 15(b). These pocket-like regions are of significant depth and vary in lateral sizes from 10's to 100's of Ångströms. Figure 15(c) is a high-resolution STM image demonstrating a stepped appearance on the surface of some of the surface features. You et al [27] propose that enhanced ion-bombardment processes may account for the generation of the terraced and stepped slopes seen on hillock-like features on samples from the higher powered etches. The features in this image seem to a certain extent unresolved when compared to those seen in figure 15(b). Finally, figure 15(d) is a large scale image of the region seen in figure 15(c) depicting the extension of reproducible etching over several thousands of Ångströms.

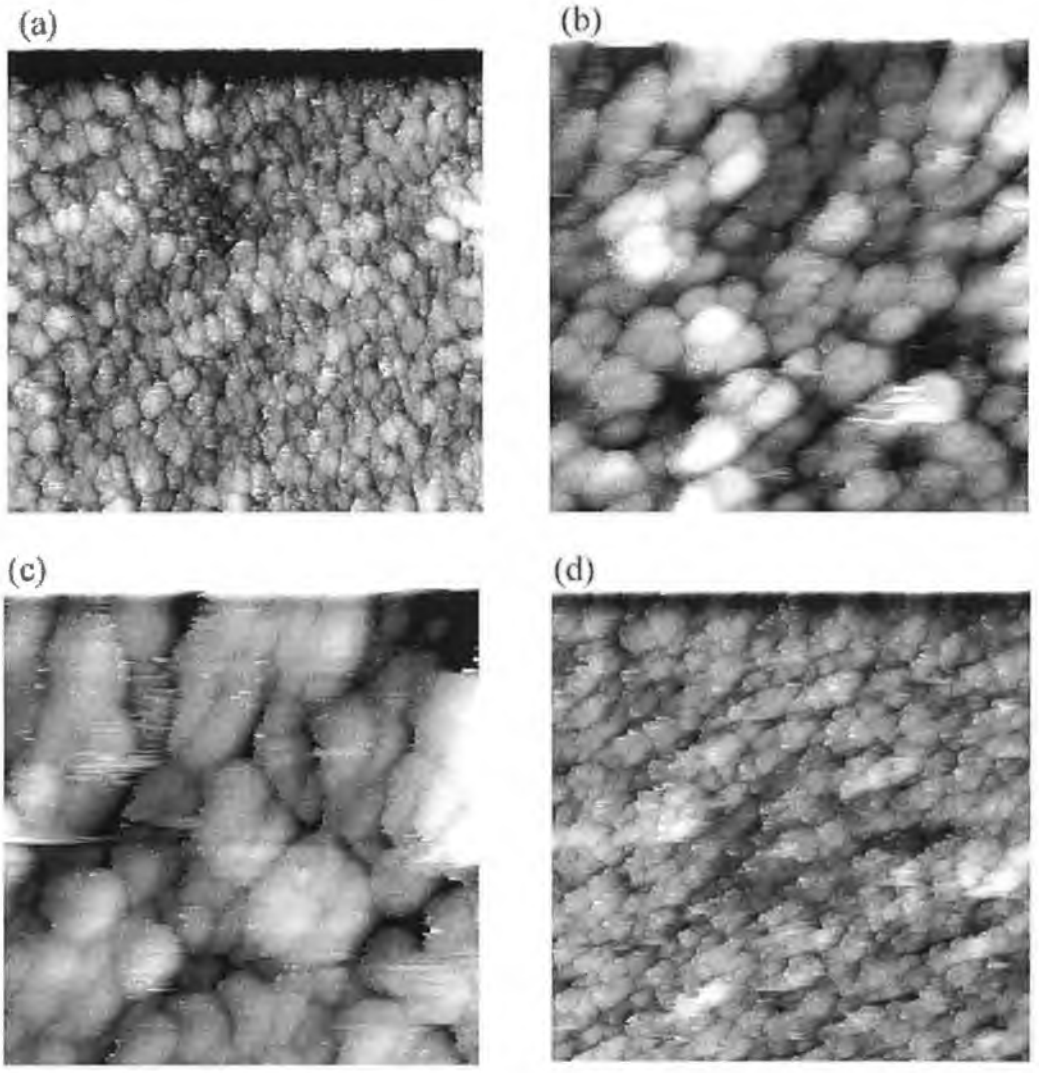

Figure 15: STM images of the surface of HOPG illustrating the characteristic rounded hillock-like structural features resulting after argon RF plasma treatment at 15 W for 10 min. (a) A large scale STM image (5000 Å x 5000 Å x 339 Å); (b) STM image (2000 Å x 2000 Å x 356 Å) revealing large, deep cavern-like regions between the hillock-like protrusions; (c) high resolution image (1000 Å x 1000 Å x 223 Å) revealing oval shaped hillocks; and (d) a large scale (5000 Å x 5000 Å x 417 Å) image of the region in (c).

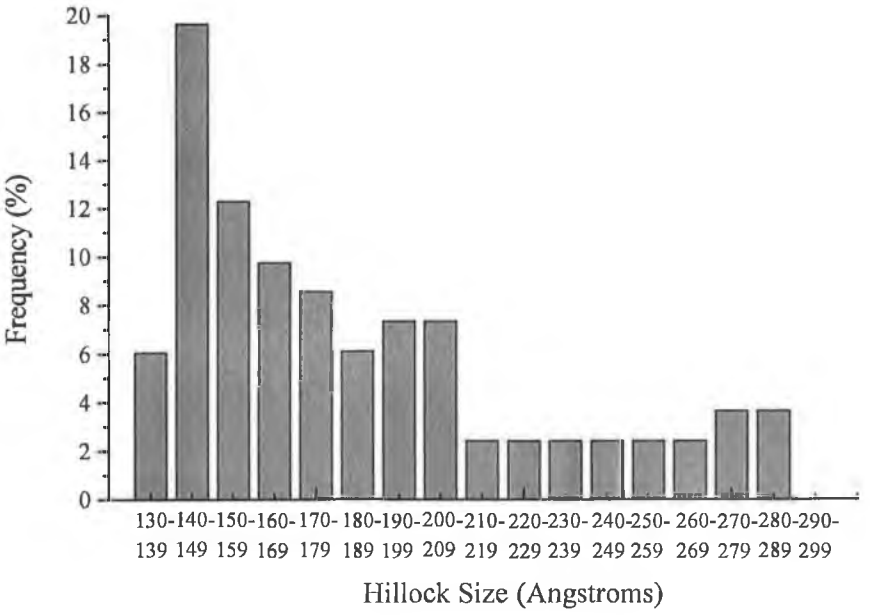

Figure 16: Measured % frequency size-distribution histogram of hillock-like protrusions deduced from STM topographs. The data shown is an average of a number of HOPG samples RF plasma etched in argon at 15 W.

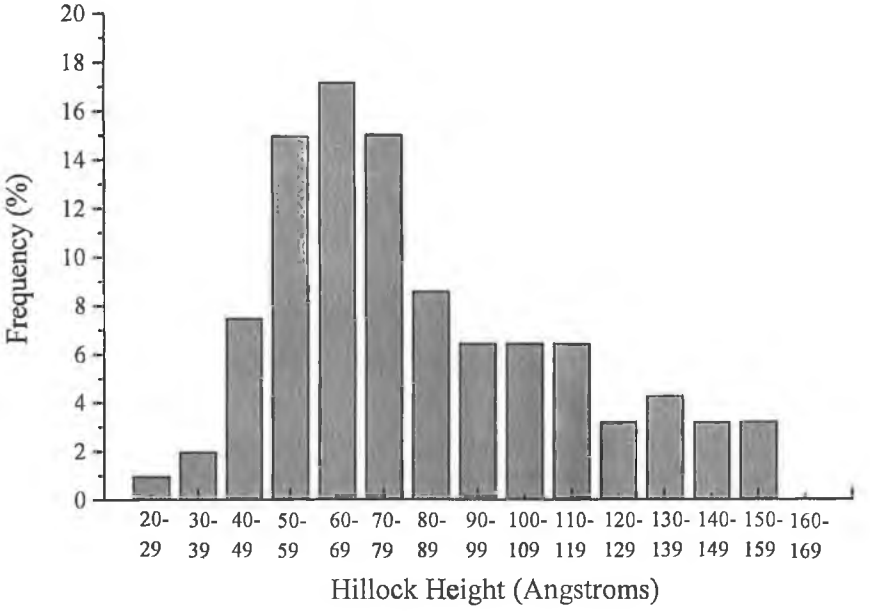

Figure 17: Measured % frequency height-distribution histogram of hillock-like protrusions deduced from STM topographs. The data shown is an average of a number of HOPG samples RF plasma etched in argon at 15 W.

A histogram of the lateral size distribution of hillock-like protrusions found on HOPG samples after 10 min of 15 W RF plasma etching is shown in figure 16. Features with lateral sizes of 140–160 Å are found to be most frequent, similar to the size-distribution histogram of features measured for 5 W samples (figure 13). Not many hillocks were found on 5 W plasma-treated samples with lateral sizes greater than this. The reasons for such similarities may be the fact that surface features on some images of 15 W plasma-treated surfaces appeared to have stepped slopes, leading to difficulties in defining exact structure sizes. Yet the vast majority of features measured (~80%) are within the lateral size range 130–210 Å. Contrary to 5 W sample distributions, almost 40% of features on samples exposed to 15 W plasmas are found with lateral sizes in the range 160–210 Å, this emphasises the differences in the topology of 5 and 15 W plasma processed surfaces.

Referring to height distributions as shown in figure 17, it is seen that a large portion of surface features (~50%) are found with heights in the range 50 to 80 Å. Significantly, only 10% of features measured have heights between 20 and 50 Å. The corresponding percentage value for feature heights measured on 5 W etched samples is 30%, i.e. the height distribution is broader for 15 W etching.

(iii) 25 W:

The increase in plasma power to 25 W during the etching process results in surface features of both greater lateral size and height compared to those seen for 5 and 15 W plasma-treated samples. Figure 18(a) is representative of STM topographs recorded for HOPG samples argon plasma-treated at 25 W for 10 min. The surface features detected are essentially more resolved than those found for the lower power experiments. A large crevice-like region present in the centre of the STM image in figure 18(b) is a typical example of the intense nature of the etching process at this power.

The extent of increase in both lateral size and hillock height in the transition from 15 to 25 W is substantially greater than that seen for the transition from 5 to 15 W. Figures 19 and 20 are the respective histogram lateral size and height distributions of surface features observed on 25 W plasma-treated samples confirming these observations.

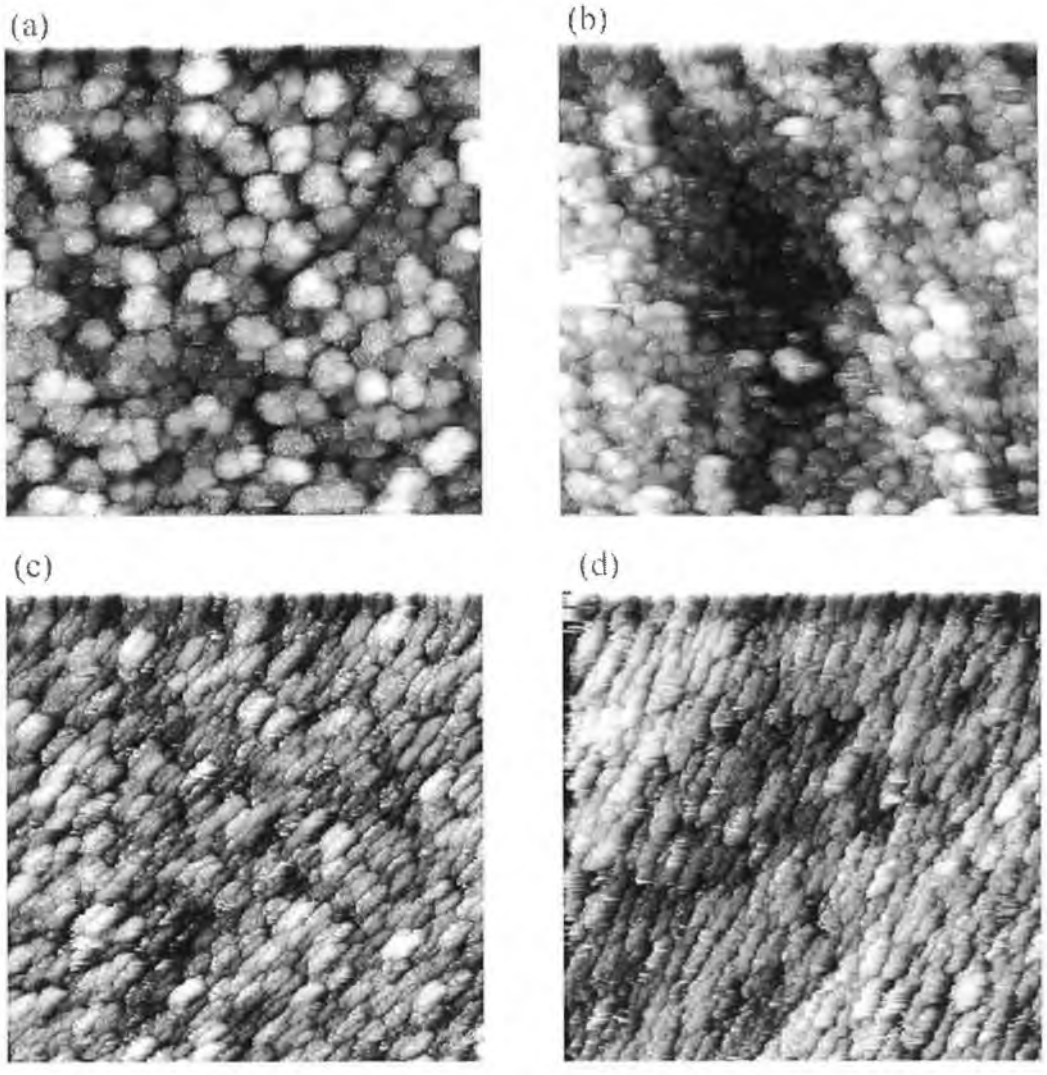

Figure 18: Topographic STM images of the surface of HOPG after argon RF plasma treatment at 25 W for 10 min revealing (a) (5000 Å x 5000 Å x 576 Å) extremely large hillock features; and (b) (5000 Å x 5000 Å x 599 Å) deep cavern-like regions between the hillock-like protrusions. STM images after plasma etching HOPG at 20 W for different lengths of time; (c) a 5 min-etched sample image (5000 Å x 5000 Å x 315 Å) revealing elliptical shaped hillocks; and (d) a 3 min-etched sample image (5000 Å x 5000 Å x 286 Å) with linear elongated features dominating the topology.

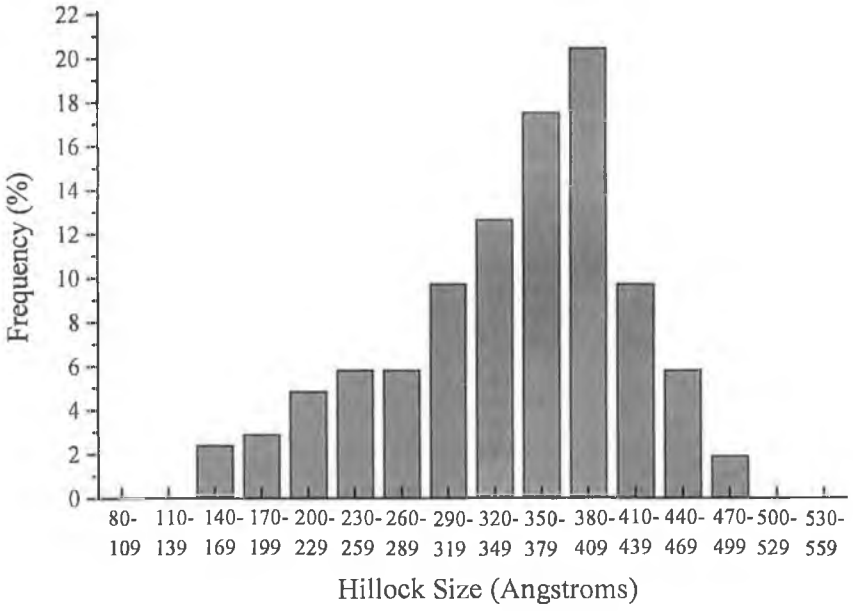

Figure 19: Measured % frequency size-distribution histogram of hillock-like protrusions deduced from STM topographs. The data shown is an average of a number of HOPG samples RF plasma etched in argon at 25 W.

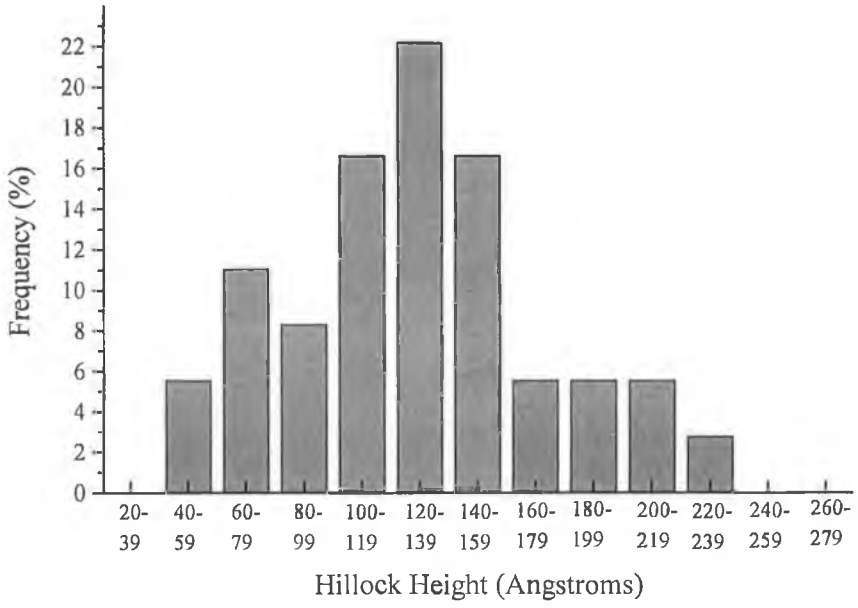

Figure 20: Measured % frequency height-distribution histogram of hillock-like protrusions deduced from STM topographs. The data shown is an average of a number of HOPG samples RF plasma etched in argon at 25 W.

R.M.S. roughness calculations

Root mean square (r.m.s.) roughness calculations were carried out on STM topographs of surface areas, which appeared to contain no defect regions for both pre-treated and plasma treated HOPG samples. The presence of random defects on the surface, such as graphitic debris and cleavage planes, complicate such calculations and prevent the accurate comparison of roughness induced exclusively by the etching process.

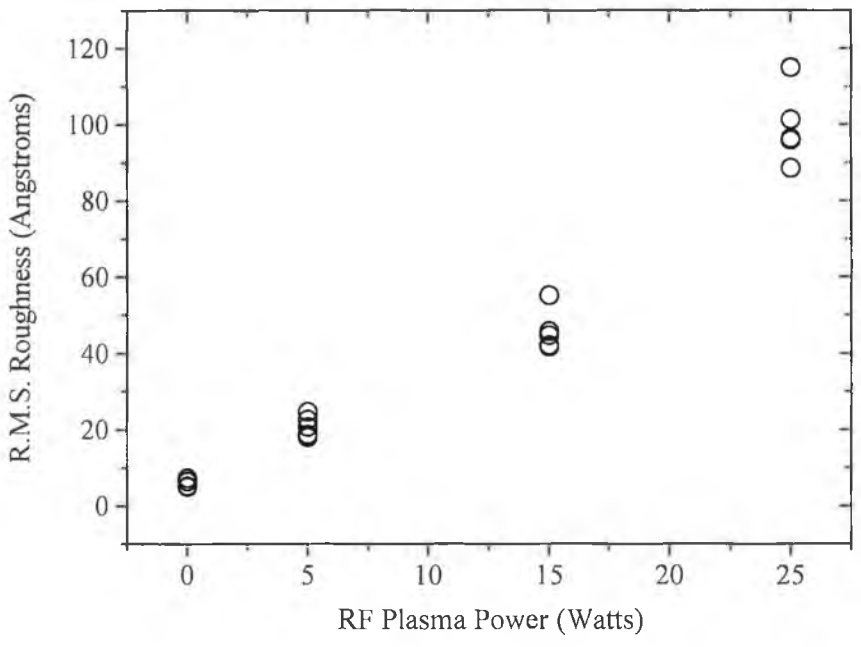

Figure 21: Dependence of the r.m.s. roughness of argon plasma-treated HOPG surfaces on the RF power levels used (etch duration = 10 min).

Roughness is plotted against plasma power for samples etched for 10 min (figure 21). Different values of roughness for the same etching power correspond to different STM topographs, not necessarily on the same sample. The data can be divided into two regions. One is from as-cleaved to 15 W plasma etching, where the scatter of roughness is small. The second region is for samples etched at 25 W where the scatter of roughness is quite large. This large increase in roughness between 15 and 25 W plasma-treated samples is consistent with both lateral size and height increases observed for features detected for both powers. Surprisingly, r.m.s.

roughness values calculated for atomically flat freshly cleaved graphitic domains were found to range from 5 and 8 Å, as opposed to an expected value of zero. These non-zero roughness values are suggested resultant of an STM imaging anomaly coupled with the presence of surface features.

4.2.3. Argon RF plasma etched HOPG - time dependence

Figure 18(c) illustrates a typical STM topograph of a 5-min etched surface at an input power of 20 W. The attendant features are quite different from those found on the surfaces of samples etched for 10 min. The elongation of the hillock-like protrusions in one direction is quite evident. Basically, they are elliptical in shape, more so than those seen during the power dependence experiments. The presence of large pocket-like regions between surface features is also less obvious. In essence, the features are more tightly packed. However, it must be emphasised that it was more difficult to image surfaces for this shorter time of etching.

Figure 18(d) (5000 Å x 5000 Å) is an example of an STM topograph of HOPG exposed to 3 min of plasma treatment at 20 W. The difficulties encountered during the imaging of these samples was again greater than that experienced during the 5 min experiments. Hillock-like protrusions were less apparent on these samples than on all other plasma-treated samples. Figure 18(d) reveals an image illustrating the most common features found on 3-min etched surfaces. These linear undefined structures, were previously reported by You et al [28]. These features were evident on a number of different samples. It is proposed that these structures may be the initial stages of hillock formation with the surface quite likely disorganised at this early stage of etching. The similar orientation of these structures and their parallel alignment is not too dissimilar to the orientation of the hillock-like protrusions found on 5-min etched surfaces.

R.M.S. roughness calculations

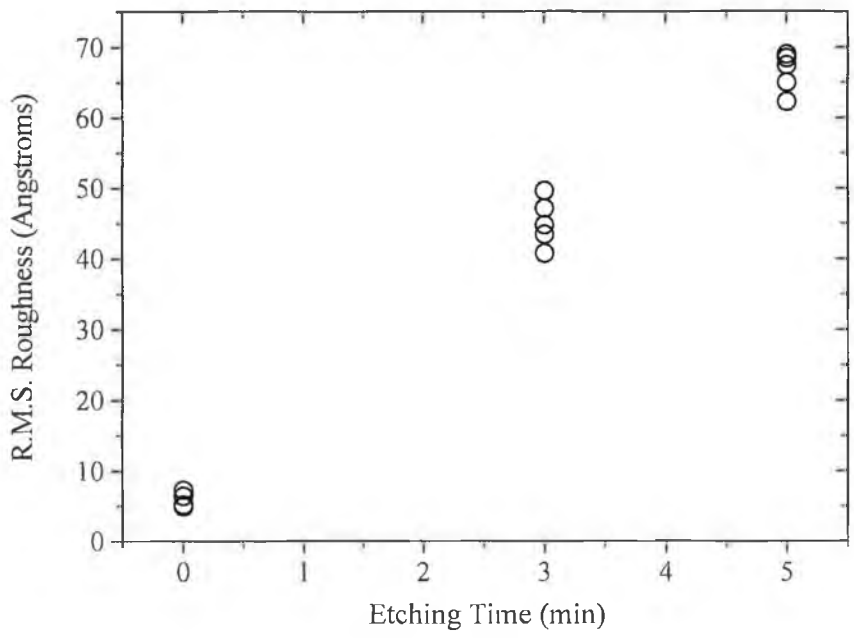

Figure 22: Etching time dependence of the r.m.s. roughness of 20 W argon plasma-treated HOPG surfaces.

Roughness (r.m.s.) is plotted against etching time in figure 22. Different values of roughness for the same etching time correspond to STM topographs of different areas on the same sample.

As would be expected, the roughness increases as etch duration is increased from 3 to 5 min. Further time-dependent studies are necessary if the mechanism of plasma-surface interactions at these early etching stages is to be successfully explained. It is also suggested that the very early stages of etching are essential to the understanding of etching processes as a whole.

The features measured on the surfaces of 3 and 5 min plasma processed samples are essentially of uniform width ranging from ~100 to 200 Å. They also reveal a localised high degree of structural uniformity. Surface features found for both etch times are orientated parallel to each other.

4.2.4. Hydrogen RF plasma etched HOPG – power dependence

(i) 15 W:

Figure 23(a) illustrates the effect of a 15 W H_2 RF plasma (etch duration = 10 min, pressure = 60 mTorr) on a HOPG sample attached to the powered electrode in the etching chamber. The characteristic atomically flat domains evident on freshly cleaved HOPG are, as expected, not found on the resultant surface. Moreover, the absence of hillock-like surface features was apparent after etching at this power. The image seen in figure 23(a) discloses a large cavity surface region almost 2500 Å in width and ~150 Å in depth. This type of surface characteristic was common for nearly all areas scanned on the sample surface.

(ii) 20 W:

An example of surface morphology similar to that found for 15 W plasma-processed surfaces is presented in figure 23(b). The r.m.s. roughness of the surface region in figure 23(a) is calculated to be 62 Å and is comparable to a value of 70 Å established for the surface area imaged in figure 23(b). Graphite samples, subject to 10 min of 20 W hydrogen plasma treatment, also exhibit topographies which seem to display surface features not too dissimilar to the hillock-like features observed during the argon RF plasma experiments. Figure 23(c) exhibits a large-scale STM image of a surface domain typical of a 20 W plasma-etched sample. Observed surface features are ellipsoidal in appearance and seem to be directional in nature. Figure 23(d) is a high resolution STM topograph of the central region of the surface domain imaged in figure 23(c).

The ellipsoidal features are essentially tightly packed throughout the surface except for the presence of pocket-like regions intermittently dispersed on the graphite plane. These pocket-like regions range in size from tens of Ångströms for the smallest to many hundreds of Ångströms for the largest. These features are comparable, in size and shape with those found during STM examination of samples exposed to 5 min of argon RF plasma processing at 20 W (figure 18(c)).

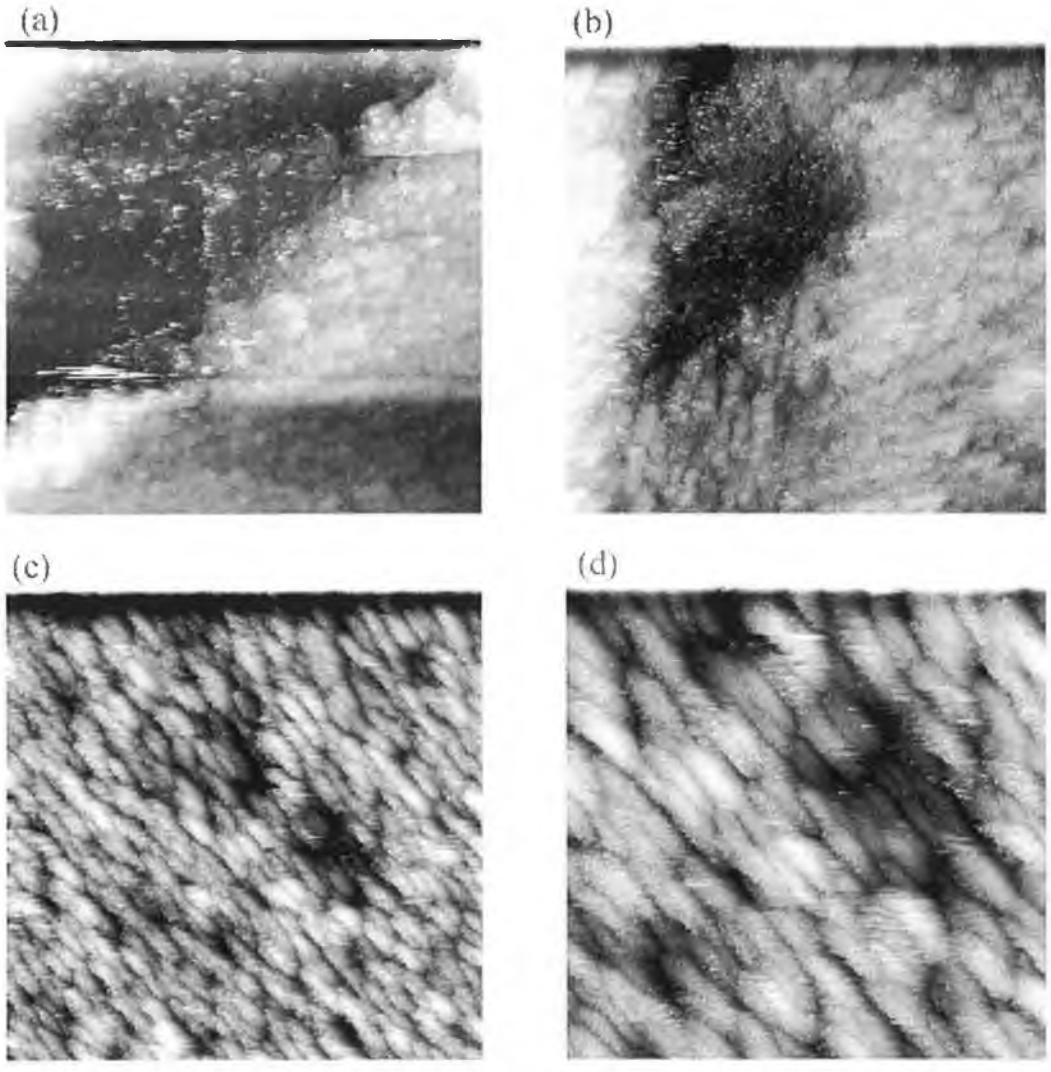

Figure 23: Topographic STM images of the surface of HOPG after hydrogen RF plasma treatment at various powers for 10 min revealing (a) a 15 W image (5000 Å x 5000 Å x 344 Å) with the noted absence of a hillock-like protrusion dominated topography; (b) a 20 W-etched sample (5000 Å x 5000 Å x 599 Å) image with surface structure similar to that seen at 15 W; (c) (7000 Å x 7000 Å x 254 Å); and (d) (3500 Å x 3500 Å x 293 Å) 20 W-etched surface images illustrating elliptical-shaped structural features.

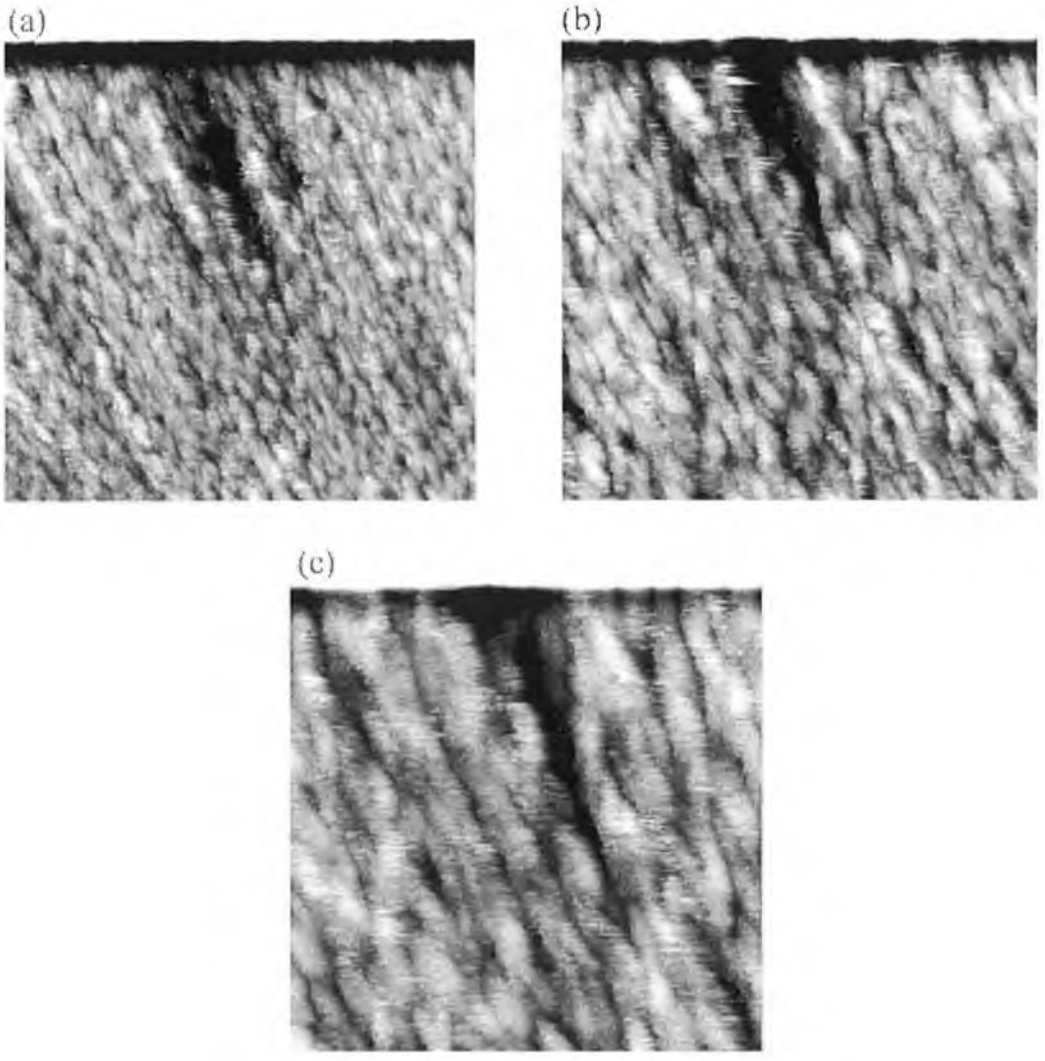

Figure 24: Topographic STM images of the surface of HOPG after hydrogen RF plasma treatment at 30 W for 10 min. (a) (8000 Å x 8000 Å x 353 Å); (b) (5000 Å x 5000 Å x 269 Å); and (c) (3000 Å x 3000 Å x 229 Å) images illustrating fully and clearly the narrow, elongated features and long narrow trenches inherent to these surfaces, quite different to 20 W-etched surfaces.

Almost half of all features measured on 20 W exposed surfaces are in the size range of 320–360 Å (figure 25). Feature sizes are again expressed as the square root of the product of the feature length in the short and long axis directions. In contrast to the semi-regular rounded protrusions observed on argon RF plasma-processed samples, those resulting from RIE in hydrogen are ellipsoidal in shape. Hence, the statistical measurements used for rounded features may not be totally applicable to such structures. Nevertheless, height distributions are relevant and are shown in figure 26.

Approximately 40% of all features measured are found in the narrow height range 80–100 Å, while ~ 45% are calculated to have heights in the range 30–80 Å.

(iii) 30 W:

The elliptical shape observed for features seen on surfaces exposed to 20 W hydrogen RF plasmas is no longer dominant on 30 W-etched surfaces, as shown in figure 24(a). Rather these surface structures are rather unresolved. A more detailed examination of the surface reveals the presence of narrow trenches running throughout the image. The left-hand side of the image illustrated in figure 24(a) illustrates several examples of this etch feature. The central area of the surface domain imaged in figure 24(a) is presented in figure 24(b). The surface morphology is more clearly illustrated. The narrow, elongated nature of the features apparent on the surface seem to diverge from the more ellipsoidal-like structures noticed on the surfaces of samples exposed to 20 W H_2 RF plasma. Figure 24(c) is a further magnification of 24(b). Ellipsoidal shaped features were also observed to a lesser degree on the surface of 30 W H_2 RF plasma-processed HOPG.

Figure 27(a) is an example of a typical STM image from a graphite surface exposed to a H_2 RF plasma at 40 W for 10 min. The characteristic cavern-like regions noticed on 30 W plasma-treated samples are also found during 40 W processing. The structures observed are of similar shape and size to those recorded for the previous power (30 W). Table 2 in section 4.1.2 provides us with some insight into hydrogen RF plasma parameter variation over the input power range employed. The ion-current along with both ion and electron densities show marked increases over the power range 10–50 W.

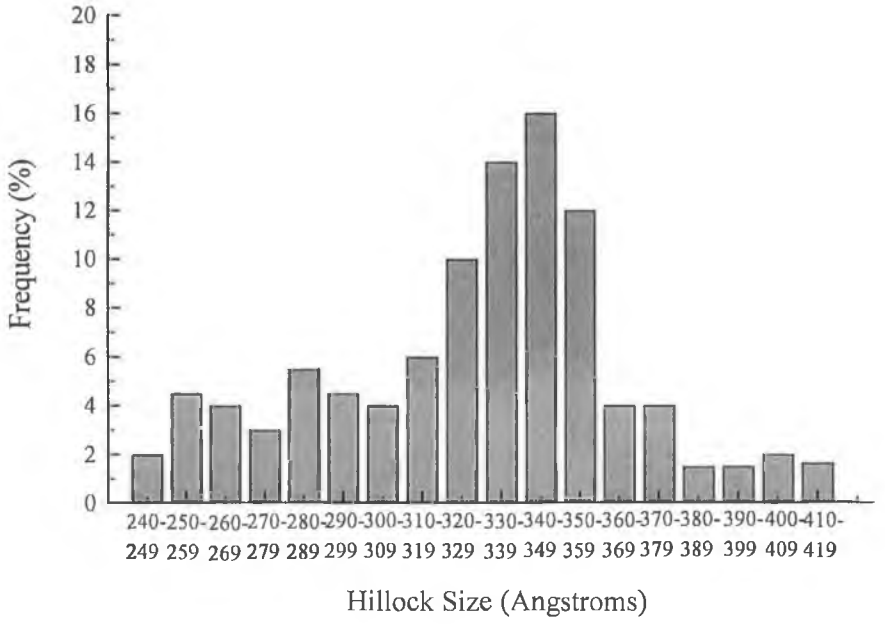

Figure 25: Measured % frequency size-distribution of surface features deduced from STM topographs. The data shown is an average of a number of HOPG samples reactive ion RF plasma etched in hydrogen at 20 W.

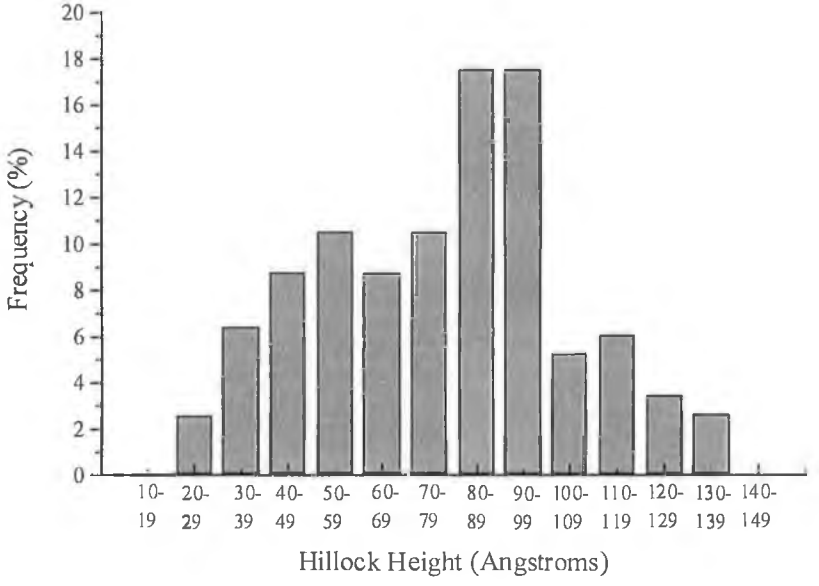

Figure 26: Measured % frequency height-distribution of surface features deduced from STM topographs. The data shown is an average of a number of HOPG samples reactive ion RF plasma etched in hydrogen at 20 W.

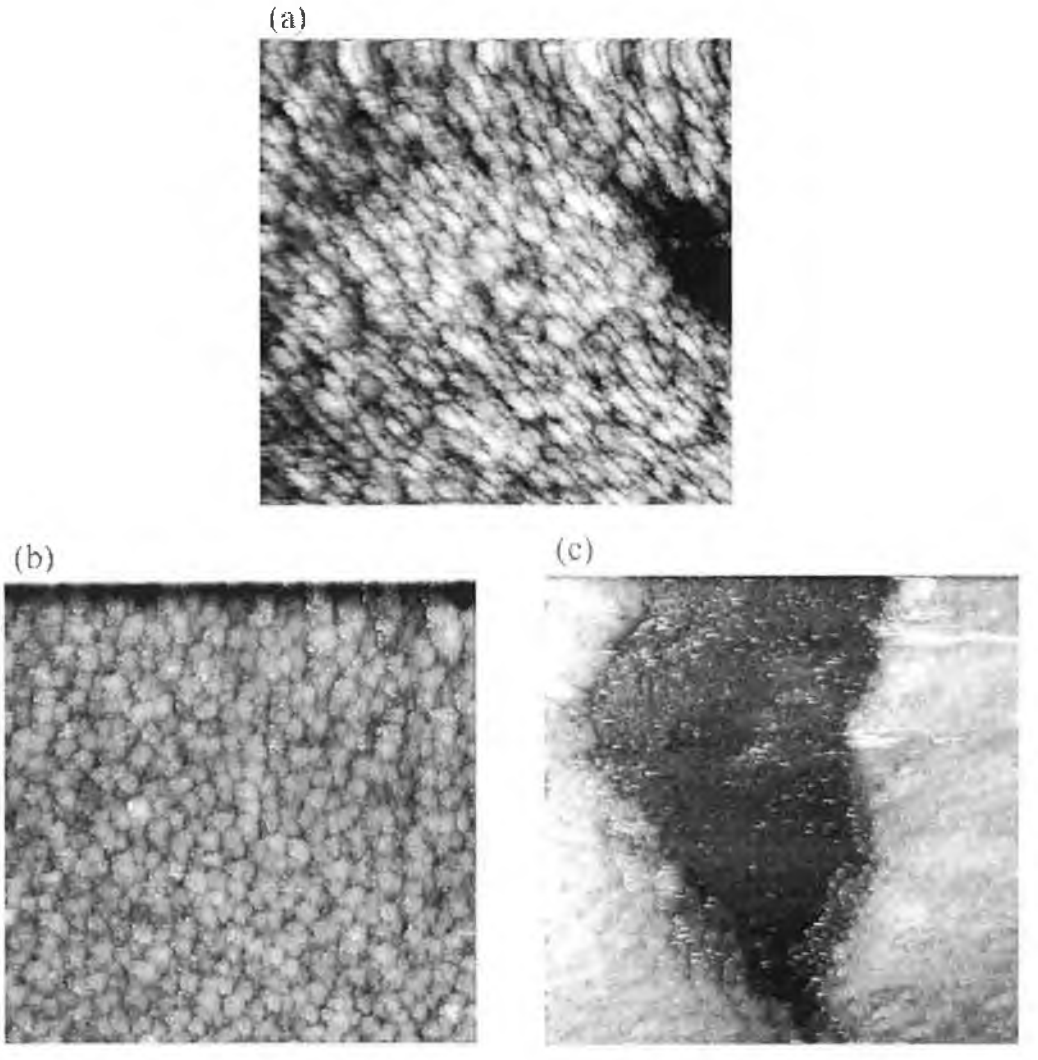

Figure 27: (a) Large scale STM image (10000 Å x 10000 Å x 313 Å) of 40 W plasma processed HOPG. (b) (4500 Å x 4500 Å x 330 Å) and (c) (4000 Å x 4000 Å x 322 Å) STM images after hydrogen RF plasma treatment at 15 W for 5 min illustrating fully the local structural variation evident after plasma processing.

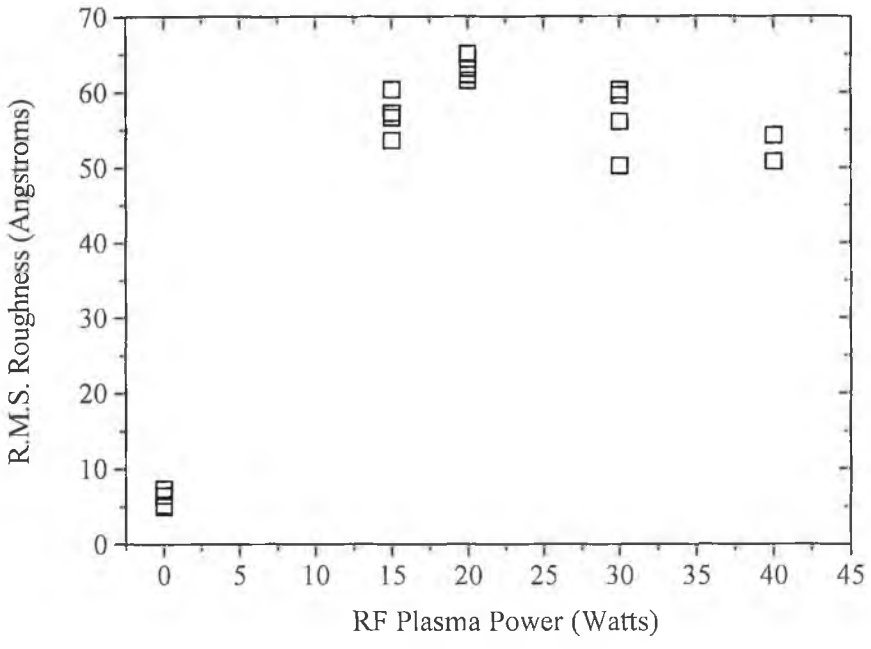

Figure 28: RF plasma power dependence of the r.m.s. roughness of hydrogen plasma-treated HOPG surfaces (etch duration = 10 min).

R.M.S. roughness calculations

Figure 28 is a plot of the calculated r.m.s. roughness of the hydrogen plasma-etched HOPG surfaces versus the RF plasma power levels used. Different roughness values for the same power correspond to r.m.s. data of several STM images from the same sample. From figure 28 and the STM images shown, it is clear that HOPG surfaces are more uniformly roughened at low RF plasma powers. This is in agreement with roughness values calculated for argon plasma-processed HOPG surfaces (see figure 21). There is an indication of a slight decrease in r.m.s. surface roughness with increasing plasma power. The exact opposite was noted for argon RF plasma etched surfaces, with roughness found to increase with increasing plasma power. This expected trend is clearly absent for reactive ion etching (RIE) experiments involving hydrogen. The increase in HOPG surface r.m.s. roughness witnessed for increasing RF plasma power during physical argon sputtering experiments is attributable to both increasing ion energies and densities bombarding the surface. The fact that this trend does not hold true for hydrogen implies that energetic ion bombardment may not be

the dominant process in the higher powered hydrogen discharges. A few proposed reasons for this will be discussed below.

Although physical sputtering maybe the most important consequence of an energetic ion-solid interaction, there are other phenomena which occur. It is not without probability that spatially very small, short-lived cascades of moving lattice atoms resulting from an ion-solid collision may promote chemical reactions which do not proceed at all or proceed very slowly under ambient conditions at the temperature of the surface. Often, the reaction, which is enhanced by energetic ion bombardment, involves reactive species from the gas phase. In the case of hydrogen RF plasma etching, the reaction rate of atomic hydrogen and other chemically reactive species at the surface is presumed to increase at higher plasma powers. H^0 production, predominantly through H_2^+/H_2 and H_3^+/H_2 collisions under the plasma conditions used here should be substantially enhanced at elevated plasma powers. The chemical erosion afforded by sub-eV H^0, producing C_2- and C_3- containing hydrocarbons [29], may in some way compete with the energetic ion bombardment process at elevated plasma powers.

4.2.5. Hydrogen RF plasma etched HOPG - time dependence

The hillock-like protrusions shown in the STM image illustrated in figure 27(b), were detected on a surface of HOPG RIE etched in a 15 W hydrogen RF plasma for 5 min. Surface features were found with lateral sizes between 100 and 220 Å with heights ranging from ~40 to 100 Å. A typical surface area observed on 5-min plasma-treated HOPG is recorded in figure 27(c) and matches the surface characteristics of samples (figure 23(a)) exposed to a longer etch time (10 min) at the same power (15 W).

It should be stressed that imaging problems were encountered during the examination of surfaces exposed to shorter etching times. Generally, the quality and reproducibility of the STM images obtained were found to be rather poor. This problem was also evident during the imaging of samples exposed to shorter etch times during the argon experiments (3–5 min).

R.M.S. roughness calculations

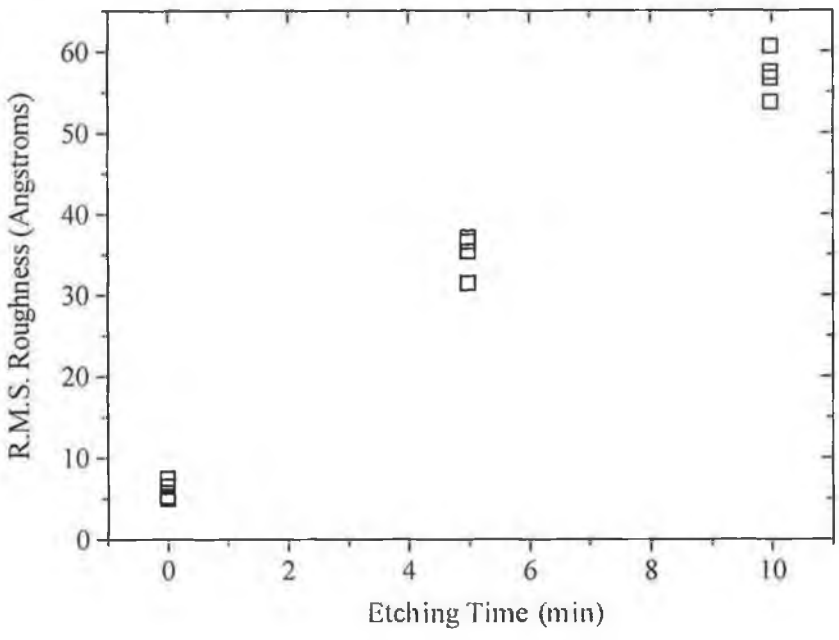

Figure 29: Etching time dependence of the r.m.s. roughness of 15 W plasma-processed HOPG.

In figure 29 a plot of the r.m.s. roughness obtained from STM topographs of 15 W plasma exposed HOPG samples versus etch duration is shown. It is evident that the r.m.s. roughness of hydrogen etched HOPG surfaces increases as a function of etching time.

Brighter spots or corrugation lines, usually found to lie parallel to either the x- or y-scanning direction, were sometimes observed in the recorded topographs, as can be seen in some of the STM images shown. These may be due to the STM tip picking up graphitic debris from the plasma processed HOPG surfaces.

4.2.6. XPS of hydrogen and argon plasma etched HOPG

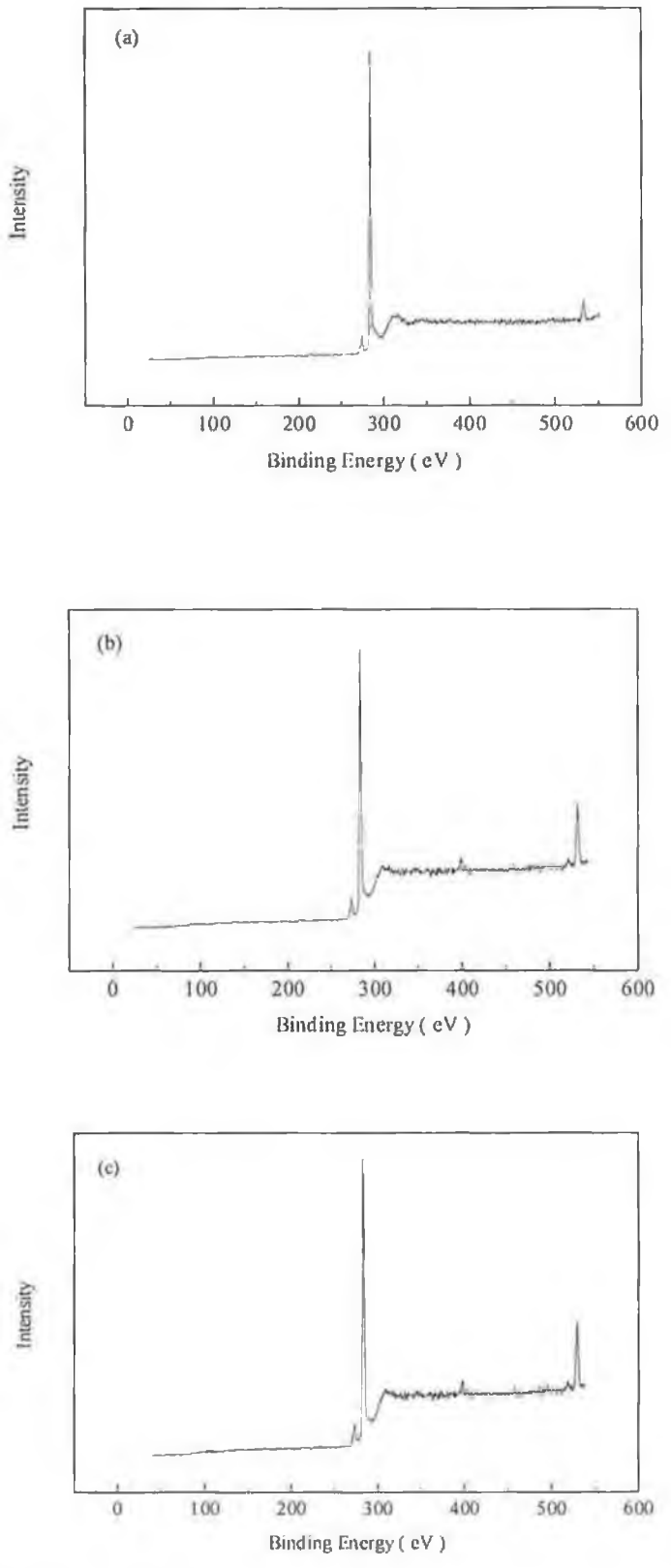

Figure 30: Survey scan spectra of (a) freshly cleaved HOPG; (b) hydrogen (40 W, 10 min) and (c) argon (25 W, 10 min) plasma treated HOPG.

The XPS examination of hydrogen and argon plasma-etched HOPG was carried out using a custom built combined XPS ultrahigh vacuum spectrometer equipped with a rapid insertion sample load lock and a VG CLAM (Combined Lens Analyser Module) 100 energy analyser with an unmonochromated Al Kα excitation source used for all spectra taken. An increase in the O 1s/C 1s ratio was recorded for all plasma treated samples when compared to that of freshly cleaved graphite. An oxygen signal is observed on freshly cleaved HOPG directly after insertion, probably due to physisorption of oxygen containing hydrocarbons in the rotary pumped load-lock system. Sample preparation protocol was the same for all samples transfer from the plasma chamber to the XPS chamber through the use of a nitrogen glove box. An increase in carbon-oxygen ratio has been reported for almost all plasma treated graphite studies to date [30,31].

Survey scan spectra of freshly cleaved, hydrogen and argon plasma treated HOPG are illustrated in figure 30 revealing the C 1s and O 1s core levels. The presence of a small peak at binding energy of ~ 400 eV seen for the etched samples is assigned to the N 1s core level, possibly resulting from a small air leak in the chamber allowing the introduction of small quantities of nitrogen into the plasma. Many common nitrogen functionality's give N 1s binding energies in the narrow region 399–401 eV. No annealing facilities were available in-situ, so oxygen contamination of freshly cleaved graphite is evident. The lack of any core levels indicative of metal contamination eliminates plasma-induced metal sputtering from the electrodes onto the HOPG samples.

A significant increase in the FWHM of the C 1s is observed upon hydrogen etching with additional intensity on the higher binding energy side of the peak (figure 31). This may be partially due to oxidation of the carbon surface after etching. Moreover, this increase may be indicative of a defected carbon surface and the presence of physically and chemically non-equivalent carbon due to its greater tendency to chemically bond upon crystalline break-up. The asymmetry in the C 1s peak observed at the high binding energy is consistent with the work of others [32,33,34]. It is possible that another contributory factor to C 1s broadening is the development of a sp^3 bonded component within the matrix contributing intensity at a different binding energy in the C 1s envelope. The difference in binding energy between sp^3 and sp^2 hybridised carbon is reported to be ~0.9 eV for diamond and graphite,

respectively [35]. The sp^3 component is shifted to higher binding energy. The presence of sp^3 and sp^2 components within the C 1s envelope of samples of diamond-like carbon have also been reported with subsequent deconvolution revealing a ~0.7 eV binding energy separation for these components [36].

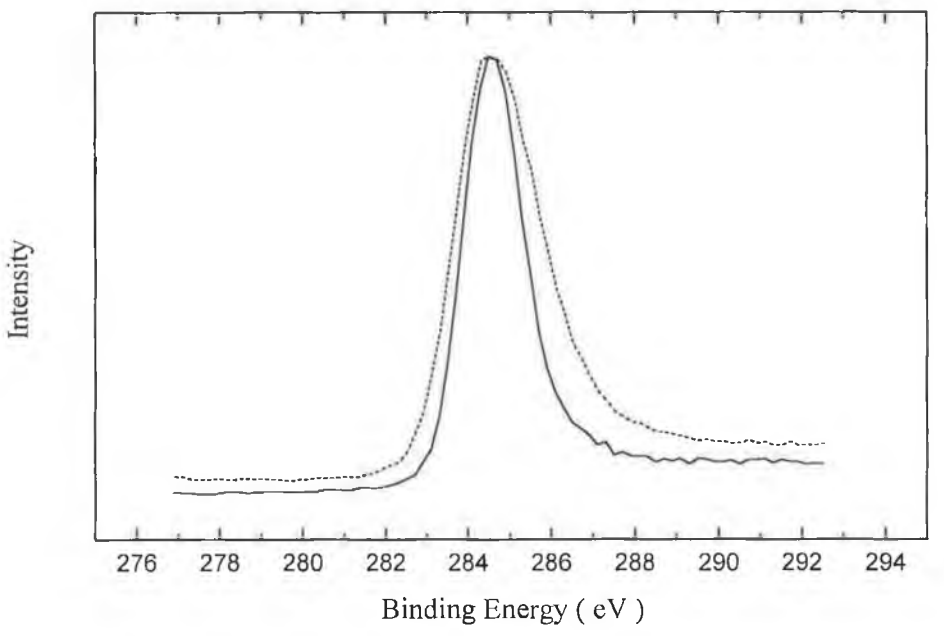

Figure 31: Al Kα C 1s spectra of hydrogen plasma etched (40 W, 10 min) HOPG (dotted line, FWHM = 2.7 eV) and freshly cleaved HOPG (solid line, FWHM = 1.8 eV).

In the case of hydrogen etched HOPG it should be emphasised that the broadened C 1s may also contain a component due to carbon–hydrogen bonding, resulting from exposure to various hydrogen species produced during etching. The binding energy of the C 1s core level for carbon particularly in a C–H bond is higher than a C–C bond [37]. The broadening of the C 1s peak on the high binding energy side might to some extent be attributable to C–H, $=CH_2$ and $-CH_3$ group formation, as well as carbon–oxygen species. Tong Lee et al [38], using HREELS, have confirmed the presence of $=CH_2$ and $-CH_3$ attributable to two deconvoluted components on the higher binding energy side of the C 1s peak after exposing diamond to atomic hydrogen (60,000 L). Graupner et al [39] propose that an additional feature resulting from moderate atomic hydrogen exposure may be attributable to a surface terminated

by residual C–H bonds. The charge transfer involved in C–H bonding effectively induces a chemical shift of 0.5 eV to higher energy on the C 1s binding energy [40]. Figure 31 reveals the characteristic broadening of the C 1s on the higher binding energy side. No attempt was made to deconvolute the C 1s spectra owing to the poor resolution of laboratory Al Kα sources combined with the complexity of species found in a hydrogen plasma allowing the formation of various carbon–hydrogen (along with oxidation) species on the surface of HOPG.

Interestingly, the FWHM and lineshape of the C 1s for both argon and hydrogen plasma processed HOPG is found to be similar. This contradicts the suggestion that the C 1s envelope broadening afforded after hydrogen plasma treatment is mainly a chemical effect. The actual reasoning for this is at the moment unclear although the oxidised carbon present for both samples results in broadening of the C 1s on the high binding energy side. Further high resolution XPS studies (e.g. at the RUSTI unit at Daresbury Laboratories using a monochromated small line width X-ray source) are required. In the case of no oxygen contamination, the broadening of the C 1s seen after argon plasma etching is purely a consequence of a highly defected carbon surface with the loss of crystalinity. The physical sputtering process possibly resulting in areas of sp^2 (graphite) and sp^3 (diamond) hybridised carbon along with argon atoms embedded in the carbon lattice. The work of Jackson et al [41] suggests that prior to ion bombardment, while graphite and diamond had very different bonding structures, afterwards, the XPS C 1s lineshapes were remarkably similar. Jackson et al tentatively hypothesise that ion bombardment may cause an equilibration of bonding types in the surface of carbon materials.

The $\pi \rightarrow \pi^*$ shake-up features of freshly cleaved and hydrogen plasma treated HOPG are shown in figure 32. The $\pi \rightarrow \pi^*$ transition is at ~6.5 eV higher binding energy than the C 1s peak maximum in graphite. The reduction in the π plasmon for hydrogen plasma etched HOPG is quite evident. Aromatic systems reveal shake-up satellites with intensities up to 5–10% of the primary peak. The intensity drop in the $\pi \rightarrow \pi^*$ transition may be a consequence of the development of sp^3 hybridised carbon. The absence of the π plasmon in the spectra of amorphous carbon films, despite the presence of sp^2 and π bonded electrons, has been reported [42]. One suggestion for this is the localisation of the π electronic charge induced by disorder which is applicable to our system. Disorder is proposed to affect the π plasmon intensity for

two reasons. Firstly, because the overlap of the p orbitals to form the π bonds is degraded compared to crystalline graphite. Secondly, the excited state has a shorter life than in graphite and hence the feature broadens in the spectra.

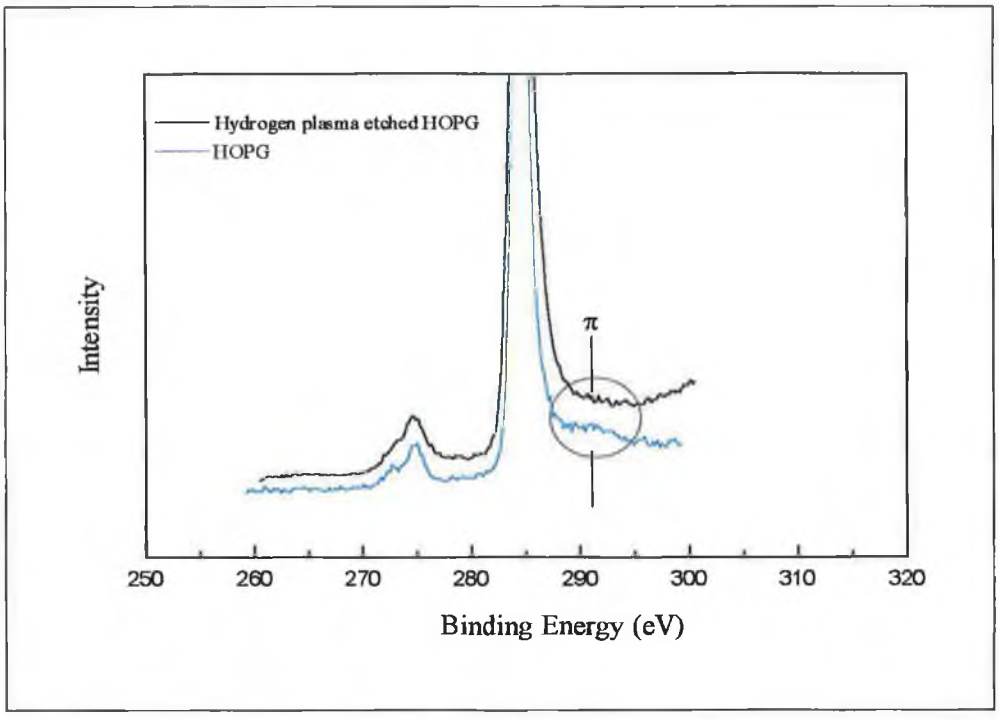

Figure 32: C 1s shake-up $\pi \rightarrow \pi^*$ satellite of hydrogen plasma etched graphite compared to that of freshly cleaved graphite.

To summarise, as expected plasma etching leads to a substantial broadening of the C 1s core level indicative of plasma induced disorder hence a range of carbon geometric and chemical environments (as determined by STM). Moreover, and most importantly no significant plasma induced sputtering from the etching chamber onto the sample surface occurs and hence the observed STM features represent true changes in the topography of HOPG.

5. Discussion

5.1. Plasma parameters

The measurement of plasma parameters was achieved through the use of cylindrical tuned Langmuir probe technology. The consistency of the measurements made demonstrate effectiveness and reliability. The results collected revealed trends which agreed with the work of others [19,20,21]. Compensating for sheath resistance allowed the accurate measurement of both electron temperature and plasma potential. Precise measurement of these parameters is not possible without taking this into account.

Tables 1 reveals marked increases in ion and electron densities, respectively, as the applied discharge power is increased at a set pressure in the argon discharge. Increased ion and electron densities were also observed for measurements made in hydrogen plasma (table 2). This is consistent with an increased ionisation rate as more energy is being fed into the plasma. The observed differences between electron and ion densities is consistent with other work carried out on similar processing systems. It is commonly believed that electron and ion density values taken for a given set of discharge parameters should be considered tentatively and too much weight should not be placed on the difference in absolute values. It is of interest to note, however, that theoretically modelled plasmas appear to have larger positive ion densities for electronegative gases than for electropositive gases partly as a result of the low mobility of the negative ions present in the former gases.

You et al [28] have reported RF plasma parameters using langmuir probe technology for a capacitively coupled argon RF discharge at a pressure of 20 mTorr. For a 5 W plasma, ion and electron densities were 0.52×10^9 cm^{-3} and 0.41×10^9 cm^{-3}, respectively, comparable to values of 0.76×10^9 cm^{-3} and 0.43×10^9 cm^{-3} measured for our system. Increasing the power to 25 W reveals an expected increase in both values. A four-fold increase in both ion and electron densities was reported by You et al while we observe densities of almost seven times that seen at 5 W. This is expected as a result of the higher argon pressure used during these experiments (75 mTorr). You et al also measured the maximum energy of argon ions. These were found to be ~95 eV and ~290 eV for 5 and 25 W plasmas, respectively.

The diagnostics of etching systems using a number of different gases has received much interest over the last few years [11,15,43]. The data obtained in such studies has illustrated the usefulness of Langmuir probe technology in the characterisation of plasmas used in etching processes. It is clear that such data may be used to check on the day-to-day reproducibility of the operation of the processing system employed and as a means of achieving etching process parameter optimisation. It is important to note that it is not our purpose to present an extensive and detailed diagnostic profile of the etching chamber for a wide range of plasma conditions, but to confirm the tuned probe as a reliable and useful plasma diagnostic tool.

5.2. Argon RF plasma etched HOPG surfaces

From STM topographs of argon RF plasma etched HOPG, it is clear that the cleaved surface of HOPG increases in roughness with increasing input power at a fixed etch duration. The hillock-like features become progressively higher while valleys between them become progressively deeper. Furthermore, the lateral sizes of the surface features also increase with increasing power.

The number of argon ions (N_A), which bombard the graphite surface during etching, is defined as:

$$N_A = \frac{I}{e}$$

where I is the current density, and $e = 1.602 \times 10^{-19}$ C is the electron charge. Table 1 (section 4.1.1) reveals ion-current densities (I) for the plasma powers employed during etching. It is recognised that I increases linearly with increasing power from 0.04–0.14 mA cm^{-2}, as the input power is increased from 5 to 25 W. It follows that N_A (ion flux to the sample surface) will also increase with increasing power. This accounts for the increased surface roughness recorded at higher plasma powers.

The argon RF plasma etching of HOPG is basically a physical phenomenon. Sputtering theory [44] predicts that the sputter yield is inversely proportional to the binding energy of surface atoms to the lattice. At defect sites on the graphite surface the binding energy of carbon atoms to the lattice decreases thus increasing the

sputtering yield, possibly producing the cavern-like regions highly evident on the surface of argon RF plasma etched HOPG.

The atomic scale phenomena affording surface etching in graphite include C–C bond breakage quoted at ~ 480 kJ mol^{-1} (4.93 eV), sputter removal of carbon atoms from the lattice, argon implantation into the graphite lattice, impurity permeation i.e. argon ion or neutral implantation (the threshold energy required for the first layer penetration of graphite is 10 eV), and graphite lattice break-up believed to occur at ~ 28 eV [26]. Particles emitted as a consequence of physical sputtering are desorbed within at most 10^{-11} s of ion impact and have a cascade-type energy distribution. The distribution is described as follows:

$$N(E) = 2UE/(E+U)^3$$

where E is the energy of the sputtered particle and U is its binding energy to the surface. When E is large compared to U, $N(E)$ decreases as $1/E^2$. The maximum in this distribution occurs when $E = 0.5U$. Hence, the binding energy of the sputtered particle to the surface can be estimated from the position of the maximum in the energy distribution.

In argon plasma-treatment of HOPG, plasma surface interactions are dominated by energetic positive ion bombardment. It is felt that although electrons and photons can influence surface processes [45,46,47], their energy and/or flux in the plasma environment is such that their contributions to plasma-surface interactions is quite insignificant. You et al [28] suggest that at higher powers of argon RF plasma etching, electron energies are sufficiently high to cause C–C bond breakage. These electrons referred to as "fast electrons" are contemplated as a contributor to increased damage at higher powers. You et al hypothesise that UV-visible photons may also have a contributory affect to the etching process at higher powers. During our argon experiments the average electron temperature (kT_e) was seen to fall as the plasma input power was increased as expected for an increased rate of electron collision at higher powers. Moreover, it is suggested that ions as opposed to electrons are the major players in creating surface damage.

The hillock-like features observed on argon plasma-treated HOPG are suggested resultant of a "collision cascade" - induced when an ion collides with a solid surface,

the collision between quasi-independent particles causing a cascade of moving target atoms. Consequences of the collision cascade include sputtering, radiation-enhanced diffusion, backscattering of the incident ion, ion-induced chemical reactions, production of lattice damage, etc. The initial collision involves an energetic ion (or atom) and a stationary (neglecting thermal energy) target atom. Subsequent collisions may involve moving atoms colliding with stationary atoms or alternatively the collision of moving atoms with each other. Porte et al [48] propose that the perturbation and raising of the area surrounding ion impact (hillock formation) is a direct consequence of the "collision cascade". The interplanar stresses afforded by this damage may also assist the process of hillock formation.

The sputtering yield of carbon by argon is essentially low. The yield is only 0.15 atoms/ion for 600 eV Ar^+ [49]. Donnelly et al [50] propose that the expansion and delamination of the graphite layers occurs, as opposed to the sputter removal of the surface atoms when exposed to energetic helium ion fluxes (10 keV, $\mathbf{Q} = 10^{17}$ ions cm^{-2}). The implantation of ions into graphite may lead to the formation of small bubbles (agglomerates of vacancies) increasing the volume (swelling) of the system [51,52,53]. The build up of lateral stress due to implantation may lead to the deformation of the irradiated material. The ability of an unconfined system like graphite to deform through the swelling and "wrinkling" of its weakly bound basal planes may, coupled with the bond breakage afforded by impacting ions, produce the hillock-like structure dominated topography seen on STM images of argon plasma etched graphite surfaces. The sputter removal of carbon from the surface of graphite is also likely to be a contributing factor.

Molecular dynamic simulations have been applied to investigate the sputtering of carbon atoms from a perfect graphite crystal. The study of phenomena such as the reflection of particles at low energies, the displacement energy thresholds for atoms in the graphite lattice and also bump formation on the surface of ion-bombarded graphite are all possible using such simulations [54,55].

STM results for single impact events on graphite show that low doses of impacting particles cause bumps on the surface of graphite for a wide energy range from a few hundred electronvolts to several kiloelectronvolts [56]. Molecular dynamics can illustrate the mechanism by which the bumps form and follow their dynamical evolution, which experiment cannot. At energies of 100 eV and normal incidence all the impacting atoms either adsorb at the surface or implant. The majority end up as

interstitials trapped between the first and the second layers. Upward momentum is imparted to the surface layer after impact while the second layer experiences downward momentum. Real-time studies have shown that after 0.04 ps the surface layer shows two bumps which seem to coalesce and overlap. The smaller bump occurs near the point at which the bombarding particle passes through the layer, the larger bump sits over the displaced primary knock-on carbon atom. The initial impact also produces what is described as a surface wave which has been found to be hexagonal in nature reflecting the structure of the crystal lattice. STM results have shown that both the height and breath of the bumps are all but independent of ion beam species and energy over the range 0.5–3.0 keV. The distribution of bump heights, resultant of single ion collisions, is 1–5 Å. Lateral sizes are approximately 60 Å.

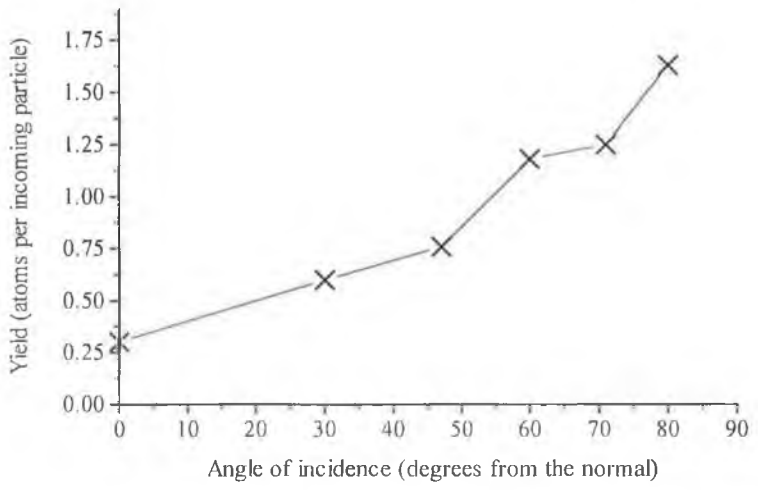

Figure 33: Experimental data revealing the ejection yield of carbon as a function of incidence angle for an ion bombardment energy of 1 keV [58].

At lower energies (<100 eV), calculations show that a large number of incident atoms reflect from the surface. For example at an energy of 25 eV, the backscattering percentage yield varies is ~25%. Graphite has a high binding energy and this is reflected in the calculated ejection yield upon incident ion bombardment, which is low. Surprisingly, it is suggested that no ejection occurs until the energy of the bombarding ion reaches 600 eV. Figure 33 reveals experimental atom ejection

yields as a function of incident angle for a bombarding ion energy of 1 keV [57]. After a certain length of time ion irradiation sputtering yields may increase and occur at lower energies as the breaking of bonds and the creation of defects destroys the rigid crystalline nature of the graphite surface. Essentially, the decrease in cohesive forces will increase the ejection probability. It has been proposed [58] that the dominant mechanism for ejection of carbon atoms from graphite for normal incidence bombardment involves an initial collision between the incoming projectile and a surface atom. This atom is subsequently guided into the second layer by its first layer neighbours. It is finally ejected after collision with a second layer atom. For incident energies of up to 1 keV the energy distribution of ejected particles is approximated in the range of 2–30 eV. For oblique angle incidences a substantial increase in ejection yield (figure 5.33) is reported [58]. The reasons for such a marked increase are unclear.

The damage of a perfect crystal by ion bombardment is initiated by the sudden transfer of a large amount of energy to a single atom within the crystal. This happens when a collision occurs between the incident ion and the primary knock-on atom (PKA). An important quantity is the minimum kinetic energy that must be transferred to the PKA to produce a permanent displacement of an atom within the crystal. Atoms in graphite occupy two distinct sites, those having carbon neighbours directly above and below (AA stacked atoms) and those with hexagon centres above and below (AB atoms). Values of 34.0 eV for AA permanent displacement and 34.5 eV for AB stacking atom displacement have been proposed [56]. Structures resulting from permanent displacements depend on whether the initial velocity is in plane or out-of-plane. An initial velocity with an out of plane component usually produces an interstitial atom that bridges two graphite layers causing the layers to move apart.

In attempting to elucidate the actual processes resulting in the formation of the hillock-like protrusions evident on the surfaces of plasma processed HOPG, we have only one avenue to follow i.e. the variation in hillock appearance and size with plasma parameter variation. Having discussed the surface possibilities upon energetic particle bombardment we find that three processes dominate. These are carbon bond breakage, carbon atom ejection and argon implantation. The formation of the hillock-like protrusions seems to proceed through the following path i.e. initial

basal plane break-up followed by bond-broken carbon atom ejection. The raising of areas of the surface as the result of "collision cascades" may also play a role.

The increasing height of the features for increasing power suggests that physical sputtering of carbon is the dominant process. Moreover, the increase in hillock lateral size and height with increasing power must be directly related to the plasma parameter changes at the higher powers i.e. the increasing degree of ionisation at higher powers, increasing ion and electron densities. Correspondingly, the ion energy, and in turn the flux density of ions per unit area (ion current) striking the HOPG surface also rise. Thus, the etching rate is increased resulting in the decreased number of rounded protrusions in a defined scanning area (a smoothing effect) as evidenced by STM for the higher power plasma etched samples. The increase in height of the protrusions with increasing power as seen for the higher powered etched samples is not so easily explained if smoothing of the surface dominates at higher powers. In fact the opposite would be expected, that is the decrease in protrusion height with increasing plasma power. This phenomenon is as of yet unexplained.

Of importance to the stabilisation of cluster catalysts on the surface of plasma treated HOPG are the small pocket-like regions found between the individual hillock-like features. Figures 11(a) and (b) emphasise that for 5 W treated samples the size of these regions is at a minimum, while their frequency throughout the surface is at a maximum. As the plasma processing power is raised beyond this (15 and 25 W) the size and depth of these regions increase with increasing hillock size. As expected their frequency on the surface subsequently decreases.

Precious metal catalysts are generally most efficient for metal cluster sizes of between 50 and 500 Ångströms. The nucleation of clusters in this size range may be best afforded on graphite surfaces processed at lower plasma powers (~5 W). The nucleation centres (regions between hillock-like protrusions) for cluster growth, found on the surface of 5 W samples are generally no more than a few nanometres in both breadth and depth.

5.3. Hydrogen RF plasma etched HOPG surfaces

The interaction of hydrogen with surfaces of various carbon and carbon based materials has been widely investigated. Common to all these studies is the observation that molecular hydrogen does not chemically interact with these surfaces. In view of the purely covalent nature of all these substrates this is not unexpected. In order to establish hydrogen–surface bonds hydrogen atoms must be supplied. Three techniques are generally used to supply hydrogen atoms to the surface: hydrogen plasmas, effusion sources, and heated filaments. Only with effusion sources can the flux of H atoms at the surface be determined with reasonable precision.

The simple scheme of H bound to C atoms in the three hybridisation states sp, sp^2, and sp^3, observed in organic molecules, is therefore a good working hypothesis to view H bonding to C based surfaces.

Pan and Yang [59] observed with transmission electron microscopy (TEM) that monolayer deep etch pits were formed at the interaction of hydrogen at the basal plane of natural single crystal graphite at 1800 K. These etch pits had a hexagonal shape and the pit boundaries had zigzag rather than armchair edges, as illustrated in figure 34. The etching was presumed to start at defect sites on the basal plane. When the edges of the graphite basal plane (0001) are exposed, two different sites exist at the plane edges, i.e. the {1011} zig-zag sites and {1121} armchair like sites. The open triangular structure of the zig-zag site reveals two unsaturated B sites on the open side and one saturated A site at the closed apex, whereas the armchair site has two unsaturated B sites at the open corners and two inner-corner saturated type A sites, of an open trapezoidal unit. Stein and Brown [60] using structure-resonance theory on large benzenoid polyaromatic molecules with different edge structures found that molecules with zig-zag edges are more reactive than those with armchair edges. By applying first-order perturbation theory to the Hückel molecular orbitals they estimated electron localisation energies (δE_π). These are the energies required to isolate a π-electron from the rest of the conjugated system for polyaromatic molecules of different sizes and edge structures. It was found that molecules with zig-zag edges are more reactive in comparison to those with armchair edges. Chen and Yang [61] used this theory to calculate the chemisorption energy of H at these

different graphite planes. They obtained adsorption energies of 3.1 and 3.8 eV at armchair and zigzag faces, respectively. Adsorption at the basal plane was found to be endothermic irrespective of the assumed adsorption geometry.

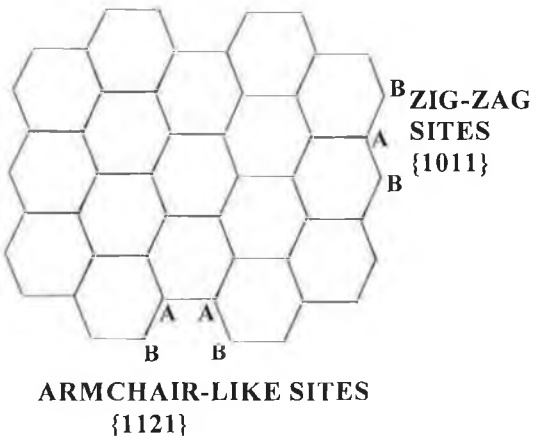

Figure 34: A schematic illustration of the active sites at the edges of the graphite basal plane (0001) [27].

The use of carbon and carbon-based materials as plasma-facing components in magnetic confinement fusion reactors has led to a great surge of interest into the understanding of processes involved in the interactions between hydrogen plasma species and carbon.

Hydrogen reactive ion etching is dominated by two processes. On one hand atomic hydrogen, produced through the electronic impact dissociation of H_2 and also through H_2^+/H_2 and H_3^+/H_2 collisions, is essentially the main chemically reactive species in hydrogen plasma. On the other hand, we must consider the effect of the ion species in hydrogen plasma such as H^+, H_2^+ and H_3^+. As the contribution of electronic dissociative ionisation is weak (requiring 29 eV electron impact) under the RF plasma conditions employed during this experiment, H^+ ions are mainly created by direct ionisation of H atoms. On the other hand H_2^+ ions are created by electron impact ionisation of H_2 molecules. Low energy H_2^+ ions (less than 10 eV) are efficiently converted into H_3^+ by non-resonant charge exchange collisions between H_2^+ and H_2. As the H_2^+ ion energy increases, the conversion becomes less effective.

The densities of the three types of ions are strongly coupled together and depend on both the magnitude of the field and the gas concentration.

The transfer of the various reactive species (H, H_3^+, H_2^+, H^+) to the substrate surface leads to their neutralisation through the following reactions:

$$(1)\ H^+ + e^- \rightarrow H_{(g)} + h\nu$$

$$(2)\ H_2^+ + e^- \rightarrow 2H_{(g)}$$

$$(3)\ H_3^+ + e^- \rightarrow 3H_{(g)}$$

Under the RF plasma conditions used during these experiments the most energetic hydrogen ions produced are expected to have energies of no more than a few hundred eV. Interestingly, it is predicated that for 50 eV ions, the erosion yield of graphite at room temperature is dominated by chemical etching rather than physical sputtering [62].

Atomic hydrogen present in hydrogen plasma is known to produce hydrocarbons upon reaction with graphite [30]. However, the detailed formation mechanism remains unclear. Early proposed mechanisms assumed the formation to occur through the interaction of carbon atoms with hydrogen atoms back-diffusing during surface implantation [63]. Carbon has been shown to trap hydrogen atoms effectively until lattice saturation is established at about 0.4 H/C [64,65], methane formation evolves only at a fluence higher than the saturation fluence [66]. Impinging hydrogen ions of less than 100 eV afforded methane formation even at room temperature [62]. Calculations of the preferred adsorption sites of hydrogen on single graphite planes [67], suggest that hydrogen atoms are adsorbed alternating on top of and below the carbon atoms, leading to tetrahedral bonding. Consequently, the formation of methane molecules, or precursors like CH_3 radicals, from such a saturated layer structure can easily be envisaged, if during implantation, carbon–carbon bonds are broken and saturated with additional hydrogen atoms.

Moreover, the microstructure of the graphite surface will determine its chemical reaction rate with atomic hydrogen. Defected graphite regions will probably yield the highest rates, with the extent of surface defects produced strongly dependent on incident ion energies and fluences. Hydrogen atoms produced via electron impact dissociation of molecules:

$$e^- + H_2 \rightarrow e^- + H + H,$$

are termed 'hot' atoms with energies of about 3.5 eV, while atoms produced via the well-known reaction $H_2^+ + H_2 \rightarrow H_3^+ + H$, have a mean energy of 0.7 eV. The dominant atomic hydrogen formation mechanism will therefore decide the extent of atomic hydrogen surface reaction. It is already known that for sub-eV atomic hydrogen, the chemical erosion of graphite affords mainly C_2- and C_3- containing hydrocarbons [29,68].

When bombarded with energetic hydrogen ions at room temperature there is an indication of a strong chemical bond between implanted hydrogen and carbon atoms at radiation damage sites in the graphite lattice. The radiation damage sites, including bond angle disorder, acetylenic bonds and, carbon Frenkel defects (interstitial carbon bond formation leaving a vacant lattice site), are formed by energetic ion bombardment with ions that can transfer a minimum energy of 25 eV to displace a carbon atom from the lattice [69]. Moreover, hydrogen maybe trapped in the lattice in the form of C–H bonds and C_2–H bridge bonds [70].

We have already discussed the saturation level of carbon with incident hydrogen ions (0.4 H/C), and the formation of hydrocarbons after this hydrogen saturation level has been reached. The co-deposition of sputtered carbon with incident hydrogen ions must also be considered. This layer is believed to consist of sputtered carbon ionised in the plasma edge and redeposited along with H^+ ions [71]. The extent to which this codeposited layer is formed on HOPG surfaces exposed to the hydrogen etching conditions used during our RF experiments is difficult to estimate. Presumably, the carbon sputtering rate from the graphite surface is the determining factor. It should also be mentioned that the difficulty encountered during the STM imaging of hydrogen plasma processed surfaces as well as the general reduction in image quality when compared to argon imaged surfaces, may in some part be due to the formation of this insulating hydrocarbon layer.

The extent of the physical radiation damage of graphite afforded through energetic ion bombardment will influence the formation of the near surface saturated layer. An enhanced saturation rate of the surface with hydrogen in the form of C–H bonds and C_2–H bridge bonds is achieved with increased surface radiation damage [72].

The activation energy necessary for hydrocarbon formation is readily obtainable at higher incident ion energies found for the higher plasma powers. An increased rate of hydrocarbon formation is therefore expected. Thus, an enhanced chemical etching rate is predicted for the higher plasma powers. The impacting distance (implantation zone) of impinging ions will determine the extent of hydrocarbon formation, subsequently, diffusing through pores or damage sites back to the surface. It is not too improbable to suggest that the long trench-like features illustrated in figures 24(a)–(c) after 30 W plasma processing may be due, in part, to the splitting of the upper graphitic layers as a consequence of hydrocarbon pressure build up in the lower surface layers.

The possible reduction of surface roughness seen at the higher plasma powers as well as the less defined nature of the ellipsoidal-shaped topographical features at these powers, evident in figures 24(a)–(c), are proposed resultant of the synergistic effects of the physical ion bombardment of high energy hydrogen ions and the reactions of chemically reactive hydrogen atoms. The degree of ionisation in hydrogen plasma, which increases at higher plasma powers and low pressures, is also of importance.

Physical surface damage accounts for the similarities in the surface features observed for argon and hydrogen plasma etched HOPG samples with concomitant chemical etching processes involved in hydrogen plasma. The relative contribution of the physical and chemical properties of hydrogen RF plasma etching to the resultant surface topography is dependant on the precise circumstances of the etching regime used, i.e. on the plasma parameters of the chosen running conditions.

Physical sputtering essentially involves ions striking the surface at normal incidence while chemical etching is a much more isotropic random process. As discussed, the anisotropic structure of graphite affords a higher rate of etching in the prismatic plane (reactive) orientation than in the basal plane (non-reactive) orientation. It is subsequently expected that the chemical erosion of surface features plays an important part in hydrogen RF plasma etching, with a somewhat smoother appearance to the surface of the oval-like and intertwined features seen on hydrogen plasma processed surfaces.

In attempting to relate argon (physical etching) and hydrogen (reactive ion etching) plasma processes, it is obvious that the mechanistic and parameter complexity is much greater in RIE relative to physical etching. The coupling of energetic ion

bombardment and the reaction of reactive atoms and radicals with the surface to form volatile compounds highlights the complexity of RIE.

As is apparent from this study, there is a large degree of empiricism to the development of plasma processes. The area of surface modification is no exception. There are many examples of situations in which a surface is exposed to a glow discharge and a change is noted in some macroscopic property with little or no understanding of the microscopic details. Hydrogen plasmas seem to be used in this way more frequently than discharges of other gases, and often the term [plasma annealing] is used to describe the process. Some of the physical characteristics influenced by plasma treatments include wettability of fabrics [73], chemical reactivity of metals [74], and nucleation characteristics [75].

6. Conclusions

Scanning tunnelling microscopy has been used to investigate the plasma-induced changes to the topography of HOPG. The RF plasma processing of HOPG with both argon (physical etching) and hydrogen (reactive ion etching) has been investigated. The presence of hillock-like surface features was noted for both etching gases in agreement with molecular dynamics studies of ion bombarded graphite surfaces [55,56,57]. A hillock-dominated (semi-regular rounded features) surface morphology is indicative of energetic ion bombardment as recorded for the physical bombarding argon experiments. In the plasma power range examined (5–25 W), the size of the generated surface features increased in size as the power increased. Time dependent studies revealed more diverse surface features with those witnessed at the lowest etch times showing a linear structure.

The presence of more ellipsoidal shaped features was observed for surfaces exposed to hydrogen RF plasma etching supposedly attributable to the synergistic effects of hydrogen ion bombardment and atomic hydrogen reactions. The topography of hydrogen RF plasma etched HOPG surfaces seems to be more strongly dependent on the plasma parameters chosen. Hydrogen plasma experiments at higher plasma powers reveal the intertwinement and elongation of surface features with a rather smoother appearance to the surface, possibly attributable to the dominance of chemical processes at these powers. The appearance of narrow trenches, extending for thousands of Ångströms, was characteristic of sample surfaces etched at these higher powers. Further investigative studies are necessary to fully explain the varying surface topographies between the different powers for hydrogen etched HOPG.

XPS examination reveals no impurity contamination of the plasma treated surfaces. The increase in the C 1s peak widths (FWHM) of etched HOPG samples is indicative of the loss of crystalline perfection of the surface and in the case of hydrogen plasma processed samples may suggest the formation of a hydrocarbon surface layer (oxygen contamination is also a contributing factor to increased C 1s peak widths). Further high resolution XPS studies are required to examine whether sp^3 hybridised (diamond-like) carbon is produced upon etching.

References

[1] Panel on Plasma Processing of Materials, National Research Council: Plasma Processing of Materials Scientific Opportunities and Technological Challenges, National Academy Press, Washington, DC, (1991).

[2] J. M. Wadehra, Appl. Phys. Lett., 35 (1979) 917.

[3] J. R. Hiskes, A. M. Karo, M. Bacal, A. M. Bruneteau and W. G. Graham, J. Appl. Phys., 53 (1982) 3469.

[4] G. C. Strutzin, Ph.D. Thesis, Spectroscopic Measurement of H(1s) and H_2(v",j") in an H^- Ion Source Plasma, Lawerence Berkeley Laboratory, University of California, (1990).

[5] B. Chapman, Glow Discharge Processes, Wiley, New York, (1980).

[6] J. V. Scanlan, Ph.D. Thesis, Dublin City University, (1991).

[7] C. Bowick, RF Circuit Design, Howard Sams and Co., Indiana, USA, (1982).

[8] V. A. Godyak, R. B. Piejak and B. M. Alexandrovich, Plasma Sources Sci. Technol., 1 (1992) 36.

[9] M. B. Hopkins and W. G. Graham, Rev. Sci. Instrum., 57 (1986) 2210.

[10] K. F. Al-Assadi, P. A. Chatterton and J. A. Rees, Vacuum, 38 (1988) 633.

[11] F. F. Chen, Plasma Physics and Controlled Fusion, Plenum Press, New York, (1980).

[12] J. V. Scanlan and M. B. Hopkins, J. Vac. Sci. Technol. A, 10 (1992) 1207.

[13] M. B. Hopkins, C. A. Anderson and W. G. Graham, Europhys. Lett., 8 (1989) 141.

[14] B. M. Annaratone and N. St. J. Braithwaite, Meas. Sci. Technol., 2 (1991) 795.

[15] P. A. Chatterton, J. A. Rees, W. L. Wu and K. F. Al-Assadi, Vacuum, 42 (1991) 489.

[16] G. Binnig and H. Rohrer, Helv. Phys. Acta, 55 (1982) 726.

[17] G. Binnig and D. P. E. Smith, Rev. Sci. Instrum., 57 (1986) 1688.

[18] G. Binnig and D. P. E. Smith, Rev. Sci. Instrum., 57 (1986) 2630.

[19] G. Oelerich-Hill, I. Pukropski and M. Kujawaka, J. Phys. D, 24 (1991) 593.

[20] A. P. Paranjpe, J. P. McVittie and S. A. Self, J. Appl. Phys., 67 (1990) 6718.

[21] D. Fang and R. K. Marcus, Spectrochim. Acta B, 45 (1990) 1053.

[22] B. Coonan, Ph.D. Thesis, Dublin City University, (1995).

[23] M. Kuwabara, D. R. Clarke and D. A. Smith, Appl. Phys. Lett., 56 (1990) 2396.

[24] J. E. Buckley, J. L. Wragg, H. W. White, A. Bruckdorfer and D. L. Worcester, J. Vac. Sci. Technol. B, 9 (1991) 1079.

[25] C. Liu, H. Chang, and A. J. Bard, Langmuir, 7 (1991) 1138.

[26] G. H. Knichin and R. S. Pease, Rep. Prog. Phys., 18 (1955) 1.

[27] H-X. You, N. M. D. Brown and K. F. Al-Assadi, Surf. Sci., 284 (1993) 263.

[28] H-X. You, N. M. D. Brown and K. F. Al-Assadi, Surf. Sci., 279 (1992) 189.

[29] E. Vietzke, K. Flaskamp, V. Philipps, G. Esser, P. Wienhold and J. Winter, J. Nucl. Mater., 145–147 (1987) 443.

[30] H-X. You, N. M. D. Brown, K. F. Al-Assadi and B. J. Meenan, J. Mater. Sci., Lett., 12 (1993) 201.

[31] F. Tuinstra and J. L. Koenig, J. Chem. Phys., 53 (1970) 1126.

[32] S. Lin, Carbon, 31 (1993) 509.

[33] D. Ugolini, J. Eitle and P. Oelhafen, Appl. Phys. A, 54 (1992) 57.

[34] H. Estrade-Scwarckopf and B. Rousseau, J. Phys. Chem. Solids, 53 (1992) 419.

[35] Y. Mizokawa, T. Miyasato, S. Nakamura, K. M. Geib and C. W. Wilmsen, J. Vac. Sci. Technol. A, 5 (1987) 2809.

[36] J. C. Lascovich and S. Scaglione, Appl. Surf. Sci., 78 (1994) 17.

[37] T. R. Anthony, Mater. Res. Soc. Symp. Proc., 162 (1990) 61.

[38] S. Tong Lee and G. Apai, Phys. Rev. B, 48 (1993) 2684.

[39] R. Graupner, J. Ristein and L. Ley, Surf. Sci., 320 (1994) 201.

[40] B. B. Pate, M. H. Hecht, C. Binns, I. Lindau and W.E. Spicer, J. Vac. Sci. Technol., 21 (1982) 364.

[41] S. T. Jackson and R. G. Nuzzo, Appl. Surf. Sci., 90 (1995) 195.

[42] J. Díaz, G. Paolicelli, S. Ferrer and F. Comin, Phys. Rev. B, 54 (1996) 8064.

[43] K. F. Al-Assadi, N. M. D. Brown, P. A. Chatterton and J. A. Rees, Vacuum, 42 (1991) 1009.

[44] P. Sigmund, Phys. Rev., 184 (1969) 383.

[45] F. A. Houle, Chem. Phys. Lett., 95 (1983) 5.

[46] T. J. Chuang, Surf. Sci. Rep., 3 (1984) 1.

[47] J. W. Coburn and H. F. Winters, J. Vac. Sci. Technol., 16 (1979) 391.

[48] L. Porte, C. H. De Villeneuve and M. Phaner, J. Vac. Sci. Technol. B, 9 (1991) 1064.

[49] L. Holland, J. Vac. Sci. Technol., 14 (1977) 5.

[50] S. E. Donnelly, W. S. Brooks, V. Vishnyakov, E. Meyer, A. Connell, C. Pearson, R. Stockmann and R. Valizadeh, J. Vac. Sci. Technol. B, 11 (1993) 141.

[51] S. E. Donnelly and J. H. Evans (Eds.), Fundamental Aspects of Inert Gases in Solids, Plenum, New York, (1991).

[52] M. Miyake, W. Saiki, T. Daimon, P. Son, C. Miyake and H. Ohya-Nishiguchi, J. Nucl. Mater., 187 (1992) 138.

[53] T. Tanabe and K. Niwase, Bull. Jpn. Inst. Met., 30 (1991) 122.

[54] H. Bergsaker, F. Lama, R. Smith and R. P. Webb, Vacuum, 44 (1993) 341.

[55] R. Smith and R. P. Webb, Nucl. Instrum. Meth. B, 59/60 (1991) 1378.

[56] R. Smith and K. Beardmore, Thin Solid Films, 272 (1996) 255.

[57] J. Roth, J. Bohdansky and W. Ottenberger, J. Nucl. Mater., 165 (1989) 193.

[58] R. Smith, Proc. R. Soc. Lond. A, 431 (1990) 143.

[59] Z. J. Pan and R. T. Yang, J. Catal., 123 (1990) 206.

[60] S. E. Stein and R. L Brown, Carbon, 23 (1985) 105.

[61] J. P. Chen and R. T. Yang, Surf. Sci., 216 (1989) 481.

[62] J. Roth and J. Bohdansky, Nucl. Instrum. Methods Phys. Res. B, 23 (1987) 549.

[63] N. P. Busharov, E. A. Gorbatov, V. M. Gusev, M. I. Guseva and Y. Martenenko, J. Nucl. Mater., 63 (1976) 230.

[64] G. Staudenmaier, J. Roth, R. Behrisch, J. Bohdansky, W. Eckstein, T. Staib, S. Matteson and S. K. Erents, J. Nucl. Mater., 84 (1979) 149.

[65] B. L. Doyle, W. R. Wampler, D. K. Brice and S. T. Picraux, J. Nucl. Mater., 93/94 (1980) 551.

[66] C. M. Braganza, S. K. Erents and G. M. McCracken, J. Nucl. Mater., 76/77 (1978) 220.

[67] R. Dovesci, C. Pisani, F. Ricca and C. Roetti, Surf. Sci., 72 (1978) 140.

[68] J. W. Davis, A. A. Haasz and P. C. Strangeby, J. Nucl. Mater., 155–157 (1988) 234.

[69] L. T. Chadderton, Radiation Damage in Crystals, Methuen, London, (1965) p. 19.

[70] V. Kh. Alimov, A. E. Goderetsky and A. P. Zakaharov, J. Nucl. Mater., 186 (1991) 27.

[71] R. A. Causey, J. Nucl. Mater., 162–164 (1989) 15.

[72] K. Sone and G. M. McCracken, J. Nucl. Mater., 111/112 (1982) 600.

[73] T. L. Ward, H. Z. Jung, O. Hinojosa and R. R. Benerito, Surf. Sci., 76 (1978) 257.

[74] D. F. Klemperer and D. J. Williams, Vacuum, 33 (1983) 301.

[75] C. J. Robinson, Thin Solid Films, 57 (1979) 285.